U.S./JAERI Collaborative Program on Fusion Neutronics

Phase IIA and IIB Fusion Integral Experiments, The U.S. Analysis

December 1989

Fusion Nuclear Technology
Mechanical, Aerospace & Nuclear Engineering Dept
University of California Los Angeles
Los Angeles, CA USA

Japan Atomic Energy Research Institute
Tokai, Ibaraki, Japan

U.S./JAERI Collaborative Program on Fusion Neutronics, Phase IIA and IIB Fusion Integral Experiments, The U.S. Analysis

Mahmoud Z. Youssef
Mohamed A. Abdou
Yoichi Watanabe*
Peter M. Song

Mechanical, Aerospace, and Nuclear Engineering Department
University of California at Los Angeles

December, 1989

---

*Current address: Innovative Nuclear Space Power Institute,
College of Engineering
University of Florida, Gainesville, FL 32611

ABSTRACT

The U.S./JAERI Collaborative Program on Fusion Neutronics is in progress using the FNS facility at JAERI. Integral experiments are performed on a test assembly (Li_2O) that has the engineering features of a fusion blanket (e.g. First Wall, neutron multiplier) and the results are compared to the analytical predictions performed by various transport codes and nuclear data. The objective is to derive information on the uncertainties involved in key design parameters, such as tritium production rate, nuclear heating, radioactivity build-up, and afterheat, and to identify the sources of these uncertainties and means to reduce them. In addition to the usefulness of considering these uncertainties by blanket designers, the program aims at examining the impact of the selection of various configurations to maximize the blanket performance (e.g. TBR) and evaluating the prediction uncertainties in each configuration.

Phase I experiments (open geometry) were performed and analyzed and the results can be found elsewhere. Phase II (A, B, and C) experiments (closed geometry) have been completed and independently analyzed by the U.S. and JAERI using their own codes and data. In these two phases, emphasis was placed on measuring tritium production rate, foil activation reaction rates, and neutron spectrum by various measuring techniques. This report documents the U.S. analysis for Phase IIA and IIB. The counterpart reports of JAERI's analysis and experiments are published separately. Activities on Phase IIC experiments (beryllium multi-layer and coolant channels effect) will be published in the near future.

ACKNOWLEDGEMENTS

The authors wish to thank Dr. A. Kumar for his valuable remarks regarding the experiments and analysis for Phase IIA and IIB. The early work of Mr. C. Gung on Phase IIA is greatly appreciated. Special thanks to Ms. Bobi O'Neill for typing and assembling this report. The U.S. contributions to the Joint Collaborative Program is supported by the United States Department of Energy, Office of Fusion Energy, under contract No. DE-FG03-86ER52123.

Table of Contents:

List of Tables:

List of Figures:

I. Introduction

I.1. Scope

The prediction accuracy of tritium breeding in a fusion blanket is a prime design issue since a slight uncertainty in tritium breeding inside those breeders that have marginal tritium breeding capability could lead to failure in achieving tritium self-sufficiency, a costly penalty that requires reliance on an external tritium supply. For that purpose, an Integral Experiments Program[1] has been initiated between the U.S. and JAERI to evaluate the overall uncertainties involved in breeding tritium inside a Li_2O test assembly. Several experiments have been conducted at the Fusion Neutron Source (FNS) facility at the Japanese Atomic Energy Research Institute (JAERI) with the objective of verifying the potential for tritium breeding in a simulated fusion blanket that has engineering features (e.g., first wall, multiplier) and making comparisons between analytical predictions and measurements to arrive at estimates for the uncertainties associated with tritium breeding as well as other neutronics parameters. The results obtained from this Program will provide a data base for selection of materials, blanket configuration, and advancing the neutronics technology required for the next experimental device, such as FER, ITER[2], etc.

Phase I experiments and their associated analyses have been completed and joint reports and papers have been issued[3 - 5]. This report discusses the analysis performed by the U.S. for Phase II experiments while the JAERI's analysis for that phase can be found in Refs. (6 - 7). Several Papers were also published on the present work on Phase II and can be found in Refs. (8-14).

The test assembly used in Phase I proceeded from a simple one (single material: Li_2O) of a pseudo-cylindral shape (D ~ 60 cm, L ~ 60 cm.) to an assembly that included the engineering features of a fusion blanket (e.g. simulated coolant channel and first wall, neutron multiplier, etc.). The test assembly was placed in a cavity impeded in the concrete wall of 4.96m x 4.96 m x 4.5 m room where the D-T neutron source was placed at its center. In this Phase, focus was placed on tritium production rate (TPR) measurements [TPR From $^6Li(T_6)$ and from $^7Li(T_7)$] at selected locations inside the test assembly in addition to in-system spectra measurements and several foil activation measurements. The source was characterized by NE213 spectrum and Time-of-Flight (TOF) measurements. However, due to the complexity involved in modeling the large room and the rotating neutron target (RNT), the prediction for the reflected component (room-returned component) of the incident neutron source involved large uncertainties and hence large

uncertainties in the prediction of parameters that depend on low-energy neutrons such as T_6 and $^{197}Au(n,\gamma)$ reactions.

The configurations for Phase II experiments have been carefully selected (through pre-analysis) such that better simulation to the incident neutron source found in fusion reactors has been achieved. A description of the configurations and the experiments for that phase is given below.

I.2. Brief Description of Phase II Experiments and Measured Parameters

Phase II experiment consists of three classes of experiments, namely; Phase IIA, Phase IIB, and Phase IIC experiments. The experiments and the associated analysis for the latter phase will be issued separately. (That focuses on the effect of heterogeneity and multi-layered Be/Li_2O configuration on TPR and other parameters, including nuclear heating and activation.) In this report, the U.S. Analyses for Phases IIA and IIB are given.

In Phase IIA a rectangular test assembly of dimensions 86.4 cm x 86.4 cm x 60.71 cm is placed at one end of a rectangular enclosure made of Li_2CO_3 and the D-T neutron source is placed inside the cavity at a distance of ~ 78 cm from the square front surface of the test assembly, as shown in Fig. I-1. The dimensions of the inner cavity are 87 cm x 87 cm x 124 cm and the thickness of the Li_2CO_3 enclosure is 20.5 cm. A 5 cm thick polyethylene layer (PE) was included at the outer surface of the enclosure in order to eliminate the low-energy, room returned component of the neutrons reflected by the room walls and re-entering the test zone. Two (central and off-central) drawers were installed throughout the axial direction of the test assembly where measurements were performed. In addition, two radial drawers were also installed at Z=12.4 cm (front drawer) and at Z=42.76 cm (back drawer) from the front surface of the assembly as shown in Fig. I.1.

Three experiments were performed in Phase IIA. The first is the reference (REF) experiment where only Li_2O material constituted the test assembly. In the second experiment, the first five centimeters at the front were replaced by beryllium (Beryllium front, BEF system). In the third experiment, a 5 cm-thick beryllium layer was sandwiched between a 5 cm-thick Li_2O front layer and the rest of the Li_2O test zone (Beryllium Sandwiched, BES system). The configurations for these experiments of Phase IIA are shown in Figure I.2.

In Phase IIA, the TPR from ^6Li (T_6) and ^7Li(T_7) were measured by various methods (Li-glass detectors, Li-metal detectors, Li_2O pellet detectors) along the axial and

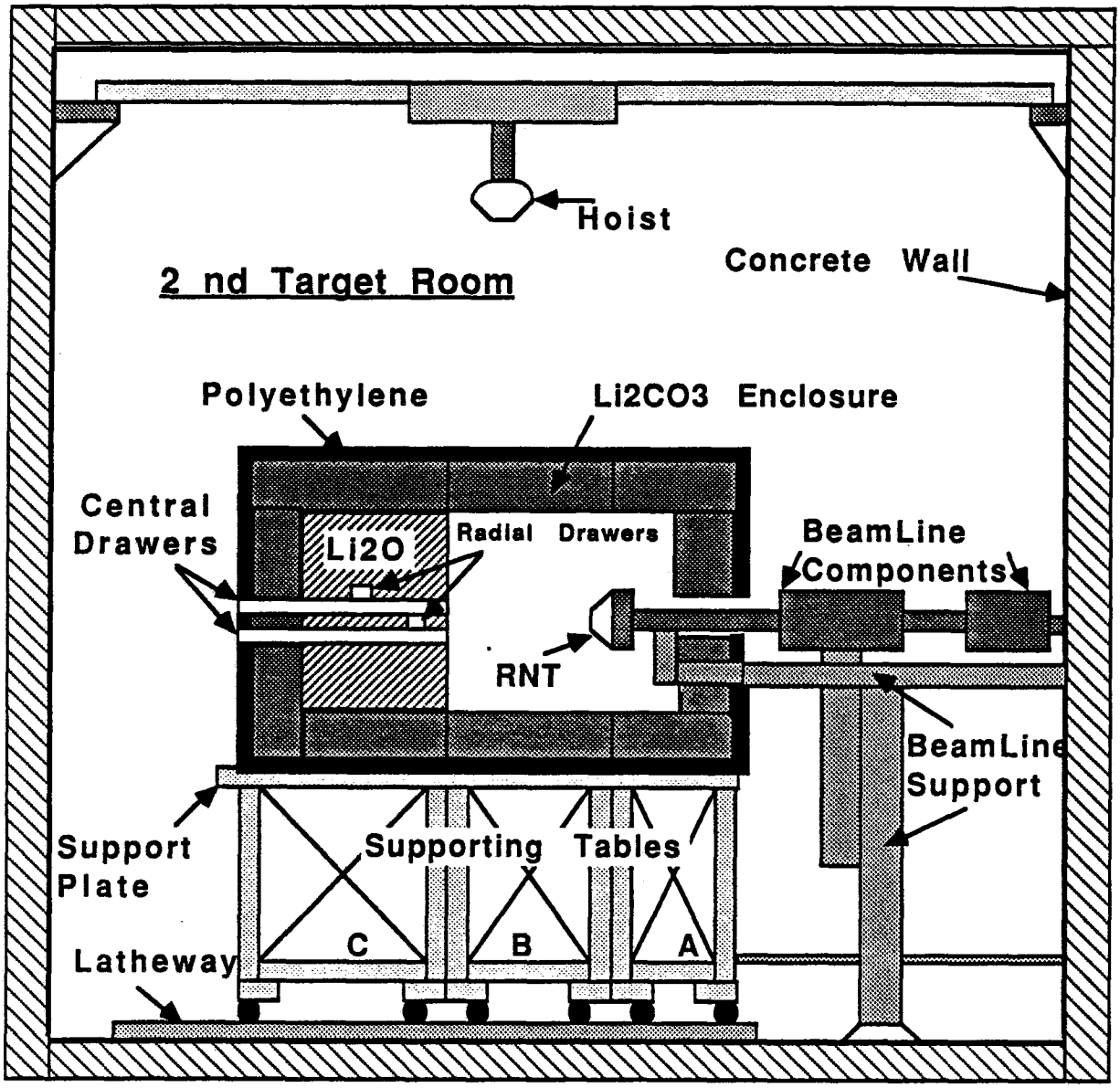

Fig. I.1: The Geometrical Arrangement for Phase II Experiments

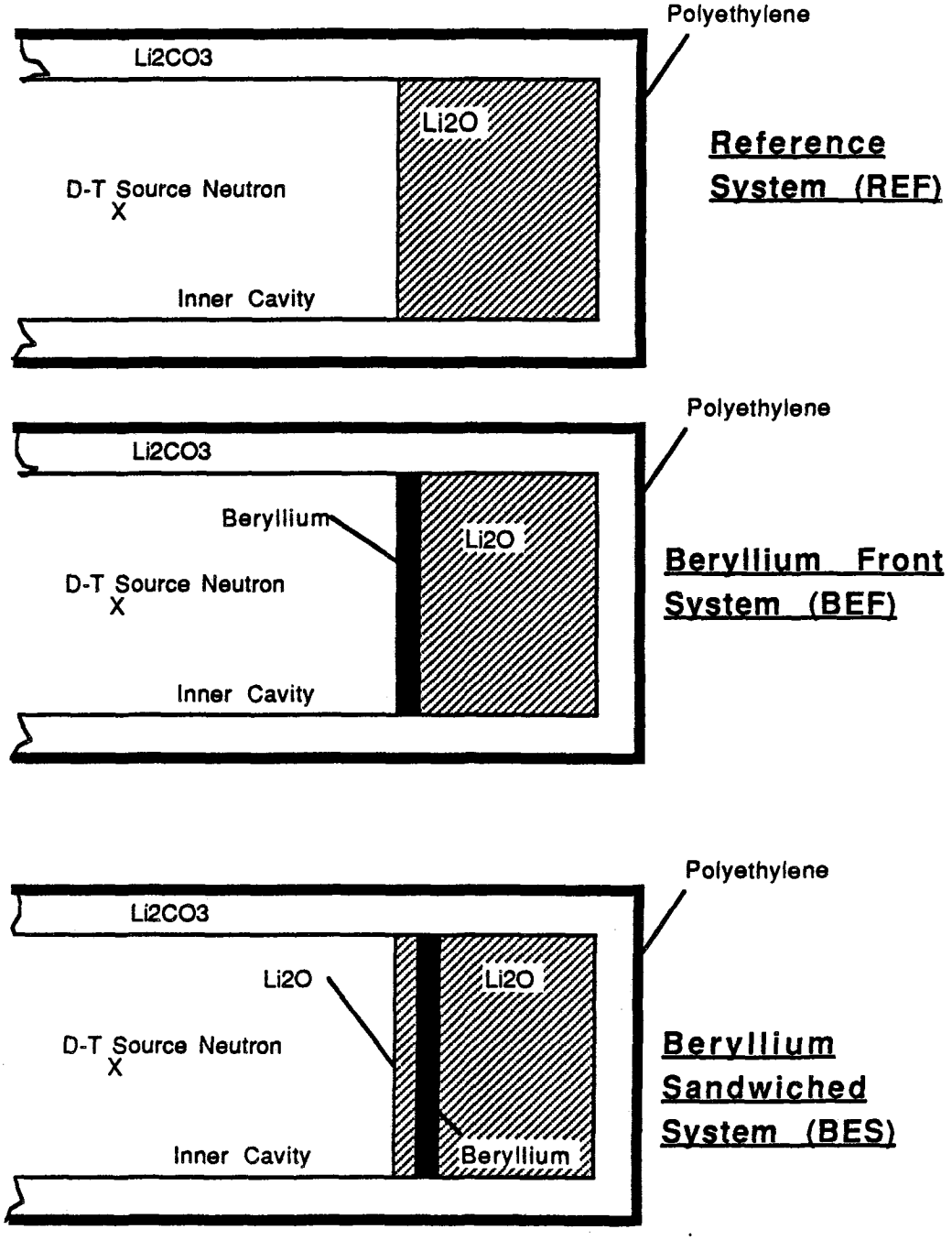

Fig. I.2: Geometrical Arrangement for Phase IIA Experiments

radial drawers. The T_7 was also measured by folding the spectrum measured by NE213 spectometer with the response $^{7}Li(n,n,\alpha)t$ cross section (NE213 indirect method). The in-system spectrum measurements were performed by using small spherical NE213 in the energy range E_n>1 MeV and by using a small size proton recoil counter (PRC) in the energy range 1 Kev < E_n < 1 MeV. Foil activation measurements along the axial drawers were performed in the REF and the BES systems which included the reactions $^{58}Ni(n,2n)$, $^{58}Ni(n,p)$, $^{27}Al(n,\alpha)$, $^{93}Nb(n,2n)^{92m}Nb$, $^{197}Au(n,2n)$, $^{115}In(n,n')^{115m}In$, and $^{197}Au(n,\gamma)$. Since the cross-sections for these reactions have different threshold energy and energy dependence, comparisons between measurements and calculations provide useful information on the neutronics characteristics inside the Li_2O assembly. Zonal TPR from natural lithium (T_N), ^{7}Li and ^{6}Li were also measured in several designated zones along the central drawer (5.08 cm x 5.08 cm x 60 cm) in the REF and BES systems. The experimentally-evaluated integrated TPR along the central drawer was then compared to the calculated values (indicative of tritium breeding ratio, TBR). In addition to performing the above-mentioned in-system measurements, the nuclear field inside the cavity, at the inner surface of the Li_2CO_3 enclosure, and at the front surface of the Li_2O assembly has been characterized by carrying out spectrum and foil activation measurements that included the reaction rate $^{58}Ni(n,2n)$, $^{58}Ni(n,p)$, $^{93}Nb(n,2n)$, $^{27}Al(n,\alpha)$, $^{197}Au(n,2n)$, and $^{197}Au(n,\gamma)$. These source characterization measurements were necessary to perform prior to Phase II experiments in order to estimate the uncertainties in predicting the incident neutron source to the Li_2O assembly.

The experiments performed in Phase IIB are similar to those of Phase IIA except that the inner surface of the Li_2CO_3 enclosure was covered by a 5 cm-thick beryllium layer in addition to a 0.5 cm-thick SUS-304 first wall as shown in Fig I.3. Three experiments were performed. The reference experiment (no Be layer in front of the Li_2O test zone), the beryllium front experiment (a 5 cm-thick Be layer preceeding the Li_2O assembly) without a first wall (BEFWOFW) and the beryllium front experiment with a first wall (BEFWFW) of a thickness of 0.5 cm.

The objective of these experiments was to study the impact of including a Be liner (similar to the Be-tiles on the inboard shield of fusion reactors) on the breeding performance of the Li_2O assembly. The massive amount of beryllium utilized in Phase IIB enabled us to examine the accuracy of beryllium neutron cross-sections and the consequent impact on tritium breeding enhancement due to neutron multiplication in beryllium through the $^{9}Be(n,2n)$ reactions. The TPR from ^{6}Li in this phase was measured by the Li-glass on-line

method while T_7 was measured by the NE213 indirect method. The T_6 and T_7 local values were also measured by the Li-metal and Li_2O-pellet detectors in the Be-front with FW experiment in addition to the in-system spectrum measurements by the NE213 and PRC. Foil activation measurements were also performed in that phase to determine the incident neutron spectrum.

Phase IIC experiments are aimed at examining the heterogeneity effect (multilayers of Be and inclusion of several coolant channels inside the test zone) on the TPR and heating rates profiles. Activities on that Phase will be reported separately.

Table I.1 summarizes the measured parameters in Phase IIA and IIB experiments for which the calculations were performed and compared. Details of the calculations performed by the U.S. can be found in the next Sections.

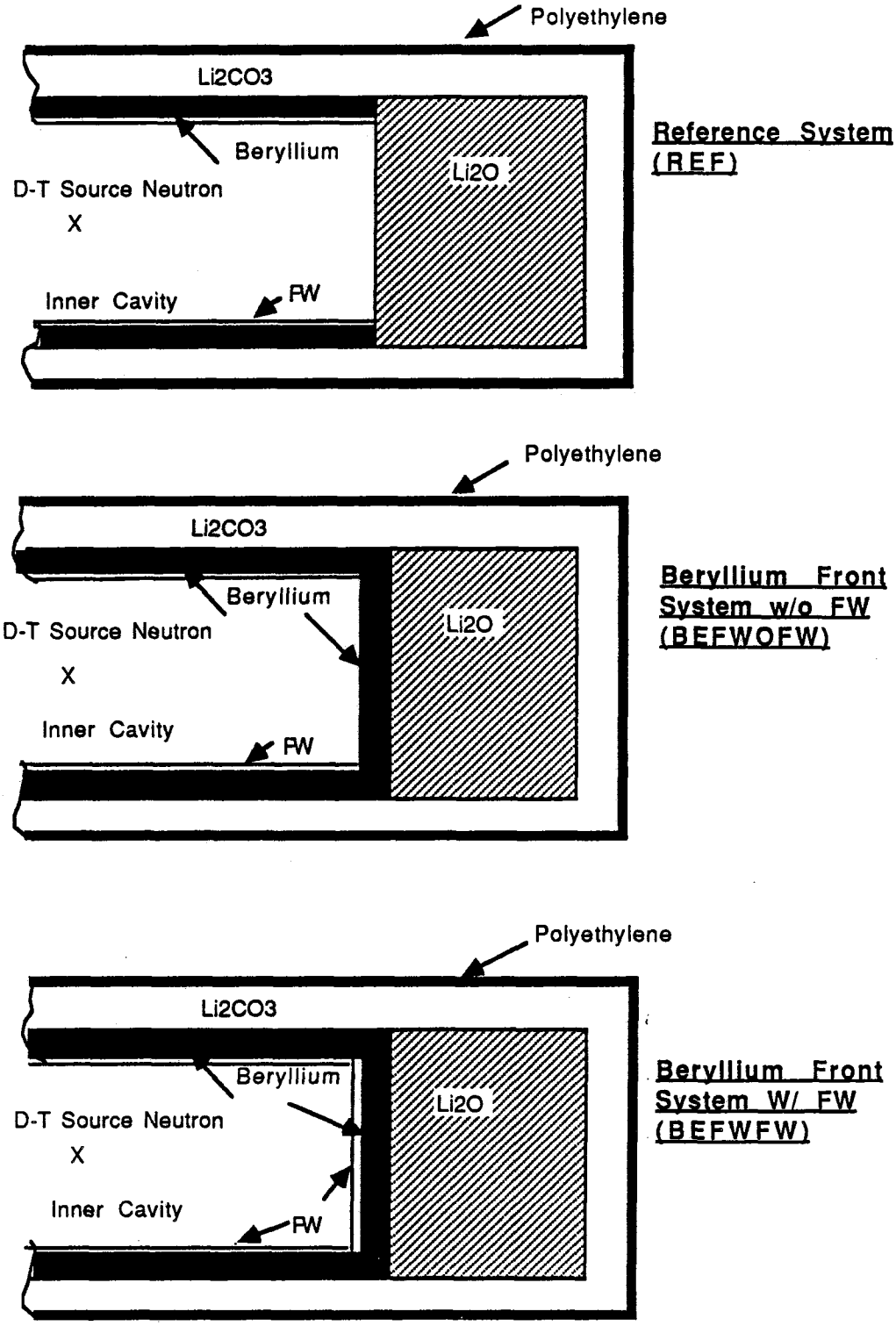

Fig. I.3: Geometrical Arrangement for Phase IIB Experiments

Table I.1: Measured Parameters in Phase IIA and IIB for which calculations were performed.

Parameter	Phase IIA			Phase IIB		
REF	BEF	BES	REF	BEFWOFW		BEFWFW
Source Characterization						
NE213	X	--	--	--	--	X
PRC	--	--	--	--	--	X
foil activation	X	--	--	--	--	X
Tritium Production Rate						
NE213 (for T_7)	X*	X*	X*	X	X	X
Li-glass (for T_6)	X*	X*	X*	X	X	X
Li-metal (for T_6 &T_7)	X	X	X	--	--	X
Zonal TPR (for Tn,T_7)	X	--	X	--	--	X+
Li_2O pellets	--	--	X	--	--	X+
In-system foil activation	X*	--	X*	--	--	X
In-system spectrum						
NE213	X*	X*	X*	X	X	X
PRC	X	X	X	--	--	X

*measurements performed in the radial and axial drawers.
+Experimental data not processed

II. Analytical Methods, Nuclear Data, and Calculational Model

II.1. Transport Codes

The analysis for Phase II experiments has been performed using both the Monte Carlo and discrete ordinates methods. The MCNP version 3A code[15] was used to perform the Monte Carlo calculations where the geometrical details of the rotating neutron target (RNT) and its surroundings (e.g. motor) as well as the Li_2CO_3 enclosure and the Li_2O test zone have been considered in three dimensional simulation. The DOT4.3[16] and DOT5.1[17] were used to perform the two-dimensional calculations where the target, the enclosure, and the test assembly were modeled in 2-D cylindrical geometry.

The DOT4.3 and DOT5.1 are similar except for the way the scratch files needed for the calculations are handled and the acceleration schemes used to speed the conversion. A special feature of the DOT code is "variable meshing." This allows the number of first-dimension (i) mesh interval to vary with the second dimension (j) index. The directional quadrature set can be chosen from an arbitrary number of input sets, and the choice can vary with spatial position and energy group. This feature can reduce the computational time considerably by concentrating the calculation in areas needing attention, such as streaming gaps. Unsymmetric direction sets can also be used in cases where streaming is directed either upward or downward. In the present analysis, the variable mesh feature was used. The S_8 symmetrical direction set was used throughout the geometry for all energy groups. There are a variety of input format that can be handled by these codes to simulate the external source (e.g., distributed source, external boundary source, etc.). In our case, the external source is generated at a point and therefore strong ray-effect could occur. To mitigate such an effect, the first collision source (which is an analytical first-flight scattering source) should be first calculated and inputed to the DOT code. For that purpose, the RUFF[18] code was used to generate the first collision source file and the final flux is the sum of the collided flux (calculated by DOT) and the uncollided flux (calculated by RUFF). The RUFF code (developed by Princeton Plasma Physics Laboratory, PPPL) is a modified version of the GRTUNCL[19] code developed at Oak Ridge National Laboratory (ORNL) and is compatible with the variable mesh feature of the DOT4.3 and DOT5.1 codes. With this code, the uncollided flux can be calculated for several point sources that are not necessarily on the central axis of the 2-D geometry. The code can also treat sources that vary in their angular distribution (symmetry around the Central Axis is required) for every

energy group used in the calculations (i.e. variations in the energy/angular distributions of the external point source(s) can be handled by RUFF.)

The Monte Carlo calculations were carried out using the MCNP code [15]. In characterizing the source by foil activation method, the U.S. participants from ORNL used the MORSE-CG [20] Monte Carlo code.

MCNP is a general purpose, continuous energy, generalized geometry, time-dependent, coupled neutron-photon Monte Carlo transport code. MCNP treats an arbitrary, three-dimensional configuration of materials in geometric cells bounded by first-and-second-degree surfaces and some special fourth-degree surfaces. Pointwise cross-section data are used (RMCCS library). A unique advantage of using pointwise data is to eliminate approximations in data due to group averaging. MCNP embodies numerous types of variance reduction methods. Some of them are: (1) importance sampling, (2) weight cutoff with Russian roulette, (3) time and energy cutoff, (4) implicit capture and analog capture (5) exponential transformation, (6) forced collisions, (7) energy splitting and Russian roulette, (8) correlated sampling, (9) source biasing, (10) point detectors, (11) DXTRAN, and (12) weight windows. Readers are referred to Ref. (15) for more information on these techniques.

MORSE-CG[20] is a multipurpose neutron and photon transport Monte Carlo code. Through the use of multigroup cross-sections, the solution of neutron, photon, or coupled neutron-photon problems may be obtained in either the forward or adjoint mode. General three-dimensional geometry may be used with an albedo option available at any material surface. Standard multi-group cross-sections such as those used in discrete-ordinates codes may be used as input. Anisotropic scattering is treated for each group-to-group transfer by utilizing a generalized Gaussian quadrature technique (PL expansion method). MORSE provides versatile types of variance reduction techniques including energy-space-dependent splitting and Russian roulette and exponential transformation. Source energy biasing is an option, as well as energy biasing at each collision.

II.2 Calculational Models

(A.) Two-Dimensional Model

In determining the specifications (energy and angular distribution) of the point neutron source used in the 2-D calculations for all the experiments that have been carried out, the following procedures were used. First a single Monte Carlo calculation was performed

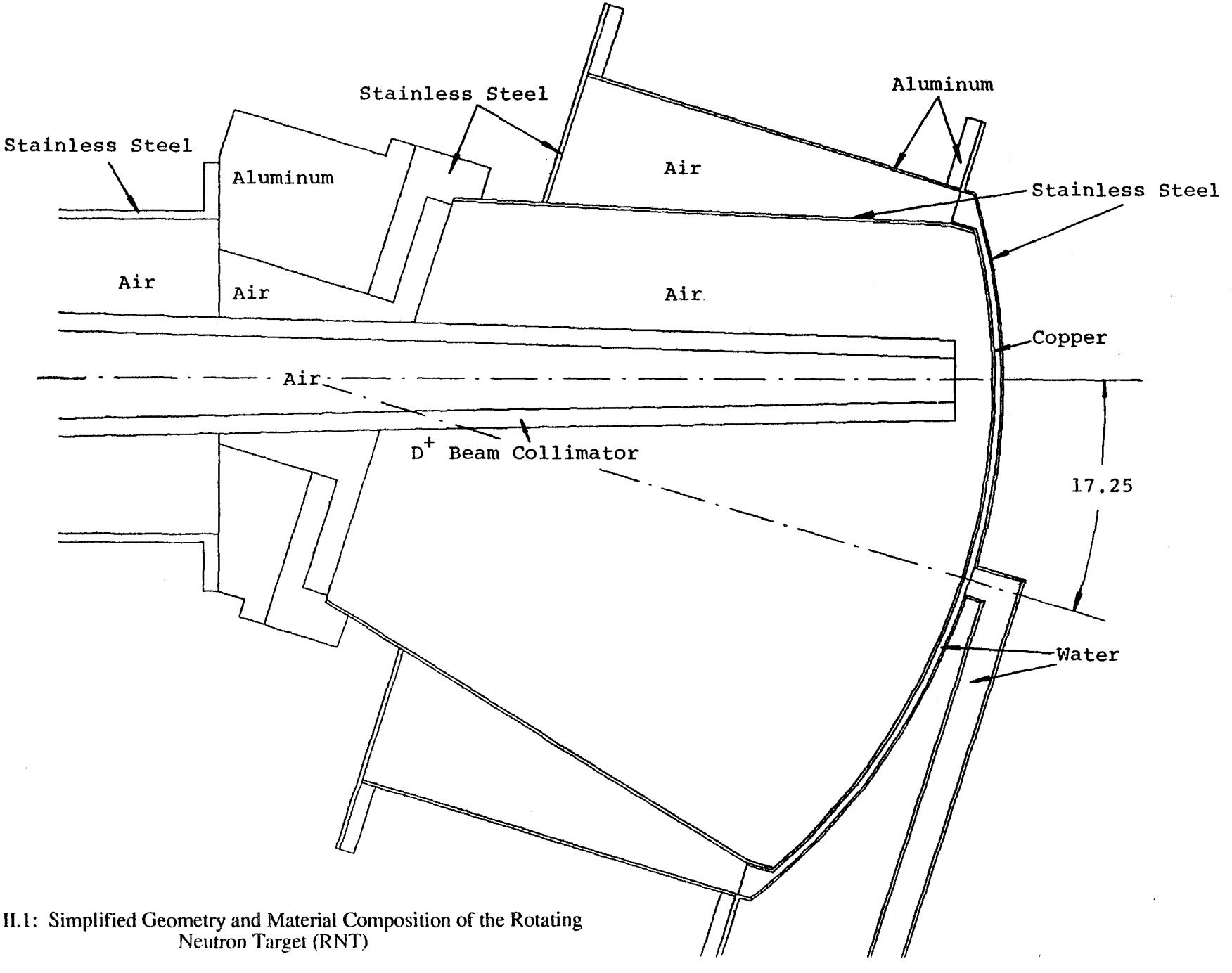

Fig. II.1: Simplified Geometry and Material Composition of the Rotating Neutron Target (RNT)

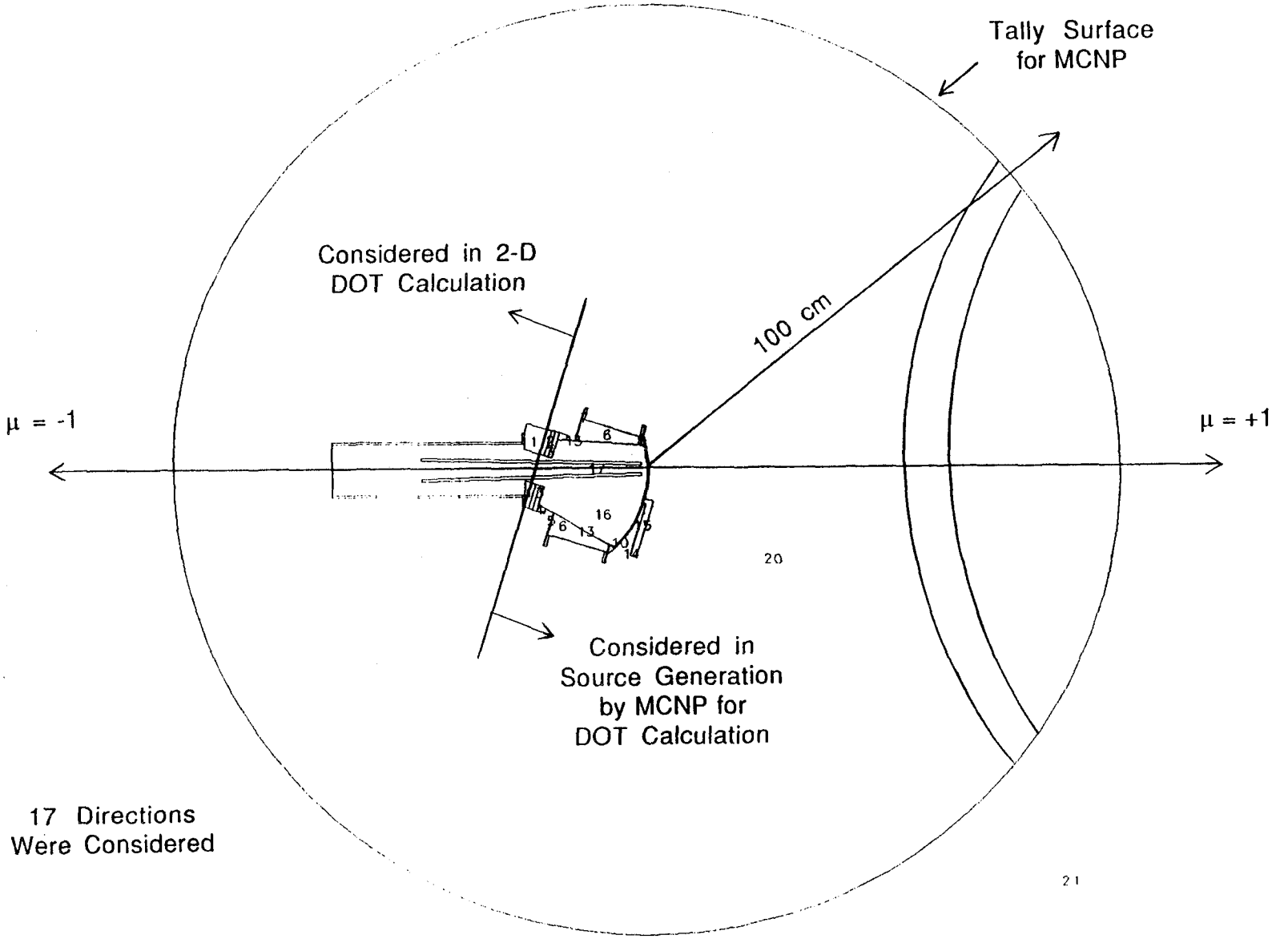

Fig. II.2: Geometrical Model for Determining D-T Input Source for 2-D Calculation

where part of the rotating neutron target (see the simplified geometry of the RNT in Fig. II.1) is considered and the energy and angular distribution of neutrons going into seventeen directions are computed as shown in Fig. II.2. The surface tally that surrounds that part of the target was considered at a distance of 1m from the point space where the D^+ beam hits the titinium-tritiated target. In the second step of the calculation, the other part of the RNT was considered in the RUFF and DOT calculations in each prospective geometrical arrangement and was modeled in a cylindrical geometry as shown in Fig II.3. The atomic densities ($x10^{-24}$) of the target materials that were used in the calculations are also shown in Fig. II.3. The two steps mentioned above are equivalent to MCNP/DOT calculations for the model shown in Fig. II.4.

Fig. II.5 shows the 2-D (R-Z) calculational model used for the reference system (REF) in Phase IIA. As shown, the D-T neutron source is located at Z=r=0.0 and part of the rotating target is considered as discussed above. The central drawer (5.08 cm x 5.08 cm x L) was simulated as cylinder with an effective outer radius of 2.886 cm. The cylinder inner Li_2O blocks of the drawer (excluding the SUS-304 clad) has an effective radius of 2.719 cm. Because the number of Li_2O blocks and shape used in the drawer and the outer Li_2O zone are different, the amount of the SUS-304 cladding is different and hence different atomic densities were used in these two Li_2O zones. Conserving the volume of the Li_2O test assembly, the effective radius is ~48.78 cm while the effective radius of the Li_2CO_3 enclosure is 69.48 cm. The thickness of the polyethylene (PE) layer was taken as is (5 cm). In the model, the volume of the experimental room was also preserved and the effective dimensions are shown in Fig II.5. The thickness of the concrete wall was considered as 60 cm which was judged to be adequate. Although the effect of the room-returned neutrons on the TPR and other reaction rates along the cental axis of the Li_2O assembly is small due to the inclusion of the PE layer, the room was considered in the modeling to accurately calculate various reaction rates measured in the back Li_2CO_3 zone that is located behind the Li_2O assembly. Note from Fig. II.5 that the outer supporting structure (made of aluminum) was accounted for in the modeling. The model used for the beryllium front system (BEF) of Phase IIA is similar to that shown in Fig. II.5 except that the first 5 cm of Li_2O zone was replaced by beryllium. Fig. II.6 shows the calculational model used for the beryllium sandwiched system (BES) of Phase IIA.

In Fig. II.7, the model used for the beryllium front system with first wall (BEFWFW) in Phase IIB is shown where a Be layer of thickness 5.08 cm surrounds the inner surface of the Li_2CO_3 enclosure and in front of the Li_2O test assembly with a 0.5 cm-

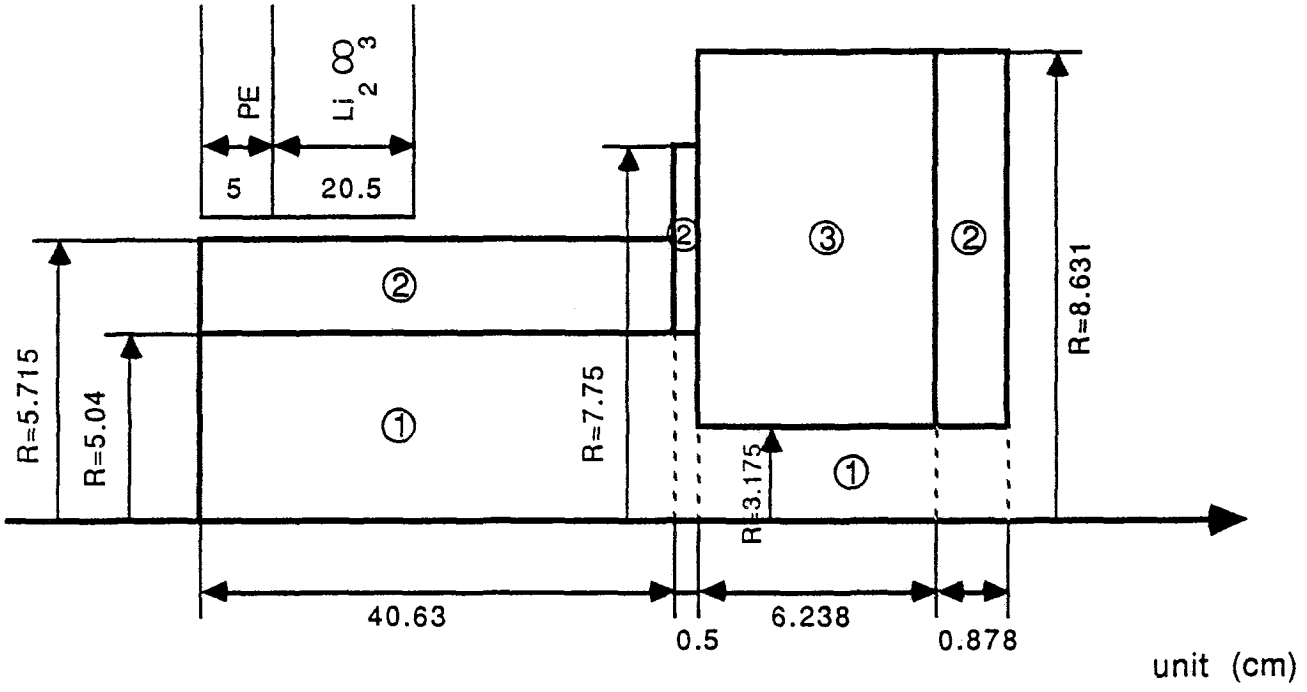

Material ①	Air	N	3.8810-5
		O	1.0400-5
②	SUS 316	Cr	1.7408-2
		Fe	6.1733-2
		Ni	8.1116-3
③	Al	Al	6.0038-2

Fig. II.3: Part of the RNT Used in the 2-D Calculations

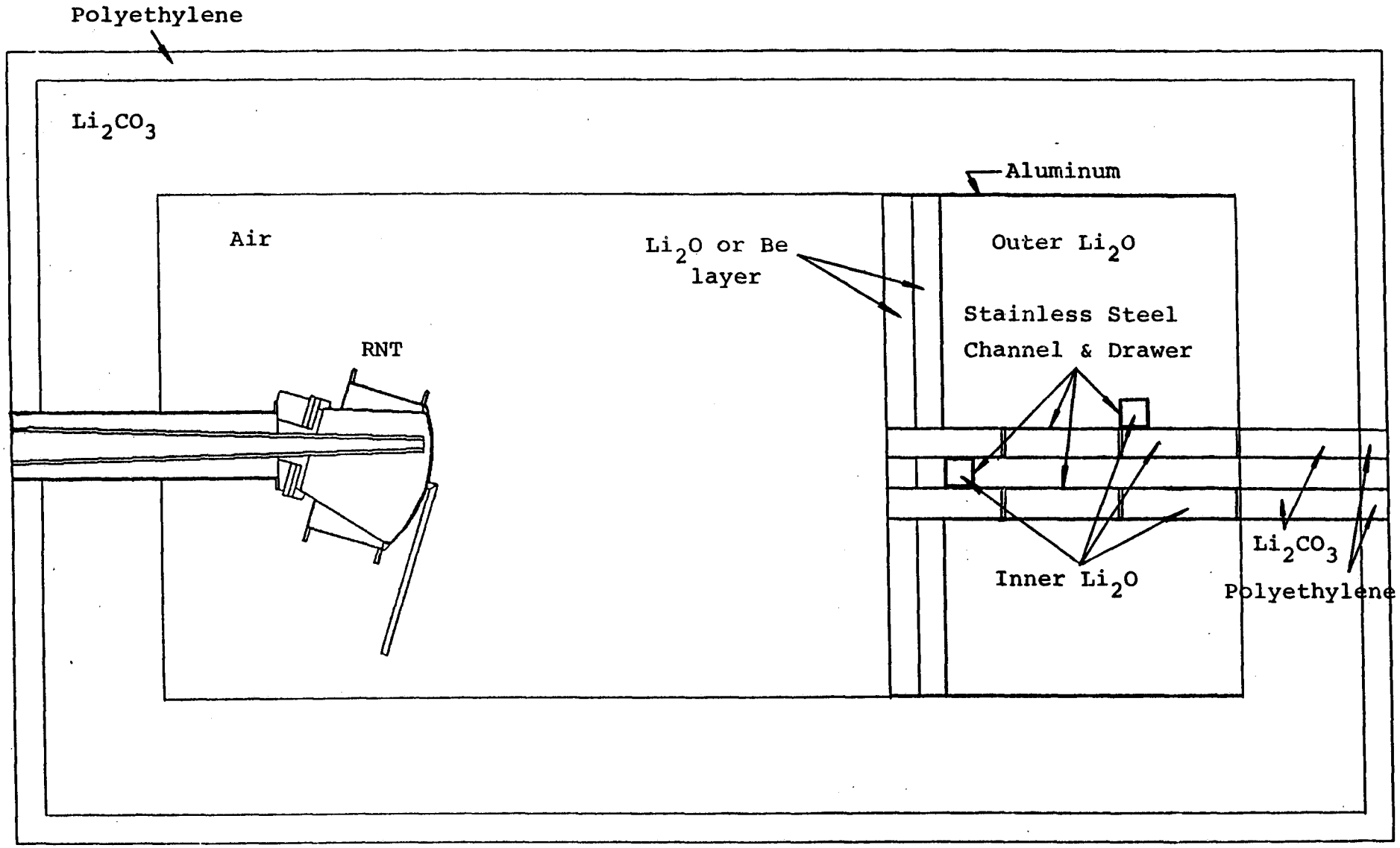

Fig. II.4: Schematic of Phase IIA Arrangement Showing the RNT, Central, and Radial Drawers

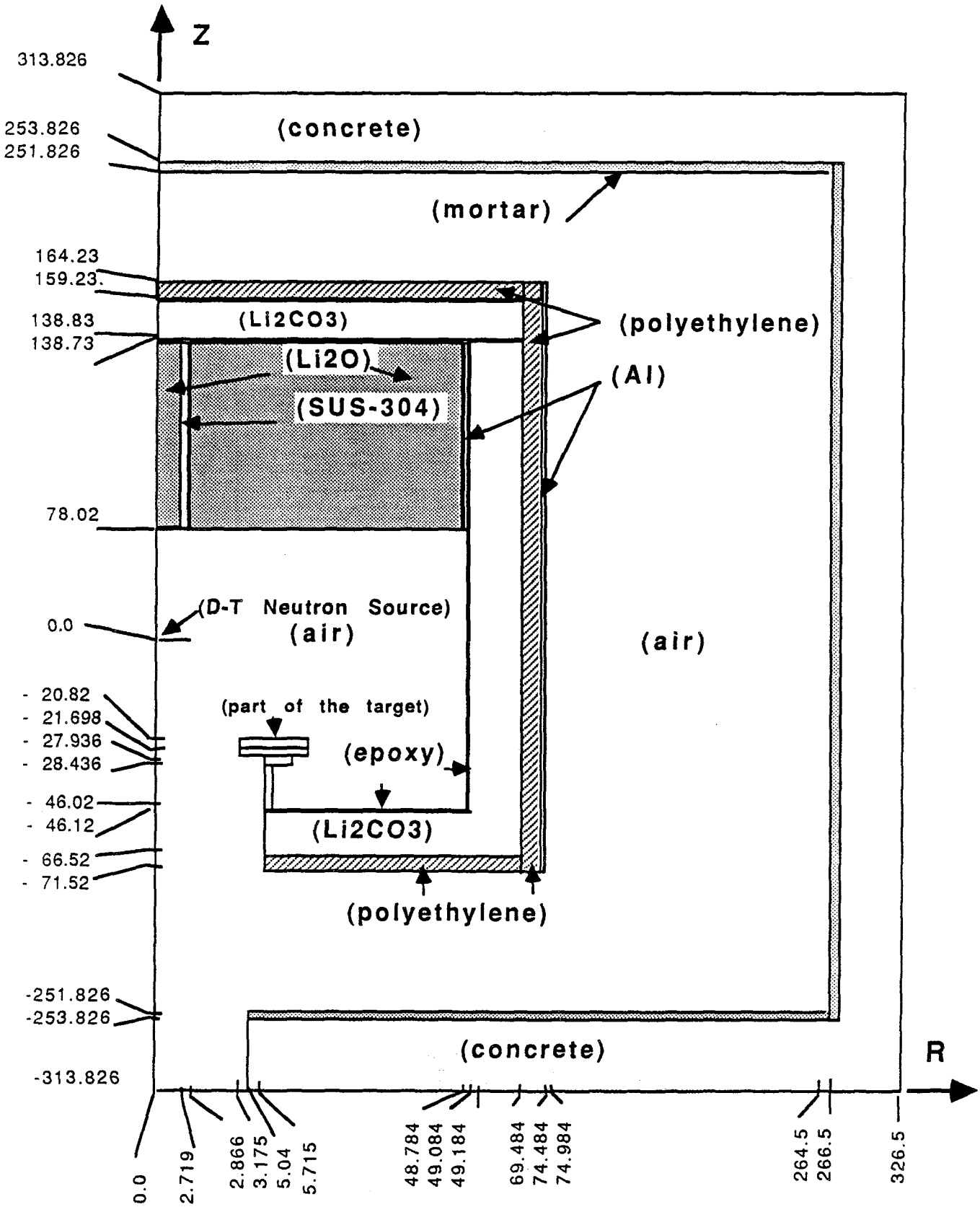

Fig. II.5: Geometrical Model Used in 2-D DOT5.1 Calculation
(Reference System - Phase IIA)
(REF)

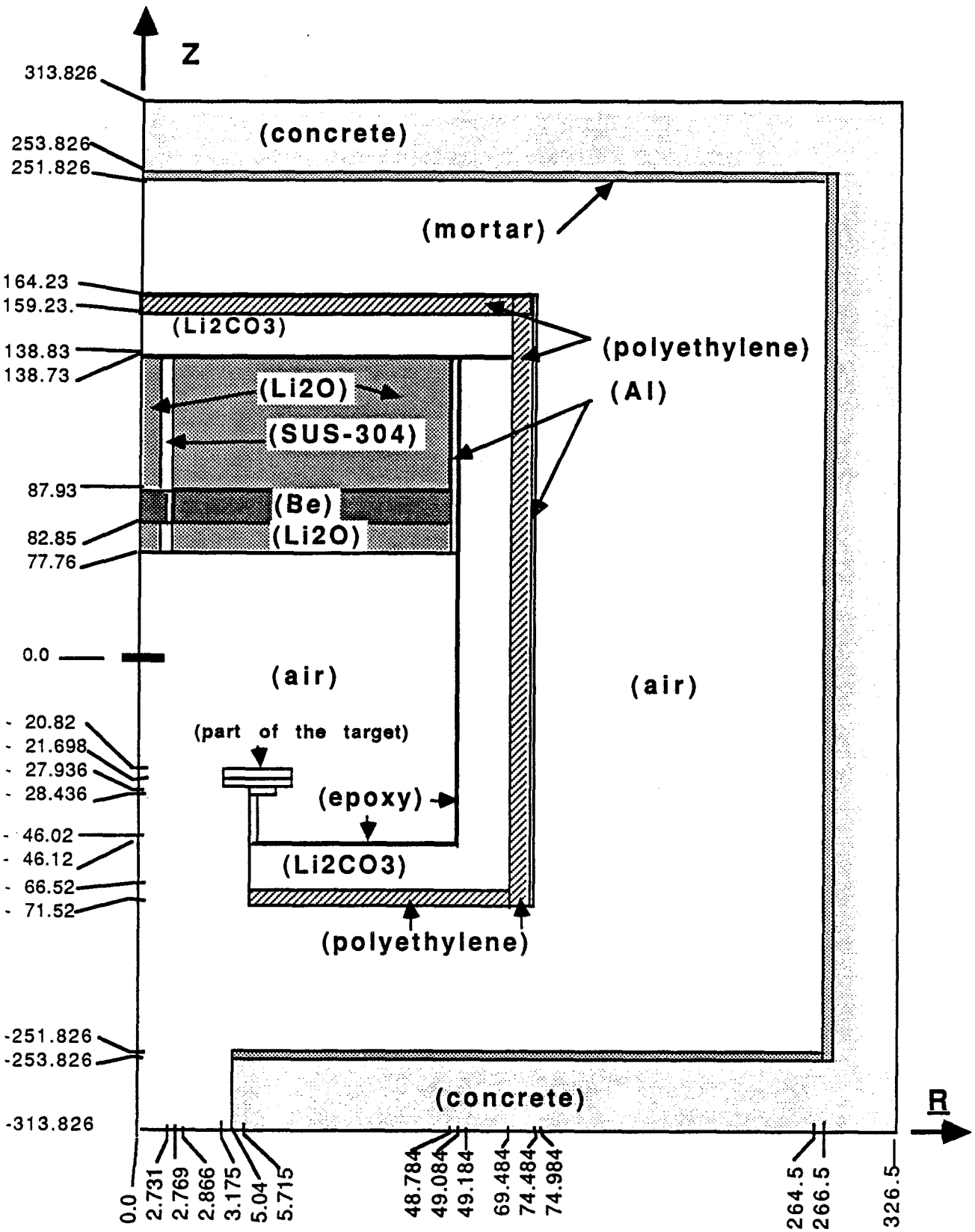

Fig. II.6: Geometrical Model Used in 2-D DOT5.1 Calculation
(Beryllium-Sandwiched System - Phase IIA)
(BES)

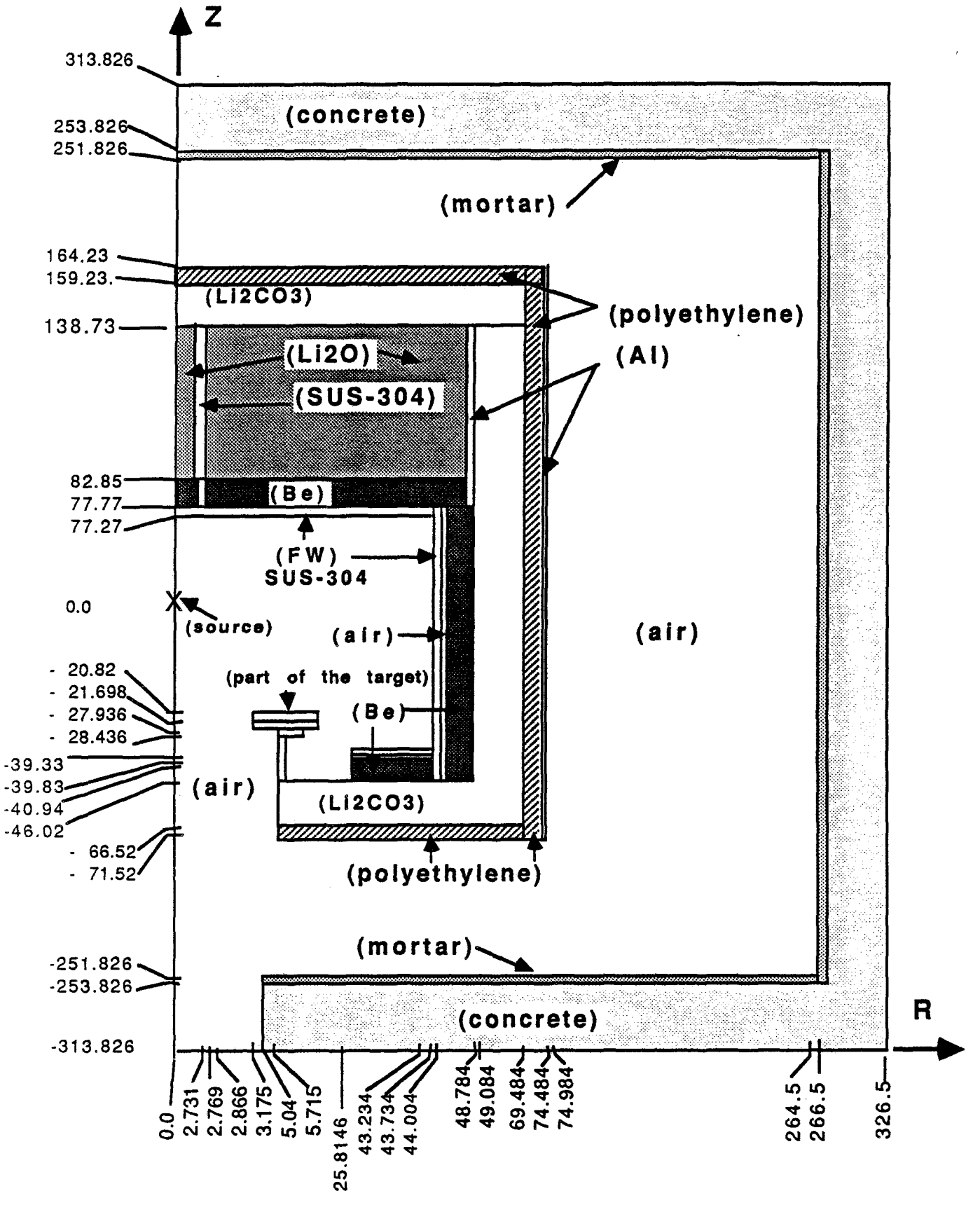

Fig. II.7: Geometrical Model Used in 2-D DOT5.1 Calculation
Beryllium-Front with FW-Phase IIB
(BEFWFW)

thick SUS-304 first wall. The back inner surface of the Li_2CO_3 enclosure was not fully covered by beryllium. The volume of beryllium used to cover this surface was calculated and an effective layer (which preserves that volume) of an equivalent inner radius of 25.81 cm was considered in the calculations. The reference system for Phase IIB is similar to that shown in Fig. II.7 except that the front beryllium zone (with the FW) that preceeds the Li_2O assembly is excluded. The model used for the beryllium front without a FW (BEFWOFW) system is similar to that of the BEFWFW except that the 0.5-thick FW was excluded from the front Be layer.

(B.) Monte Carlo Model

The Monte Carlo model used in the calculations employed either direct importance assignment to neutrons or weight window method to trance neutron's importance as function of energy and location in a spatial cell.

In the source characterization in Phase IIB, the reactions $^{197}Au(n,\gamma)^{198}Au$ and $^{93}Nb(n,2n)^{92m}Nb$ were mapped at the inner surface of the Li_2CO_3 enclosure and at the front of the assembly (see Section III) using direct neutron importance method. Figs. II.8 and II.9 show the importances used to calculate the $^{197}Au(n,\gamma)$ reaction at various cells for the side and top view, respectively. Notice that the higher the importance value assigned to a particular cell, the larger the neutrons are followed in that region. As shown in these figures, neutrons' importance were considered small inside the outer regions of the geometry and at deep locations in the assembly since flux mapping were performed at the inner surfaces only. Figs. II.10 and II.11 are the corresponding figures for the case of the $^{93}Nb(n,2n)^{92m}Nb$ reaction in the BEFWFW system. Notice that zero importance indicated in these figures does mean that neutrons carry very low importance, close to zero.

The Monte Carlo model for the REF system of Phase IIA is shown in Figs. II.12 and II.13 (side and top view, respectively) for all the calculated parameters (except TLD measurements) using the weight window method. Shown in these figures are the lower bounds of the weight windows at various cells. Lower numbers indicate that neutrons are followed till their weight drops below the values shown before deciding their fate. Therefore, one may notice from these figures that more importance is given to those neutrons that are within (or close to) the central drawers. Again, zero values mean that the lower weight window bounds are very close to zero. The weight window method was also applied to the BEF, and BES systems of Phase IIA (not shown).

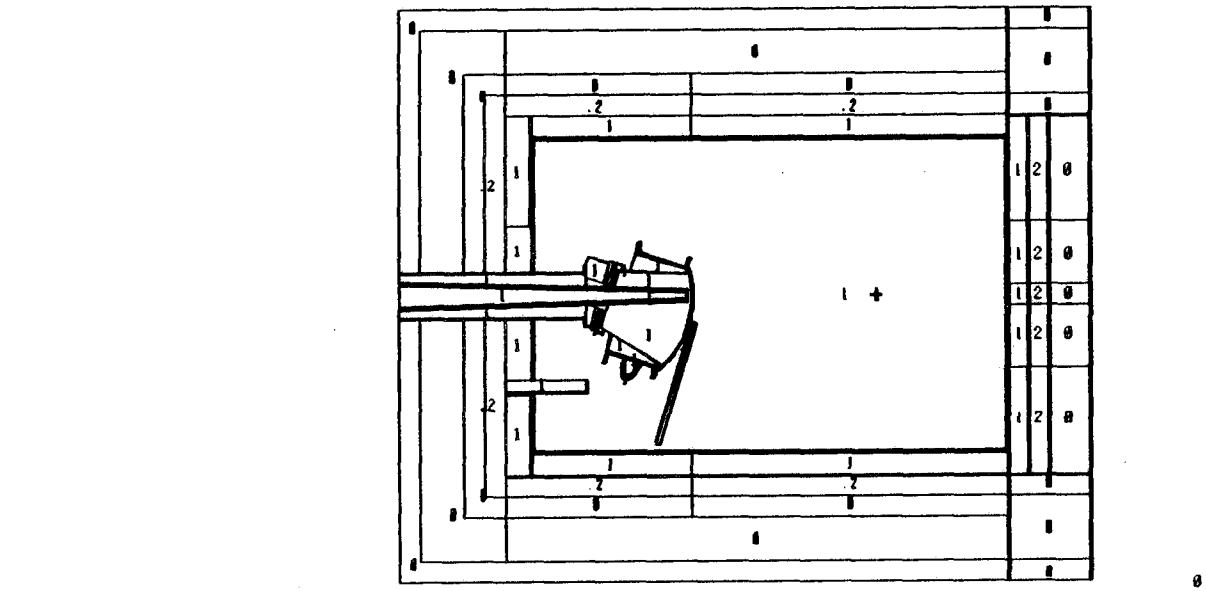

Fig. II.8: Side View of the Monte Carlo Model Used for Mapping of the $^{197}Au(n,\gamma)$ Reaction in the Be-Front System (W/FW) of Phase IIB

```
F 07/21/89 15:44:15
FNS PHASE IIB.BE-FRONT W. FW:
 FLUX MAPPING  AU(N,GAMMA)
 (04/25/88)
PROBID - F 07/21/89 15:12:58
BASIS:
( 1.000000, 0.000000, 0.000000)
( 0.000000, 0.000000, 1.000000)
ORIGIN:
(    45.00,     0.00,     0.00)
EXTENT - (   120.00,   120.00)
CELL LABELS ARE
 NEUTRON IMPORTANCES
```

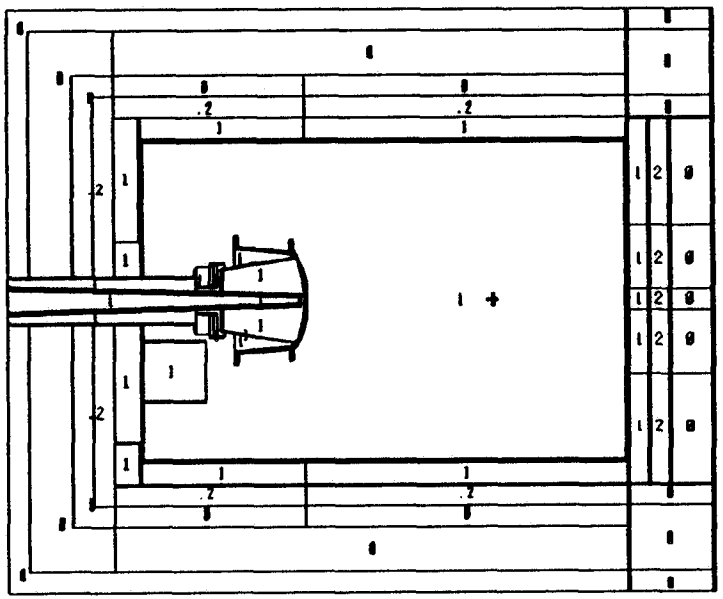

Fig. II.9: Top View of the Monte Carlo Model used for Mapping of the $^{197}Au(n,\gamma)$ reaction in the Be-Front (W/FW) System of Phase IIB

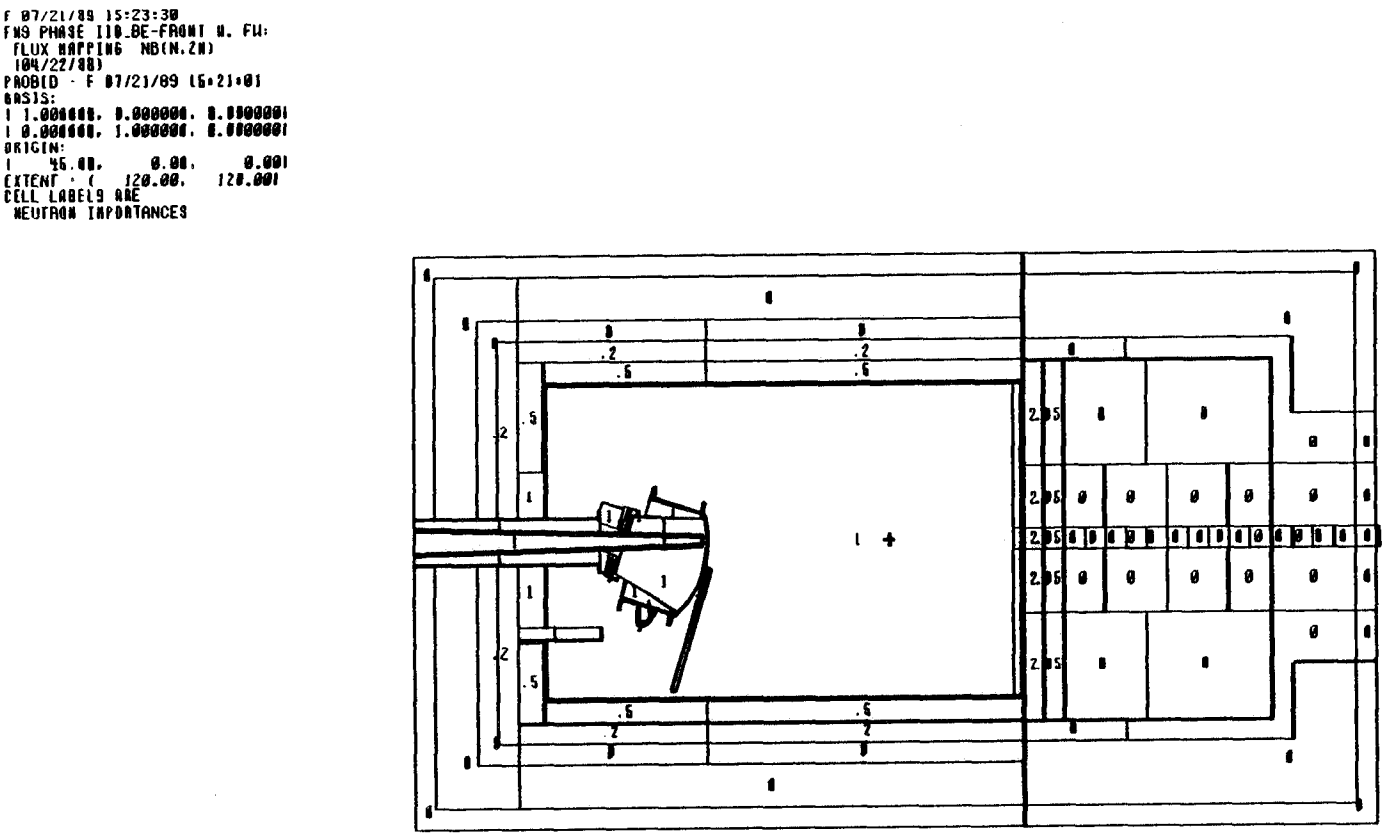

Fig. II.10: Side View of the Monte Carlo Model Used for Mapping of the ^{93}Nb(n,2n) Reaction in the Be-Front (W/FW) System of Phase IIB

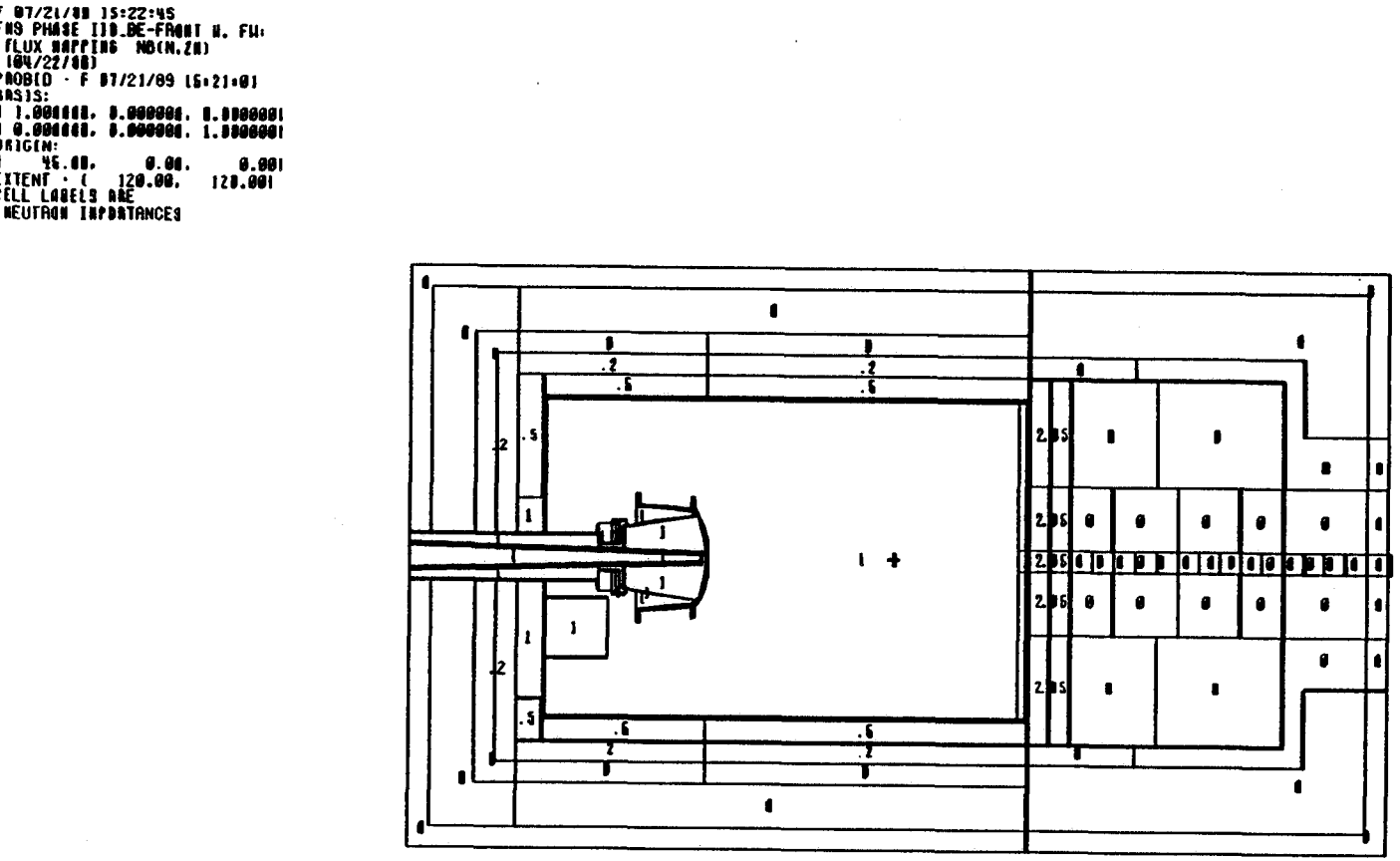

Fig. II.11: Top View of the Monte Carlo Model Used for Mapping of the $^{93}Nb(n,2n)$ Reaction in the Be-Front (W/FW) System of Phase IIB

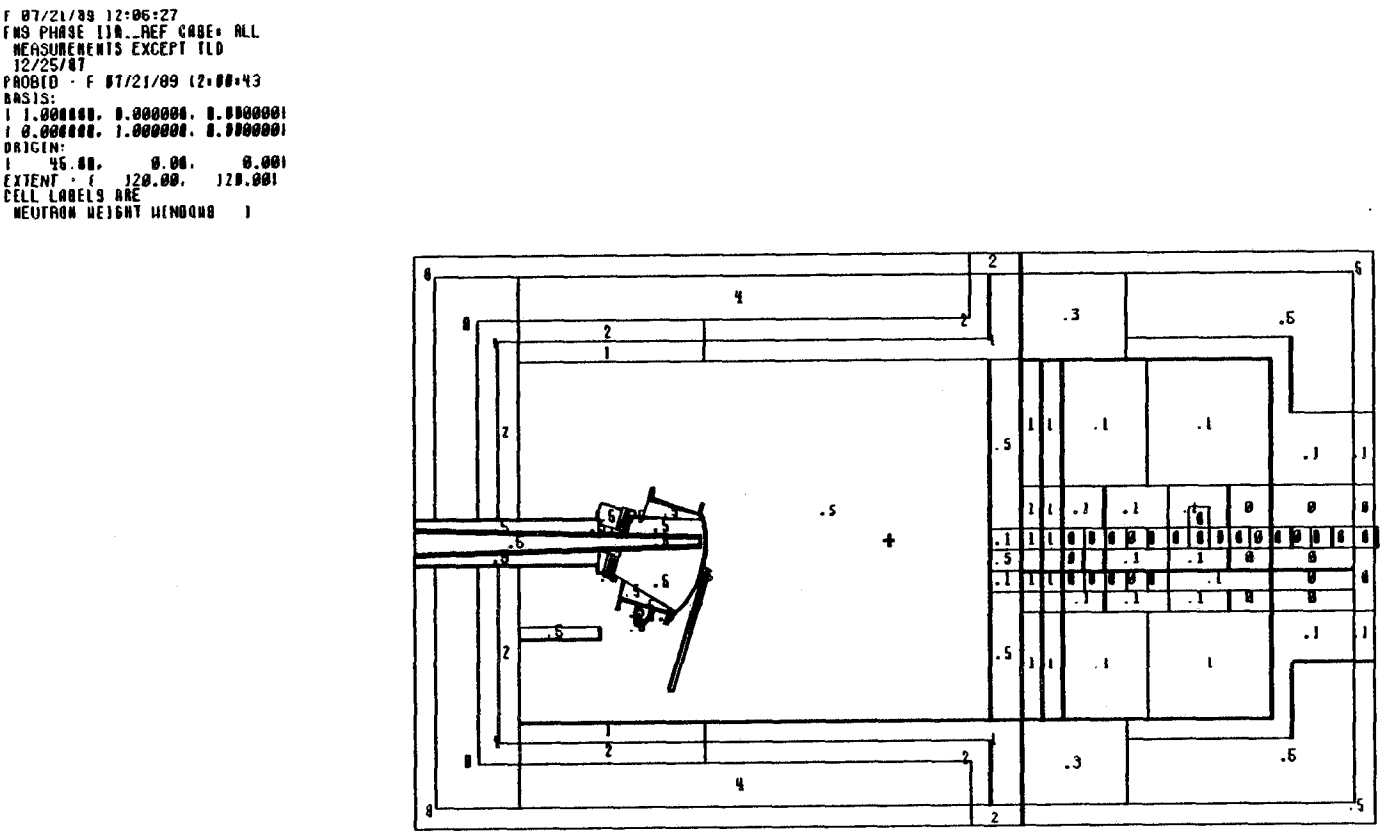

Fig. II.12: Side View of Monte Carlo Model Used in the REF System of Phase IIA

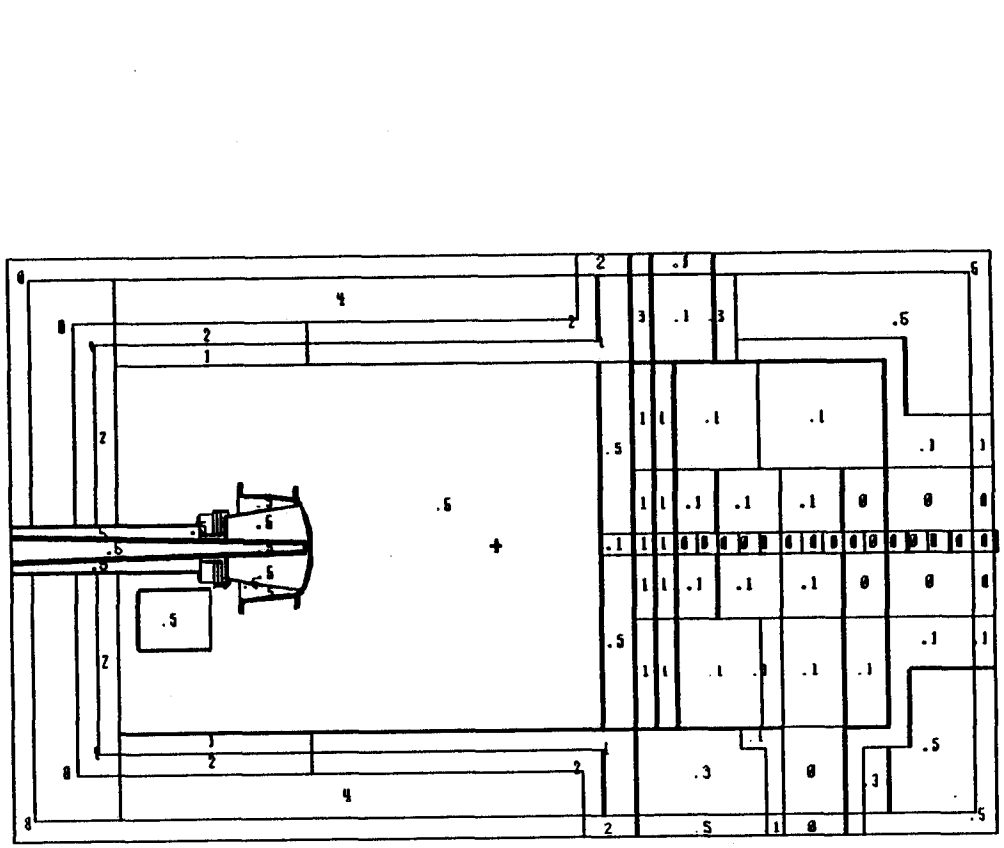

Fig. II.13: Top View of the Monte Carlo Model Used in the REF System of Phase IIA

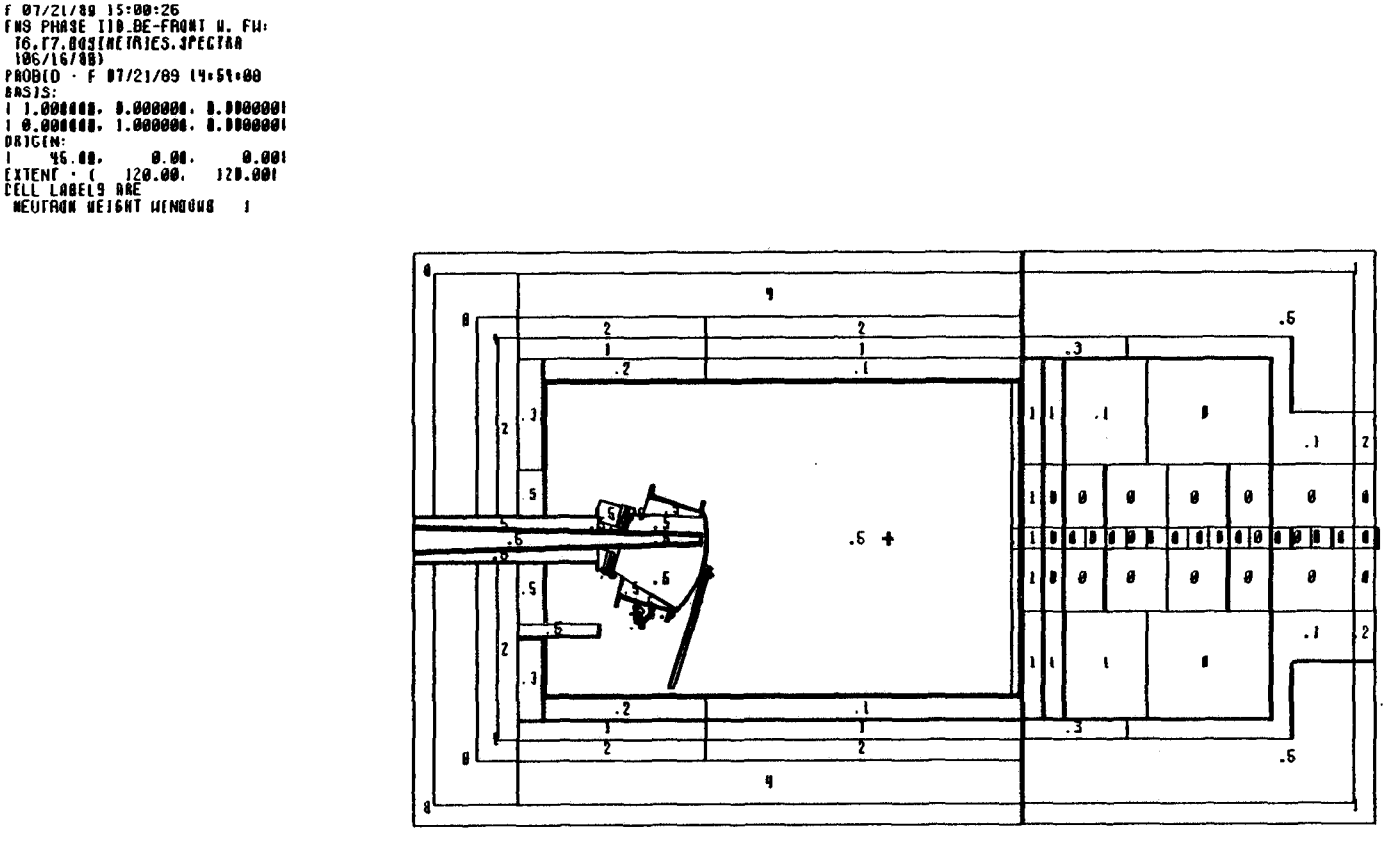

Fig. II.14: Side View of the Monte Carlo Model Used in the BEFWFW System of Phase IIB

```
F 07/21/89 14:58:39
FNS PHASE IIB_BE-FRONT W. FW:
 16.T7.GEOMETRIES.SPECTRA
 (06/16/88)
PROBID - F 07/21/89 14:51:00
BASIS:
( 1.000000, 0.000000, 0.0000001
( 0.000000, 0.000000, 1.0000001
ORIGIN:
(    46.00,     0.00,     0.001
EXTENT - (   120.00,   120.001
CELL LABELS ARE
 NEUTRON WEIGHT WINDOWS   1
```

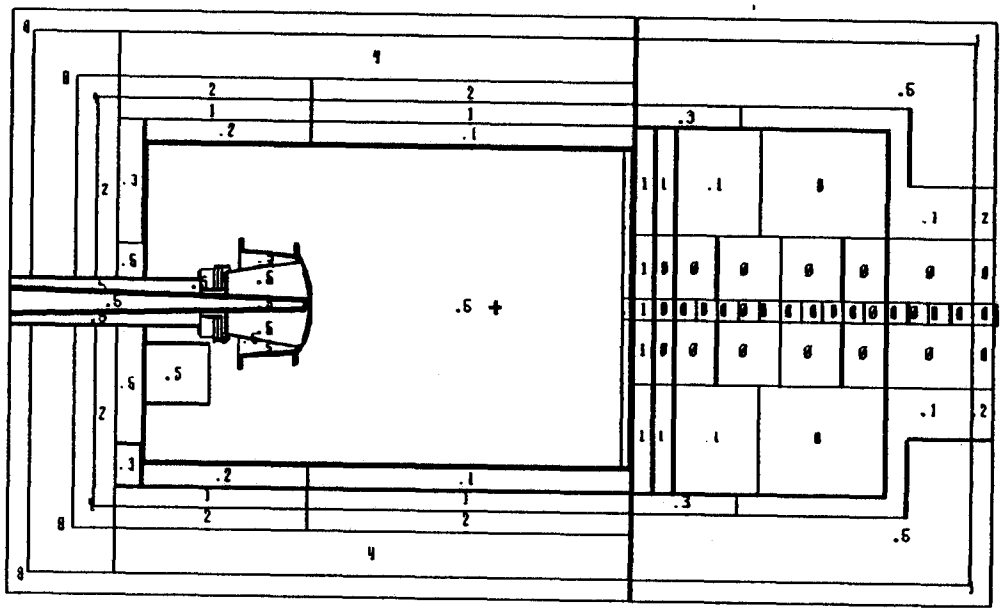

Fig. II.15: Top View of the Monte Carlo Model Used in the BEFWFW System of Phase IIB

The Monte Carlo model adopted (with weight window method) in the REF system of Phase IIB is very similar to the one shown in Figs. II.12 and II.13. The calculations for T_6, T_7, activations rates, and spectra in the Be-front (W/FW,BEFWFW) system of Phase IIB were also performed using weight window method whose lower weight bounds are shown in Figs. II.14 and II.15.

In both Phase IIA and IIB, track length estimators were used for calculating the reaction rates and spectrum inside the central drawer. Table II.1 shows the lower boundaries of each cell along the central axis of the central drawer (measured from the D-T neutron source location). Also shown are the number of regions considered in each cell as well as their width. Table II.2 shows the energy bin structure for the neutron spectrum computation used in the Monte Carlo calculations. The number of bins considered (113 bins) is larger than the number of the energy groups used in the MATXS6[21] library deployed in the DOT calculations.

II.3 Nuclear Data

For the Monte Carlo analysis, most of the calculations were based on the default Recommended Monte Carlo Cross-Section Library, RMCCS, of the MCNP code which includes data for 77 materials and isotopes. This library is based on pointwise cross-section data generated by using the ACER routine of the NJOY[22] processing code. For most materials, the data in this library are based on the ENDF/B-V data file. With general energy grids, the length of the cross-section tables in the RMCCS library is usually shorter than that in the ENDF/B-V file. If the resonance absorption is not important, the results obtained from the RMCCS library and from the direct ENDF/B-V file are similar. Besides the default library, data from the cross-section file BMCCS3, ENDF5P3 and ENDF5U3 were utilized. The cross-section data file for activation and reaction rates are based on ACTL library generated at Lawrence Livermore National Laboratory (LLNL). Tables II.3 to II.5 give the nuclide I.D., source of evaluation and the name of data file used in Phase IIA calculatiosn which are basically the same as those used in Phase IIB.

In characterizing the source by foil activation method, the U.S. participants from ORNL[23] used MORSE-CG along with a 53 neutron group cross-section library generated from the 174 neutron group of VITAMIN-E (ENDF/B-V) library.[24] In their calculations, the activation cross-sections used are from the ORACT[25] library.

Table II.1: Regions of Track Length Estimators Used in Test Channel
(Dimension: 4.84 x 4.84 x ΔZ)

Cell Number	Phase IIA			Phase IIB		
	Lower Boundary (cm)	Regions	Region Widths ΔZ's (cm)	Lower Boundary (cm)	Regions	Region Widths ΔZ's (cm)
0	77.76	5	1.0, 1.0, 1.0, 1.0, 1.08	77.76	5	1.0, 1.0, 1.0, 1.0, 1.08
1	82.84	5	1.0, 1.0, 1.0, 1.0, 1.08	82.84	5	1.0, 1.0, 1.0, 1.0, 1.08
2	87.92	2	2.54, 2.54	87.92	2	2.54, 2.54
3	93.00	2	2.54, 2.54	93.00	2	2.54, 2.54
4	98.08	2	2.54, 2.54	98.08	2	2.54, 2.54
5	103.16	2	2.54, 2.54	103.16	2	2.54, 2.54
6	108.24	2	2.54, 2.54	108.24	2	2.54, 2.54
7	113.32	2	2.54, 2.54	113.32	2	2.54, 2.54
8	118.40	2	2.54, 2.54	118.40	2	2.54, 2.54
9	123.48	2	2.54, 2.54	123.48	2	2.54, 2.54
10	128.56	2	2.54, 2.54	128.56	2	2.54, 2.54
11	133.64	2	2.54, 2.55	133.64	2	2.54, 2.55
12	138.73	2	2.28, 2.79	138.73	2	2.28, 2.79
13	143.80	5	1.0, 1.0, 1.0, 0.96, 0.96	143.80	5	1.0, 1.0, 1.0, 0.96, 0.96
14	148.72	5	1.0, 1.0, 1.0, 1.0, 1.25	148.72	5	1.0, 1.0, 1.0, 1.0, 1.25
15	153.97	5	1.0, 1.0, 1.0, 1.0, 1.26	153.97	5	1.0, 1.0, 1.0, 1.0, 1.26
16	159.23	3	1.0, 1.0, 3.0	159.23	3	1.0, 1.0, 3.0

As for the library used in the deterministic calculations, the MATXS6[21] library was utilized. This library has a 80-group energy structure and is based on ENDF/B-V data.[26] This library is also generated by using the NJOY[22] processing code with P5 Legendre coefficients and a fusion peak + 1/E + Maxwellian weighting function. The U.S. calculations were based on the latest evaluations for beryllium[27] and ^{7}Li ENDF/B-V, version 2 carried out at LANL[28] as it is the case in the Monte Carlo calculations. As for beryllium, comparison was also made to results based on ENDF/B-V and ENDF/B-VI data.[29] The neutron group structure of the MATXS6 library is given in Table II.6.

Table II.2: Energy Bin Structure for Neutron Spectrum Computation by MCNP (113 Bins)

Bin	Upper Bound MeV)	Bin	Upper Bound (MeV)	Bin	Upper Bound (MeV)	Bin	Upper Bound (MeV)
1	7.889E-05	31	9.804E-02	61	2.691	91	11.51
2	1.301E-04	32	1.111E-01	62	2.865	92	11.69
.3	2.144E-04	33	1.259E-01	63	3.050	93	11.88
4	3.536E-04	34	1.426E-01	64	3.267	94	12.06
5	5.829E-04	35	1.616E-01	65	3.456	95	12.25
6	9.611E-04	36	1.832E-01	66	3.679	96	12.45
7	1.234E-03	37	2.075E-01	67	3.916	97	12.64
8	1.585E-03	38	2.352E-01	68	4.169	98	12.84
9	2.035E-03	39	2.665E-01	69	4.437	99	13.04
10	2.613E-03	40	3.020E-01	70	4.724	100	13.25
11	3.355E-03	41	3.422E-01	71	5.028	101	13.66
12	4.307E-03	42	3.877E-01	72	5.353	102	13.67
13	5.531E-03	43	4.396E-01	73	5.698	103	13.88
14	7.102E03	44	4.979E-01	74	6.065	104	14.10
15	9.119E-03	45	5.642E-01	75	6.465	105	14.32
16	1.171E-02	46	6.893E-01	76	6.873	106	14.55
17	1.503E-02	47	7.299E-01	77	7.316	107	14.78
18	1.930E-02	48	8.208E-01	78	7.788	108	15.01
19	2.187E02	49	9.301E-01	79	8.290	109	15.25
20	2.479E-02	50	1.054	80	8.825	110	15.49
21	2.809E-02	51	1.196	81	9.394	111	15.73
22	3.183E-02	52	1.353	82	10.00	112	15.98
23	3.607E-02	53	1.534	83	10.16	113	16.23
24	4.087E-02	54	1.738	84	10.32		
25	4.631E-02	55	1.850	85	10.48		
26	5.247E-02	56	1.969	86	10.65		
27	5.946E-02	57	2.096	87	10.81		
28	6.738E-02	58	2.231	88	10.98		
29	6.635E-02	59	2.375	89	11.16		
30	8.652E-02	60	2.528	90	11.33		

Table II.3: Nuclear Cross Section Sources for Reference and Be-Sandwich Cases of Phase II.A

Nuclide	Nuclide I.D. Number in MCNP	Source Evaluation	Cross Section File Name
^{1}H	1001.50c	ENDF/B-V	RMCCS
^{6}Li	3006.50c	ENDF/B-V	RMCCS
^{7}Li	3007.55c	T - 2	RMCCS
^{9}Be	4009.03c	LASL-SUB	BMCCS3
C	6012.50c	ENDF/B-V	RMCCS
^{14}N	7014.50	ENDF/B-V	RMCCS
^{16}O	8016.50c	ENDF/B-V	RMCCS
^{23}Na	11023.50c	ENDF/B-V	ENDF5P3
^{27}Al	13027.50c	ENDF/B-V	RMCCS
^{32}S	16032.51c	ENDF/B-V	RMCCS
K	19000.51c	ENDF/B-V	RMCCS
Ca	20000.51c	ENDF/B-V	RMCCS
Cr	24000.50c	ENDF/B-V	RMCCS
^{55}Mn	25055.51c	ENDF/B-V	RMCCS
Fe	26000.55c	T - 2	RMCCS
Ni	28000.50c	ENDF/B-V	RMCCS
Cu	29000.50c	ENDF/B-V	RMCCS

Table II.4: Nuclear Cross Section Sources for Be Front Case of Phase IIA

Nuclide	Nuclide I.D. Number in MCNP	Source/Evaluation	Cross Section File Name
^{1}H	1001.50c	ENDF/B-V	RMCCS
^{6}Li	3006.50c	ENDF/B-V	RMCCS
^{7}Li	3007.55c	T - 2	RMCCS
^{9}Be	4009.03c	LASL-SUB	BMCCS3
C	6000.50c	ENDF/B-V	RMCCS
^{14}N	7014.50c	ENDF/B-V	RMCCS
^{16}O	8016.50c	ENDF/B-V	RMCCS
^{23}Na	11023.50c	ENDF/B-V	ENDF5P3
^{27}Al	13027.50c	ENDF/B-V	RMCCS
^{32}S	16032.50c	ENDF/B-V	ENDF5U3
K	19000.50c	ENDF/B-V	ENDF5U3
Ca	20000.50c	ENDF/B-V	ENDF5U3
Cr	24000.50c	ENDF/B-V	RMCCS
^{55}.Mn	25055.50c	ENDF/B-V	ENDF5U3
Fe	26000.55c	T - 2	RMCCS
Ni	28000.50c	ENDF/B-V	RMCCS
Cu	29000.50c	ENDF/B-V	RMCCS

Table II.5: Dosimetry Cross Section for Reaction Rate Calculation

Reaction type	Nuclide I.D. Number in MCNP	ENDF/B Reaction type Identification MT	Source File Name
$^{6}Li(n,\alpha)T$	3006.50c	205	RMCCS
$^{7}Li(n,n',\alpha)T$	3007.55c	205	RMCCS
$^{27}Al(n,\alpha)^{24}Na$	13027.50c	107	RMCCS
$^{58}Ni(n,2n)^{57}Ni$	28058.26y	16	532dos2
$^{58}Ni(n,p)^{48}Co$	28058.26y	103	532dos2
$^{93}Nb(n,2n)^{92m}Nb$	41093.30y	1016	LLLdos2
$^{197}Au(n,2n)^{196}Au$	79197.55c	16	RMCCSA3
$^{197}Au(n,\gamma)^{198}Au$	79197.55c	102	RMCCSA3
$^{115}In(n,n')^{115m}In$	49115.26y	51	532dos2
$^{115}In(n,\gamma)^{116}In$	49115.30y	102 & 2102	LLLdos2

Table II.6: Neutron Group Structure for the MATXS6 (ENDF/B-V) Library and the Weighting Spectrum

Group	Upper Energy	Upper Lethargy	Group Flux
1	2.00000 + 7	-6.931 - 1	7.1543 - 4
2	1.69046 + 7	-5.250 - 1	6.2937 - 3
3	1.49182 + 7	-4.000 - 1	2.1704 - 1
4	1.34986 + 7	-3.000 - 1	3.2477 - 2
5	1.19125 + 7	-1.750 - 1	6.0709 - 2
6	1.00000 + 7	0.0	1.9733 - 1
7	7.78801 + 6	2.500 - 1	3.6194 - 1
8	6.06531 + 6	5.000 - 1	6.6346 - 1
9	4.72367 + 6	7.500 - 1	1.0208
10	3.67879 + 6	1.000	1.3507
11	2.86505 + 6	1.250	1.6508
12	2.23130 + 6	1.500	1.8749
13	1.73774 + 6	1.750	2.1286
14	1.35335 + 6	2.000	1.1702
15	1.19433 + 6	2.125	1.2472
16	1.05399 + 6	2.250	1.3291
17	9.30145 + 5	2.375	1.4167
18	8.20850 + 5	2.500	1.5100
19	7.24398 + 5	2.625	1.6092
20	6.39279 + 5	2.750	1.6934
21	5.64161 + 5	2.875	1.7606
22	4.97871 + 5	3.000	1.8273
23	4.39369 + 5	3.125	1.8992
24	3.87742 + 5	3.250	4.0239
25	3.01974 + 5	3.500	4.3431
26	2.35177 + 5	3.750	4.6917
27	1.83156 + 5	4.000	5.0039
28	1.42642 + 5	4.250	4.9479
29	1.11090 + 5	4.500	4.8307
30	8.65170 + 4	4.750	4.7157

Table II.6 (cont'd)

Group	Upper Energy	Upper Lethargy	Group Flux
31	6.73795 + 4	5.000	4.6038
32	5.24752 + 4	5.250	4.4531
33	4.08677 + 4	5.500	4.0835
34	3.18278 + 4	5.750	1.9006
35	2.80879 + 4	5.875	1.0973
36	2.60584 + 4	5.950	7.1421 - 1
37	2.47875 + 4	6.000	1.7270
38	2.18749 + 4	6.125	1.6465
39	1.93045 + 4	6.250	1.5698
40	1.70362 + 4	6.375	1.4963
41	1.50344 + 4	6.500	1.4267
42	1.32678 + 4	6.625	1.3602
43	1.17088 + 4	6.750	1.2968
44	1.03330 + 4	6.875	1.2363
45	9.11882 + 3	7.000	1.1785
46	8.04733 + 3	7.125	1.1140
47	7.10174 + 3	7.250	1.0447
48	6.26727 + 3	7.375	9.7956 - 1
49	5.53084 + 3	7.500	9.1837 - 1
50	4.88095 + 3	7.625	8.6105 - 1
51	4.30743 + 3	7.750	6.0739 - 1
52	3.80129 + 3	7.875	7.5711 - 1
53	3.35463 + 3	8.000	7.0976 - 1
54	2.96045 + 3	8.125	6.6562 - 1
55	2.61259 + 3	8.250	6.2409 - 1
56	2.30560 + 3	8.375	5.8515 - 1
57	2.03468 + 3	8.500	5.4863 - 1
58	1.79560 + 3	8.625	4.8838 - 1
59	1.58461 + 3	8.750	4.1230 - 1
60	1.39842 + 3	8.875	3.4811 - 1
61	1.23410 + 3	9.000	2.9390 - 1

Table II.6(cont'd)

Group	Upper Energy	Upper Lethargy	Group Flux
62	1.08909 + 3	9.125	2.4813 - 1
63	9.61117 + 2	9.250	3.8637 - 1
64	7.48518 + 2	9.500	2.7540 - 1
65	5.82947 + 2	9.750	1.9632 - 1
66	4.53999 + 2	1.000 + 1	1.3993 - 1
67	3.53575 + 2	1.025 + 1	9.7274 - 2
68	2.75364 + 2	1.050 + 1	8.8975 - 2
69	1.67017 + 2	1.100 + 1	2.8386 - 2
70	1.01301 + 2	1.150 + 1	8.9265 - 3
71	6.14421 + 1	1.200 + 1	4.4279 - 3
72	3.72665 + 1	1.250 + 1	4.4281 - 3
73	2.26033 + 1	1.300 + 1	4.4281 - 3
74	1.37096 + 1	1.350 + 1	4.4278 - 3
75	8.31529	1.400 + 1	4.4285 - 3
76	5.04348	1.450 + 1	4.4278 - 3
77	3.05902	1.500 + 1	8.8563 - 3
78	1.12535	1.600 + 1	8.8557 - 3
79	4.13994 - 1	1.700 + 1	8.8562 - 3
80	1.52300 - 1	1.800 + 1	1.2650 - 2
81	1.38879 - 4[a]	2.500 + 1	

(a) Lower Energy Boundary of the Last Group

III. Neutron Source Characterization

III.1. Generation of the D-T neutrons

The rotating neutron target (RNT) used in Phase II is the same target used for Phase I. Deuteron beam, D^+, of energy 350 Kev is incident on a tritiated-titinium (T-Ti) rotating target to generate the fusion neutrons. The energy and angular distributions of the emitted neutrons at the point of reaction were calculated taking into account the slowing down process in the T-Ti target and the relativistic effect.

Two approaches were used in the MCNP calculations to calculate the energy/angle distribution of the emitted neutrons. In one approach, and for each history, the angular distribution of the emitted neutron was sampled from the formula

$$\frac{\sigma(\theta)}{\sigma(0^o)} = 0.998 + 0.0213 \text{ Cos } \theta - 0.019 \text{ Cos}^2 \theta$$

given by Benveniste et al [30] for incident deuteron of energy En = 350 KeV. The angular distribution, ϕ, in the laboratory system and the emission energy were calculated from the formula

$$\sin \phi = \pm \sin \theta / \sqrt{1 + 2\gamma \text{ Cos } \theta + \gamma 2}$$

where

$$1/\gamma^2 = \frac{M_\alpha}{M_n} \circ \frac{M_D + M_T}{M_D} \left(\frac{M_T}{M_D + M_T} + \frac{Q}{E_D} \right)$$

M_D = mass of incident deutron

M_T = mass of target triton

M_α = mass of emitted α particle

M_n = mass of the emitted neutron

Q = 17.6 MeV; the released kinetic energy of the neutron and α particle

E_D = kinetic energy of the incident deuteron.

The energy of the emitted neutron E_n is, then, calculated as follows:

$$E_n = W_n - M_n.$$

$$W_n = \frac{1}{2a}(b \pm \sqrt{b^2-4ac})$$

$$a = (W_D + M_T)^2 - (W_D^2 - M_D^2)\,\mathrm{Cos}^2\,\phi$$

$$b = (W_D + M_T)\,(M_D^2 + M_T^2 + M_n^2 - M\alpha^2 + 2W_D M_T)$$

$$c = \frac{1}{4}(M_D^2 + M_T^2 + M_n^2 - M\alpha^2 + 2W_D M_T)^2 + (W_D^2 - M_D^2)\,M_n^2\,\mathrm{Cos}^2\phi,$$

where

$$W_i = M_i + E_i \text{ (total energy of particle i)}$$

In the above approach, a source subprogram including the D-T reaction kinematic listed above is directly used for each history in the MCNP calculation performed for each geometrical arrangement.

In the second approach, (denoted "Table Sampling Method") a table for energy and angle distributions of the fusion neutrons is created using MCNP with a source patch (subprogram) that includes the D-T reaction kinematic. Thirteen (13) energy intervals in the range 12.84 MeV to 15.49 MeV and thirty-two (32) angle intervals are used to represent the distribution. This table is used to generate the neutrons in the MCNP analysis of each experiment. Two problems were solved by using these two approaches. The approach of direct Monte Carlo method is about 40 % slower than the Table Sampling Method although the differences between the two methods in calculating threshold reactions and flux spectrum is negligible. Hence, the MCNP results reported here were obtained from the Table Sampling Method.

The source intensities of the emitted D-T neutrons as a function of energy and angle is shown in Fig. III.1. In the forward direction (0^o) the peak energy is around 15 MeV while it tends to peak toward lower energies (about 13 MeV) in the backward direction.

III.2. Source Characterization

III.2.1. Phase IIA

To characterize the emitted D-T neutron source, several foil activations reaction rates were measured at various locations on the inner surface of the Li_2CO_3 enclosure and

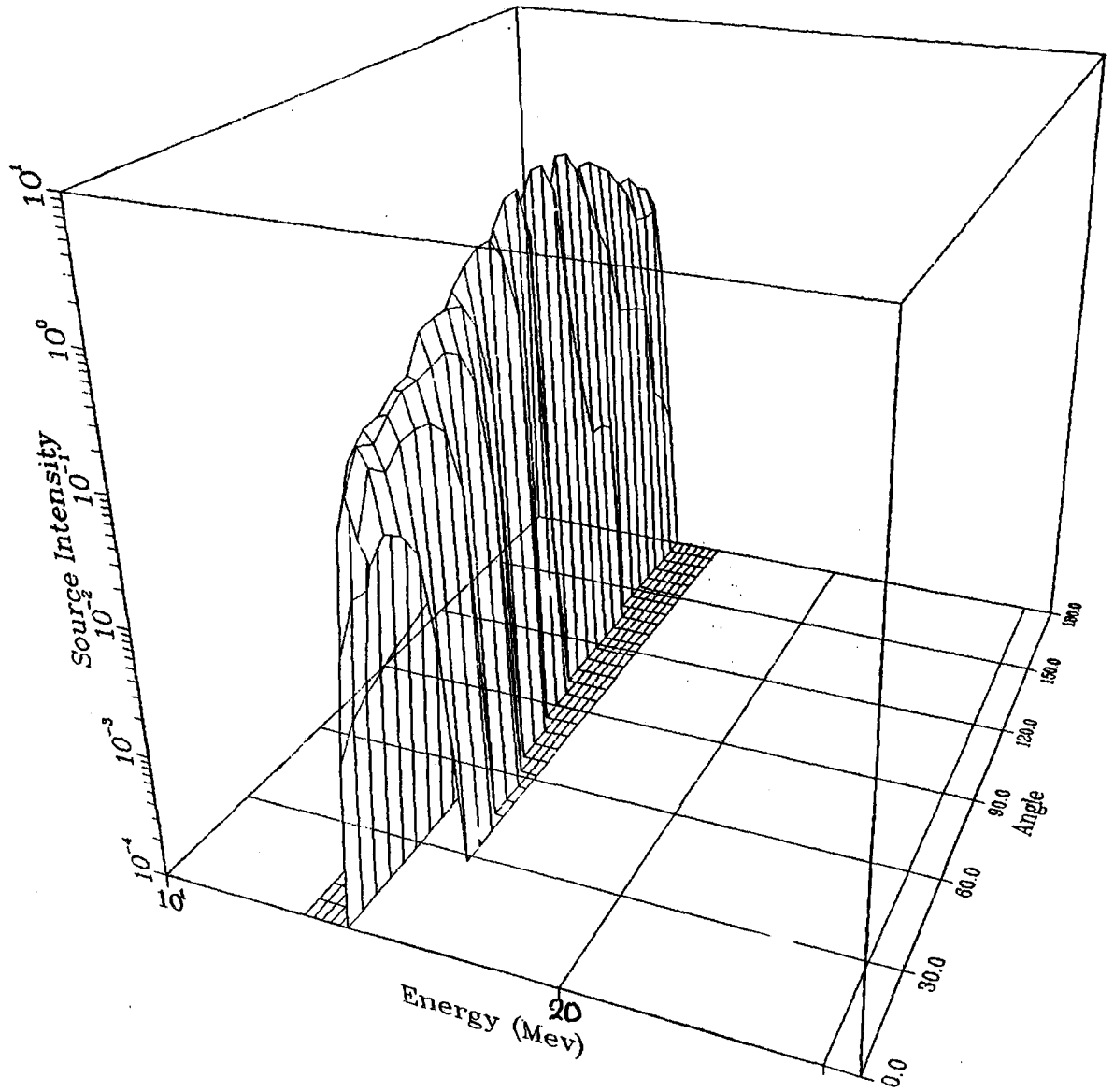

Fig. III.1: Energy and Angulal Distribution of the FNS D-T Neutron Source used in DOT and MCNP Calculations

at the front surface of the Li_2O test assembly in the reference experiment of Phase IIA. The reactions considered in this case are $^{93}Nb(n,2n)^{92m}Nb$, $^{58}Ni(n,2n)^{57}Ni$, $^{58}Ni(n,p)^{58}CO$, $^{197}Au(n,2n)^{196}Au$, $^{27}Al(n,\alpha)$, and $^{197}Au(n,\gamma)^{198}Au$. The accuracy of predicting the high-threshold reactions [e.g $^{58}Ni(n,2n)$, $^{93}Nb(n,2n)^{92m}Nb$] will indicate the accuracy of predicting the high-energy component (En> 10 MeV) of the incident neutron spectrum. On the other hand, the accuracy of predicting non-threshold reactions [e.g. $^{197}Au(n,\gamma)$] gives information on the prediction accuracy of the low-energy component of those neutrons that were slowed down and reflected by the enclosure walls.

Mapping of the calculated to experimental values (C/E) for the $^{93}Nb(n,2n)$ reaction is shown in Fig. III.2 at the mid-plane of the experimental configuration that is parallel to the room floor. The calculations [performed by the analysts of ORNL, see Ref. (23)] were not carried out for all the indicated locations for which measured values have been obtained. The prediction accuracy for $^{93}Nb(n,2n)$ reaction is within a few percent at the forward locations but large discrepancy is observed at locations that are behind the RNT. This large discrepancy at these back locations was observed for all high-energy reactions [e.g. $^{58}Ni(n,2n)$,$^{197}Au(n,2n)$]. Behind the RNT and on its side, a motor is located in addition to the tubes containing the cooling water. The inaccuracy of modeling these equipments and improper accounting for their atomic densities that are subject to large uncertainties is the reason for the large discrepancies observed at the back locations.

The C/E values for $^{197}Au(n,2n)$ and $^{27}Al(n,\alpha)$ reactions are shown in Fig. III.3 and III.4, respectively. The former reaction seems to be underpredicted by a few percent but the prediction accuracy for the latter is slightly better. Nevertheless, one can say that these two reactions are predicted with reasonable accuracy based on the ORACT data (ENDF/B-V), particularly at the forward direction.

As for $^{58}Ni(n,2n)$ reactions, all the C/E values (except those at the back locations) are lower than unity by as large as 33% as shown in Fig. III.5. Since the other high-energy reactions are reasonably predicted, it follows that the values for the $^{58}Ni(n,2n)$ cross-section, as currently implemented in ENDF/B-V, is underpredicted by $\sim$ 15 - 30 %. This was also pointed out in the analysis for Phase I experiments[3],[4]. However, the prediction accuracy for the $^{58}Ni(n,p)$ reaction is within 5 - 10 %, as shown in Fig. III.6. Note that the C/E values are greater than unity at most of the locations. Since the threshold

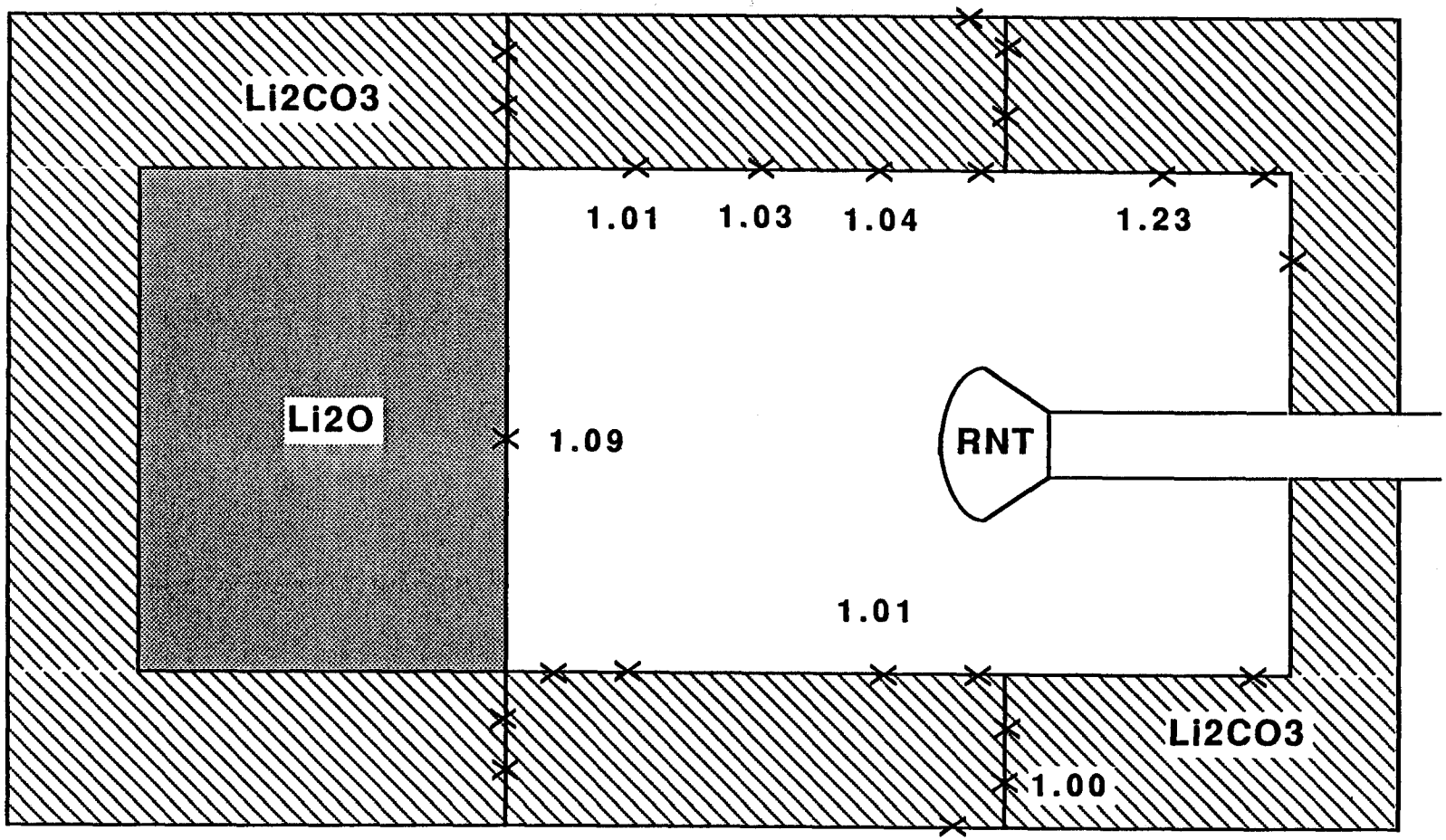

Fig. III.2: C/E Mapping of ^{93}Nb(n,2n) Reaction Rate at the Mid-Plan

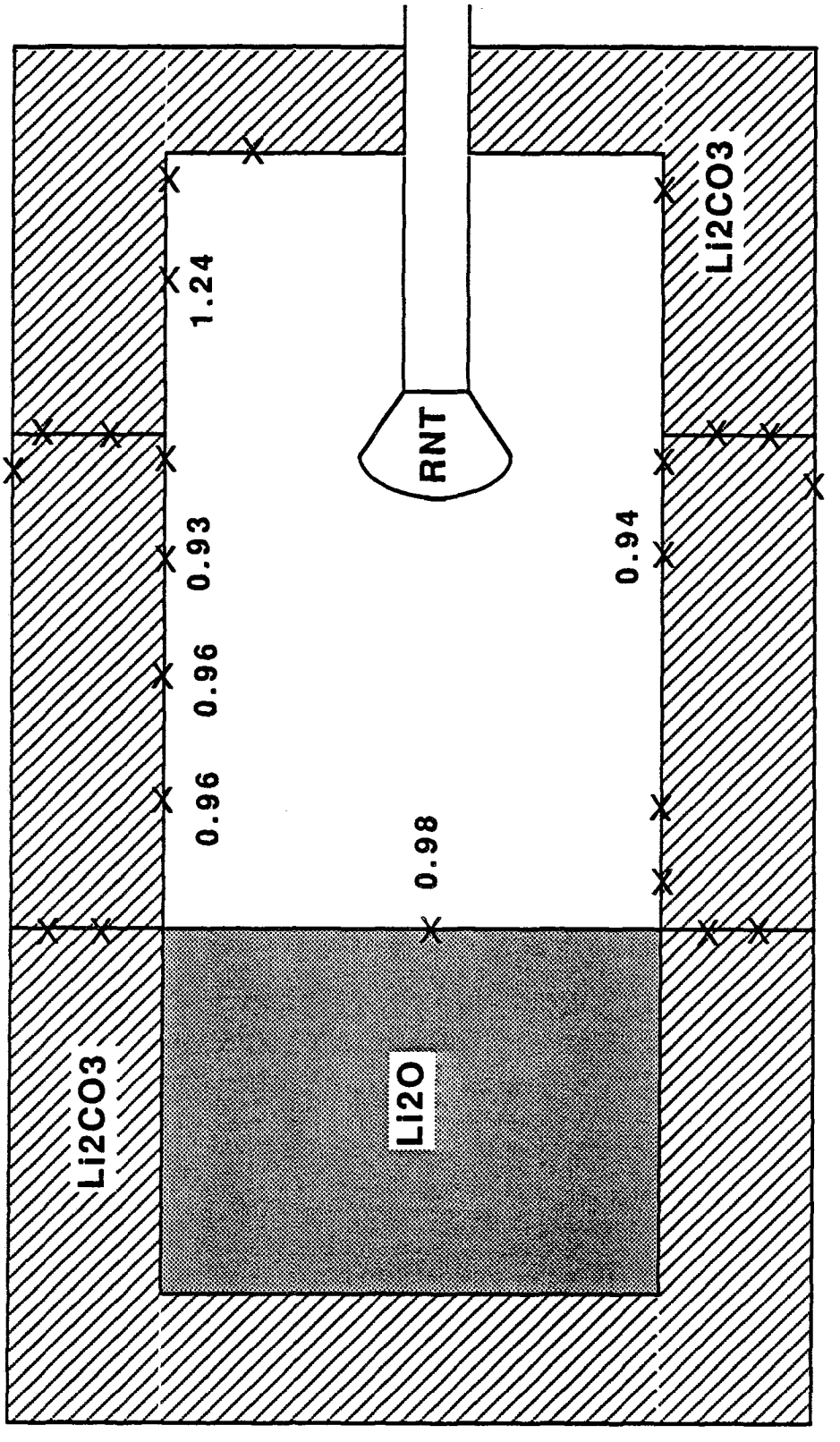

Fig. III.3: C/E Mapping of ^{197}Au(n,2n) Reaction Rate at the Mid-Plan

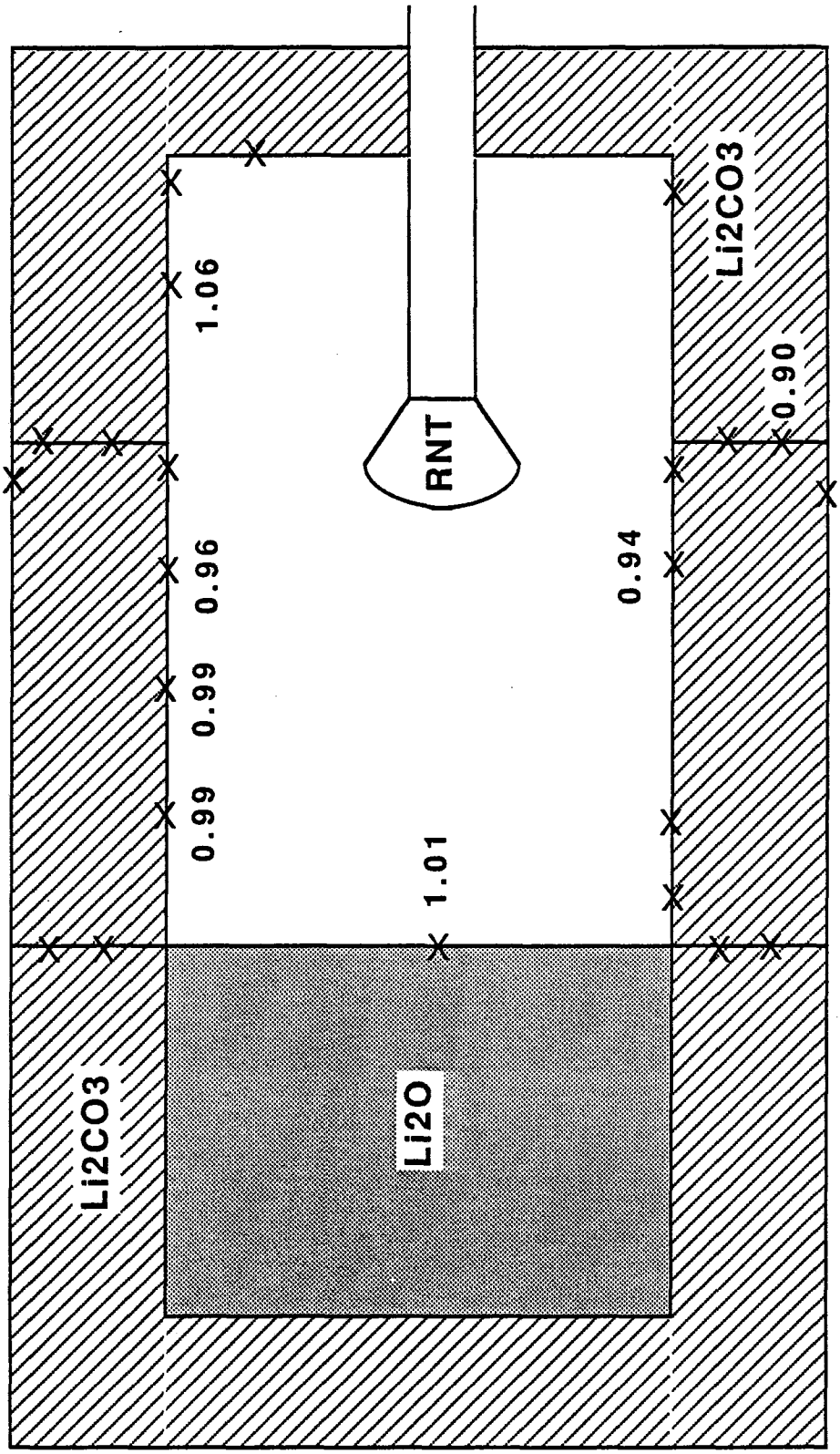

Fig. III.4: C/E Mapping of $^{27}Al(n,\alpha)$ Reaction Rate at the Mid-Plan

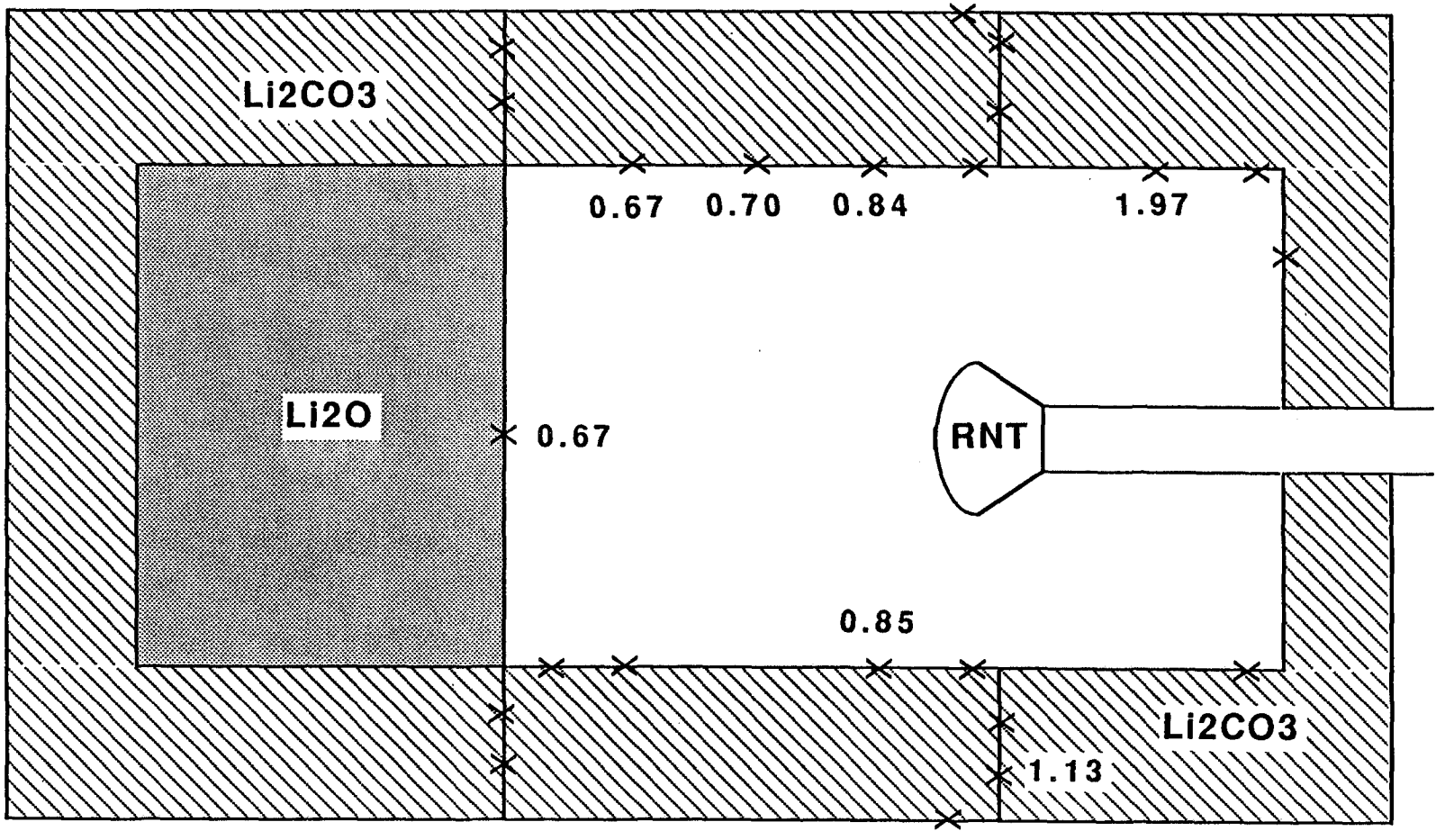

Fig. III.5: C/E Mapping of $^{58}Ni(n,2n)$ Reaction Rate at the Mid-Plan

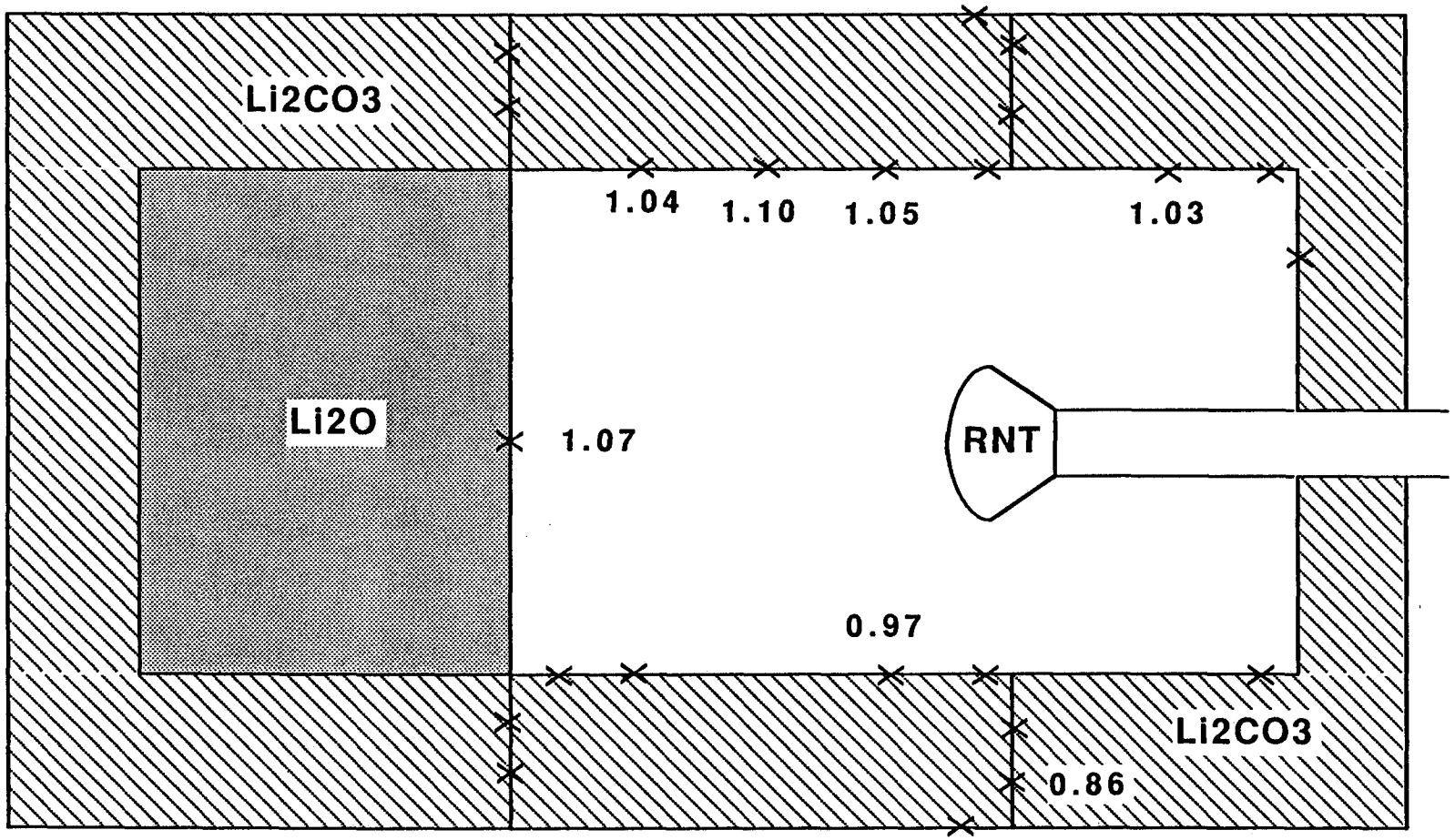

Fig. III.6: C/E Mapping of $^{58}Ni(n,p)$ Reaction Rate at the Mid-Plan

for that reaction is low (En ~ 1 MeV), the overprediction could be caused by an overprediction for the neutron spectrum in the energy range 1- 10 MeV.

As mentioned earlier, the above foil activation analysis was performed by ORNL participants using the MORSE-CG and ORACT library. Foil activation measurements were also performed at the front surface of the Li_2O assembly in the REF experiment, both in the horizontal and vertical directions. The analyses for these reactions were performed by MCNP code along with RMCCS library, as discussed in Chapter II. Figs. III.7 and III.8 show the C/E values for several reaction rates in the horizontal and vertical direction, respectively.

The C/E values for the $^{93}Nb(n,2n)\ ^{92m}Nb$ in the horizontal direction (Fig. III.7) is larger than the unity (by 2 - 8%) at all locations. The threshold for this reaction is ~ 8MeV and hence the integrated incident neutron spectrum could be either overestimated above this energy or, the value of the cross-section itself is overestimated. This is also true in the vertical direction as shown in Fig. III.8 and is consistent with the result obtained by the ORNL participants as shown in Fig. III.2. Another set of cross-section for $^{93}Nb(n,2n)^{93m}Nb$ was prepared by the T-2 group at LANL where a correction factor was applied to account for the correct branching ratio for this reaction. This cross-section was used to calculate the $^{93}Nb(n,2n)^{93m}Nb$ reaction rates inside the Li_2O assembly in the REF system and comparison was made to the results obtained from the cross-section used in Figs. III.7 and III.8. The C/E values for this reaction rate with the corrected cross-section is shown in Fig. III.9, where they are now closer to unity. This cross-section was therefore used in subsequent calculations.

As for $^{197}Au(n,2n)^{196}Au$ and $^{27}Al(n,\alpha)$ reactions, (Eth ~ 7 and ~ 6 MeV, respectively,) the C/E values, on the average, are slightly less than unity by several percent as shown in Fig. III.7 and III.8. The prediction accuracy for $^{58}Ni(n,p)^{58}Co$ is reasonable (2 - 9 %) and the C/E values at the center location is larger than unity by 5% which may be caused by an overestimation in the incident neutron spectrum in the energy range 1 - 10MeV, as was discussed earlier. The C/E values for $^{58}Ni(n,2n)\ ^{57}Ni$ are always lower than unity by ~20% (at all the front locations of the Li_2O assembly) as it was indicated in Fig. III.5. The cross-section for this reaction (as currently implemented in ENDF/B-V) should thus be increased by several percent. This was further emphasized by the work of Pavik , et. al.[31] as shown in Fig. III.10.

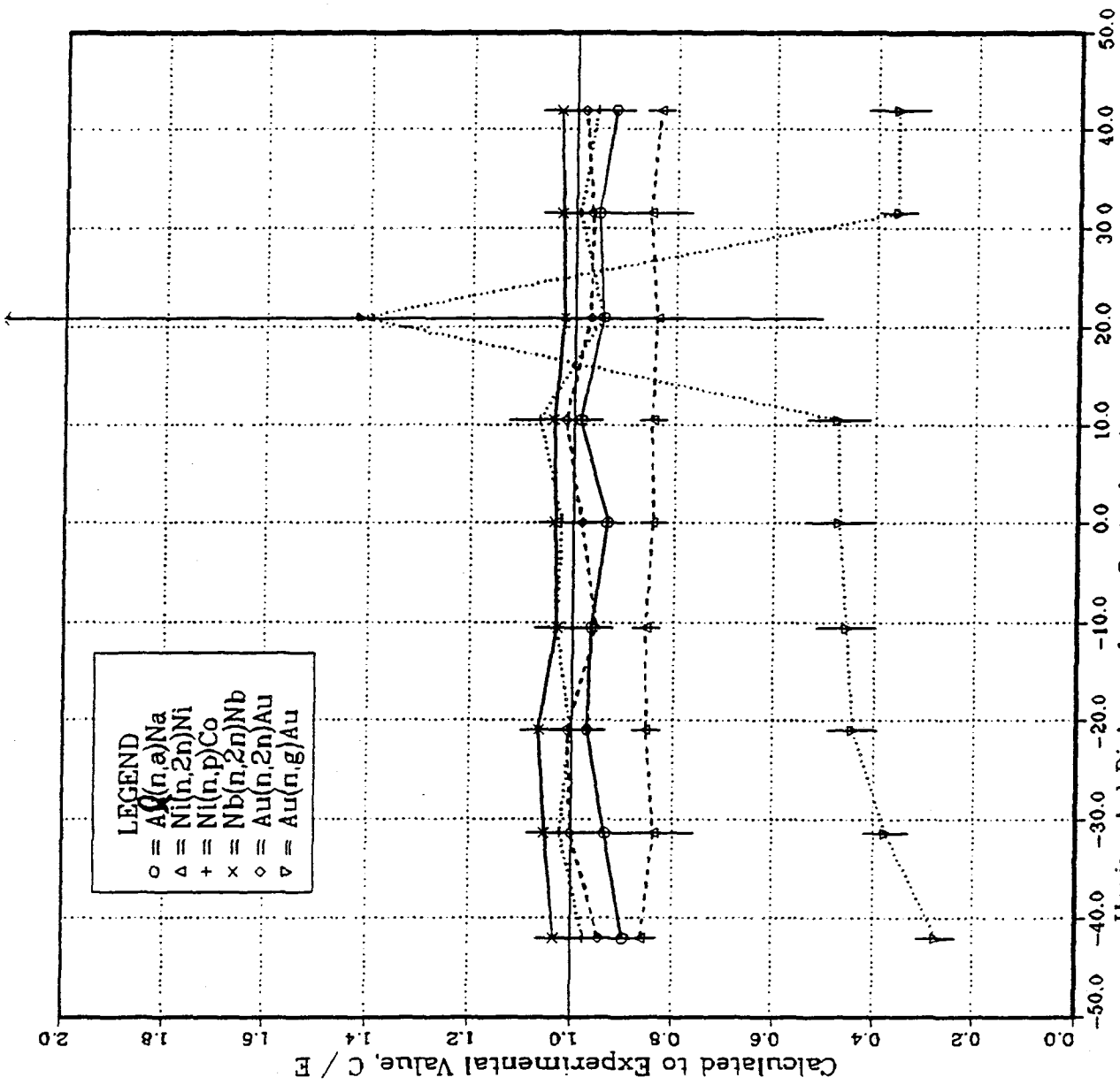

Fig. III.7: Computed to Experimental Value of the Reaction Rates Measured by Foils for Phase IIA on Front Surface of Li_2O Assembly (REF System - Horizontal distribution)

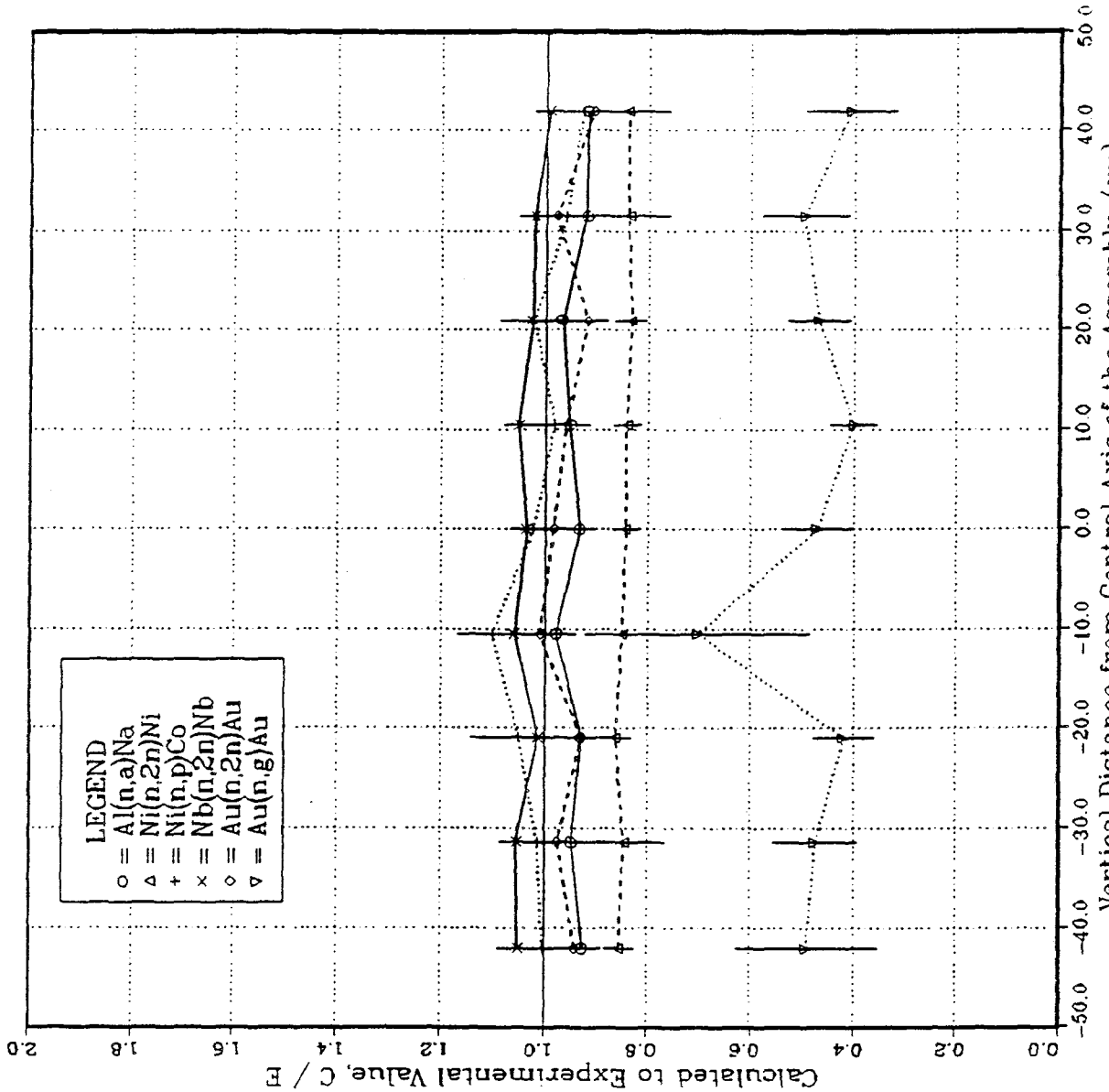

Fig. III.8: Computed to Experimental Values as the Reaction Rates Measured by Foils for Phase IIA on Front Surface of Li_2O Assembly (*REF* System - Vertical Distribution)

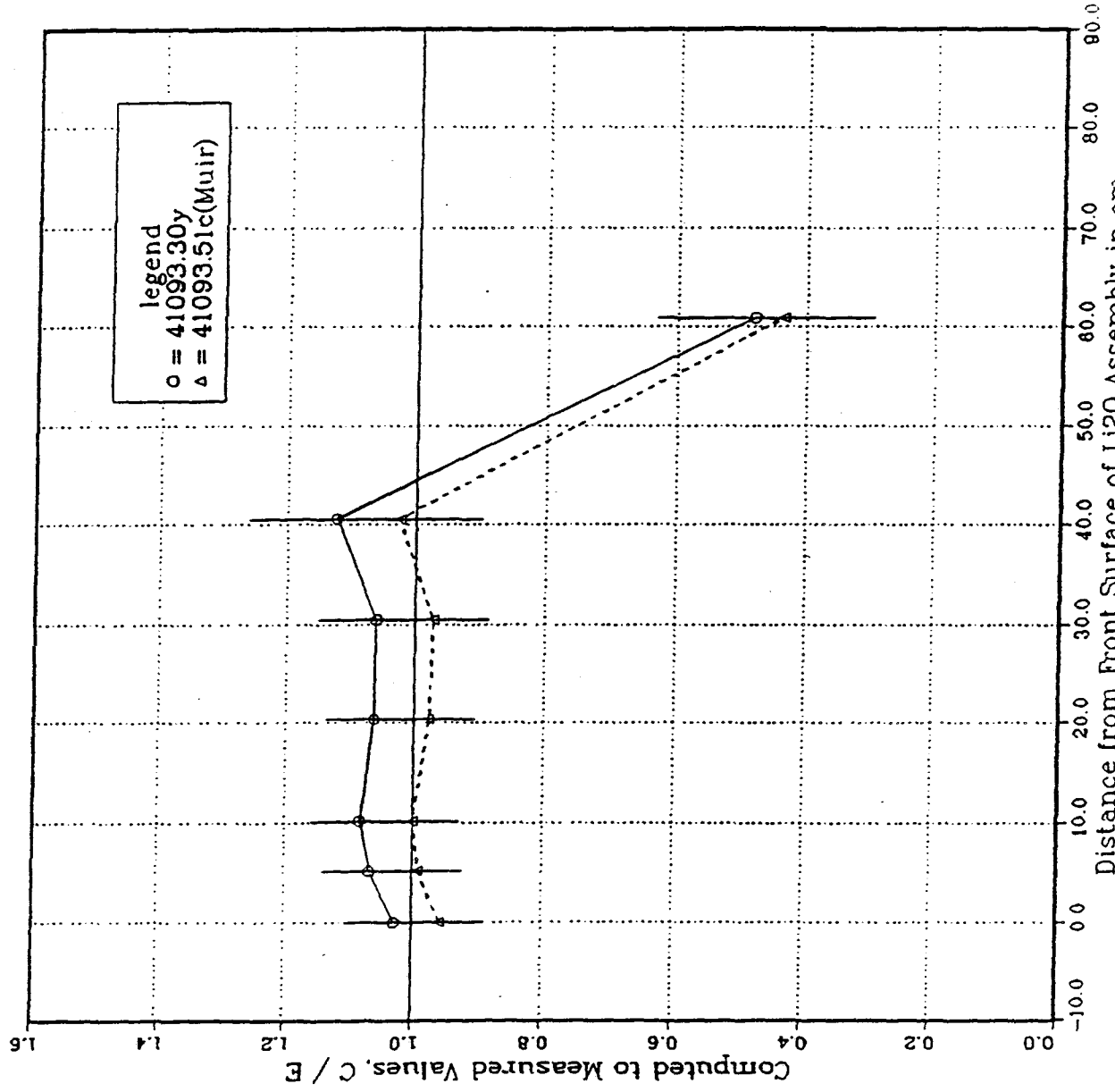

Fig. III.9: Comparison of Two C/E Values Obtained by Two Evaluations for $^{93}Nb(n,2n)^{92m}Nb$ Cross-Section (REF System - Phase IIA - MCNP Calculation)

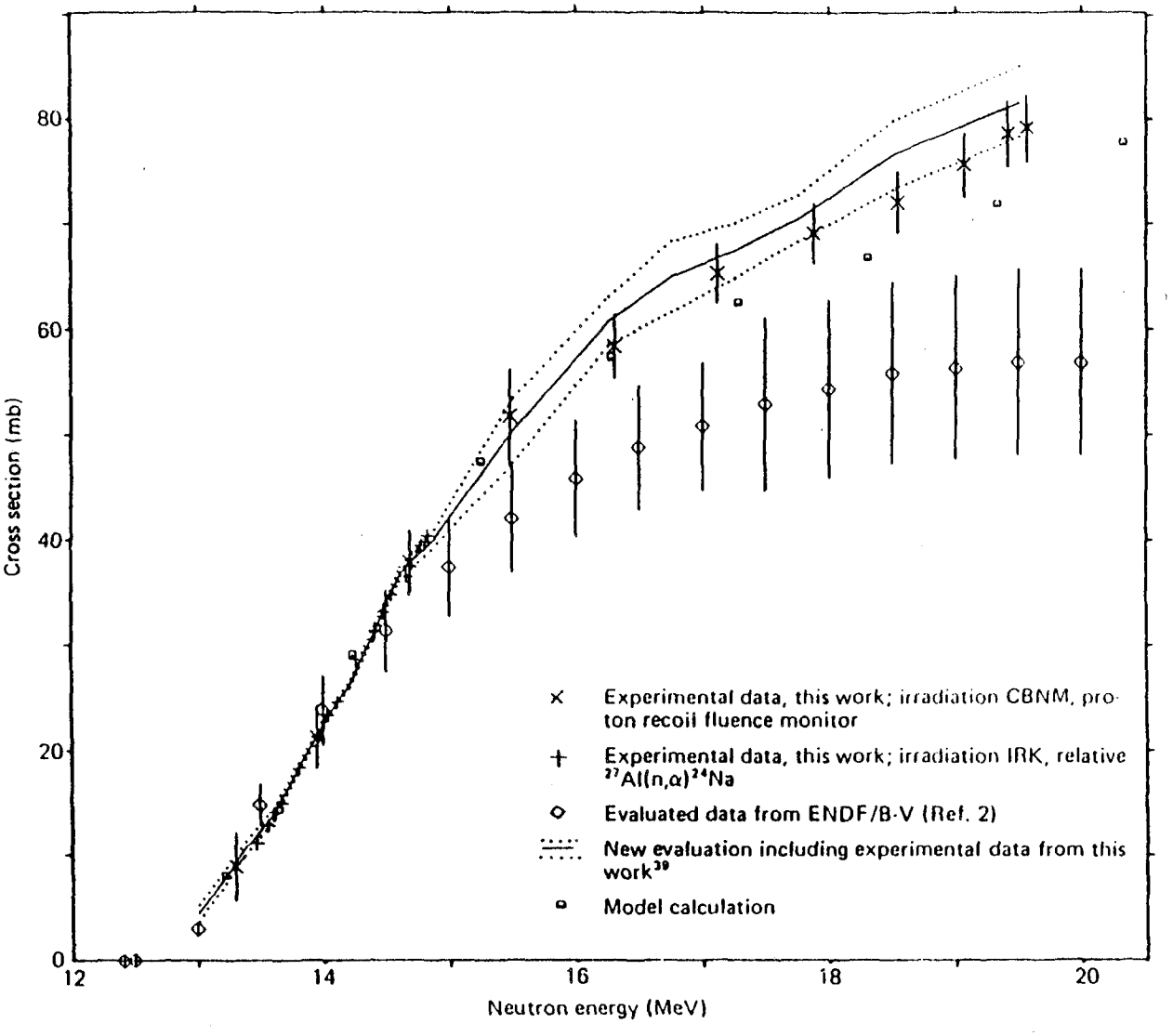

Fig. III.10: Measured $^{58}Ni(n,2n)^{57}Ni$ Cross-Sections and Evaluation Based on New Data as Compared with the Results from the Model Calculations and the ENDF/B-V Evaluation. [See Ref (31)]

It can be noticed from Figs. III.7 and III.8, that the C/E values for $^{197}Au(n,\gamma)$ reactions are always less than unity at all locations by as large as 60% (except at one location where the statistical error from the Monte Carlo calculation is large.) The $^{197}Au(n,\gamma)$ reaction is sensitive to the low-energy neutrons reflected by the Li_2CO_3 enclosure walls. Epoxy paint (rich in its hydrogen contents) was used to cover the Li_2CO_3 bricks, and the way this paint was modeled in the calculations will noticeably affect the prediction accuracy of those reactions that are sensitive to low-energy neutrons. In the Monte Carlo model used in this particular calculation, the epoxy coating on the Li_2CO_3 bricks was not included, though it was included in subsequent calculations (see Section IV.).

Neutron Spectrum in the cavity that surrounds the D-T neutron source was also measured by NE213 spectrometer in the energy range above 1MeV and by proton recoil counters (PRC) in the energy range 1 KeV - 1 MeV. Figs. III.11 to III.15 show a comparison between the calculated spectrum (by MCNP) and the measured one (by NE213) in the energy range above 1 MeV in the reference system. The coordinates used indicate that the intercomparison was made at a distance of 5 cm in front of the Li_2O assembly and at several locations in the horizontal direction. As shown, the 14 MeV peak is underpredicted at all locations, but on the average, the integrated spectrum between 1 - 12 MeV is overestimated. The impact of this overestimation is reflected and consistent with the foil activation results shown in Figs III.2 to III.8.

III.2.2. Phase IIB

Spectrum measurements by NE213 and PRC were also carried out in Phase IIB at the front of the test assembly. In addition, $^{93}Nb(n,2n)^{93m}Nb$ reaction rate was measured at the outer surface of the first wall in the Be-front with FW(BEFWFW) system.

Fig. III.16 shows three cross-sectional locations where the $^{93}Nb(n,2n)$ reactions were measured in the BEFWFW system (cross-sections A-A, B-B, and C-C). Cross-section A-A is at the backward location behind the RNT while both cross-sections B-B and C-C are at the front of the RNT.

The C/E values for $^{93}Nb(n,2n)^{93m}Nb$ reactions are shown in Fig. III.17,a,b, and c at cross-sections A-A, B-B, and C-C, respectively. (Note: the C/E values shown are at selected locations; more measurements were taken at other locations, denoted by circled

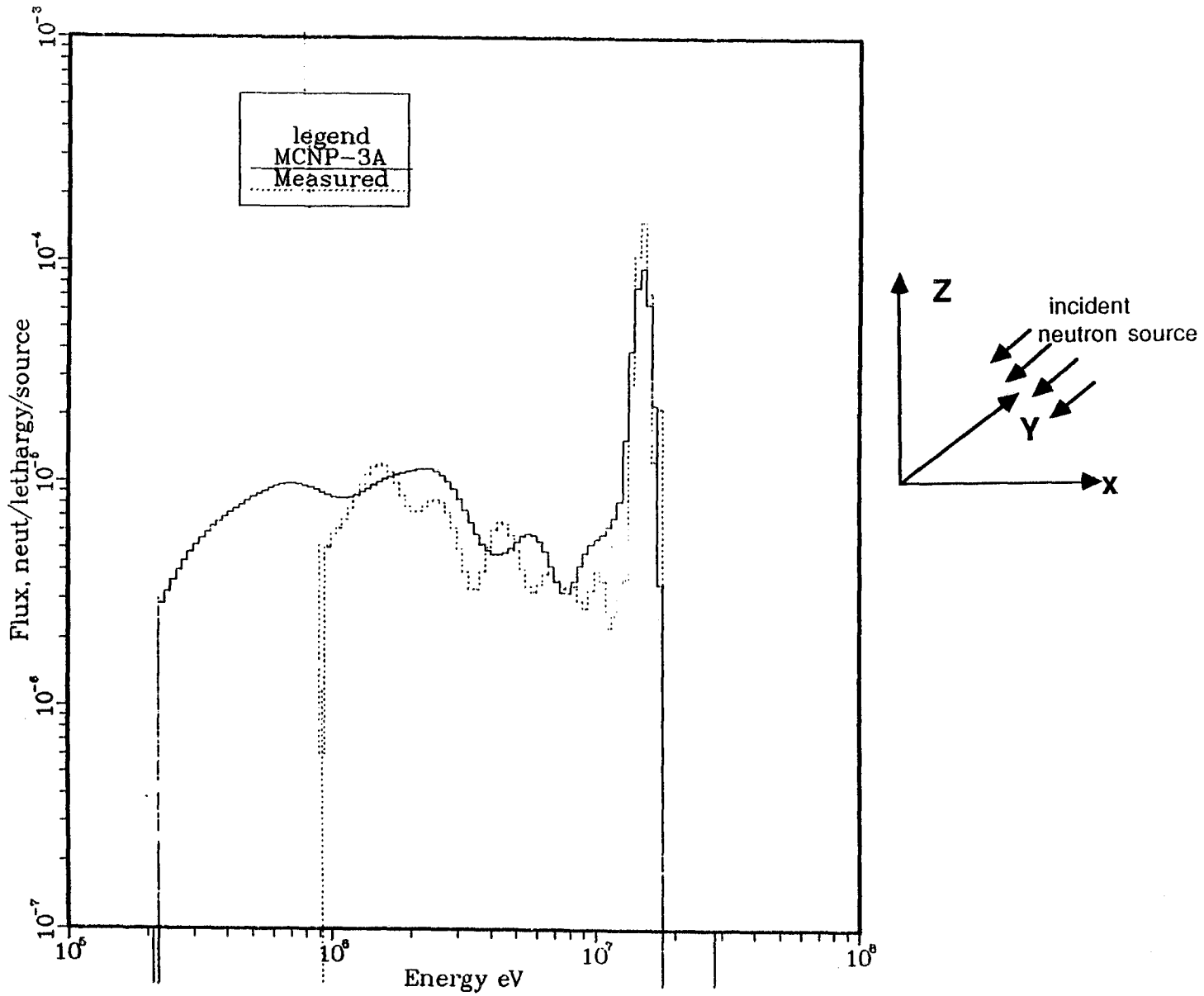

Fig.III.11: Measured and Calculated Neutron Flux at Position (0,5,0)

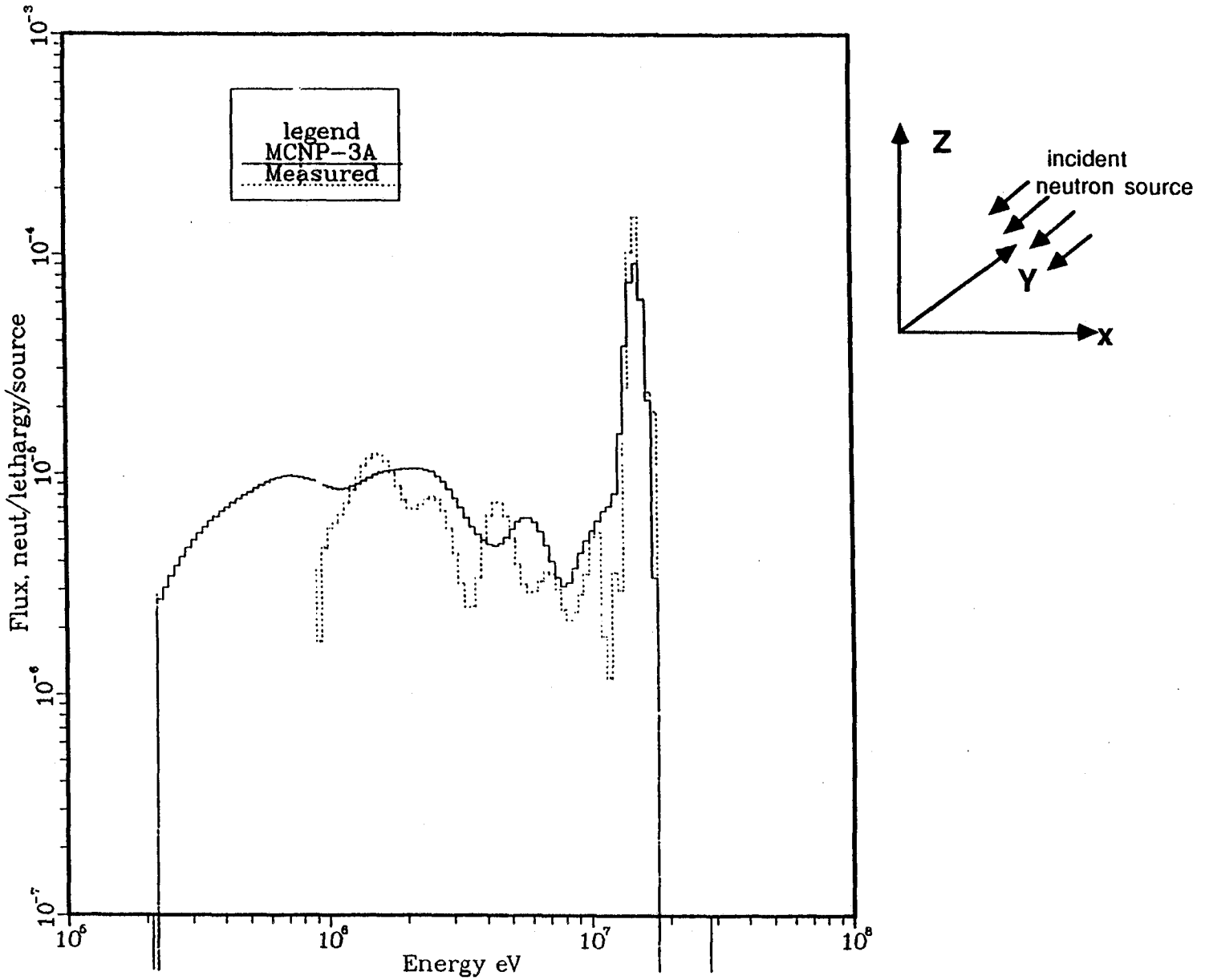

Fig. III.12: Measured and Calculated Neutron Flux at Position (10,5,0)

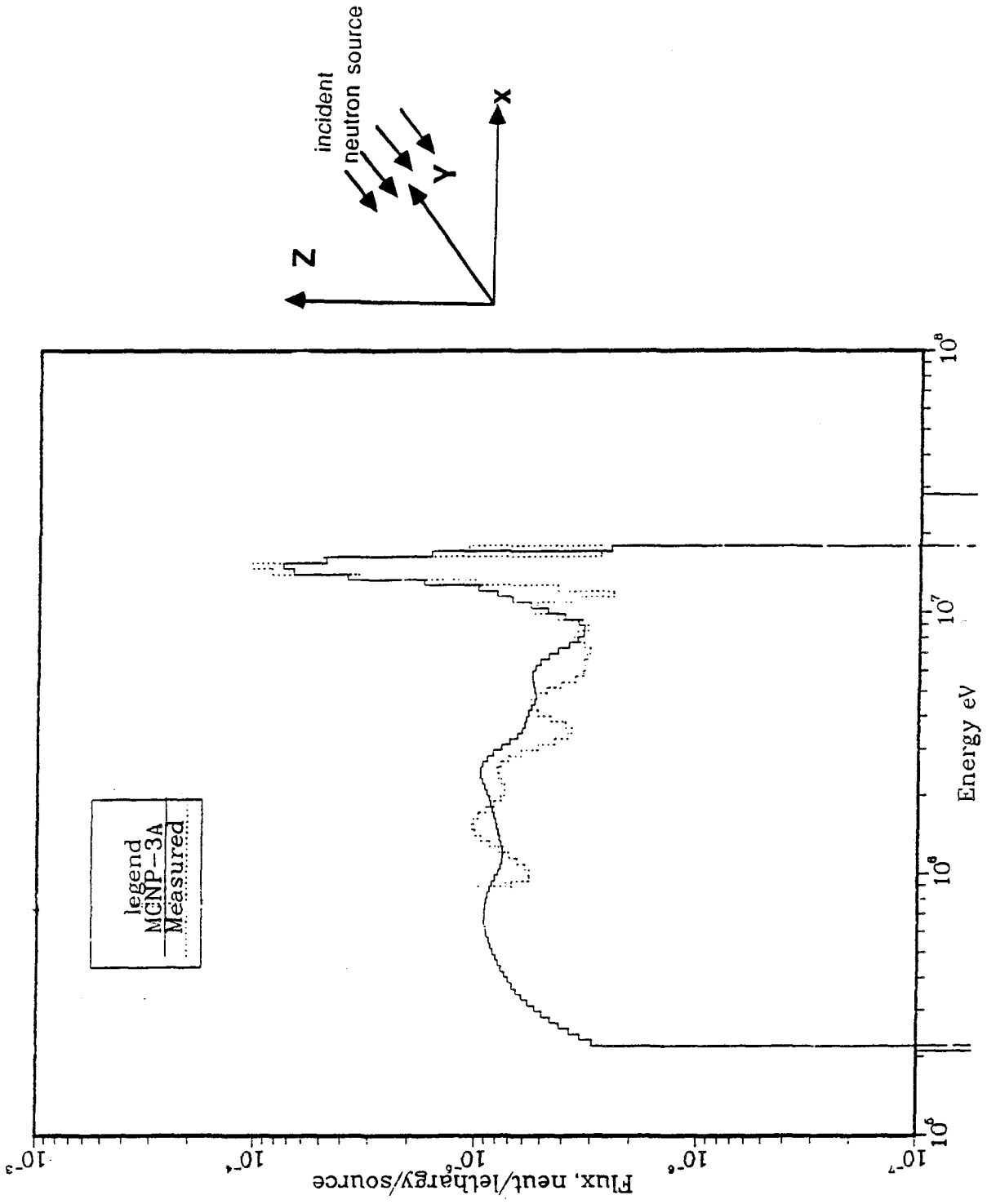

Fig. III.13: Measured and Calculated Neutron Flux at Position (30,5,0)

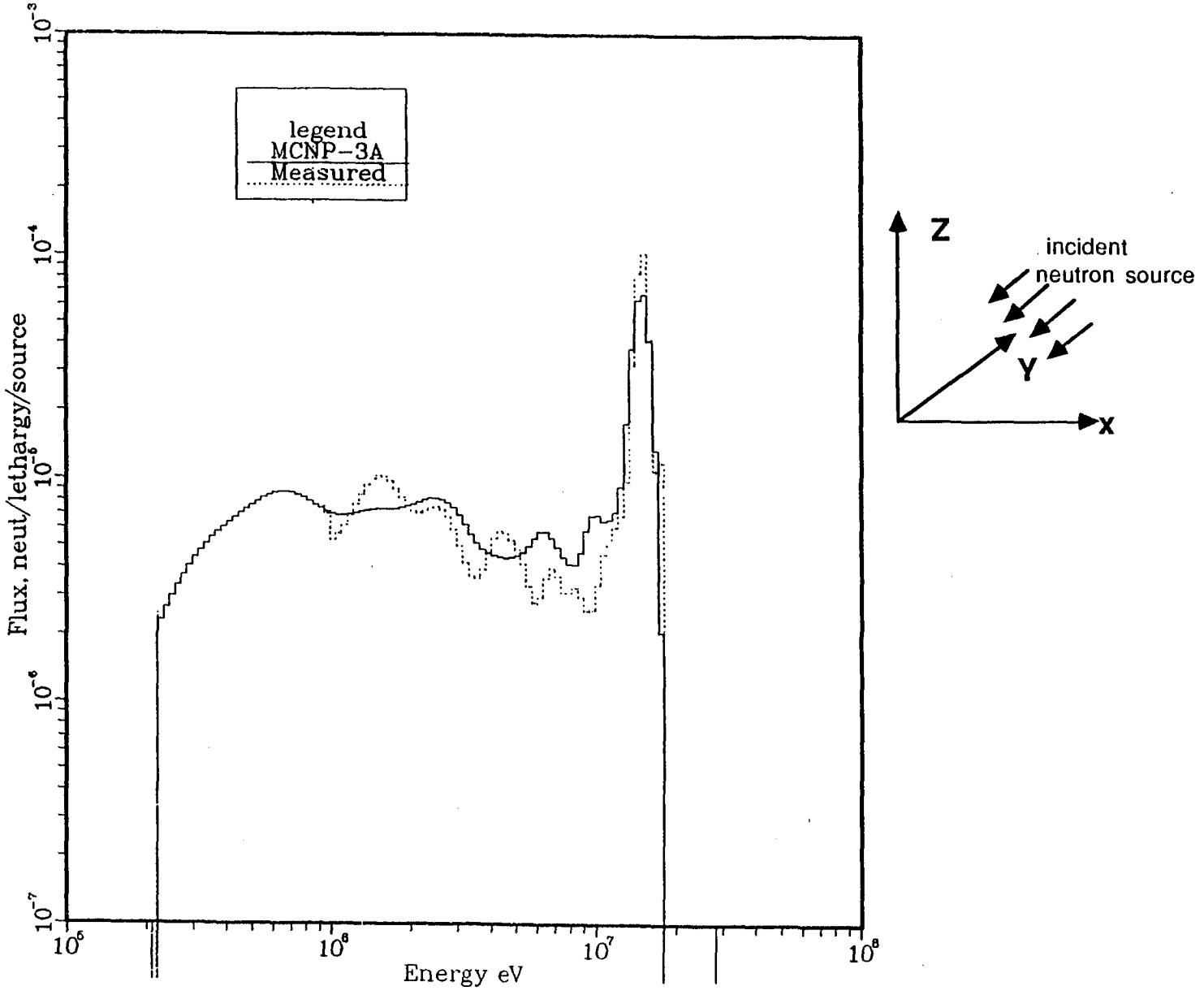

Fig. III.14: Measured and Calculated Neutron Flux at Position (40,5,10)

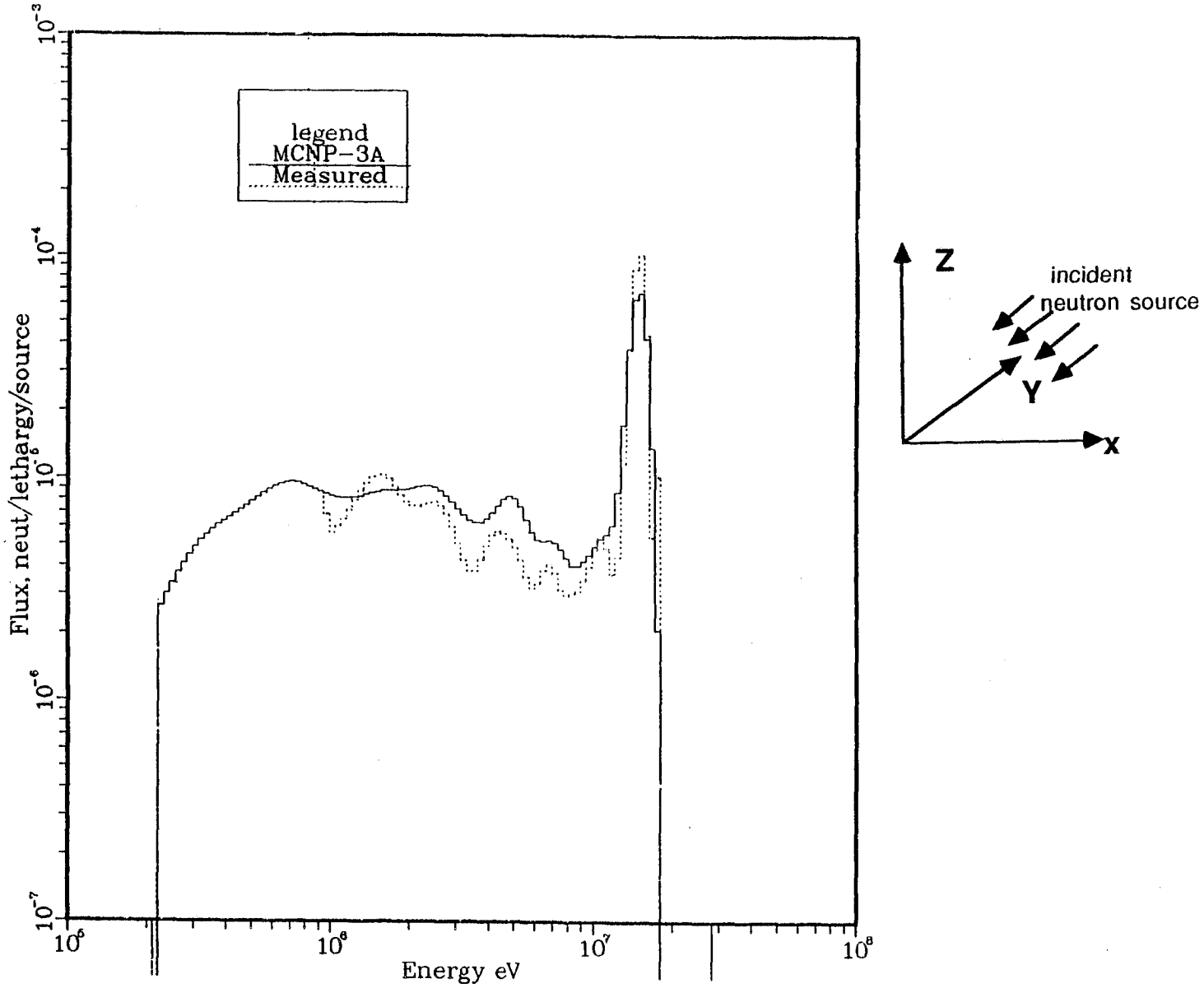

Fig. III.15: Measured and Calculated Neutron Flux at Position (-30,5,0).

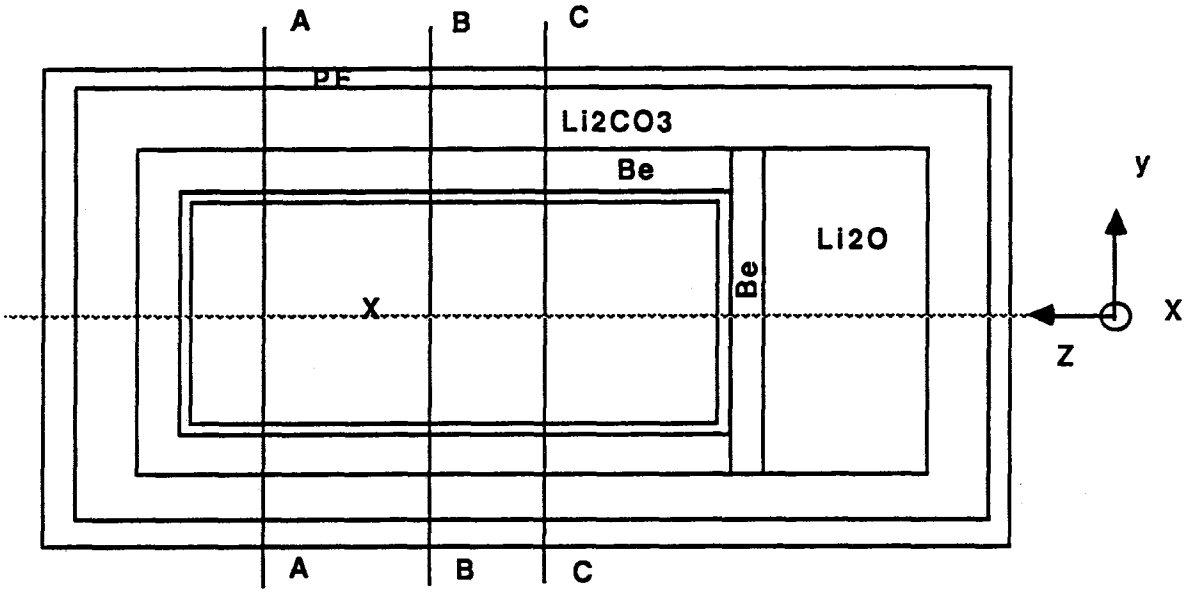

Fig. III.16: Side View of Phase IIB Be-Front with First Wall Experiment

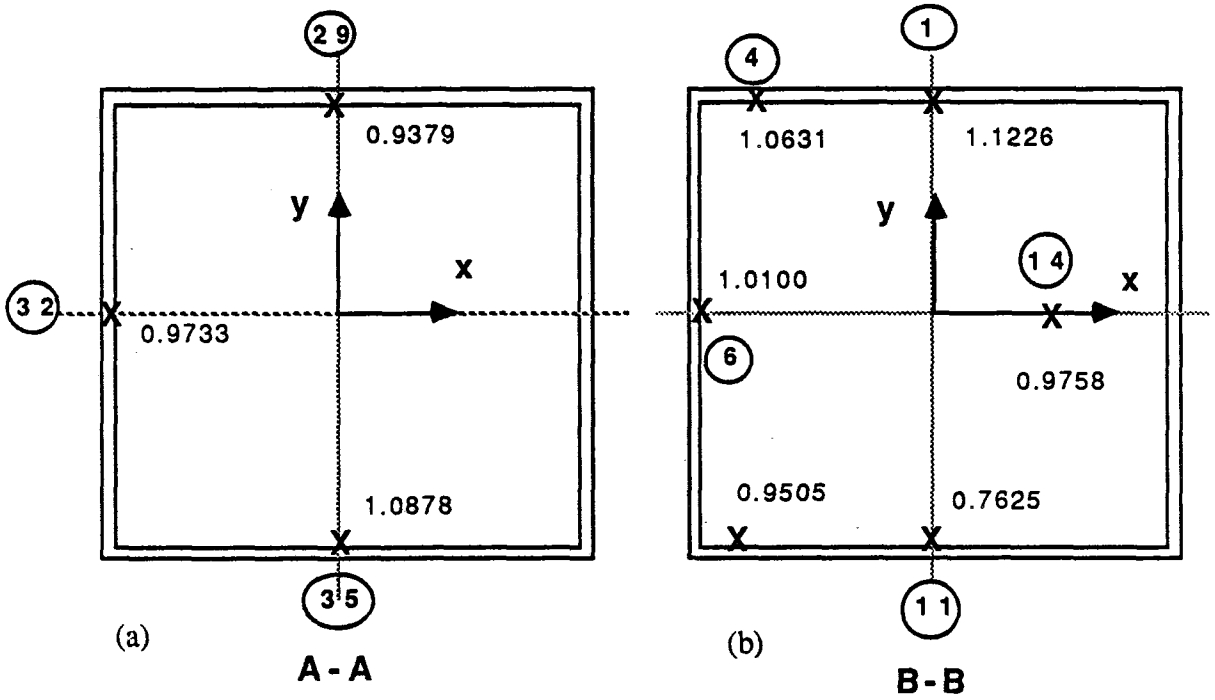

Fig. III.17: Calculated to Measured Values (C/E) of $^{93}Nb(n,2n)^{92m}Nb$ Reaction Rate at Cross-Section A-A, B-B, and C-C (Be-Front w/ FW-BEFWFW)

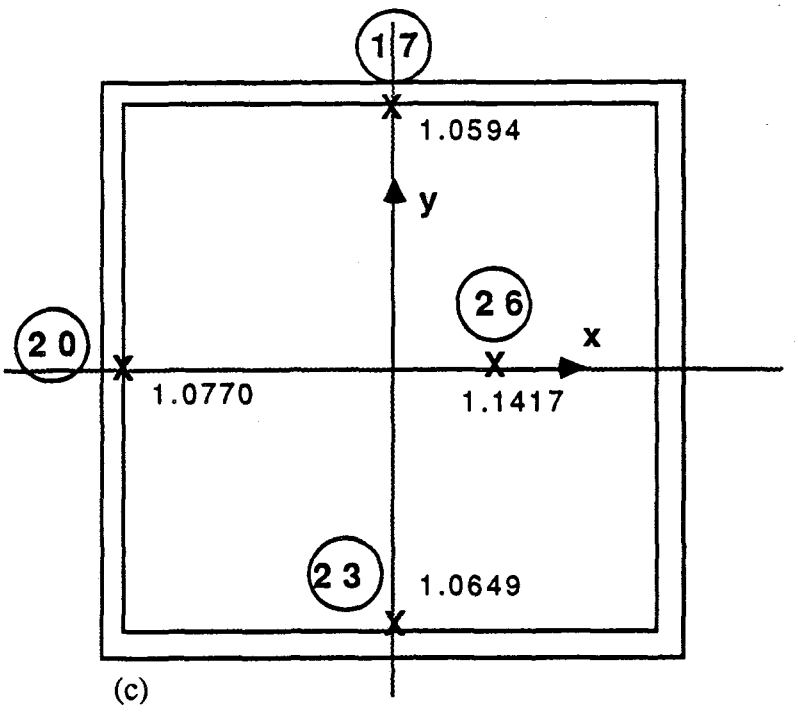

Fig. III.17: Calculated to Measured Values (C/E) of $^{93}Nb(n,2n)^{92m}Nb$ Reaction Rate at Cross-Section A-A, B-B, and C-C (Be-Front w/ FW-BEFWFW)

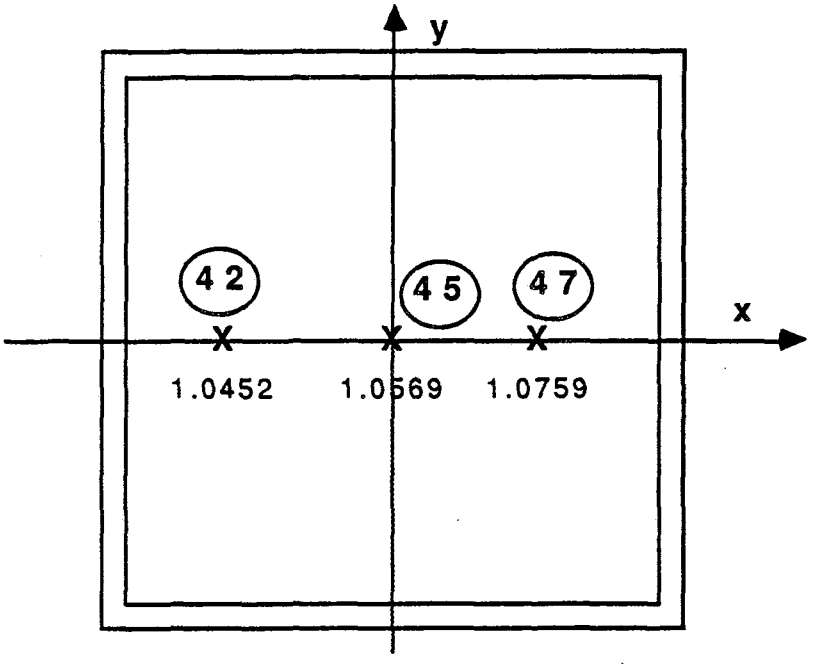

Fig. III.18: Calculated to Measured Values (C/E) of $^{93}Nb(n,2n)^{92m}Nb$ Reaction Rate at the Front Surface of the Test Assembly (Be-Front W/ FW-BEFWFW)

numbers.) At cross-section A-A, the values are lower that unity by 2 - 6% (except at few locations at the bottom and the right-hand side of the cross-section). At the cross-section B-B, the C/E values are larger than unity at locations, 1, 4, and 6 but below unity at locations 8, 11, and 14. Since the cross-section B-B is close to the spatial point where the D^+ beam interacts with the T-Ti target, the prediction accuracy for the threshold reaction $^{93}Nb(n,2n)$ depends on the degree of details used in modeling the RNT target. Newly-born D-T neutrons could suffer several collisions with other parts of the target before reaching these close locations of the cross-section B-B. However, the prediction accuracy of the $^{93}Nb(n,2n)$ reactions at the forward directions is better as shown in Fig. III.17-c where the C/E values are improved (except for few locations.) At the front surface of the test assembly the C/E values are within 4 - 7% as shown in Fig. III.18.

Fig. III-19 shows a comparison between the neutron spectrum measured by NE213 (above 1MeV) and the calculated spectrum by DOT 5.1. The comparison is made at 5 cm distance from the front surface of the test assembly in the BEFWF system. The 14 MeV peak is slightly larger, as predicted by the calculation. Also, the measured spectrum in the energy range 3 - 13 MeV is generally lower than the calculated values with several peaks and dips that could be attributed to the unfolding method used to derive the measured spectrum by the NE213 method. Fig. III.20 shows the comparison to the NE213 and PRC measurements in the energy range above few KeV. There are several structures that appear in the calculated spectrum in the energy range of several KeV - 30 KeV. This could be attributed to the fact that the cross-section library used in the calculations (MATXS6 library) does not account for the iron self-shielding effect but the prediction of the spectrum trend is reasonable.

Since beryllium is used as a liner in Phase IIB, the low-energy component of the incident neutron spectrum to the test assembly is appreciable in comparison to Phase IIA. No experimental verification of this component (below several KeV) is possible by using the NE213 and/or the PRC counters.

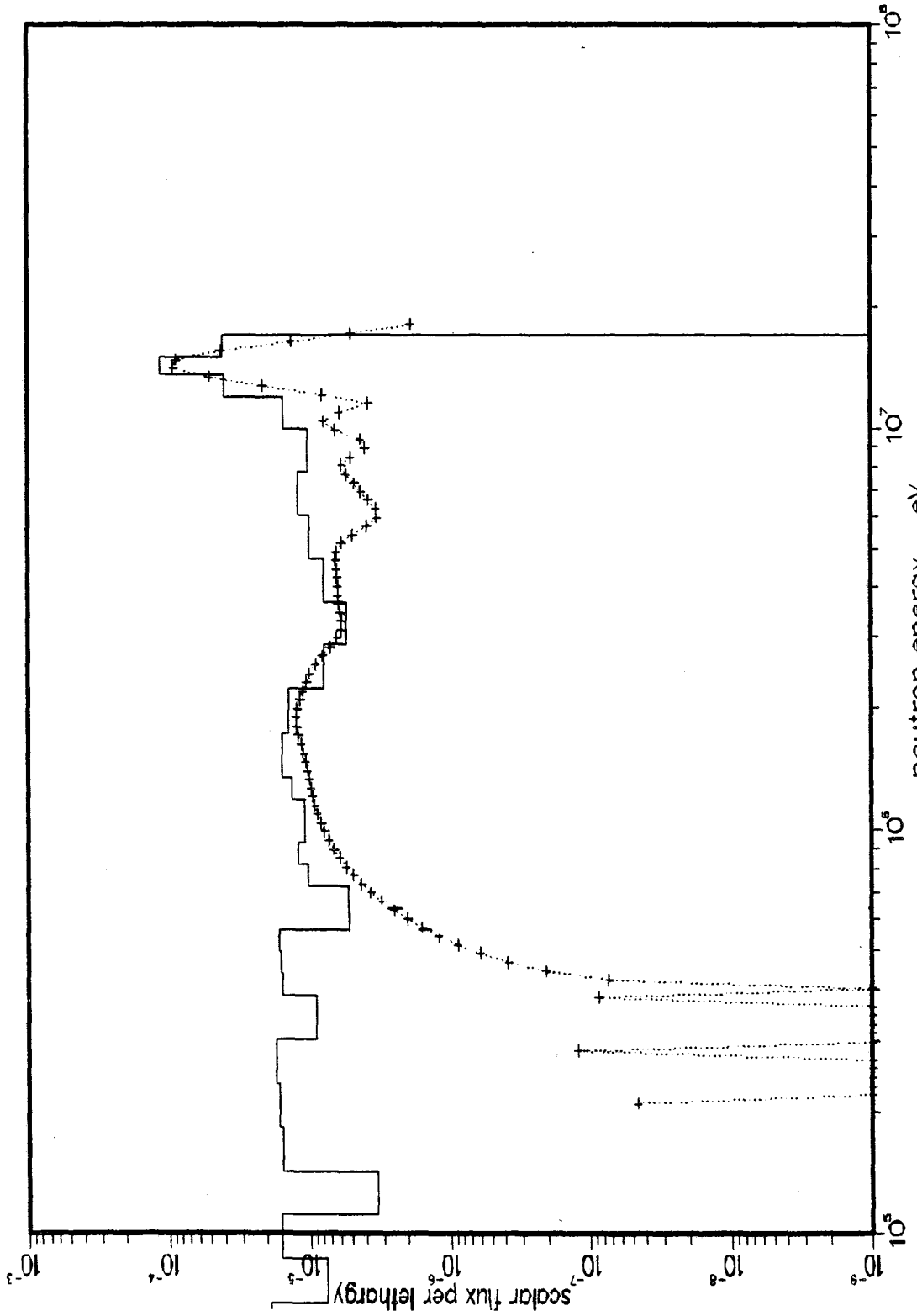

Fig. III.19: Calculated (Solid Line - DOT) and Measured (NE213) Spectrum at Z = -5 cm in the BEFWFW System of Phase IIB

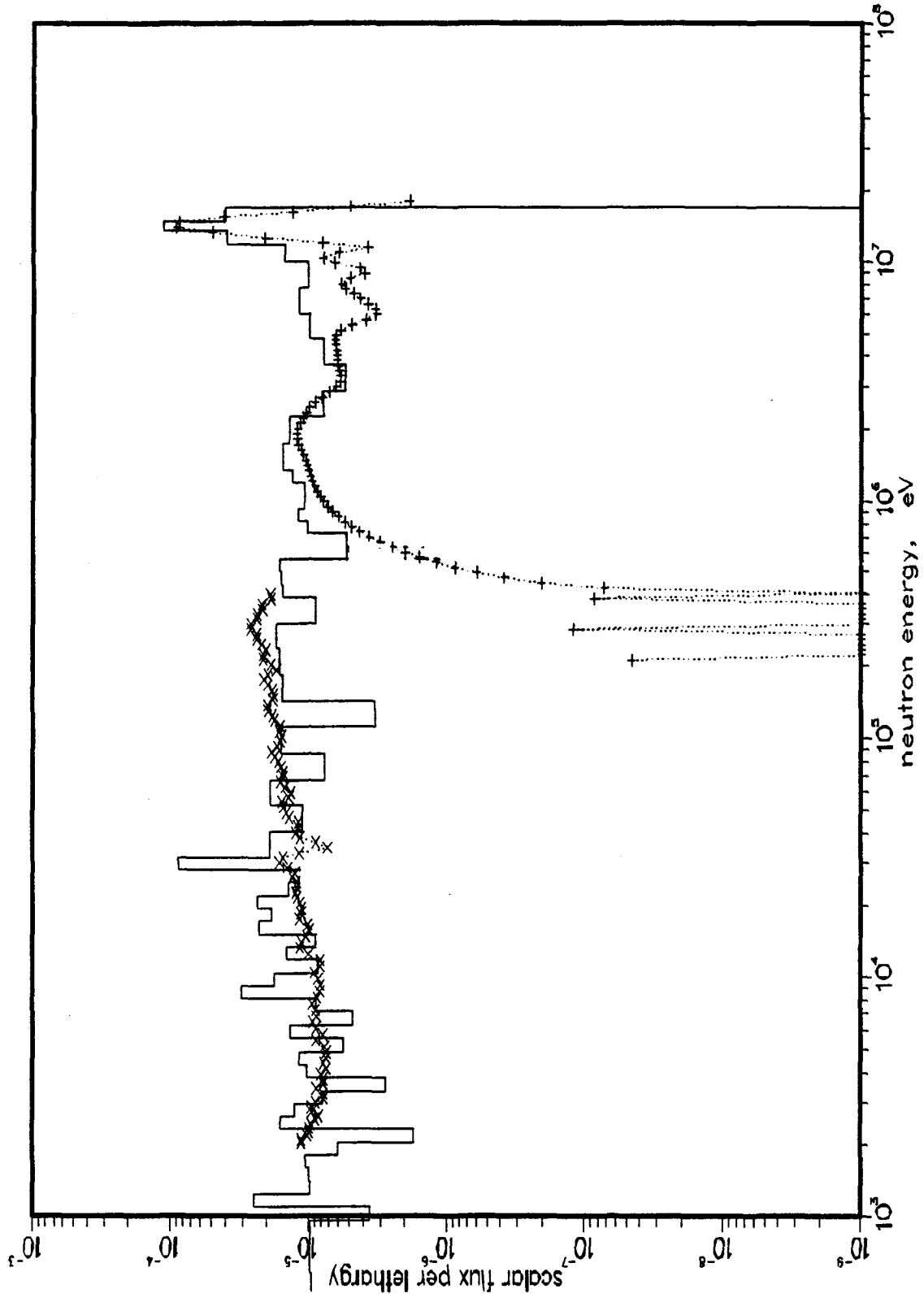

Fig. III.20: Calculated (Solid Line - DOT) and Measured (NE213-PRC) Spectrum at Z = 5 cm in the BEFWFW System of Phase IIB

IV. Analysis of Tritium Production Rate

IV.1 Introduction

As was discussed in Section I, the emphasis of the collaborative program in Phase IIA and IIB was placed on estimating the uncertainty involved in predicting local tritium production rate (TPR), both from ^6Li and ^7Li. The estimated uncertainty is used to infer the uncertainty in tritium breeding ratio (TBR) in a fusion blanket that utilizes Li_2O breeding material provided the number of the selected locations where measurements are performed are large enough and scattered everywhere inside the breeding material. Since the processing of the measurement data for a numerous number of locations is impractical, the TPR measurements were performed only throughout the central axis of the assembly (inside the central drawer) and at two radial directions (radial drawers), as discussed in Section I. Several measuring techniques were used to measure T_6 and T_7 for cross-checking among these techniques. On the other hand, measuring the TPR in the entire assembly at once is still under development. JAERI, however, has developed a technique for measuring the TPR in blocks of Li_2O of typical dimension of 5 cm x 5 cm x 5 cm (zonal TPR measurements). These measurements were performed in the central drawer ($\sim$ 5 cm x $\sim$ 5 cm x $\sim$ 60 cm) inside predesignated zones and were compared to the estimated integrated values in these zones. The prediction accuracy could, therefore, be used to better infer the uncertainty in the TBR.

The distribution of TPR (and other reaction rates) inside the test assembly is largely dependent on the incident neutron spectrum and its relative changes inside the assembly. Fig. IV.1 shows contours of the total neutron flux (per incident D-T neutron) inside the geometrical arrangement of the REF system (including the room walls) of Phase IIA. Fig. IV.2 shows further details of these contours inside the Li_2O and the Li_2CO_3 enclosure. As shown, the flux is slowly-varying in the radial direction inside the Li_2O assembly. The contours of the flux components in the energy ranges $E_n > 10$ MeV, 1.05 MeV $< E_n < 10$ MeV, and $E_n < 1.05$ MeV are shown in Figs. IV.3 to IV.5, respectively. These contours indicate that the variation in the neutron flux (and its several components) in the radial direction is small, and therefore, the prediction accuracy of the TPR (and other reactions) inside the central drawer in the axial direction will be a fairly good indicative of the prediction accuracy of these reactions everywhere inside the Li_2O assembly. Notice that the weak space-dependence of the C/E values of several reaction rates in the horizontal and vertical directions were observed in Figs. III.7 and III.8 where their curves are almost flat.

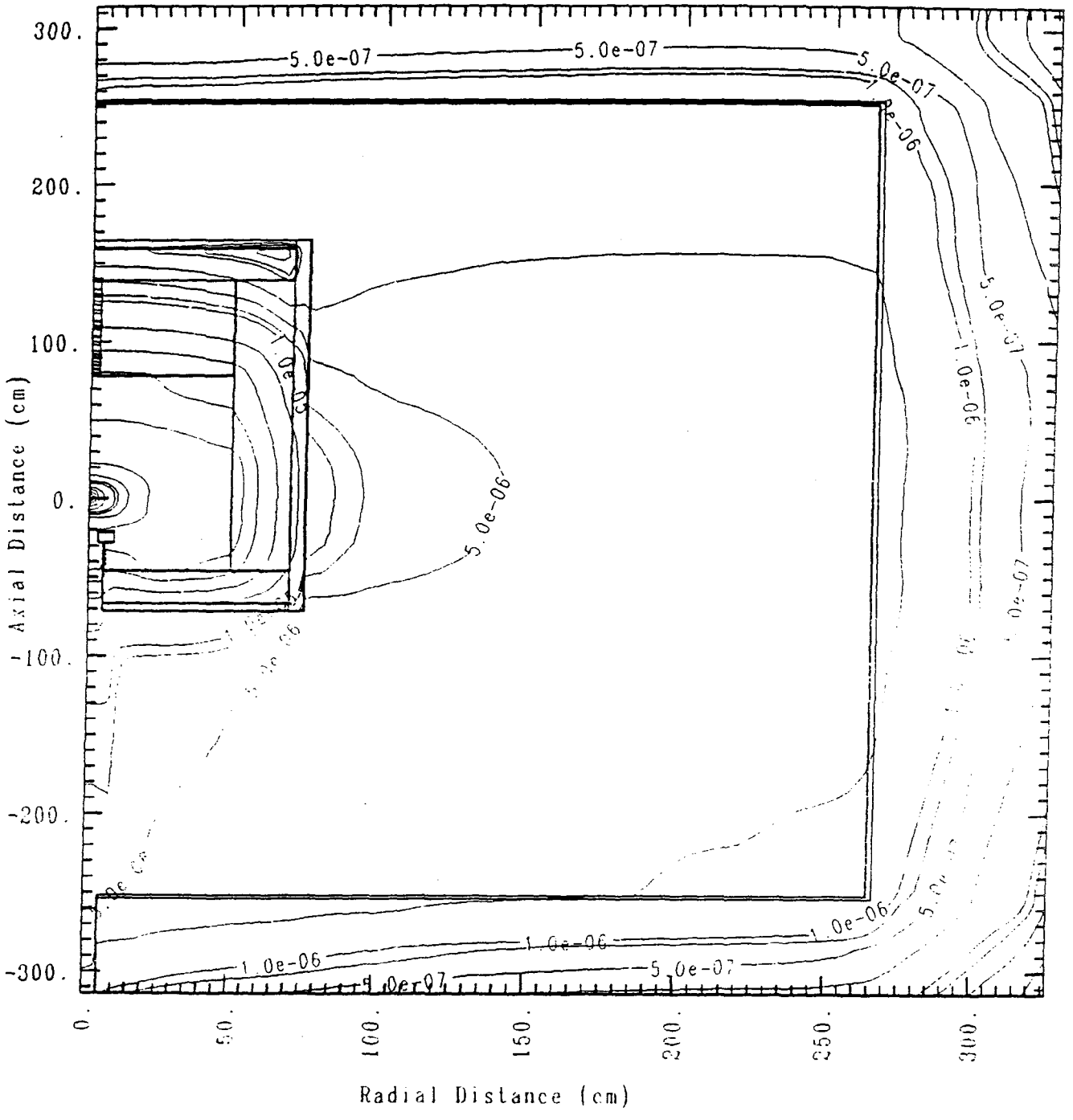

Fig. IV.1: Geometry and Total Flux Contours of Phase IIA Reference Experiment (Room Included)

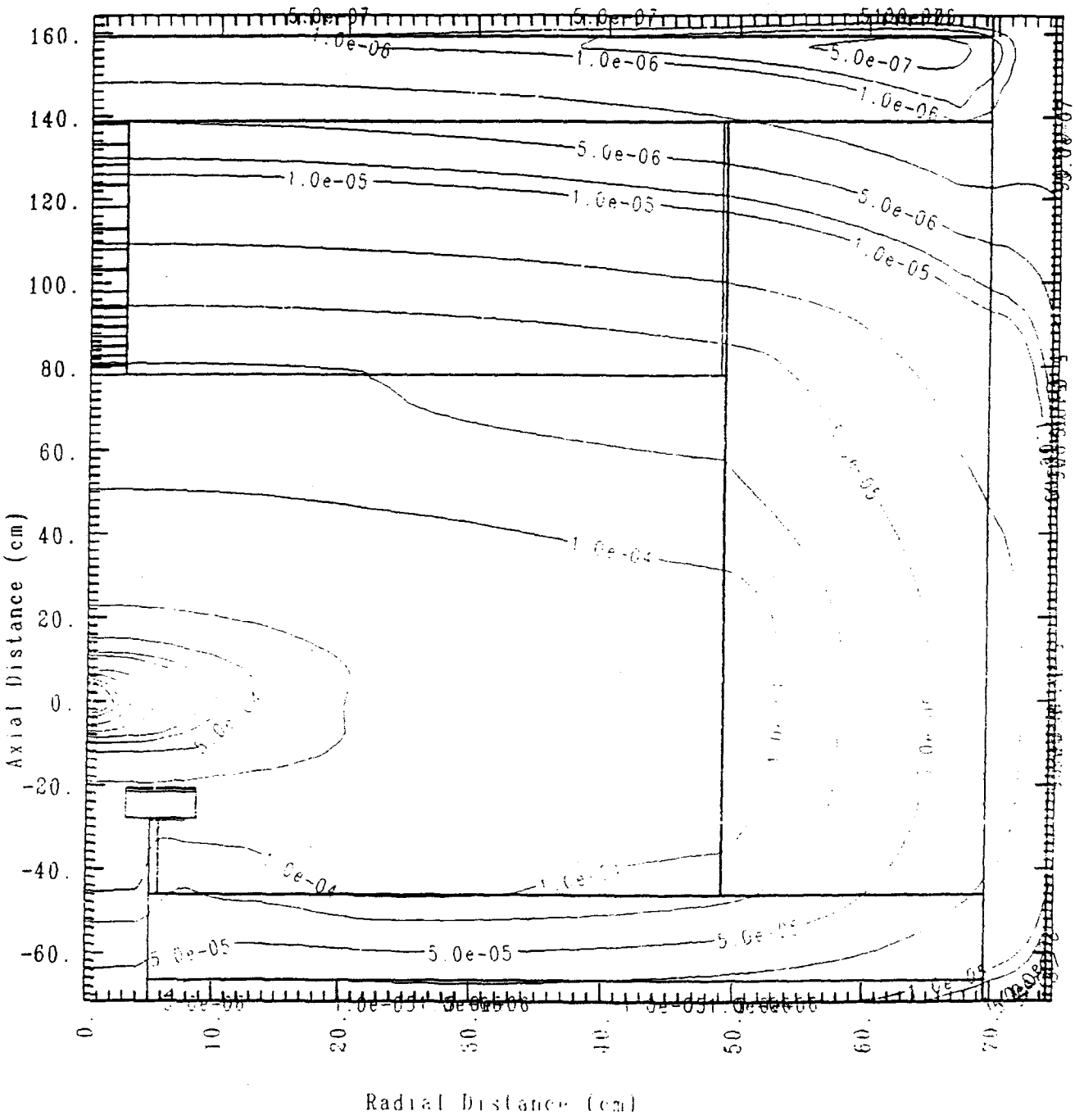

Fig. IV.2: Geometry and Total Flux Contours of Phase IIA Reference Experiment (Room Excluded)

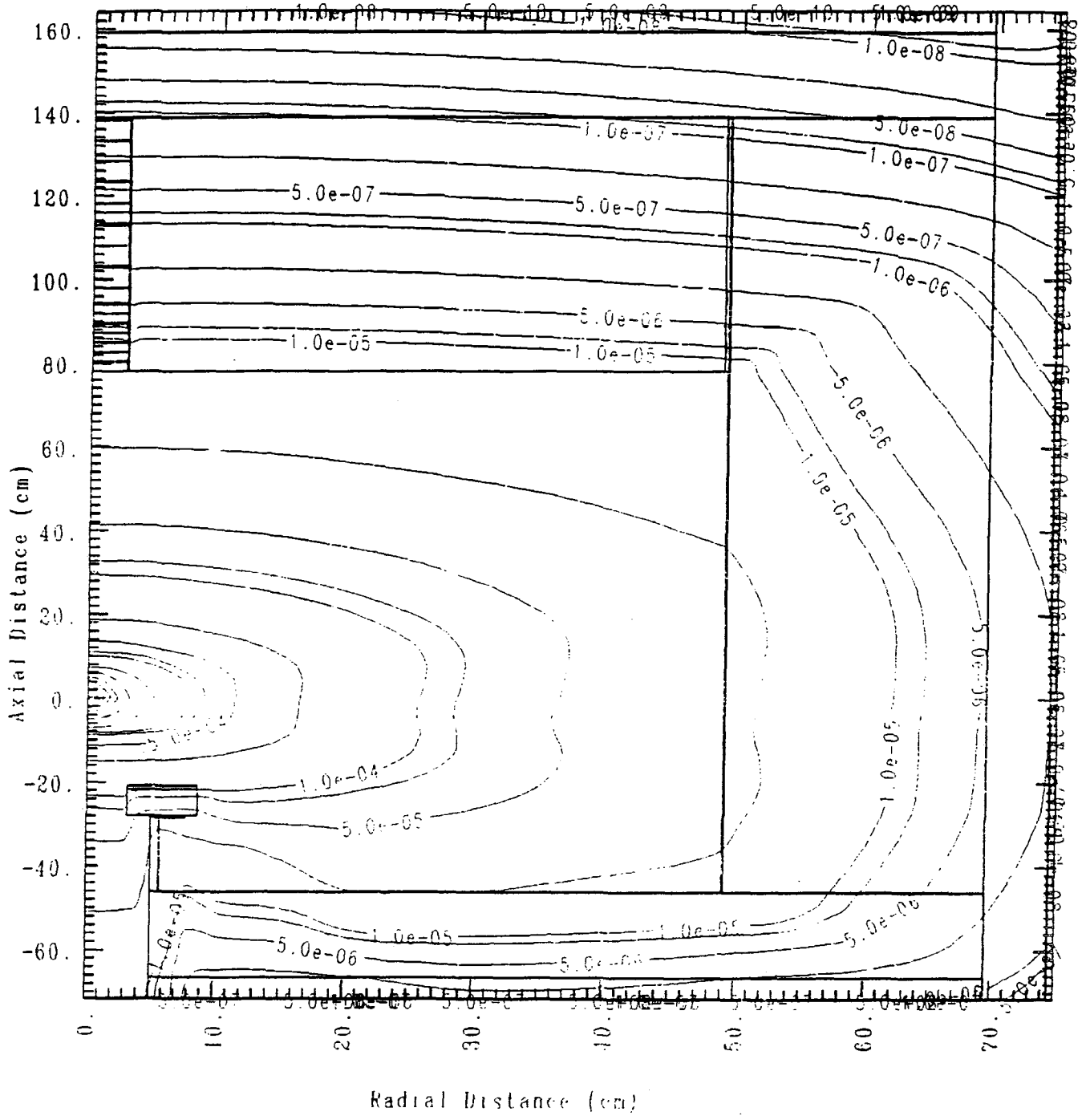

Fig. IV.3: Contours of Integrated Flux (En>10.0 MeV)
(Phase IIA - REF System)

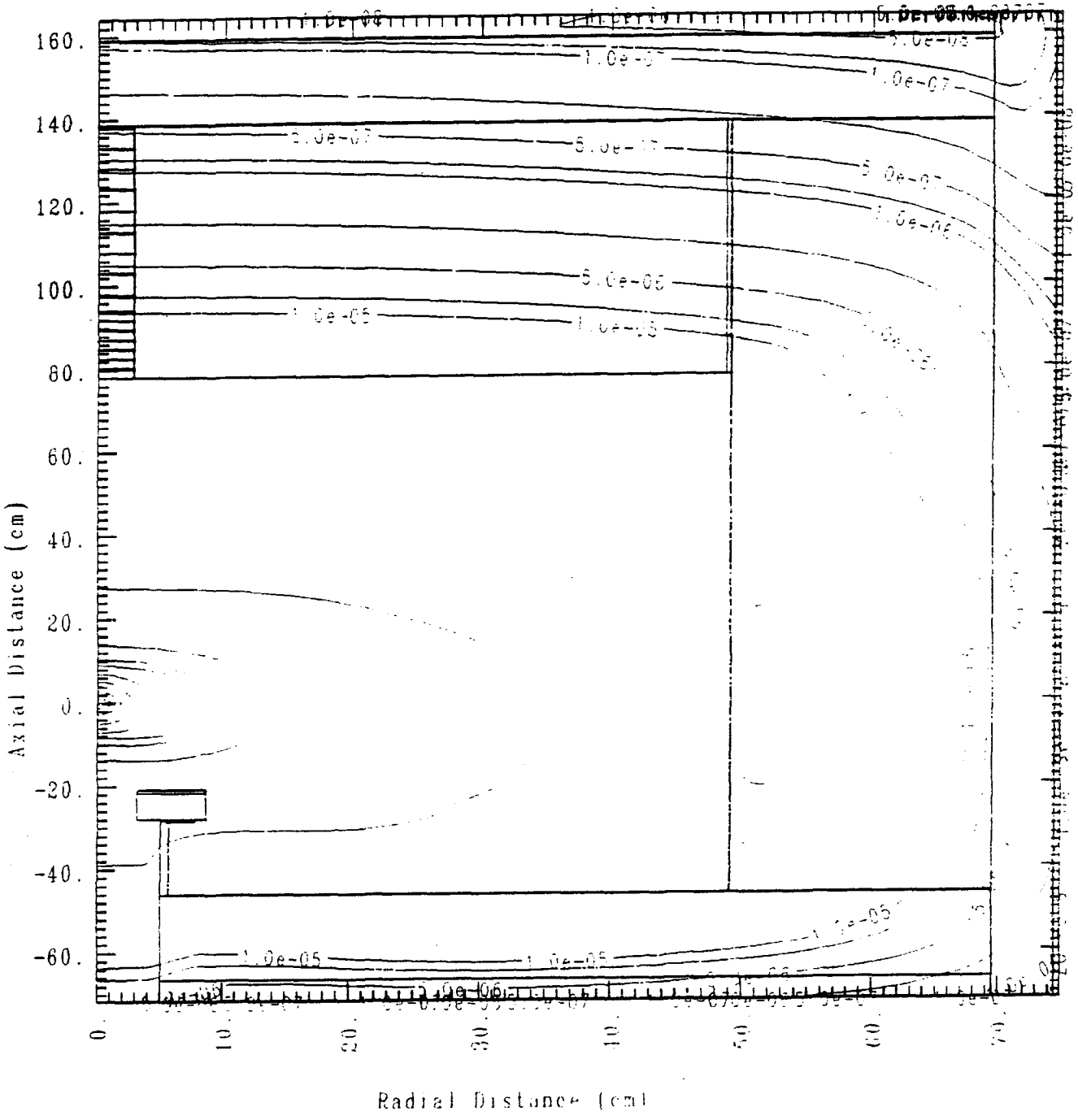

Fig. IV.4: Contours of Integrated Flux (1.01 MeV<En<10. MeV) (Phase IIA - REF System).

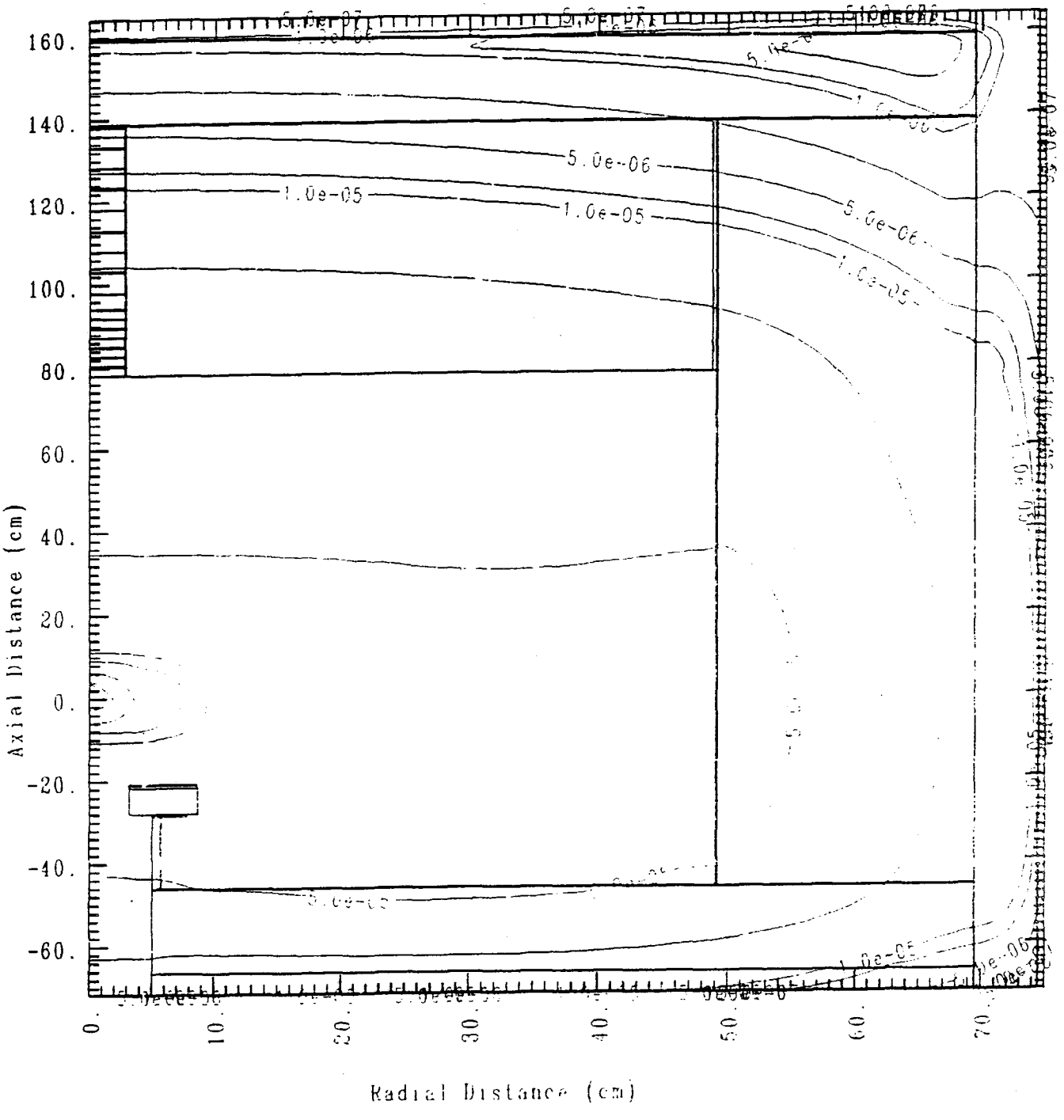

Fig. IV.5: Contours of Integrated Flux (En<1.01 MeV)
(Phase IIA- REF System)

IV.2 Phase IIA

The T_6 and T_7 profiles throughout the central axis of the test assembly are shown in Figs. IV.6 and IV.7, respectively for the REF, BEF, and BES systems of Phase IIA. These profiles were obtained through measurements by Li-glass detectors (for T_6) and by folding the spectrum measured by NE213 detectors with the $^7Li(n,n'\alpha)t$ cross-section of JENDL3-PR1 data.[32] As shown for the REF system, the decrease in T_7 in the axial direction is exponential while it is less steep for T6. The T_6 profiles start to increase steeply inside the Li_2CO_3 as one proceeds towards the outer boundaries where the effect of the slow-neutrons reflected by the room walls is noticeable. The T_6 values inside the Be layer in the BEF and BES systems are large due to the soft spectrum inside this layer but the T_7 profiles do not exhibit such large changes inside this layer.

(A) Tritium Production Rate from $^6Li(T_6)$

The effect of using beryllium as a neutron multiplier on T_6 profiles is that an enhancement occurs (by a factor of 2 - 3) in the local values at locations adjacent to the beryllium zone in both the BEF and BES systems in comparison to the reference system. However, no noticeable increase in T_6 is observed at deep locations. In addition, T_6 values measured in the beryllium region are noticeably large (a factor of 7.8, and 7.2 increase in the BES and BEF system, respectively) due to the fairly soft spectrum encountered inside the beryllium zone. This is shown in Fig. IV.8 where the changes in the T_6 profiles relative to the one found in the REF system are shown (as calculated by the DOT5.1 code). Fig. IV.9 shown the change in T_7 profiles resulting from including the Be layers relative to the T_7 profile of the REF system. As shown, while T6 is enhanced around the Be layer in the BEF and BES systems, T_7 profiles show large decrease in (by 10 - 20%) in the BEF system (due to slowing down the incident neutron spectrum through the $^9Be(n,2n)$ reactions; an adverse effect on the $^7Li(n,n'\alpha)t$ reactions) behind this layer and that decrease is less pronounced in the BES system. (There is slight increase in T_7 inside the Be layer due to the increase in neutron multiplication by the $^9Be(n,2n)$ reactions.)

The C/E values for the T6 in the REF system are shown in Figs. IV.10 to IV.12 for the axial drawer, front, and rear drawer, respectively, where the calculations are performed by MCNP and DOT5.1, independently. As shown, T_6 is generally overestimated by the codes and libraries used along the central axis of the Li_2O assembly where Li-glass detectors were used in the measurements. The C/E values range from 0.9 to 1.25 but in the

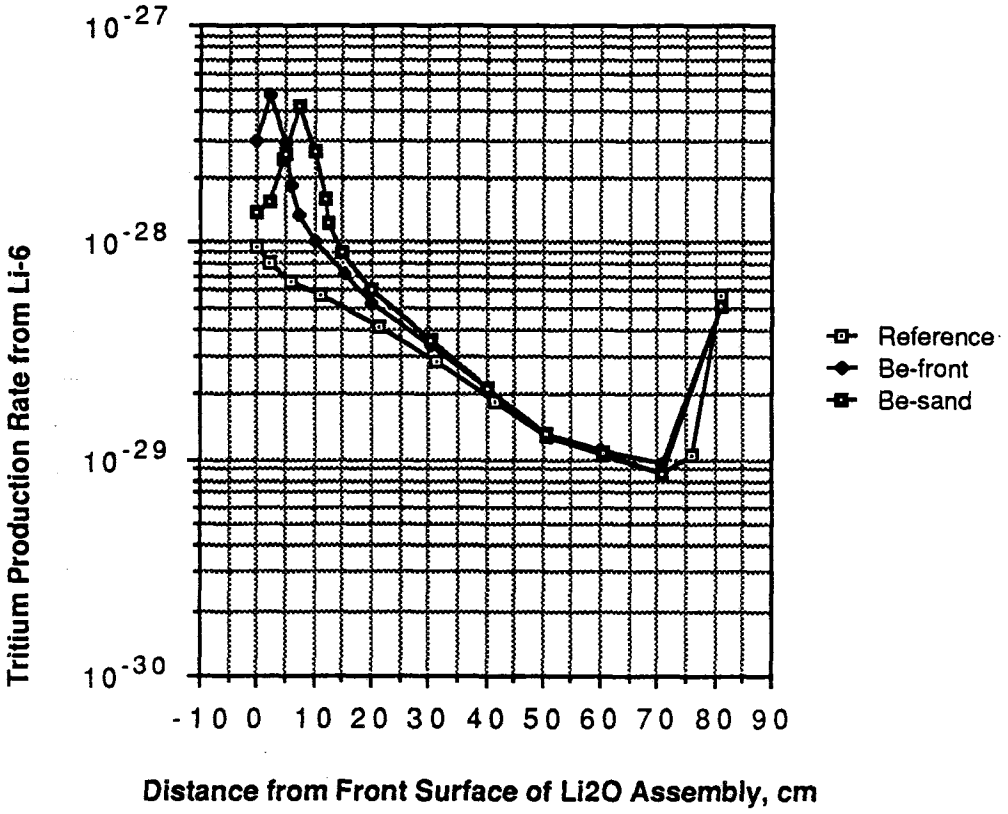

Fig. IV.6: Comparison of Measured T_6 for the Three Systems of Phase IIA

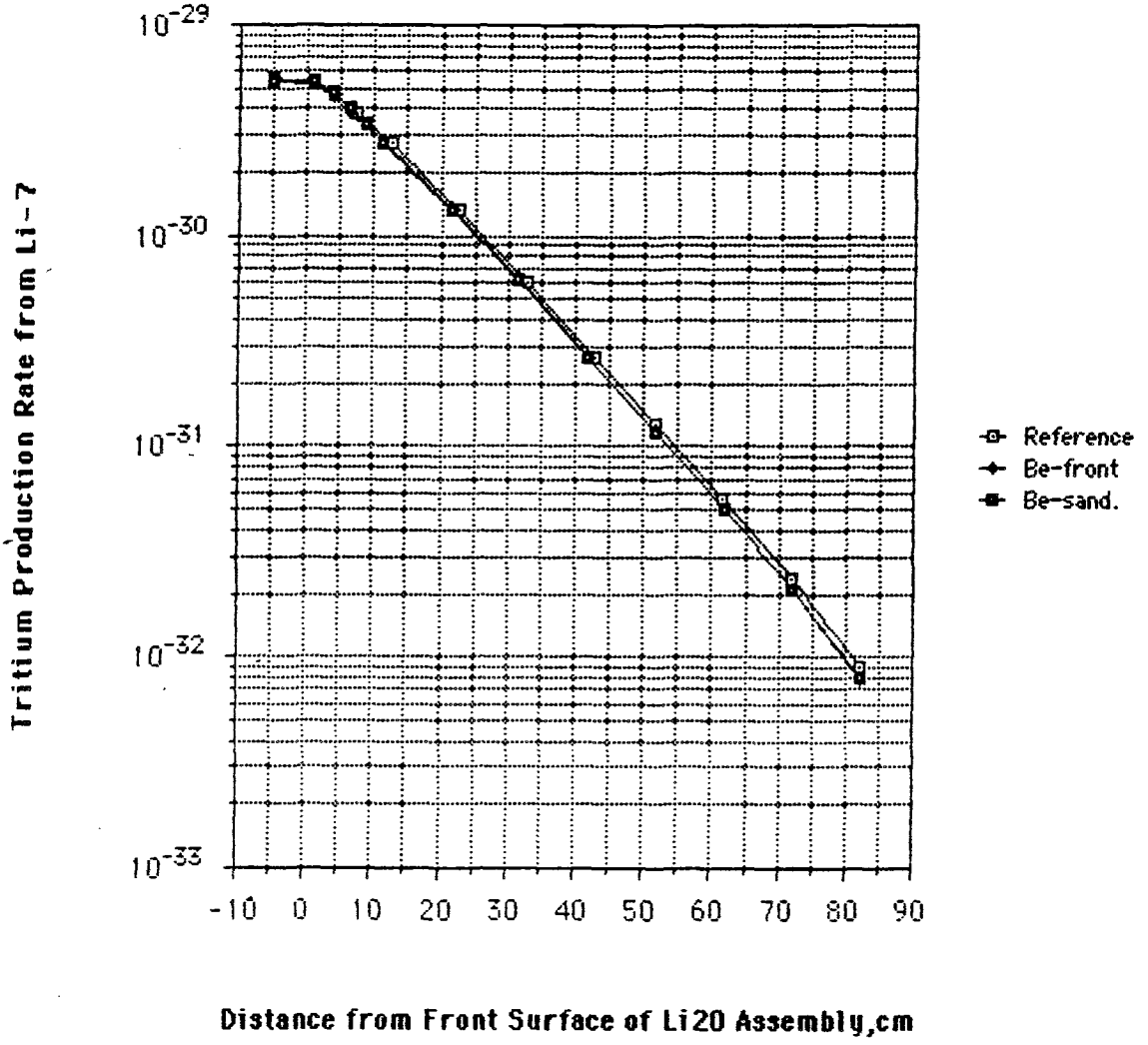

Fig. IV.7: Comparison of the Measured T_7 for Three Systems of Phase IIA

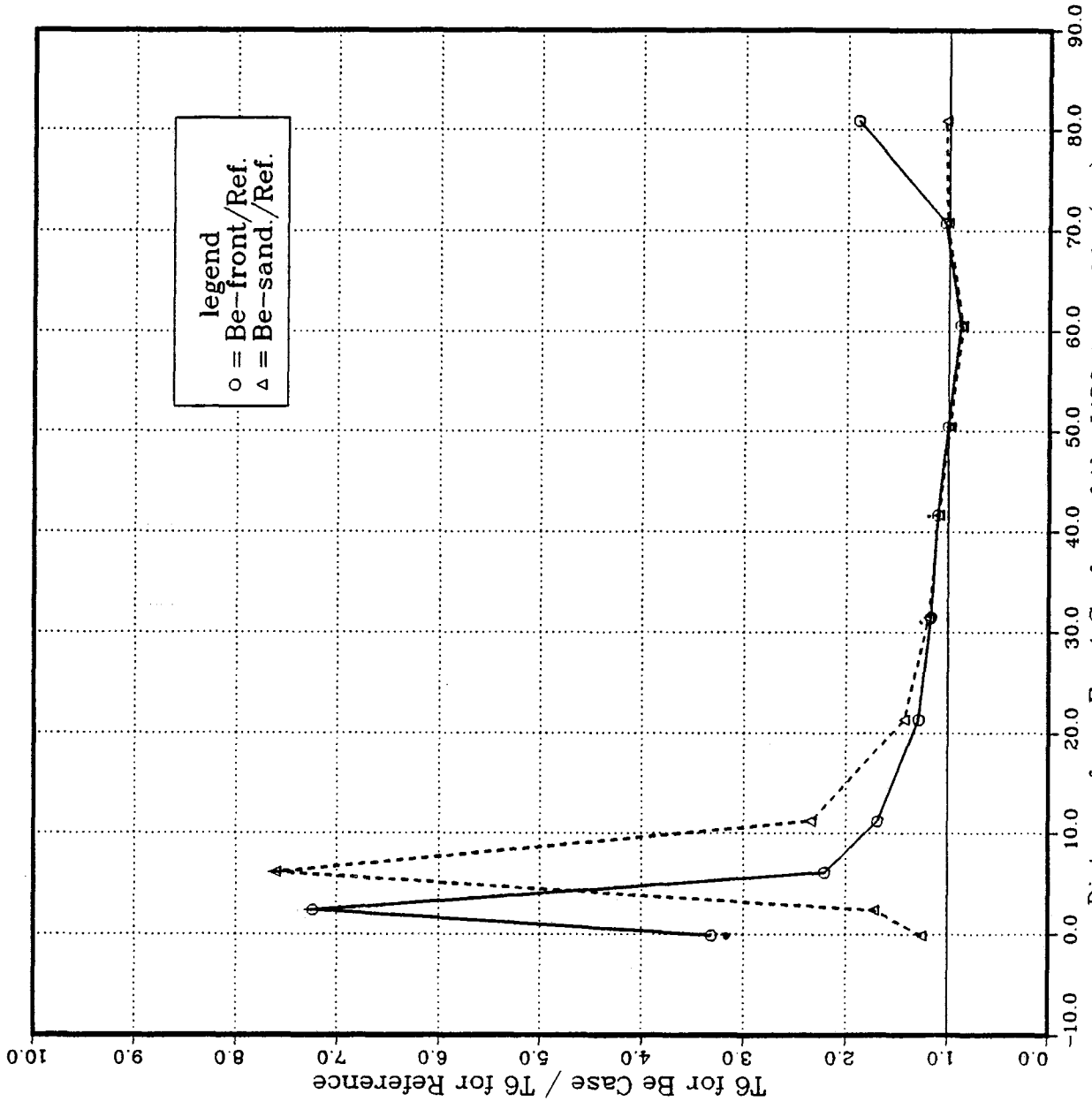

Fig. IV.8: Comparison of T6 Measured by Li-Glass Detector for REF, BEF, and BES Systems of Phase IIA (DOT Calculation)

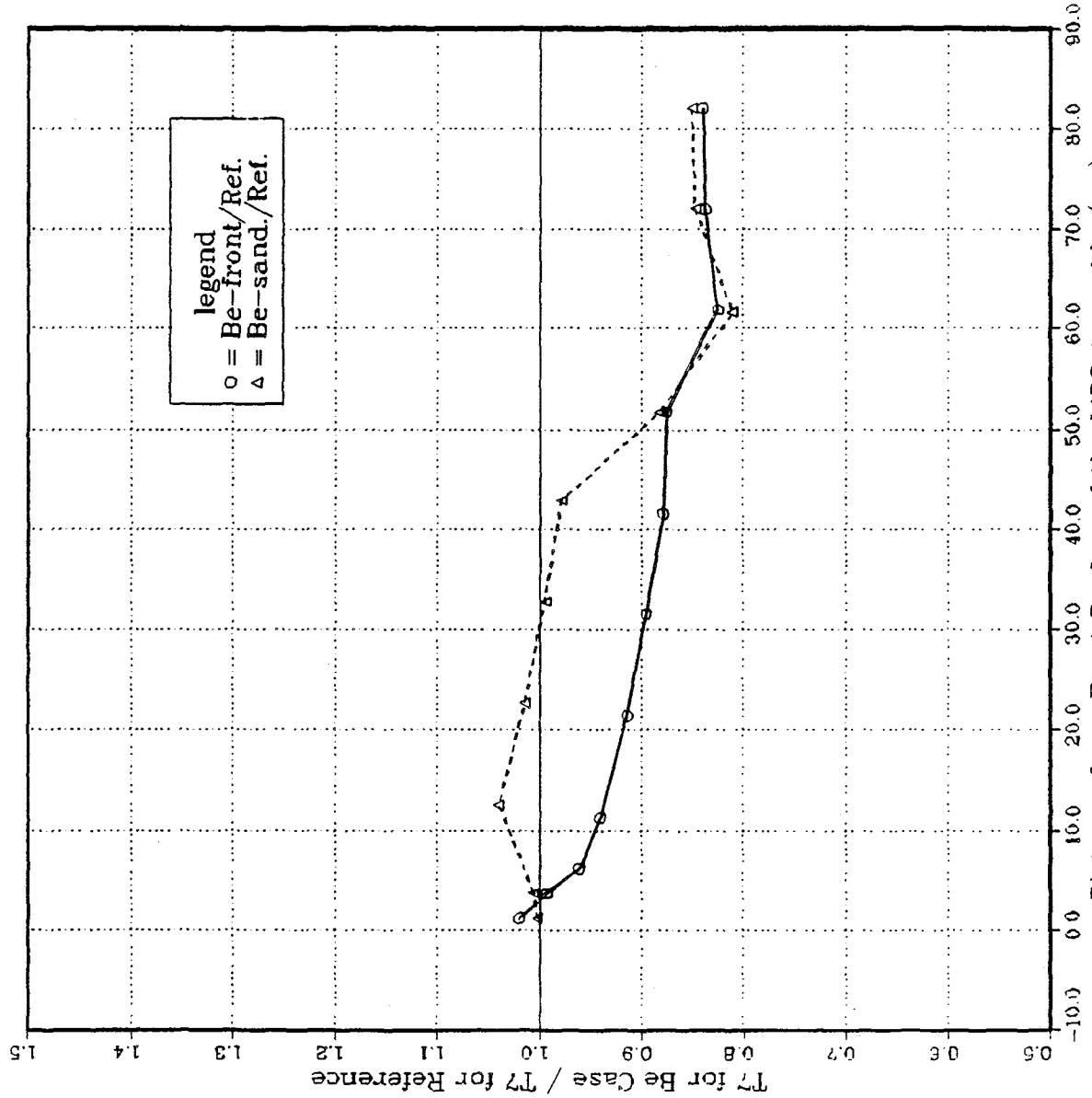

Fig. IV.9: Comparison of T7 Measured by NE213 Detector for REF, BEF, and BES Systems of Phase IIA (DOT Calculation)

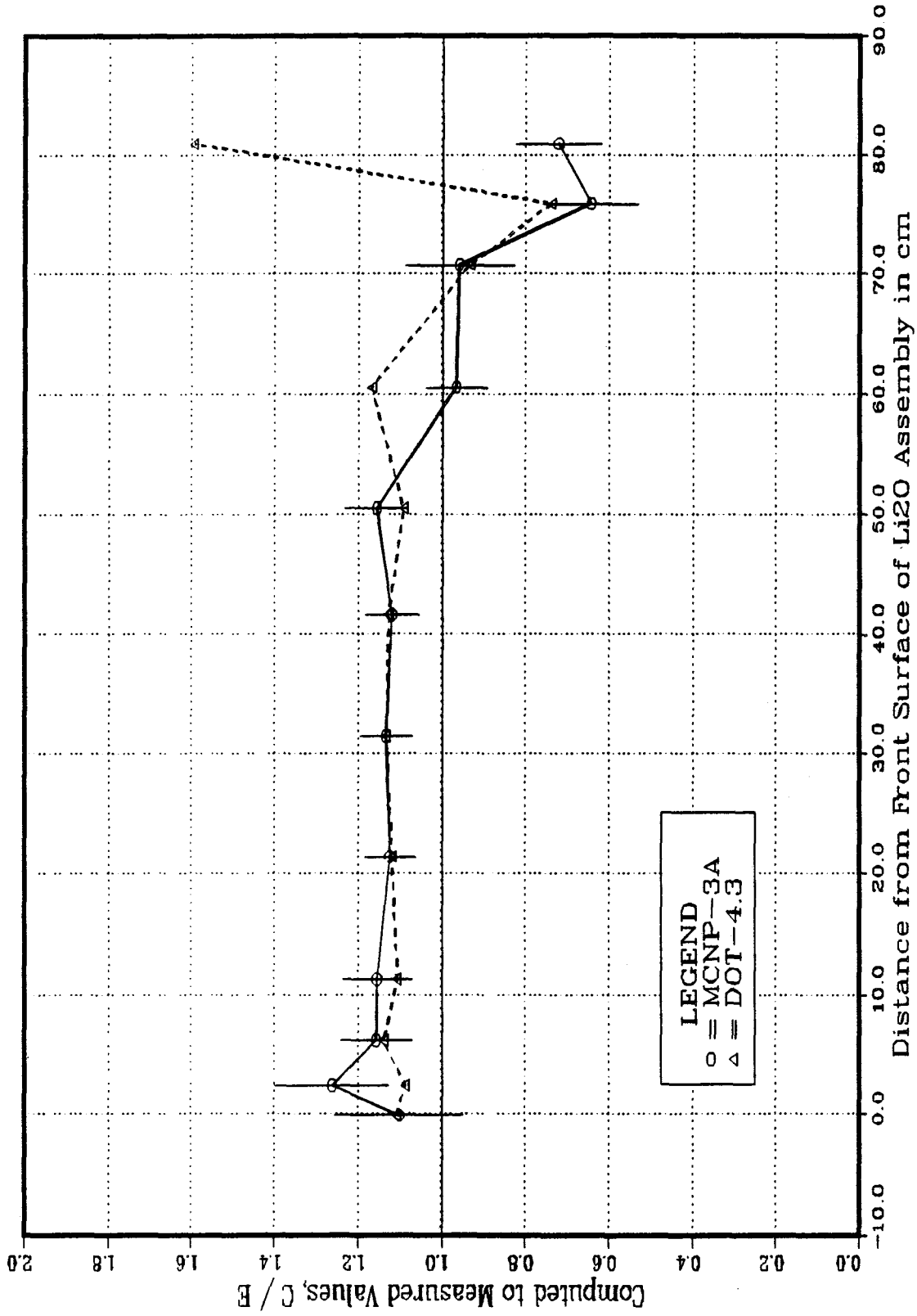

Fig. IV.10: C/E Values for T_6 Using Li-Glass Detector in the Central Drawer (REF System of Phase IIA)

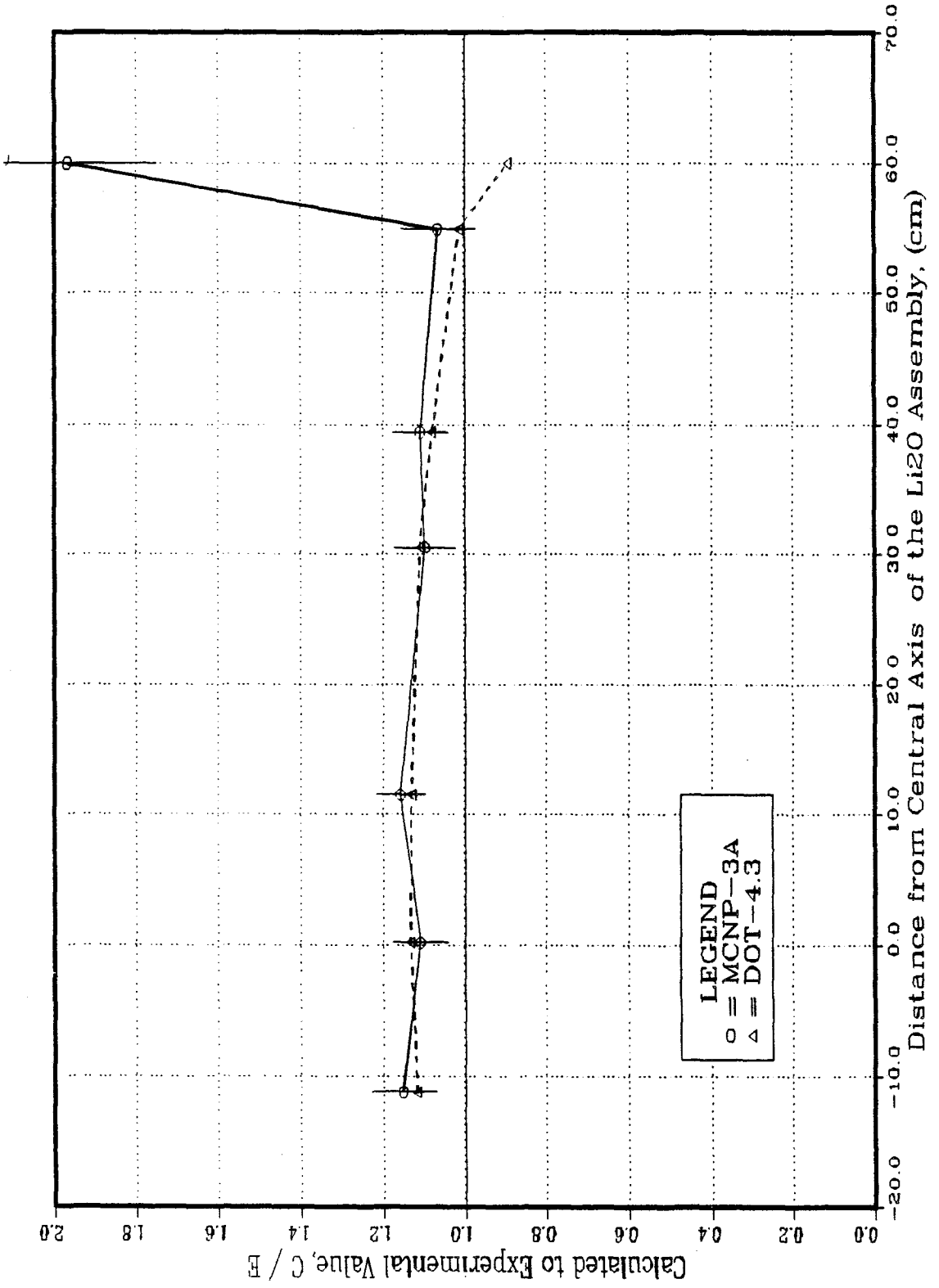

Fig. IV.11: C/E Values for T_6 Using Li-Glass Detector in the Front Radial Drawer (REF System of Phase IIA)

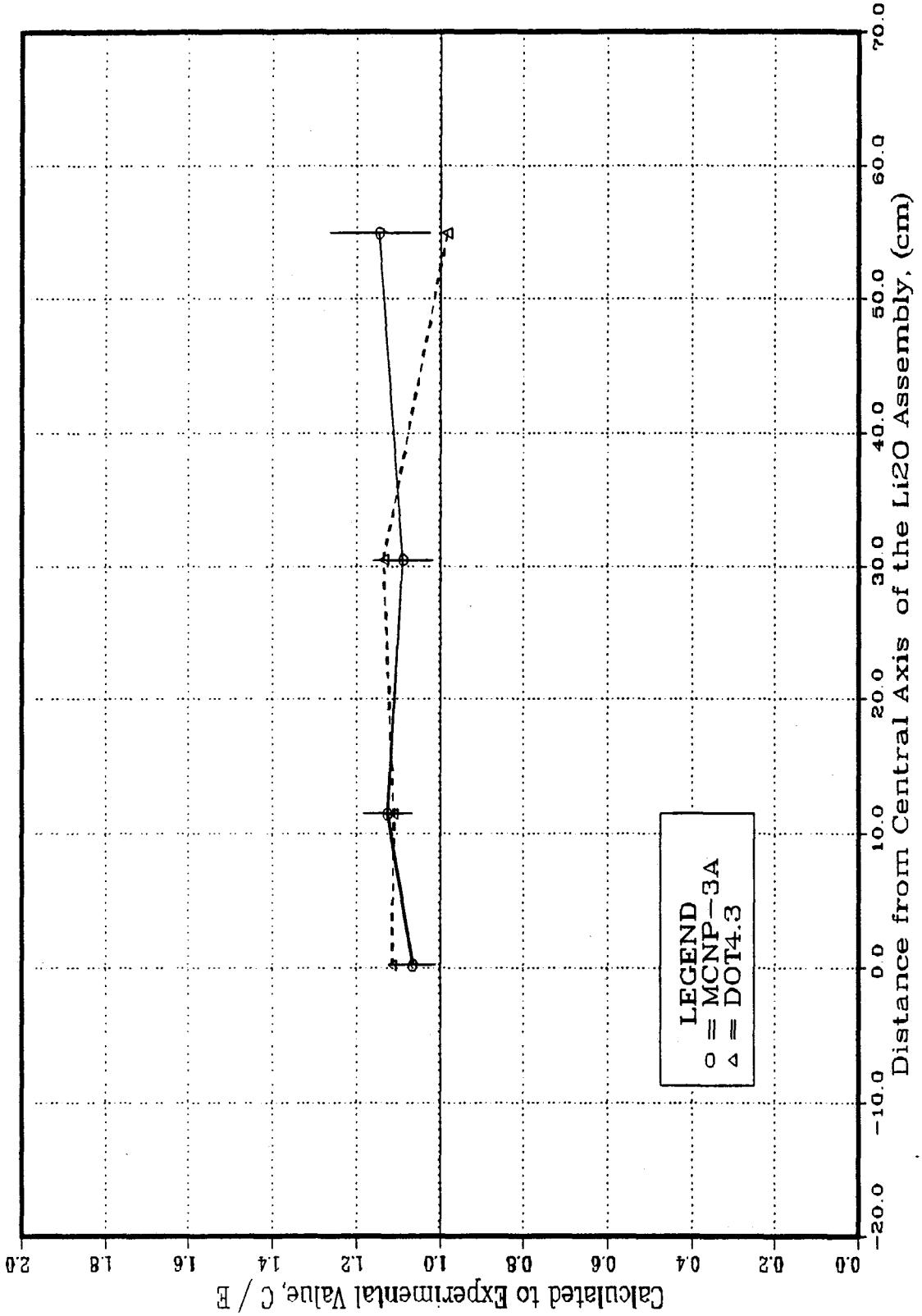

Fig. IV.12: C/E Values for T_6 Using Li-Glass Detector in the Rear Radial Drawer (REF System of Phase IIA)

bulk of the assembly, the C/E values are around 1.1 (experimental errors are - 3 - 4%). The discrepancy is large in the Li_2CO_3 layer due to the uncertainties in the specifications of the Li_2CO_3 blocks, e.g., atomic densities, epoxy paint content, etc. With the Li-metal detectors, the C/E values were closer to unity (1 - 1.1) but the overestimation still persists as shown in Fig. IV.13. The C/E values for T_6 in the radial directions are ~ 1-1.1, as can be seen from Figs. IV.11 and IV.12. Notice from these figures that the results obtained by the MCNP and by the DOT calculations are similar (within the statistical errors of the Monte Carlo calculations) and that there is very small space-dependence in the C/E curves in the radial directions, as was discussed earlier.

The curves for the C/E values for T_6 in the BEF and BES systems are shown in Figs. IV.14 and IV.15, respectively. There are common features in these curves, namely (a) large values are observed inside the Be layer, (C/E ~1.4, MCNP/B5) (b) sudden drop in the C/E values below unity just behind the Be layer (C/E ~ 0.8 - 0.9) followed by a gradual increase where the values are leveled above unity in the bulk of the Li_2O zone then gradual decrease in their values occurs thereafter, (c) large discrepancy occurs between measurements and calculations inside the Li_2CO_3 layer for the reasons discussed earlier, and (d) generally, the C/E values are closer to unity in the bulk of the Li_2O zone as compared to those found in the reference system.

The reasons for the sudden drop in the C/E value just behind the Be layer could be related to secondary energy/angular distribution of the emitted neutrons from the $^9Be(n,2n)$ reactions. This is further investigated and discussed in V where a comprehensive cross-section sensitivity analysis was performed to explore this feature. The large C/E values inside the Be layer is attributed mainly to flux perturbation by the Li-glass components and to self-shielding effect as explained below.

The reasons for the large values for T_6 in the beryllium zone were examined by direct calculations. Note that the measured values shown in Figs. IV.10 to IV.15 were not corrected for detector self-shielding effect. The correction factor is large in the beryllium zone where soft neutron spectra are encountered. To calculate this factor, the geometrical details of the Li-glass scintillator, the light guide and the photo multiplier tube (PMT ~ 10% Al) contained in the outer aluminum tube were modeled in the R-Z 2-D model and T_6 in the Li-glass scintillator was calculated. In this particular calculation, it was found that the calculated T_6 in the BES case, where the details of the Li-glass detector were ignored, is larger by about 50% than the value obtained by the model shown in Fig. IV.16. This

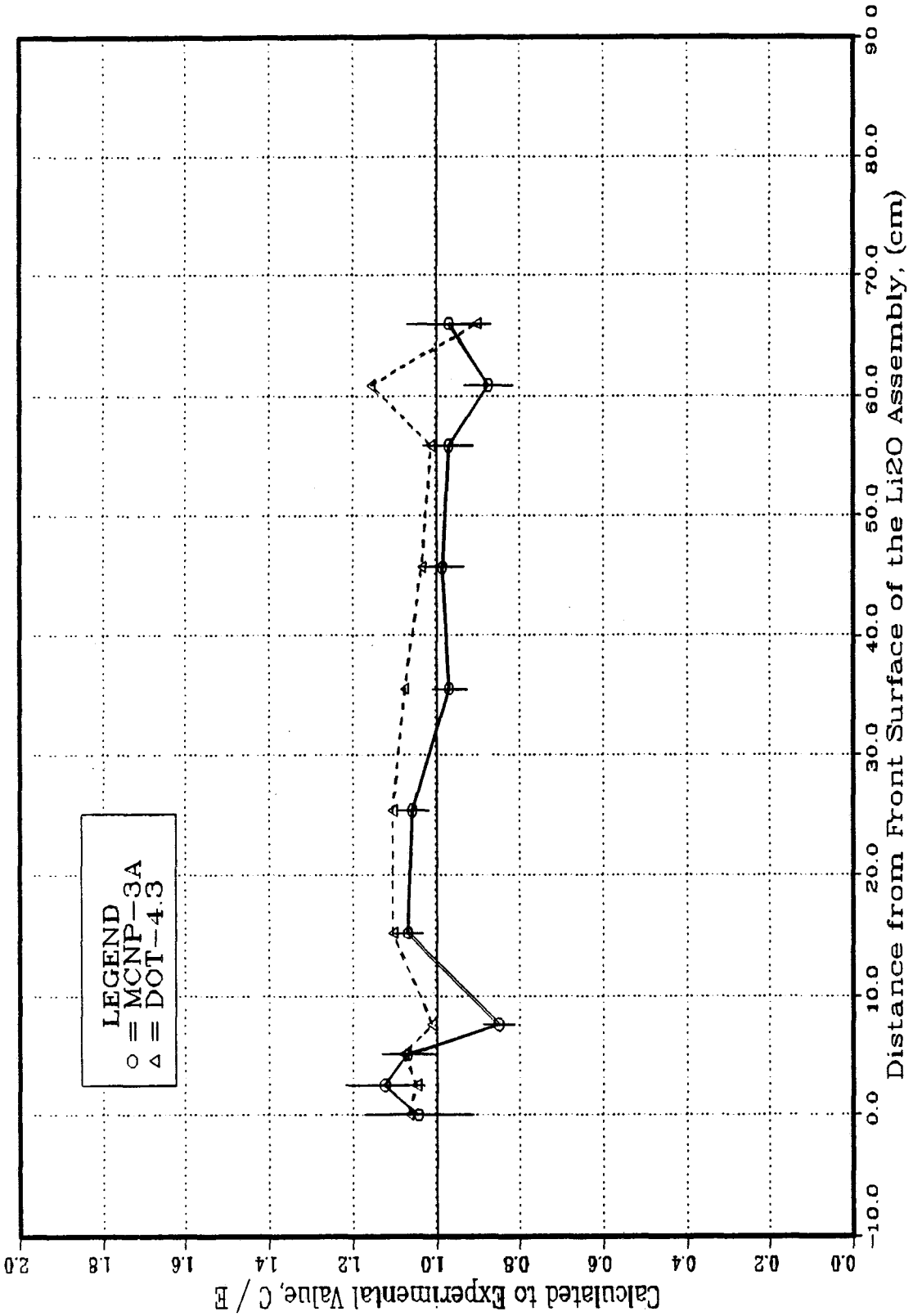

Fig. IV.13: C/E Values for T_6 Using Foils in the Central Drawer (REF System - Phase IIA)

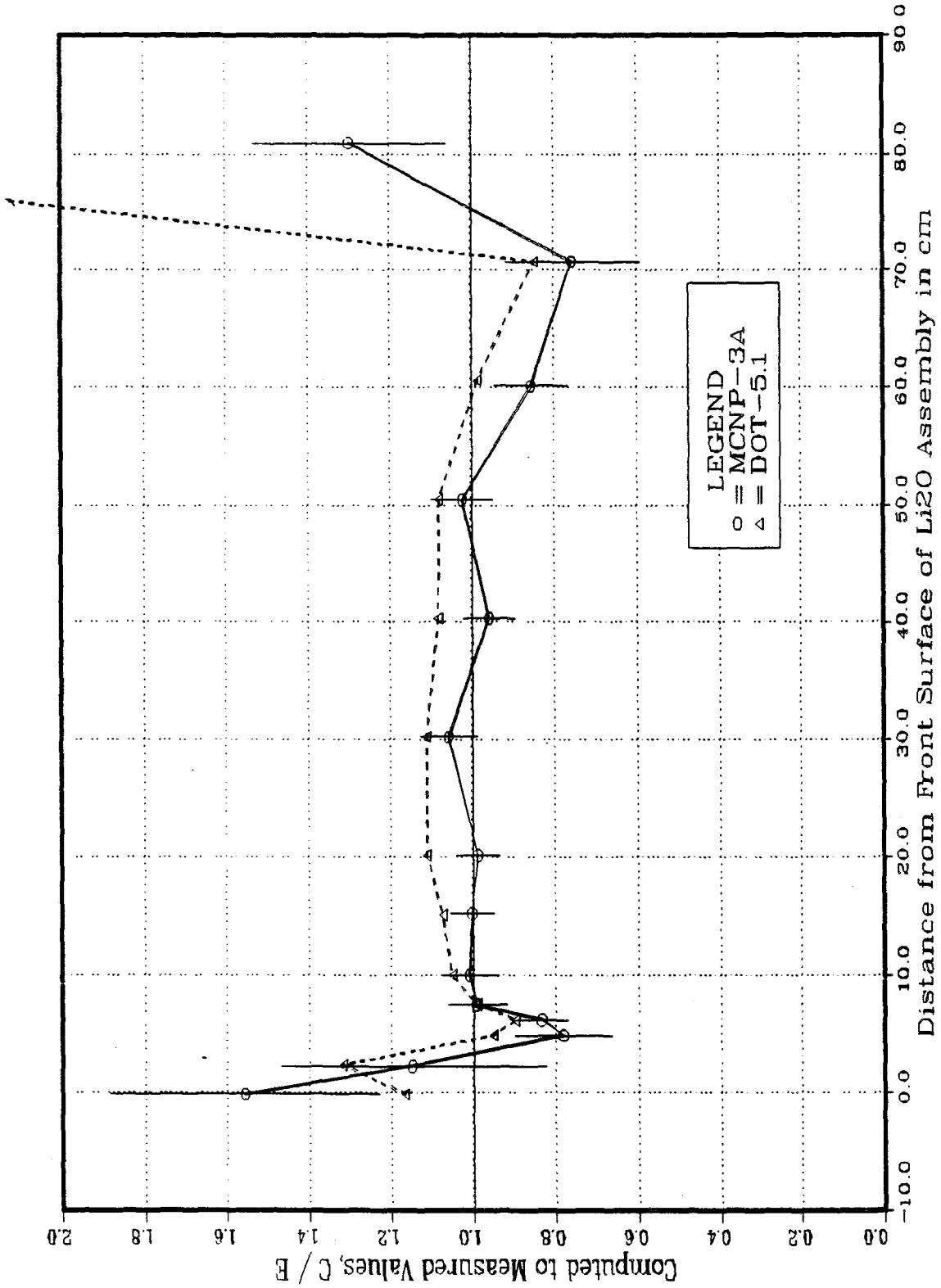

Fig. IV.14: C/E Values for T_6 Using Li-Glass Detector in the Central Drawer (BEF System - Phase IIA)

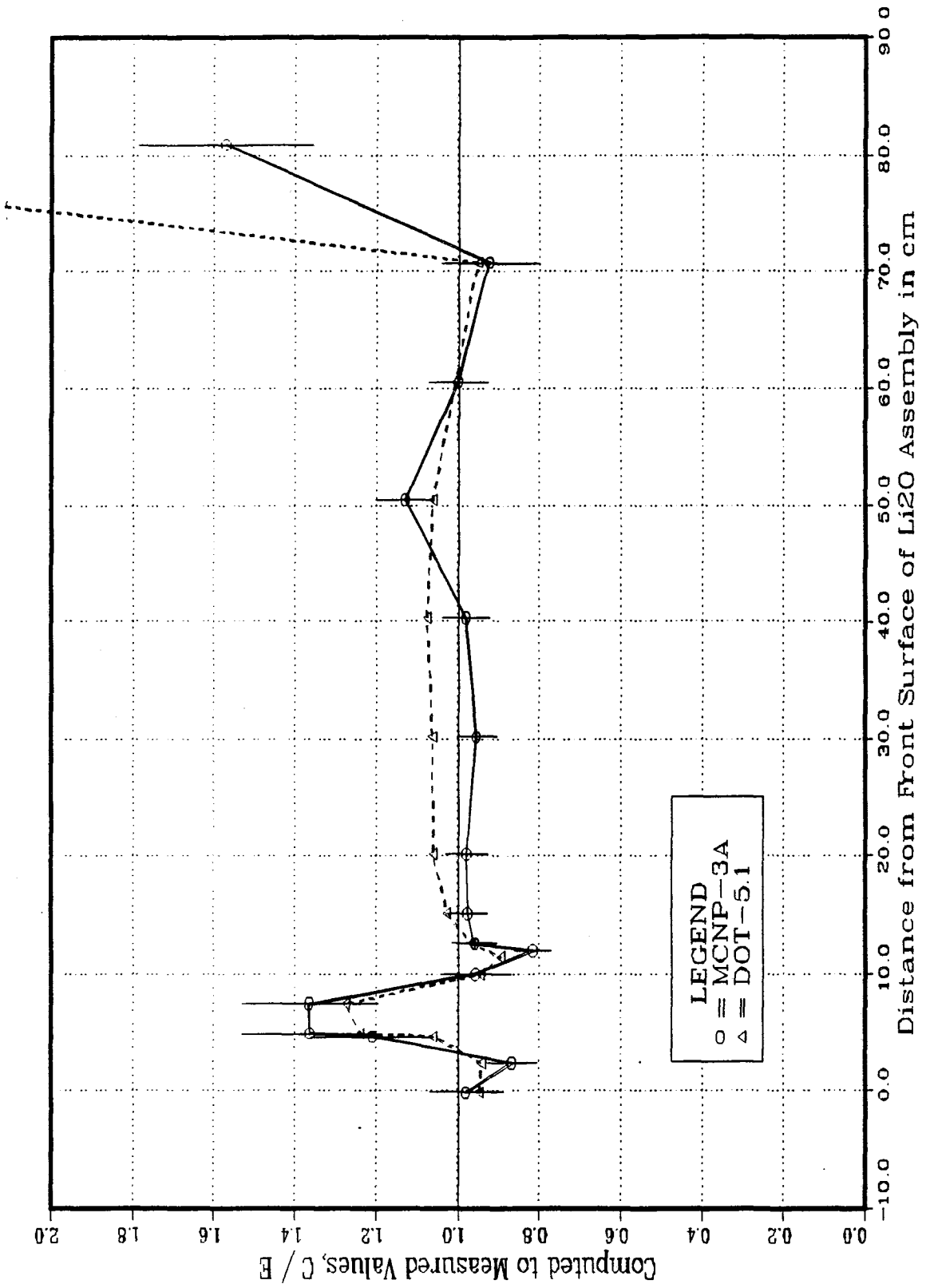

Fig. IV.15: C/E Values for T_6 Using Li-Glass Detector in Central Drawer (BES System - Phase IIA)

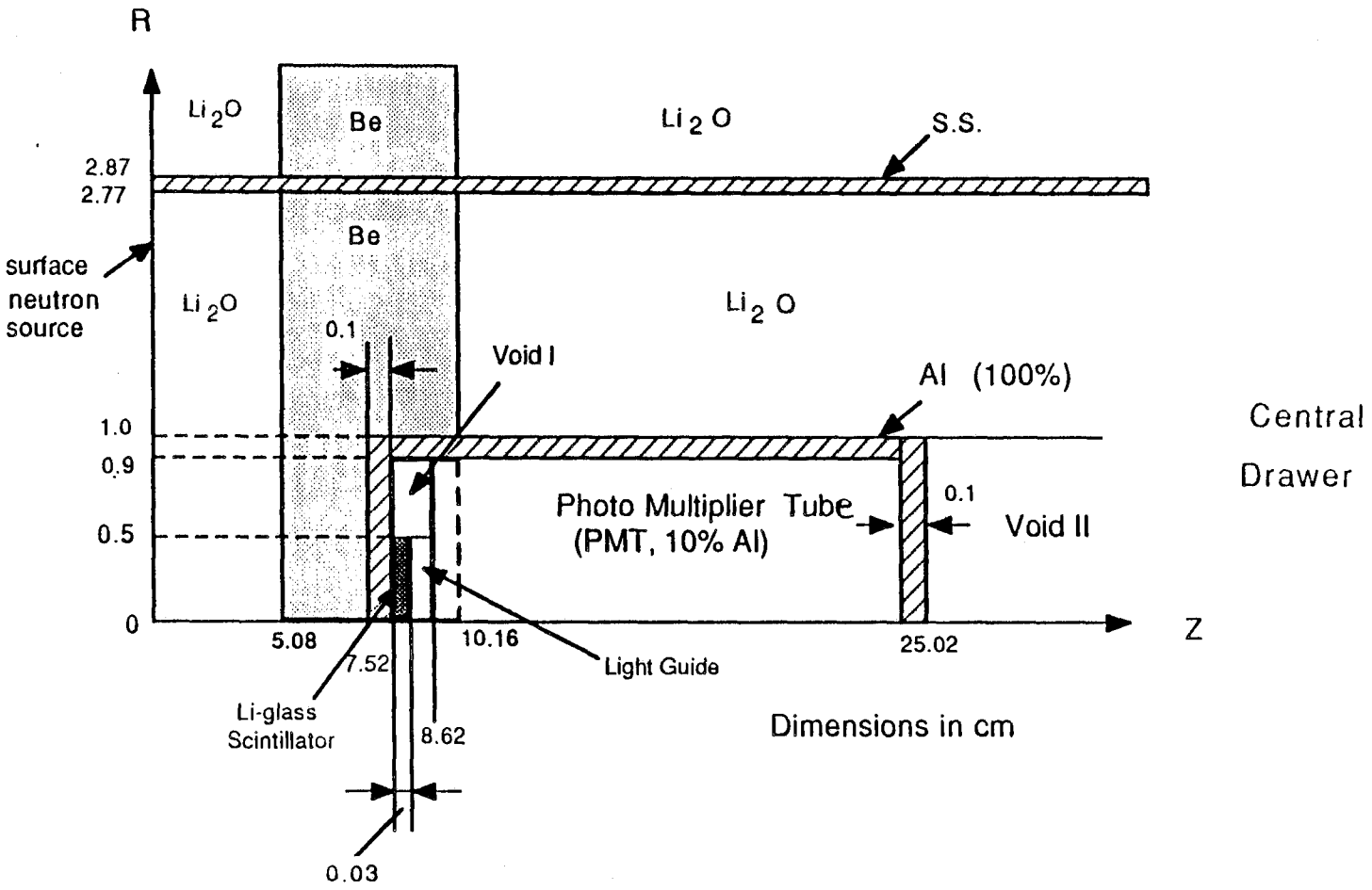

Fig. IV.16: Two-Dimensional Model of T_6 Measurement by Li-Glass Detector in Beryllium Zone

difference is basically due to the detector perturbation to the neutron flux and to the self-shielding effect. To further estimate contributions to this difference that is attributed to flux perturbation, each component of the Li-glass detector was replaced in the model by the corresponding material where that particular component physically exists and several separate calculations for the T6 in the Li-glass scintillator were performed. It was found that replacing the light tube zone by beryllium leads to ~8% increase in T_6 while replacing the PMT by Li_2O between z = 10.16 cm and z = 25.02 cm and by beryllium between z = 8.62 cm and z = 10.16 leads to ~7% increase in T_6. Also, replacing the void zone (Void I) by beryllium leads to ~4% increase. Thus, flux perturbation due to considering the components of the Li-glass detector (other than the Li-scintillator) in the calculation leads to ~ 20% difference in the calculated T_6. The contribution to the 50% difference mentioned above that is due to self-shielding effect was estimated by calculating T_6 in a case where only the volume occupied by the Li-glass scintillator is filled by the actual material of the scintillator while the rest of the detector geometry is ignored in the model and comparison was made to the calculated T_6 in the reference BES case in which this volume was filled with beryllium. It was found that T6 in the latter case is larger by ~ 30%. Indeed, separate calculations for the self-shielding factors in the beryllium zone based on Hanna's approximation[33] were shown to be ~ 0.78. It was concluded that the large C/E encountered in the beryllium zone is basically due to neglecting the geometrical details of detector in the calculational model. However, the analysis has also shown that neglecting these details when measurements are taken in the Li_2O zone leads only to ~2% change in T_6. Several methods for correcting for the self-shielding effect are discussed in Section IV.3.

As shown in Fig. IV.15, the C/E values for T_6 at the Be-Li_2O boundaries are 1.2 and 0.97 at the front and back boundary of the BES system, respectively, as calculated by DOT5.1 code. Since the T_6 profiles are steep near the boundaries, any deviation in the interpolation of T_6 to the exact measurement locations leads to a large variation in the C/E values. Sensitivity study showed that a deviation of 1 mm leads to a change in the C/E values by ~2% and 8% at back and front boundaries, respectively. Thus, the C/E values of 0.97 at the Be-Li_2O back boundary could possibly be caused by uncertainty in the order of 1 mm in the exact measuring location. This is shown in Fig. IV.17 where hypothetical deviation in the Z direction of dZ = -1 mm and dZ = -3 mm were applied and the calculated T_6 values based on this assumption were interpolated to the new locations and compared to the experimental values. Larger deviations obviously lead to larger relative changes in the C/E values at these boundaries. This is also true at the Li_2O/Li_2CO_3 boundaries. This

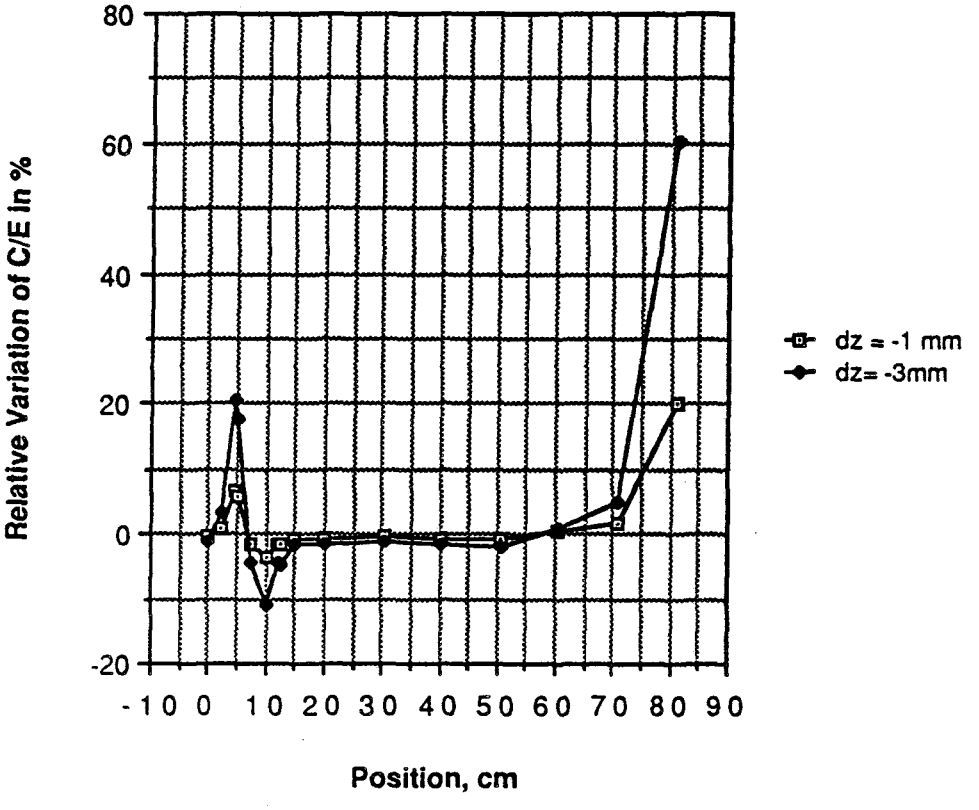

Fig. IV.17: Sensitivity of the C/E Values of T_6 Due to Variations in the Axial Positions

effect is small, however, in the bulk of the Li_2O zone where the T_6 profiles are not as steep as they are at material boundaries, as shown in Fig. IV.17.

(B) Tritium Production Rate From $^7Li(T_7)$

The profiles of T_7 in the REF and the BES systems are shown in Fig. IV.18 and IV.19, respectively. The measurements data are those obtained by the NE213 indirect method and the calculations are those obtained by MCNP. The agreement between these two sets of data is good at front locations, but large discrepancies are seen at the back locations and inside the Li_2CO_3 layer where the stastical errors are large.

The C/E values for T_7 measured by the NE213 method in the REF system are shown in Figs. IV.20, IV.21, and IV.22 throughout the central axis, the front, and the back radial drawer, respectively. The C/E values in Fig. IV.20 are $\sim$ 1.1 - 1.2 as obtained by DOT4.3 calculations and are, on the average, closer to unity in the Monte Carlo calculations (C/E $\sim$ 1.0 - 1.2). Note that the values obtained by DOT code are always larger than unity. The C/E values in the radial directions are similar (C/E = 1 - 1.20) as seen in Fig. IV.21 and IV.22.

The C/E values for T_7 in the BEF and BES systems along the central axis of the assembly are shown in Figs. IV.23 and IV.24, respectively. The DOT calculations are larger than measurements by 5 - 20% and by 5 - 18% in the BEF and BEB systems, respectively, while the corresponding values obtained by MCNP code are $\pm$ 12 - 20% and $\pm$ 5 - 25%. The deviations from T_7 measurements in the Li_2CO_3 layer are large but the statistical errors in that layer are also large. Based on DOT calculations, it could be seen from Figs. IV.23 and IV.24 that the C/E values are lower (by 2 - 3%) in the BEF and BES systems as compared to the values found in the REF system (see Fig. IV.20).

Based on T_7 measurements by the Li-foil detectors, the C/E values in the REF system are lower by $\sim$ 10 - 20% than those based on the NE213 indirect method. This could be seen by observing the C/E curves shown in Fig. IV.25 and those in Fig. IV.20. The T_7 measurements by Li-foils are a direct method and require irradiating the foils for a long time as compared to the on-line NE213 measurements (low irradiation).

Unlike T_6, the C/E values for T_7 do not change drastically between the locations inside and outside the Be layer. In addition, the microstructure treatment that considers the geometrical details of the detector used (whether the detector is a single foil or multicomponent as is the case of Li-glass detectors) was shown to be unnecessary for T_7 which depends mainly on high-energy neutrons.

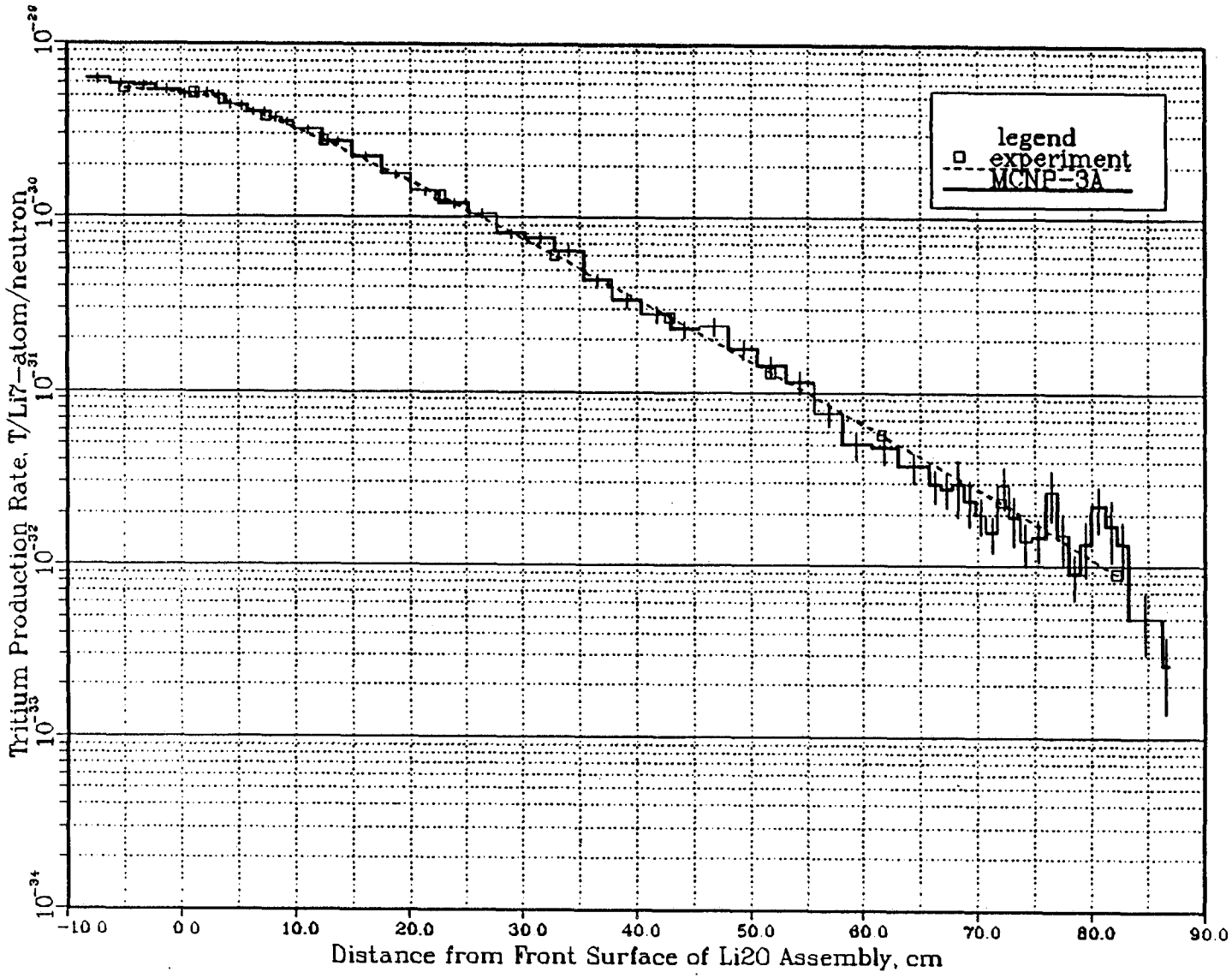

Fig. IV 18: Calculated (MCNP) and Measured (NE213) Values
for T_7 in the Central Drawer
(REF System - Phase IIA)

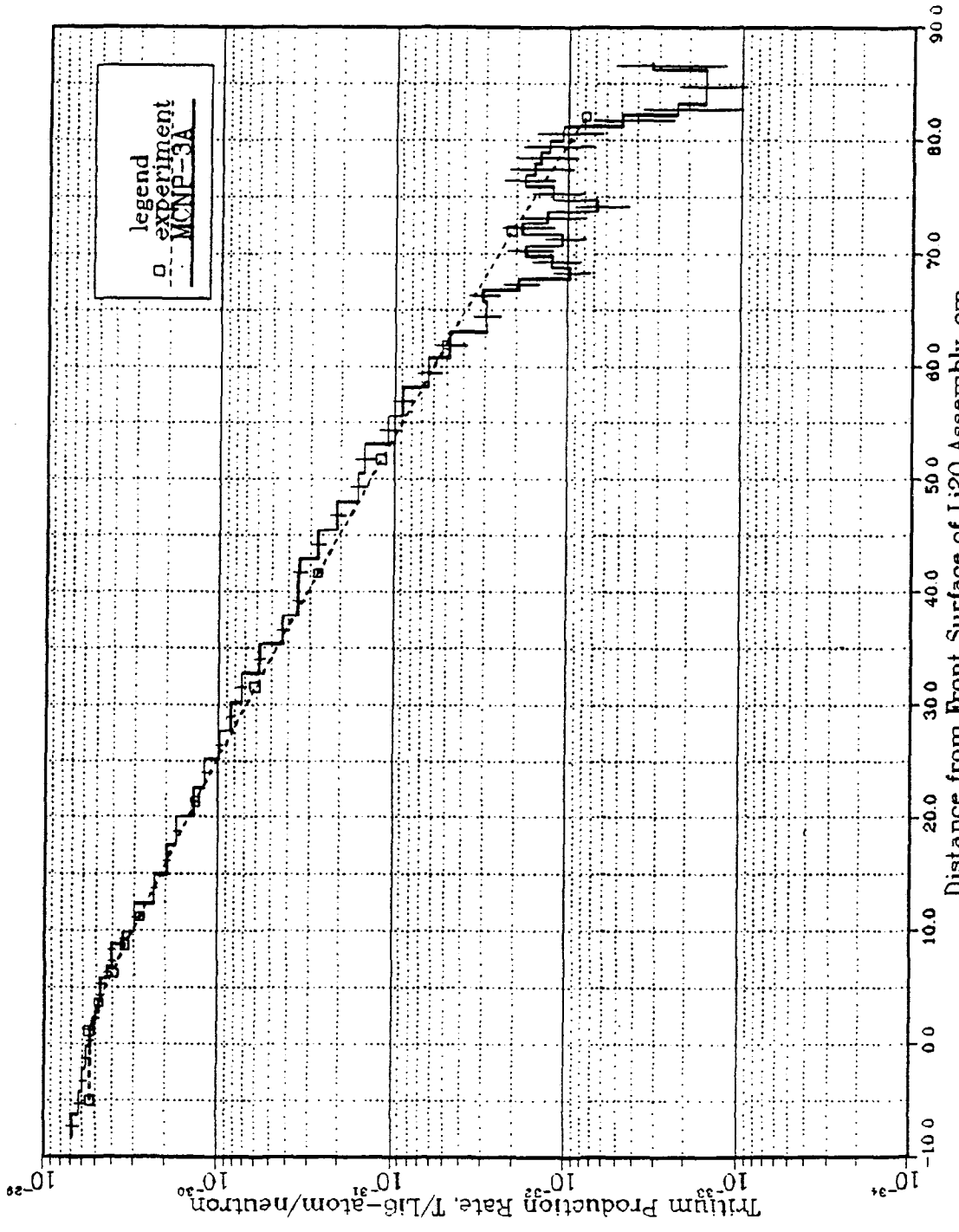

Fig. IV.19: Calculated (MCNP) and Measured (NE213) Values for T_7 in the Central Drawer (BES System - Phase IIA)

(C) Zonal Tritium Production Rate

As mentioned earlier, JAERI has developed a method for measuring the TPR inside blocks of Li_2O using the liquid scintillation method. A typical size of these blocks is 5 cm x 5 cm x 5 cm, but it could be larger. Different enrichment could be used. This method was applied in the REF and the BES systems where blocks (natural enriched and ^7Li-enriched) of different sizes inside the central drawers were used. Tritium production rate from natural lithium, T_N, and from $^7Li(T_7)$ were measured in each block(s) and the TPR from $^6Li(T_6)$ was calculated by subtracting T_7 from T_N.

The C/E values for T_N in the REF system is shown in Fig. IV.26. The deviation from the measured values is ~ 5 - 8% in the front region (up to Z ≅ 30 cm) but larger deviation (~ 13%) is obtained at back locations, as predicted by DOT4.3 code. The C/E values based on MCNP calculations show oscillatory feature; they are below unity by (2 - 17%) up to a depth Z = 15 cm, larger than unity by (5 - 10%) at Z = 15 cm to Z = 38 cm; then they are below unity thereafter. One can thus say that the prediction accuracy of TPR from natural lithium (per atom of natural Li) is ~ ± 13 - 17% (C/E = 0.83 - 1.13). The C/E for T_7 is always lower than unity (by ~ 7 - 27%), as shown in Fig. IV.27, based on MCNP calculations. The corresponding C/E values for T_6 obtained by these zonal measurements are in the range 0.86 - 1.15, as shown in Fig. IV.28. Note that the C/E values for T_7 in this case are close to the values obtained by the Li-foil method (see Fig. IV.25.)

In the BES system, the C/E values for T_N are 0.99 - 1.09 (DOT5.1) and 0.83 - 1.29 (MCNP). The largest deviation from the measured values is observed near the front boundary of the Be layer in the MCNP calculations. The C/E values for T7 is near unity throughout the assembly as predicted by DOT5.1 calculations (see Fig. IV.30) but there is fluctuation in the C/E curve obtained by MCNP code. This is also true for the derived C/E curves for T_6 shown in Fig. IV.31. Because of the cancellation effect, one can say that the prediction accuracy for T_N is better than those for T_6 and T_7 and this accuracy is within - 17% and + 13% and within - 17% and + 29% in the REF and the BES systems, respectively.

The measured and calculated zonal TPR from natural Li are given in Table IV.1-a for the REF and the BES systems. The values shown are integrated results over the entire volume of the central drawer (~ 5.08 x 5.08 x 60 cm) per atom of natural Li per source

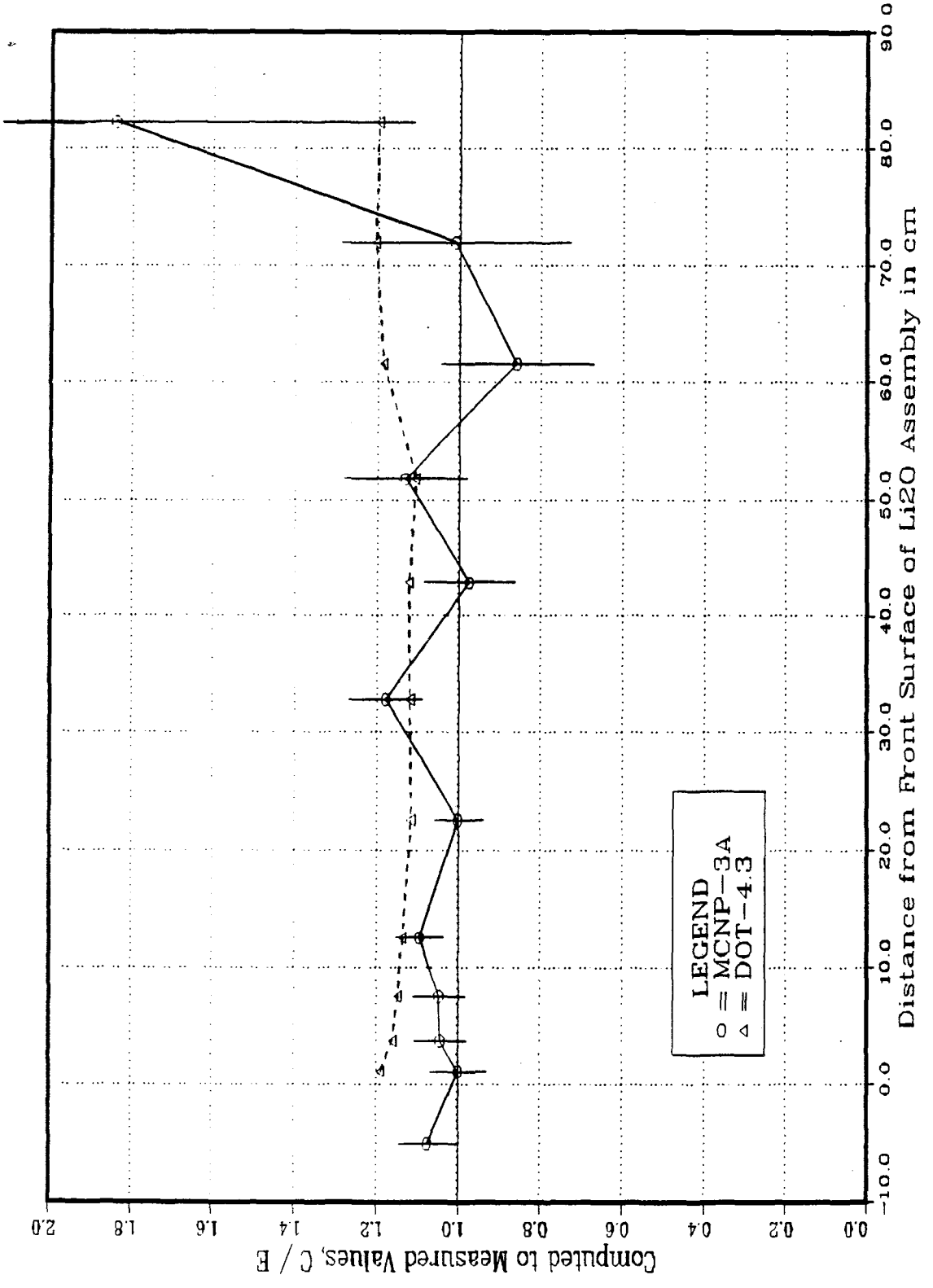

Fig. IV.20: C/E Values for T_7 Using NE213 Detector in the Central Drawer (REF System - Phase IIA)

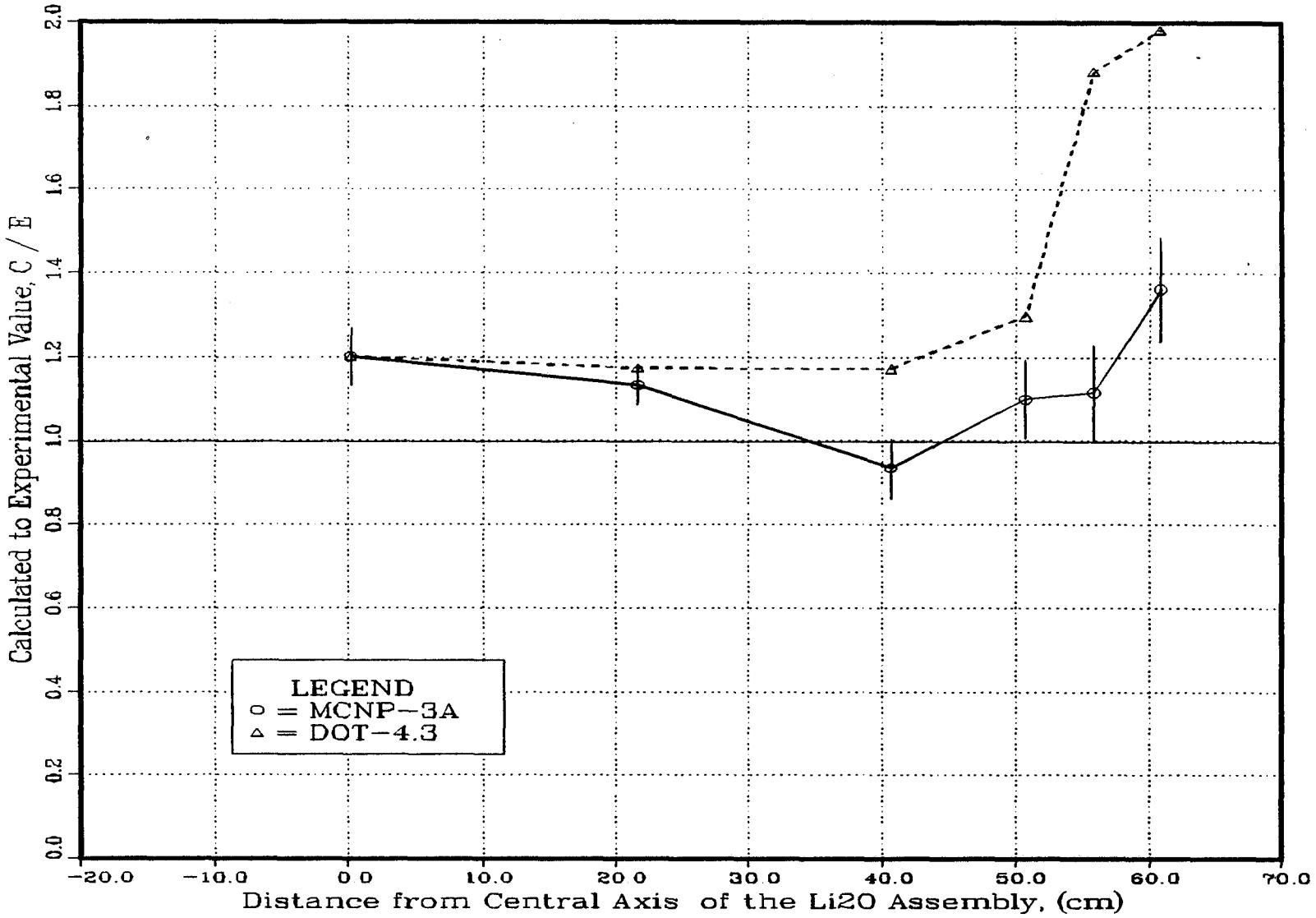

Fig. IV.21: C/E Values for T_7 Using NE213Detector in the Front Radial Drawer (REF System - Phase IIA)

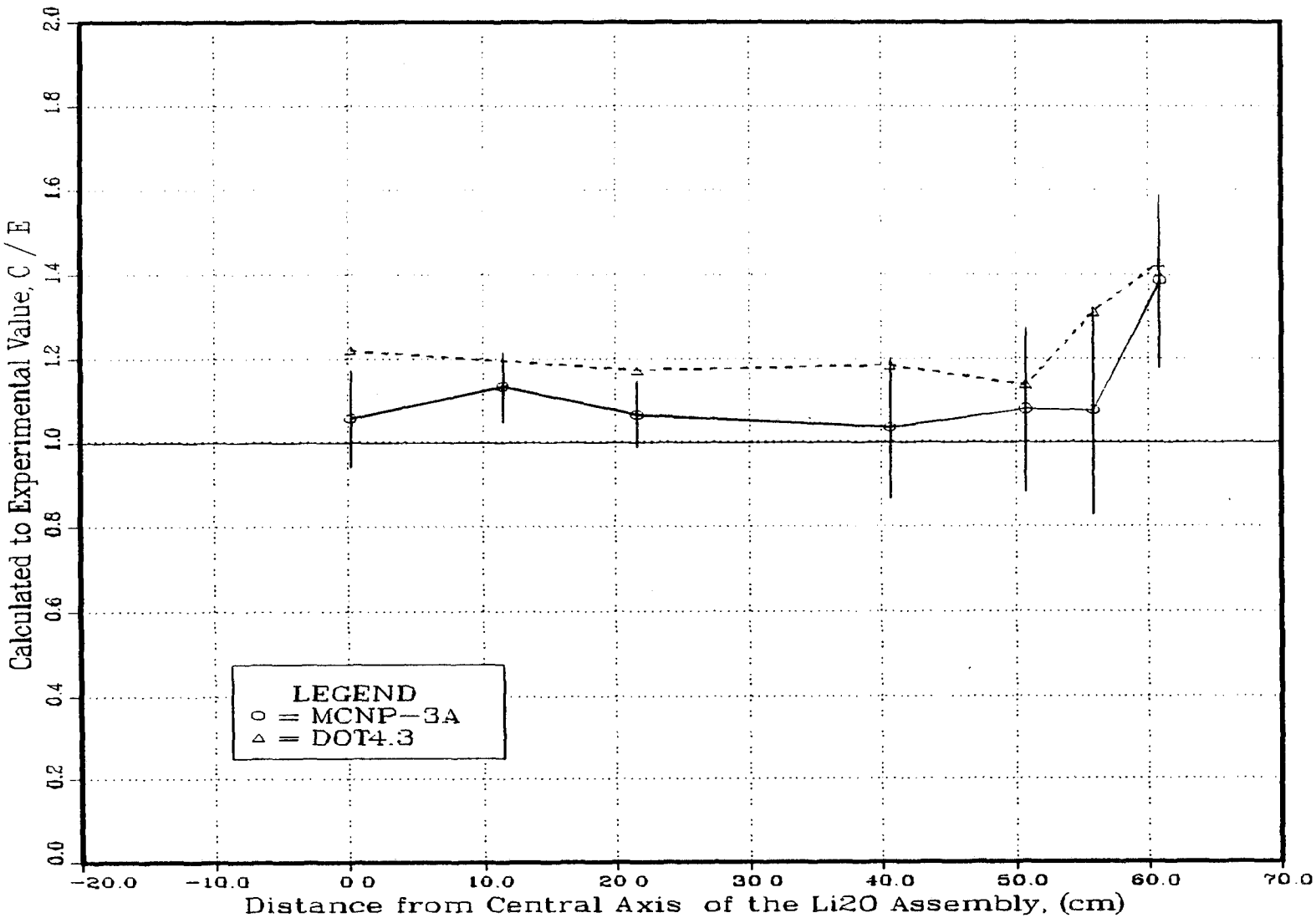

Fig. IV.22: C/E Values for T_7 Using NE213 Detector in the Rear Radial Drawer
(REF System - Phase IIA)

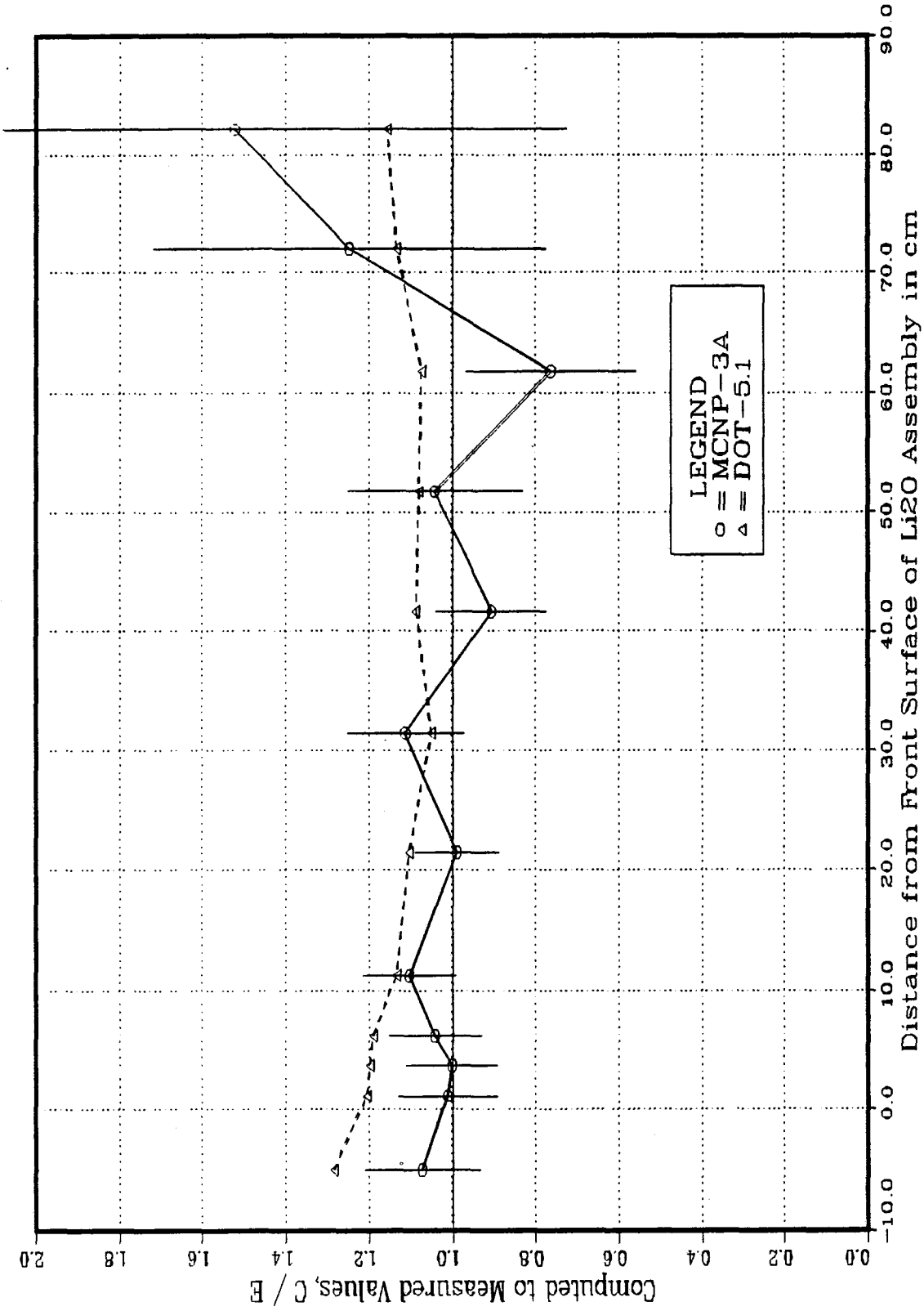

Fig. IV.23: C/E Values for T_7 Using NE213 Detector in the Central Drawer (BEF System - Phase IIA)

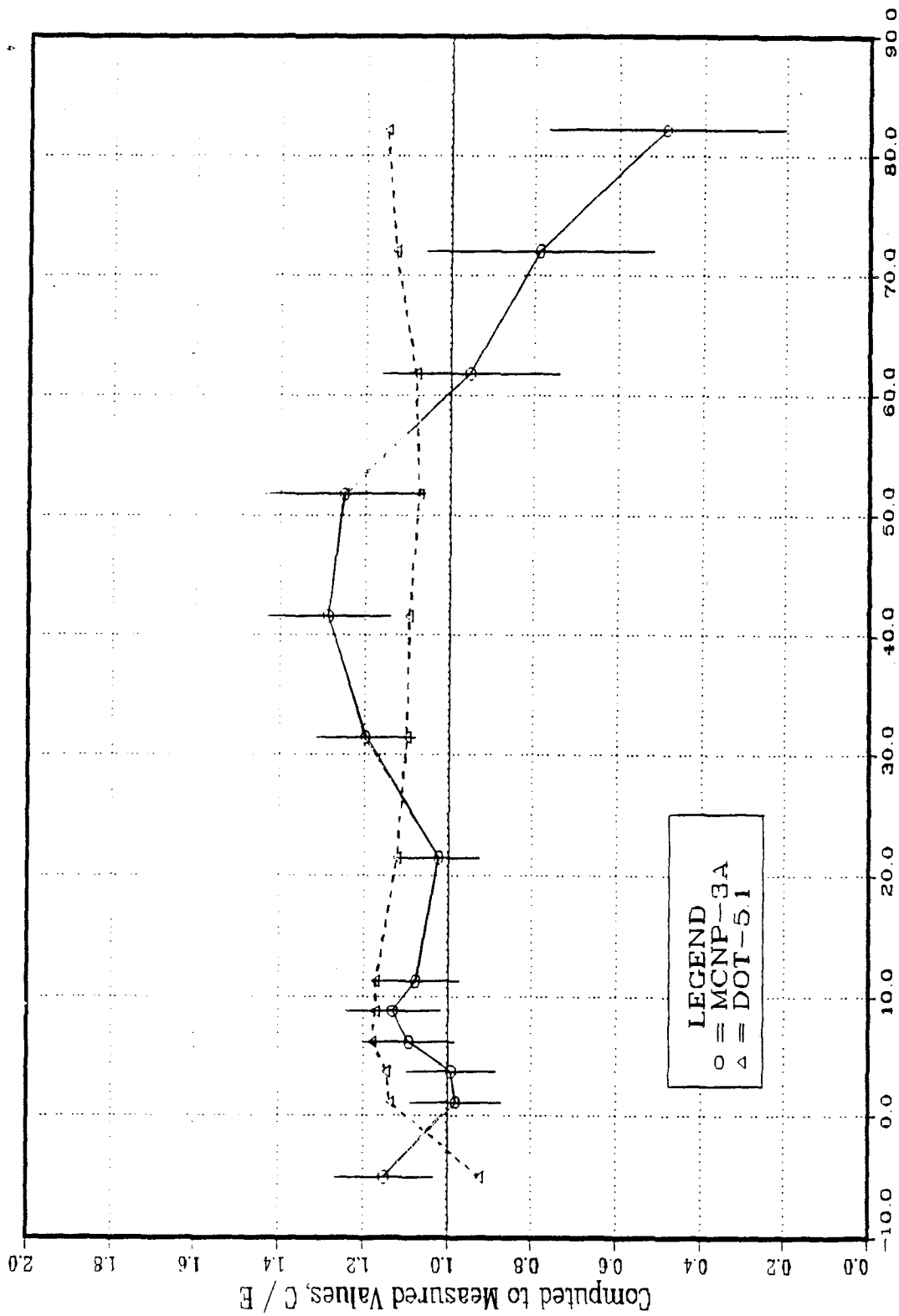

Fig. IV.24: C/E Values for T_7 Using NE213 Detector in the Central Drawer (BES System - Phase IIA)

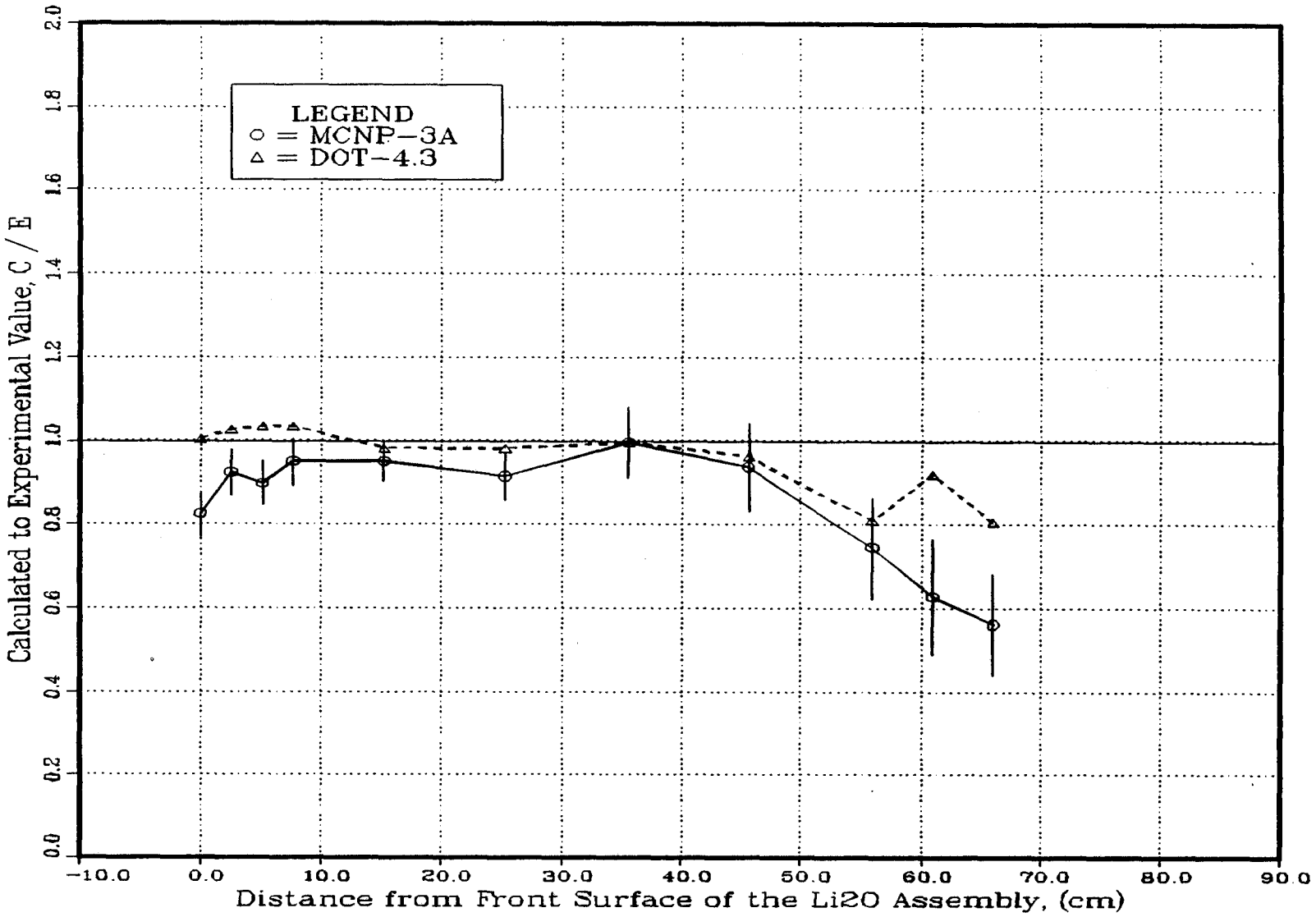

Fig. IV.25: C/E Values for T_7 Using Foils in the Central Drawer
(REF System - Phase IIA)

neutron. Values in parentheses are the relative values with respect to the reference system and thus indicate the tritium breeding potential in the central drawer. As shown, the TPR from natural Li in the BES system has been increased by ~ 18% as predicted by MCNP. The predicted increase by DOT5.1 is ~ 20%. However, the experimentally measured increase in the TPR from natural Li is ~ 17%. Table IV.1-b shows the C/E values for the integrated zonal TPR in both systems. As shown, the MCNP results are lower than measurements by ~ 1% in both systems. The DOT results, however, are larger by 7% and 10% in the two systems, respectively. It is clear, therefore, that the prediction accuracy of TPR over large volume of the breeding material (Li_2O in our case) is better than the prediction accuracy at local points due to the cancellation effect of the over-and-under-prediction at several locations.

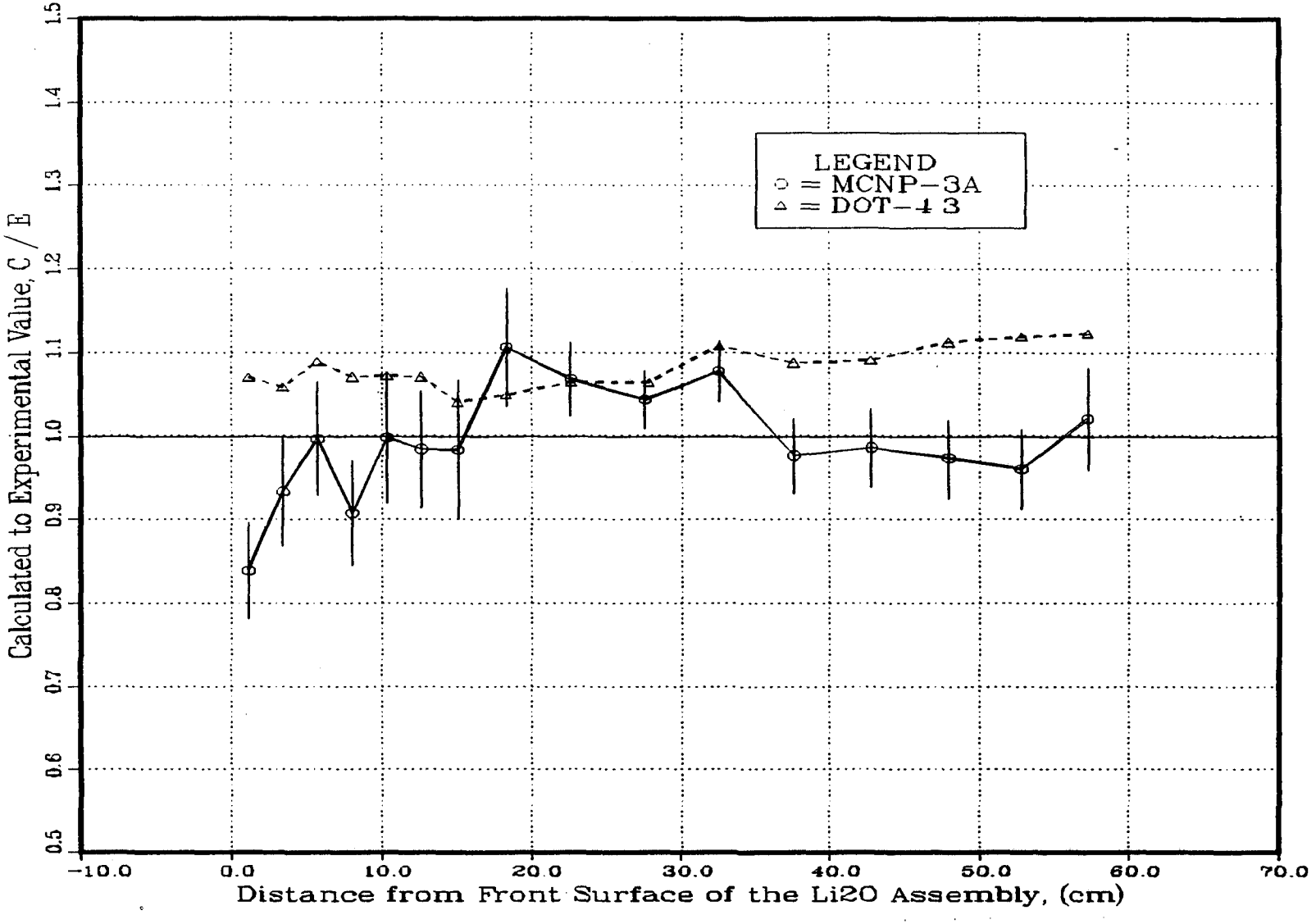

Fig. IV.26: C/E Values for Tritium Production Rate From Natural Lithium (Zonal TPR) in the Central Drawer (REF System - Phase IIA)

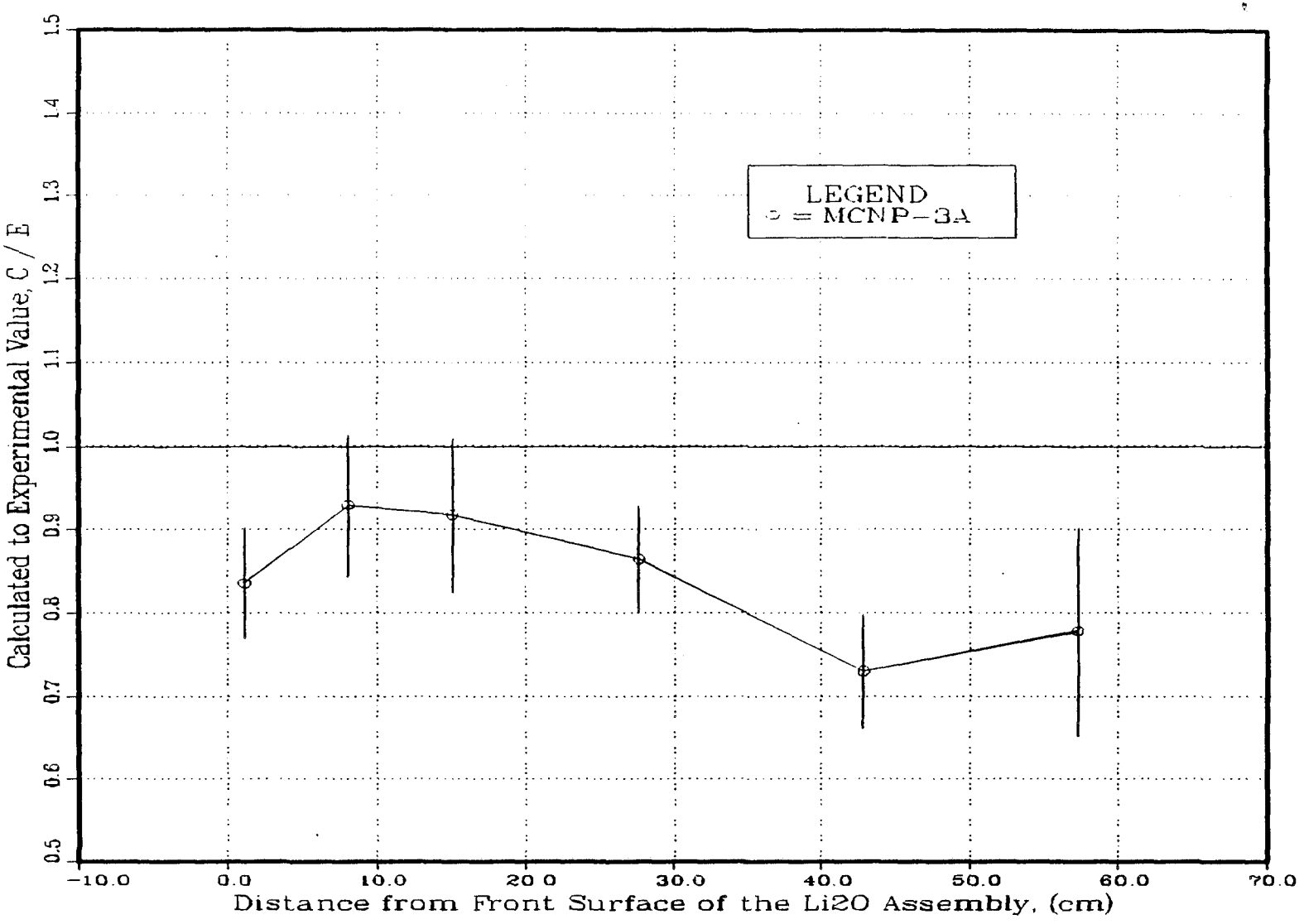

Fig. IV.27: C/E Values for Tritium Production Rate from ^{7}Li (Zonal TPR)
in the Central Drawer
(REF System - Phase IIA)

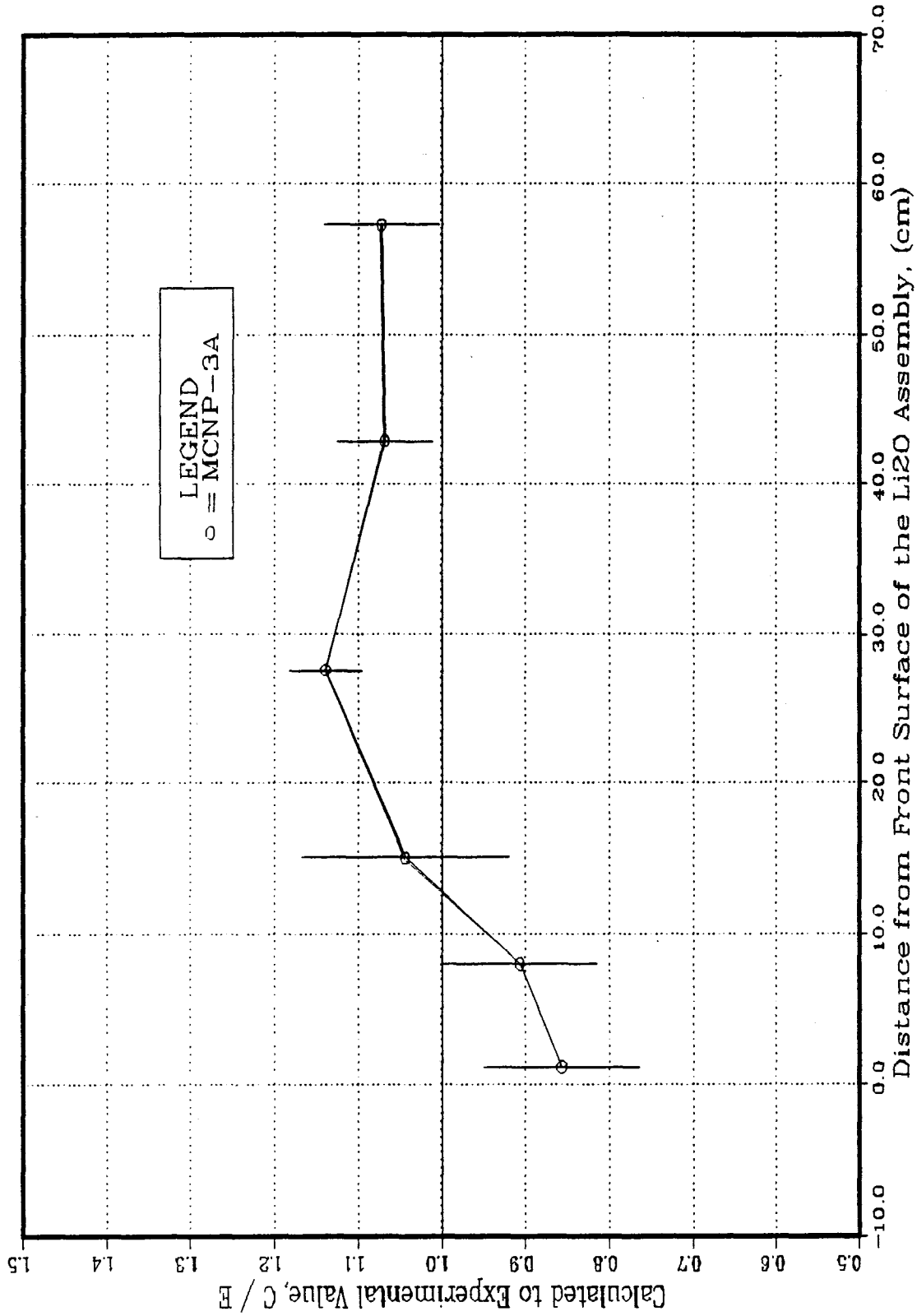

Fig. IV.28: C/E Values for Tritium Production Rate from ^{6}Li (Zonal TPR) in the Central Drawer (REF System - Phase IIA)

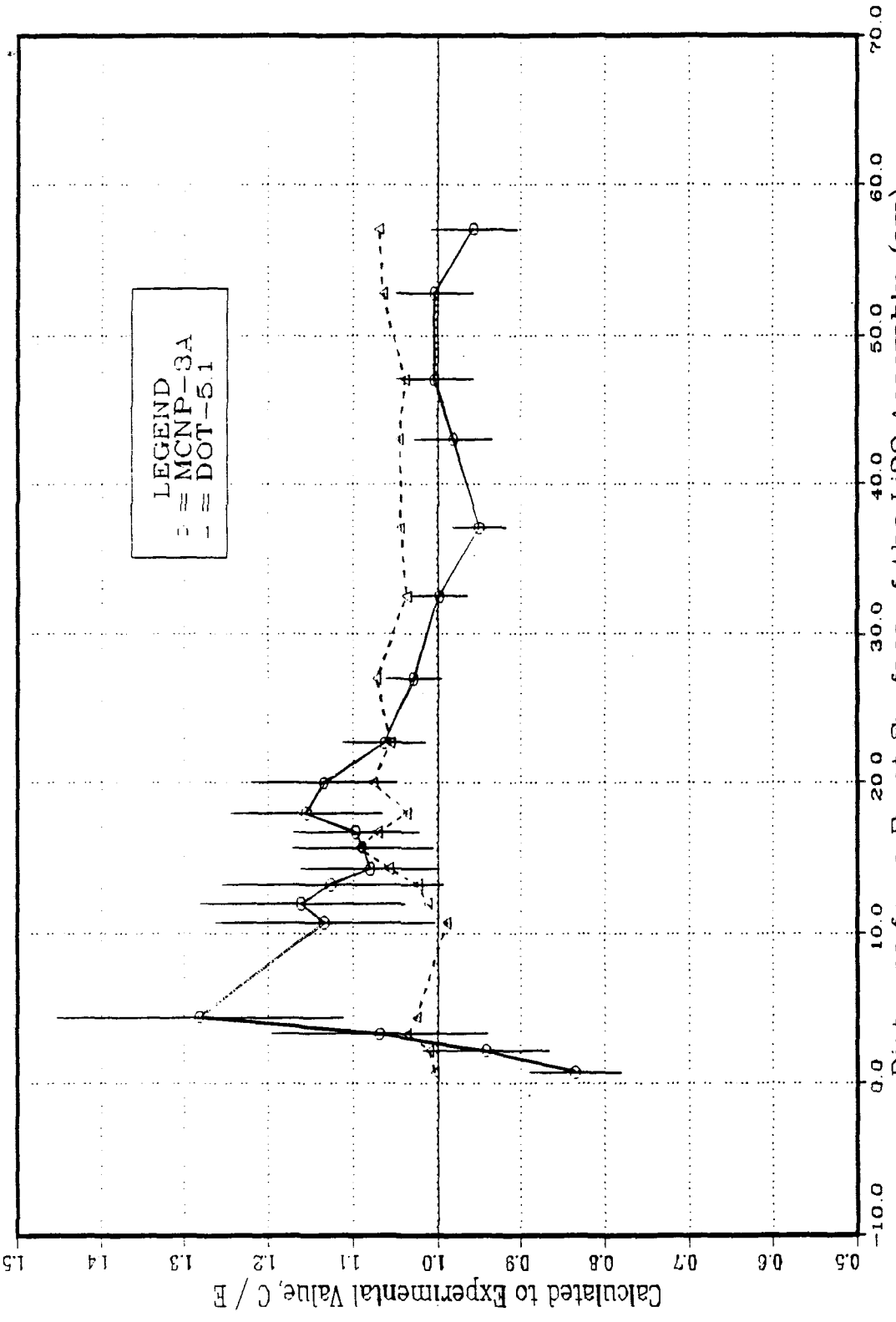

Fig. IV.29: C/E Values for Tritium Production Rate from Natural Lithium (Zonal TPR) in the Central Drawer (BES System - Phase IIA)

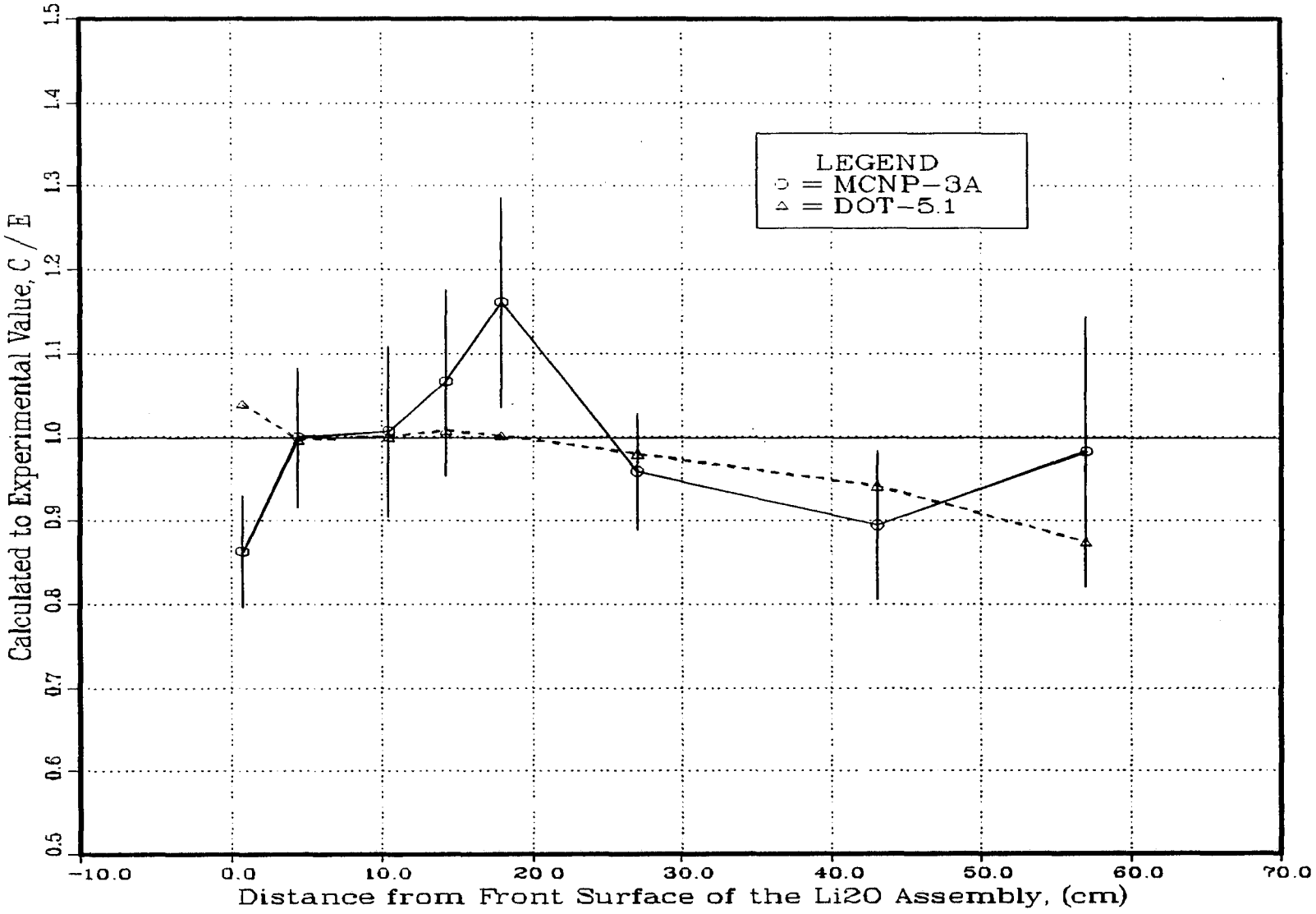

Fig. IV.30: C/E Values for Tritium Production Rate from ^{7}Li (Zonal TPR)
in the Central Drawer
(BES System - Phase IIA)

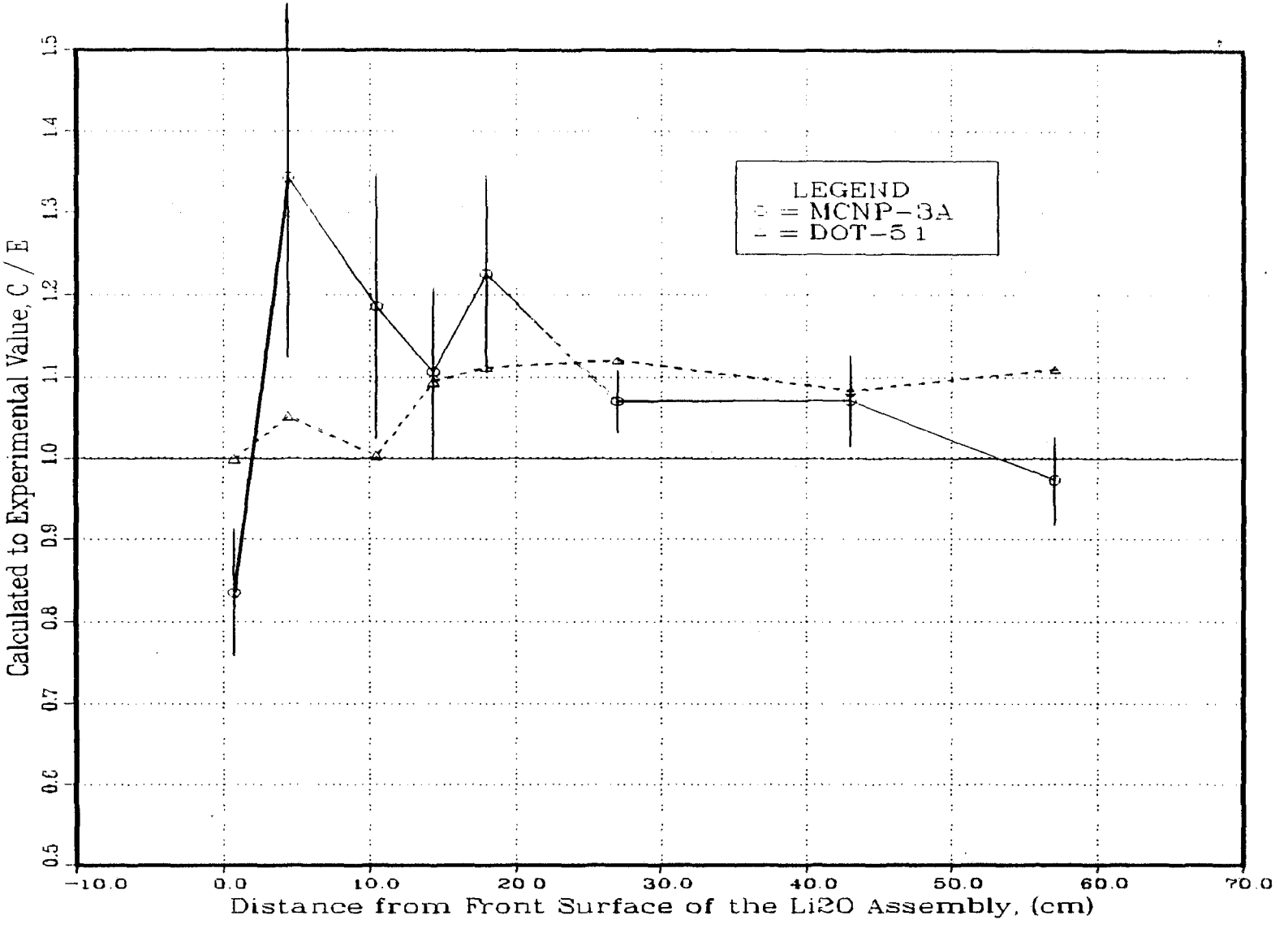

Fig. IV.31: C/E Values for Tritium Production from ^{6}Li (Zonal TPR)
in the Central Drawer
(BES System - Phase IIA)

Table IV.1. Integrated zonal TPR from natural lituium in the reference and the Be-sandwiched system

a. Increase in the tritium breeding potential

Method	Reference		Be-Sandwiched
MCNP	2.434-28*	(1.0)	2.860-28+ (1.175)
DOT	2.646-28	(1.0)	3.184-28+ (1.203)
Measurement	2.467-28	(1.0)	2.889-28+ (1.171)

b. C/E Values

Method	Reference	Be-Sandwiched
MCNP	0.987	0.990
DOT	1.073	1.102

* Units: tritium atom/source neutron. Nat. Li atom. sec.

+ Tritium produced in the beryllium zone is excluded

IV.3 Phase IIB

The main difference between Phase IIA and IIB experimental configuration is that an additional beryllium liner was added where the interior surface of the Li_2CO_3 enclosure was covered by a 5 cm-thick beryllium layer to simulate Be tiles placed on the inboard blanket in a Tokamak fusion reactor. As it was discussed in Section I, three experiments were performed in this phase, namely: (a) the reference experiment: similar to the REF system of Phase IIA but with the Be liner in place, (b) the beryllium front experiment: similar to the BEF experiment of Phase IIA but with the Be liner in place. No stainless steel first wall (FW) preceeded the front Be layer. This system is denoted BEFWOFW, and (c) the Be-front experiment with FW: similar to system (b) but an SUS304 FW of thickness of 0.5 cm was added in front of the Be layer. This system is denoted BEFWFW. Schematic configurations for these systems are shown in Fig. I.3.

IV.3.1 Effect of Beryllium Liner on T_6 Profiles

The inclusion of a 5 cm-thick beryllium liner on the inner surface of the Li_2CO_3 enclosure tends to soften the incident spectrum at the entrance of the Li_2O assembly and hence an increase in T_6 occurs as depected in Fig. IV.32, which shows the ratio of the local T_6 along the central axis in the reference and the BEFWOFW systems of Phase IIB to the corresponding values in Phase IIA (no Be liner). The ratios shown (enhancement factor, M_6) are those predicted by the DOT5.1 calculations, M^C_6, and as measured by the Li-glass detectors, M^E_6. In the reference system, the enhancement factor at the front surface is $M^E_6 = 23$ while the enhancement factor is $M^C_6 = 14$ as predicted by the DOT calculations. Note that the low-energy component of the incident spectrum gets absorbed rapidly by ^6Li throughout the first 10 - 20 cm inside the assembly and the ratio M_6 is close to unity at deeper locations. In the BEFWOFW system, the inclusion of the Be-liner tends to further increase T_6 behind the front Be layer but the local increase at these locations is less pronounced than in the reference system. However, since the incident spectrum gets further softened inside the front Be layer, a remarkable increase in T_6 occurs inside this layer [by a factor of $\sim$ 21(DOT) and a factor of $\sim$ 17 (measurements)].

The C/E values in the REF, BEFWOFW, and the BEFWFW systems are shown in Figs. IV.33 to IV.35, respectively. The C/E values are lower than unity at the front surface of the Li_2O assembly in the reference system (MCNP: C/E = 0.63, DOT5.1: C/E = 0.72). This could be attributed to the observation that in Young's evaluation for the Be(n,2n)

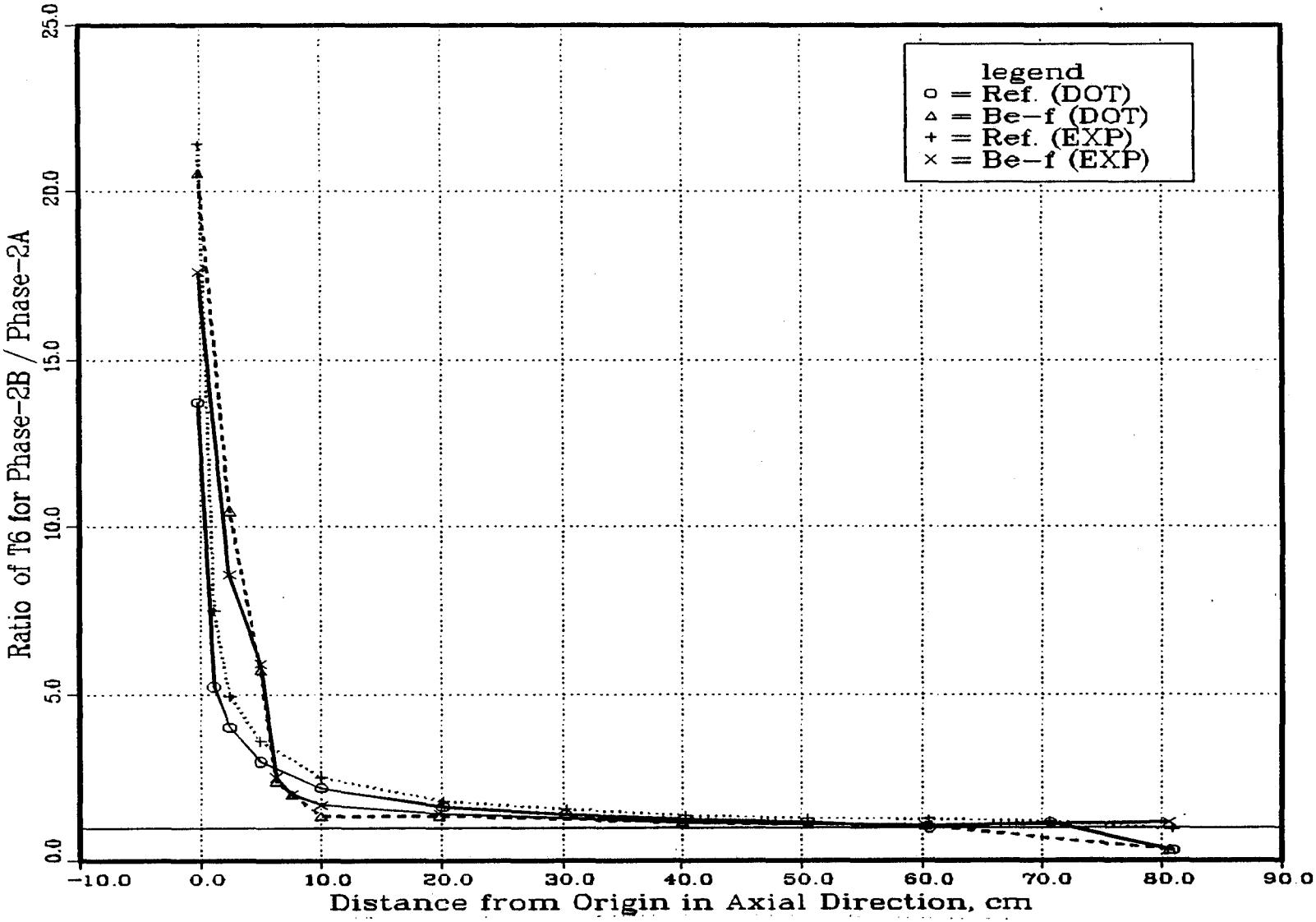

Fig. IV.32: Comparison of Phase IIA and IIB Experiments for T_6
(REF and BEFWOFW-DOT5.1 and Li-Glass)

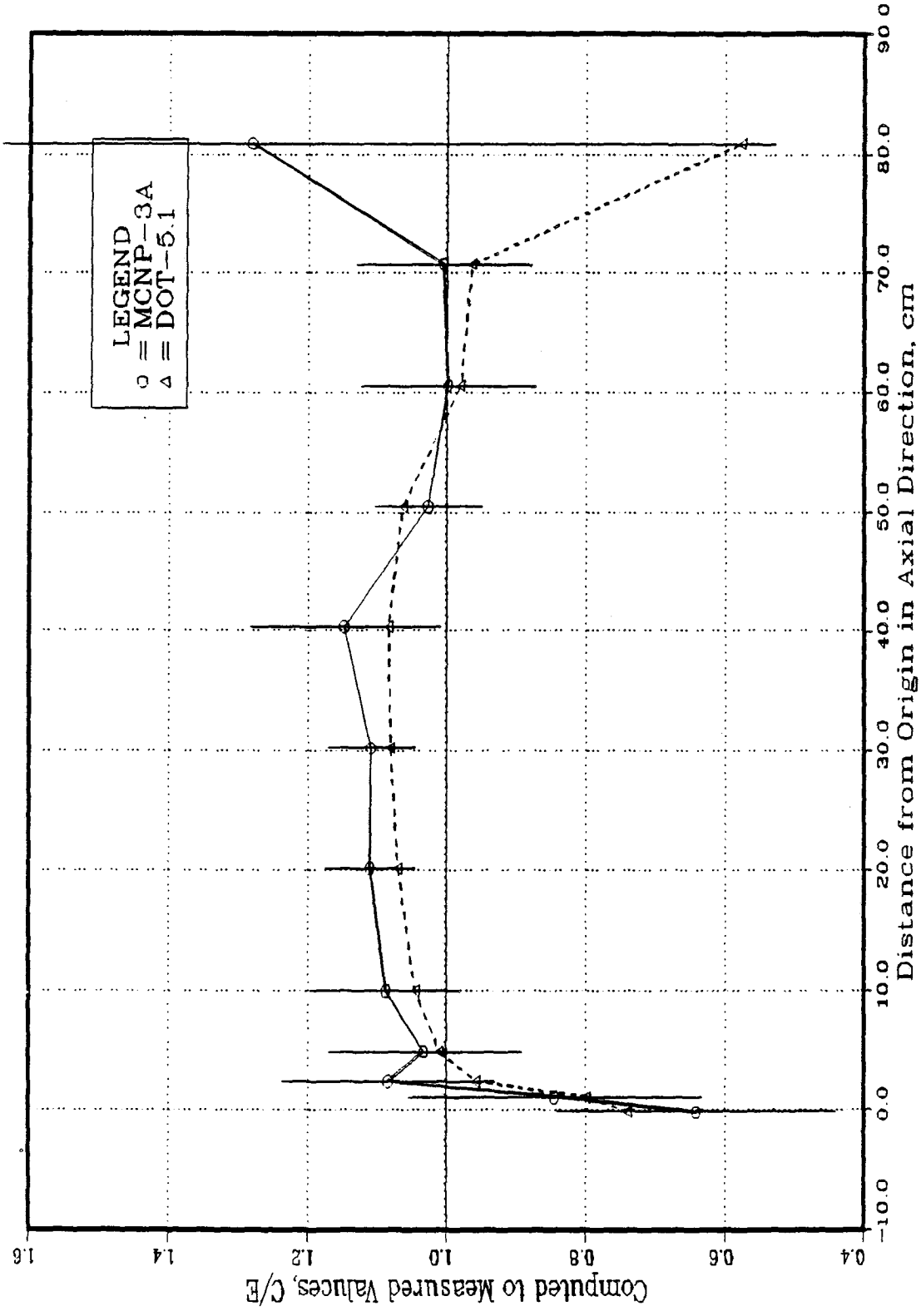

Fig. IV.33: C/E Values for T_6 Measured by Li-Glass Detector in the Central Drawer of Phase IIB (REF System)

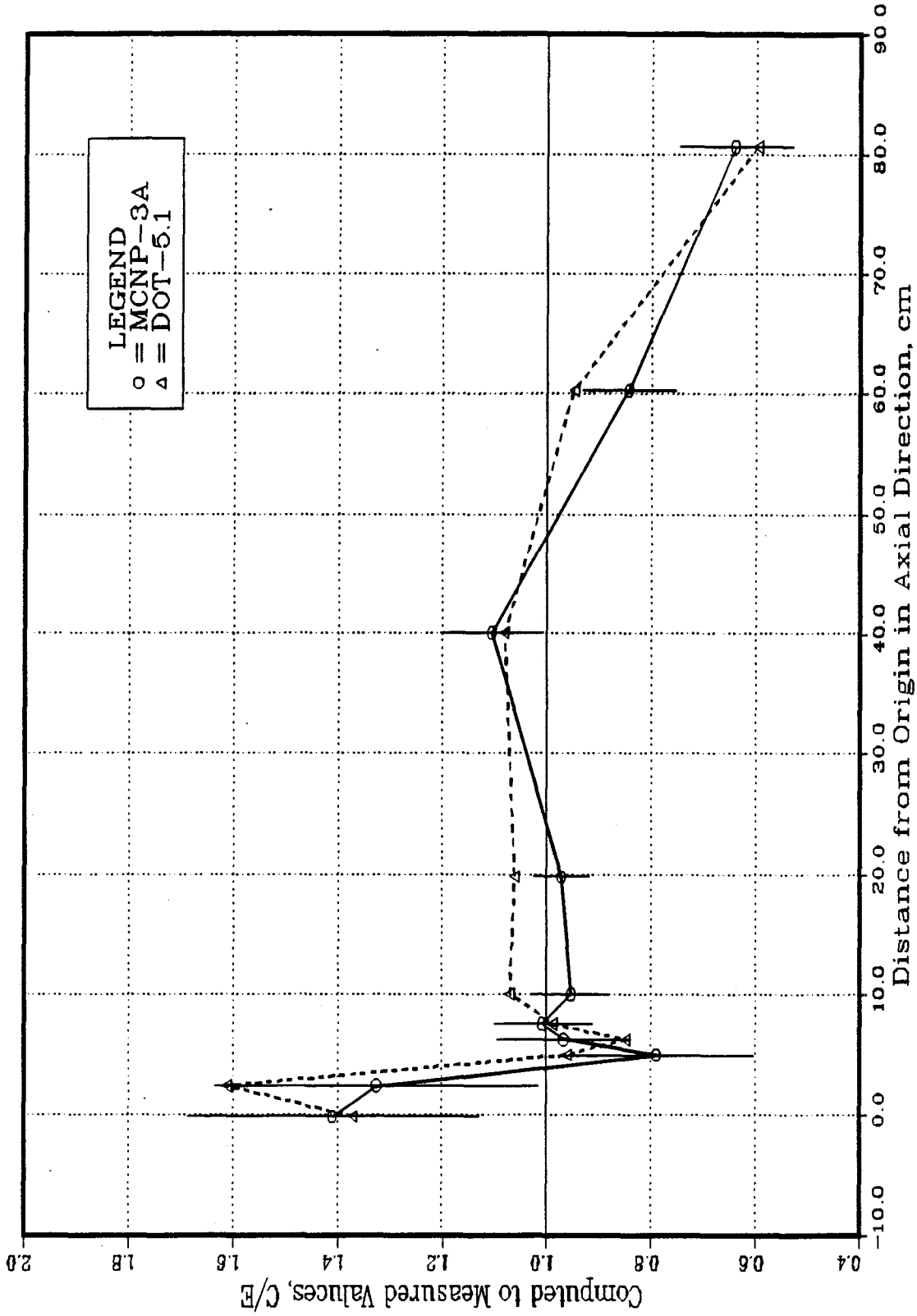

Fig. IV.34: C/E Values for T_6 Measured by Li-Glass Detector in the Central Drawer of Phase IIB (BEFWOFW System)

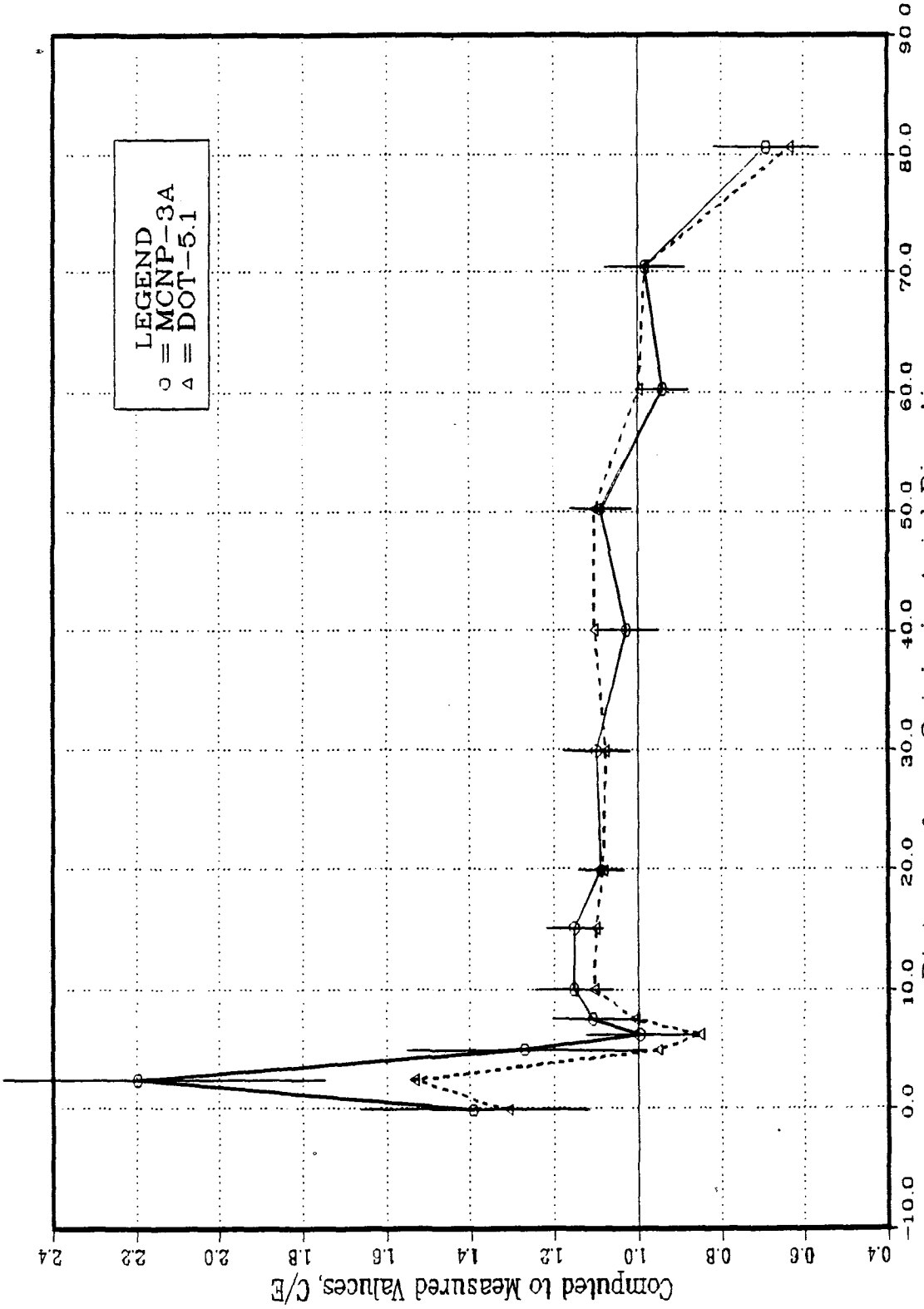

Fig. IV.35: C/E Values for T_6 Measured by Li-Glass Detector in the Central Drawer of Phase IIB (BEFWFW System)

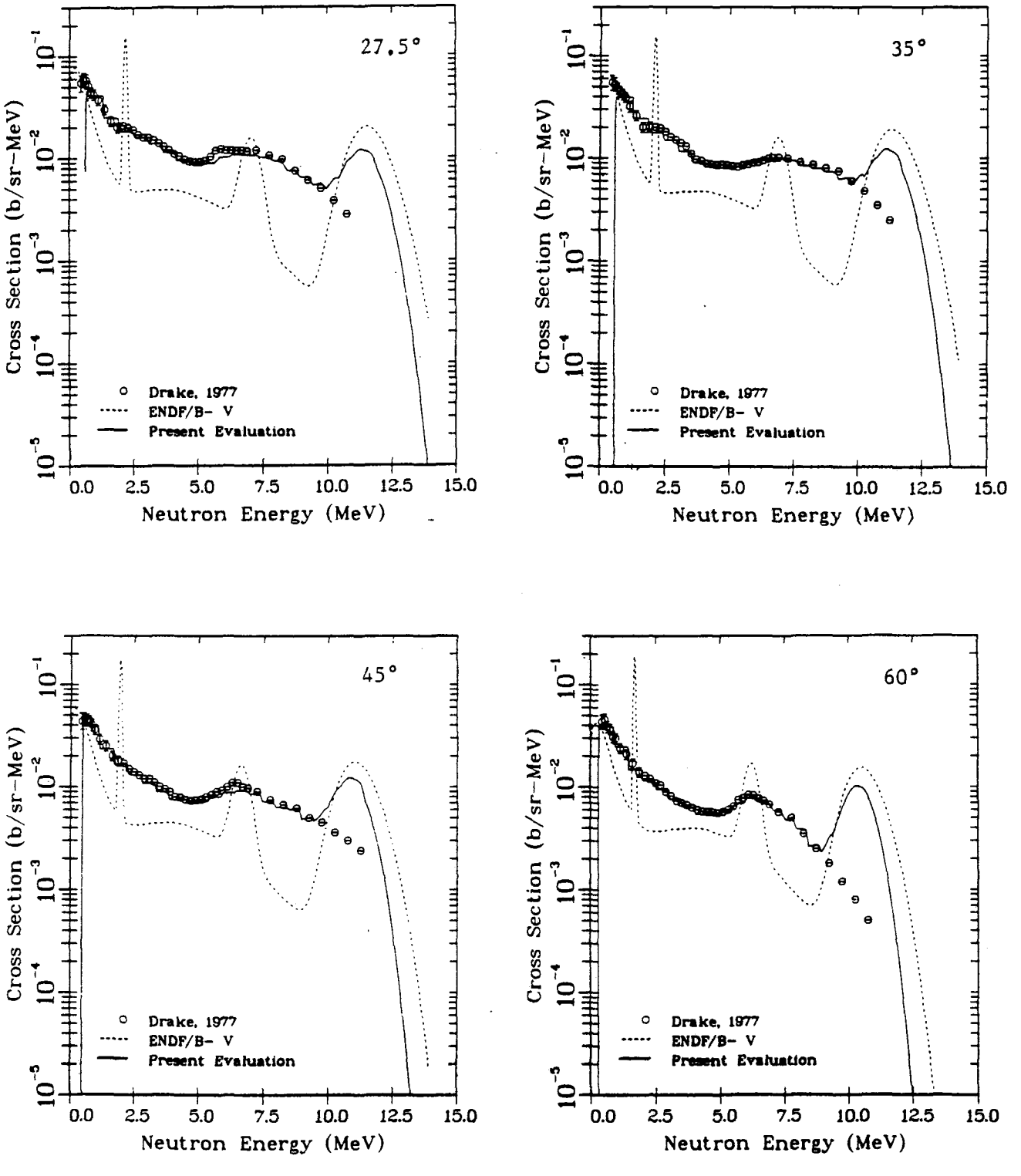

Fig. IV.36: Measured and Evaluated Neutron-Emission Spectra at 27.5, 35, 45, and 60° Induced by 14.2-MeV Neutrons
[From Ref. (27)]

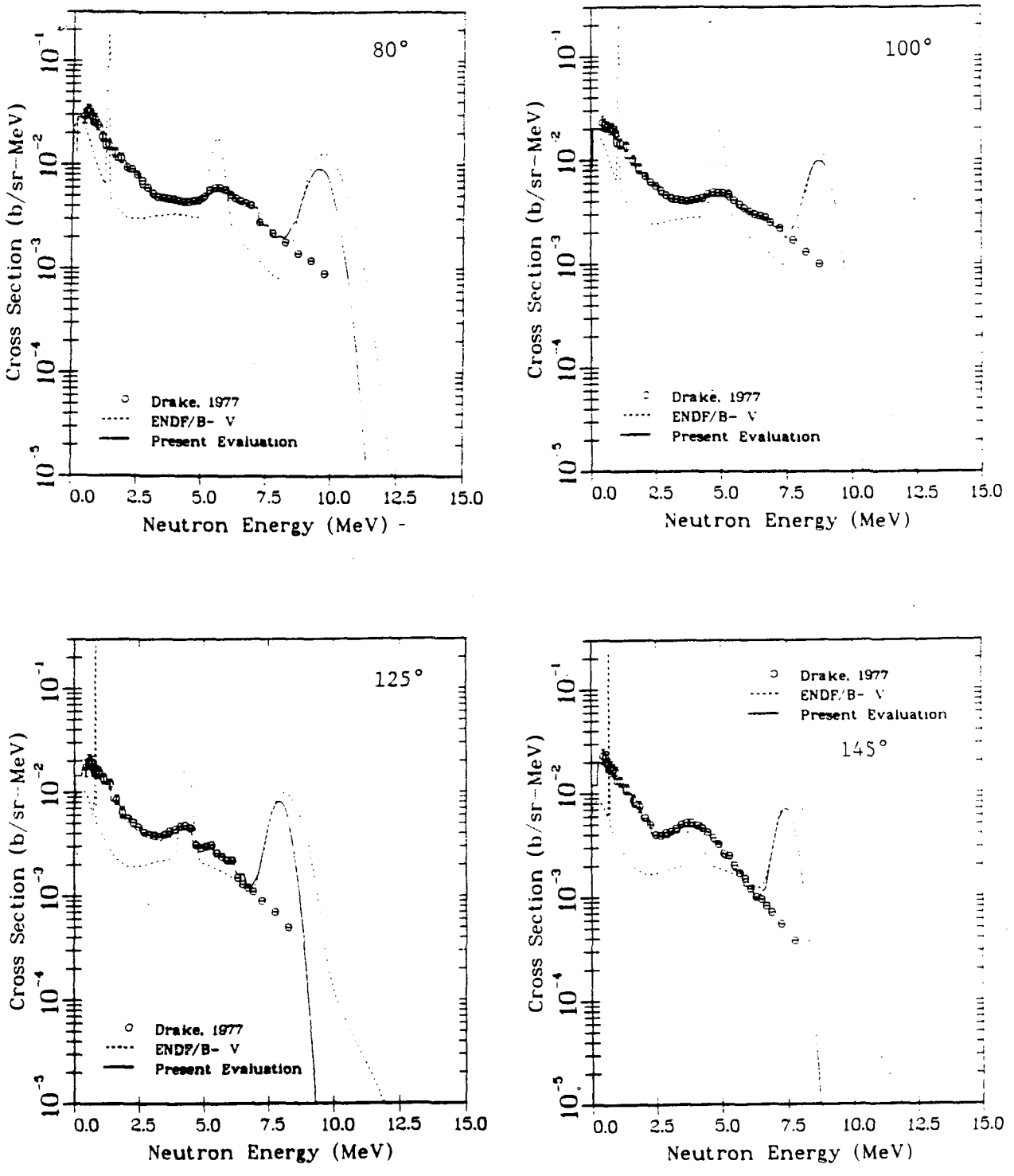

Fig. IV.37: Measured and Evaluated Neutron-Emission Spectra at 80, 100, 125, and 145° Induced by 14.2 -MeV Neutrons
[From Ref. (27)]

reaction, at high energies, the emission spectrum has a low energy component (E<0.5 MeV). This could be seen from Figs. IV.36 and IV.37 which show the energy distribution of the secondary neutrons emitted from the $^{9}Be(n,2n)$ reactions for incident energy of 14.2 MeV and at various angles. The solid-line curves are the Young's cross-sections which are vanishing below ~ 0.5 MeV. This is also true for other incident energies. Note that the Young's evaluation (LANL) for Be cross-sections was deployed in both the Monte Carlo and the discrete ordinates codes used. Therefore, neutrons interacting with the Be liner and reflected toward the test assembly have small low-energy component below 0.5 MeV resulting in underestimating T_6 at the front few centimeters in the Li_2O test assembly. In the bulk of the Li_2O, however, the C/E values are 1 -1.15. The C/E values in the BEFWOFW and BEFWFW systems are ~ 1 - 1.08 and ~ 1 - 1.15 in the bulk of this Li_2O zone, respectively. The large C/E values inside the Be layer are due to the self-shielding effect and flux perturbation by the Li-glass detector as explained earlier in Section IV.1. More on correction for self-shielding effect is given in Section IV.3.4. Note also from Figs. IV.33 - 35 that the C/E values fall below unity just behind the front Be layer, then sharply rise after 3 - 5 cm to reach more or less steady values and then decrease toward the back locations. These features were found in the BEF and BES systems of Phase IIA, as was pointed out earlier and could be related to the beryllium cross-sections as explained below. Section V is devoted to further investigating these features.

The C/E values for T_6 in the case where Li-foil detectors were used are shown in Fig. IV.38 for the BEFWFW system. In comparison to Fig. IV.35, one notices that the C/E values inside the beryllium layer are less than the case where Li-glass detectors are used to measure T_6. Also, in the bulk of the Li_2O zone, the C/E values are generally closer to unity as compared to those shown in Fig. IV.35. Thus the divergence between the Li-foil and the Li-glass measurements is ~ 10 - 20 % where the former gives lower values. However, the features discussed above on the shape of the C/E curves for T_6 (as obtained by MCNP and DOT codes) are the same.

IV.3.2 Effect of Beryllium Liner on T_7 Profiles

The ratio of the local T_7 in the cases where the inner surface of the Li_2CO_3 enclosure is covered by Be liner to the corresponding values without a liner in the reference and the Be-front (w/o FW, BEFWOFW) are shown in Fig. IV.39. While DOT calculations predict an increase in T_7 of 2 - 5% up to 10 cm - depth in the REF system and a decrease of 2 - 10% thereafter, measurements indicate an increase of 10 - 15% throughout

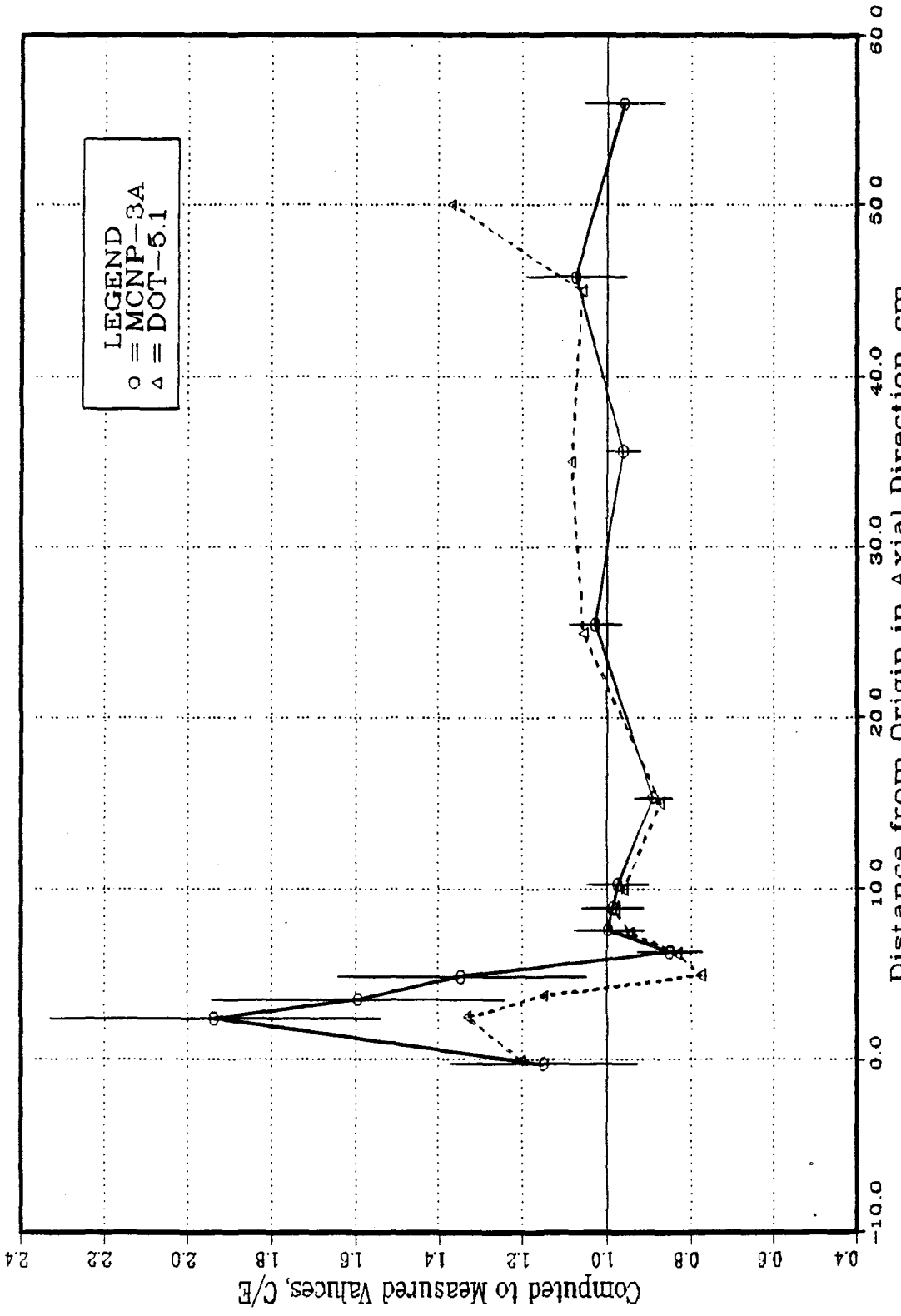

Fig. IV.38: C/E Values for T_6 Using ANL Foils in the Central Drawer (BEFWFW System - Phase IIB)

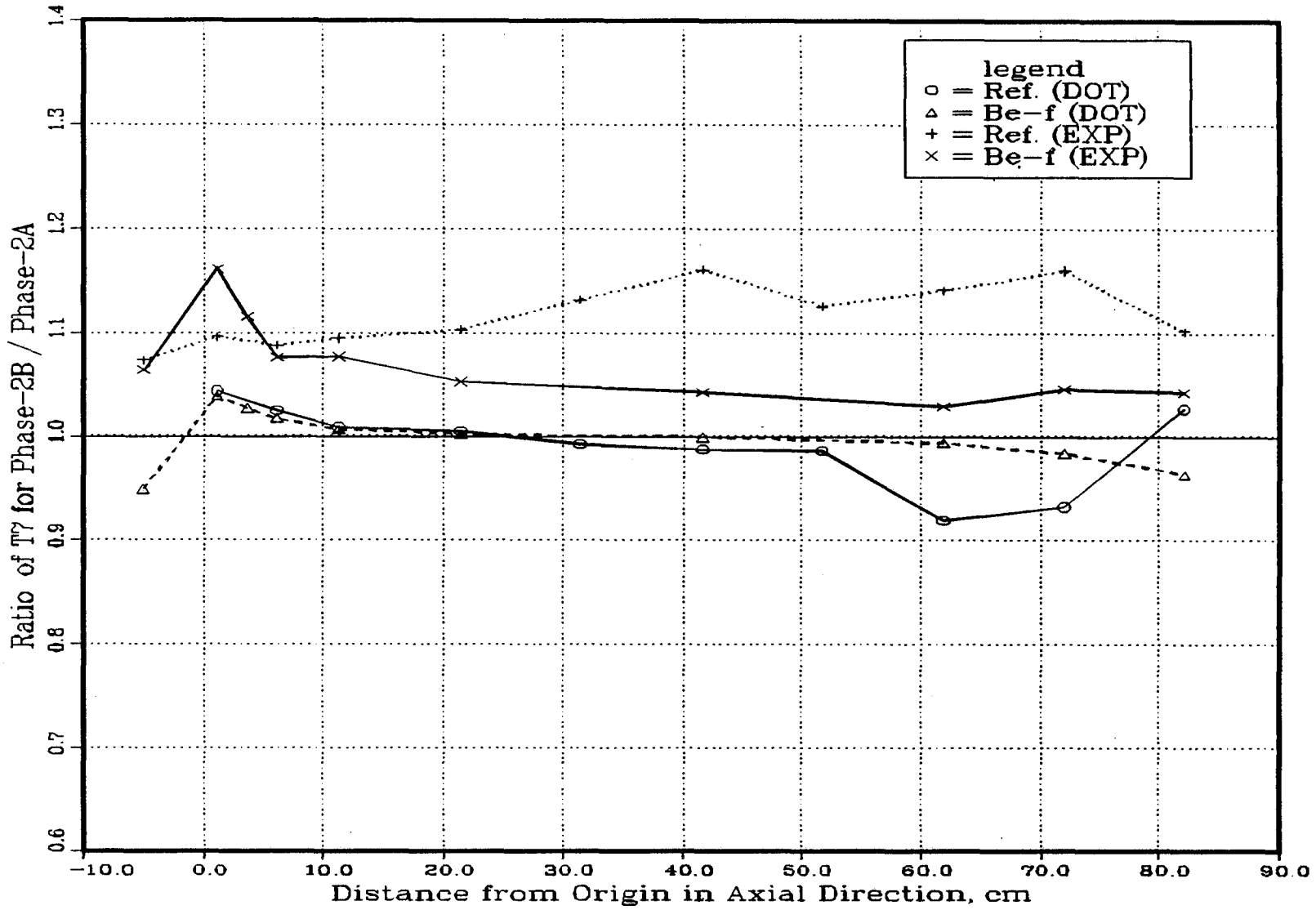

Fig. IV.39: Comparison of Phase IIA and IIB Experiments for T_7 in the Reference and BEFWFW System (DOT5.1 & NE213)

the Li_2O zone. In the BEFWOFW system, the predicted change is similar to the reference system but measurements show an increase of 5 - 15%.

The C/E curves for T_7 is the REF, BEFWOFW, and the BEFWFW systems are shown in Figs. IV.40 to IV.42, respectively. Their values in these systems are C/E ≈ 0.92 - 1.15, 0.88 - 1.10, and 0.98 - 1.22, respectively. The C/E values for T_7 using the ANL foils are shown in Fig. IV.42' for the BEFWFW system. Unlike the values shown in Fig. IV.42, the C/E values are lower than unity by ~ 15% up to a depth of 10 cm, as predicted by both MCNP and DOT calculations, but they are ~ 1.5 - 1.12 in the bulk of the Li_2O zone. Note that the statistical errors in the MCNP calculations for T_7 are large at almost all locations considered, as shown in Fig. IV.42. In comparison to the C/E curves for T_7 in Phase IIA shown in Figs. IV.20 and IV.23, the values in Phase IIB tend to be lower than those of Phase IIA (by ~ 10%). In addition, the C/E curves in Phase IIB exhibit a slope toward the back locations in the Li_2O assembly where the C/E values fall below unity at these locations, as shown in Figs. IV.40 and IV.41. This behavior in the C/E curves could be related to the uncertainty associated with the $^9Be(n, 2n)$ cross section and the energy/angle distributions of the secondary neutrons emitted from this reaction as discussed below.

IV.3.3 Remarks on the Enhancement in T_6 and T_7 Upon Including Beryllium Liner/Layer

One notices from Fig. IV.32 that the enhancement factors, M^C_6, are always less than M^E_6 except inside the beryllium zone in the BEF system, that is, the calculations underestimate the local increase in T_6 in the Li_2O assembly in the reference system and behind the Be layer in the Be-front system upon including the Be liner. This is further illustrated in Fig. IV.43 which shows the ratios of M^C_6 to M^E_6 in both systems. The enhancement in T_6 is underestimated by ~ 35% at the front surface in the reference system and the discrepancy between M^C_6 and M^E_6 gets less in the bulk of the Li_2O assembly. These features are the same behind the Be zone in the Be-front system but the discrepancy is less pronounced. Note that the ratio M^C_6/M^E_6 is equal to the ratio of C/E values in each system of Phase IIB to the C/E values of that system in Phase IIA.

The reason for the above mentioned features could be explained by comparing the computed enhancement factor M^C_6 (ratio of the local T_6 in the case where a Be layer is included to the corresponding value in the reference system) to the measured one, M^E_6, in the BEF and BES systems of Phase IIA and in the Be-front system of Phase IIB (BEFWOFW), as shown in Fig. IV.44. It is clear form the figure that M^C_6/M^E_6 is always

less than unity in the Li_2O zone(s) of Phase IIA and that the discrepancy is more pronounced just behind the Be layer. Note from Fig. IV.44 the similarity (in shape) to the C/E curves shown in Fig. IV.14 and IV.35. The enhancement in T_6 is underestimated by $\sim$ 30% behind the Be layer and by $\sim$ 10% in the bulk of the Li_2O zone in both systems of Phase IIA. The range of this discrepancy is similar to the one shown in Fig. IV.43 due to the inclusion of the Be liner in the reference system of Phase IIB. In Phase IIB, the discrepancy in the enhancement factor between calculations (DOT5.1) and measurement upon including a front Be layer is less pronounced and is $\sim$ 20% behind the Be layer and $\sim$ 2% in the bulk of the Li_2O zone, as shown in Fig. IV.44. These features could be explained if the emerging neutrons from the Be layer are underestimated in the low-energy range (below 0.5 MeV) and overestimated in the energy range 2 - 10 MeV. The underestimation in the low-energy component leads to the large discrepancy in the enhancement factor just behind the Be layer. However, the overestimation in the emerged neutrons in the energy range 2MeV <E<10 MeV tends to improve the discrepancy since these neutrons are slowed down as they travel inside the Li_2O zone, and thus lead to an increase in the local values of T_6 by distance and the discrepancy caused by the underestimation in the emerged spectrum below 0.5 MeV tends to decrease.

Oyama and Maekawa[34] have shown that the spectrum of the emerged neutrons from a 5 cm-thick beryllium slab is indeed underestimated in the energy range 0.1- 0.5 MeV upon using LANL (Young's), JENDL3-PR1, and ENDF/B-IV data for beryllium. They have also shown that this spectrum is overestimated in the energy range 2 - 10 MeV with LANL evaluation by $\sim$ 10 - 20% but is underestimated by $\sim$ 20 - 40% with the JENDL3-PR1 evaluation while the spectrum above 10 MeV is underestimated by 20 - 30% with both evaluations. Since the $^9Be(n,2n)$ reactions are appreciable inside the Be layer, one can suspect that the emission spectrum from these reactions is underestimated in the energy range below 0.5 MeV and overestimated (in Young's evaluation) in the energy range 2 MeV < E < 10 MeV. Since more such interactions occur if the incident spectrum is hard (as in Phase IIA), the discrepancy in the computed and measured enhancement factor for T6 is more pronounced in Phase IIA than in Phase IIB behind the front Be layer, as shown in Fig. IV.44.

The fact that the enhancement in T_6 upon including the Be liner in Phase IIB is also underestimated, as shown in Fig. IV.43, is consistent with the results of Oyama and Maekawa's experiment. Neutrons emitted from the $^9Be(n, 2n)$ reactions in the Be-liner and reflected toward the test assembly could be underestimated in the energy range below 0.5

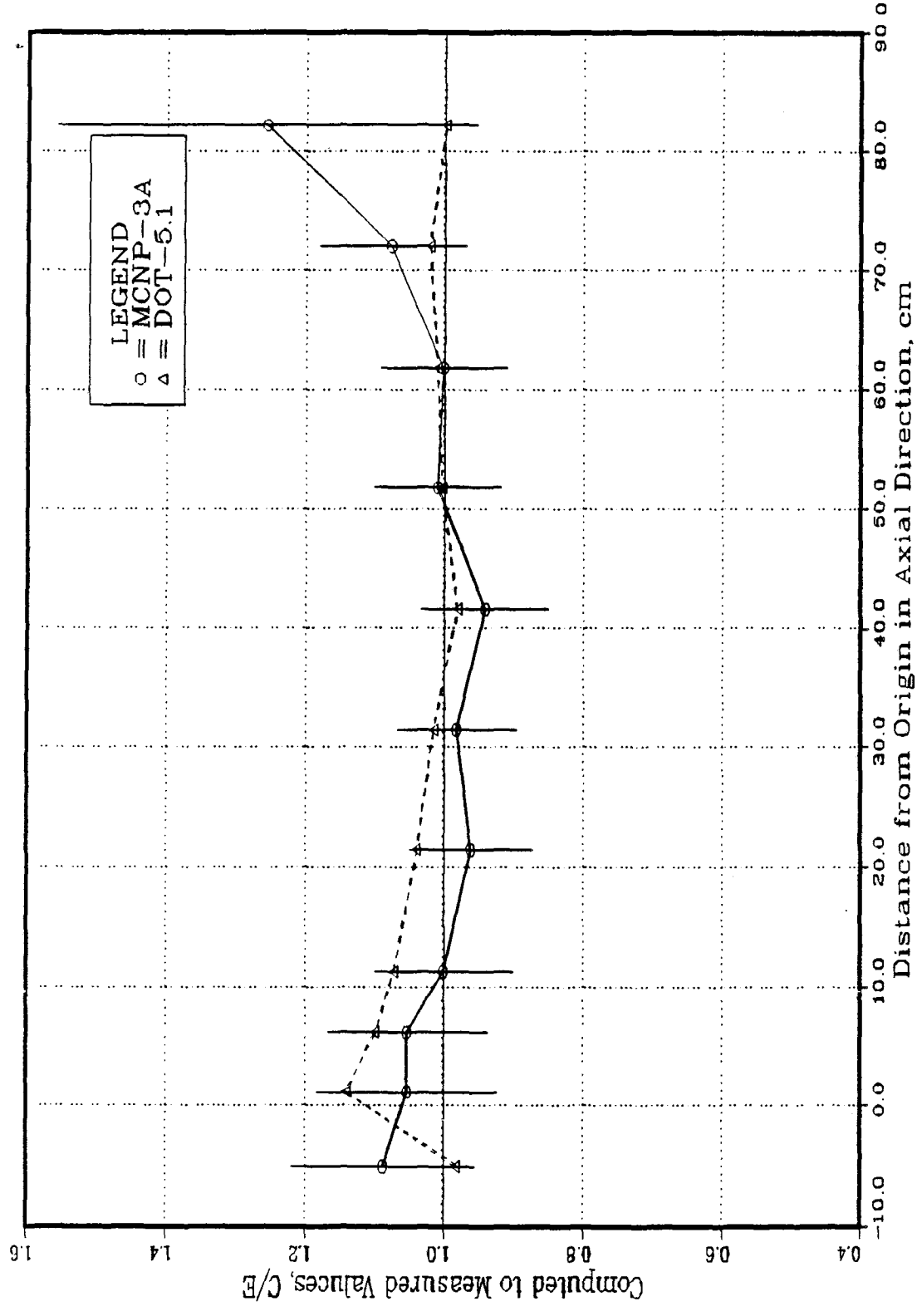

Fig. IV.40: C/E Values for T_7 Measured by NE213 Detector in the Central Drawer of Phase IIB (REF System)

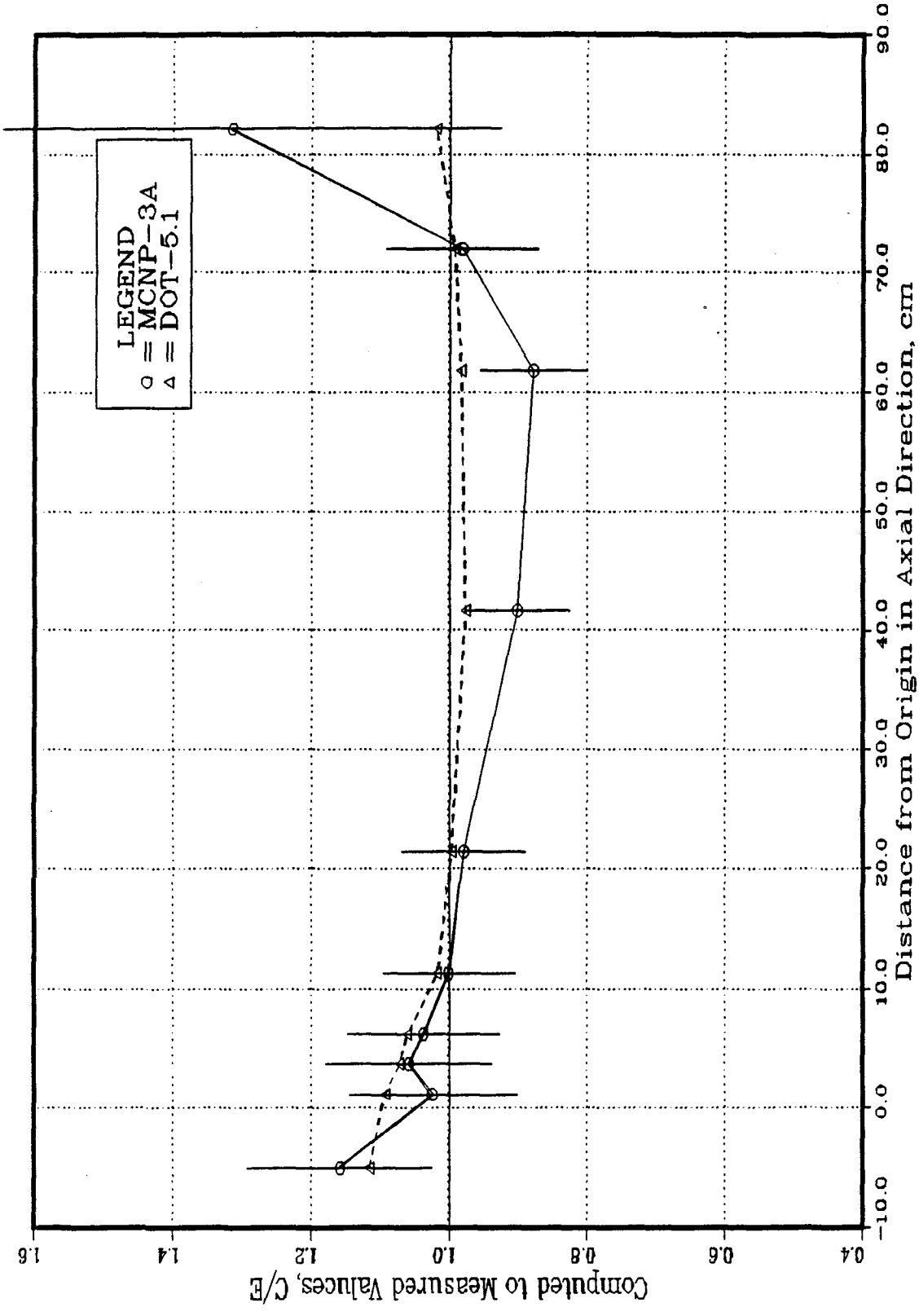

Fig. IV.41 C/E Values for T_7 Measured by NE213 Detector in the Central Drawer of Phase IIB (BEFWOFW System)

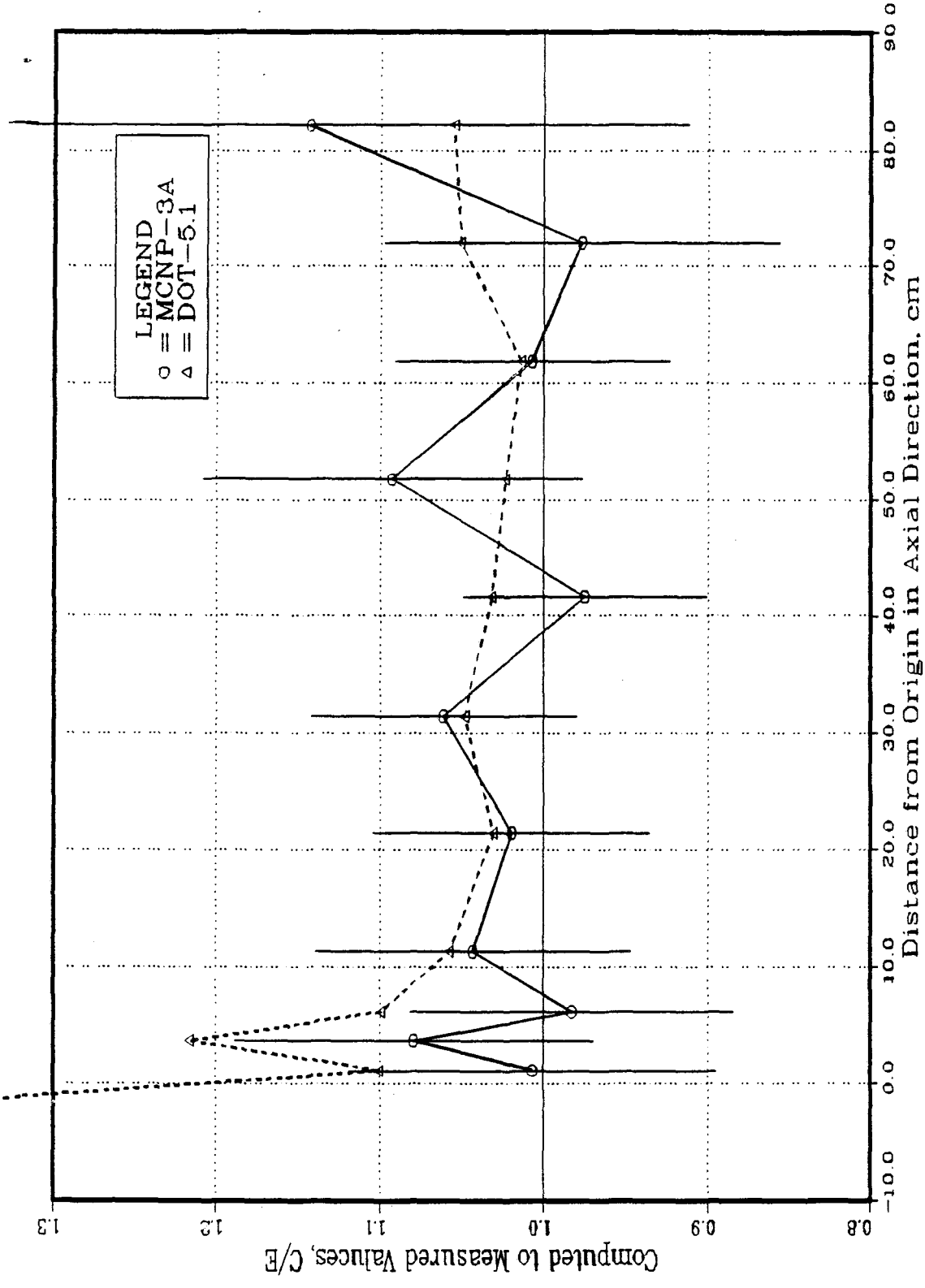

Fig. IV.42: C/E Values for T_7 Measured by NE213 Detector in the Central Drawer (BEFWFW System - Phase IIB)

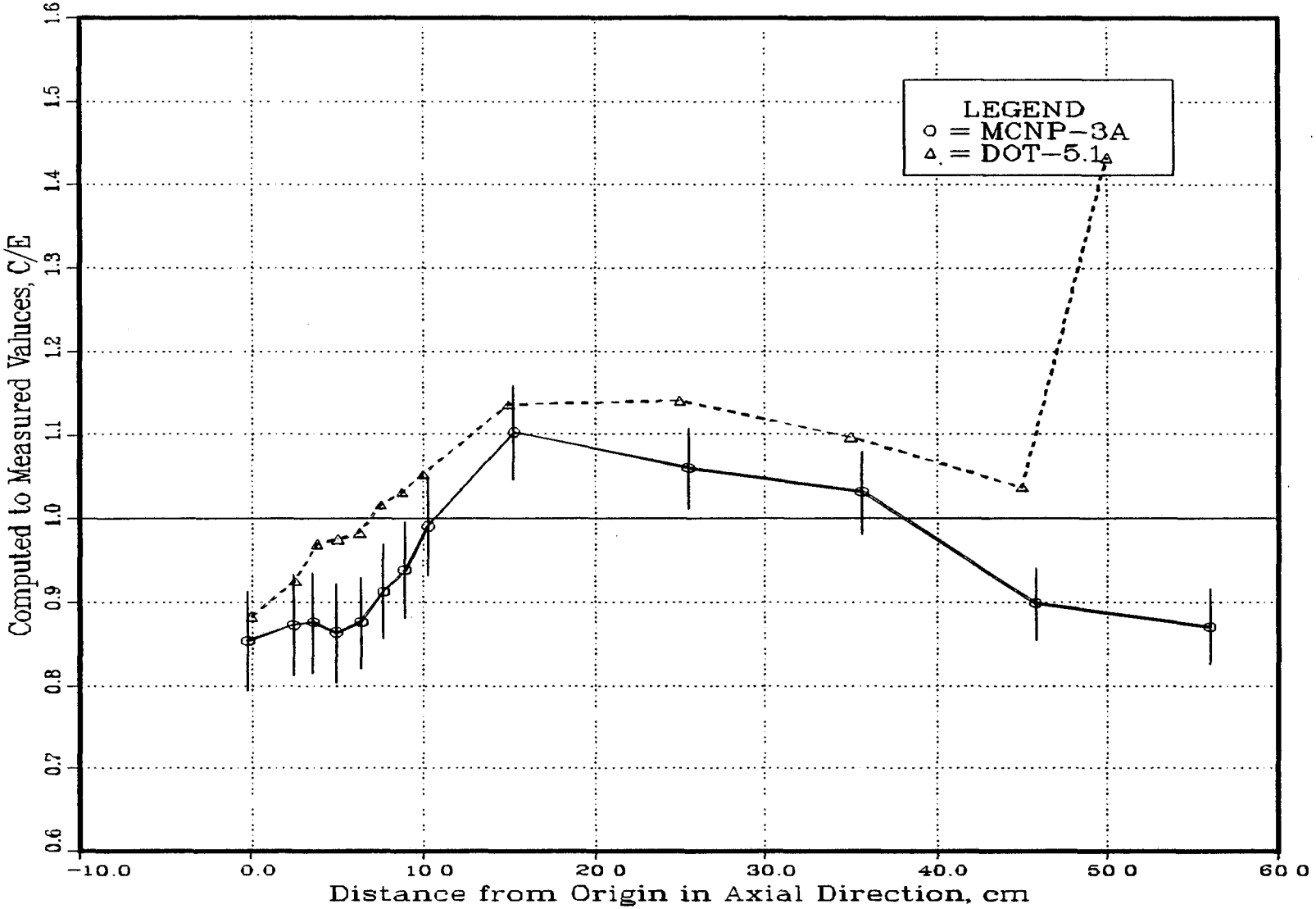

Fig. IV.42': C/E Values for T_7 Using ANL Foils in the Central Drawer
(BEFWFW System - Phase IIB)

MeV and overestimated in the energy range 2 MeV < E < 10 MeV. The overestimation of the incident spectrum in the energy range 2 MeV < E < 10 dMeV could be seen from Fig. IV.45 which shows comparison to the measured spectrum by NE213 measurements at the surface of the Li_2O assembly in the reference system of Phase IIB. Note that NE213 measurements below 1 MeV are not reliable due to the inherent inaccuracy of this method below this energy. Detailed discussion on spectra measurements and their analysis is given in Section VII.

As for T_7, it was indicated in Fig IV.39 that calculations underpredict T_7 upon including the Be-liner in Phase IIB, as compared to measurements by NE213 method. The ratio of the computed enhancement factor, M^C_7, to the measured one, M^E_7, is shown in Fig. IV.46 for the REF and BEFWOFW systems. Similar to T_6, the enhancement factor is underestimated by calculations throughout the entire test assembly and the underestimation is larger in the reference system in comparison to the Be-front system.

As was shown in Fig. IV.44 for T_6, the ratios of the computed enhancement (or rather a decrease) factor, M^C_7, (ratio of local T_7 in the case where a Be front layer is included to the corresponding value in the reference system) to the measured one, M^E_7, in the Be-front (BEF) and Be-sandwiched (BES) systems of Phase IIA and in the BEFWOFW system of Phase IIB are shown in Fig. IV.47. As shown these ratios are always less than unity throughout the Li_2O zone in both systems of Phase IIA but slightly larger than unity inside the Be layer. Thus, the calculations overestimate the relative decrease in local T_7 inside the Li_2O zone (or underestimate T_7) upon the inclusion of the Be layer. (The Be layer acts as a moderator and hence local T_7 are decreased in the Li_2O zone.) Similar features were found in the Be-front system of Phase IIB, as also shown in Fig. IV.47.

The underestimation in the local T_7 upon including the Be layer could be related to the accuracy of the total $^9Be(n,2n)$ cross-section as currently implemented in LANL evaluation. This cross-section is overestimated above 10 MeV and therefore neutron moderation at high energy throughout $^9Be(n,2n)$ reactions are overestimated. This is supported by the observation made by Oyama and Maekawa in their experiment where the emerged spectrum from the 5 cm-thick Be slab is underestimated above 10 MeV. This can also be seen from Fig. IV.48 that shows a comparison of the calculated neutron spectrum behind the Be layer in the BEFWFW system of Phase IIB where the 14 MeV peak is underestimated by calculations. The underestimation of the 14 MeV peak can also be seen in Fig. IV.45 due to the collisions in the Be liner where overestimation in the $^9Be(n,2n)$

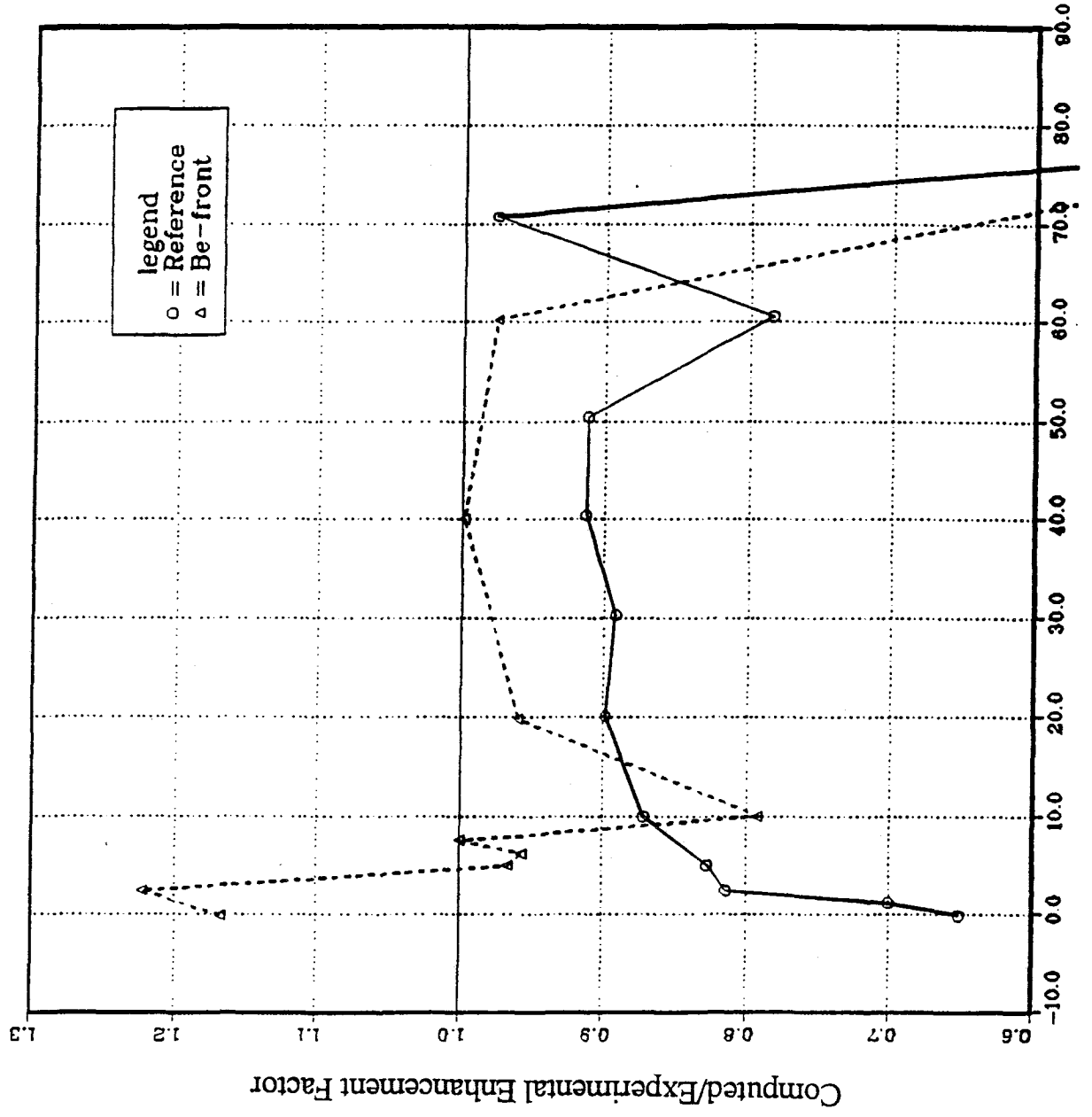

Fig. IV.43: Calculated to Measured Enhancement Factor in T_6 due to the Beryllium Liner in Phase IIB

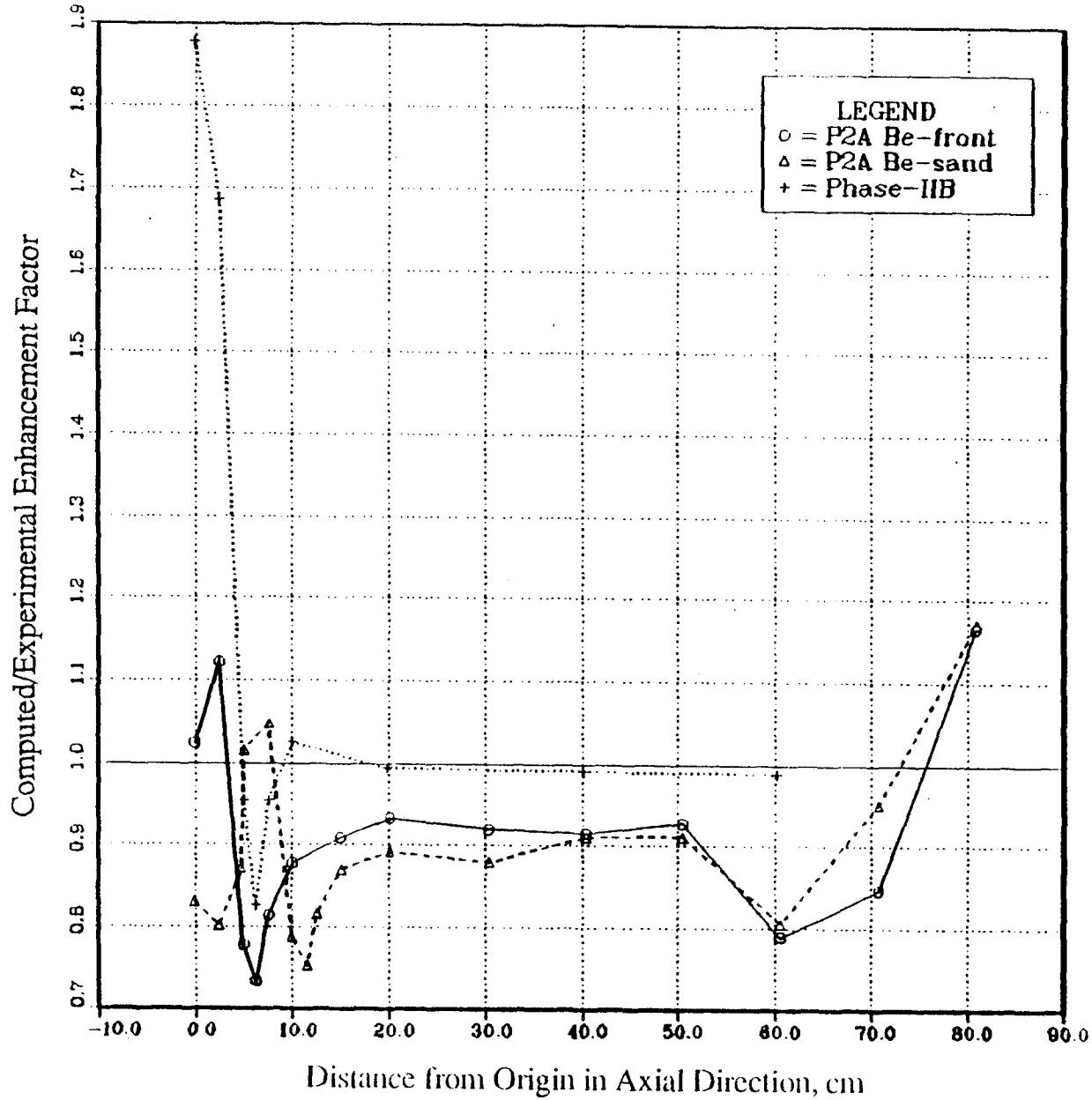

Fig. IV.44: Calculated to Measured Enhancement Factor in T_6 Due to the Beryllium Front Layer in Phase IIA and IIB

reactions exists. The underestimation in the 14 MeV peak was observed in all the spectra that were measured at various locations inside the assembly in Phase IIB as discussed in Section VII. In Section VIII, a comprehensive comparison between the impact of various evaluations of the beryllium cross-sections on T_6 and T_7 (and other reaction rates and spectra) is given, where it is shown that ENDF/B-VI data for beryllium narrows the discrepancy between calculations and measurements. One can also notice in Fig. IV.47 that the discrepancy between M^C_7 and M^E_7 gets larger at the back locations since the effect of the underestimation in the high-energy component of the emerged neutrons from the Be-layer is more pronounced at deep locations. Furthermore, cross-section sensitivity analysis has indicated that T_7 has negative sensitivity coefficient to an increase in the ^{9}Be(n,2n) cross-section at high-energy and that this coefficient gets larger as one proceeds deeper into the Li_2O zone behind the Be layer. Further discussion on the cross sections sensitivity analysis and their impact on T_6 and T_7 is given in Section V. Since less ^{9}Be(n,2n) reactions occur if the incident spectrum is soft, the discrepancy between M^C_7 and M^E_7 is smaller in Phase IIB, as shown in Fig. IV.47.

The overestimation in the relative decrease in T_7 upon including a front Be layer in Phase IIA and the underestimation in the enhancement factor for T_6 lead to underestimation in the enhancement in tritium breeding upon including the beryllium multiplier. This is supported by the results shown in Table IV.1 where calculations underestimate the enhancement in the integrated zonal TPR by ~ 3% relative to measurements. Note that this underestimation is for the natural Li_2O breeder and the results could be different for other breeding materials that are enriched in ^{6}Li. Also, the overestimation in the relative decrease in local T_7 upon including a Be liner in Phase IIB [see Fig. IV.46] and the underestimation in the enhancement factor for local T_6 in that phase [see Fig. IV.43] lead to underestimation in the integrated values throughout the Li_2O zone.

IV.3.4 Self-Shielding Correction Factors

Due to the finite nature of the detectors used to measure T_6 (Li-glass, Li-foil), there is a flux depression in the low-energy neutron flux inside these detectors. This effect was not taken into consideration when the calculations were performed. The calculated values for T_6 and T_7 should thus be reduced by a factor to account for this self-shielding effect. In zones characterized by having soft-spectrum, such as inside the beryllium zone in the BEF and BES systems of Phase IIA and BEFWFW in Phase IIB, the correction factors are significant. However, in the Li_2O zone, where relatively harder spectra are found in

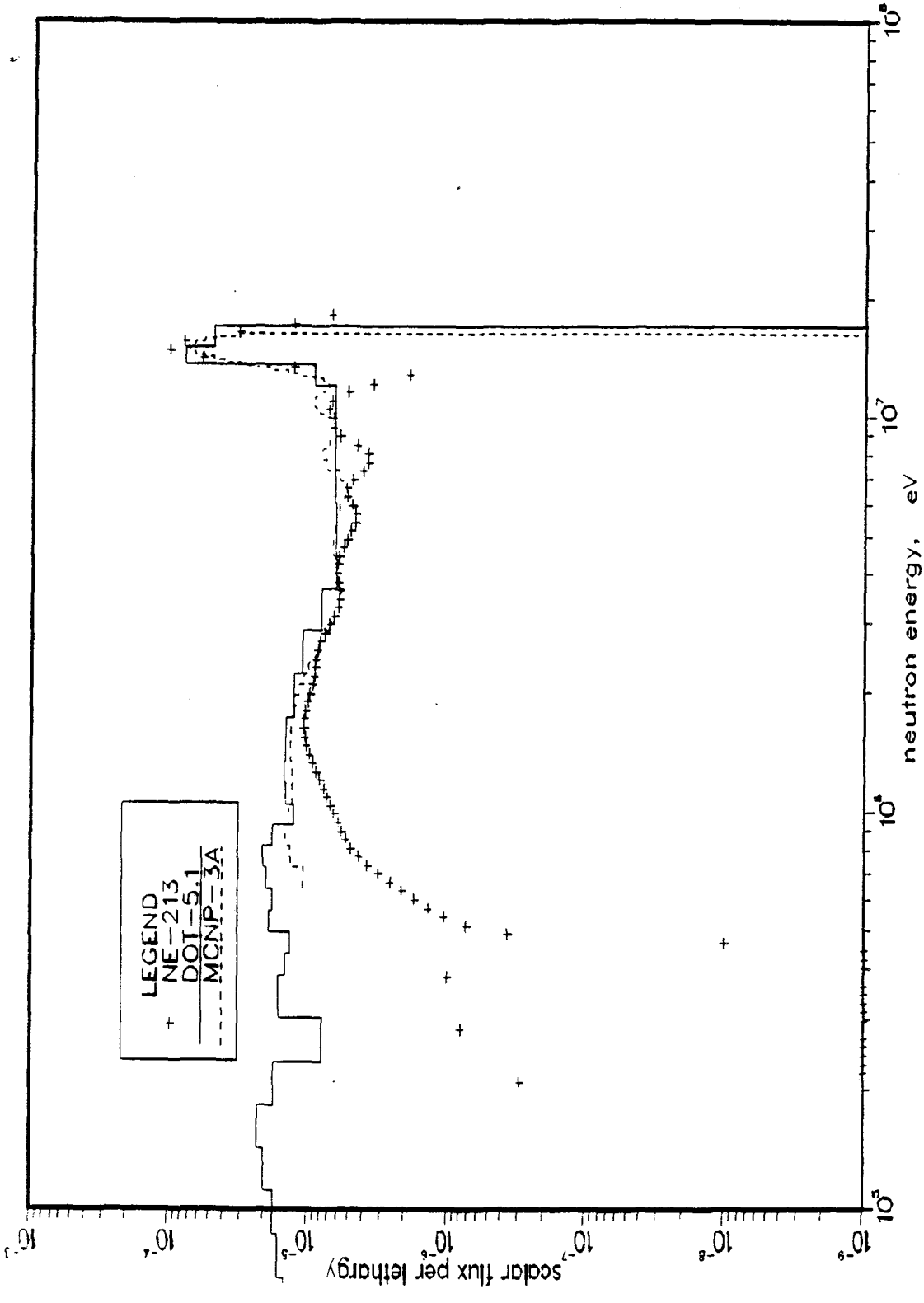

Fig. IV.45: Incident Neutron Spectrum at the Front Face of the Test Assembly (BEFWOFW System - Phase IIB)

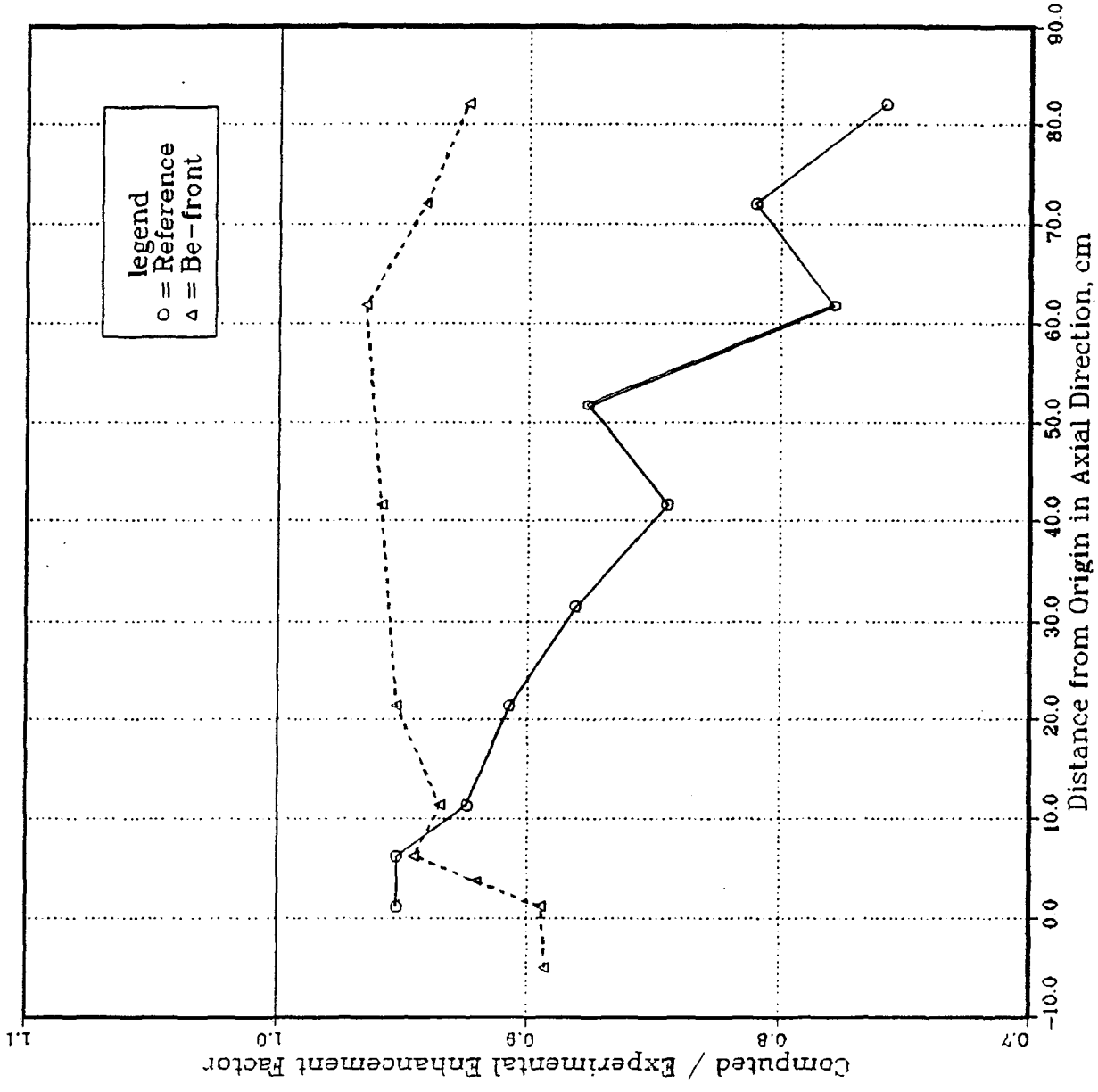

Fig. IV.46: Calculated to Measured Enhancement Factor in T_7 Due to the Beryllium Liner in Phase IIB

comparison to the Be zone, applying these correction factors is not necessary and leads to insignificant errors.

The foil perturbation correction factor, f is defined as:

$$f(r) = \frac{\int \Sigma_r(r,E)\phi_o(r,E)g(r,E)dE}{\int \Sigma_r(r,E)\phi_o(r,E)dE}, \qquad \text{(IV.1)}$$

where g(r,E) is the correction factor which is dependent on location, r, and neutron energy, E.

For an infinite plate in vaccuum with an isotropic flux, the factor g is given by

$$g(E) = \alpha/2\tau \qquad \text{(IV.2)}$$

where

$\alpha = 1 - 2E_3(\tau)$

$\tau = \Sigma_a\delta$,

$\Sigma_a \equiv$ absorption cross-section of the plate

$\delta \equiv$ plate thickness

In Hanna's formula[33], the foil edge effect is accounted for, as follows:

$$g(E) = \frac{\alpha}{2\tau}(1 + \varepsilon)$$

where

$$\varepsilon = \frac{2\tau}{\alpha} \cdot \frac{2}{\pi n}[I(\tau) - \Delta(n\tau)] \cdot \qquad \text{(IV.3)}$$

Here,

$n = 2R/\delta$

$R =$ foil radius.

when $\tau << 1$,

$$g \approx \frac{2}{\pi n}\left(1 - \frac{\pi\tau}{6}\right) \qquad \text{(IV.4)}$$

When the activation correction is performed,[35 - 37] the correction factor g becomes

$$g = \frac{\alpha}{2\tau}\,\frac{1 + \varepsilon}{1 + \chi}. \qquad \text{(IV.5)}$$

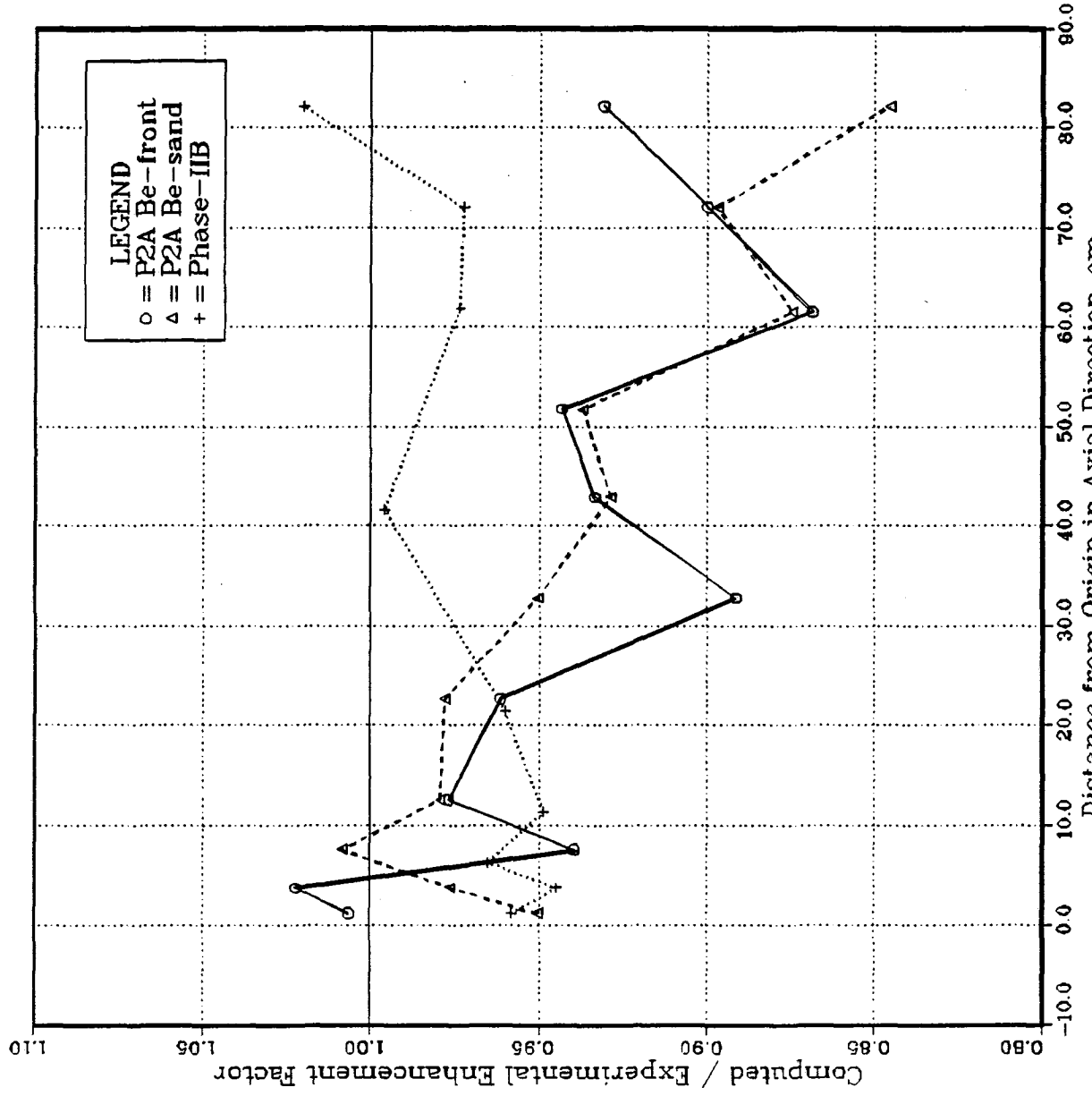

Fig. IV.47: Calculated to Measured Enhancement Factor in T_7 due to the Beryllium Front Layer in Phase IIA and IIB

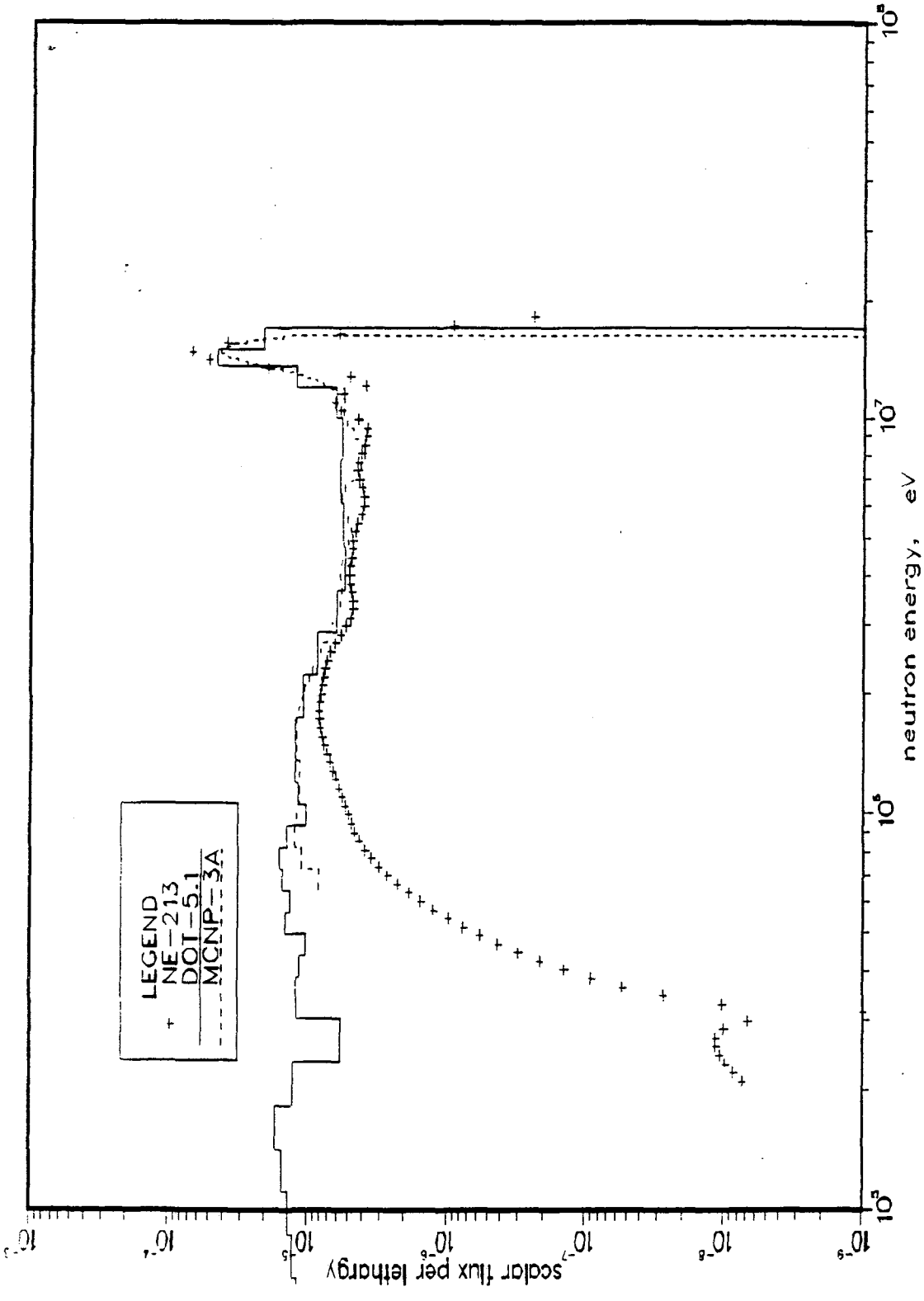

Fig. IV.48: Calculated and Measured Neutron Spectrum at Depth Z = 5 cm in the BEFWFW System of Phase IIB

Where in the case $R << \lambda tr$, we have

$$\chi = \frac{2}{\pi} \circ \frac{R}{\lambda_s} h(\tau)\alpha, \text{ (Meister}^{(37)} \text{ approximation)} \qquad \text{(IV.6)}$$

and in the case $R \geq \lambda tr$, we have

$$\chi = \frac{3}{4}\left\{\frac{L}{\lambda} S\left(\frac{2R}{L}\right) - \frac{2}{3} K\left(\frac{2R}{\lambda}\gamma\right)\right\}\alpha \text{ (Skymre}^{(35)} \text{ approximation),} \qquad \text{(IV.7)}$$

where

$\lambda_s = 1/\Sigma_s$

Σ_s = scattering cross-section of surrounding medium

$\lambda tr = \lambda_s /(1 - \bar{\mu}_o)$

$\bar{\mu}_o \equiv$ average cosine of the scattering angle

$\gamma = \Sigma_s /\Sigma_t$

Σ_t = total cross-section of the scattering medium

The self-shielding correction factor, f, for T_6, as obtained by Hann's, Meister's, and Skymre's approximation has been calculated in the BEFWFW system of Phase IIB, as a function of the location inside the test assembly and the results are shown in Fig. IV.49. This factor is small (large correction) inside the beryllium zone and tends to be unity just behind that layer. The smallest values occur in the middle of the Be layer, as expected, where softer spectrum is encountered. These factors were calculated using the 2-D neutron spectrum obtained from the DOT results. The dimensions of the foil are those of the natural foils used in measuring T_6 and T_7 ($R \approx 9$mm, $\delta = 2$mm.) When these factors were used, the C/E values for T_6 become those shown in Fig. IV.50 to IV.52 (See Fig. IV.38 for the C/E values of T_6 before correction). One notices from Fig. IV.49 that the correction factors applied are $\sim$ 0.64 - 0.73 and that the Skymre's approximation gives the lowest values. Inside the Be-layer, the Meister's approximation is more valid since the condition $R << \lambda tr$ holds in this zone. However, we observe large differences between the Monte Carlo and the discrete ordinates results in this zone and that the C/E values fall below unity. Note that the results based on the MCNP calculations have large statistical errors, as shown in Fig. IV.38.

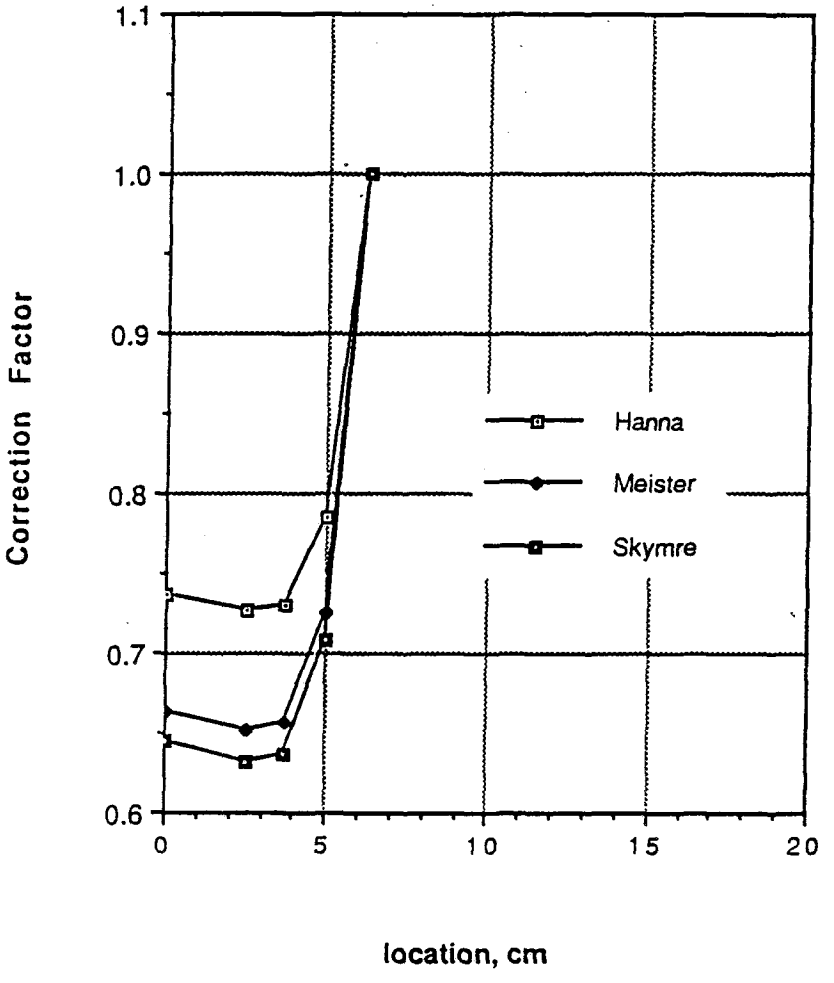

Fig. IV.49: Correction Factor for T_6 Measured by ANL Natural Foil in Phase IIB (BEFWFW System)

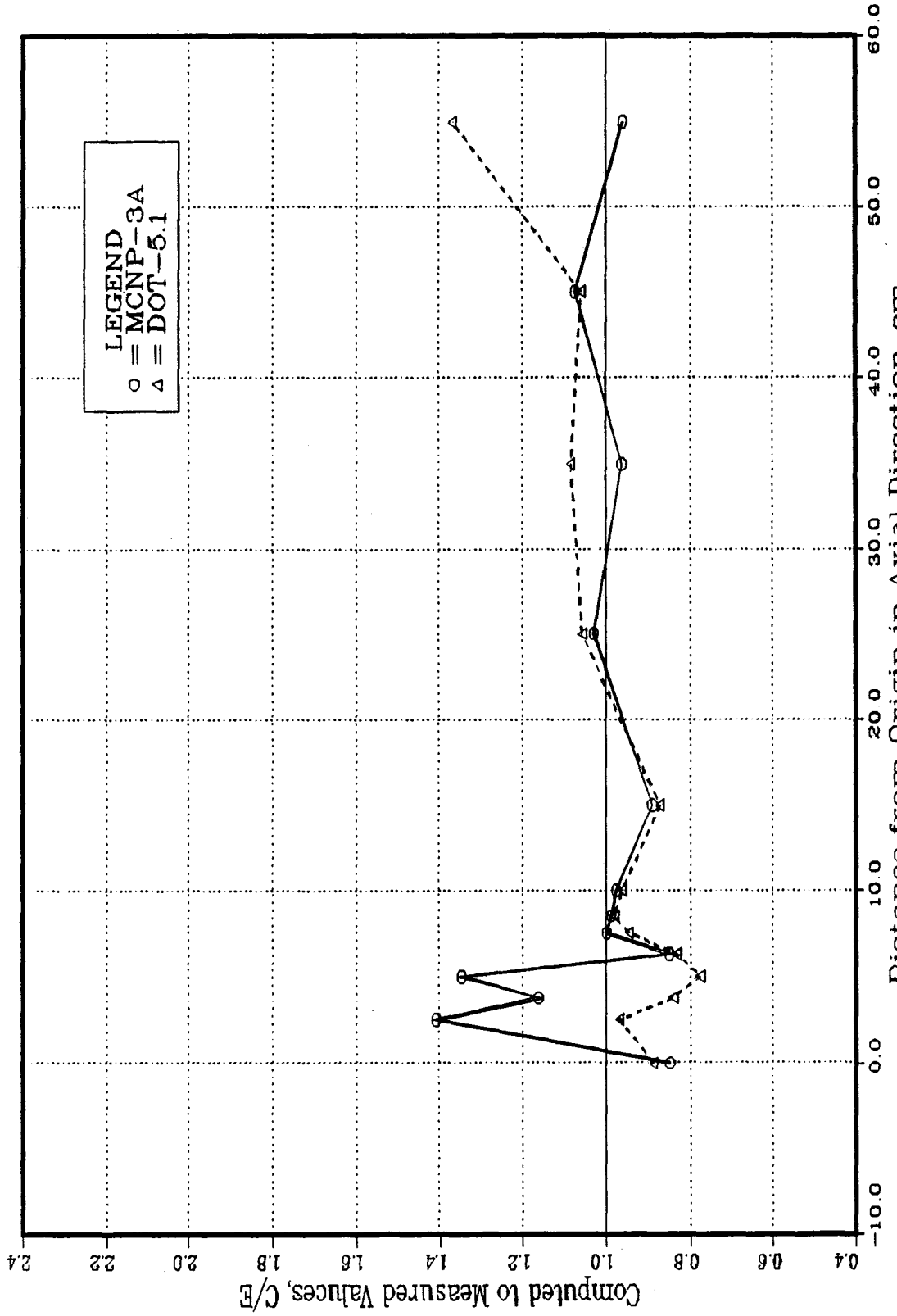

Fig. IV.50: C/E Values for T_6 Measured by the ANL Foils in the Central Drawer (Hanna Approximation - BEFWFW System of Phase IIB)

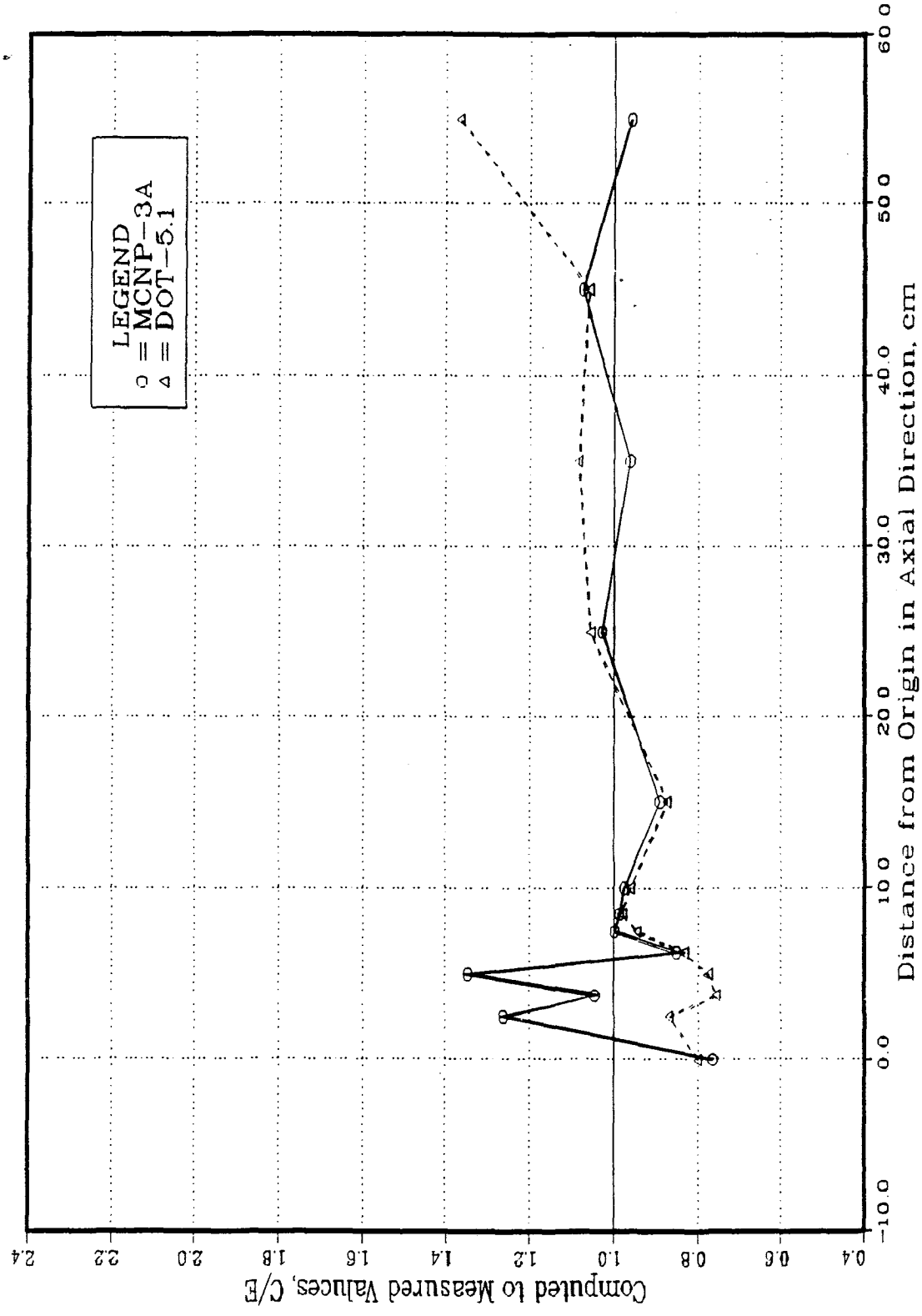

Fig. IV.51: C/E Values for T_6 Measured by the ANL Foils in the Central Drawer (Meister Approximation - BEFWFW System of Phase IIB)

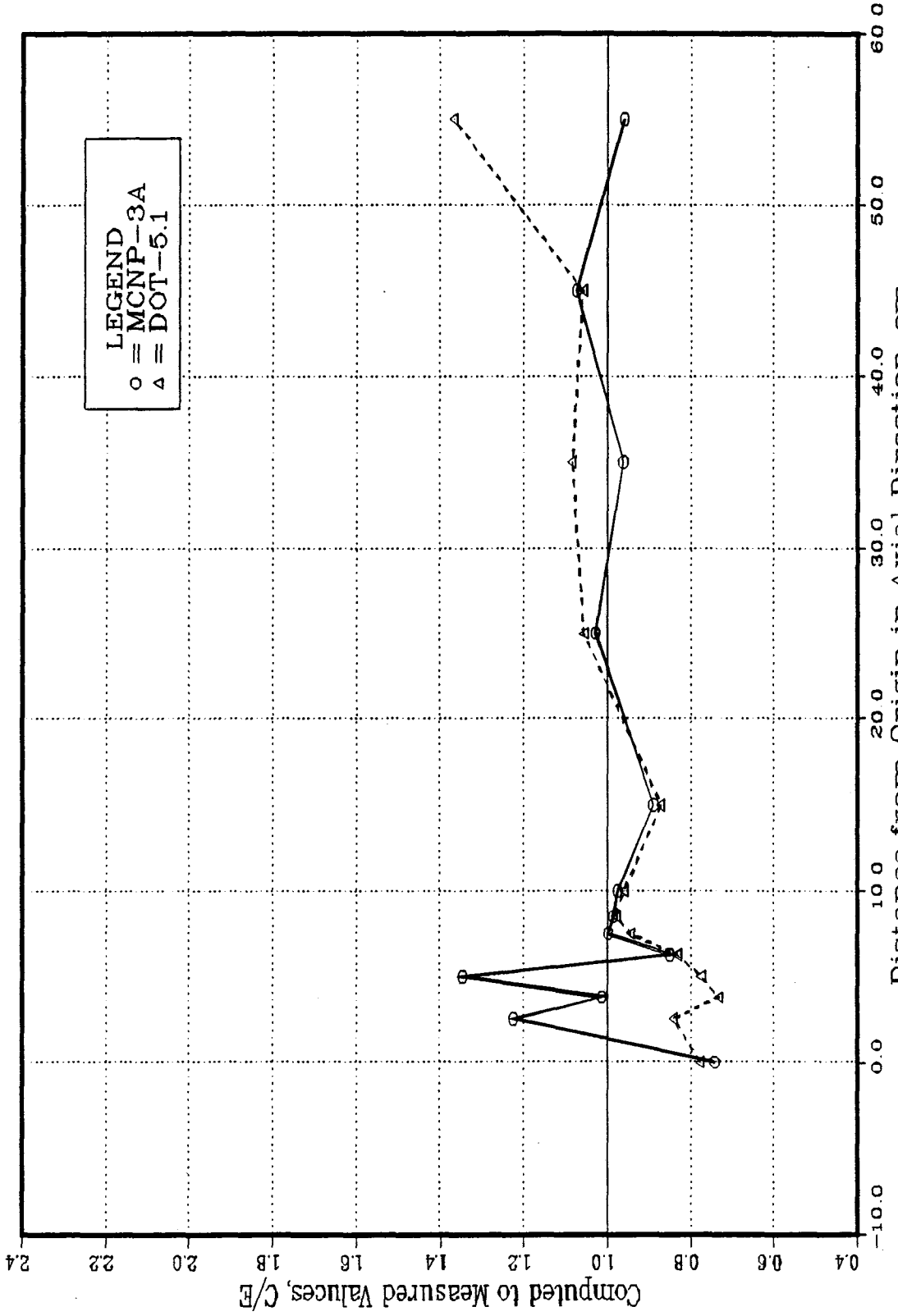

Fig. IV.52: C/E Values for T_6 Measured by the ANL Foils in the Central Drawer (Skymre Approximation - BEFWFW System of Phase IIB)

V. Sensitivity Analysis of the Beryllium Cross-Sections and Their Emission Spectrum and the Impact on Tritium Production Rate

V.1. Introduction and Status of Beryllium Data

The shape of the C/E values for T_6 observed in Phase IIA (see Fig. IV.14 and IV.15) and in Phase IIB (see Figs IV.34 and IV.35) indicate that there is underestimation in the TPR from ^{6}Li just behind the beryllium layer. The C/E values then sharply increase within the next few centimeters to reach more or less steady values, then their curves start to decrease. As it was pointed out in Section IV.3.3, this feature could be related to the beryllium cross-sections. Several integral experiments have indicated that the basic nuclear cross-section data of the ^{9}Be(n,2n) reaction may be overestimated because of inadequate representation of the energy/angle distribution of the emitted neutrons. The importance of considering the uncertainty involved in secondary energy distribution (SED) and secondary angular distribution (SAD) of emitted neutrons from reactions such as (n,2n), (n,inelastic), etc. is due to the fact that neutron transport and subsequent interactions with various nuclides of the transport media depend on the incident neutron energy and direction of those secondary neutrons.

Although the corresponding integrated (over energy and angle) cross-section could be known to a better accuracy, these SAD and SED of the ^{9}Be(n,2n) cross section are subject to large uncertainties. The ^{9}Be(n,2n) reaction proceeds by transitions through excitation levels in ^{9}Be, ^{8}Be, ^{6}He, and ^{5}He. The ^{9}Be(n,2n) reaction produces the first neutron, n_1, through ^{9}Be(n,n_1)^{9*}Be. The excited ^{9*}Be decays immediately to ^{8*}Be and n_2 where n_2 is the second neutron. The ^{8*}Be breaks to 2α's (See Fig. V.I for the excitation levels in ^{9*}Be). The levels involved are wide and unstable with the end result of the reaction always being two neutrons and two alpha particles. In the ENDF/B-IV and V, only four of the ^{9}Be excitation levels, 1.68, 2.43, 6.76, and 11.28 MeV, have been considered, each having zero width and with the energy-angle correlation between the emitted neutrons ignored, although the measured (n,2n) neutron emission of ^{9}Be shows a strong energy-angle correlation.

A concept of pseudolevels is used in which 33 inelastic levels are chosen to fit the neutron emission spectrum measurements of Drake, et al.[38] Young and Stewart[27], from LANL, have made an improvement of ENDF/B-IV and V data for beryllium. The LANL evaluation is the one used in the present study, as indicated earlier.

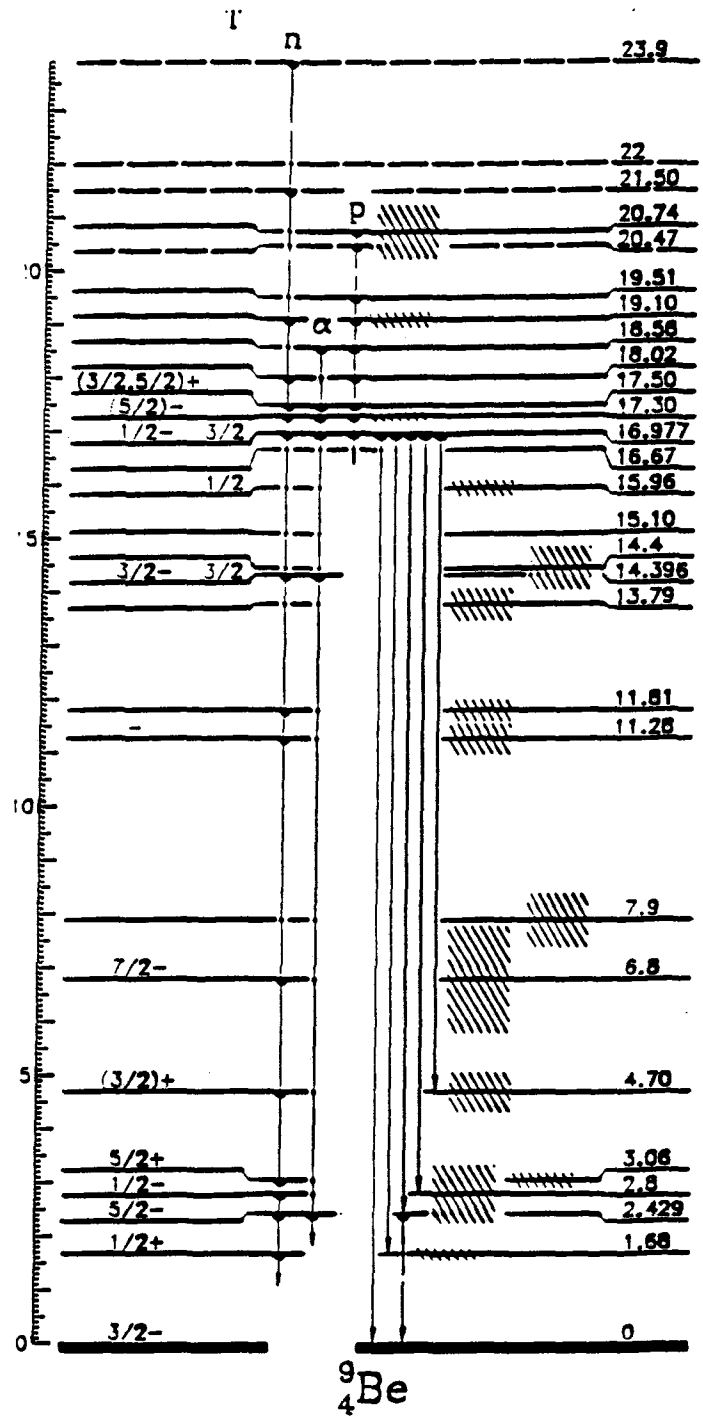

Fig. V.I: Excitation Levels in ^{9*}Be

In the LANL-Be evaluation, (n,2n) distributions are based on data for a cluster of real levels near Ex = 2.429 MeV and 32 excitation energy bins to represent the (n,2n) continuum levels. The excitation energy bins have half widths of 0.25 MeV. Comparison with the neutron emission spectrum with ENDF/B-IV and V beryllium cross-sections shows that the importance of the low-lying states was overemphasized in ENDF/B-IV and -V. Baba, et al.[39], also measured the double differential cross-section of ^{9}Be(n,2n)2α for several incident energies in the range of 3.25-7.0 MeV and support the data of Drake, et al.[38] rather than those in ENDF/B-IV. Basu, et al.[40 - 42], measured the multiplication of 14 MeV neutrons in a Be-metal assembly and found a value approximately 20 - 25% lower than that calculated using ENDF/B-IV.

Takahashi, et al.[43] have measured the double differential cross-section at 14 MeV for a number of nuclides including ^{9}Be, and their measured emission spectrum of the ^{9}Be(n,2n) cross-section deviates applicably from the values which are in JENDL-3T[44] and ENDF/B-IV. Recently, Perkins, et al.[45], evaluated the double differential cross-section using a Monte Carlo technique and compared evaluated data with those of Drake, et al.[38], Baba, et al.[39], and Takahashi, et al.[43] The ENDF/B-VI data for Be is based on Perkins, et al, evaluation of LLNL. Section VIII is devoted to studying this new evaluation and its impact on the TPR in Phase IIB experiments. A comparison is also made to the results obtained from ENDF/B-V and LANL evaluations for Be cross-sections. In this Chapter emphases are placed on studying the impact of variations in SED and SAD of the ^{9}Be(n,2n) cross-section on T_6 and T_7 and whether or not such variations could explain the discrepancies observed in the C/E curves discussed in Section IV.

V.2 Variations in the SED of the ^{9}Be(n,2n) cross section:

Variations in the secondary energy distribution (SED) of the emitted neutrons from the ^{9}Be(n,2n) reactions could be achieved in several ways. As mentioned above, the ^{9}Be(n,2n) cross-section is the summation of the cross-sections of the several inelastic levels that describe this reaction. Each level has its own SED and by varying the contribution from a particular excitation level to the total SED, meanwhile the SED of other levels are also varied such that the total integrated SED is kept the same (i.e. no variation in the total ^{9}Be(n,2n) cross-section takes place), we obtain a new SED distribution. This approach is denoted "excitation level approach." Another approach is to carry out direct variations in the total SED. By comparing the SED from two evaluations, for example, one can derive variation factors that are applied in each energy interval of a particular evaluation to arrive at the SED of the second evaluation. One can thus study the impact of the

difference in the SED's of the two evaluations (e.g. ENDF/B-V, LANL...) on an integrated parameter without the need to perform separate transport calculation. These two approaches are discussed below.

V.2.1 Excitation Level's Approach

In this approach, one varies the contribution of a particular level's cross-section to the total cross-section by applying a variation factor, the variations in the cross-section of other excitation levels could be ahcieved such that the total cross-sections remain the same. If the transfer cross section of the ^{9}Be(n,2n) reactions is described, in multigroup treatment, by $\sigma gg'$, then:

$$\sigma_{gg'} = \sigma^{\chi 1}_{gg'} + \sigma^{\chi 2}_{gg'} + \ldots + \sigma^{\chi n}_{gg'}$$

$$= \sum_{i} \sigma^{\chi i}_{gg'} \qquad \text{(V.1)}$$

where

$\sigma_{gg'}$; $\sigma_g f(g \rightarrow g')$

$f(g \rightarrow g')$; Probability distribution function. It is the probability that neutron scattered at group g will be transfered to group g'

χi ; i^{th} excitation level

n ; number of excitation levels involved.

Now, if cross-section of a particular level, $\sigma^{\chi m}_{gg'}$, is changed by a factor α^{m}_{g}, (this level is denoted "prime level") and at the same time the cross-sections of other levels, $\sigma^{\chi i}_{gg'}$ are varied by factors α^{i}_{g}, we get

$$\sigma^{new}_{gg'} = \sum_{\substack{i=1 \\ i \neq m}}^{n} (1 + \alpha^{i}_{g})\, \sigma^{\chi i}_{gg'} + (1 + \alpha^{m}_{g})\, \sigma^{\chi m}_{gg'} \qquad \text{(V.2)}$$

and

$$\sigma_g^{new} = \sum_{g'} \sigma_{gg'}^{new} = \sigma_g^{old} \qquad (V.3)$$

By summing over the exit energy, g', we get,

$$\sigma_g^{new} = \sum_{\substack{i=1 \\ i\neq m}}^{n} (1+\alpha_g^i)\,\sigma_g^{\chi i} + (1+\alpha_g^m)\,\sigma_g^{\chi m}$$

$$= \sigma_g^{old} + \sum_{\substack{i=1 \\ i\neq m}}^{n} \alpha_g^i \sigma_g^{\chi i} + \alpha_g^m \sigma_g^{\chi m}$$

Since we force the condition V.3 above to hold in order to keep the total cross-section the same at incident energy group g, we get,

$$\sum_{\substack{i=1 \\ i\neq m}}^{n} \alpha_g^i \sigma_g^{\chi i} = -\alpha_g^m \sigma_g^{\chi m} \qquad (V.4)$$

There are several ways to vary the cross-sections of the excitation levels involved. One method is denoted "the level-independent treatment," in which the variation factors that are applied to each excitation level are assumed the same, i.e.:

$$\alpha_g^1 = \alpha_g^2 = \alpha_g^3 = \ldots\ldots\ldots = \alpha_g^i = \alpha_g, \quad i \neq m \qquad (V.5)$$

From Eq. V.4, the variation factor that is applied to each excitation level is then given by:

$$\alpha_g \left[\sigma_g - \sigma_g^{\chi m}\right] = -\alpha_g^m \sigma_g^{\chi m}$$

$$\alpha_g = -\frac{\alpha_g^m \sigma_g^{\chi m}}{\sigma_g - \sigma_g^{\chi m}} \qquad \text{(V.6)}$$

By using the level-independent variation factor, α_g, we get a new SED distritution. This can be shown by using Eq. V.6 in Eq. V.2,

$$\sigma_{gg'}^{new} = \sum_{\substack{i=1 \\ i\neq m}}^{n} (1+\alpha_g)\sigma_{gg'}^{\chi i} + (1+\alpha_g^m)\,\sigma_{gg'}^{\chi m}$$

$$= \sigma_{gg'}^{old} + \sum_{\substack{i=1 \\ i\neq m}}^{n} \alpha_g \sigma_{gg'}^{\chi i} + \alpha_g^m \sigma_{gg'}^{\chi m}$$

$$= \sigma_{gg'}^{old} + \frac{-\alpha_g^m \sigma_g^{\chi m}}{\sigma_g - \sigma_g^{\chi m}} \sum_{\substack{i=1 \\ i\neq m}}^{n} \sigma_{gg'}^{\chi i} + \alpha_g^m \sigma_{gg'}^{\chi m}$$

By noticing that ,

$$\sum_{\substack{i=1 \\ i\neq m}}^{n} \sigma_{gg'}^{\chi i} = \sigma_{gg'}^{old} - \sigma_{gg'}^{\chi m},$$

we get

$$\sigma_{gg'}^{new} = \sigma_{gg'}^{old} - \alpha_g^m \sigma_{gg'}^{\chi m} \left(\frac{\sigma_{gg'}^{old} - \sigma_{gg'}^{\chi m}}{\sigma_g - \sigma_g^{\chi m}} - 1 \right) \qquad \text{(V.7)}$$

Notice also that the integrated cross-section is unchanged. This can be shown by summing Eq. V.7 over the exit energy group g' to get

$$\sigma_g^{new} = \sigma_g^{old} - \alpha_g^m \sigma_g^{\chi_m} \quad \{1-1\}$$

$$= \sigma_g^{old}$$

Another way of varying the cross-section of the excitation levels involved is that the absolute variation in the cross-section of other excitation levels is assumed the same, i.e.

$$\alpha_g^1 \sigma_g^1 = \alpha_g^2 \sigma_g^2 = \alpha_g^3 \sigma_g^3 = \ldots = \alpha_g^i \sigma_g^i, \; i \neq m \qquad (V.8)$$

This method is denoted "level-dependent treatment." From Eq. V.4, the variation factor applied to excitation level χ_i is now given by

$$\alpha_g^i = \frac{-\alpha_g^m \sigma_g^{\chi_m}}{(n-1)\sigma_g^{\chi_i}} \qquad (V.9)$$

Here, n is the number of excitation levels that are considered in the treatment. It could be all levels that are energetically possible and contributing to the total cross-section or it could be a selected number of levels. The new SED in this case is given by:

$$\sigma_{gg'}^{new} = \sigma_{gg'}^{old} + \sum_{\substack{i=1 \\ i \neq m}}^{n} \alpha_g^i \sigma_{gg'}^{\chi_i} + \alpha_g^m \sigma_{gg'}^{\chi_m}$$

$$= \sigma_{gg'}^{old} - \frac{\alpha_g^m \sigma_g^{\chi_m}}{(n-1)} \sum_{\substack{i=1 \\ i \neq m}}^{n} \frac{\sigma_{gg'}^{\chi_i}}{\sigma_g^{\chi_i}} + \alpha_g^m \sigma_{gg'}^{\chi_m}$$

$$= \sigma^{old}_{gg'} - \frac{\alpha^m_g \sigma^{\chi m}_g}{(n-1)} \left(\sum_{\substack{i=1 \\ i\neq m}}^{n} \frac{\sigma^{\chi i}_{gg'}}{\sigma^{\chi i}_g} - \frac{(n-1)\sigma^{\chi m}_{gg'}}{\sigma^{\chi m}_g} \right) \qquad (V.10)$$

and, the result from the summation over the exit energy group, g', shows that the total cross-section remains as the same, i.e.

$$\sigma^{new}_g = \sigma^{old}_g - \frac{\alpha^m_g \sigma^{\chi m}_g}{(n-1)} \{(n-1) - (n-1)\}$$

$$= \sigma^{old}_g$$

One important remark about the above treatments is that the variation factors, α^i_g, could be treated as dependent or independent on each excitation level; however, the dependency on the exit energy group, g', does not lead to a new distribution. For example, in the case of level-independent treatment, if we assume the factors $\alpha gg'$ to be dependent on the exit energy group g', we get

$$\alpha_{gg'} \sigma^{\chi 1}_{gg'} + \alpha_{gg'} \sigma^{\chi 2}_{gg'} \ldots + \alpha_{gg'} \sigma^{\chi m-1}_{gg'} + \alpha_{gg'} \sigma^{\chi m+1}_{gg'} + \ldots = -\alpha^m_{gg'} \sigma^{\chi m}_{gg'}$$

$$\alpha_{gg'} \sum_{\substack{i=1 \\ i\neq m}}^{n} \sigma^{\chi i}_{gg'} = -\alpha^m_{gg'} \sigma^{\chi m}_{gg'}$$

i.e. $$\alpha_{gg'} = \frac{-\alpha^m_{gg'} \sigma^{\chi m}_{gg'}}{\sigma_{gg'} - \sigma^{\chi m}_{gg'}} \qquad (V.11)$$

The new distribution from these variation factors is exactly the same as the old distribution, i.e.

$$\sigma^{new}_{gg'} = \sigma^{old}_{gg'} - \sum_{\substack{i=1 \\ i\neq m}}^{n} \frac{\alpha_{gg'} \sigma^m_{gg'}}{\sigma_{gg'} - \sigma^{\chi m}_{gg}} \sigma^{\chi i}_{gg} + \alpha^m_{gg'} \sigma^{\chi m}_{gg'}$$

$$= \sigma^{old}_{gg'} - \frac{-\alpha^{m}_{gg'}\sigma^{\chi m}_{gg'}}{\sigma gg' - \sigma^{\chi m}_{gg'}} \sum_{\substack{i=1 \\ i\neq m}}^{n} \sigma^{\chi i}_{gg'} + \alpha^{m}_{gg'}\sigma^{\chi m}_{gg'}$$

$$= \sigma^{old}_{gg'} - \alpha^{m}_{gg'}\sigma^{\chi m}_{gg'}[1 - 1]$$

$$= \sigma^{old}_{gg'}$$

where

$$\sigma_{gg'} - \sigma^{\chi m}_{gg'} = \sum_{\substack{i=1 \\ i\neq m}}^{n} \sigma^{\chi i}_{gg'}$$

V.2.2 Direct variation's Approach

One can proceed by applying variations factors, $\beta_{gg'}$, to the total SED instead of applying these factors to the cross-sections of the excitation levels involved. This can be seen by noticing that,

$$\sigma^{new}_{gg'} = \sigma^{old}_{gg'} \left(1 + \left(\sum_{\substack{i=1 \\ i\neq m}}^{n} \alpha^{i}_{g} \sigma^{\chi i}_{gg'} + \alpha_m \sigma^{\chi m}_{gg'} \right) X \frac{1}{\sigma^{old}_{gg'}} \right)$$

$$= \sigma^{old}_{gg'} \left(1 + \left(\sum_{i=1}^{n} \alpha^{i}_{g} \sigma^{\chi i}_{gg'} \right) X \frac{1}{\sigma^{old}_{gg'}} \right)$$

$$= \sigma^{old}_{gg'} [\, 1 + \beta^{m}_{gg'}] \qquad (V.12)$$

Where the variation factor $\beta^{m}_{gg'}$, is now given by

$$\beta_{gg'}^{m} = \left(\sum_{i=1}^{n} \alpha_g^i \sigma_{gg'}^{\chi i} \right) \times \frac{1}{\sigma_{gg'}^{old}} \qquad (V.13)$$

The condition that σ_g^{new} should be the same as σ_g^{old} leads to,

$$\sum_{g'} \sigma_{gg'}^{old} \beta_{gg'}^{m} = \sum_{i=1}^{n} \alpha_g^i \sigma_g^{\chi i} = 0 \qquad (V.14)$$

In this treatment, the $\beta_{gg'}$ factors are derived from Eq. V.13, depending on the variation factor of the 'prime' level χ^m, and the variation factors for other level. However, in practice, one can increase the cross-section $\sigma_{gg'}^{old}$ by an assumed factor $\beta_{gg'}^{i}$ for a specified exit energy range, i, meanwhile, the cross-section $\sigma_{gg'}^{old}$ for other possible exit energy ranges, k≠i, is decreased such that the total cross-section, σg, remains the same. In this case, the factors $\beta_{gg'}^{i}$ are not calculated from the level variation factors α_g^i described by Eq. V.13.

V.3. Variation in the SAD of the ^{9}Be(n,2n) cross-section

To achieve variations in the SAD of neutrons emitted from the ^{9}Be(n,2n) reactions one can assume that the space of the scattering angle is partitioned into three regions (FORWARD, UPWARD, and BACKWARD). These regions are defined as region 1($0.5<\mu<1.0$), region 2($-0.5<\mu<0.5$), and region 3($-1.0<\mu<-0.5$), where μ is the cosine of the scattering angle in the laboratory system. In the present analysis, the P_3 approximation is used to represent the scattering cross section at a particular angle, μ. That is:

$$\sigma_{gg'}(\mu) \cong \sigma_{gg'}^{0} + \sigma_{gg'}^{1} P_1(\mu) + \sigma_{gg'}^{2} P_2(\mu) + \sigma_{gg'}^{3} P_3(\mu)$$

$$= \sigma^{0}_{gg'} + \sigma^{1}_{gg'} \cdot \mu + \sigma^{2}_{gg'} \frac{(3\mu^2 - 1)}{2} + \sigma^{3}_{gg'} \frac{(5\mu^3 - 3\mu)}{2} \qquad \text{(V.15)}$$

Integrating the angular cross-section over the three regions defined above and over the entire angular space, we get

$Igg',_1 = \int \sigma gg'(\mu)d\mu \qquad (0.5 < \mu < 1.0)$
$Igg',_2 = \int \sigma gg'(\mu)d\mu \qquad (-0.5 < \mu < 0.5)$
$Igg',_3 = \int \sigma gg'(\mu)d\mu \qquad (-1.0 < \mu < -0.5)$, and
$Igg',_t = \int \sigma gg'(\mu)d\mu \qquad (-1.0 < \mu < 1.0)$.

Here, we have

$$Igg'_t = Igg'_1 + Igg'_2 + Igg'_3 \qquad \text{(V16)}$$

and to preserve the SAD, the condition,

$$Igg'_t = \text{Constant} \qquad \text{(V.17)}$$

should hold. This implies no variation in the P_o component of the cross section, $\sigma^{0}_{gg'}$.

Performing these integrations, we get

$$\begin{pmatrix} 4a & 0 & 0 & 0 \\ a & b & c & d \\ 2a & 0 & -2c & 0 \\ a & -b & c & -d \end{pmatrix} \cdot \begin{pmatrix} \sigma^{0}_{gg'} \\ \sigma^{1}_{gg'} \\ \sigma^{2}_{gg'} \\ \sigma^{3}_{gg'} \end{pmatrix} = \begin{pmatrix} Igg't \\ Igg'1 \\ Igg'2 \\ Igg'3 \end{pmatrix} \qquad \text{(V.18)}$$

where a, b, and c are constants. Fig. V.2 shows the variations assumed in the present study in the SAD. From Eq. V-18, if we increase Igg'1 by a factor $\alpha_m, \sigma^{1}_{gg'1}$ will be increased by a factor $\chi_{gg'1}$ expressed as

$$(\chi_{gg'})_1 = \frac{Igg'1(\alpha_m)}{b.\sigma^{1}_{gg'}}, \qquad \text{(V.18-a)}$$

with the assumption that $\sigma^{3}_{gg'}$, $\sigma^{2}_{gg'}$, and Igg'2 do not change. This is the "forward" variation considered here. If we increase Igg'2 by a factor α_m, $\sigma^{2}_{gg'}$ will be increased by a factor $\chi_{gg'2}$ expressed as

$$(\chi_{gg'})_2 = \frac{Igg'2(\alpha_m)}{-2c \cdot \sigma^{2}_{gg'}} , \qquad \text{(V.18-b)}$$

and the conservation condition Igg't = Igg'1 + Igg'2 + Igg'3 necessitates that no change in $\sigma^{1}_{gg'}$ and $\sigma^{3}_{gg'}$ takes place (upward variation). If we increase Igg'3 by a factor α_m, $\sigma^{1}_{gg'}$ will be increased by a factor $\chi_{gg'1}$ expressed as;

$$(\chi_{gg'})_1 = \frac{Igg'3(\alpha_m)}{-b \cdot \sigma^{1}_{gg'}} \qquad \text{(V.18-c)}$$

with the assumption that $\sigma^{3}_{gg'}$, $\sigma^{2}_{gg'}$, and Igg'2 do not change (backward variation).

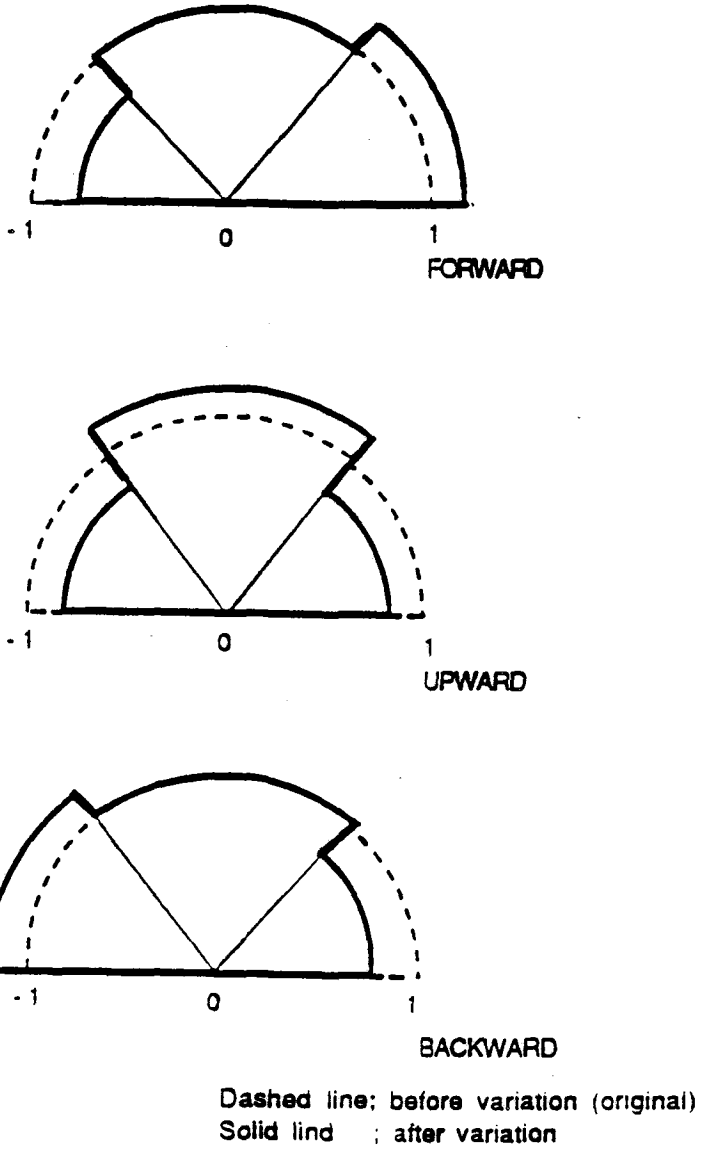

Fig. V.2: Three Different Variations Considered in the SAD Analysis

V.4 Sensitivity Profiles

The relative sensitivity Profile, $P_{\Sigma x}(E)$, is defined as the percentage change in the integrated parameter under consideration (T_6 or T_7 in our case) due to a 1% increase in a particular type of cross-section, Σ_x, at the energy E, and this variation is assumed to take place within a particular region in space. This coefficient is given by

$$P_{\Sigma_x}(E) = -\frac{1}{R}\langle \phi^*, L_{\Sigma_x}\phi \rangle_E, \qquad (V.19)$$

where ϕ and ϕ^* are the forward and the adjoint angular flux and they are the solutions of the transport equation $L\phi = S$ and $L^*\phi^* = \Sigma_r$, respectively. Here, the integrated response, $R(T_6$ or $T_7)$ is given by

$$\begin{aligned} R &= \langle \Sigma_r, \phi \rangle \\ &= \langle S, \phi^* \rangle, \end{aligned} \qquad (V.20)$$

where Σr is the response function [macroscopic cross-section of the $^6Li(n,\alpha)t$ or $^7Li(n,n'\alpha)t$ reactions] and S is the external neutron source. Note from Eq. V.19 that the L_{Σ_x} is the part of Boltzmann operator that includes the perturbed cross-section, Σ_x. The notation ,<,>$_E$, indicates integration over the phase space $\underline{\Omega}$, and $\underline{r}$ only while the notation, <,>, indicates integration over the whole phase space $\underline{\Omega}$, $\underline{r}$, and E. The perturbation theory used to derive Eq. V.19 can be found in Refs. (46 - 52).

In the multigroup treatment, and based on the excitation level's approach discussed in Section V.2.1, the relative sensitivity profile for variation in the cross-section of an excitation level i is given by:

$$P^{g}_{\Sigma^i_x}(SED) = \frac{4\pi}{R\Delta U g}\left[\sum_{g'=g}^{G_{max}}\sum_{\ell=0}^{L_{max}}(2\ell+1)\alpha^i_g\Sigma^{\chi ig\to g'}_{S\ell}\sum_{k=0}^{\ell}\sum_{j=1}^{Jmesh} V_j\phi^{kg}_{\ell}(j)\phi^{*kg'}_{\ell}(j)\right.$$

$$\left. - \sum_{\ell=0}^{L_{max}}(2\ell+1)\alpha^i_g\Sigma^{\chi ig}_{xT}\sum_{k=0}^{\ell}\sum_{j=1}^{Jmesh} V_j\phi^{kg}_{\ell}(j)\phi^{*kg}_{\ell}(j)\right]. \qquad (V.21)$$

The first term is the "scattering gain" term and the second is the "collisional loss" term. The total relative sensitivity profile for SED is the summation of all the excitation levels' sensitivity coefficients and is given by

$$P^{g}_{\Sigma_x}(SED) = \sum_{i=1}^{n} P^{g}_{\Sigma^{i}_{x}}$$

$$= \frac{4\pi}{R\Delta U^g}\left[\sum_{i=1}^{n}\left\{\sum_{g'=g}^{G_{max}}\sum_{\ell=0}^{L_{max}}(2\ell+1)\alpha_g^i\Sigma^{\chi_{ig\to g'}}_{S\ell}\sum_{k=0}^{\ell}\sum_{j=i}^{Jmesh}V_j\phi^{kg}_{\ell}(j)\phi^{*kg'}_{\ell}(j)\right.\right.$$

$$\left.\left.-\sum_{\ell=0}^{L_{max}}(2\ell+1)\alpha_g^i\Sigma^{\chi_{ig}}_{x_T}\sum_{k=0}^{\ell}\sum_{j=1}^{Jmesh}V_j\phi^{kg}_{\ell}(j)\phi^{*kg}_{\ell}(j)\right\}\right], \qquad (V.22)$$

where

V_j = volume of spatial mesh j

ΔU^g = lethargy width of energy group g

G_{max} = maximum number of the energy group used in the multigroup calculations

L_{max} = maximum number of the polynomials used in the P_ℓ approximation.

$\phi^{kg}_{\ell}, \phi^{*kg}_{\ell}$ ≡ the forward and the adjoint flux component of the associated Legendre polynomials.

Notice that the second term of the SED sensitivity profile is cancelled out (see Eq. V.14) because the total cross-section was kept the same when the SED was varied. Thus, the SED sensitivity profile can be rewritten as

$$P\backslash A(g,\Sigma\backslash A(\ ,x))\,(SED) = \backslash F(4\pi,R\Delta U^g)\ \backslash A(_n,\Sigma_{,i=1})\ \backslash A(G_{max},\Sigma,g'=g)$$

$$\sum_{\ell=0}^{L_{max}}(2\ell+1)\alpha_g^i\Sigma^{\chi_{ig\to g'}}_{S\ell}\sum_{k=0}^{\ell}\sum_{j=1}^{Jmesh}V_j\phi^{kg}_{\ell}(j)\phi^{*kg'}_{\ell}(j) \qquad (V.23)$$

However, in the "direct variation treatment", the variation factors β^m_{gg} could be applied to the old SED distribution as mentioned in Section V.2.2. In this case, the SED sensitivity profile is given by

$$P^{g}_{\Sigma_x}(SED) = \frac{4\pi}{R\Delta U^g}\sum_{i=1}^{n}\sum_{g'=g}^{G_{max}}\sum_{\ell=0}^{L_{max}}(2\ell+1)\alpha_g^i\Sigma^{\chi_{ig\to g'}}_{S\ell}\sum_{k=0}^{\ell}\sum_{j=1}^{Jmesh}V_j\phi^{kg}_{\ell}(j)\phi^{*kg'}_{\ell}(j)$$

$$= \frac{4\pi}{R\Delta U^g} \sum_{g'=g}^{G_{max}} \sum_{\ell=0}^{L_{max}} (2\ell+1)\, \beta^m_{gg'} \Sigma^{g\to g'}_{S\ell} \sum_{k=0}^{\ell} \sum_{j=1}^{Jmesh} V_j \phi^{kg}_{\ell}(j) \phi^{*kg'}_{\ell}(j) \quad (V.24)$$

Likewise, the sensitivity profiles for SAD can be obtained by using the variation factors $(\chi_{gg})_i$ discussed is Section V.3 in a similar fashion. The three scattering regions considered in the present analysis are:

$$P^{forward}_{g(SAD)} = -\sum_{g'=g}^{G_{max}} \frac{1}{R} \langle \phi^*, \chi^{forward}_{gg'1} L_{\Sigma_{gg'1}} \phi \rangle_{gg'}$$

$$P^{upward}_{g(SAD)} = -\sum_{g'=g}^{G_{max}} \frac{1}{R} \langle \phi^*, \chi^{upward}_{gg'2} L_{\Sigma_{gg'2}} \phi \rangle_{gg'}$$

$$P^{backward}_{g(SAD)} = -\sum_{g'=g}^{G_{max}} \frac{1}{R} \langle \phi^*, \chi^{backward}_{gg'1} L_{\Sigma_{gg'1}} \phi \rangle_{gg'} . \quad (V.25)$$

V.5 Calculational Procedures

The cross-sections needed for the forward and the adjoint transport calculations was generated from the DLC-113/VITAMIN-E[24] master interface fine-group library (174 groups), using the CHOX and MALOCS codes of the AMPX[53] processing system and from the MATXS6 multigroup cross-section file by using the TRANSX-CTR[21] program. These 30 group transport forward and adjoint cross-section libraries were converted to group-organized cross-section sets by using the GIP code.

The total and partial cross-sections for the sensitivity analysis were also prepared from the VITAMIN-E[24] master library into 30-group structure by using the NITAWL module of the AMPX processing system. The ANISN-formatted transfer matrices of the total and partial cross-section libraries were converted to the MATXS format which is required for the sensitivity analysis by using the ANTMX code of the cross-section sensitivity/uncertainty analysis system, FORSS.[54] This code system was developed at Oak Ridge National Laboratory and is applied in the present analysis. However, some modifications in that system were required to carry out the SED/SAD sensitivity analysis. The calculational procedures carried out are summarized in Fig. V.3.

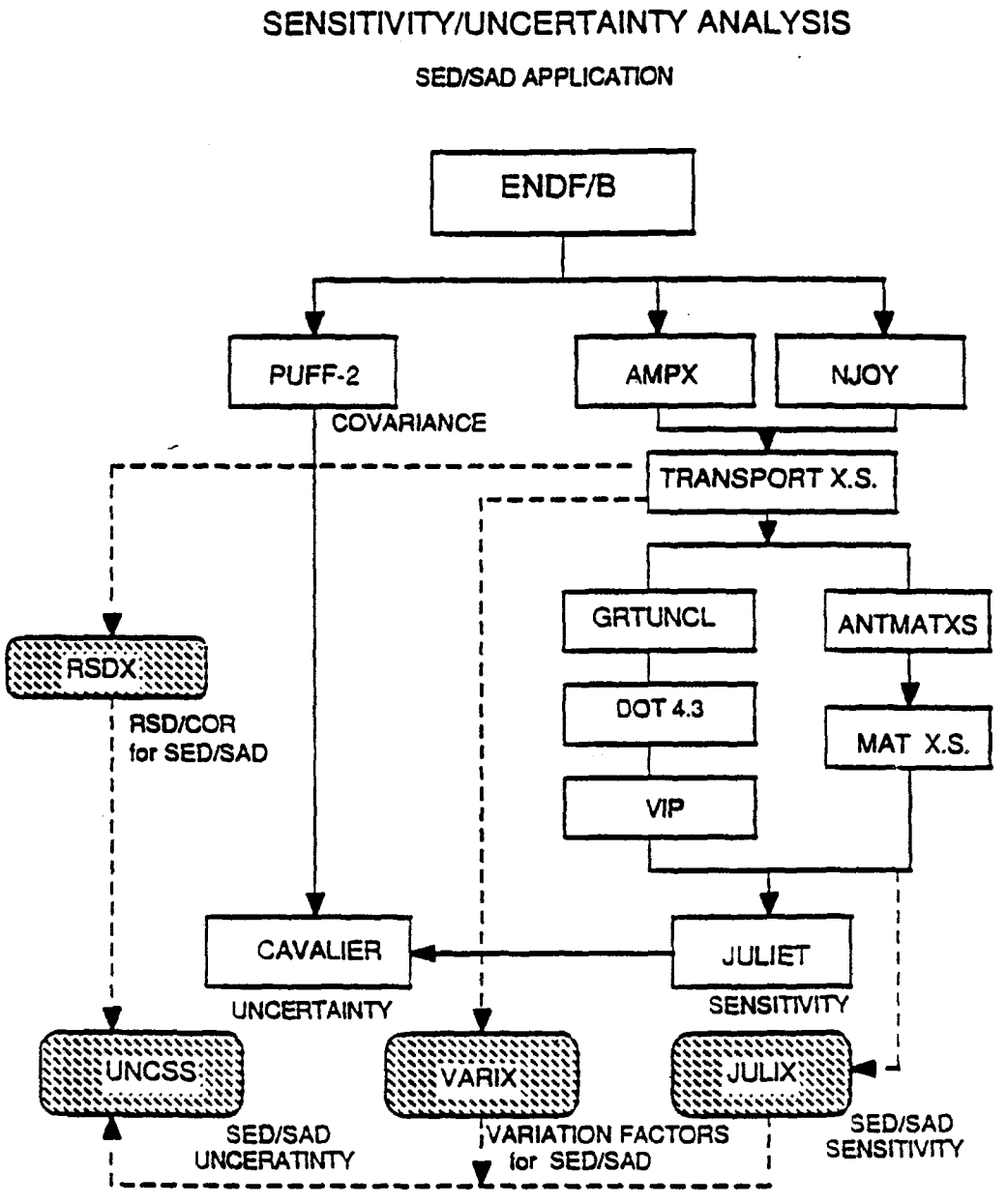

Fig. V.3: Calculational Procedure of FORSS SED/SAD Sensitivity/Uncertainty Analysis

The unshaded boxes represent the calculational procedures and codes used to perform the sensitivity/uncertainty analysis for the "smooth" cross-sections while the shaded boxes indicate the calculational path followed in carrying out the sensitivity and uncertainty analysis for the SED/SAD variations. As shown, some same modifications were required in the modules of the FORSS code to perform the SED/SAD sensitivity/uncertainty analysis. In the present work, only the results of the sensitivity analysis for the SED/SAD are reported. The complete uncertainty analysis is currently in progress and will be published in the near future.

The volume-integrated product code, VIP, was used for the preparation of $\langle\phi_K,\phi^*\rangle$ in two-dimensional form. This code was developed by Childs, et. al.[55 - 56] and is used for each response considered in the present analysis. The MATXS partial cross-sections and the volume-integrated flux file $<\phi_K,\phi^*>$ were used as input to the modified JULIET code of the FORSS module[54] to get the sensitivity profiles for each partial cross-section. The end product of the JULIET sensitivity profiles are placed in a SENPRO file. In the case of SED/SAD analysis, after calculating the variation factor for each excitation levels using the VARIX code, these factors were applied to each sensitivity profile generated by the JULIX code, the modified version of JULIET.

The beryllium-sandwiched system (BES) of Phase IIA was chosen for the analysis in the present study. Five locations were selected for T_6 and T_7 inside the test assembly at distance 2.55, 6.72, 8.22, 10.72, and 35.72 cm from the front surface of the test assembly. These locations are denoted P_1, P_2, P_3, P_4, and P_5, respectively, as shown in Fig. V.4. The first location is inside the front Li_2O layer; the second two locations are inside the Be-layer, and the other two locations are in the Li_2O zone that follows the Be layer. The locations at Z=10.72 cm is at a distance 0.55 cm behind the Be layer.

One forward calculation was performed using the DOT4.3 in 2-D R-Z geometry along with the uncollided flux file obtained by the GRTUNCL code[57]. The calculations were performed with a P_5S_8 approximation with the 30-group neutron library. Ten adjoint calculations were needed (five for T_6 and five for T_7) to calculate the adjoint flux. The response function [^{6}Li(n,α)t or ^{7}Li(n,n'α)t macroscopic cross-section] was considered, at each location separately, as the source to the adjoint equation and the adjoint fluxis (ϕ_6^* and ϕ_7^*) were calculated using an adjoint cross-section library generated by using the GIP code.

Note that the uncollided adjoint fluxes were first genered by the GRTUNCL code since the responses considered (T_6 and T_7) are at spatial points in space.

V.6 Calculational Results

V.6.1 Variations in SED of the ^{9}Be(n,2n) Cross-Section

The ENDF/B-V data for beryllium was used in the present analysis. The ^{9}Be(n,2n) cross-section is the sum of the cross-sections of four inelastic levels, as mentioned in Section V.1. Fig. V.5 shows the transfer cross-section $\sigma_{gg'}$ for each level for an incident energy group g = 13.5 MeV - 15 MeV. As shown, the largest $\sigma_{gg'}$ for g' below 1 MeV is the transfer cross-section of the 2nd excitation level while the smallest is that corresponding to the 4th level. The $\sigma_{gg'}$ of the 1st level is comparable to that of the 2nd level. The transfer cross-sections at other incident energies are shown in Fig. V.6 to V.9 for each level, respectively. Note that the integration under each curve yields the total cross-section at the incident energy (energy group) under consideration (i.e. $\sigma_g^i = \sum_{g'} \sigma_{gg'}^i$, i = 1,2,3, or 4). The axis of these figures are labeled in the power of 10 (e.g. E - out = 10^{-3}eV). Note from Fig. V.9 that the 4th level can only be excited at incident energies above the threshold of that level.

The C/E values for T_6 and T_7 are shown in Fg. V.10 based on the 30-group library used. Also shown are the values obtained upon using ENDF/B-VI and LANL evaluation for beryllium cross-sections. (Note that the LANL evaluation is the data used for all results reported in the other sections in this report.) As shown, the C/E values for T_6 inside the Be layer are larger with the ENDF/B-V than those obtained by the LANL and ENDF/B-VI evaluations due to: (a) larger ^{9}Be(n,2n) cross-section which leads to larger neutron multiplication, and (b) larger low-energy component in the SED of neutrons emitted from the ^{9}Be(n,2n) reactions. The latter reasoning can be seen from Figs. V.11 to V.13 which show the transfer cross-section $\sigma_{gg'}$(n,2n) of ENDF/B-V, LANL, and ENDF/B-VI (evaluated by LLNL), respectively. More details on the impact of these three evaluations on the prediction accuracy of T_6 and T_7 (and on other reaction rates) are discussed in Section VIII. For the purpose of the present analysis, the SED sensitivity results are based on ENDF/B-V evaluation for beryllium.

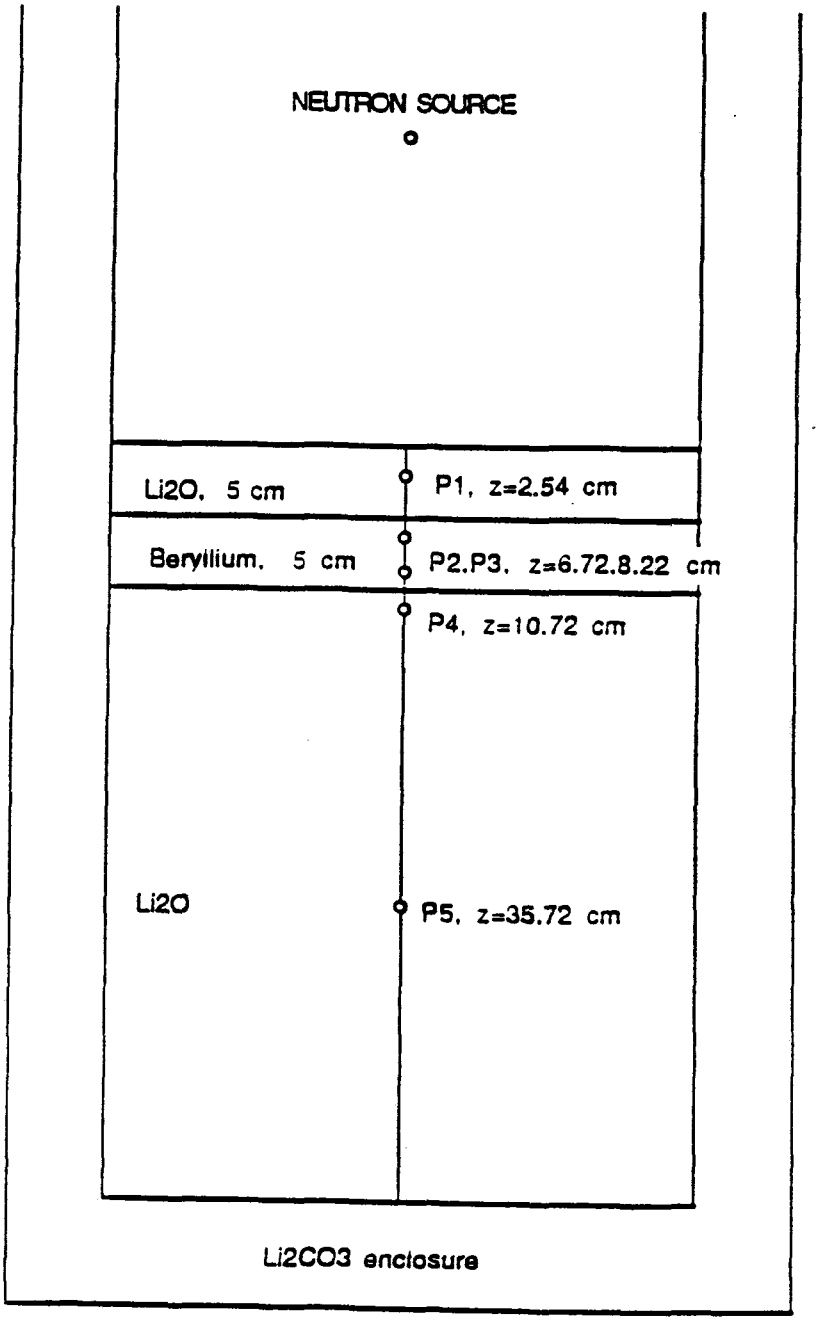

Fig. V.4: Different Detector Locations Considered in the Sensitivity Analysis for the BES System of Phase IIA

(A) Analysis of Excitation Level's Variations

Based on the level-independent treatment for variations in the SED of the ^{9}Be(n,2n) cross-section, if we assume a 1% increase in the cross-section $\sigma^1_{gg'}$ of the 1st excitation level at incident group energy g = 13.5 - 15MeV, the required variation factors for other levels, $\alpha^2_g = \alpha^3_g = \alpha^4_g$, are obtained from Eq. V.6. Eq. V.7, then, gives the new cross-section $\sigma^{new}_{gg'}$. The resultant variation factors $\beta^1_{gg'}$, given by Eq. V.13, which relates the old and new distributions are shown in Fig. V.14. Similarly, we increase the cross-section of the 2nd level by 1%, we can evaluate the variation factors $\beta^2_{gg'}$, which are also shown in Fig. V.14. The factors $\beta^3_{gg'}$, and $\beta^4_{gg'}$, are depicted in Fig. V.14 for comparison where the horizontal axis represents the exit energy group g'. Note from that figure that the factors are generally large (in absolute values in the energy range $E_{g'} > 0.5$ MeV and are almost constant below this energy. Also the trend of these factors for variations in the 1st and 2nd levels (by α^m_g = 1%; m = 1,2) are similar and more or less opposite in their sign to the corresponding variations in the 3rd and 4th levels (m = 3,4). In the case of the level-dependent treatment, the variation factors are very similar (see Fig. V.15) to those shown in Fig. V.14.

When these variation factors are used to calculate the total relative sensitivity profiles, P^g(SED), given by Eq. V.24, and when summation is performed for all the incident energy group, we obtain the total integrated sensitivity coefficient, $P(SED) = \sum_g P^g(SED)$, shown in Fig. V.16 for T_6 at the five locations P_1 through P_5. This figure gives the percentage change in T_6 at these locations upon increasing the cross-section of the ith level (i=1,2,3,4,) by 1% and compensating the cross-sections of other levels by the factor α^i_g obtained from Eq. V.6. As shown, the coefficients corresponding to the 1st excitation level (χ1) are the largest and positive inside the beryllium layer. The coefficients are also positive outside the Be layer, however, the coefficients for considering an increase in the 2nd excitation level (2.43 MeV) is the largest nearby the beryllium boundaries. This

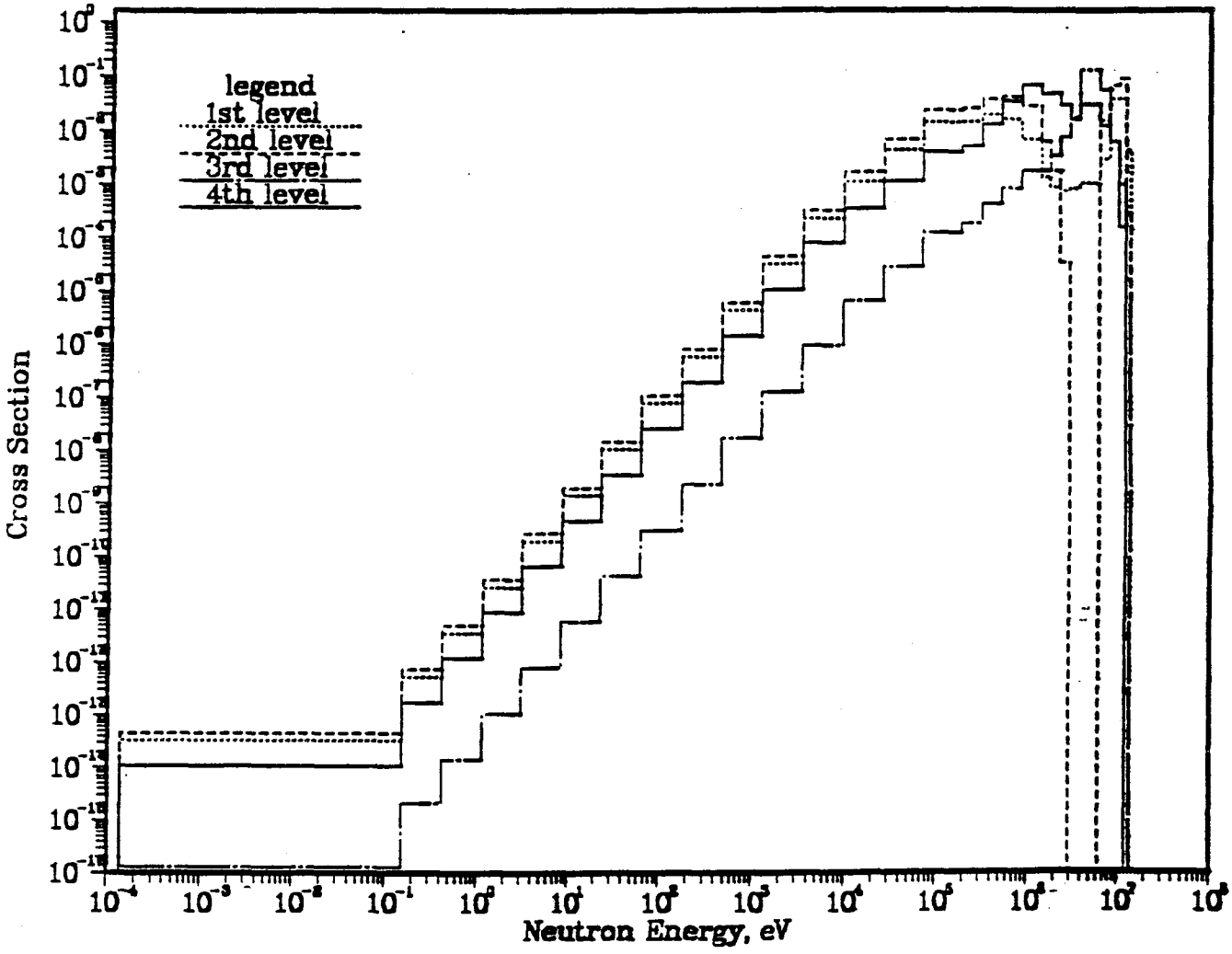

Fig. V.5: The $^{9}Be(n,2n)$ Total Cross-Section from the Four Different Levels of ENDF/B-V (Ein = 13.5 MeV to 15 MeV)

is due to emphasizing (i.e. increasing) the low-energy component of the total SED that is due to the 2nd emitted neutron.

Note that the SED for each excitation level shown in Fig. V.5 is a composite of the SED of the 1st and the 2nd neutrons emitted from the $^{9}Be(n,2n)$ reaction. Fig. V.17 shows this SED ($\sigma_{gg'}^{\chi_i}$, not normalized) for each excitation level. For example, if the incident neutron energy is ~ 14 MeV, the 1st neutron emitted from exciting the 1st excitation level will have energy around 10 MeV while the 2nd neutron will have broader energy spectrum which has a peak around 1 MeV; an important range for contributing to T_6. Note that for the 3rd excitation level, the 1st and 2nd emitted neutrons will have energies around 5 - 7 MeV, a range that is not largely contributing to T_6. Therefore, increasing the cross-section of the 3rd (6.76 MeV) or the 4th (11.28 MeV) excitation level with a decrease in the cross-section of other levels leads to negative coefficients. This is due to emphasizing (i.e., increasing) the high-energy component of the total SED that is due to the 2nd emitted neutron. As for T_7, increasing the cross-section of the first or second excitation level while decreasing the cross-sections of other levels leads to an increase in T_7 inside and around the Be layer. The coefficients for the second level are the largest as shown in Fig. V.18. This is due to the emphasizing (i.e. increasing) the high energy component of the total SED that is due to the first emitted neutron. Although there is an increase in SED of the second neutron, this has little impact on T_7. Note from Fig. V.18 that increasing the cross section of the third or fourth excitation level with a decrease in the cross-section of other levels leads to negative coefficients. This is due to the decrease in the high-energy component of the total SED that is due to the first emitted neutron. Figs. V.19 and V.20 show the coefficients for T_6 and T_7 when the level-dependent treatment is adopted to vary the SED. As compared to Figs. V.16 and V.18, the treatment with either level-dependent or level-independent approach gives similar results. Note from these figures that the sensitivity coefficients for the various level's variations are larger (in absolute values) for T_7 (by a factor of ~ 4) as compared to the coefficients for T_6.

The choice of which excitation level to increase (or decrease) with a compensating decrease (or increase) in the other levels depends on the discrepancies that are observed between measurements and calculations. For example, increasing the cross-section of the second excitation level will improve the C/E values (lower than units) observed just behind the Be layer in the BES of Phase IIA. However, the sensitivity coefficients for 1% increase in that level is ~ 0.07% (small) for T_6 at location P_4, as shown in Fig.16 The observed

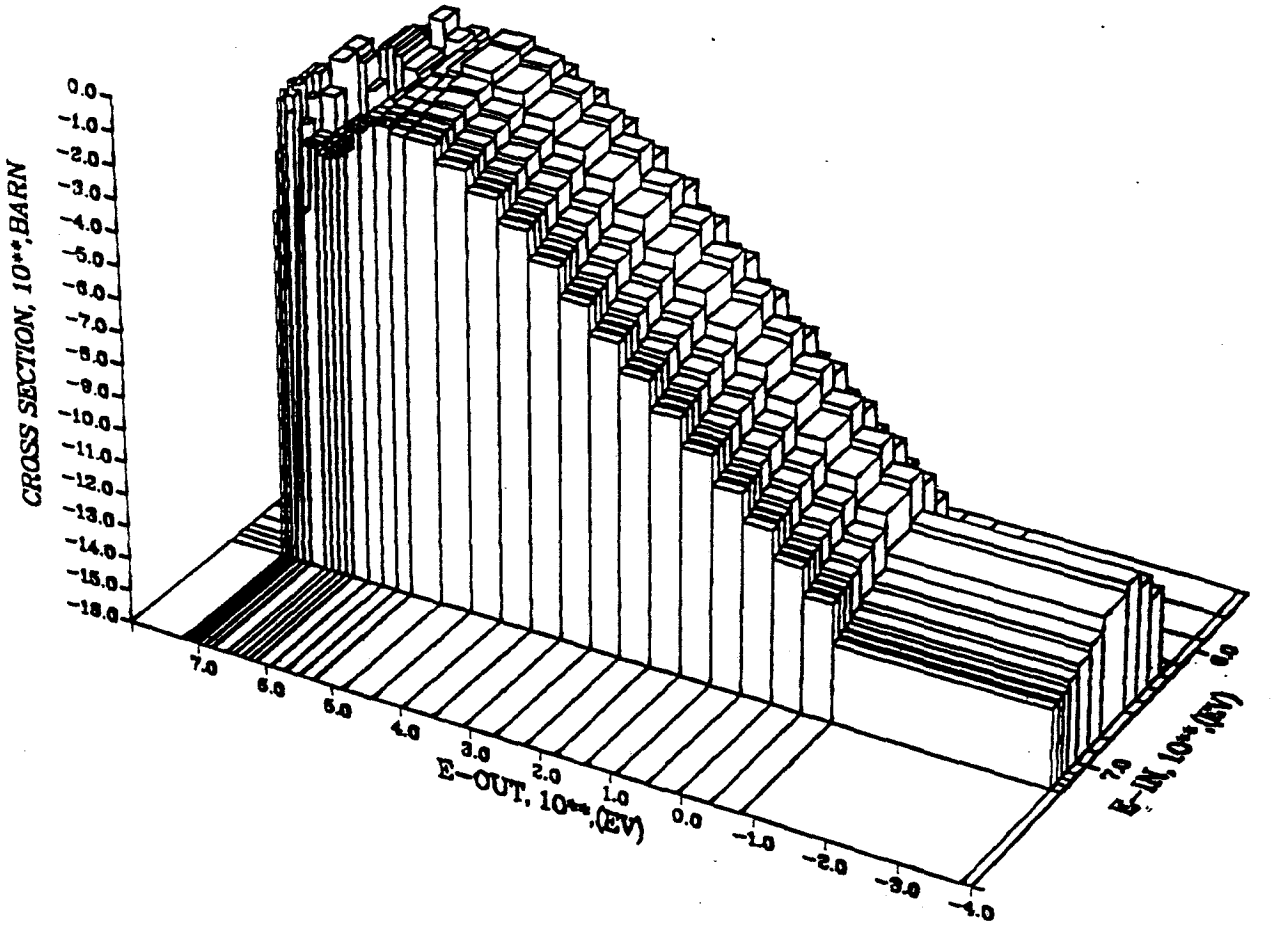

Fig. V.6: The SED from the First Level of ENDF/B-V ^{9}Be(n,2n) Cross Section

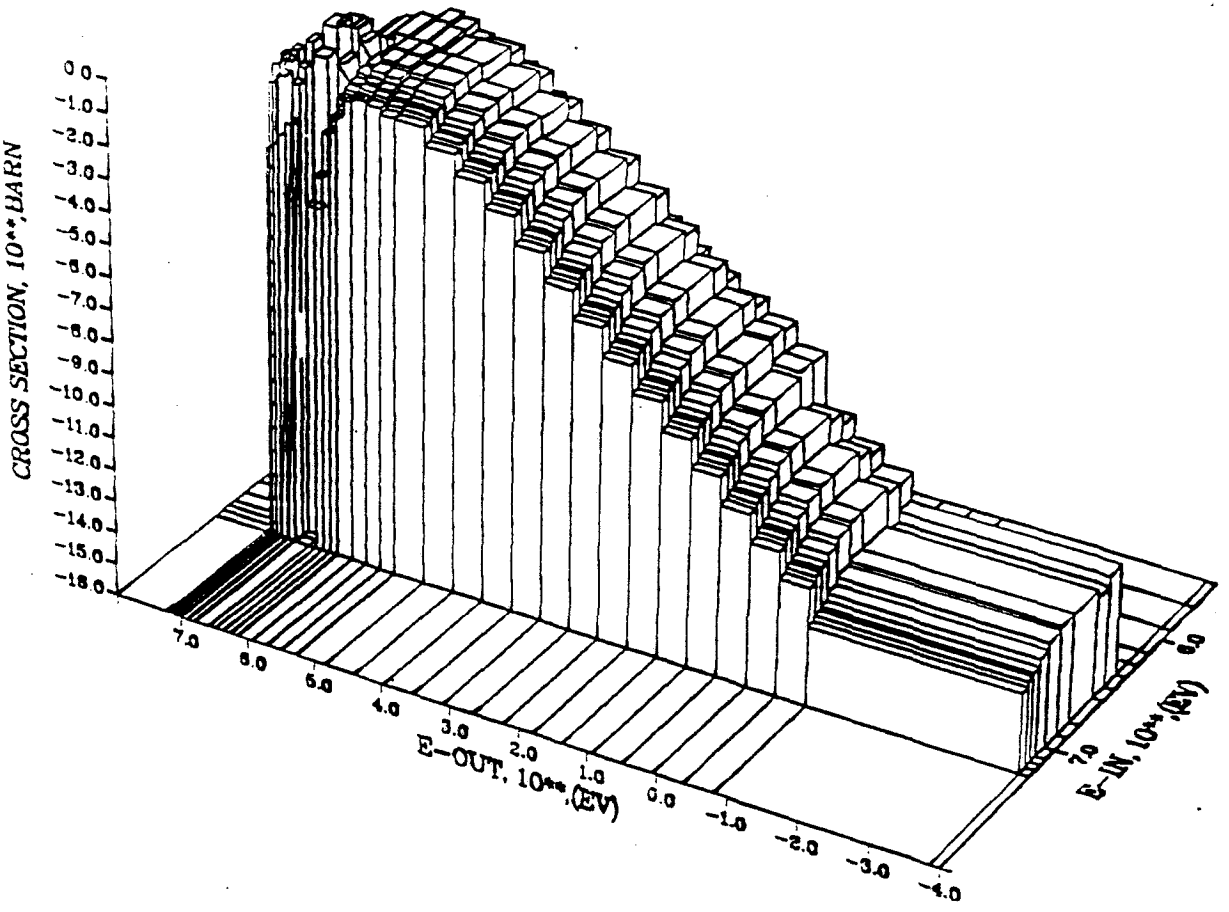

Fig. V.7: The SED from the Second Level of ENDF/B-V ^{9}Be(n,2n) Cross-Section

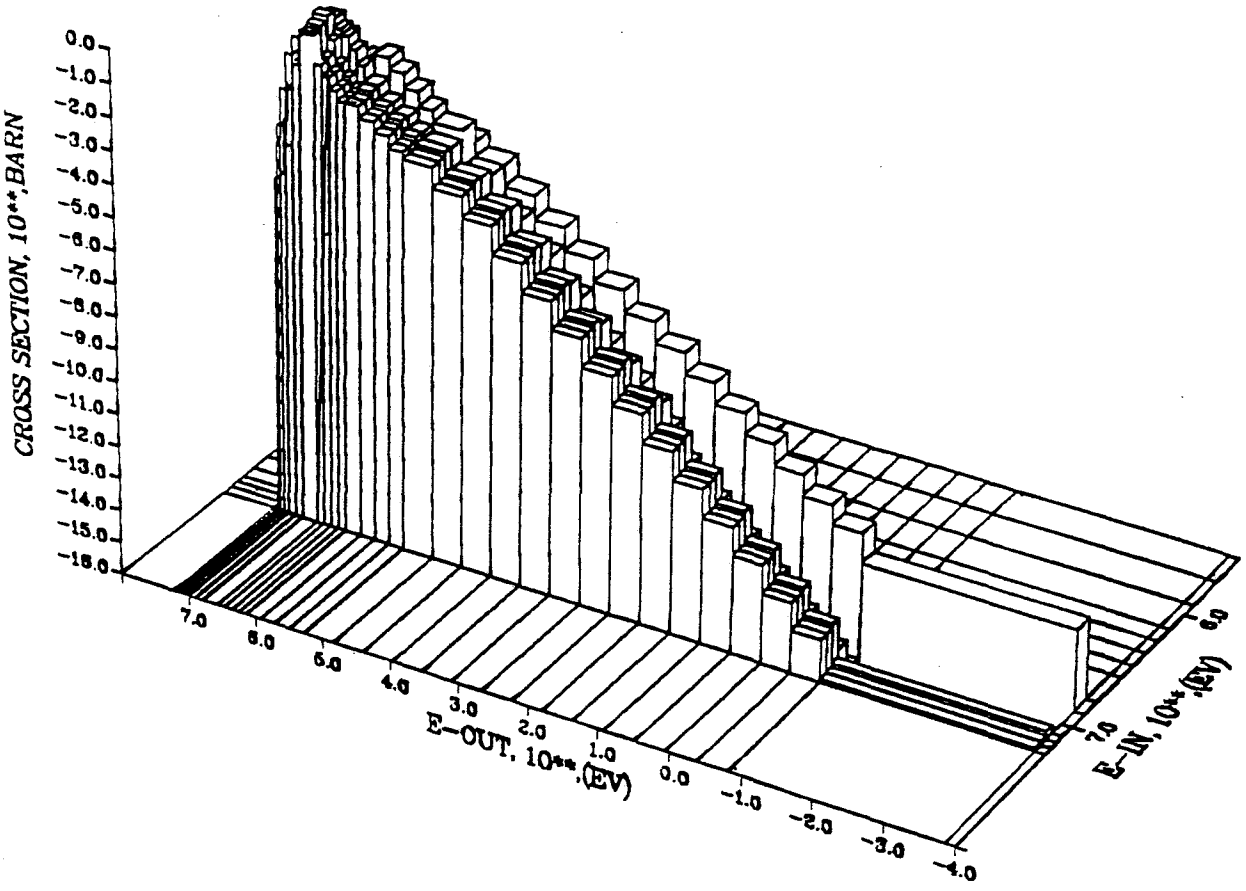

Fig. V.8: The SED from the Third Level of ENDF/B-V ^{9}Be(n,2n) Cross Section

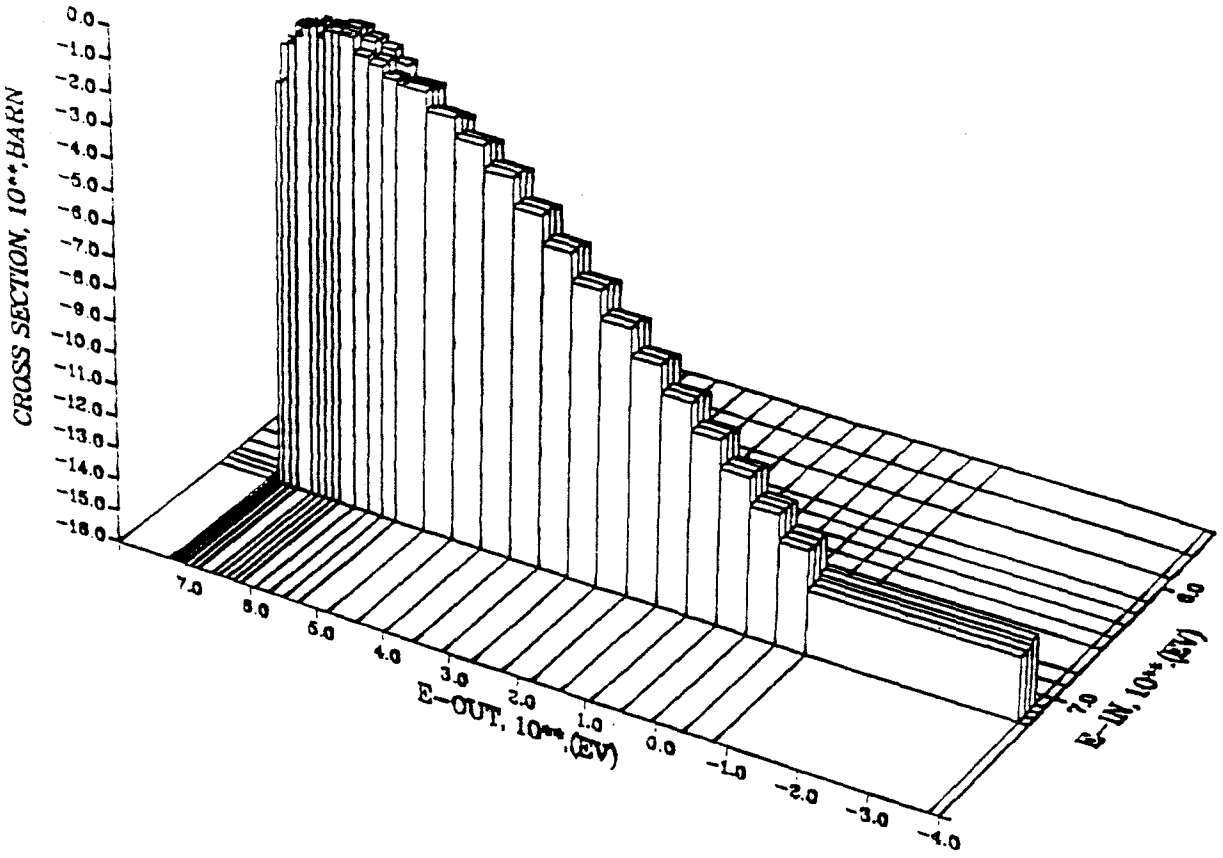

Fig. V.9: The SED from the Fourth Level of ENDF/B-V ^{9}Be(n,2n) Cross-Section

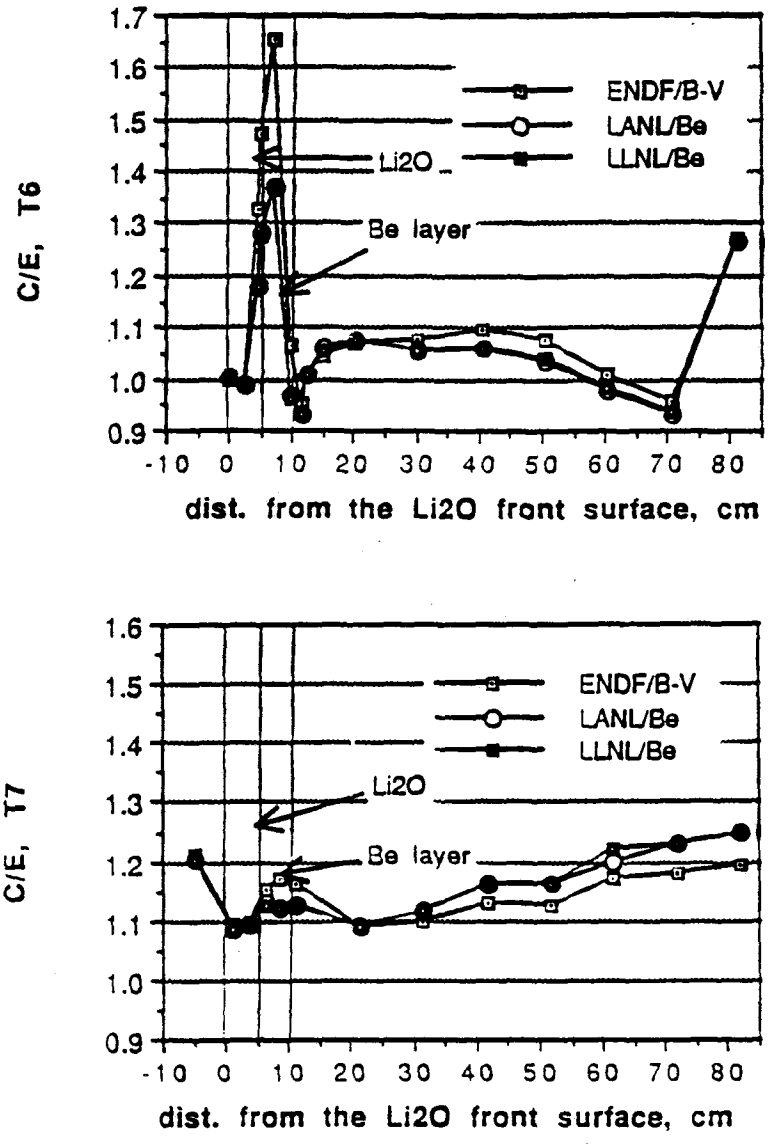

Fig. V.10: C/E Values for T_6 and T_7 in Phase IIA BES Experiment

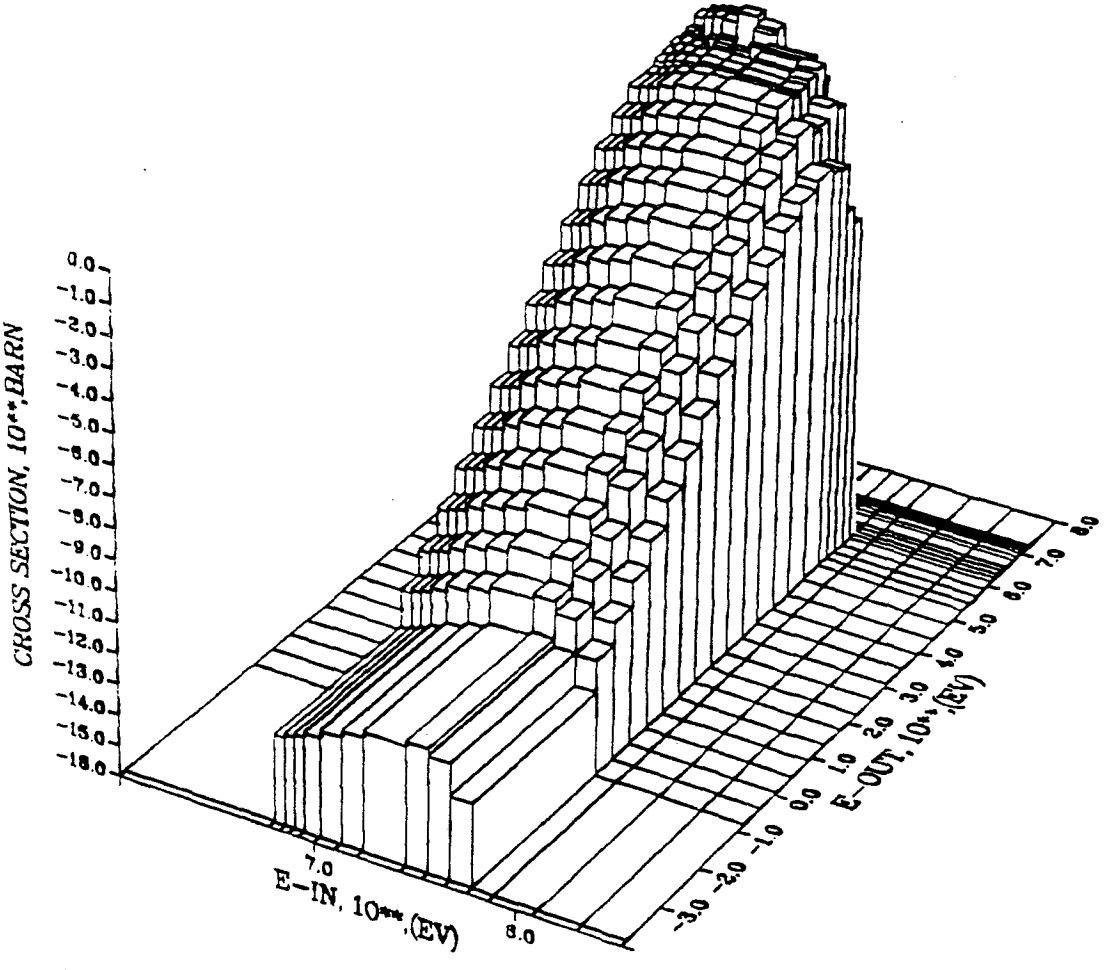

Fig. V.11: The SED (Cross-Section) of Neutrons Emitted from the ^{9}Be(n,2n) Reaction (ENDF/B-V)

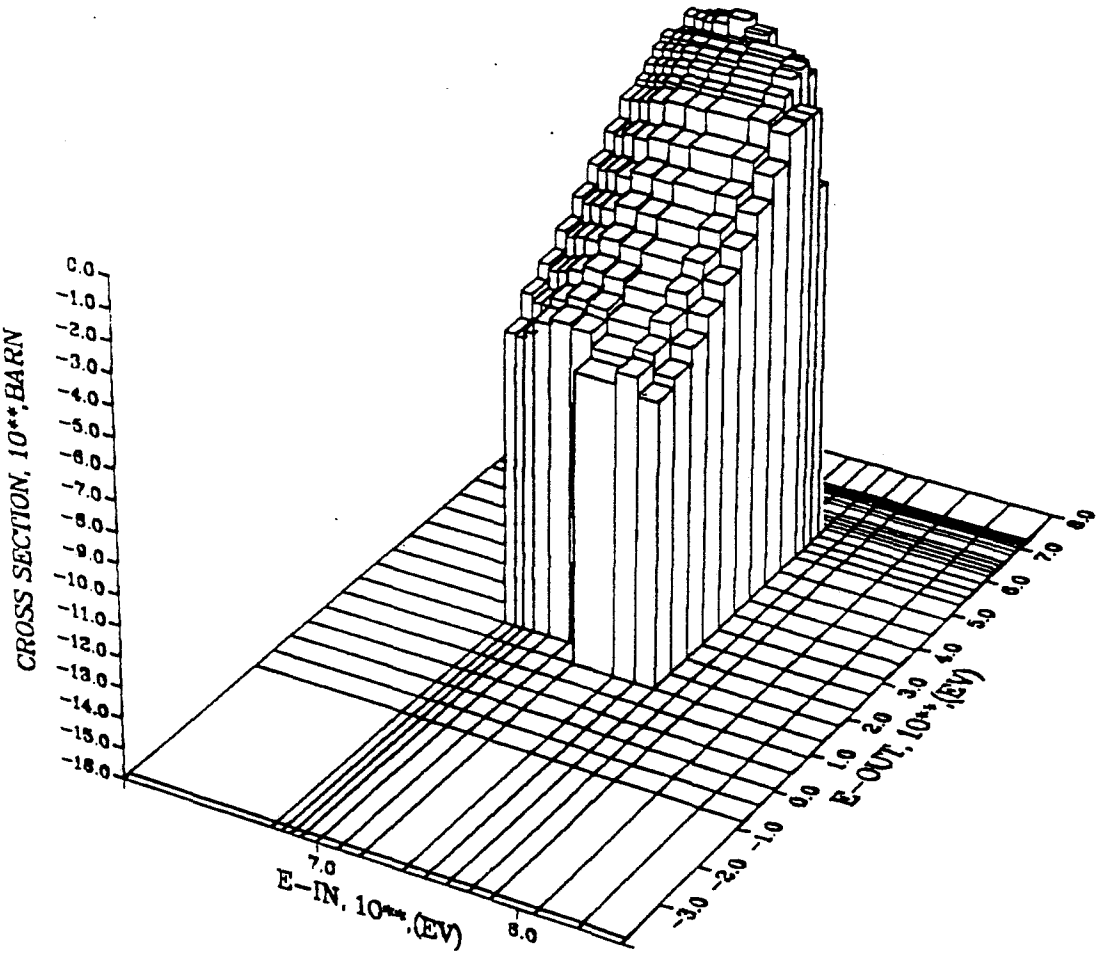

Fig. V.12: The SED (Cross-Section) of Neutrons Emitted from the ^{9}Be(n,2n) Reaction (LANL)

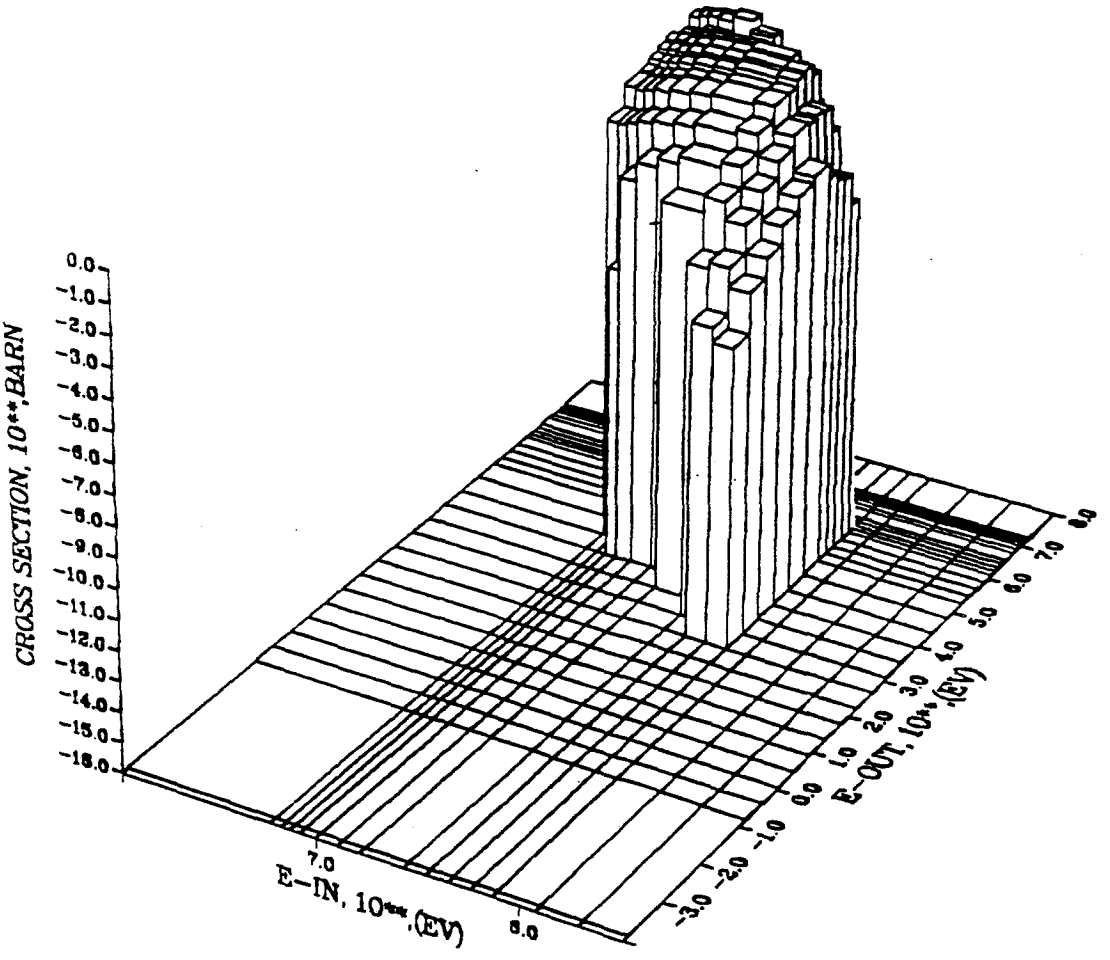

Fig. V.13: The SED (Cross-Section) of Neutrons Emitted from the ^{9}Be(n,2n) Reaction (LLNL)

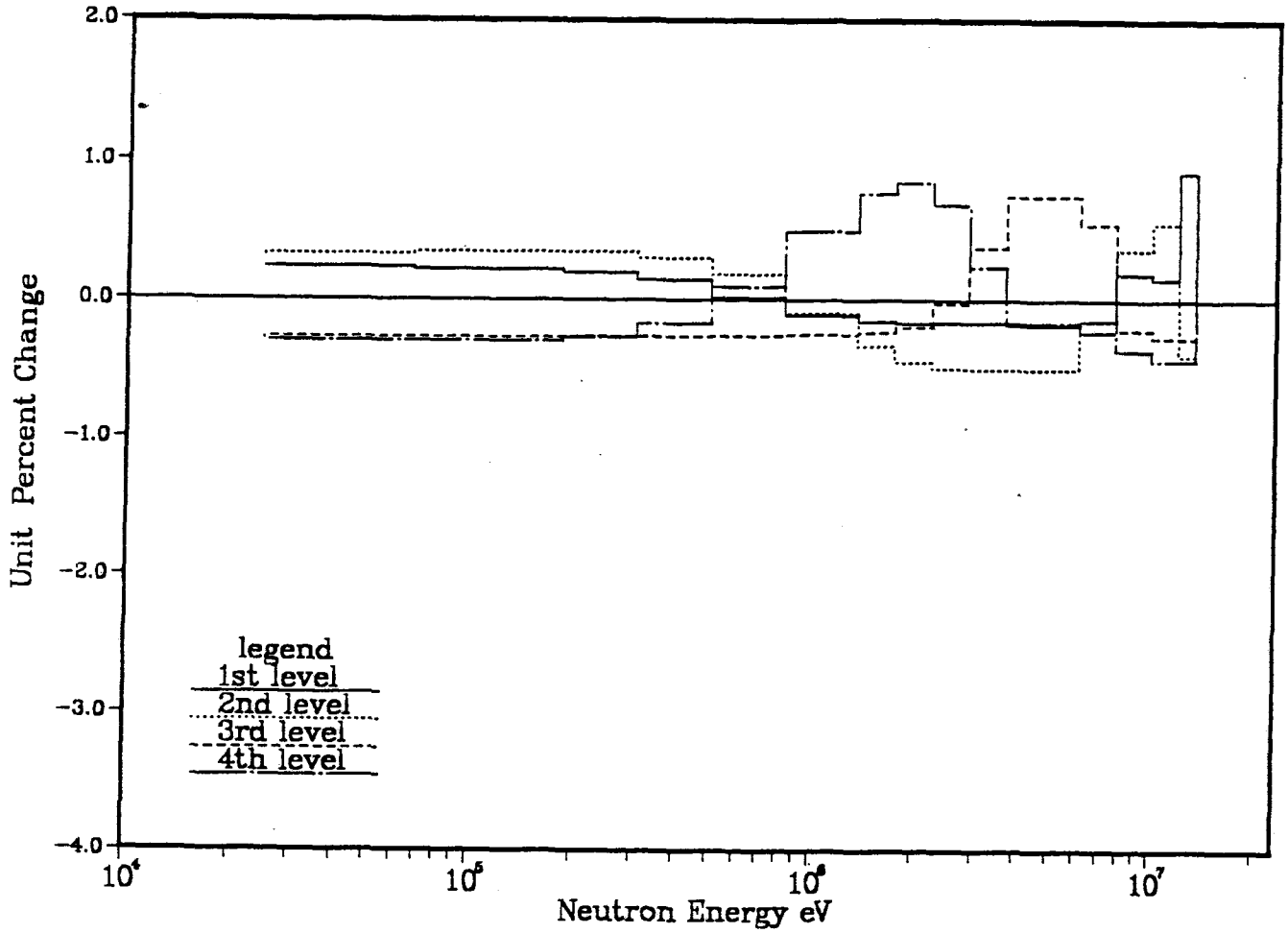

Fig. V.14: Variation Factors for the Level-Independent Treatment of the ENDF/B-V Berylium Data for Incident Neutron Energy Group 15-13.5 MeV

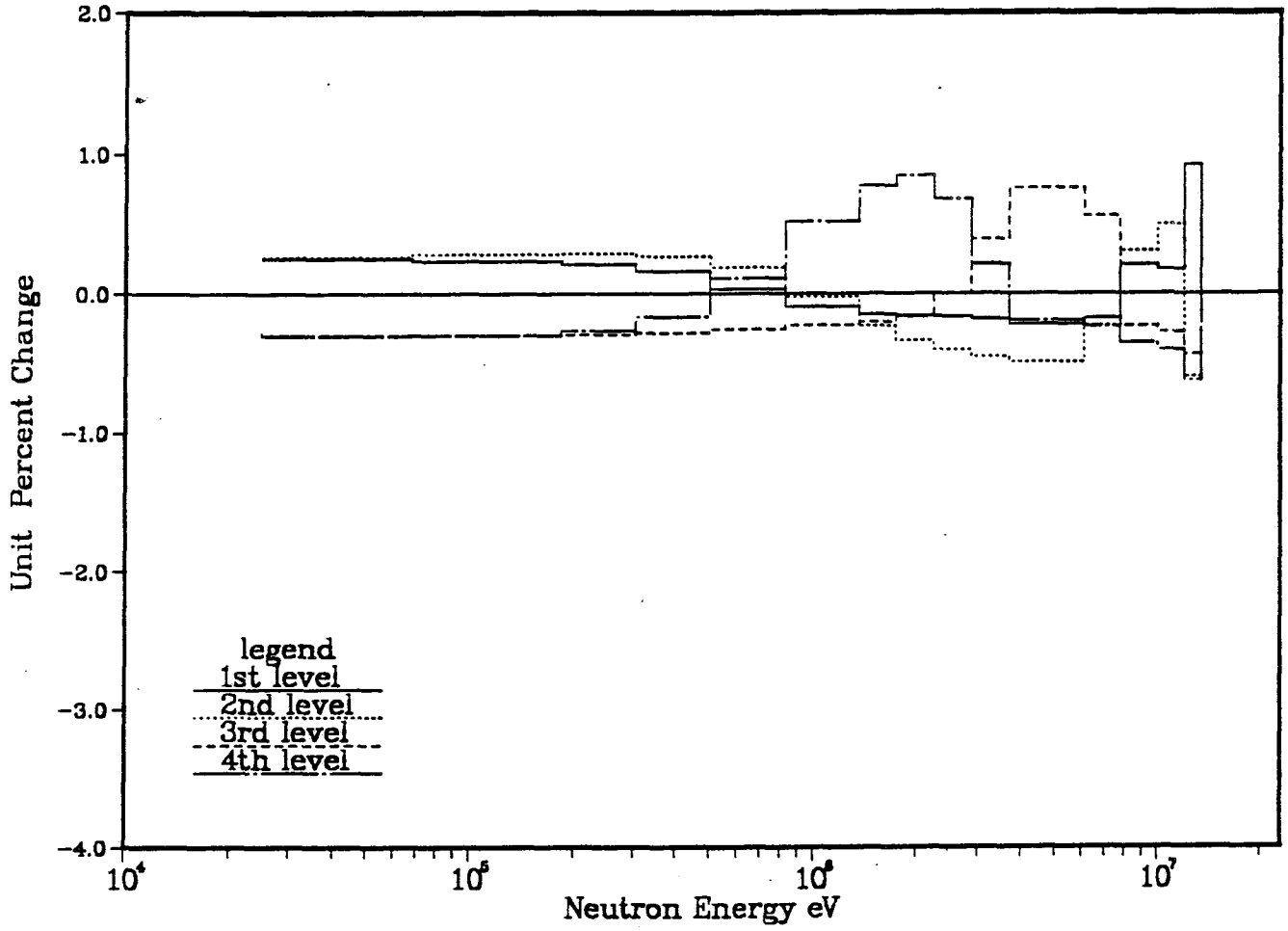

Fig. V.15: Variation Factors for the Level-Dependent Treatment of the ENDF/B-V Berylium Data for Incident Neutron Energy Group 15-13.5 MeV

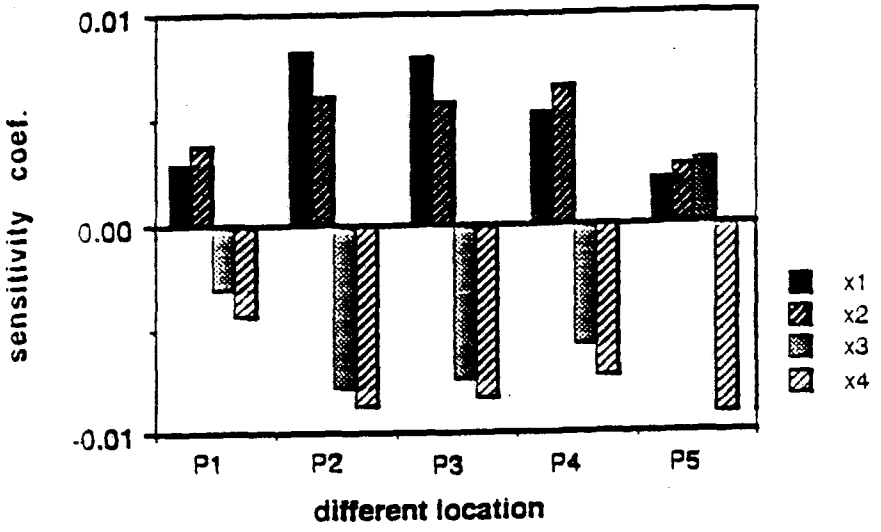

Fig. V.16: Integrated Sensitivity Coefficient for T6 Due to Variation in SED of ^{9}Be(n,2n) Cross-Section-Level-Independent Treatment (ENDF/B-V)

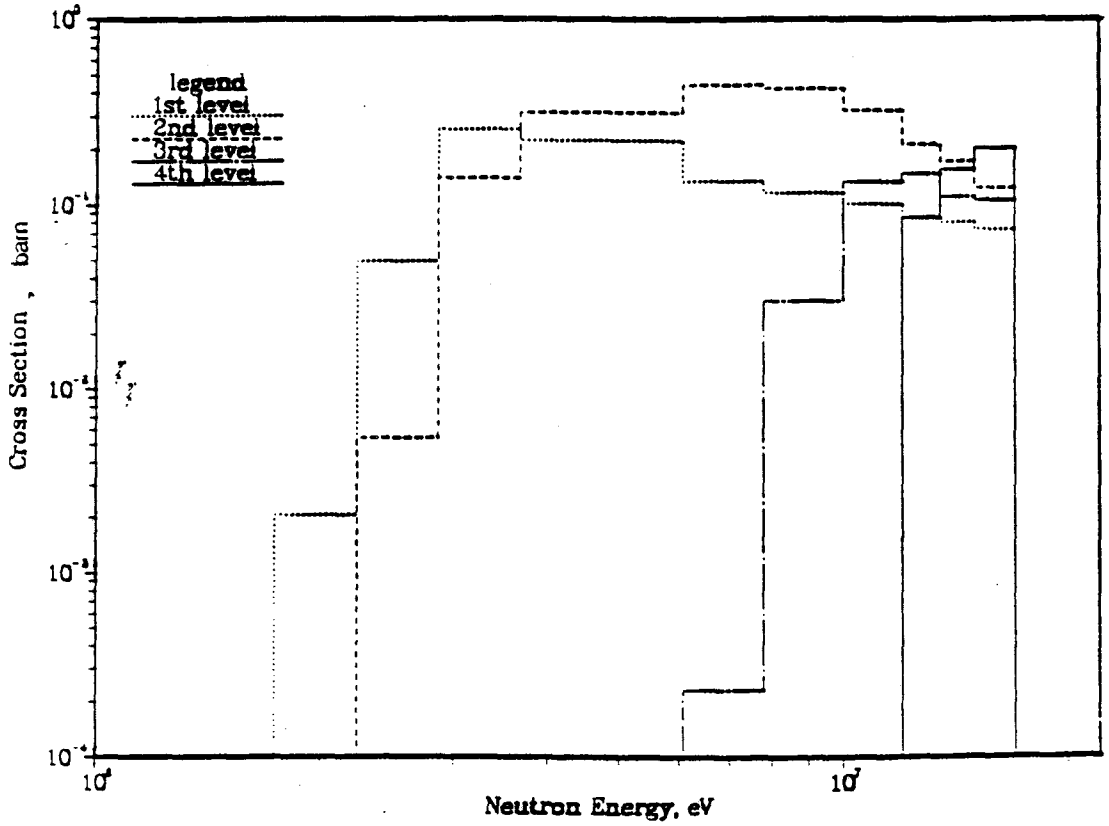

Fig. V-17: The $^{9}Be(n,2n)$ Total Cross-Section from the Four Different Levels of ENDF/B-V (Ein - 13.5 MeV to 15 MeV)

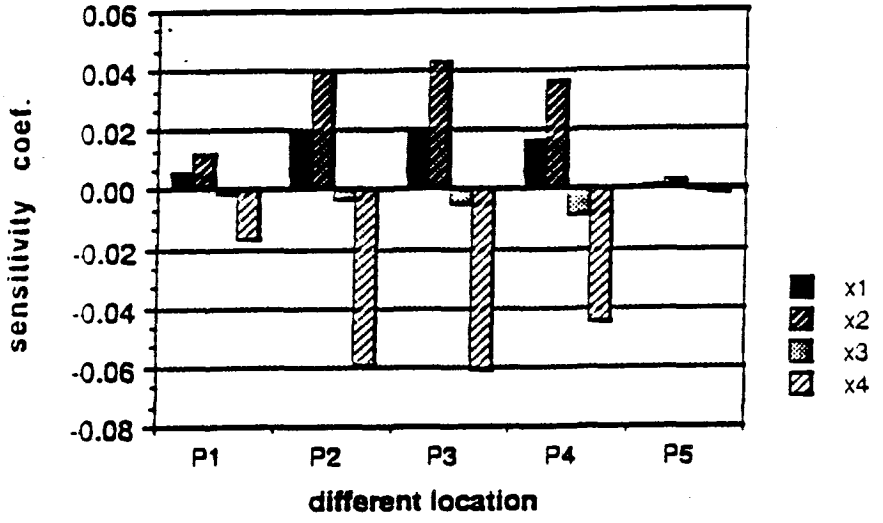

Fig. V.18: Integrated Sensitivity Coefficient for T_7 Due to Vairation in SED of $^{9}Be(n,2n)$ Cross-Section (Level-Independent Treatment) (ENDF/B-V)

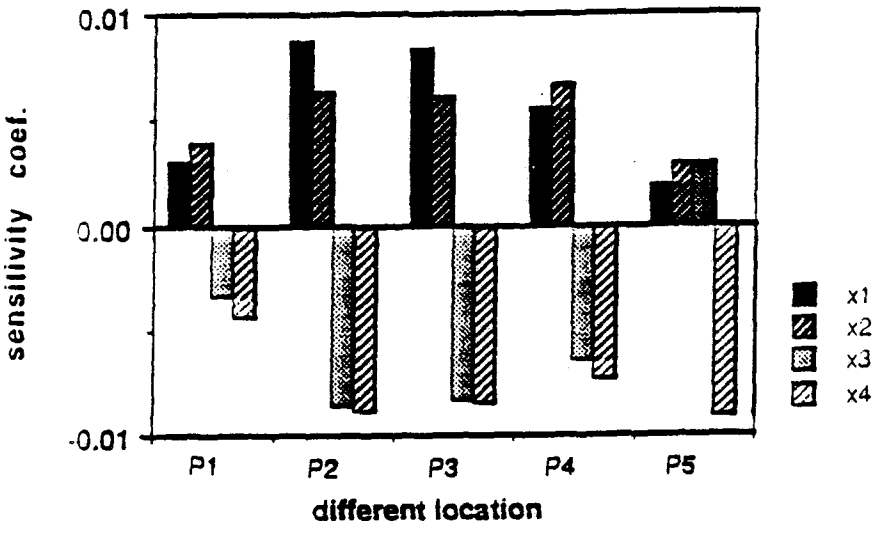

Fig. V.19: Integrated Sensitivity Coefficient for T_6 Due to Variation in SED of $^{9}Be(n,2n)$ Cross-Section (Level-Dependent Treatment) (ENDF/B-V)

discrepancy of ~ 5 - 7% shown in Fig. V.10 can not be explained by the 1% variation assumed in the cross-section of the 2nd excitation level, unless this variation is 100%.

(B) Analysis of Direct Variation in the SED of ^{9}Be(n,2n) Cross-Section Over Several Energy Intervals

Direct variations in the SED of the ^{9}Be(n,2n) was performed and the sensitivity coefficients were calculated according to Eq. V.24. The results of Oyamaya and Maekawa's experiment[34] on the leakage spectrum behind a 5cm-thick beryllium slab with Be (LANL) data showed that the calculated spectrum is

under-estimated in the energy range 0.1 MeV $<E_{out}<$0.5 MeV
over-estimated in the energy range 0.5MeV $< E_{out} <$10 MeV, and
under-estimated in the energy range $E_{out} >$ 10 MeV.

Assuming that these discrepancies are due to the inadequacy of the SED of the total ^{9}Be(n,2n) cross-section, we carried out two types of SED variations:

In case 1 variation, the overestimated part of the integrated spectrum (0.5MeV$<E_{out}$ <10MeV) was decreased by 1%. The necessary increase in the underestimated parts (E_{out}>10MeV, 0.1 MeV $< E_{out} <$0.5MeV) was calculated (by assuming that the decreased amount in the overestimated part is equally distributed in the other underestimated parts) such that the total integrated spectrum was kept the same. The variations were also assumed to be for all incident energies (above the threshold energy of the ^{9}Be(n,2n) reaction).

In case 2 variation, the lower energy part of the SED below 0.1 MeV was increased by 1% and the necessary decrease in the SED above 0.1 MeV was carried out for all incident energies. This type of variation was applied to investigate the impact of variation in the lower energy tail of the SED of the ^{9}Be(n,2n) reactions on T_6. The required variation factors were derived in the above two cases and the relative integrated sensitivity coefficients were calculated for both T_6 and T_7

Fig. V.21 displays these sensitivity coefficients at the five locations considered. In case 1, the integrated coefficients are positive for T_6 inside and around the Be layer. Since T_6 is increased behind this layer, the drop in the C/E curves observed at this location will be lessened. However, the coefficients are still small in absolute values. For a 1% decrease in the overestimated part of the spectrum (with the necessary increase in the other

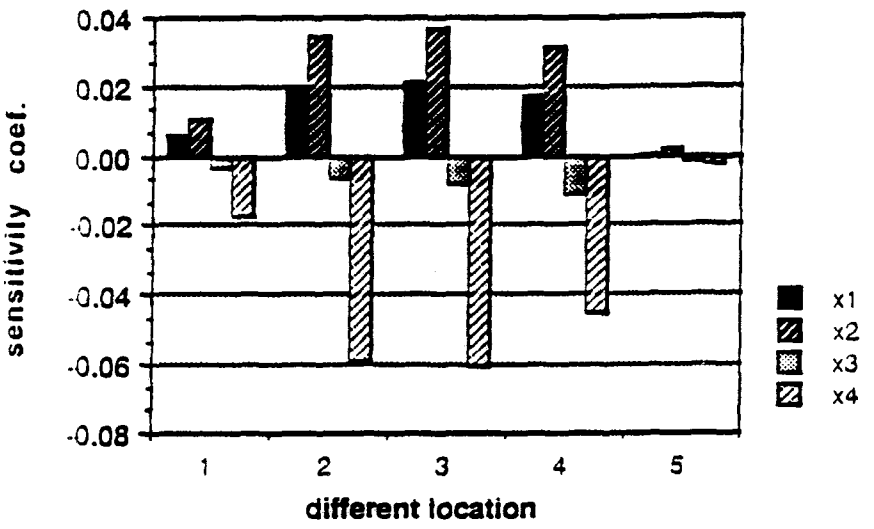

Fig. V.20: Integrated Sensitivity Coefficient for T_7 Due to Variation in SED of $^{9}Be(n,2n)$ Cross-Section (Level-Dependent Treatment) (ENDF/B-V)

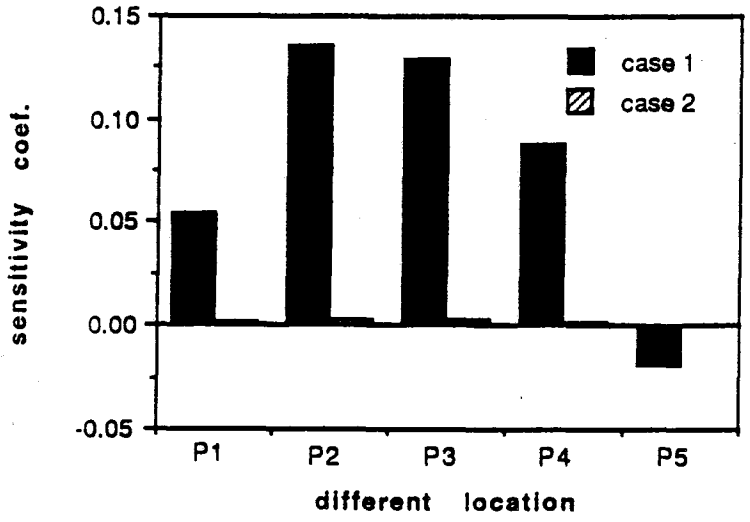

Fig. V.21; Integrated Sensitivity Coefficient for T_6 Due to Two Types of Vatiations in the SED of the $^9Be(n,2n)$ Cross-Section

parts of the SED), the T_6 coefficient is ~ 0.09% behind the Be layer. To cover the observed discrepancy of ~ 7.0% at this location, the required decrease in the overestimated part should be ~ 70 - 80%.

Fig. V.22 shows the breakdown of the contribution to the sensitivity coefficients of T_6, at each location, that comes from various energy ranges, namely 10MeV<E_{out}<17MeV, 0.5 MeV<E_{out}<10MeV, and 0.1 MeV<E_{out}<0.5 MeV. No variation in the SED was carried out below 0.1 MeV in case 1. The 1% decrease in the energy range 0.5MeV<E_{out}<10MeV resulted in a negative contribution to the sensitivity coefficients for T_6 at all locations and its absolute value is large inside the Be layer and at distance far behind that layer. However, the contributions from the necessary increase in the SED above 10MeV and in the energy range 0.1 MeV<E_{out}<0.5MeV compensate for the negative contribution resulted from the decrease in SED in the energy range 0.5MeV<E_{out}<10MeV. The net result is positive coefficients inside the Be and just behind it as shown in Fig. V.21.

In case 2 variation, the integrated sensitivity coefficients for T_6 were found to be positive in and around the Be layer as shown in Fig. V.21. However, their absolute values are very small (<0.001%). Therefore, variations in the SED of the emitted neutrons from the ^{9}Be(n,2n) reactions below 0.1 MeV have little impact on T_6; the larger impact is due to variations performed above 0.1 MeV, as in Case 1.

As for T_7, Case 1 indicates that T_7 has positive integrated sensitivity coefficient at all locations and their absolute values increase as one proceeds towards the back locations of the test assembly, as shown in Fig. V.23. Although the SED was decreased (by 1%) in the energy range 0.5 MeV <E_{out}<10MeV, where the threshold of the ^{7}Li(n,n'α)t reaction lies, however, the increase in the SED above 10MeV leads to larger and positive contribution to the total sensitivity coefficient, and that leads to net positive values. Therefore, any uncertainties in the SED of the ^{9}Be(n,2n) reactions above 10 MeV will have large impact on T_7, as expected. One notices however, that the sensitivity coefficients for T_7 are smaller than those for T_6 inside the Be layer, shown in Fig. V.21. Also, the variations performed in Case 2 leads practically to insignificant variation in T_7 (and T_6)

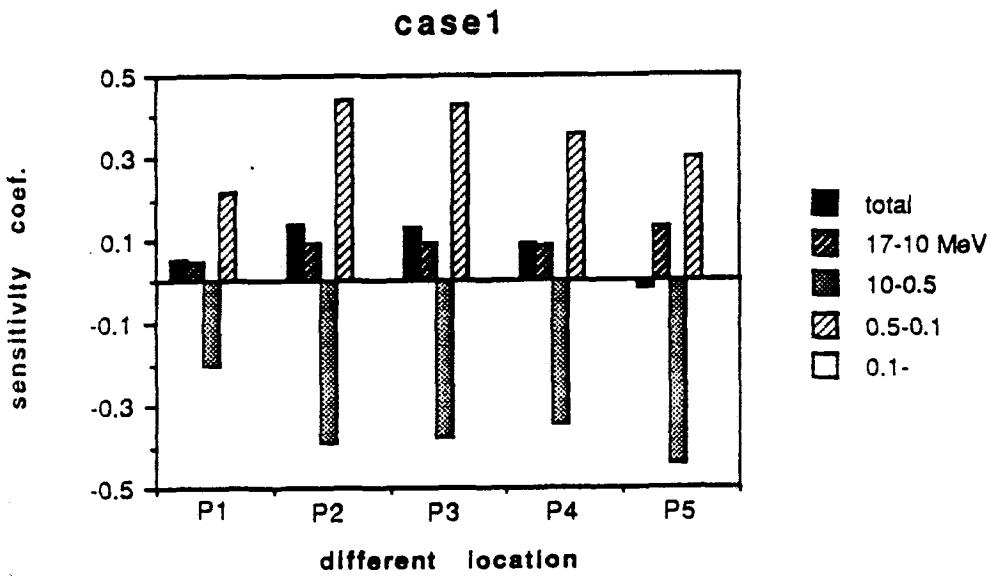

Fig. V.22: Breakdown (by Energy Range) in the Integrated Sensitivity Coefficient for T6 due to Case 1 Variation in the SED of the ^{9}Be(n,2n) Cross-Section

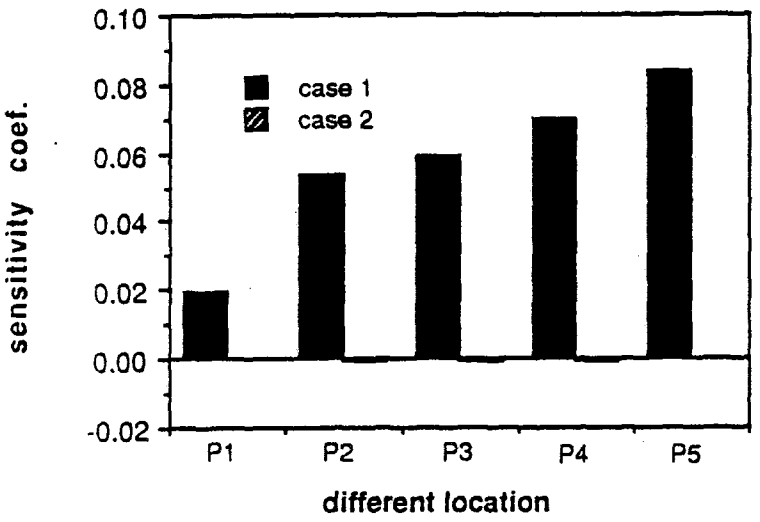

Fig. V.23: Integrated Sensitivity Coefficient for T_7 Due to Two Types of Variation in the SED of the $^{9}Be(n,2n)$ Cross-Section

V.6.2 Variations in the SAD of the ^{9}Be(n,2n) Cross-Section

The three types of variations in the angular distribution of neutrons emitted from the ^{9}Be(n,2n) reactions that were discussed in Section V.3, have been applied to investigate their impact on T_6 and T_7. Note that the LANL evaluation for beryllium was used in these particular calculations.

In the first case (forward variation), the SAD was increased by a 1% in the interval $0.5 < \mu < 1$. The upward SAD ($-0.5 < \mu < 0.5$) was kept unchanged. The required change in the backward SAD ($-1 < \mu < -0.5$) was calculated such that the integrated SAD was kept the same. In the second case (upward variation), a 1% increase in the upward SAD was applied with the corresponding decrease in the forward and backward SAD. A 1% increase in the backward SAD was applied in the third case (backward variation). The upward SAD was unchanged. The required change in the forward SAD was calculated such as the integrated SAD was kept the same. The variation factors used are those given by Eqs. V.18-a through V.18-c.

Figs. V.24 and V.27 show the integrated sensitivity coefficients for T_6 and T_7, respectively, in the three cases discussed above. The coefficients of T_6 for the forward variation in the SAD is positive inside and behind the Be layer but negative in the front Li_2O zone, as expected. These coefficients increase as one proceeds inside the back Li_2O zone because more neutrons can now reach these locations and contribute to T_6 (and T_7, see below). Notice that the coefficients shown in Figs. V.24 and V.27are the total integrated ones, i.e., the forward variation was applied for each incident neutron energy (energy group) and the resultant coefficients were added to yield the values shown in Figs. V.24 and V.27.

Fig. V.25 gives the sensitivity coefficient for each neutron incident energy (group) and at four locations. The largest coefficient is at location P_5 ($\sim$ 25 cm behind the Be layer) and for the second incident energy group (13.5 - 15 MeV). At this location, and for every incident group, the coefficients are larger than those of other locations and they are always positive (solid lines are positive values, dashed lines are negative values). The coefficients at location P_4 (0.55 cm behind the Be layer) are the next largest and they are also positive for all incident energy groups. The coefficients at P_1 (in front of the Be layer) are the smallest and they are negative, as expected, since a lesser number of neutrons reach that location when the forward variation is applied.

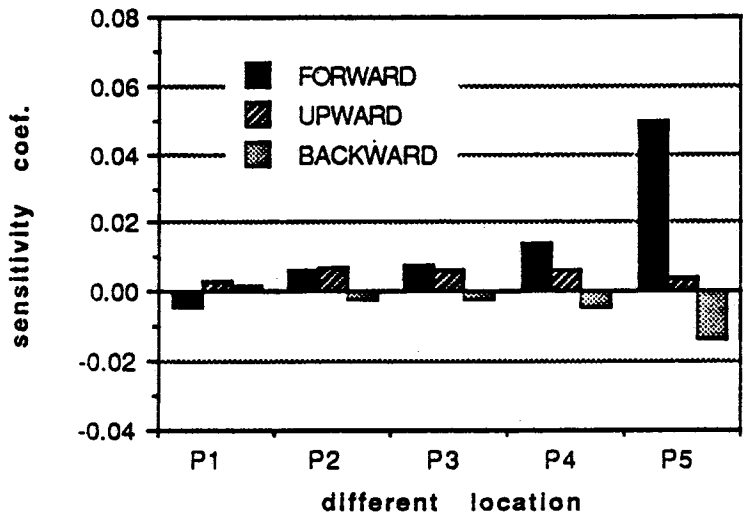

Fig. V.24: Integrated Sensitivity Coefficient for T_6 Due to Three Types of Variation in the SAD of the $^{9}Be(n,2n)$ Cross-Section (LANL Evaluation)

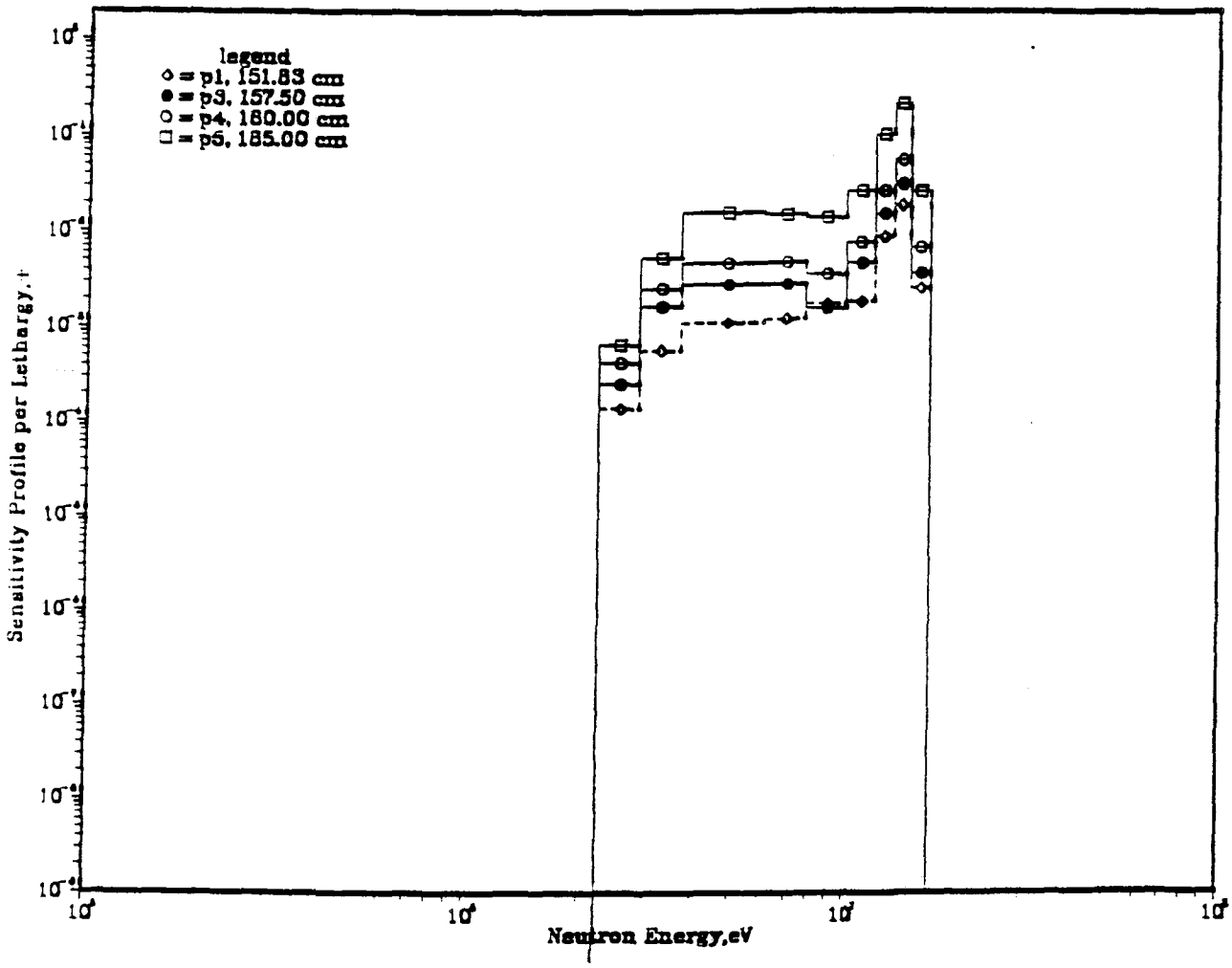

Fig. V.25: Relative Sensitivity Profile of T_6 Due to the Forward Variation in the SAD of the $^{9}Be(n,2n)$ Cross-Section

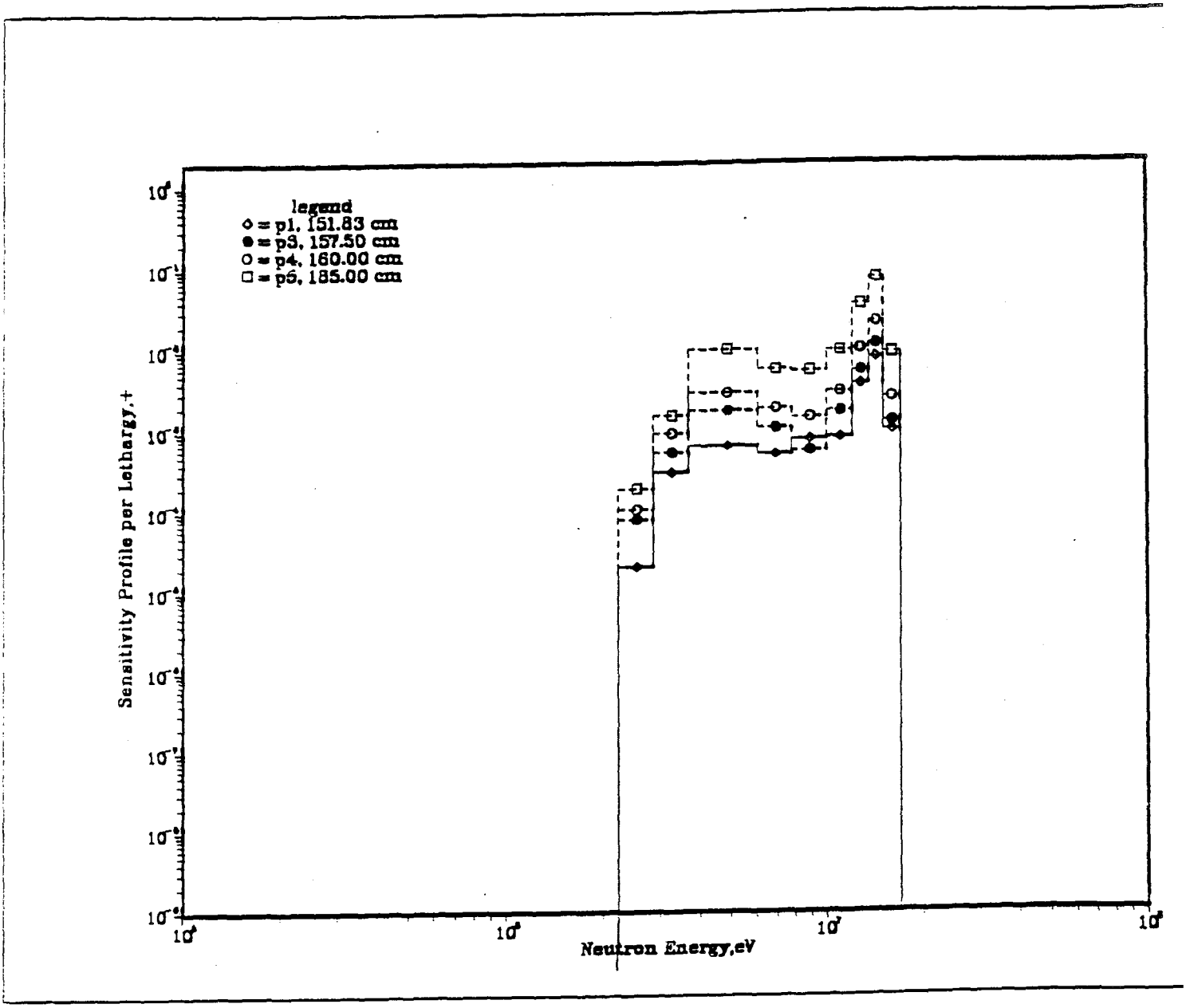

Fig. V. 26: Relative Sensitivity Profile of T_6 Due to the Backward Variation in the SAD of the $^{9}Be(n,2n)$ Cross-Section (LANL-Evaluation)

The coefficients for the upward variation in the SAD is always positive inside and around the Be layer. This is due to the increase in beryllium multiplication as neutrons are kept inside the Be zone leading to more $^{9}Be(n,2n)$ reactions that have low threshold energy ($\sim$ 1.75 MeV).

The coefficients for the backward variation are negative and they increase in absolute value as one proceeds towards the back end of the Li_2O assembly. This is as expected since fewer neutrons can now reach these back locations. Similar to Fig. V.25, the sensitivity coefficients as function of the incident neutron group are shown in Fig. V.26, where it is clear that these coefficients are always negative at all incident groups at locations P_3, P_4, and P_5 but they are always positive (solid lines) at locations P_1 since more neutrons reach this location when the backward variation is applied. Notice from Fig. V.24 that the upward and backward variations lead to positive (but significantly small) coefficients in the front Li_2O layer (location P1).

As for T_7, (see Fig. V.27) the coefficients for the forward variation are negative inside the Be layer and at the front Li_2O layer, but positive (with increasing trend) behind the Be layer since more high energy neutrons reach the bulk of the back Li_2O zone. The coefficients for the upward variation are always positive and large inside the Be layer since more neutron multiplication occurs. However, as a result of softening the incident spectrum with this type of variation, the high-energy neutrons reaching the back Li_2O zone are decreased at deep locations and hence a reduction in T_7 occurs in the bulk of the Li_2O zone.

The coefficients for the backward variation is positive (but small) inside the Be layer and at the front Li_2O layer but negative behind the Be layer, as expected.

In general, the coefficients for T_6 and T_7 are small. In comparison to the variations in the SED discussed in Figs. V.21 and V.23, the coefficients of variations in SAD are roughly an order of magnitude less than those for the variations in the SED.

V.7 Results of Variations in the Other Cross-Section of Beryllium

As we discussed above, the sensitivity coefficients for the SED and SAD of the $^{9}Be(n,2n)$ reactions are small. The sensitivity analysis was extended to include variations in the smooth integrated cross-sections $^{9}Be(n,2n)$, $^{9}Be(n,elastic)$ and $^{9}Be(n,total)$ to study

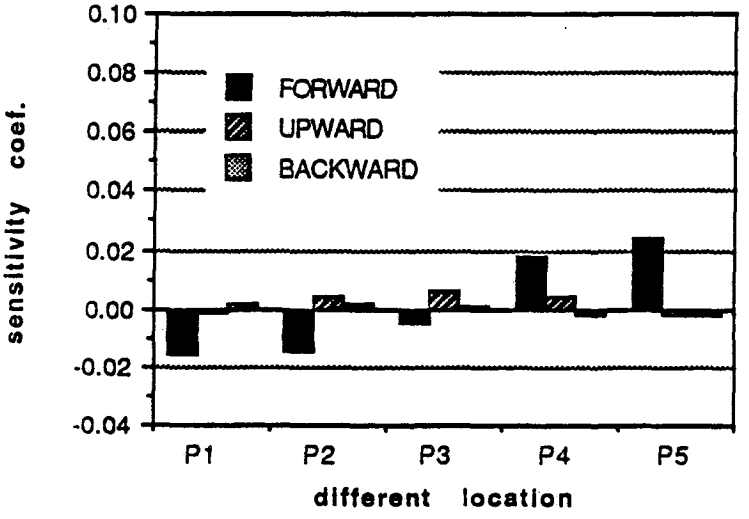

Fig. V.27: Integrated Sensitivity Coefficient for T_7 Due to Three Types of Variation in the SAD of the $^{9}Be(n,2n)$ Cross-Section (LANL Evaluation)

their impact on T_6 and T_7. The analysis was carried out for the three different evaluations for beryllium (namely; ENDF/B-V, LANL, and ENDF/B-VI).

Figs. V.28 to V.30 show the integrated sensitivity coefficients for T_6 resulting from a 1% increase in the ^{9}Be(n,total), ^{9}Be(n,eleastic), and ^{9}Be(n,2n), respectively. With all the evaluations, T_6 increases inside and around the Be layer, upon increasing the ^{9}Be(n,total) cross section, as shown in Fig. V.28. An increase in that cross-section means an increase in the (n,elastic) and (n,2n) reactions thus leading to more neutron moderation/multiplication and therefore enhancement in T_6 occurs. At the location P5, however, the coefficients are negative since high energy neutrons reaching this location are decreased upon increasing the number of interactions (particularly elastic interactions) inside the Be layer. The contribution to the sensitivitiy coefficients that is attributed to an increase (by 1%) in the ^{9}Be(n,elastic) cross-section is dominant as shown in Fig. V.29. Therefore, the values (and sign) of the sensitivity coefficients due to variation in the ^{9}Be(n,total) cross-section are basically driven by the contribution from the ^{9}Be(n,elastic) cross-section. The contriburtion from the ^{9}Be(n,2n) cross-section is small (by an order of magnitude) inside the beryllium layer, as shown in Fig. V.30, however, this contribution gets relatively larger behind that layer. Just behind the Be layer, the sensitivity coefficient of the ^{9}Be(n,2n) cross-sectin is $\sim$ 30% of that of the ^{9}Be(n,elastic) cross-section. By comparing the results shown in Fig. V.30 to those of Figs. V.21 and V.24, one can see that the sensitivity coefficients behind Be layer for variations in the total ^{9}Be(n,2n) cross-section are a factor of $\sim$3 and $\sim$15 larger than those obtained from variations in the SED and SAD, respectively.

In Figs. V.31 and V.32, the relative sensitivity profiles for T_6 are shown for the ^{9}Be(n,2n) and ^{9}Be(n,elastic) cross sections, respectively. These figures show in what energy range (or group) the variation in the cross-section under consideration will give the largest coefficient. As shown in Fig. V.31, the variation in the ^{9}Be(n,2n) cross-section in the second energy group (13.5 - 15MeV) leads to the largest coefficients at all the four locations considered. However, variations in the low energy range for the ^{9}Be(n,elastic) cross-section can lead to large variations in T_6, particularly inside and just behind the Be layer, as shown in Fig. V.32.

Figs. V.33 to V.35 show the corresponding integrated sensitivity coefficients for T_7 due to a 1% increase in the total, elastic, and (n,2n) cross-sections of beryllium, respectively. As shown, the sensitivity coefficients for the ^{9}Be(n,total) cross-sections are always negative at all locations and they are driven by the variation in the ^{9}Be(n,2n) cross-section (as opposed to ^{9}Be(n,elastic) cross-section in the case of T_6) as shown in Fig.

V.35. The coefficients for the ^{9}Be(n,elastic) cross-section are an order of magnitude less than those of the ^{9}Be(n,2n) cross-section inside the Be layer. Figs. V.36 and V.37 show the relative sensitivity profiles for T_7 for variations (by 1%) in the ^{9}Be(n,2n) and ^{9}Be(n,elastic) cross-sections, respectively. Variations in the ^{9}Be(n,2n) cross-section at any incident energy leads to negative coefficients, as shown in Fig. V.36.

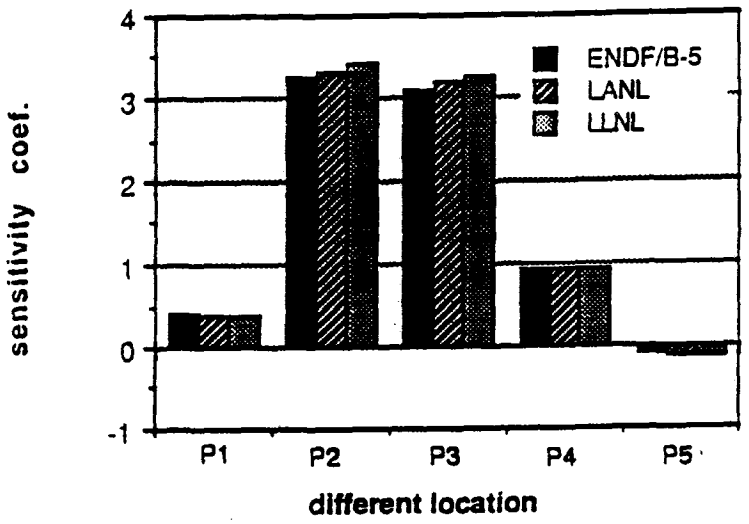

Fig. V.28: Integrated Sensitivity Coefficient for T_6 Due to a 1% Increase in the Total Cross-Section of Beryllium

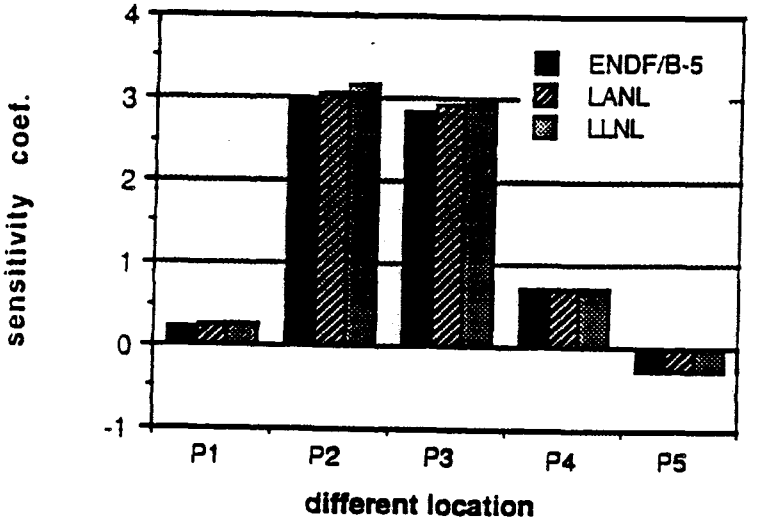

Fig. V.29: Integrated Sensitivity Coefficient for T_6 Due to a 1% Increase in the Elastic Cross-Section of Beryllium

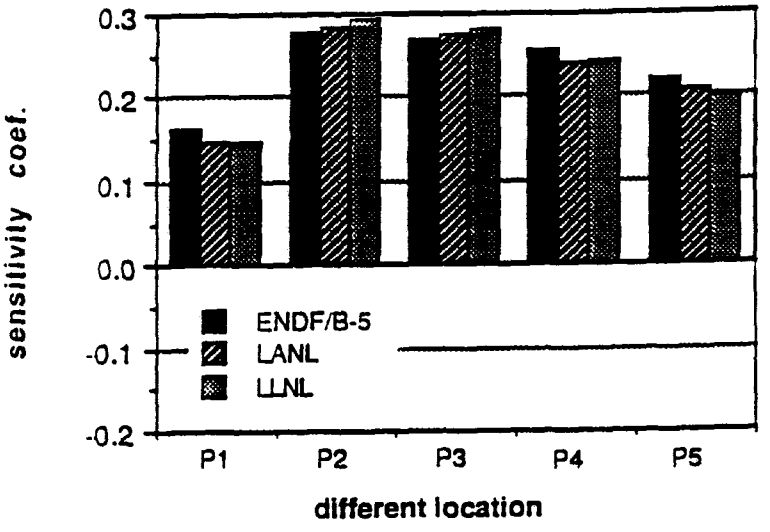

Fig. V.30: Integrated Sensitivity Coefficient for T_6 Due to a 1% Increase in the Total $^{9}Be(n,2n)$ Cross-Section

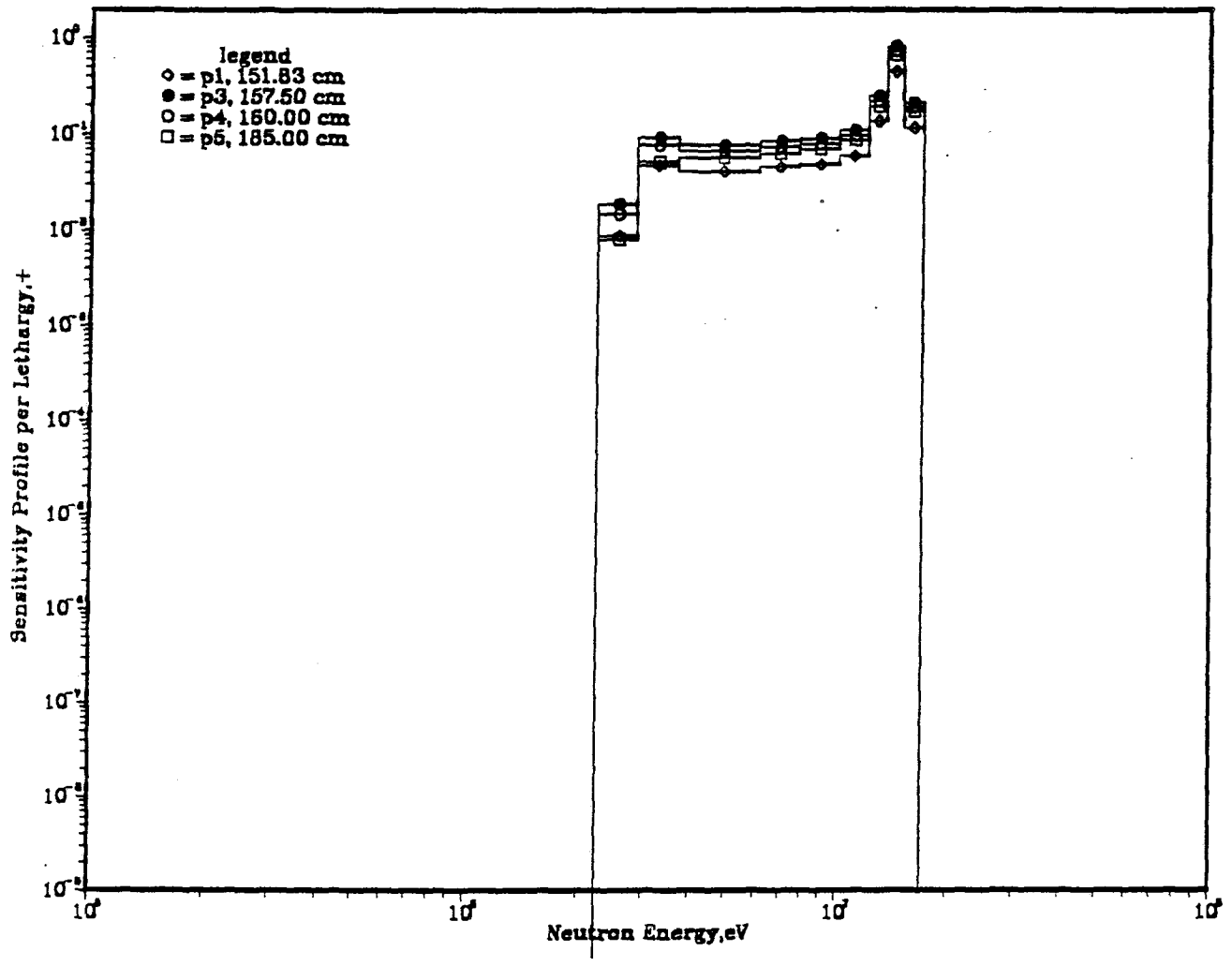

Fig. V.31: Relative Sensitivity Profile of T_6 at Various Locations Due to a 1% Increase in the Total $^{9}Be(n,2n)$ Cross-Section (LANL Evaluation)

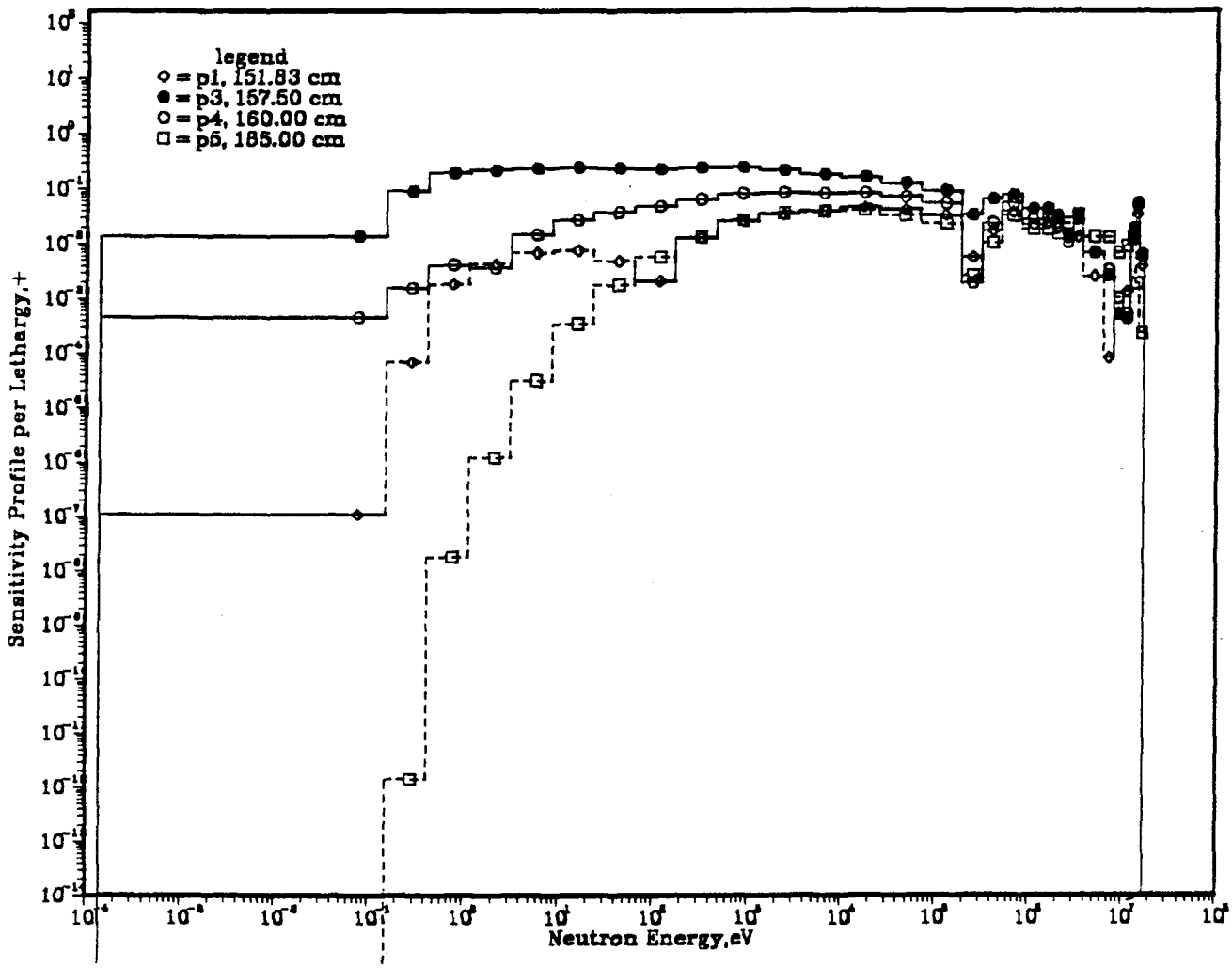

Fig. V.32: Relative Sensitivity Profile of T_6 at Various Locations Due to a 1% Increase in the ^{9}Be(n,elastic) Cross-Section (LANL Evaluation)

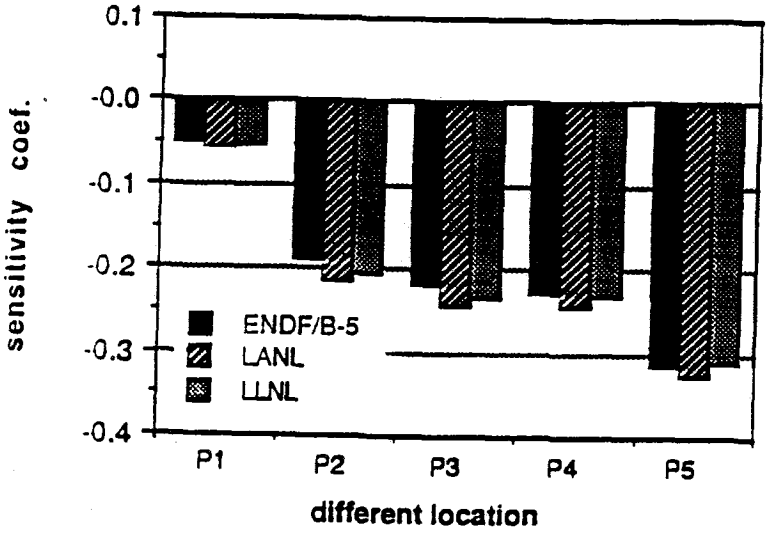

Fig. V.33: Integrated Sensitivity Coefficient for T_7 Due to a 1% Increase in the Total Cross-Section of Beryllium

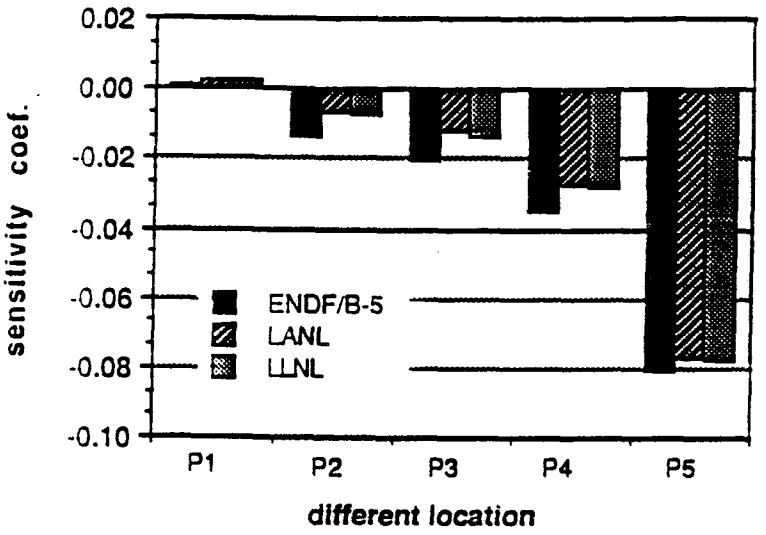

Fig. V.34: Integrated Sensitivity Coefficient for T_7 Due to a 1% Increase in the Elastic Cross-Section of Beryllium

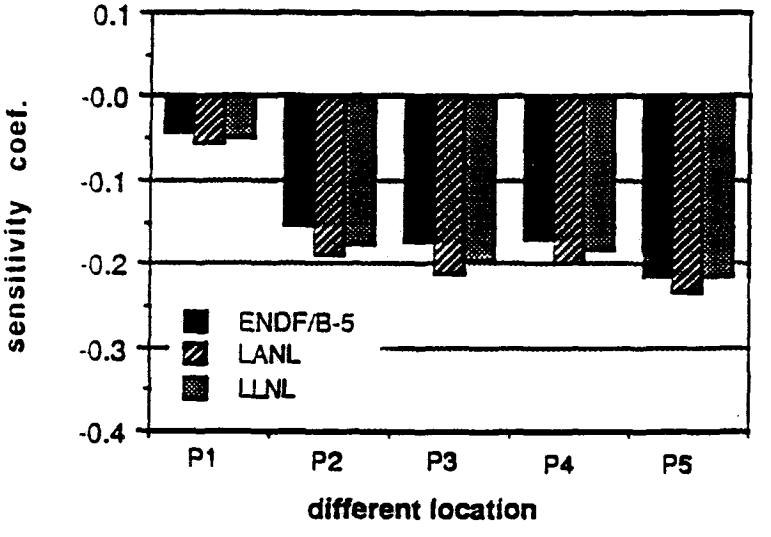

Fig. V.35: Integrated Sensitivity Coefficient for T_7 Due to a 1% Increase in the Total $^{9}Be(n,2n)$ Cross-Section

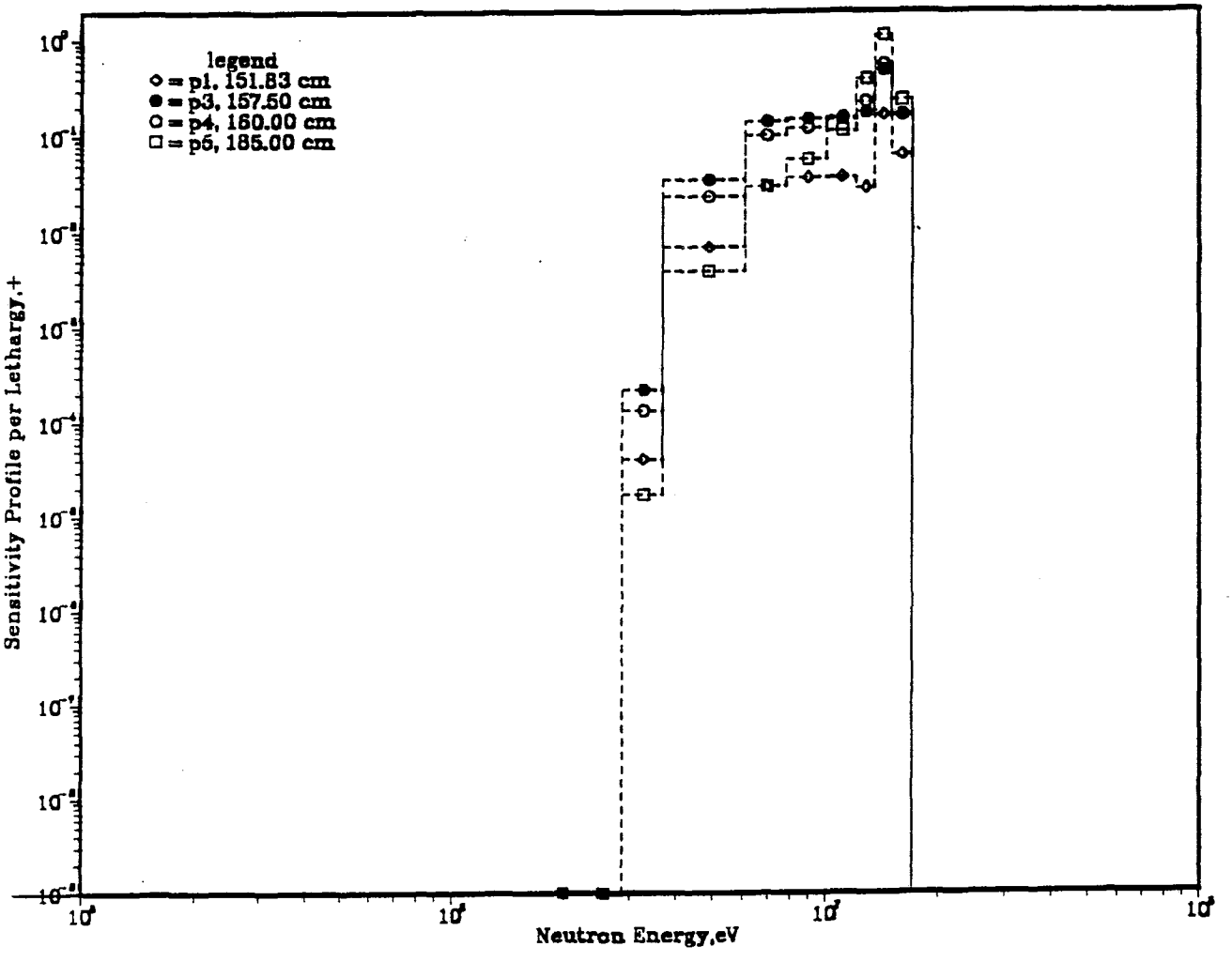

Fig. V.36: Relative Sensitivity Profile for T_7 at Various Locations Due to a 1% Increase in the $^9Be(n,2n)$ Cross-Section (LANL Evaluation)

V.8 General Remarks

The above results regarding the impact of variations in the cross-section of beryllium and in the SED and SAD of the ^{9}Be(n,2n) cross-section on tritium production rate indicate that T_6 is most sensitive to the ^{9}Be(n,elastic) cross-section while T_7 is most sensitive to the ^{9}Be(n,2n) cross-section. The positive sensitivity coefficients inside and just behind the Be layer in the former case are ~ 3% and 0.5%, respectively, while T_7 has negative coefficients for variations in the ^{9}Be(n,2n) cross-sections that are about - 0.2% inside and just behind the Be layer. These coefficients are much larger than those corresponding to variations in SED/SAD of the ^{9}Be(n,2n) cross-section. The T_6 sensitivity coefficients inside and around the Be layer in the case of level-independent treatment and in the direct variation treatment for the SED variations are ~ 0.01% and ~ 0.15%, respectively, while the corresponding T_7 coefficients are -0.06% and +0.07%, respectively. The direct variation treatment generally gives larger coefficients than those obtained by the level-independent (or dependent) treatment but, nevertheless, the SED sensitivity coeffieients are much less than those obtained with variations in the ^{9}Be(n,elastic) and ^{9}Be(n,2n) cross-sections. The coefficients are even smaller in the case of variations in the SAD. This does not mean that the uncertainties in T_6 and T_7 will be smaller in the case of SED/SAD than those for the smooth cross-sections. Direct comparison between the secondary emission spectrum of ENDF/B-V, LANL, and ENDF/B-VI data for Be indicates that the transfer cross-section $s_{gg'}$(n,2n) differes among these evaluations by more than an order magnitude in some exit energy ranges (particularly in the low-energy tail of the secondary spectrum). Therefore, upon performing a complete uncertainty analysis that takes into account these large uncertainties in the SED, one can expect large uncertainties in $T_6$and T_7 that is attributed to the uncertainty in the SED of the ^{9}Be(n,2n) cross-section. The on-going activities on completing this uncertainty analysis [this work will be published shortly[58]] indicate that the uncertainty in $T_6$and T_7 that is attributed to the uncertainty in the SED of the ^{9}Be(n,2n) cross-section could be as large as 10 - 11% and 3 - 5%, respectively, inside and just behind the Be layer. These uncertainties are comparable to those due to the uncertainties in the smooth integrated cross-sections ^{9}Be(n,elastic) and ^{9}Be(n,2n). For example, the uncertainties in T_6 inside and just behind the Be layer that is caused by the uncertainties in the ^{9}Be(n,elastic) cross-sections are 9% and 2%, respectively, but those due to the uncertainties in the ^{9}Be(n,2n) cross-section are 2% and 1.5%, respectively. Therefore, a complete uncertainty analysis should account for the contribution from the uncertainties in the SED/SAD even if their sensitivity coefficients are small. Thus, the methodology

adopted here could be useful in perfoming a comprehensive sensitivity/uncertainty analysis that includes variations in the SED/SAD of reactions that involves several inelastic levels.

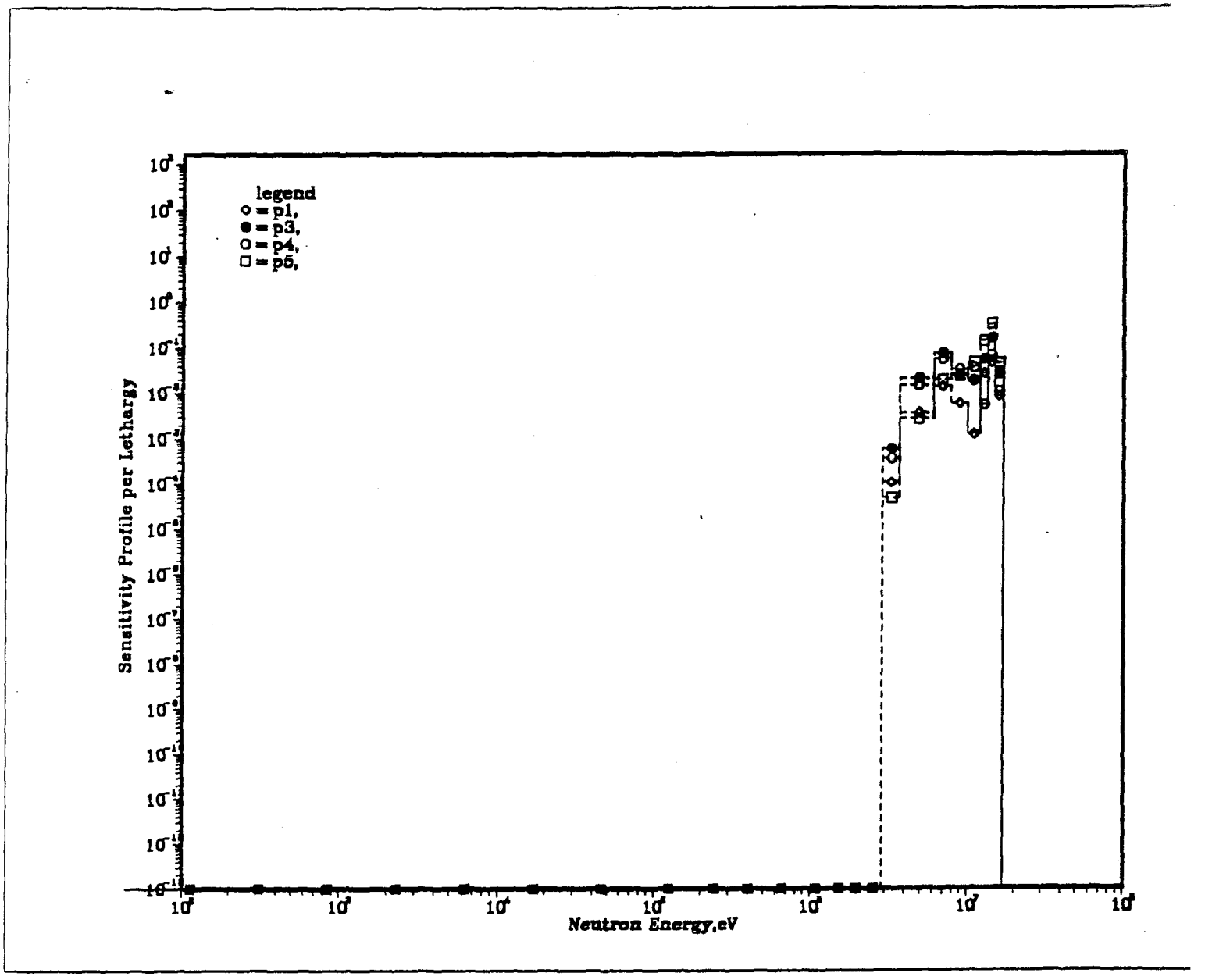

Fig. V.37: Relative Sensitivity Profile for T7 at Various Locations Due to a 1% Increase in the ^{9}Be(n,elastic) Cross-Section (LANL Evaluation)

VI. Reaction Rates of Activation Foils

Reaction rates of activation foils were measured in the reference (REF) and the Be-Sandwiched (BES) system of Phase IIA and in the Be-front system (W/FW, BEFWFW) of Phase IIB. The reaction rates chosen have different threshold energies and, therefor, the prediction accuracy of these reactions could be used to infer the accuracy in predicting the integrated spectrum as well as tritium production rates. In particular, reactions that have threshold energy similar to the $^{7}Li(n,n'\alpha)t$ reaction [e.g. $^{58}Ni(n,p)^{58}Co$] could infer the accuracy of predicting T_7. Also, among the reaction rates chosen is the $^{197}Au(n,\gamma)$ since this reaction has no threshold and can thus infer the accuracy in predicting T_6. Note, however, that this is true provided the cross-sections for these reactions are known to a high precision. As discussed below, the C/E values for some of these reactions indicate that some cross-section [e.g. $^{58}Ni(n,2n)$] needs further improvement. The reactions considered are listed below, along with their approximate threshold energies. Also, Fig. VI.1 shows the cross-sections for the several activations considered as function of incident neutron energy. This figure is taken from Ref (4).

$^{58}Ni(n,2n)^{57}Ni$	($\sim$12.5MeV)
$^{197}Au(n,2n)^{196}Au$	($\sim$ 7.5 MeV)
$^{93}Nb(n,2n)^{92m}Nb$	($\sim$8 MeV)
$^{27}Al(n,\alpha)^{24}Na$	($\sim$6 MeV)
$^{58}Ni(n,p)^{58}Co$	($\sim$2 MeV)
$^{115}In(n,n')^{115m}In$	($\sim$1 MeV)
$^{197}Au(n,\gamma)^{198}Au$	(0 Mev)

VI.1 Phase IIA

The C/E values for the $^{58}Ni(n,2n)$ reaction along the central axis are shown in Figs. VI.2 and VI.3 for the REF and BES system, respectively. At front locations, the C/E values are lower than unity by $\sim$ 20%, as predicted by both the MCNP and DOT calculations. As it was shown in Figs. III.7 and III.8, the C/E values at the front surface of the assembly were also underpredicted by $\sim$18 - 20%. It was pointed out in Section III that the $^{58}Ni(n,2n)$ cross-section, as currently implemented in ENDF/B-V, is underestimated by $\sim$15 - 20%, and this underestimation is reflected on the C/E values at the front locations shown in Figs. VI.2 and VI.3. The threshold of this reaction is high ($\sim$ 12.5MeV) and as was shown in Fig. III.15 in Section III, the 14 MeV peak of the incident

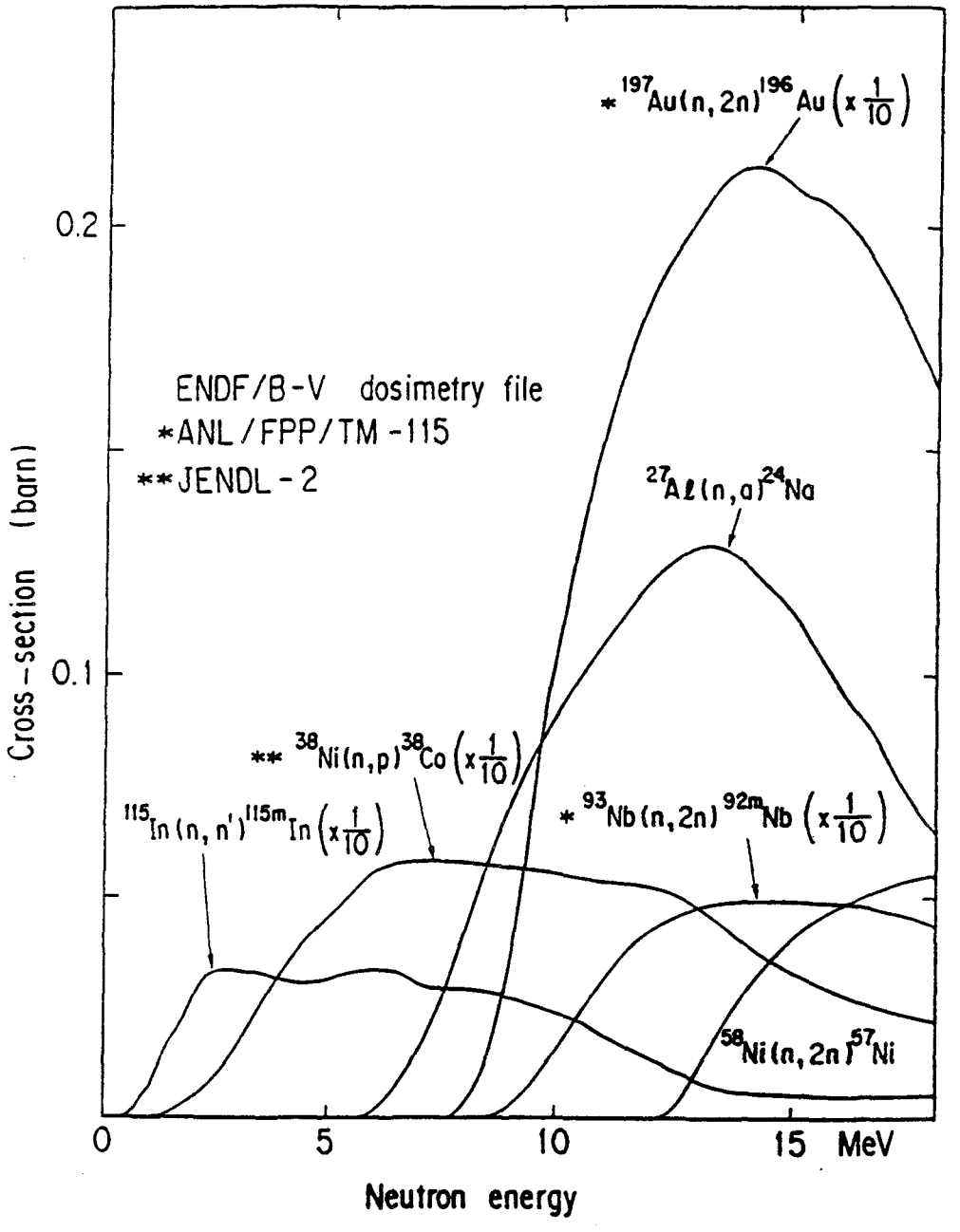

Fig. VI.1: Cross-Section for Activation Foils Used in Reaction Rates Measurements [From Ref (4)]

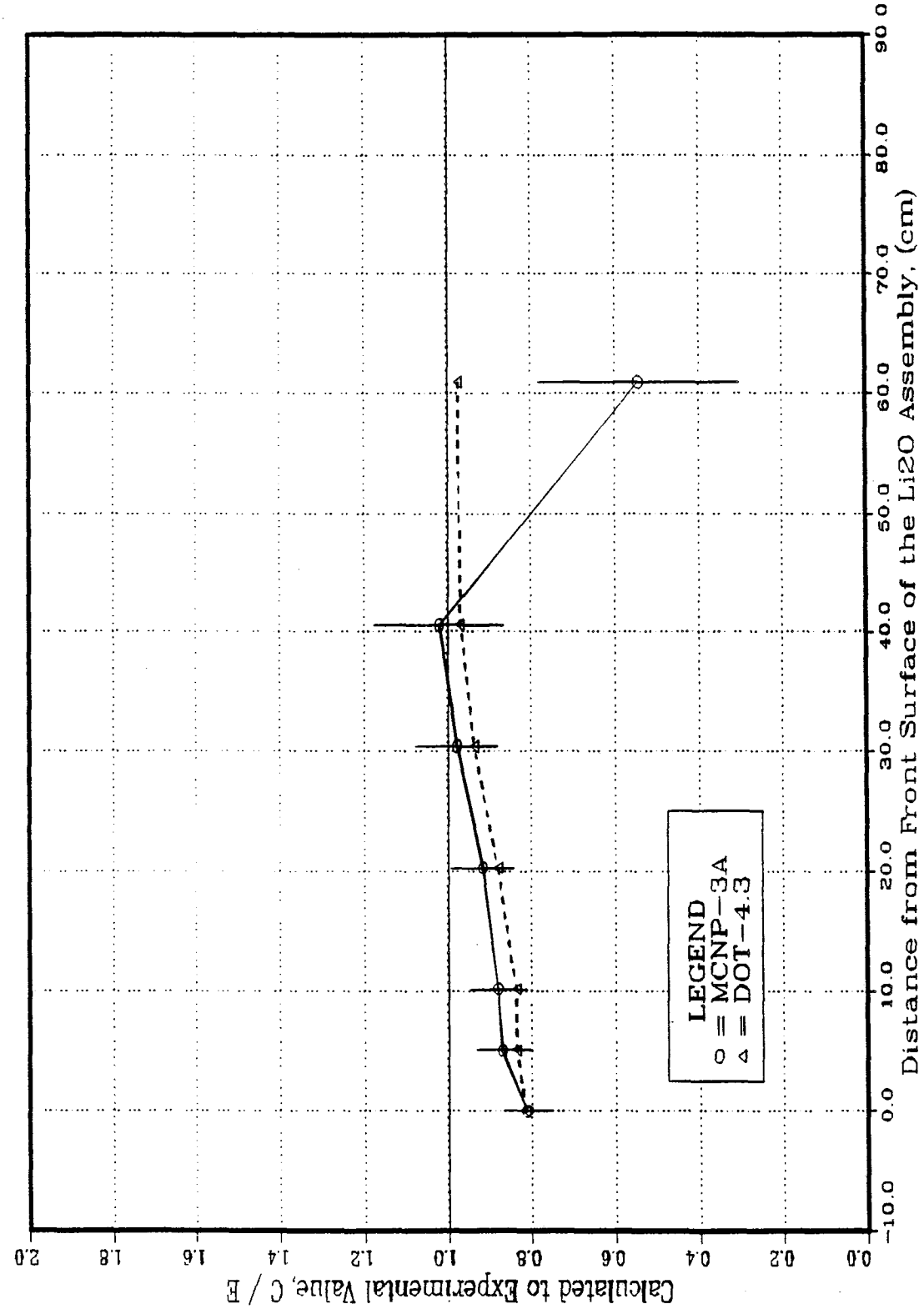

Fig. VI.2: C/E Values for the $Ni^{58}(n,2n)Ni^{57}$ Reaction In the Central Drawer (REF System of Phase IIA)

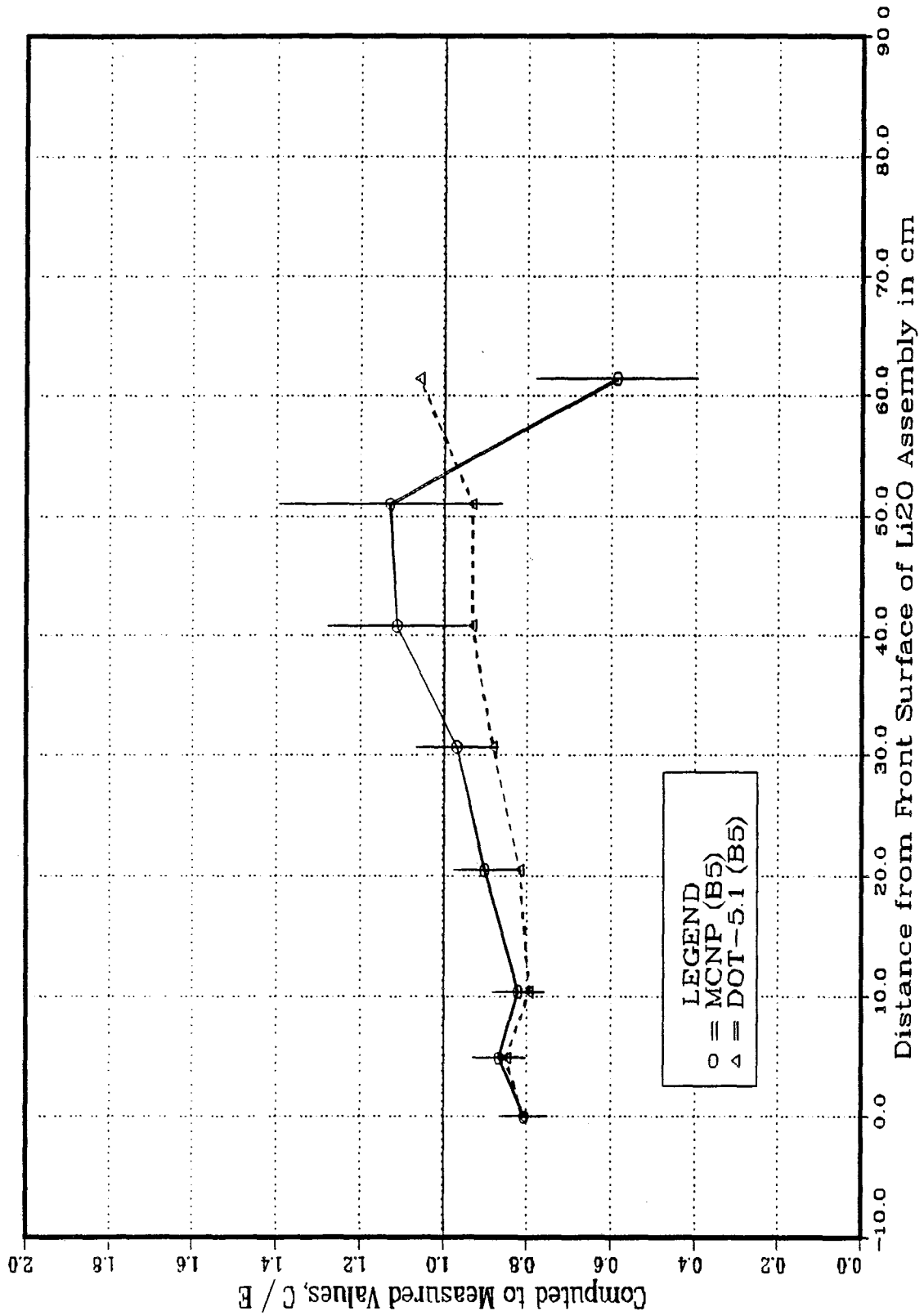

Fig. VI.3: C/E Values for the $Ni^{58}(n,2n)Ni^{57}$ Reaction in the Central Drawer (BES System - Phase IIA)

spectrum in the forward direction is also underestimated. This could add to the underestimation observed for the $^{58}Ni(n,2n)$ reactions at the front locations. Notice from Figs. VI.2 and VI.3 that the C/E values tend to increase as one proceeds towards the back locations and this feature is the same as obtained by the Monte Carlo and the discrete ordinates methods. The integrated spectrum above 10 MeV obtained by the MCNP calculations in the BES system is lower than the measured value at the front locations, but it tends to be larger at back locations (see Section VII, Fig. VII.16). This could explain the increasing trend in the C/E curves of the $^{58}Ni(n,2n)$ at the back locations. However, the integrated spectrum above 10 MeV, as predicted by the DOT code, has no such space-dependence, as shown in Fig. VII.16.

The C/E values for $^{93}Nb(n,2n)^{92m}Nb$ reaction along the central axis of the assembly are shown in Fig. VI.4 for the REF system. The cross-section for this reaction is the modified cross-section performed at LANL by the T-2 group, as was pointed out in Fig. III.9. As shown in Fig. VI.4, the C/E values are close to unity (C/E $\sim$ 1.02-1.1) throughout the entire assembly except at the location at Z = 60 cm where the value falls sharply below unity (C/E $\sim$ 0.5) which could be due to an error in the experimental value at this location.

The C/E curves for the $^{197}Au(n,2n)^{196}Au$ reaction is shown in Fig. VI.5 for the reference system. This reaction has a threshold energy of $\sim$7.5 MeV. The C/E values obtained by the DOT calculations are larger than unity by $\sim$ 2-12% but the Monte Carlo calculations give values that are lower than unity (by $\sim$ 5%) at the front locations and then fluctuate thereafter. Note that the shape of the curves obtained by the MCNP and DOT calculations is similar (but values are lower by 5-10% in the MCNP calculations) and that the C/E values at the location Z = 40 cm is much lower than unity (C/E $\sim$ 0.75).

As for the $^{27}Al(n,\alpha)$ reaction, (Eth $\sim$ 6 MeV), the C/E curves are shown in Figs. VI.6 and VI.7 for the REF and the BES system, respectively. In the REF system, the C/E values obtained by DOT calculations are steady throughout the assembly and are $\sim$ 1.08. The values fall below unity behind the Be layer in the BES system (C/E $\sim$ 0.95). The Monte Carlo calculations give, on the average, lower C/E values in the REF system (C/E $\sim$ 1 - 0.9) but larger values at the back locations (C/E $\sim$ 1- 1.2) in the BES system. Note, however, that the statistical error in the MCNP calculations are large at these locations ($\sim\pm$ 20 %). The difference between the C/E values obtained by DOT and by MCNP calculations

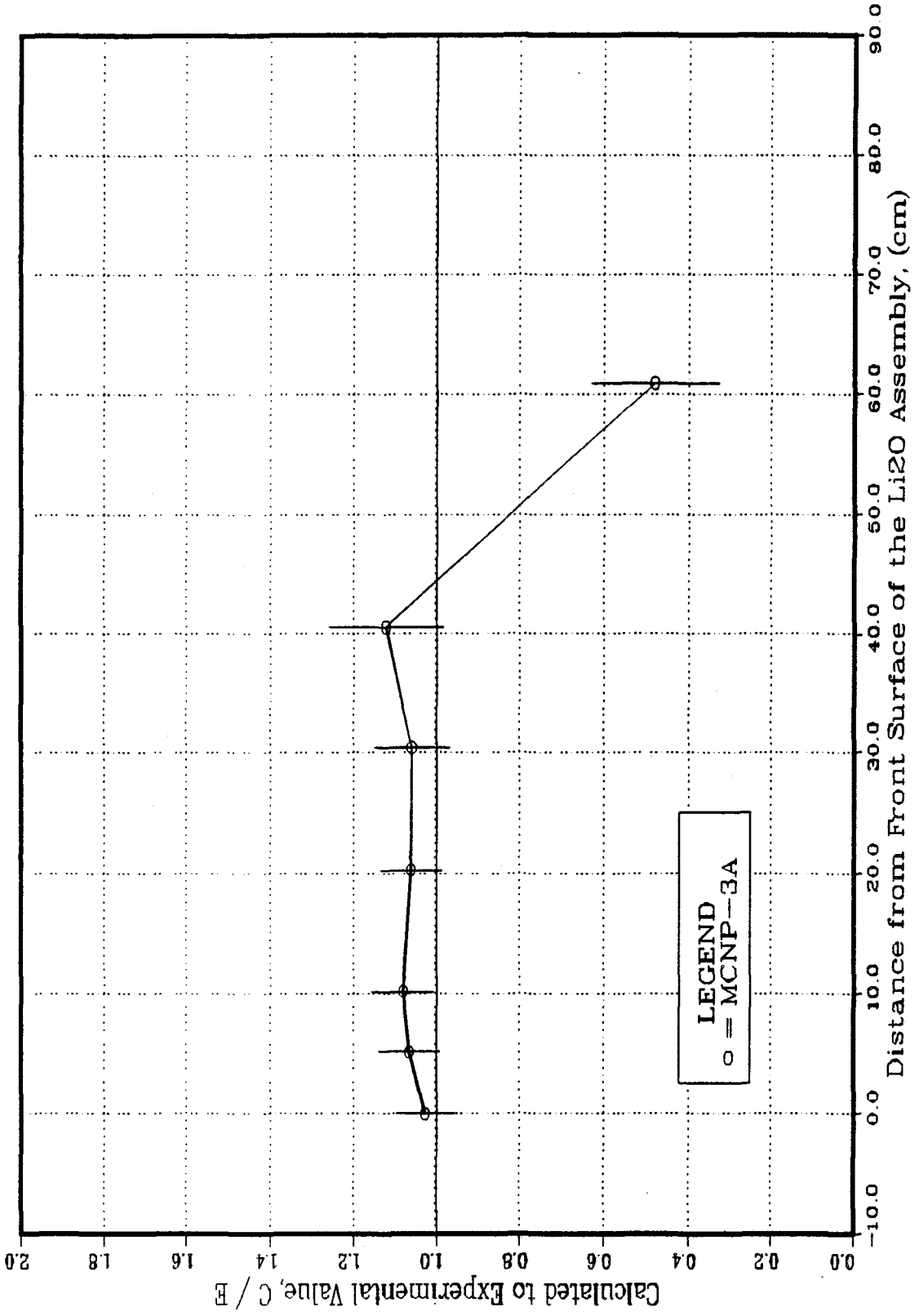

Fig. VI.4: C/E Values for the $Nb^{93}(n,2n)Nb^{92m}$ Reaction in the Central Drawer (REF System - Phase IIA)

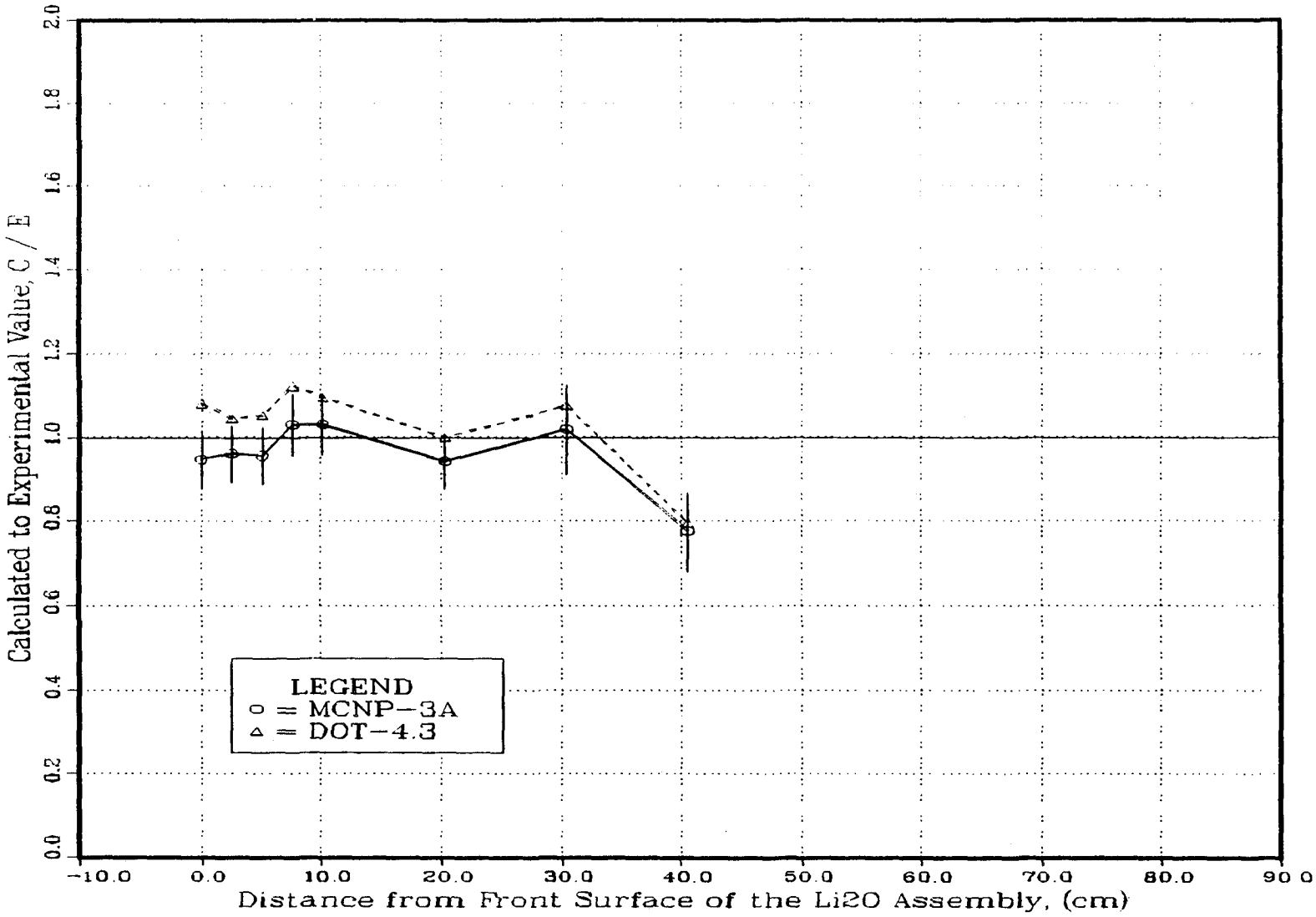

Fig. VI.5: C/E Values for the $Au^{197}(n,2n)Au^{196}$ Reaction in the Central Drawer (REF System - Phase IIA)

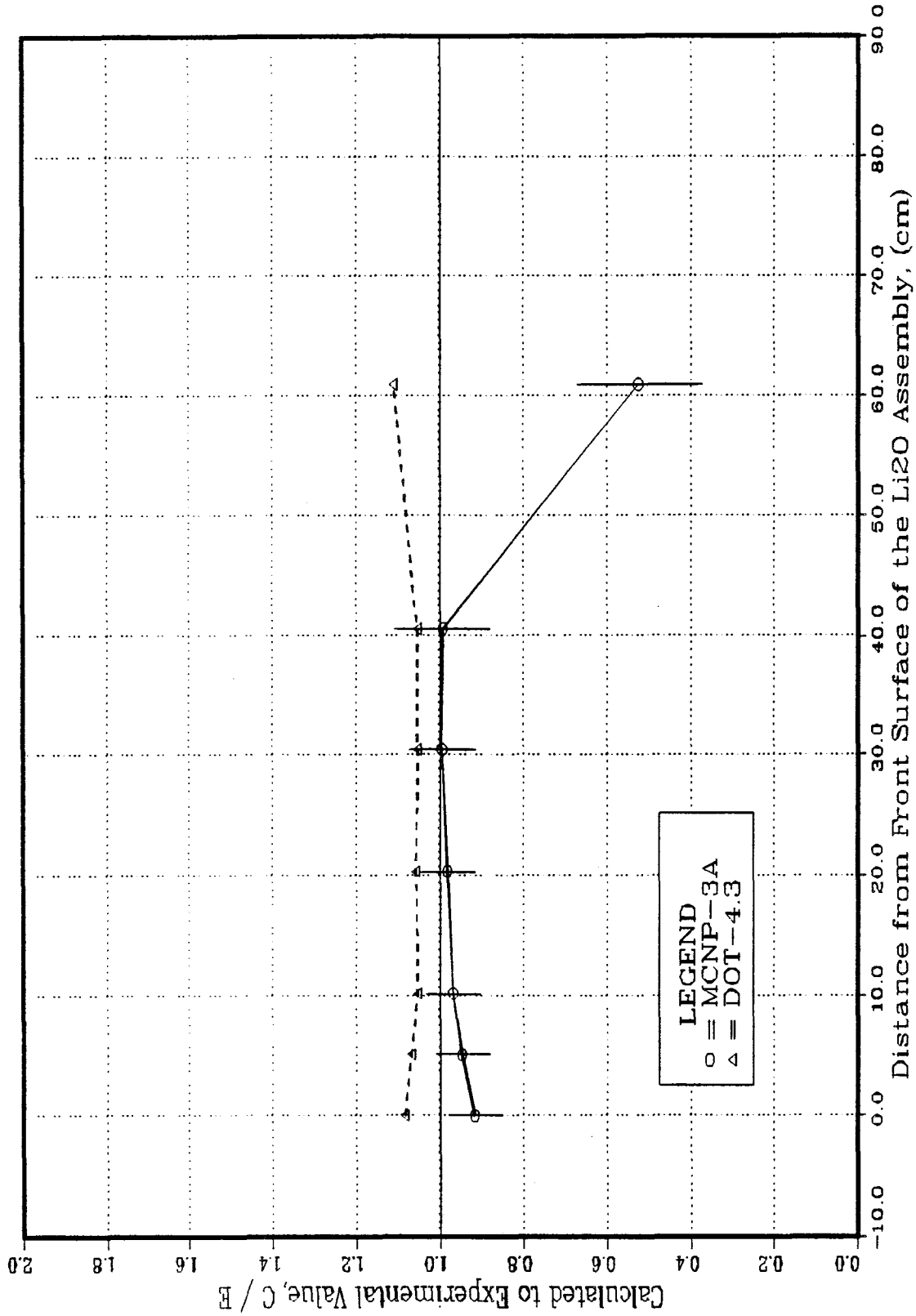

Fig. VI.6: C/E Values for the $Al^{27}(n,\alpha)Na^{24}$ Reaction in the Central Drawer (REF System - Phase IIA)

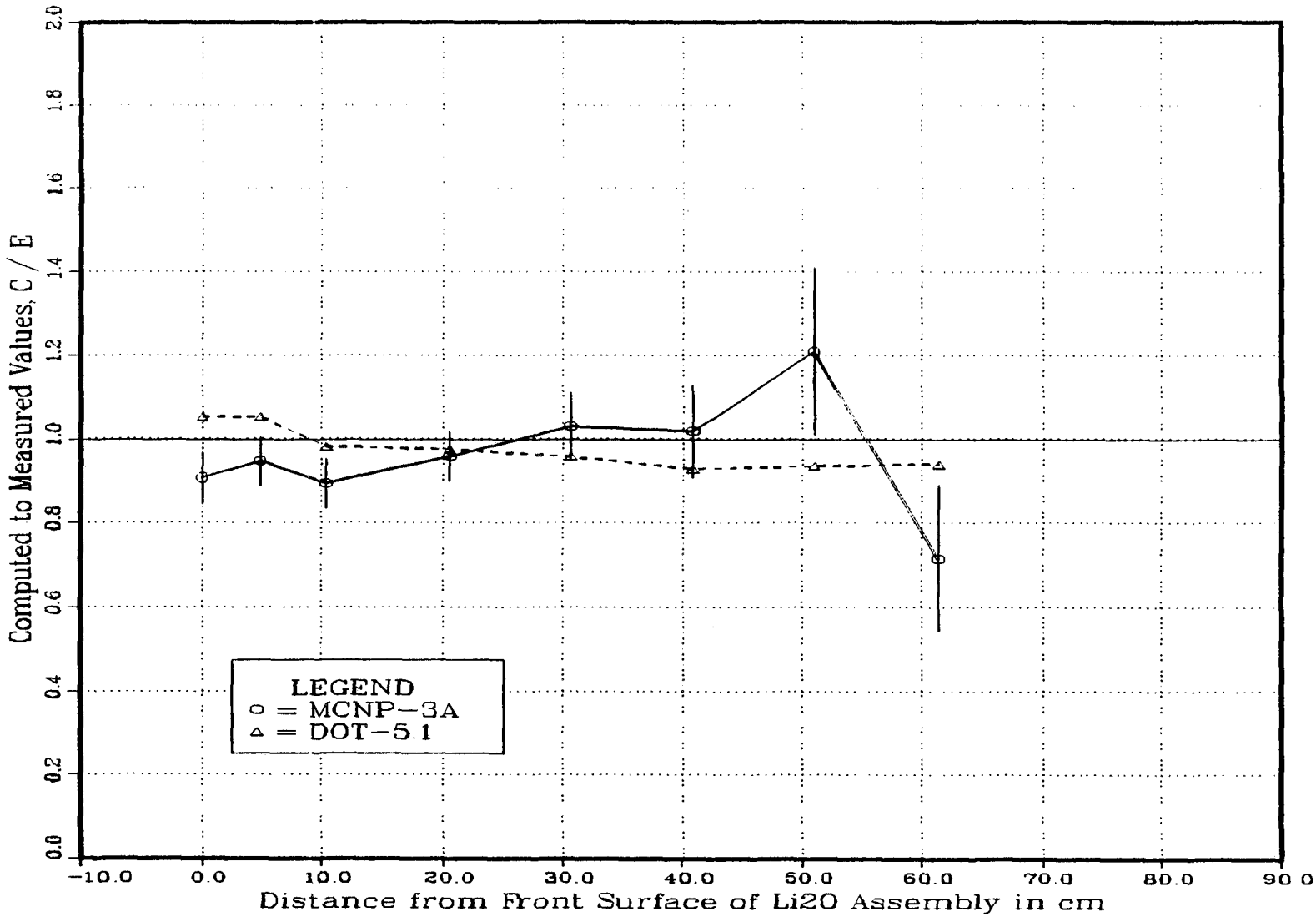

Fig. VI.7: C/E Values for the $Al^{27}(n,\alpha)Na^{24}$ Reaction in the Central Drawer
(BES System - Phase IIA)

is ~ 10 - 20% (except at the location Z = 62 cm). This difference is within the statistical error of the Monte Carlo calculations, particularly at the middle locations in the assembly.

The $^{58}Ni(n,p)^{58}Co$ reaction has a low threshold energy (~ 2 MeV) as shown in Fig. VI.1. The C/E values for this reaction in the REF and the BES systems are shown in Figs. VI.8 and VI.9, respectively. In both systems, the values obtained by the DOT calculations are always larger than unity throughout the assembly (C/E ~ 1.1 - 1.23), as is the case for the $^{27}Al(n,\alpha)^{24}Na$ reaction, while the MCNP calculations give lower C/E values in the REF system at all locations. Examining the C/E values for the integrated spectrum in the energy range 1.0 MeV<En<10 MeV (see section VII) indicates that the calculations, by both MCNP and DOT, give larger values (by about 20 - 40%) than the measurements performed by the NE213 detector in the BES system. Therefore, the overestimation of this reaction could be partly attributed to the overestimation in the integrated spectrum between 1 MeV and 10 MeV.

The C/E values for the $^{115}In(n,n')^{115m}In$ reaction, as calculated by the MCNP code, are shown in Figs. VI.10 and VI.11 for the REF and BES system, respectively. The values cluster around unity in both systems and the agreement with the measured values is very well, except at the back locations and inside the Li_2CO_3 layer, as shown in Fig. VI.10, where again the statistical errors are large.

The $^{197}Au(n,\gamma)^{198}Au$ reaction occurs at all energies and is sensitive to the low-energy component of the neutron spectrum. The C/E values for this reaction are shown in Figs. VI.12 and VI.13 for the REF and BES system, respectively. Note that the values obtained by the DOT calculations are lower than unity throughout the assembly in the REF system and behind the Be layer in the BES system. Since this reaction is sensitive to the low-energy component of the spectrum, the accuracy in specifying the epoxy content (rich in hydrogen) has direct impact on the prediction accuracy of this reaction. It was indicated in Section III on source characterization that the low-energy component of the incident spectrum is underestimated and that leads to lower C/E values for $^{197}Au(n,\gamma)$ reactions at the front suface, as shown in Figs. III.7 and III.8. Although the Monte Carlo calculations have large statistical errors, on the average, the C/E values are also lower than unity, as shown in Fig. VI.12 for the REF system. As is the case for T_6, the C/E values are large inside the Be layer in the BES system and sharply drop below unity just behind that layer. The shape of the C/E curve in this case is very similar to the corresponding curve for the T_6

and could thus be related to the observed underestimation in the emerged spectrum from the Be layer below 0.5 MeV, as was discussed in Section V.

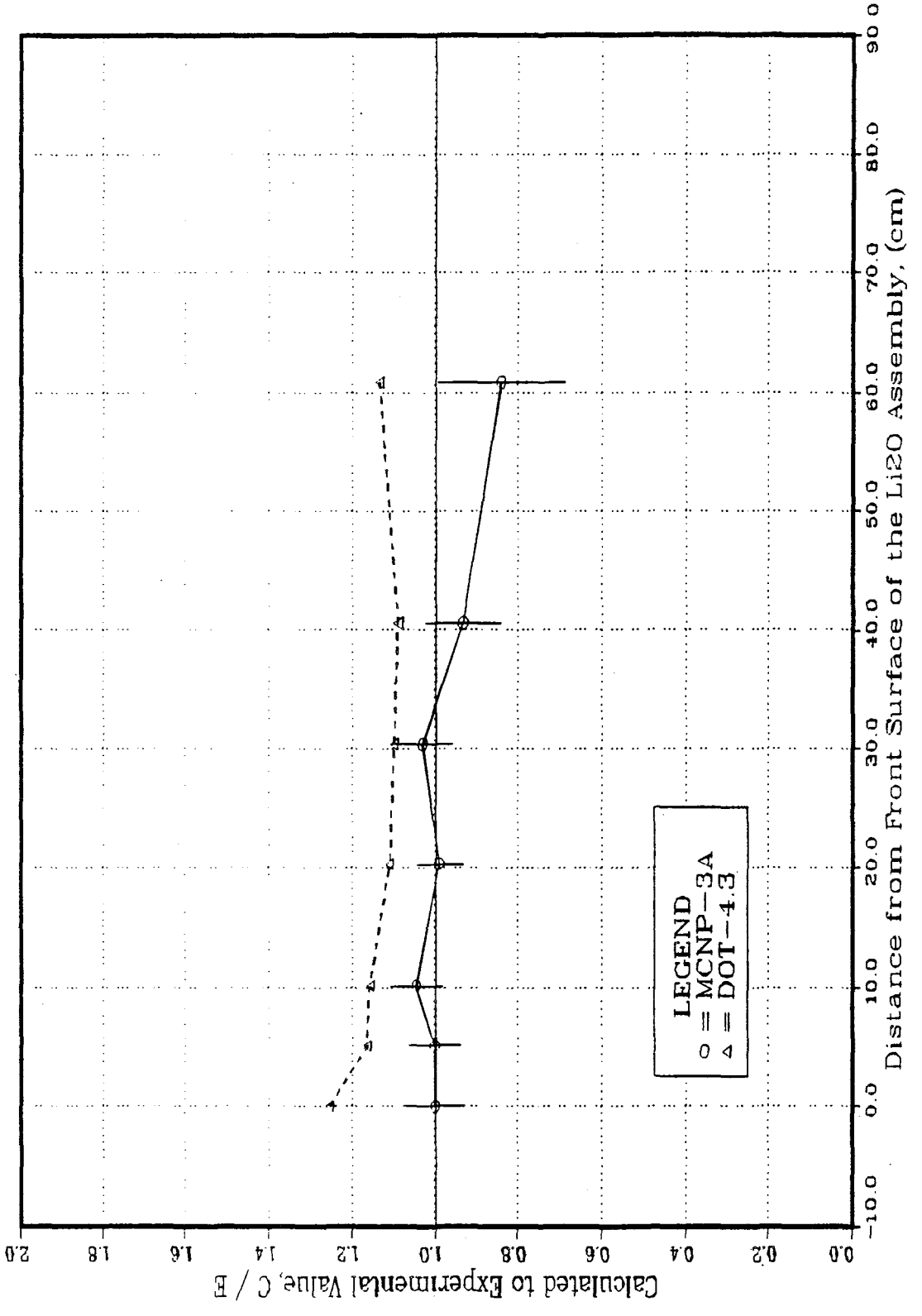

Fig. VI.8: C/E Values for the $Ni^{58}(n,p)Co^{58}$ Reaction in the Central Drawer (REF System - Phase IIA)

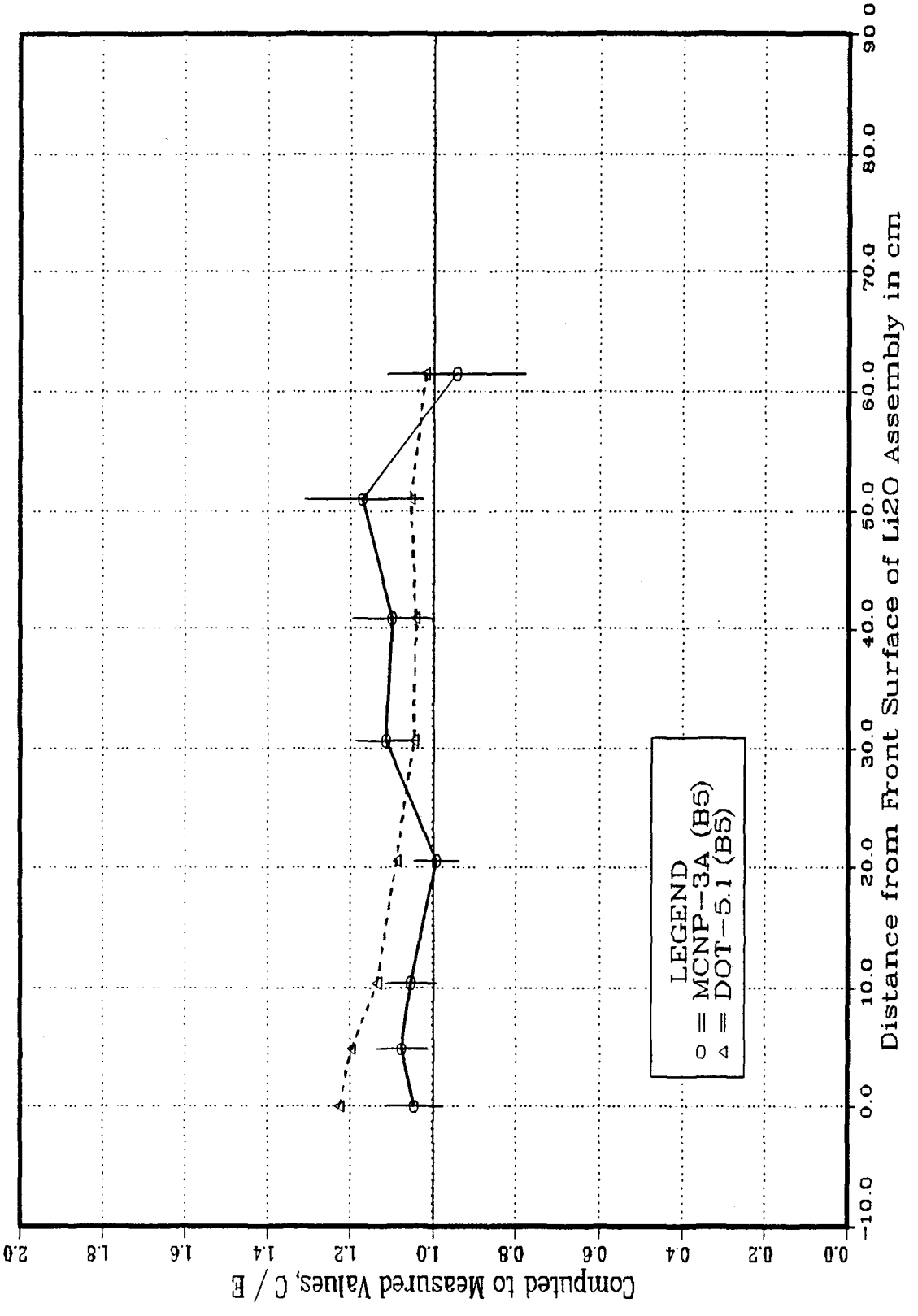

Fig. VI.9: C/E Values for the $Ni^{58}(n,p)Co^{58}$ Reaction in the Central Drawer (BES System - Phase IIA)

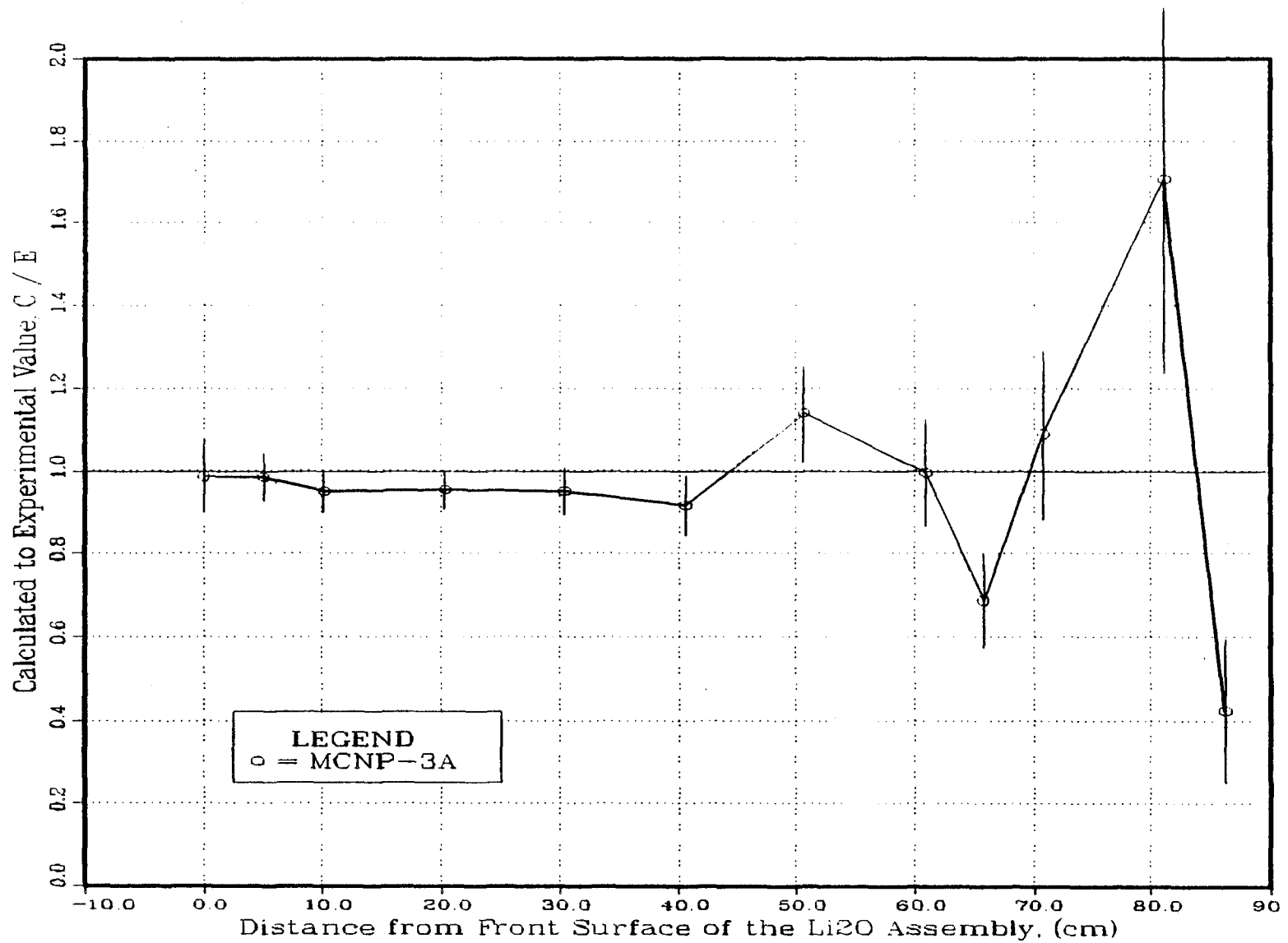

Fig. VI.10: C/E Values for the $In^{115}(n,n')In^{115m}$ Reaction in the Central Drawer (REF System - Phase IIA)

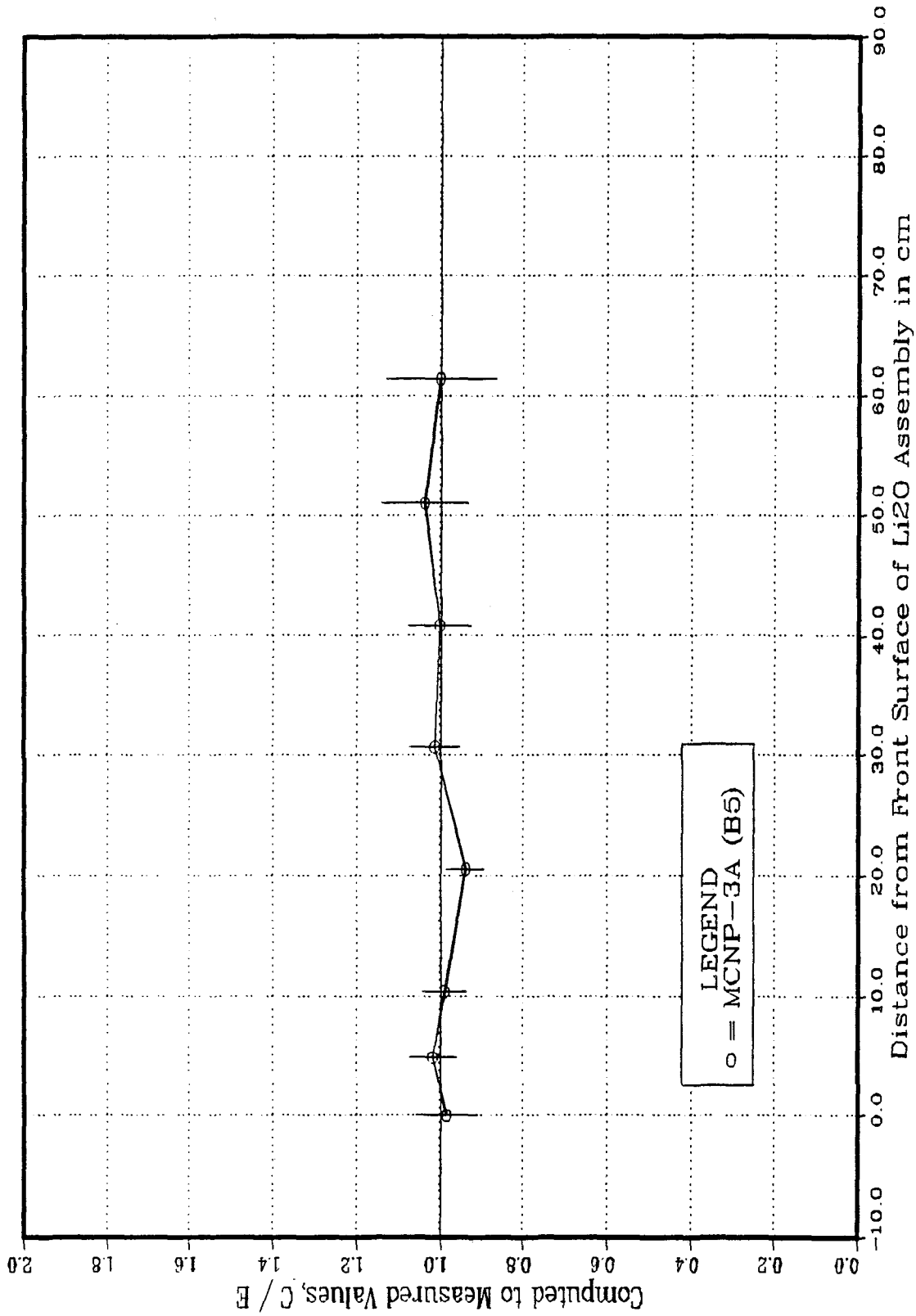

Fig. VI.11: C/E Values for the $In^{115}(n,n')In^{115m}$ Reaction in the Central Drawer (BES System - Phase IIA)

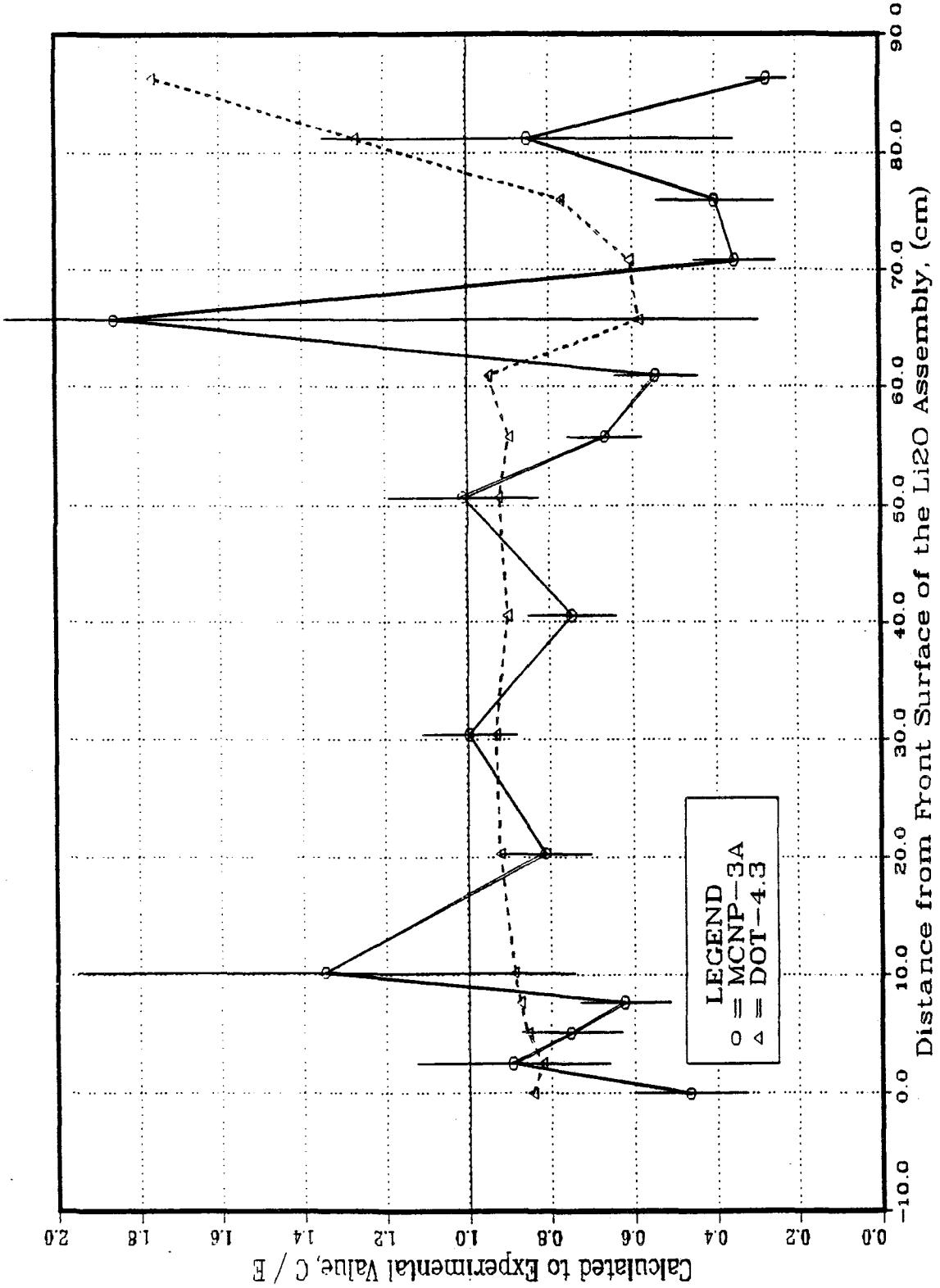

Fig. VI.12: C/E Values for the $Au^{197}(n,\gamma)Au^{198}$ Reaction in the Central Drawer (REF System - Phase IIA)

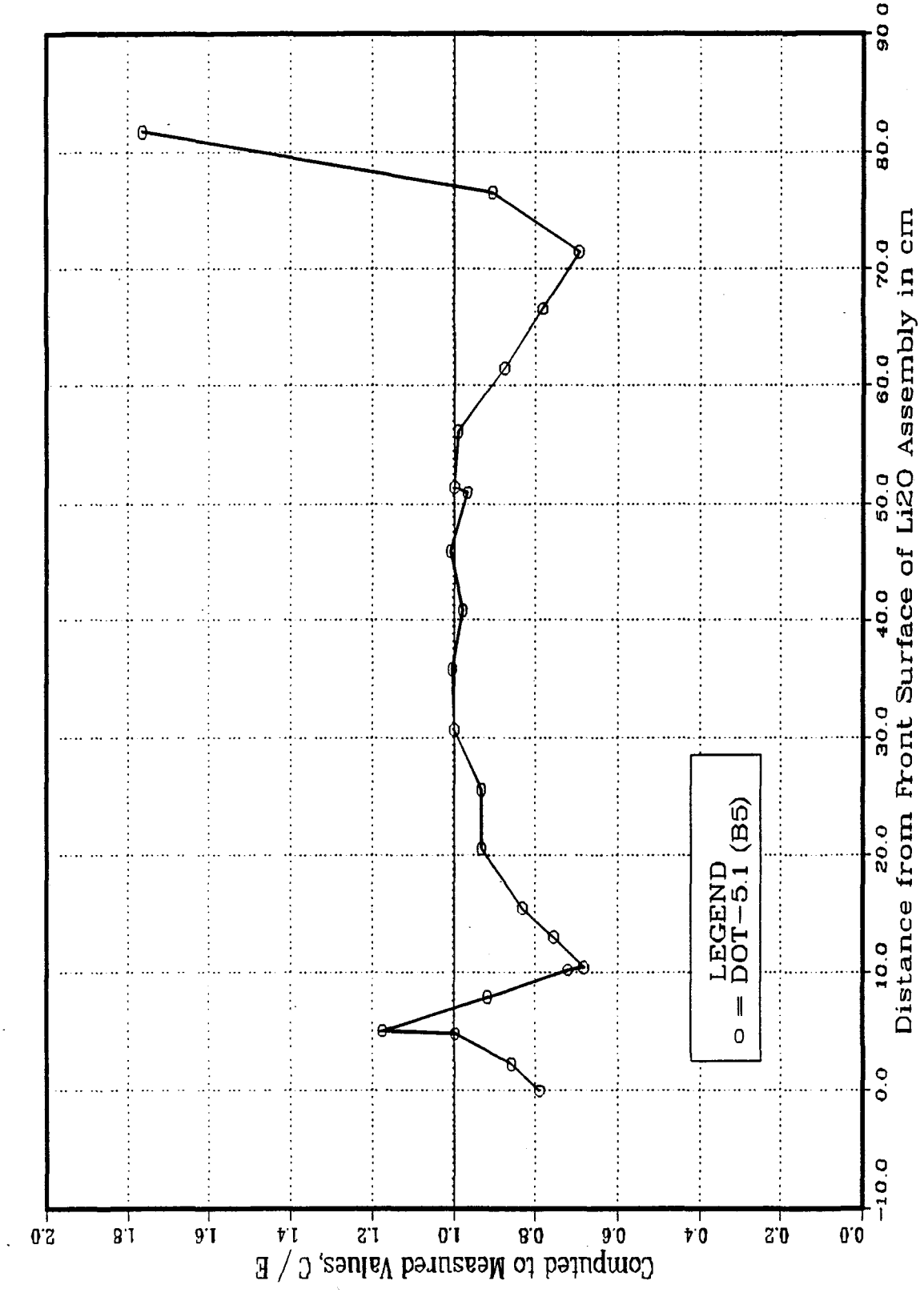

Fig. VI.13: C/E Values for the $Au^{197}(n,\gamma)Au^{198}$ Reaction in the Central Drawer (BES System - Phase IIA)

VI.2 Phase IIB

In addition to the reaction rates discussed above, the Ti(n,xp)Sc-46, Ti(n,xp)Sc-47 and Ti(n,xp)Sc-48 reactions were also measured in the Be-front system (W/FW, BEFWFW) of Phase IIB.

The C/E values for the ^{58}Ni(n,2n) reaction is shown in Feg. VI.14 where again, their values are less than unity throughout the entire assembly. In comparison to the values shown in Figs. VI.2 and VI.3, there is a decreasing trend in the C/E curve after the front Be layer and then the curve rises again with a dip at a distance around 15-20 cm from the front surface. Note from Figs. VI.2 and VI.3 that the C/E values are lower than unity by $\sim$ 2 – 20% up to a distance of $\sim$30 – 40 cm while the C/E values for this reaction are lower by 25% (DOT) and by 23% (MCNP) behind the Be layer. As pointed out earlier, the cross-section for this reaction is underestimated by $\sim$ 15 - 20% in ENDF/B-V. In addition, the rather lower C/E values observed in Phase IIB (see Fig. VI.14) as compared to the results from Phase IIA could also be attributed to the underestimation in the emerged neutron spectrum above 10 MeV behind the front Be layer, as was observed in Oyama and Maekawa's experiment [34] on Be-slab, which was discussed in Section V. The C/E curve for the ^{93}Nb(n,2n)^{92m}Nb reaction is shown in Fig. VI.15. This high-threshold reaction (E_{th} $\sim$ 8 MeV) is underestimated by $\sim$ 5 - 10% at all locations behind the front Be layer. This feature was not observed in Phase IIA where the C/E values were, on the average, larger than unity in the REF system (see Fig. VI.4). This could be attributed to the total ^{9}Be(n,2n) cross-section which is likely to be overestimated, as it is discussed in Section VIII. An overestimation in the ^{9}Be(n,2n) leads to less number of high energy neutrons that can reach the back locations and contributing to high-energy reactions, such as ^{58}Ni(n,2n) and ^{93}Nb(n,2n).

The C/E values for the ^{27}Al(n,α)^{24}Na reaction (E_{th} $\sim$ 6 MeV) is shown in Fig. VI.16. The values behind the Be layer are C/E $\sim$ 0.92 - 1.0 as predicted by both the MCNP and DOT codes. Notice from Fig. VI.16 that within the statistical errors, the values obtained by the Monte Carlo calculations give similar results to those obtained by the deterministic method. Also, and similar to the trend observed for the high-energy reactions, the C/E values tends to decrease by distance as one proceeds toward the back locations. This is not the case in Phase IIA as it was shown in Fig. VI.6 where the C/E values in this

case are more or less larger than unity, steady, and space-independent. Again, the lower C/E values for this threshold reaction indicate that the high-energy component of neutrons emerging from the front Be layer is underestimated, as pointed out above, and this could be related to the total $^{9}Be(n,2n)$ cross-section, which is overestimated. In addition, the sensitivity analysis discussed in Section V has indicated that T_7 is sensitive to variations in the $^{9}Be(n,2n)$ cross-section. Therefore, high energy reactions will decrease behind the Be layer if the $^{9}Be(n,2n)$ cross-section is overestimated. An overestimation in the high-energy (n,2n) collisions inside the Be liner/layer leads to lesser number of neutrons with high energies that can reach the back locations of the test assembly and this also leads to the slope observed in the C/E curves for the high-threshold reactions.

The C/E curves for the $^{58}Ni(n,p)^{58}Co$ reaction ($E_{th} \sim 2$ MeV) are shown in Fig. VI.17. When compared to the corresponding curves in Phase IIA shown in Fig. VI.8, the slope in these curves in Phase IIB discussed above is also observed , but to a lesser extent due to the low–threshold energy of this reaction.

The C/E values for the $^{115}In(n,n')$ ^{115m}In, Ti(n,xp)Sc-46, Ti(n,xp)Sc-47, and Ti(n,xp)Sc-48 are shown in Figs. VI.18 to VI.21, respectively. The prediction accuracy of the MCNP calculations for the $^{115}In(n,n')$ reaction is poor due to the large statistical errors involved as can be seen from Fig. VI.18. On the other hand, the DOT calculations show that the C/E values are larger than unity inside the Be layer but fall below unity with a descending trend behind that layer. The C/E values for Ti(n,xp)Sc-46 in the bulk of the Li_2O zone is $\sim$ 0.9, as predicted by the DOT code and is $\sim$ 0.8 as predicted by the MCNP code, as shown in Fig. VI.19. As for the Ti(n,xp)Sc-47 reaction, however, the C/E values are below unity at the front locations [C/E $\sim$ 0.9 (DOT), C/E $\sim$ 0.7 (MCNP)] and start to increase toward the back locations where they are closer to unity at depth Z $\sim$ 40 cm (see Fig. VI.20). There is a large deviation from the experimental values for the Ti(n,xp)Sc-48 reactions, as can be seen from Fig. VI.21.

As for the $^{197}Au(n,\gamma)^{198}Au$ reaction, (see Fig. VI.22) the C/E values are larger than unity inside the front Be layer but fall sharply below unity just behind that layer, as was the case for T_6. In the bulk of the Li_2O zone, the C/E values are lower than unity (C/E $\sim$ 0.9) in both the Monte Carlo and the discrete ordinates calculations. Note from Fig. VI.22 that the DOT results are within the statistical errors of the MCNP calculations. Improving the MCNP results for this low-energy reaction will require much longer computation which is limited by the computational resources.

One can say that the reaction rates were reasonably predicted in Phase IIA except for the $^{58}Ni(n,2n)$ reaction whose cross-section should be increased by 15 - 20% to improve its C/E curves. When compared to the results of Phase IIA, the C/E curves in Phase IIB exhibit a descending slope for high-energy reactions, such as $^{93}Nb(n,2n)^{92m}Nb$, and that their values fall below unity at the back locations. In addition, the C/E values for these reactions, as predicted by the DOT code are, on the average, larger than those obtained by the MCNP code, especially at the front locations. In the present study, the LANL data for beryllium was used. As it is discussed in Section VIII, noticeable improvement in the C/E curves was achieved when the ENDF/B-VI data for beryllium was used.

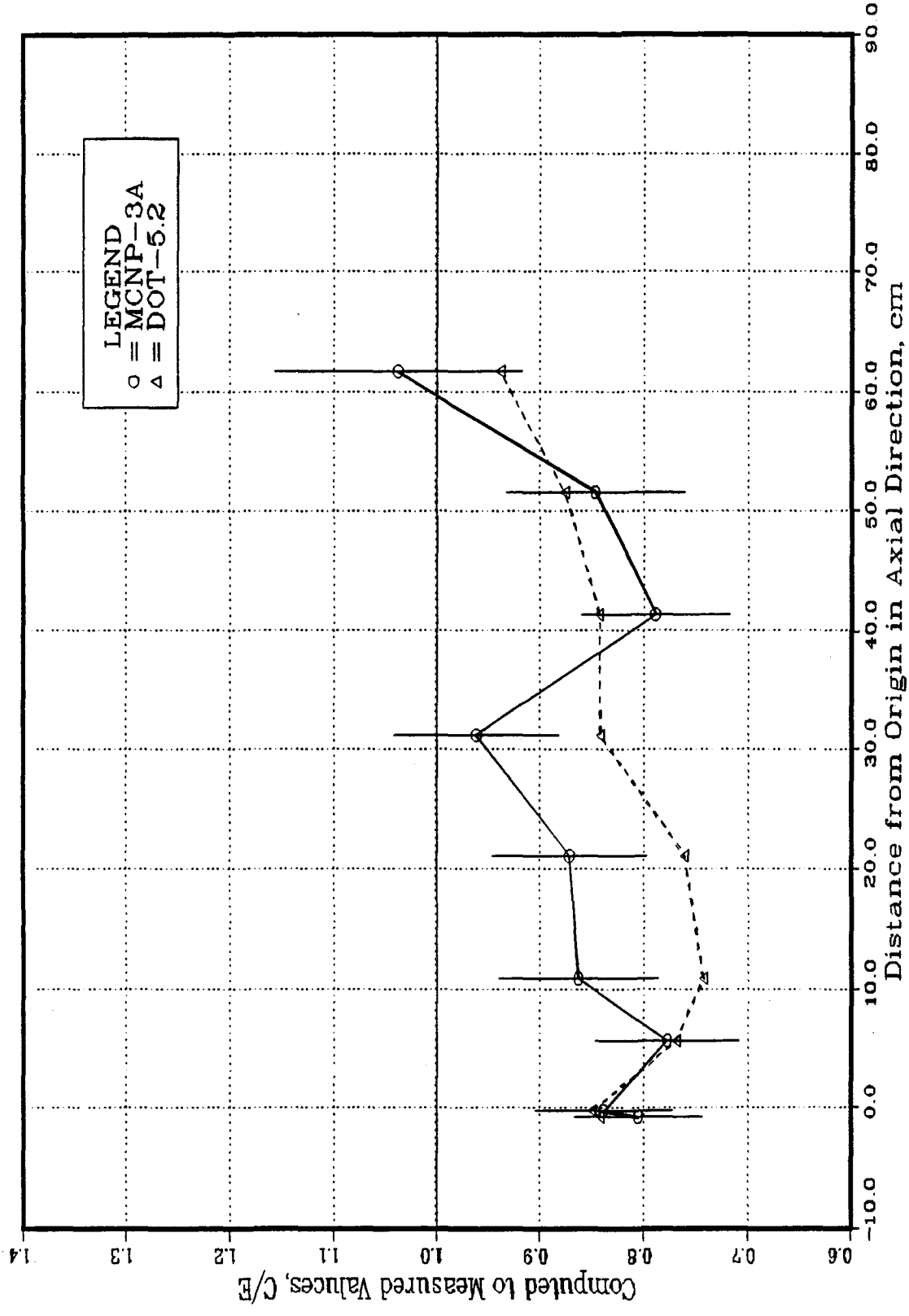

Fig. VI.14: Reaction Rates, $Ni^{58}(n,2n)Ni^{57}$, Measured by Foils in the Central Drawer (BEFWFW - Phase IIB)

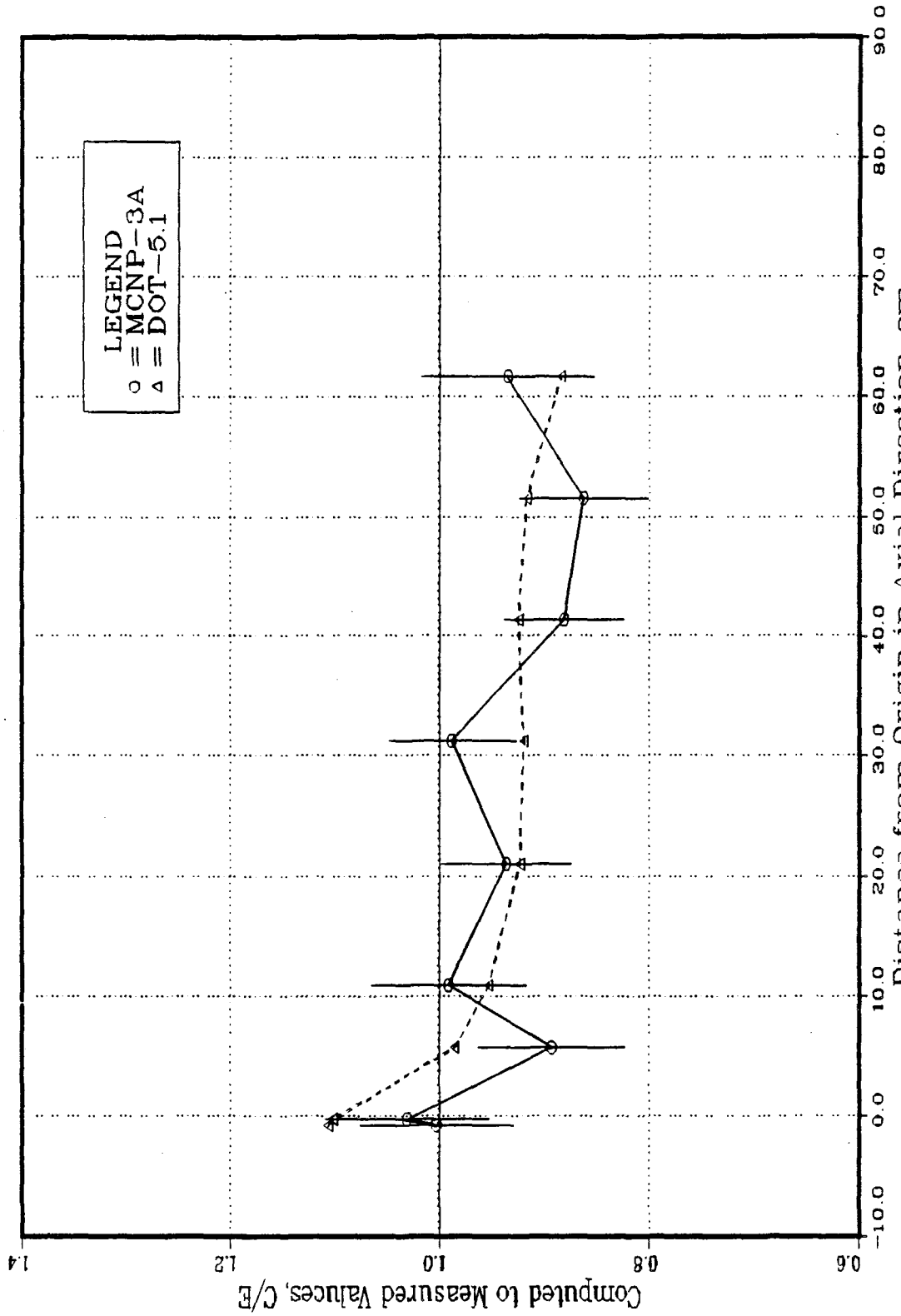

Fig. VI.15: C/E Values for the $Nb^{93}(n,2n)Nb^{92m}$ Reaction in the Central Drawer (BEFWFW System - Phase IIB)

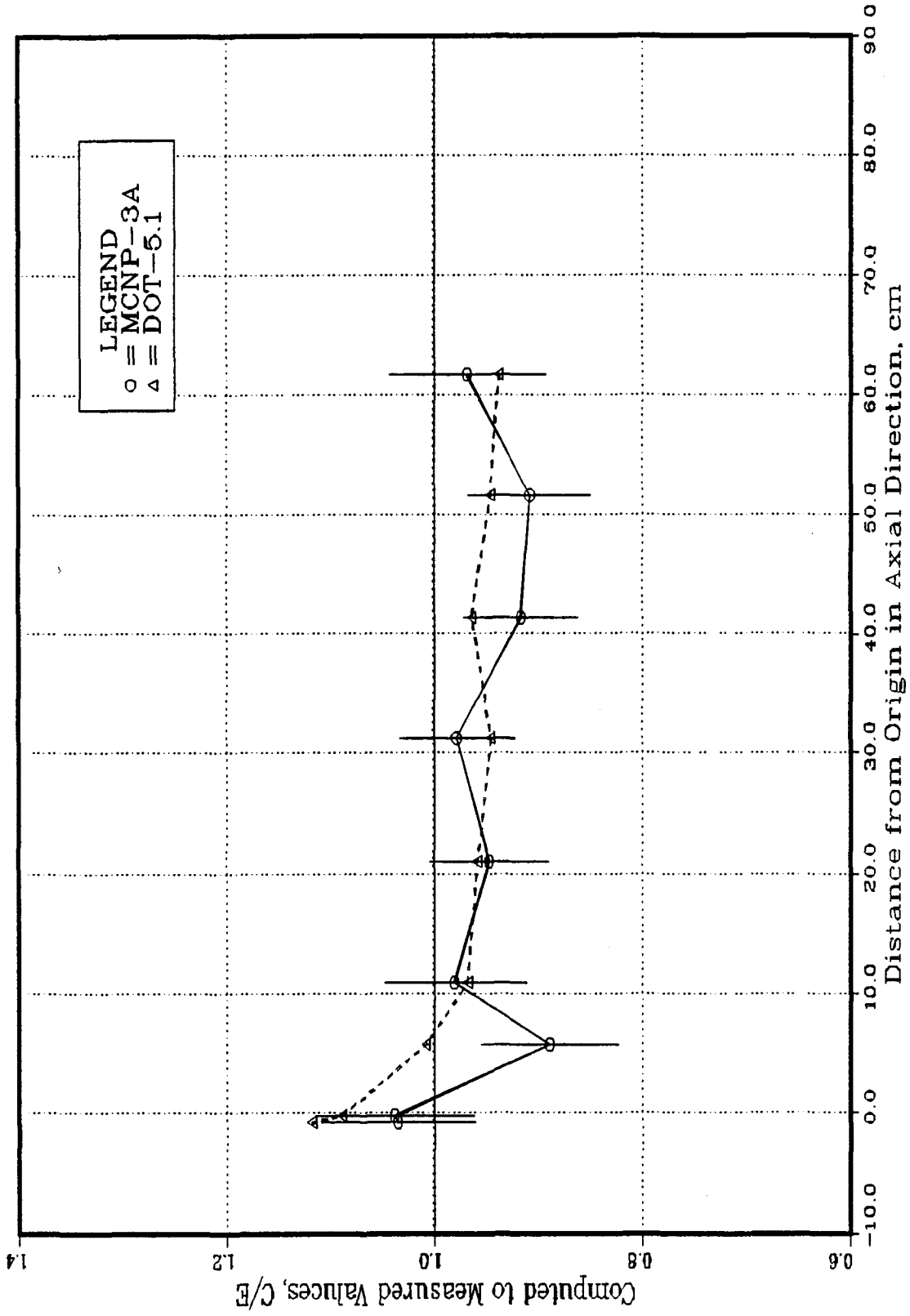

Fig. VI.16: C/E Values for the $Al^{27}(n,\alpha)Na^{24}$ Reaction in the Central Drawer (BEFWFW System - Phase IIB)

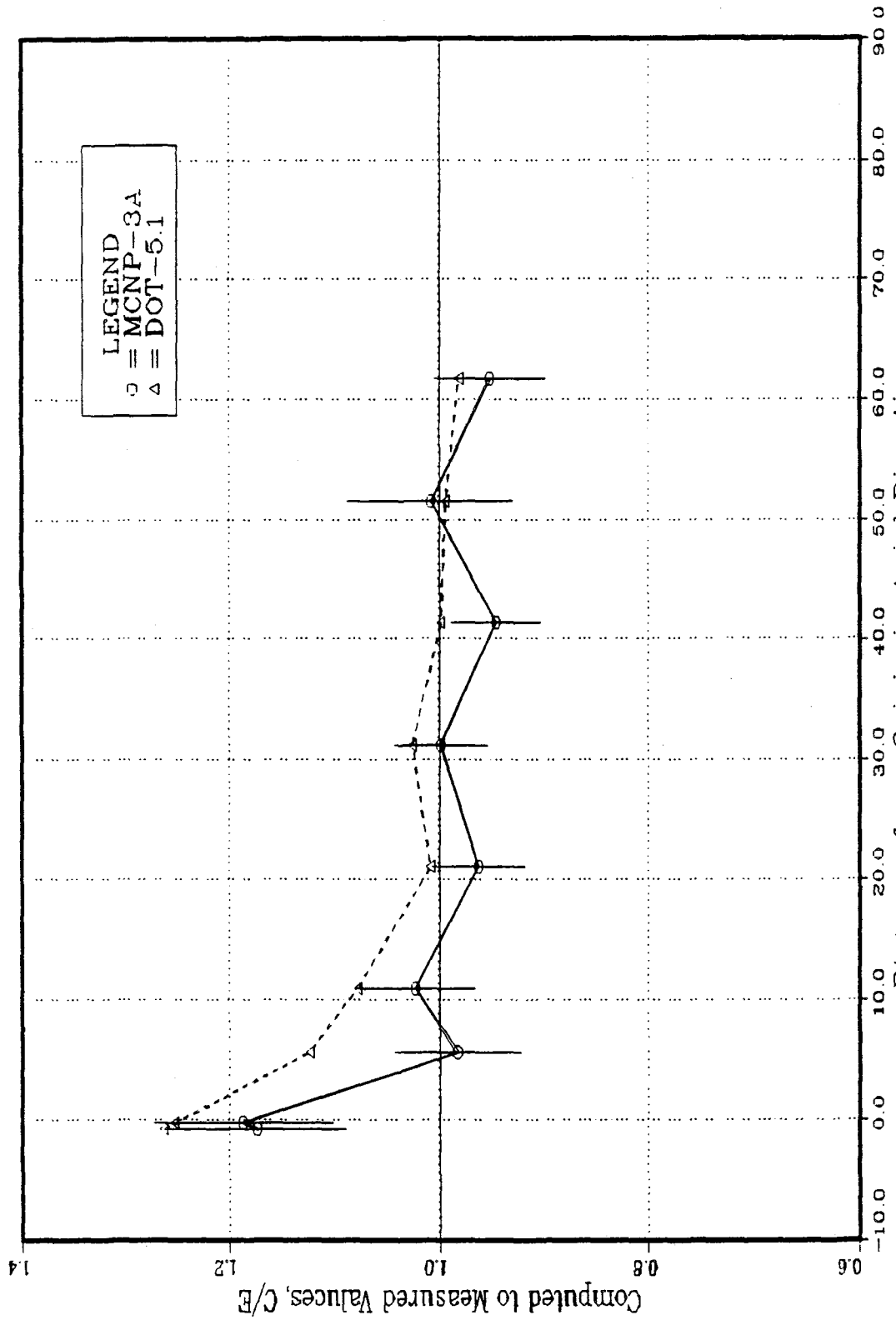

Fig. VI.17: C/Values for the $Ni^{58}(n,p)Co^{58}$ Reaction in the Central Drawer (BEFWFW System - Phase IIB)

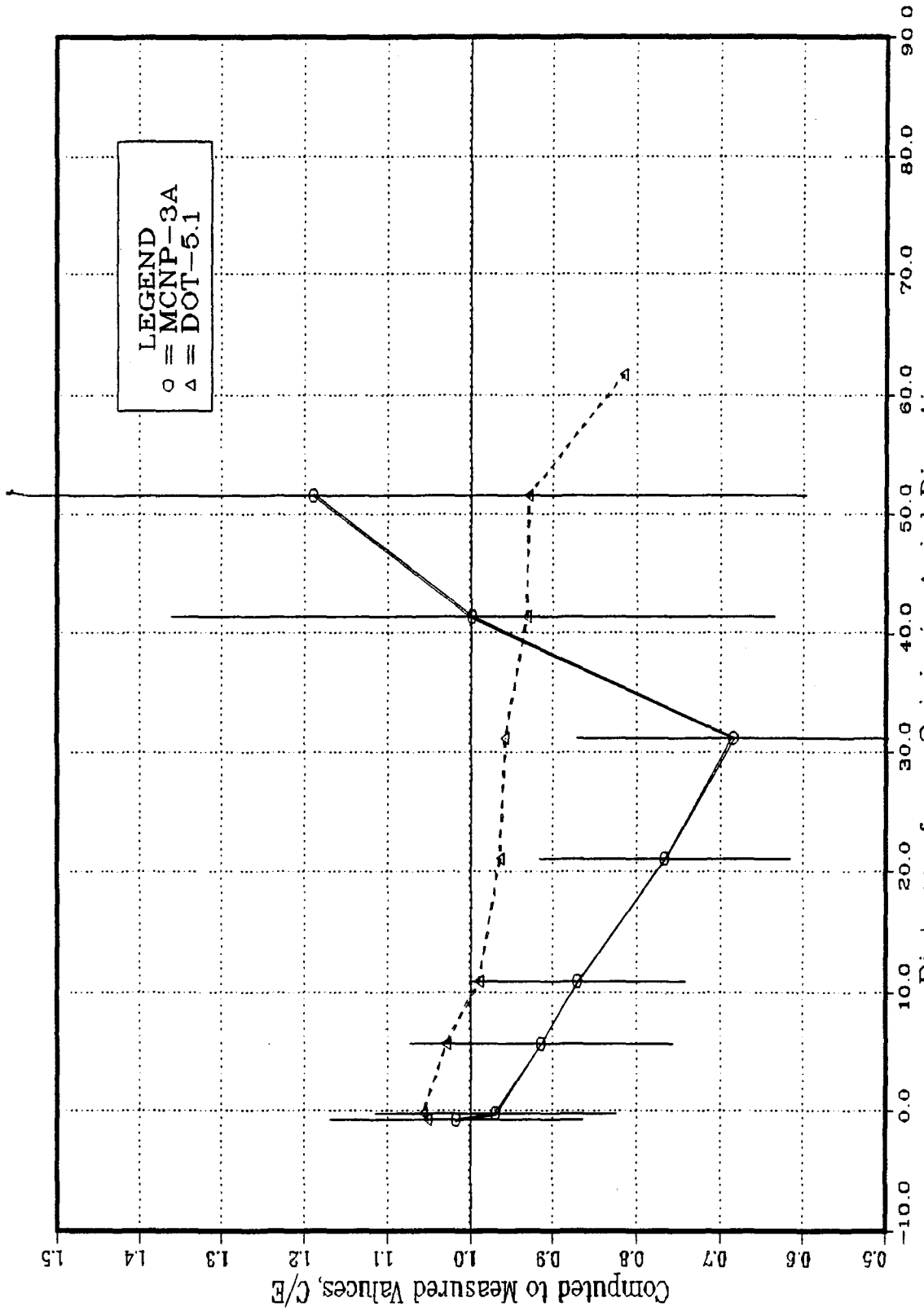

Fig. VI.18: C/E Values for the $In^{115}(n,n')In^{115m}$ Reaction in the Central Drawer (BEFWFW System - Phase IIB)

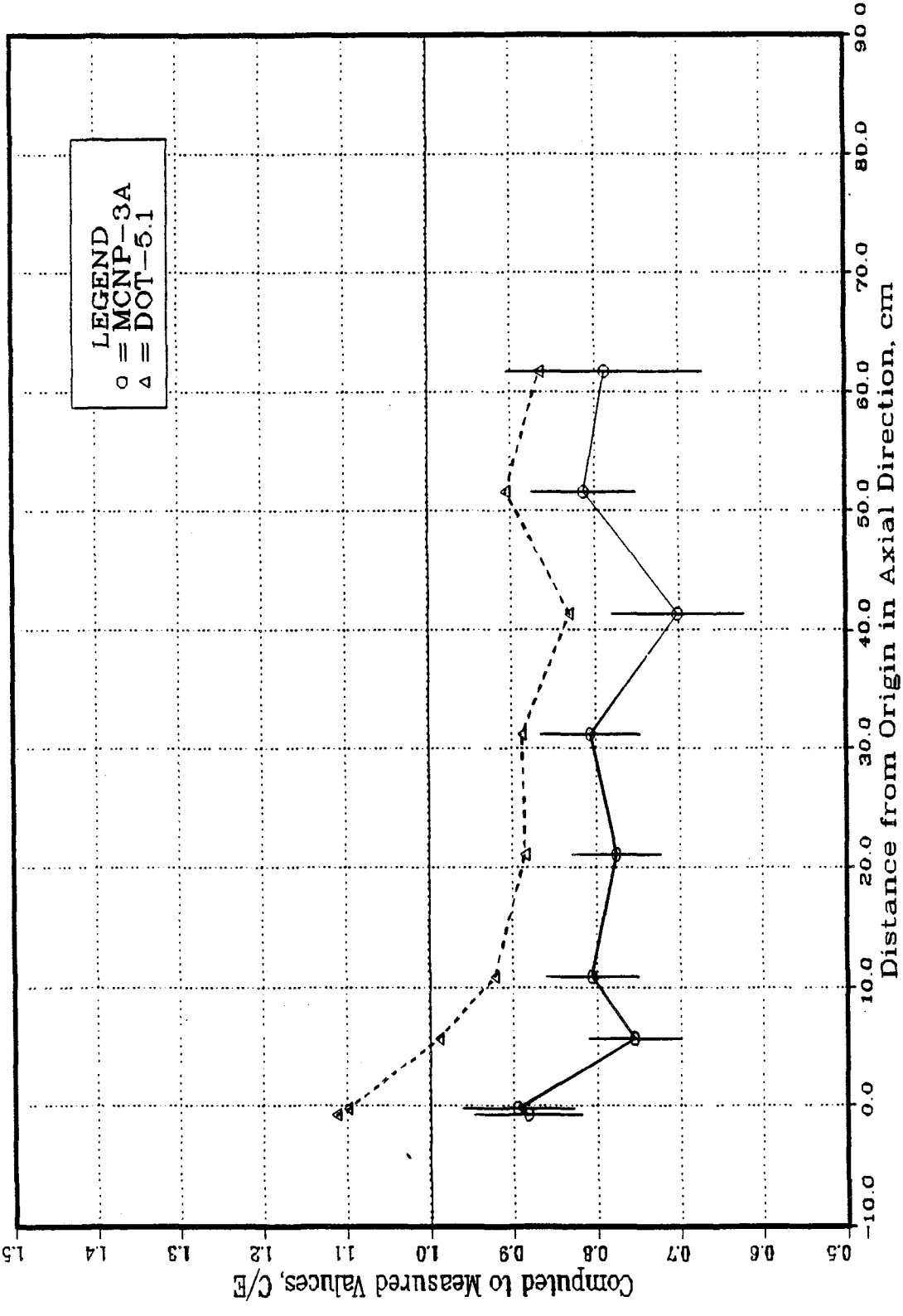

Fig. VI.19: C/E Values for the Ti(n,xp)Sc-46 Reaction in the Central Drawer (BEFWFW System - Phase IIB)

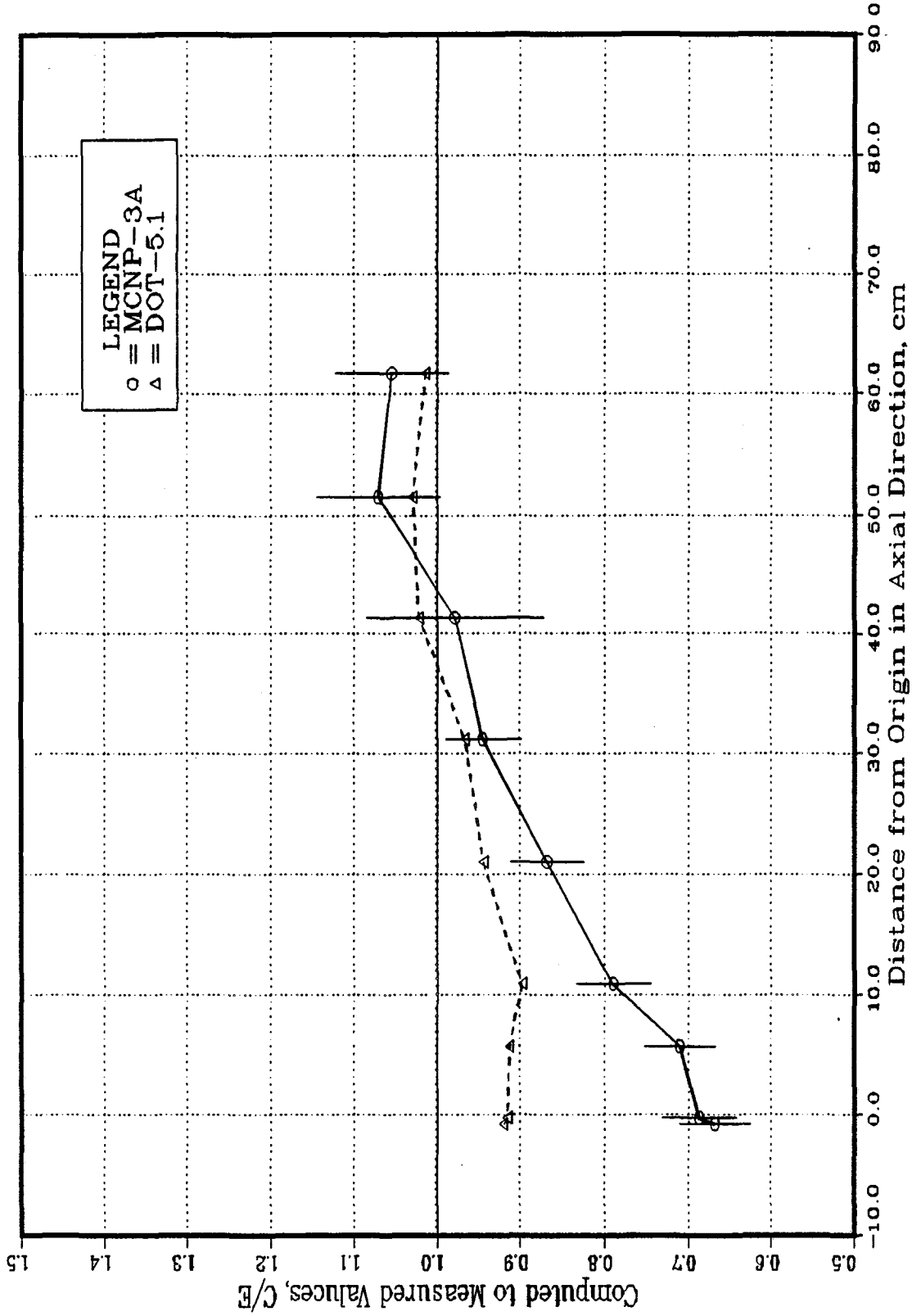

Fig. VI.20: C/E Values for the Ti(n,xp)Sc-47 Reaction in the Central Drawer (BEFWFW System - Phase IIB)

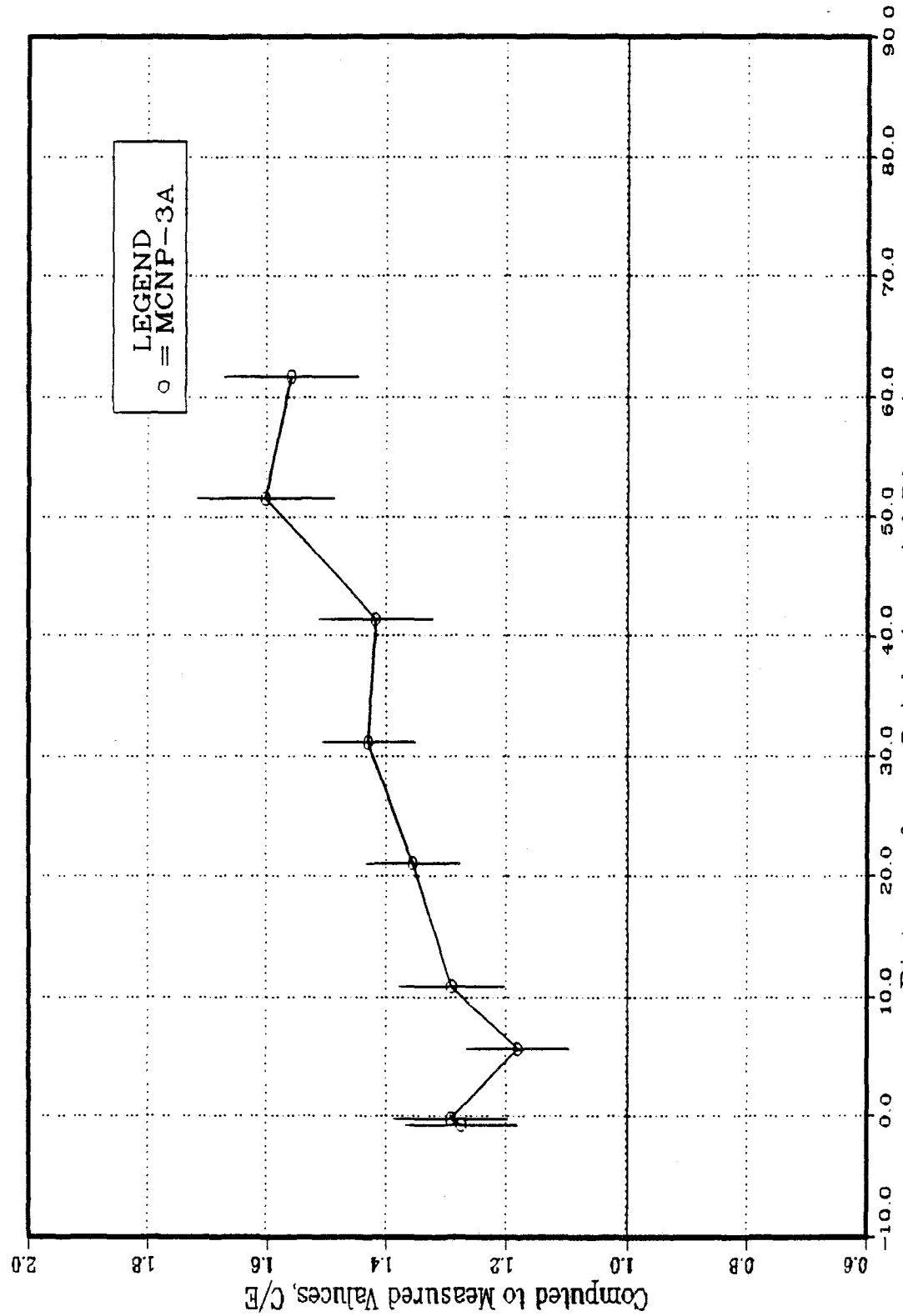

Fig. VI.21: C/E Values for the Ti(n,xp)Sc-48 Reaction in the Central Drawer (BEFWFW System - Phase IIB)

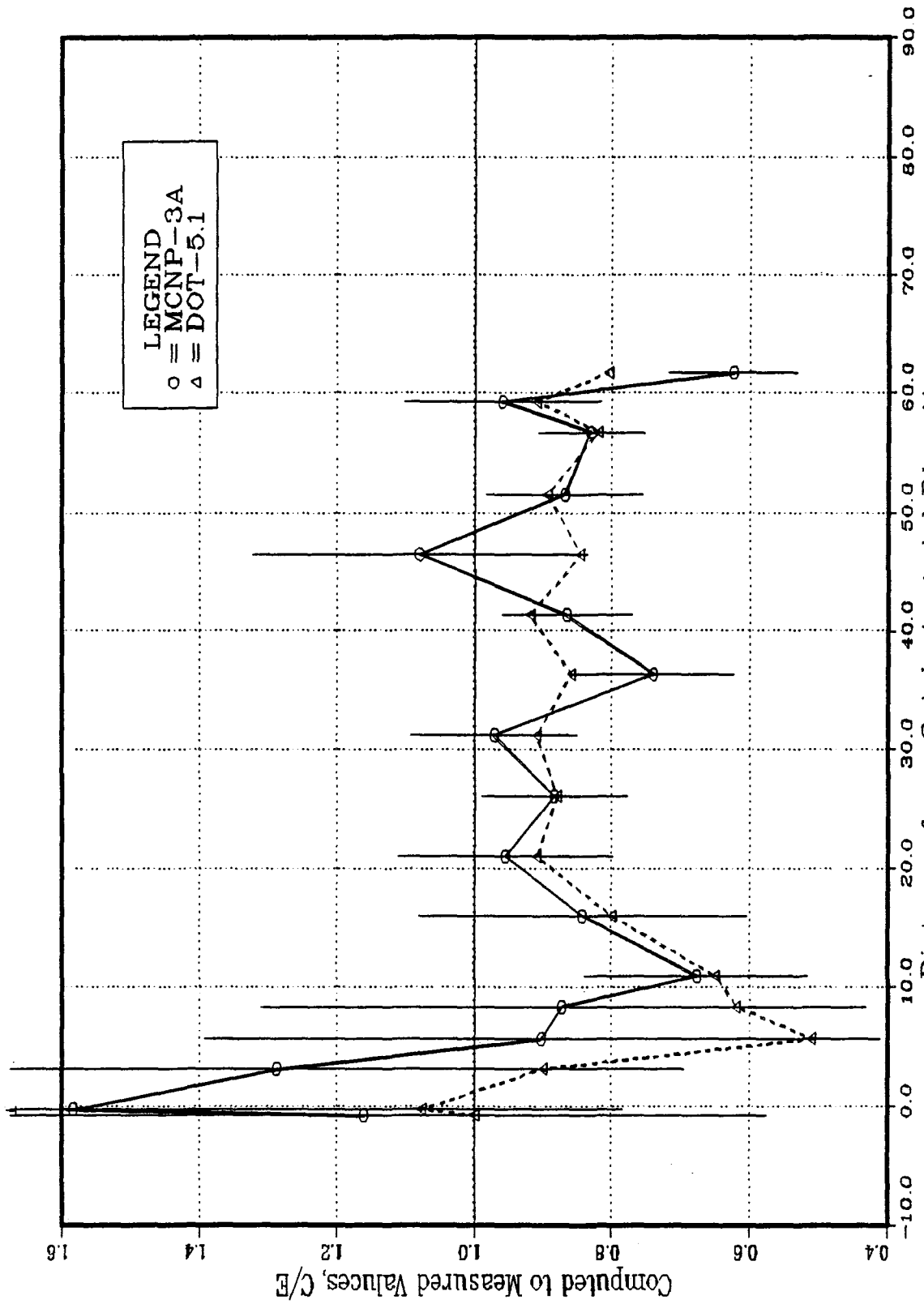

Fig. VI.22: C/E Values for the $Au^{197}(n,\gamma)Au^{198}$ Reaction in the Central Drawer (BEFWFW System - Phase IIB)

VII. In System Neutron Spectra

Specially designed small NE213 and proton recoil (PRC) detectors were used to measure neutron spectrum inside the test assembly. The former detector was used for neutron energies above 1 MeV while the latter was used for neutron energies in the range 1KeV - 1 MeV. As indicated in Table I.1, the two detectors were used in the three systems of Phase IIA and IIB while the PRC was used only in the Be-front system (w/FW,BEFWFW) of Phase IIB.

VII.1. Neutron Spectrum in Phase IIA

A comparison between the calculated neutron spectrum by MCNP code in the REF system of Phase IIA and the measured spectrum by the NE213 detector is shown in Figs. VII.1 to VII.4 at depth Z = 1.15, 3.68, 7.46, and 12.52 cm, respectively. The calculated spectrum was not smeared with the NE213 window value. The 14 MeV peak decreases as one proceeds deeper in the Li_2O zone. The calculated spectrum in the energy range 2 - 10 MeV is larger than the measured spectrum at all the locations shown in these figures. Also, the calculated 14 MeV peak seems to be underpredicted, particularly at deep locations, as can be seen from VII.4. The overestimation of the spectrum in the energy range 2 - 10 MeV leads to C/E values that are above unity for reactions whose threshold energies lie in this energy range. From Fig. IV.20, for example, the C/E values for T_7 are around 1.15. The C/E values for the $^{58}Ni(n,p)$ reaction ($E_{th} \sim$ 2MeV) shown in Fig. VI.8 are also above unity in the reference system.

A comparison to the neutron spectrum measured by the PRC in the reference system is shown in Figs. VII.5 to VII.7 at depth Z = 1.15, 12.52, and 42.88 cm, respectively. The calculated spectrum (by MCNP code) are larger than measurements in the energy range 2 - 30 KeV while the measured spectrum is larger than the calculated one in the energy around 100-200 KeV. There is good agreement with the measurements in the energy range 50 - 80 KeV.

Spectrum comparison in the BES system is shown in Fig. VII.8 to VII.12 along the central axis at locations Z = 1.15, 3.68, 6.21, 8.74, and 11.27 cm. The measurements were performed using the NE213 detector. The first two locations are in the front Li_2O layer and the second two locations are inside the Be layer. The calculated spectrum (by Monte Carlo) was not smeared using the NE213 window value, as is the case in Figs. VII.1 to VII.4. This leads to the shift observed in the 14 MeV peak. At the first location

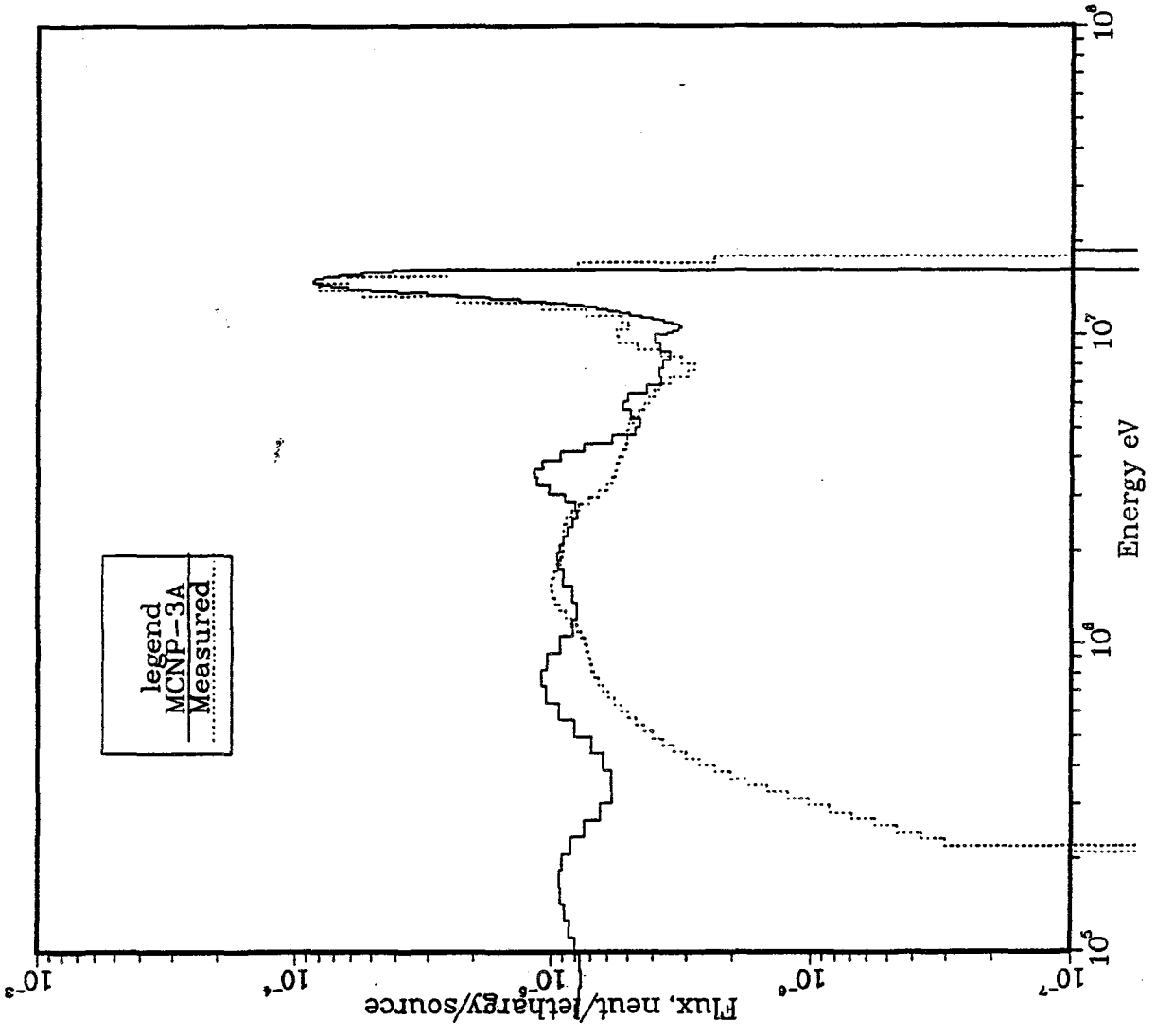

Fig. VII.1: Neutron Spectrum at Z = 1.15 cm
(REF System - Phase IIA)

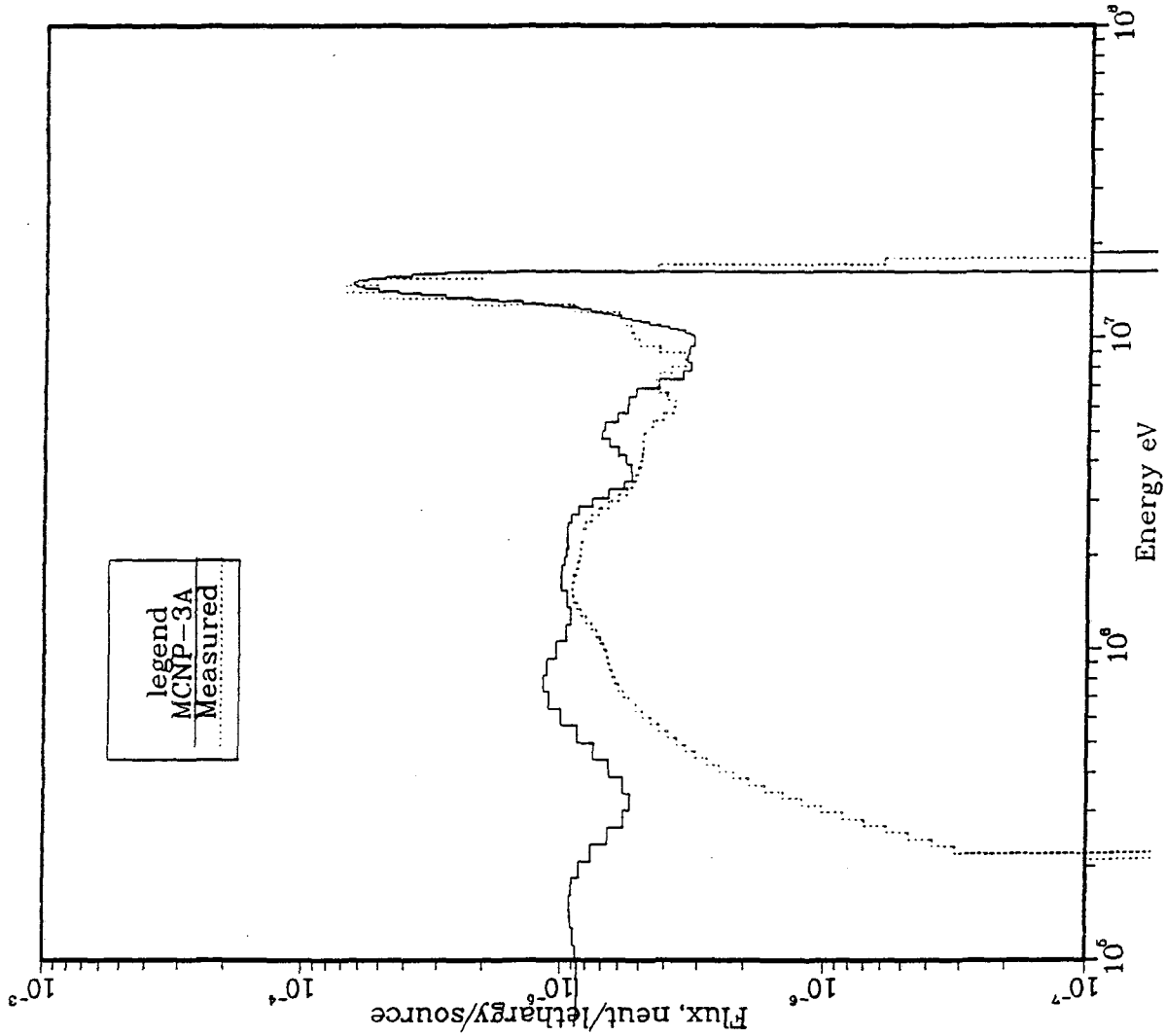

Fig. VII.2: Neutron Spectrum at Z = 3.68 cm
(REF System - Phase IIA)

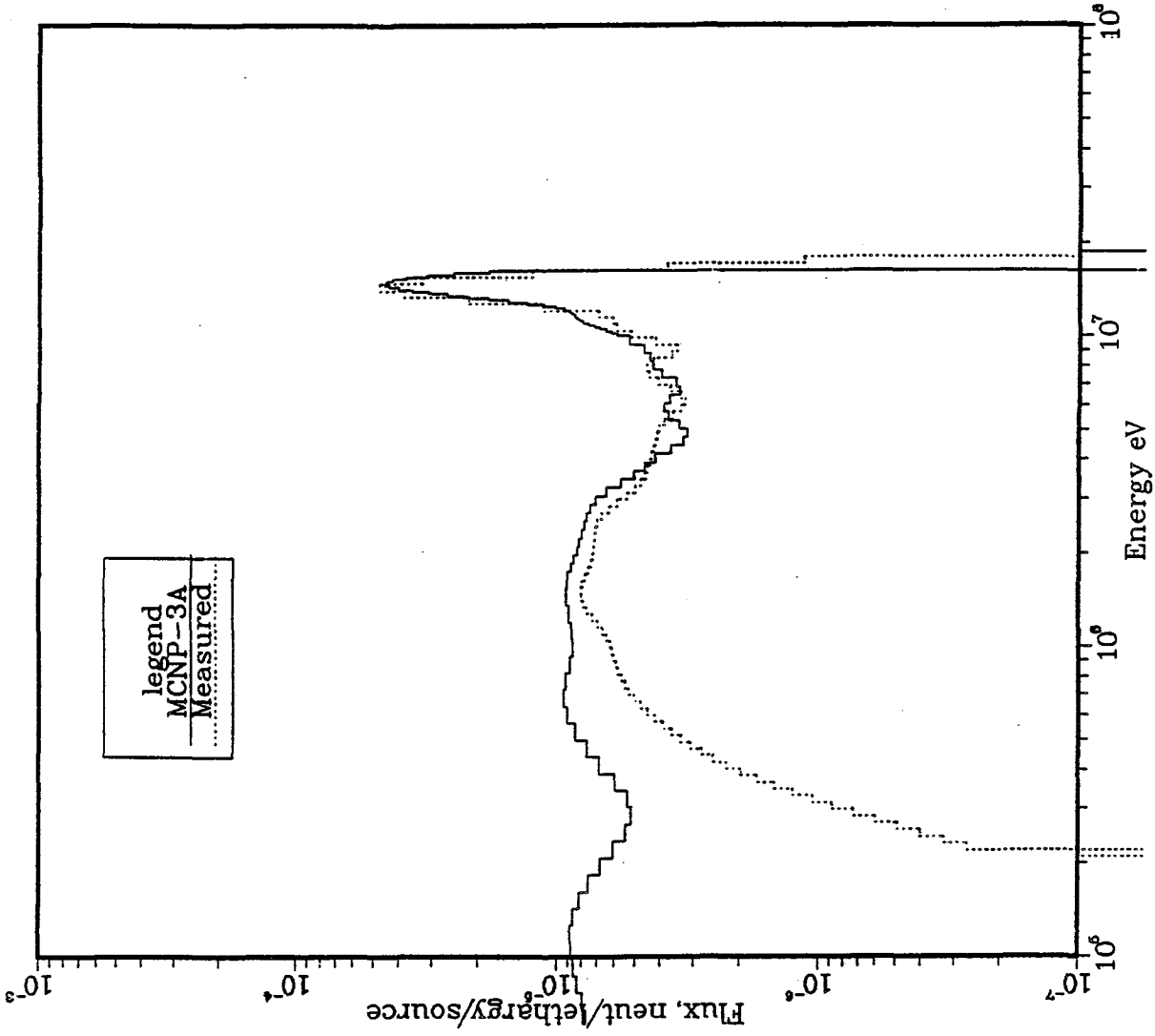

Fig. VII.3: Neutron Spectrum at Z = 7.46 cm
(REF System - Phase IIA)

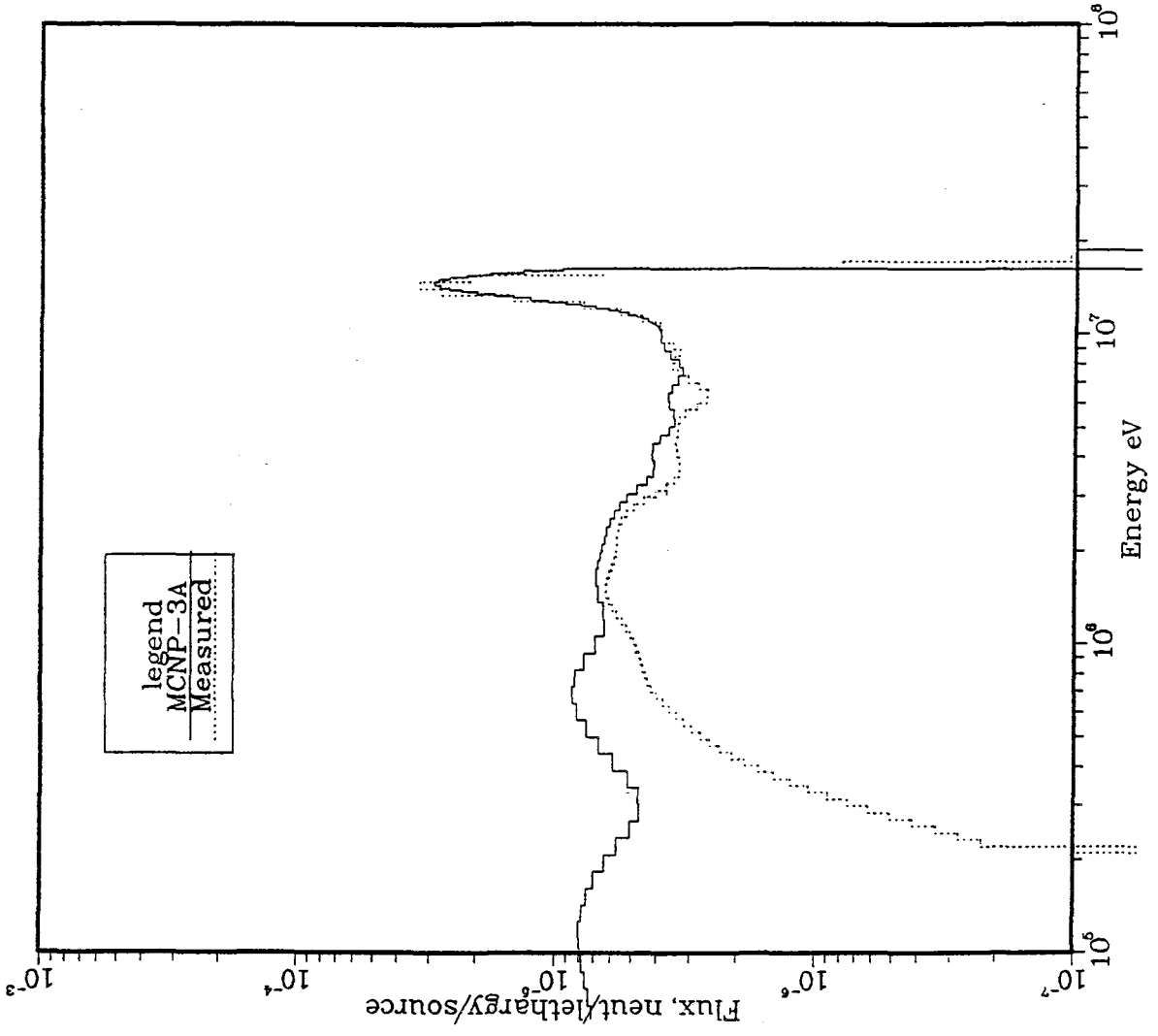

Fig. VII.4: Neutron Spectrum at Z = 12.52 cm
(REF System Phase IIA)

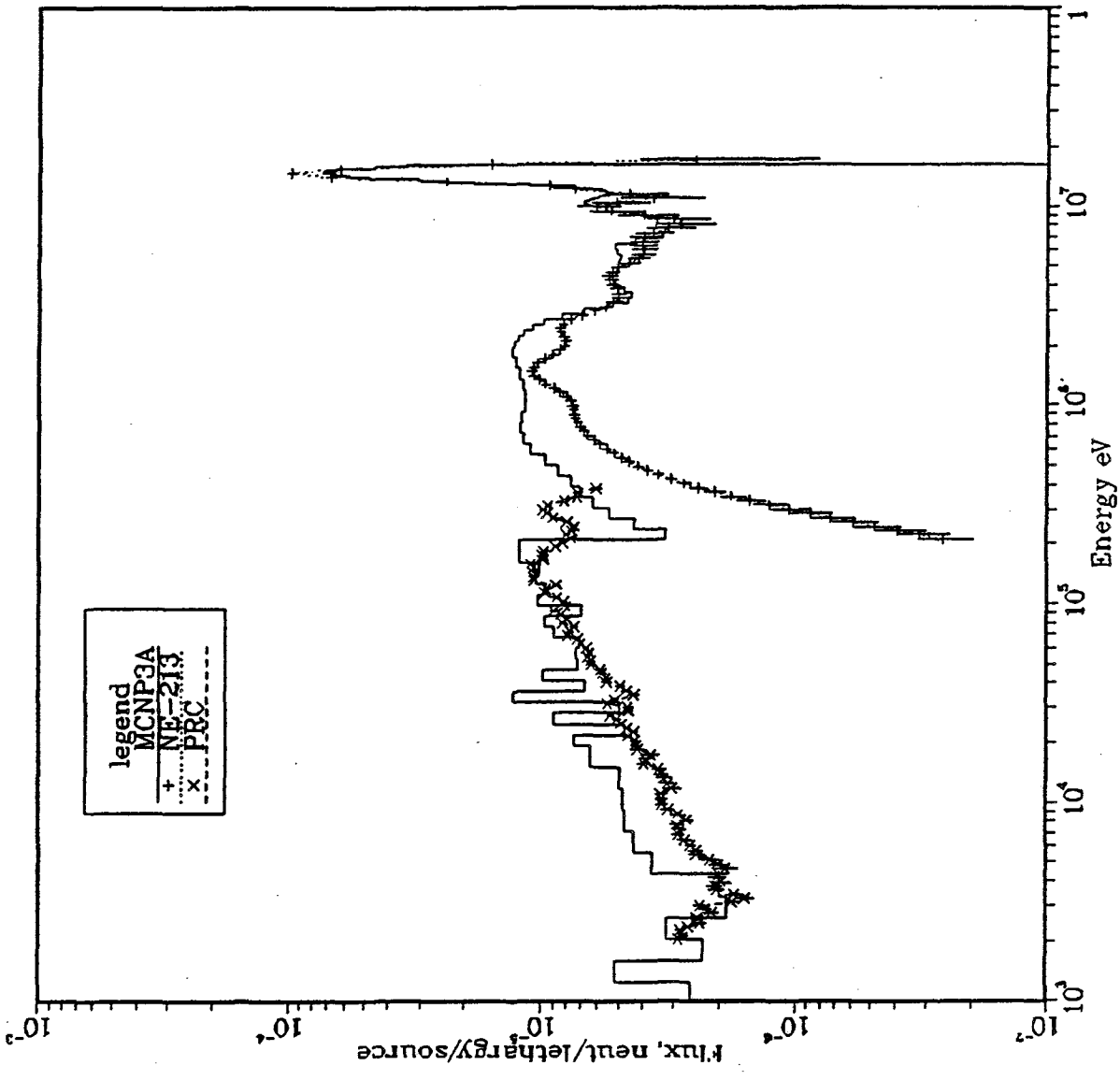

Fig. VII.5: Neutron Spectrum at Z = 1.15 cm
(REF System - Phase IIA, NE213 and PRC Measurements)

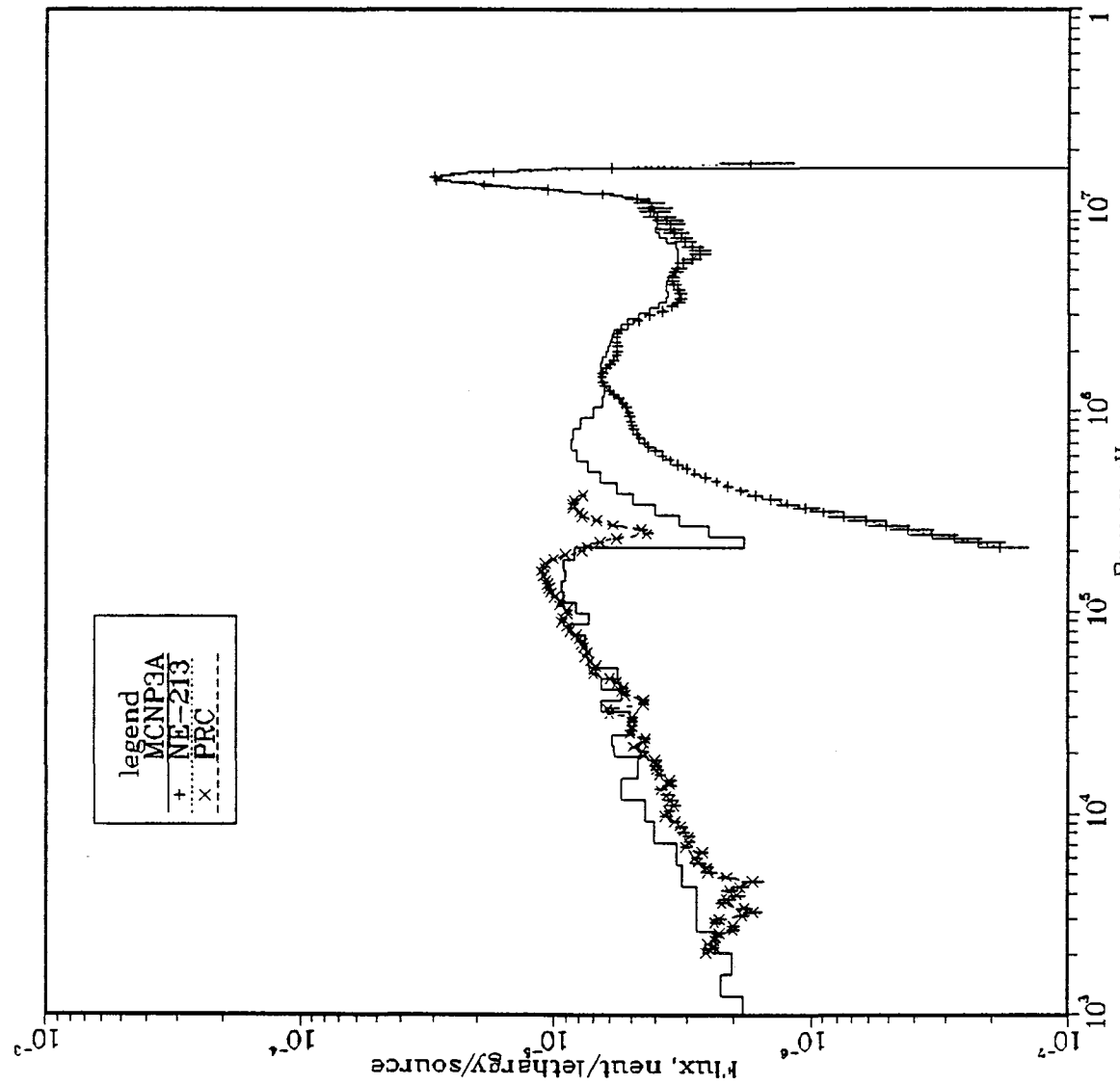

Fig. VII.6: Neutron Spectrum at Z = 12.52 cm
(REF System - Phase IIA, NE213 and PRC Measurements)

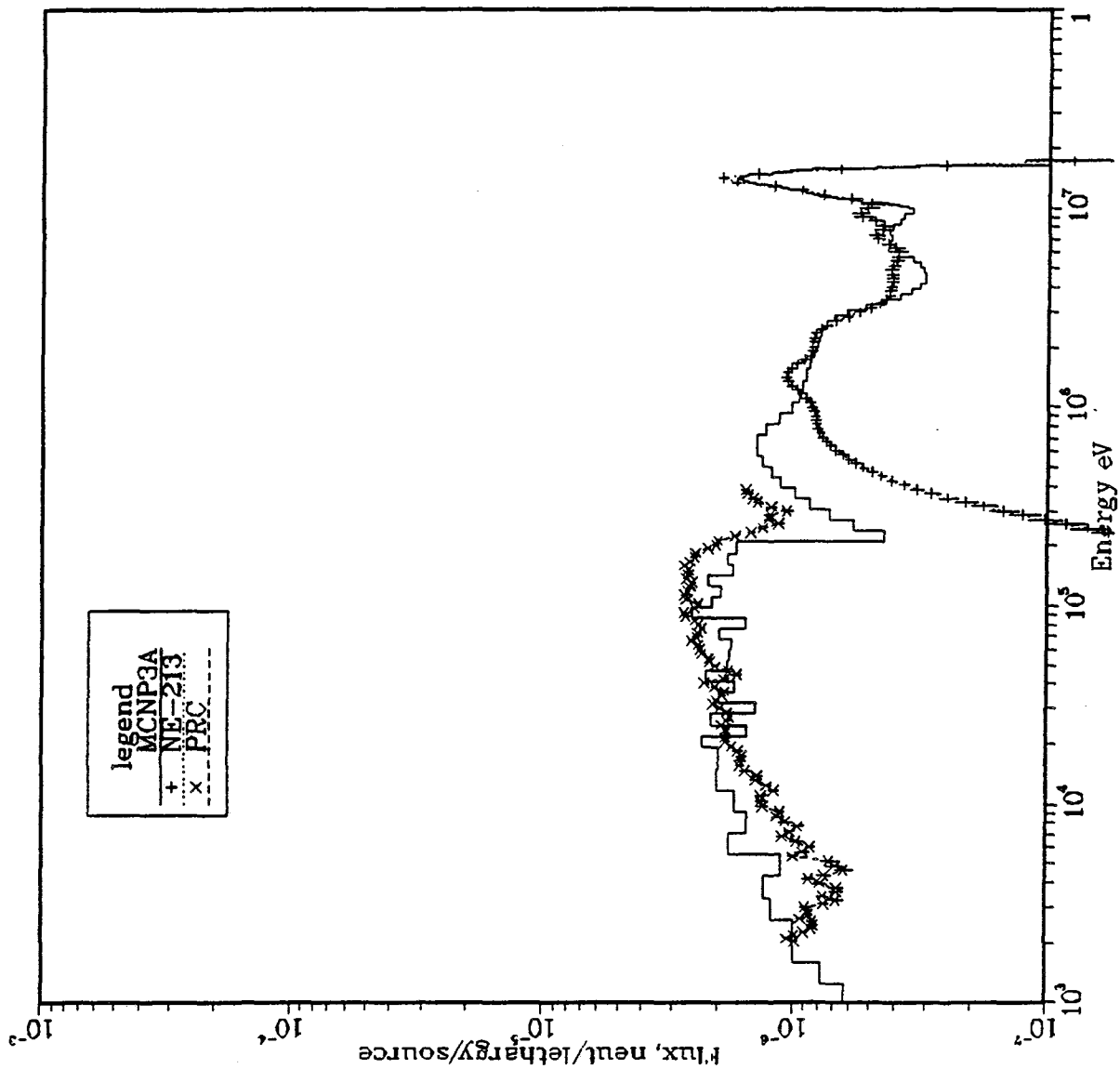

Fig. VII.7: Neutron Spectrum at Z = 42.88 cm
(REF System - Phase IIA, NE213 and PRC Measurements)

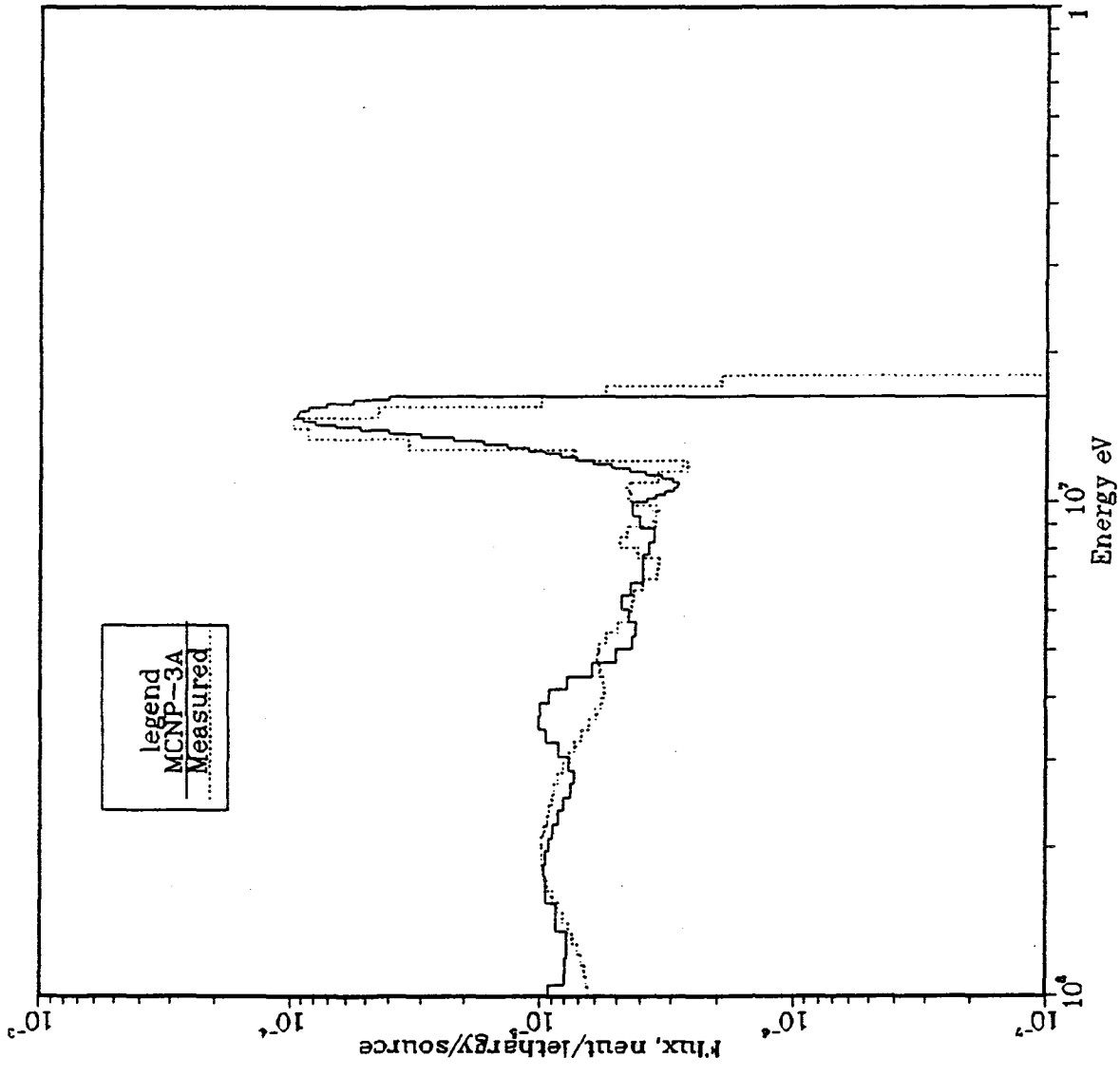

Fig. VII.8: Neutron Spectrum at Z = 1.15 cm
(BES System - Phase IIA)

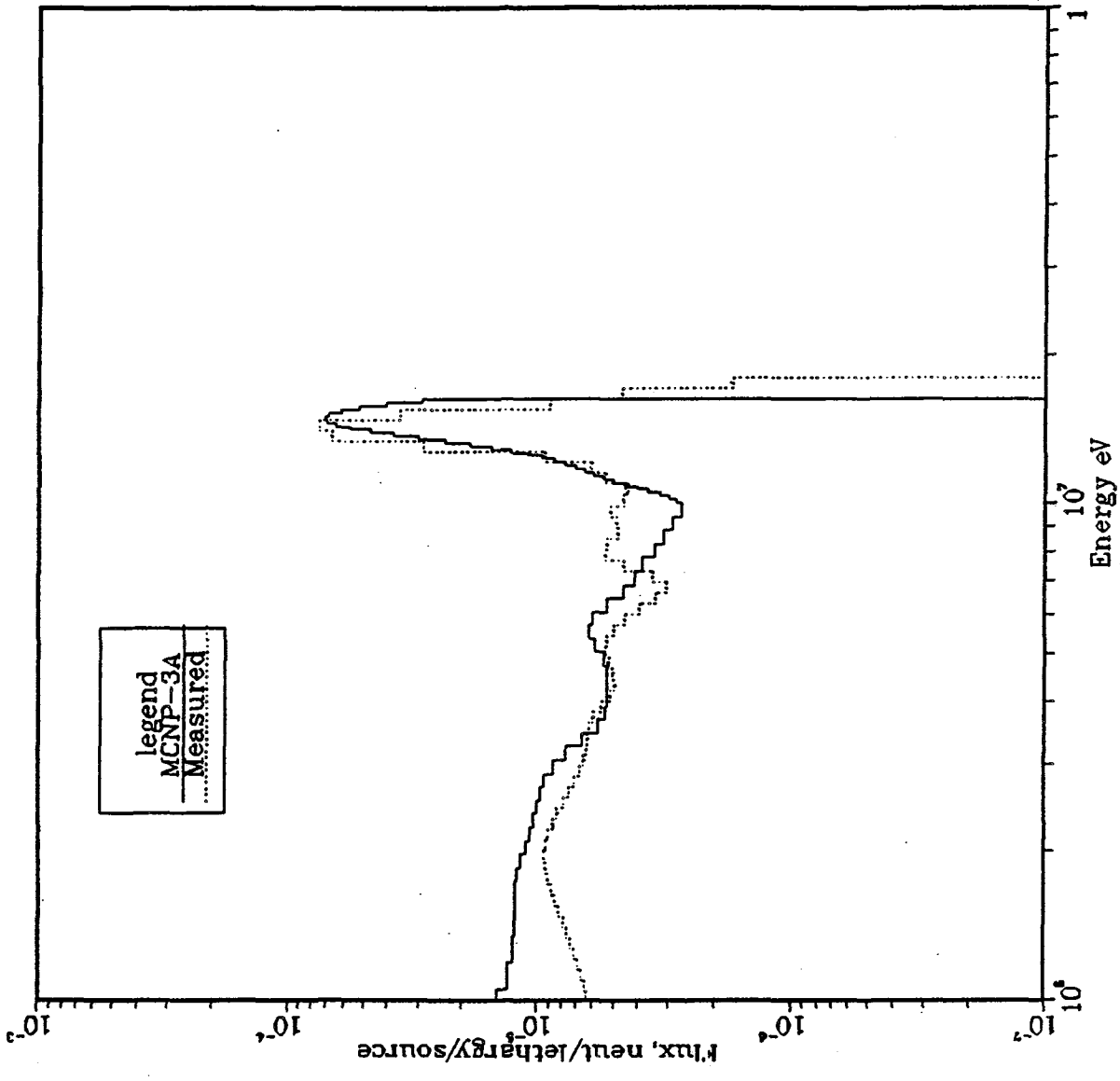

Fig. VII.9: Neutron Spectrum at Z = 3.68 cm
(BES System - Phase IIA)

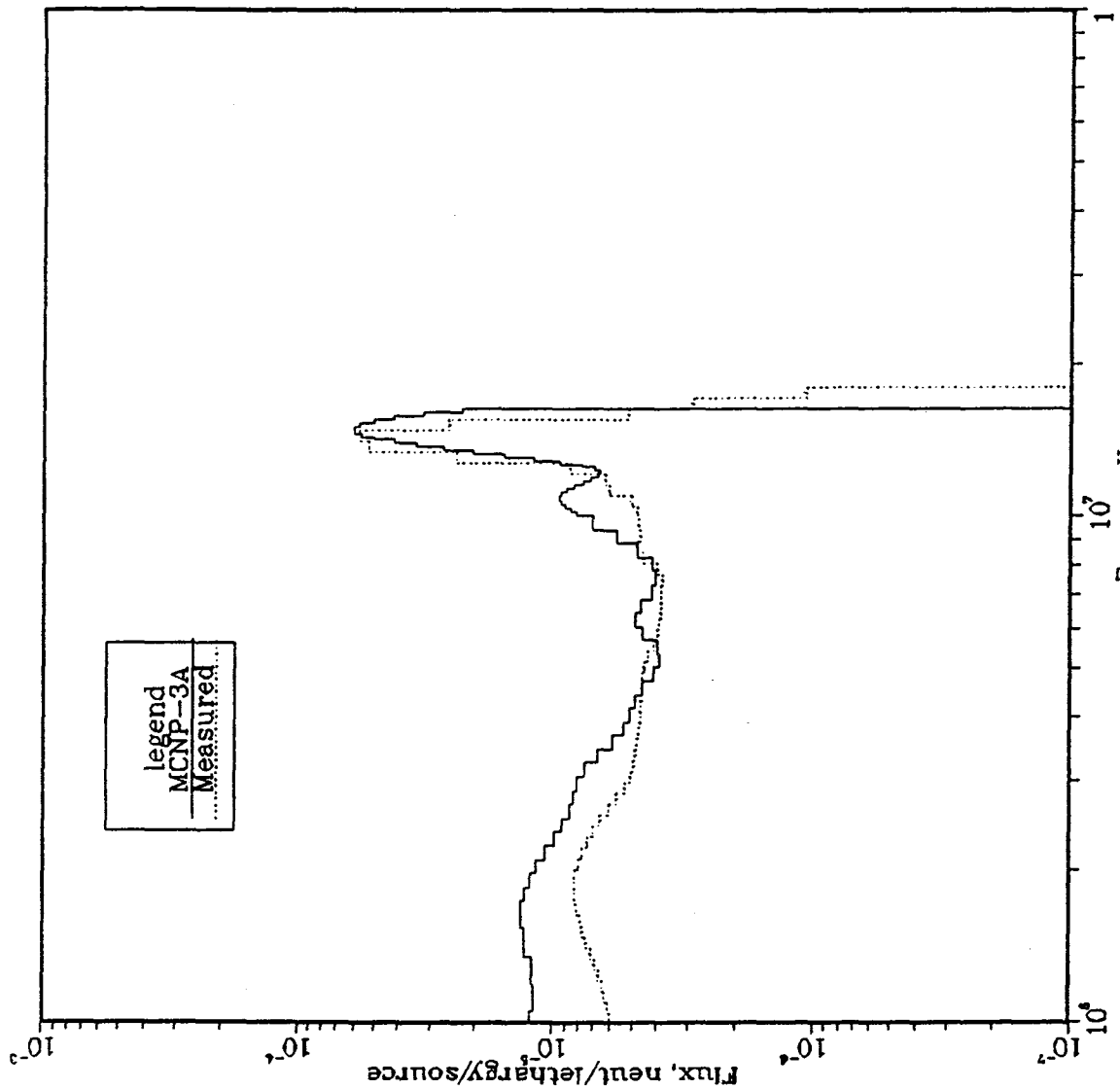

Fig. VII.10: Neutron Spectrum at Z = 6.21 cm
(BES System - Phase IIA)

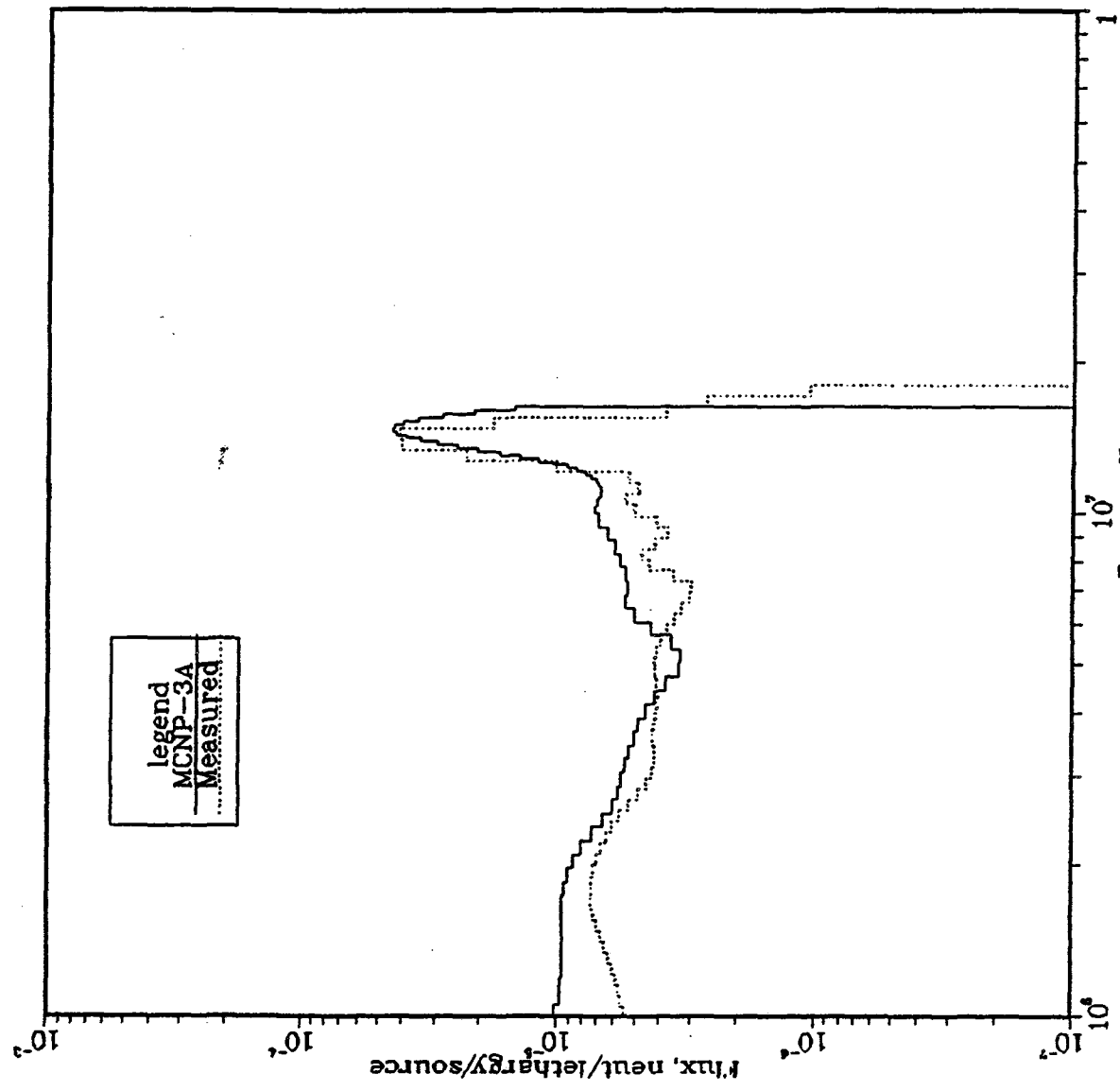

Fig. VII.11: Neutron Spectrum at Z = 8.74 cm
(BES System - Phase IIA)

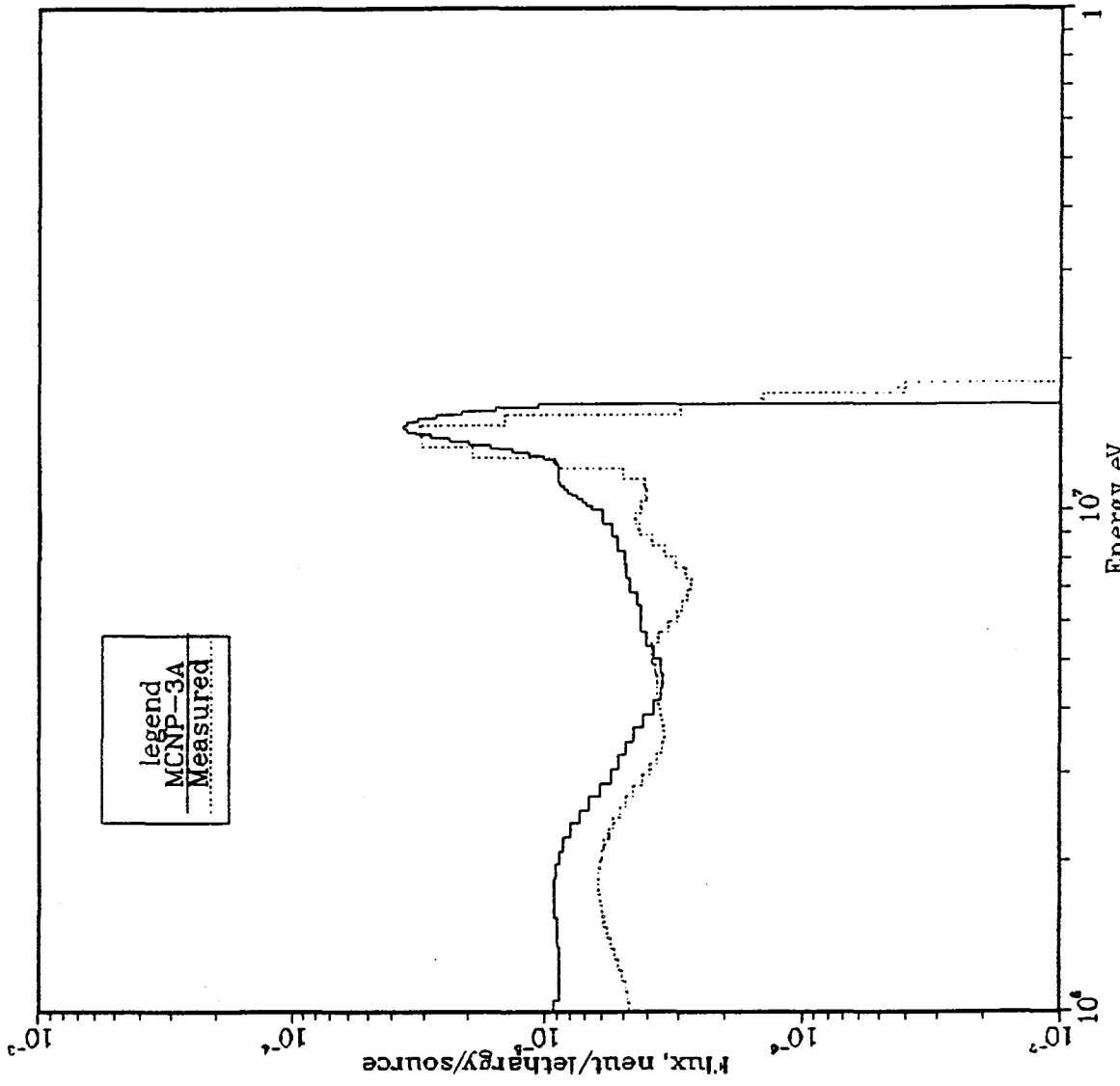

Fig. VII.12: Neutron Spectrum at Z = 11.27 cm
(BES System - Phase IIA)

(Z = 1.15cm.), the calculated spectrum in the energy range 2 - 10 MeV is, on the average, larger than the measured spectrum. Around E = 8 MeV, the measured spectrum is larger. At the location Z = 3.68 cm, the calculated spectrum is much larger than the measured values in the energy range 1 - 3 MeV but lower in the energy range 7 - 10 MeV. Inside the Be layer, the calculated spectrum is noticeably larger than the measurements in the energy range 1 - 10 MeV, as can be seen in Figs. VI.10 and VII.11. This is also true just behind the Be layer, as shown in Fig. VII.12. The overestimation in the neutron spectrum in the energy range 1 - 10 MeV is consistent with Oyama and Maekawa's experiment on the Be-slab discussed in Section V. This is also reflected on the C/E values for those reactions whose threshold energies are within this energy range (see for example Fig. IV.24 for T_7 where it is shown that the C/E values are larger than unity, particularly inside the Be layer). As for the PRC measurements, the comparison with the MCNP calculations is shown in Fig. VII.13 to VII.15. The agreement is well in the energy range 2 KeV - 100 KeV at the location Z= 11.27 cm (1.27 cm behind the Be layer) but the predicted spectrum are larger than measurements at several energies in that energy range at the locations Z = 1.15 cm and Z = 41.63 cm.

The C/E values for the integrated spectrum (measured by NE213 detector) in the energy ranges 1.01 MeV<En<10.1MeV and En>10.1MeV are shown for the BES system in Fig. VII.16. The C/E values shown are those obtained by the MCNP and DOT calculations. The integrated spectrum above 10.1 MeV is well predicted by the DOT calculations but the MCNP calculations indicated that while the spectrum is underpredicted in the front Li_2O and Be layers, it is over-predicted at depth Z > 20 cm (inside the Li_2CO_3 layer, the statistical errors are larger). This trend observed in the Monte Carlo calculations is reflected on the C/E values of the $^{58}Ni(n,2n)$ reaction discussed in Section VI.1 and shown in Fig. VI.2. As for the integrated spectrum in the energy range 1.01MeV <En <10.1 MeV, both the Monte Carlo and discrete ordinate methods predict values larger by 20 - 45% than measurements. As was discussed earlier, the integrated spectrum inside the Be layer and behind it is larger than the measurements by ~ 35 - 45% as can be ovserved from Fig. VII.16.

VII.2. Neutron Spectrum in Phase IIB

The inclusion of a Be liner on the inner surface of the Li_2CO_3 enclosure leads to a large low-energy component in the incident spectrum to the test assembly.

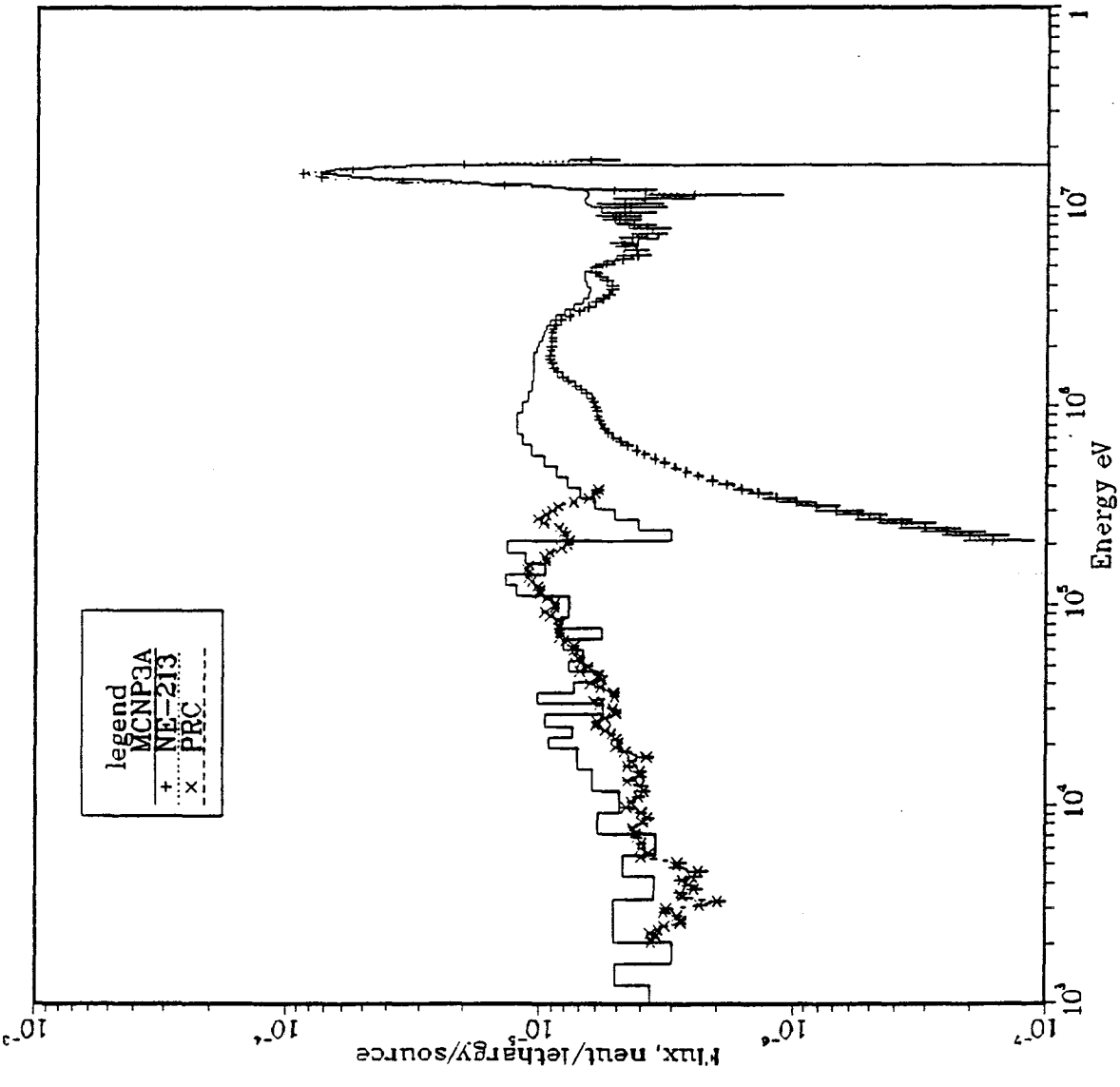

Fig. VII.13: Neutron Spectrum at Z = 1.15 cm
(BES System - Phase IIA, NE213 and PRC Measurements)

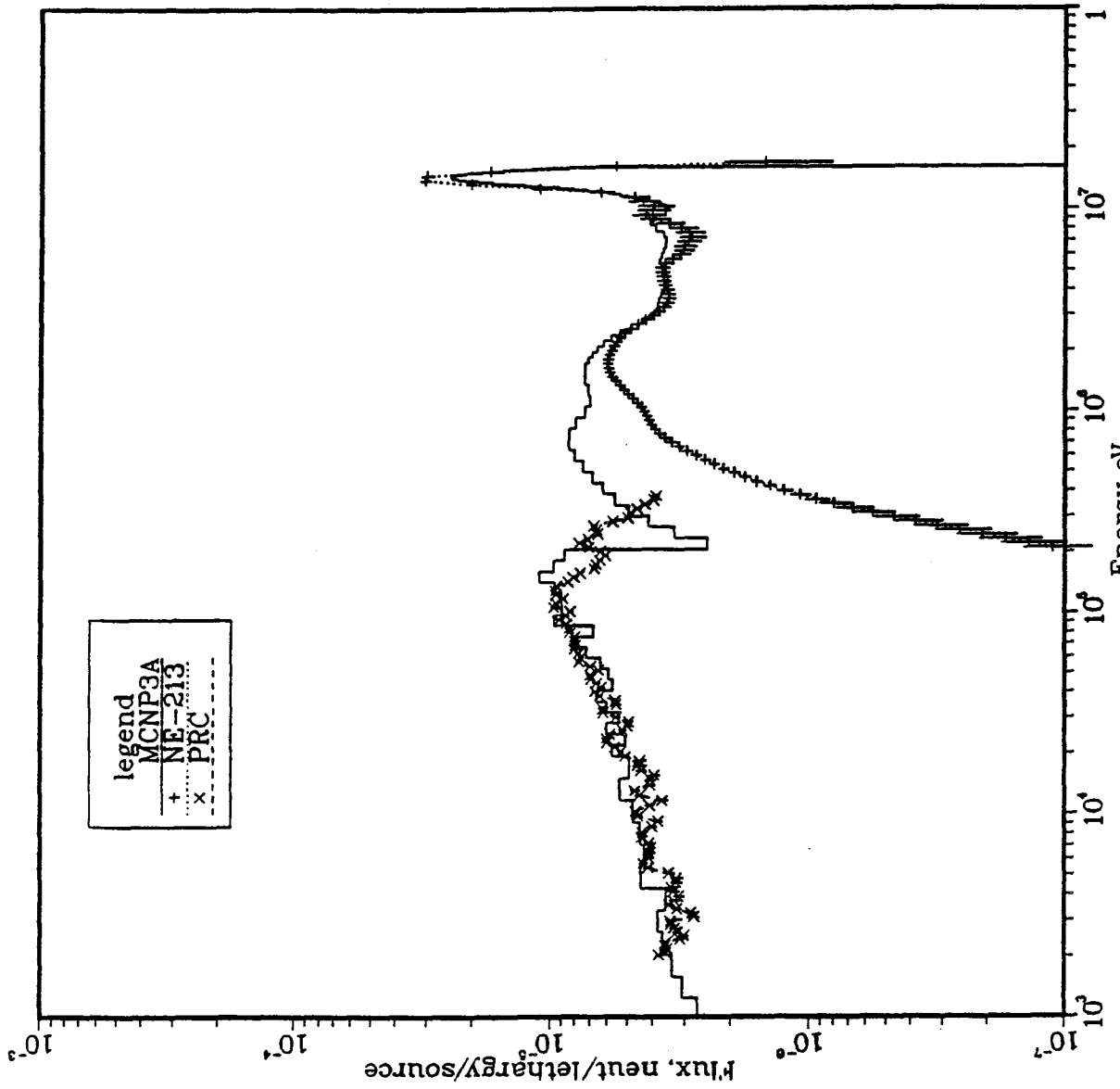

Fig VII.14: Neutron Spectrum at Z = 11.27 cm
(BES System - Phase IIA, NE213 and PRC Measurements)

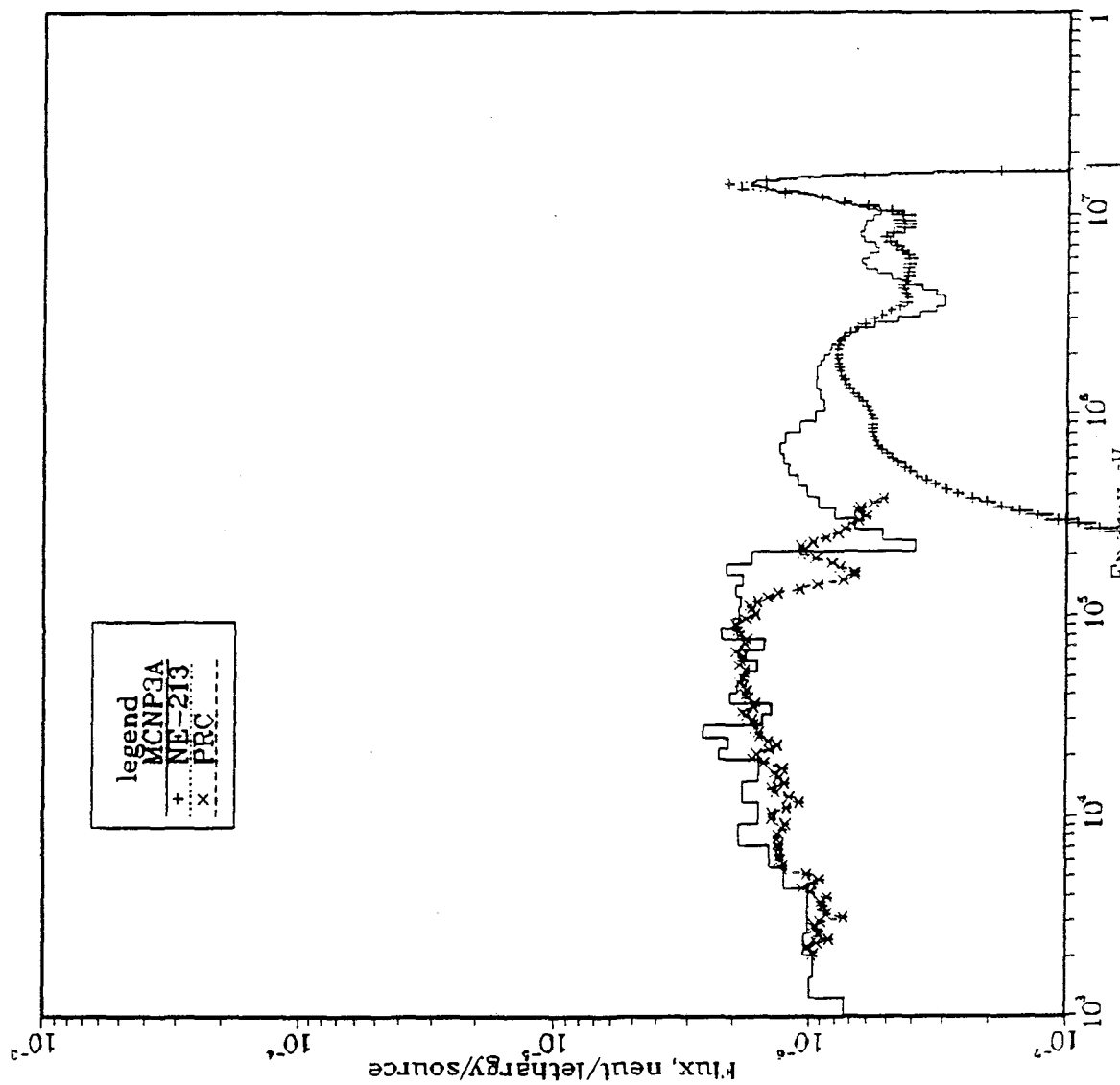

Fig. VII.15: Neutron Spectrum at Z = 41.63 cm
(BES System - Phase IIA, NE213 and PRC Measurements)

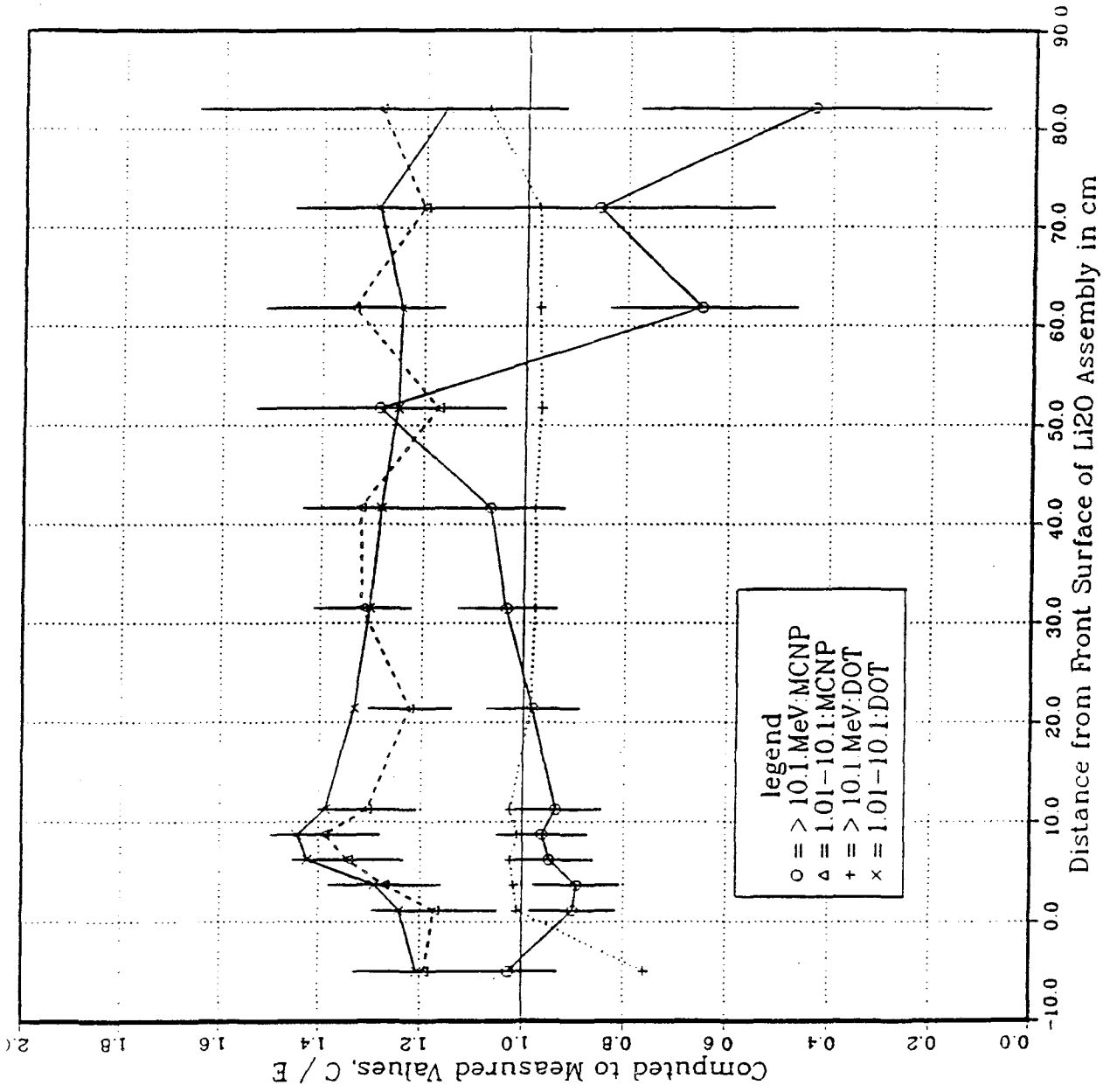

Fig. VII.16: C/E for Integrated Flux Measured by NE213 Detector in the Central Drawer (BES System - Phase IIA)

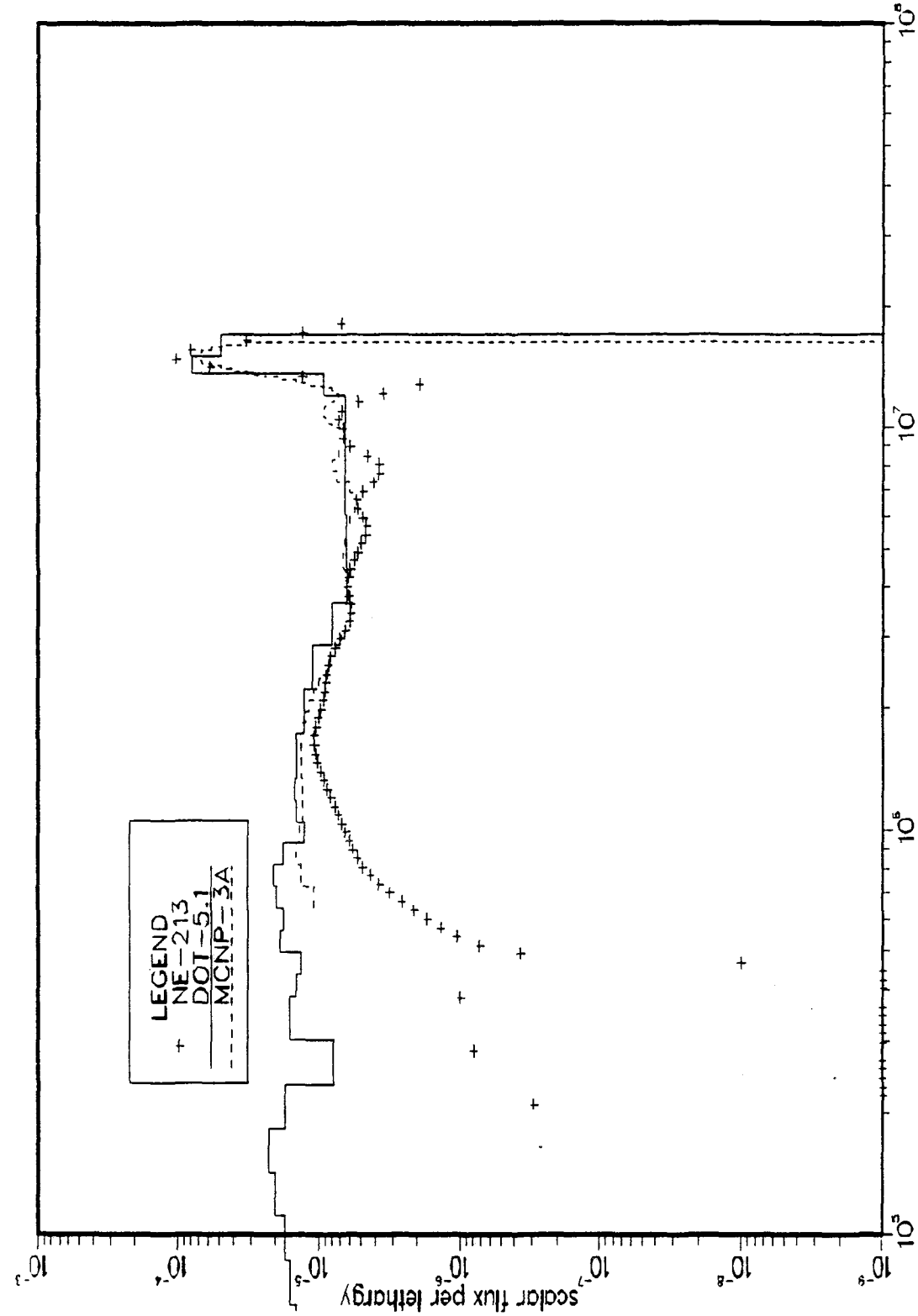

Fig. VII.17: Incident Neutron Spectrum at the Front Face (Z = 0) of the Test Assembly (REF System - Phase IIA)

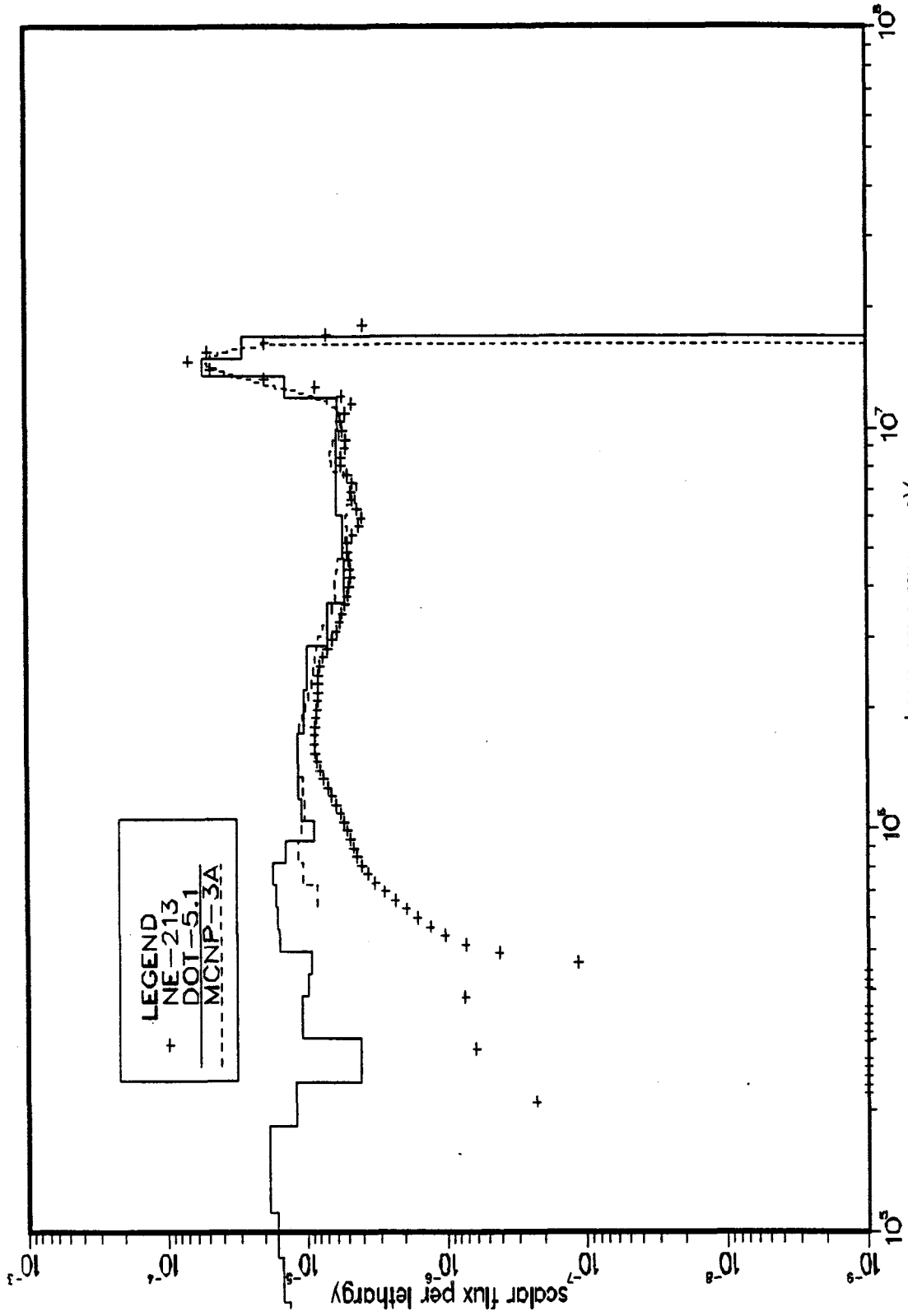

Fig. VII.18: Neutron Spectrum at Z = 5 cm
(REF System - Phase IIB)

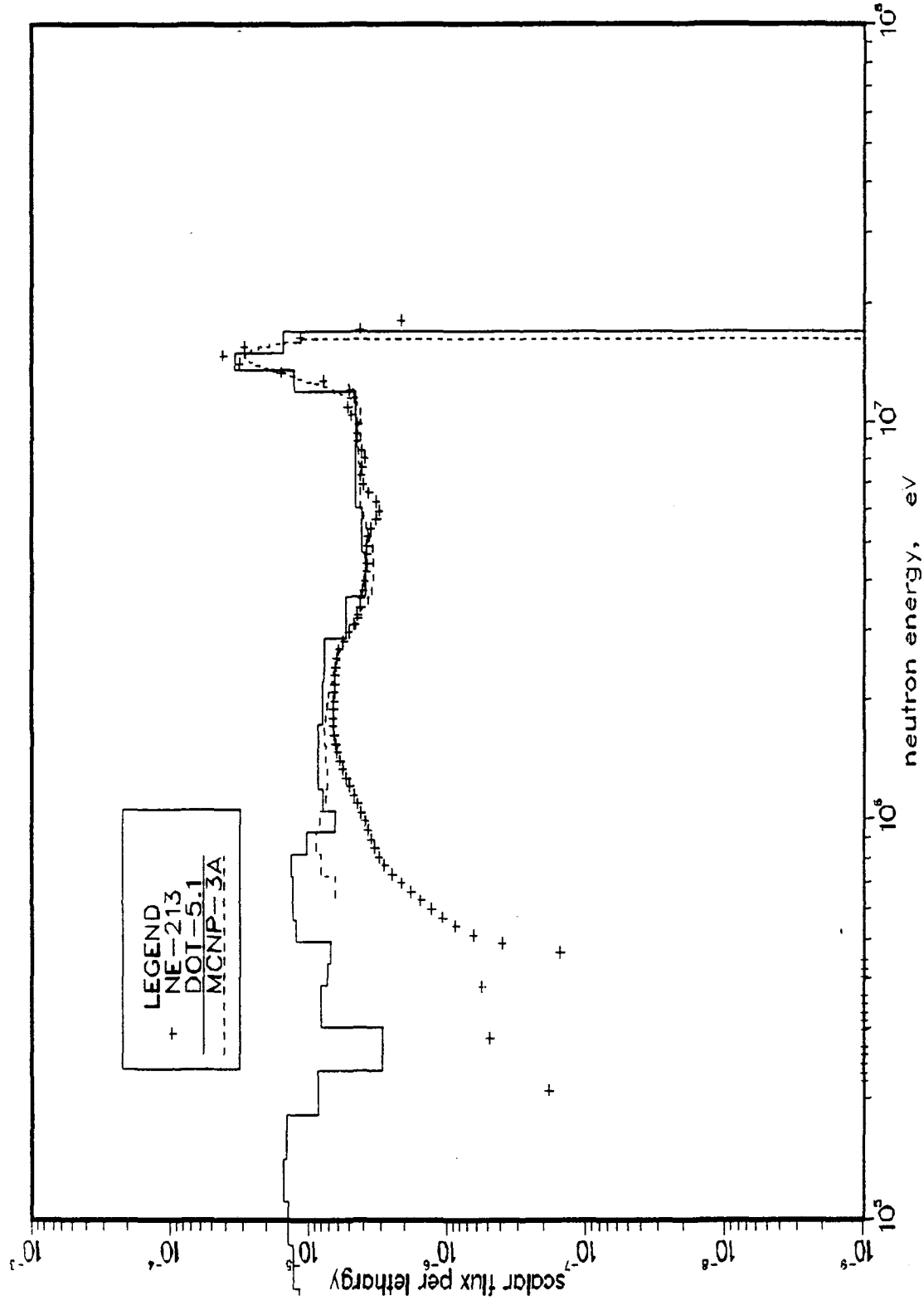

Fig. VII.19: Neutron Spectrum at Z = 10 cm
(REF System - Phase IIB)

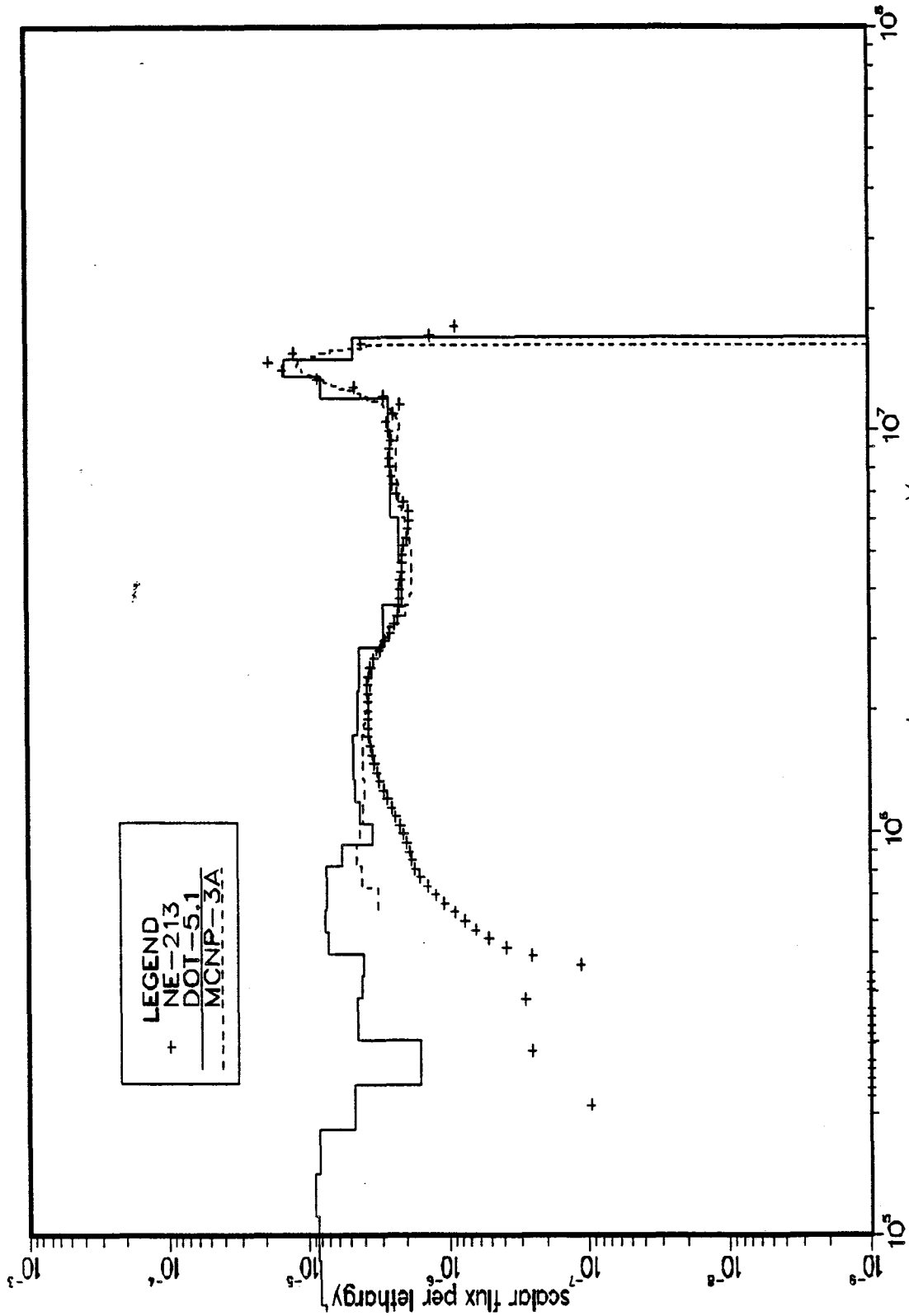

Fig. VII.20: Neutron Spectrum at Z = 20 cm
(REF System - Phase IIB)

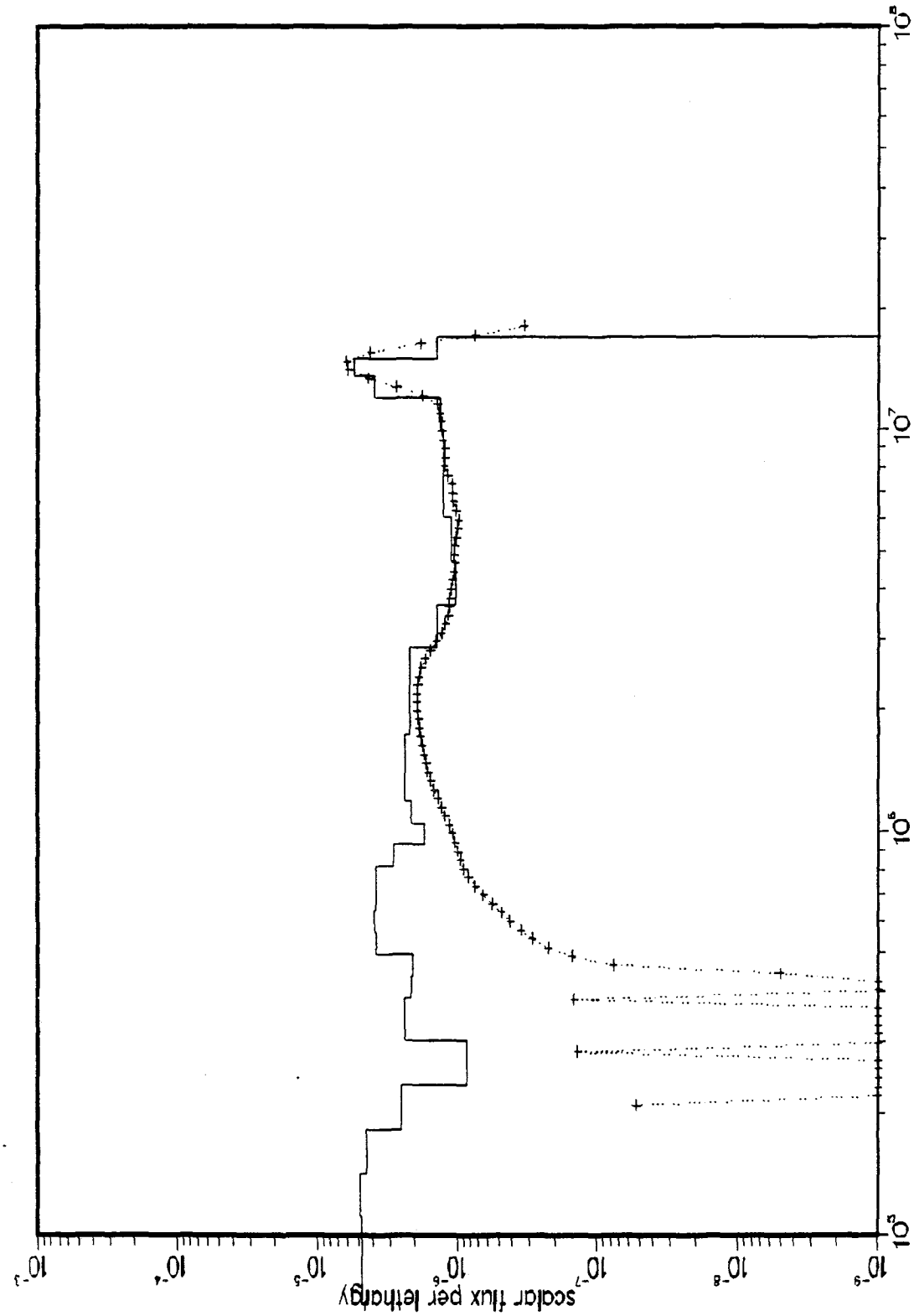

Fig. VII.21: Neutron Spectrum at Z = 30 cm
(REF System - Phase IIB)

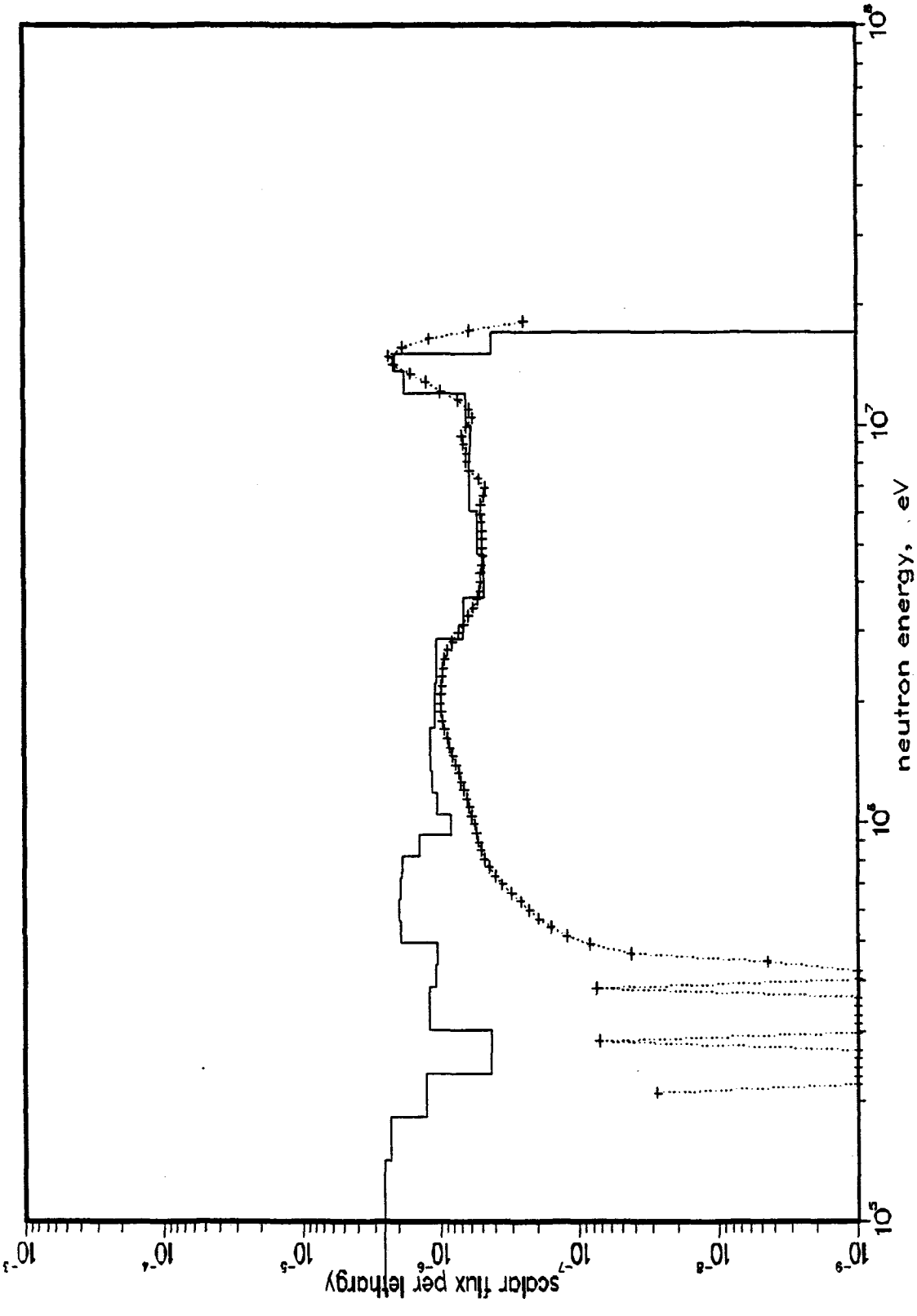

Fig. VII.22: Neutron Spectrum at Z = 40 cm
(REF System - Phase IIB)

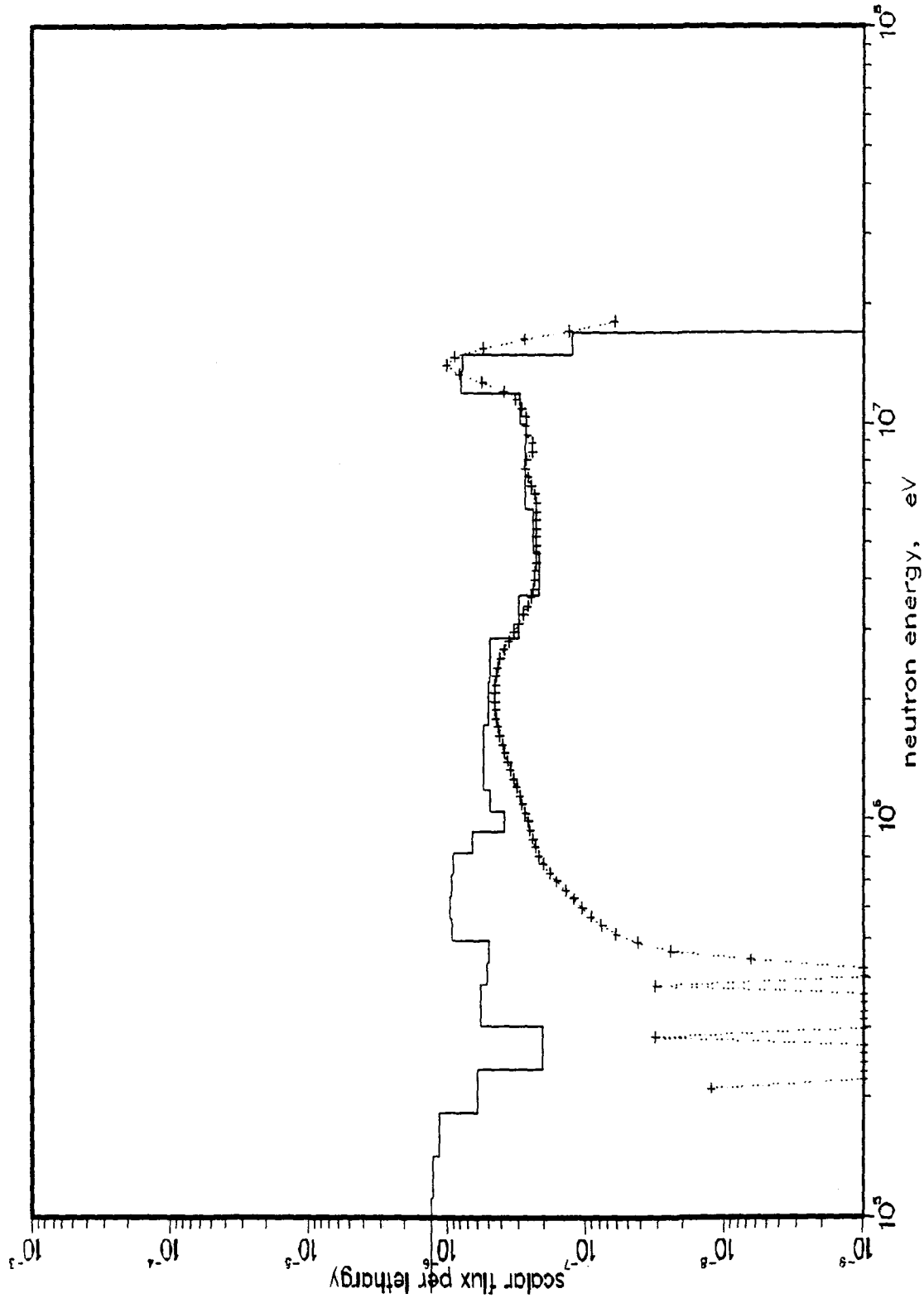

Fig. VII.23: Neutron Spectrum at Z = 50 cm
(REF System - Phase IIB)

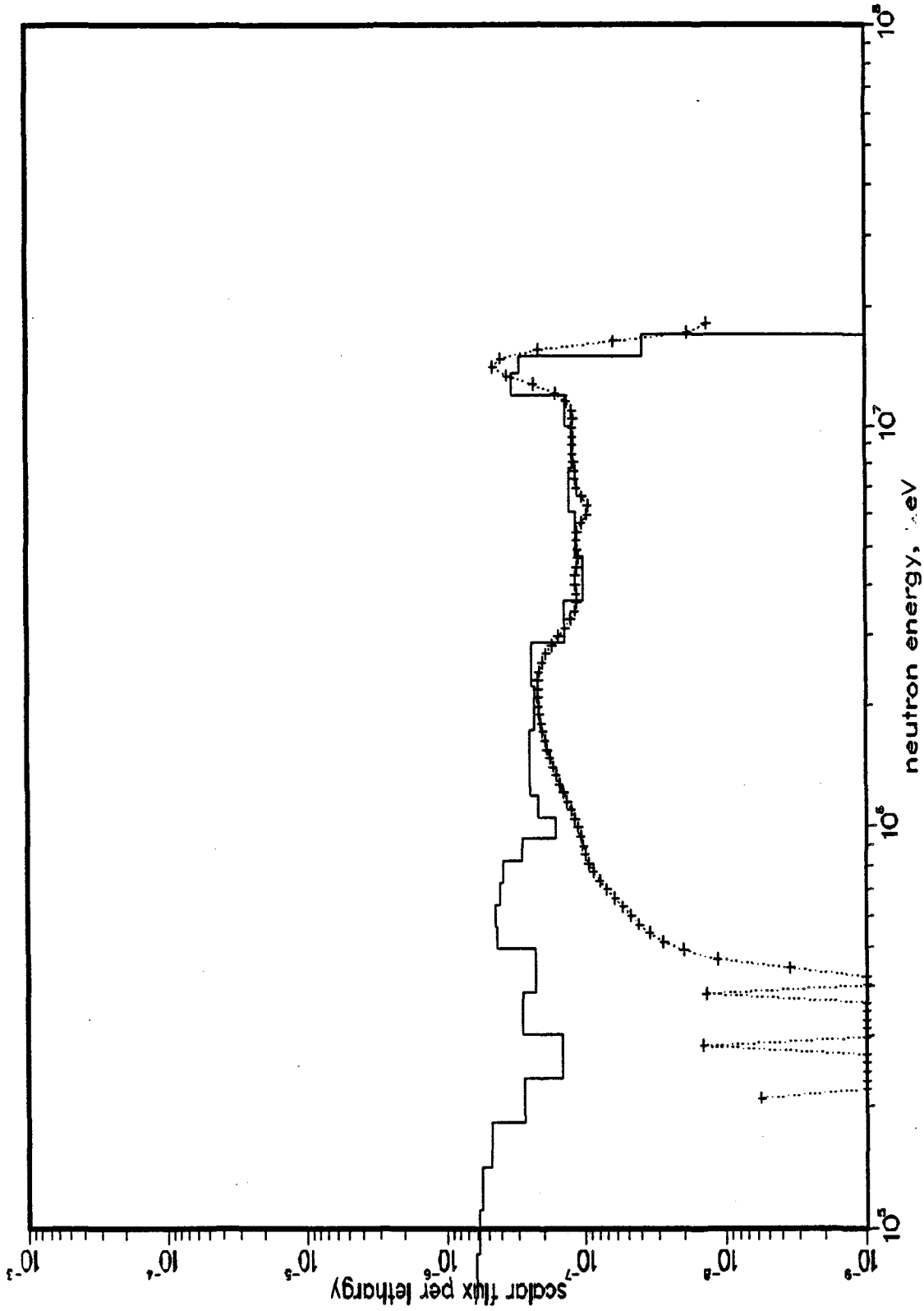

Fig. VII.24: Neutron Spectrum at Z = 60 cm
(REF System - Phase IIB)

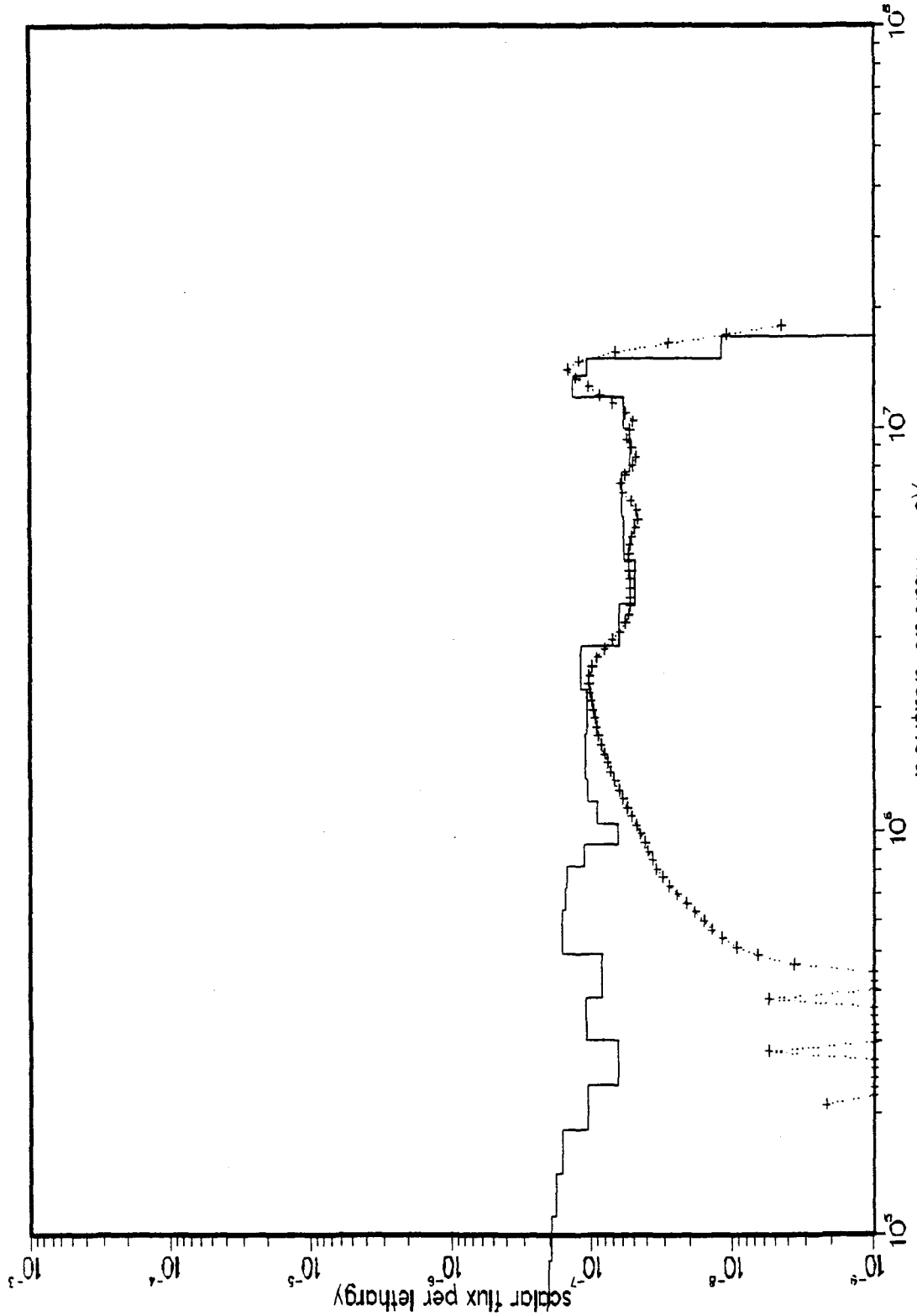

Fig. VII.25: Neutron Spectrum at Z = 70 cm
(REF System - Phase IIB)

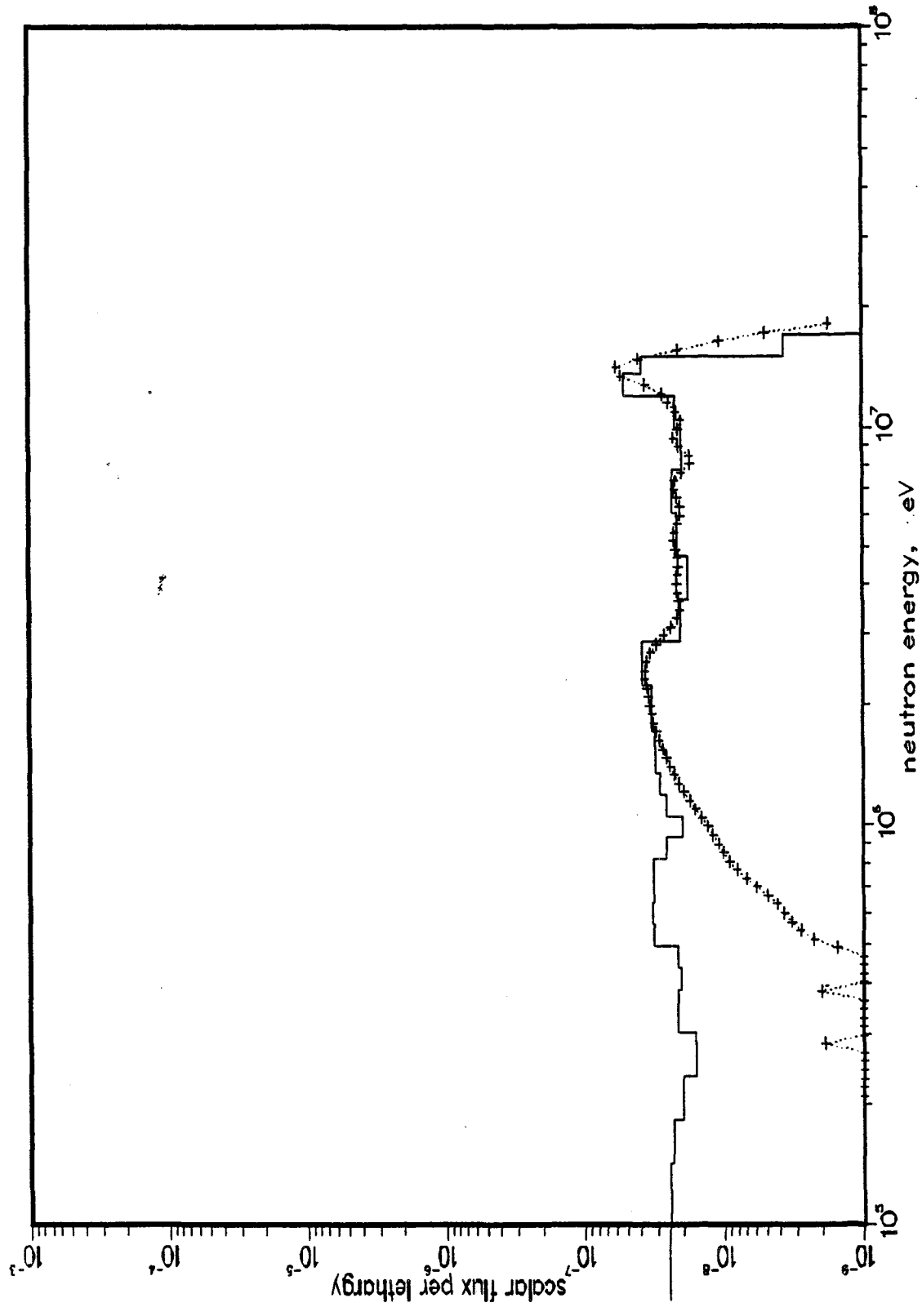

Fig. VII.26: Neutron Spectrum at Z = 80 cm
(REF System - Phase IIB)

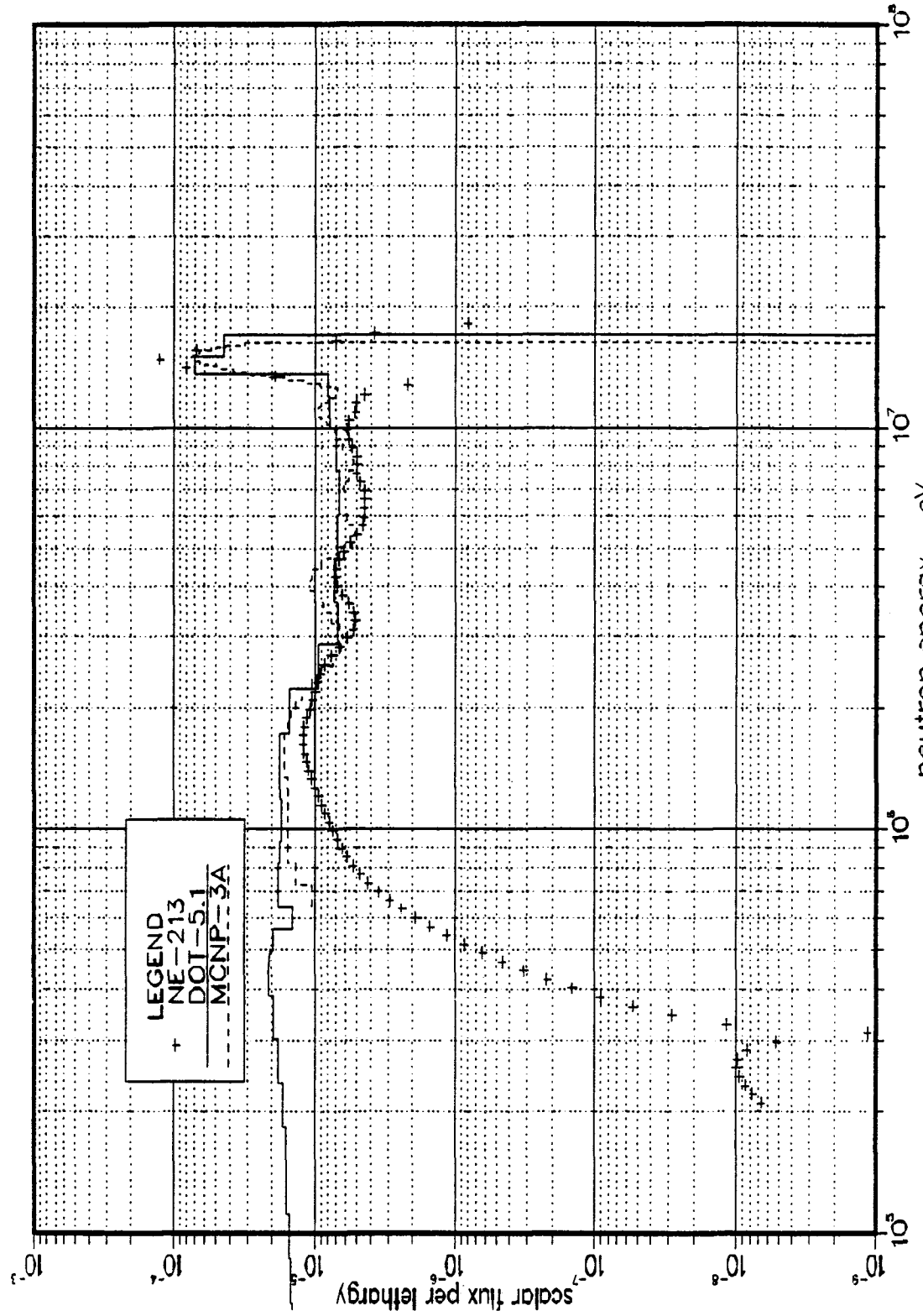

Fig. VII.27: Incident Neutron Spectrum at the Front Face (Z = 0) of the Test Assembly (BEFWFW System - Phase IIB)

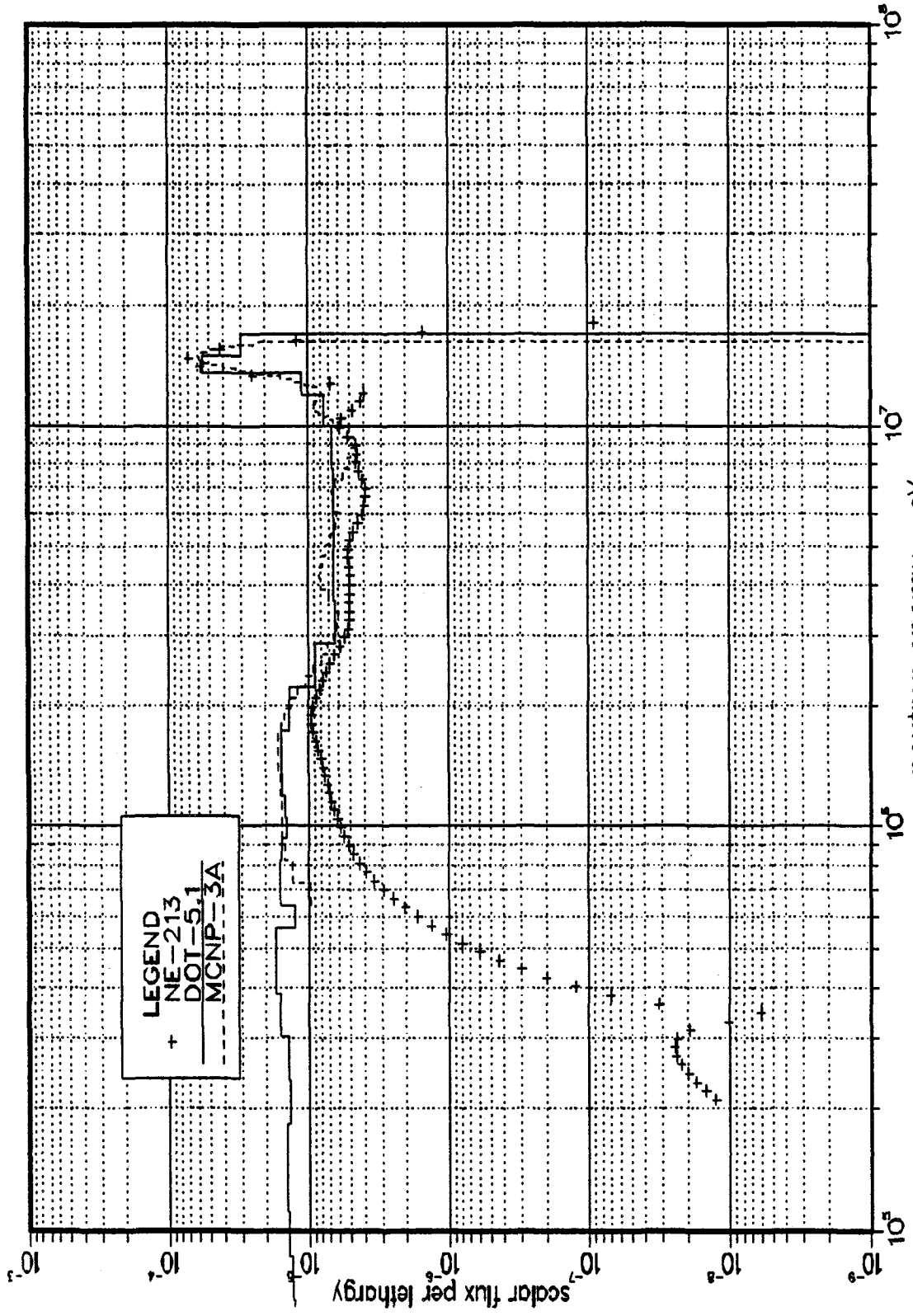

Fig. VII.28: Neutron Spectrum at Z = 2.5 cm
(BEFWFW System - Phase IIB)

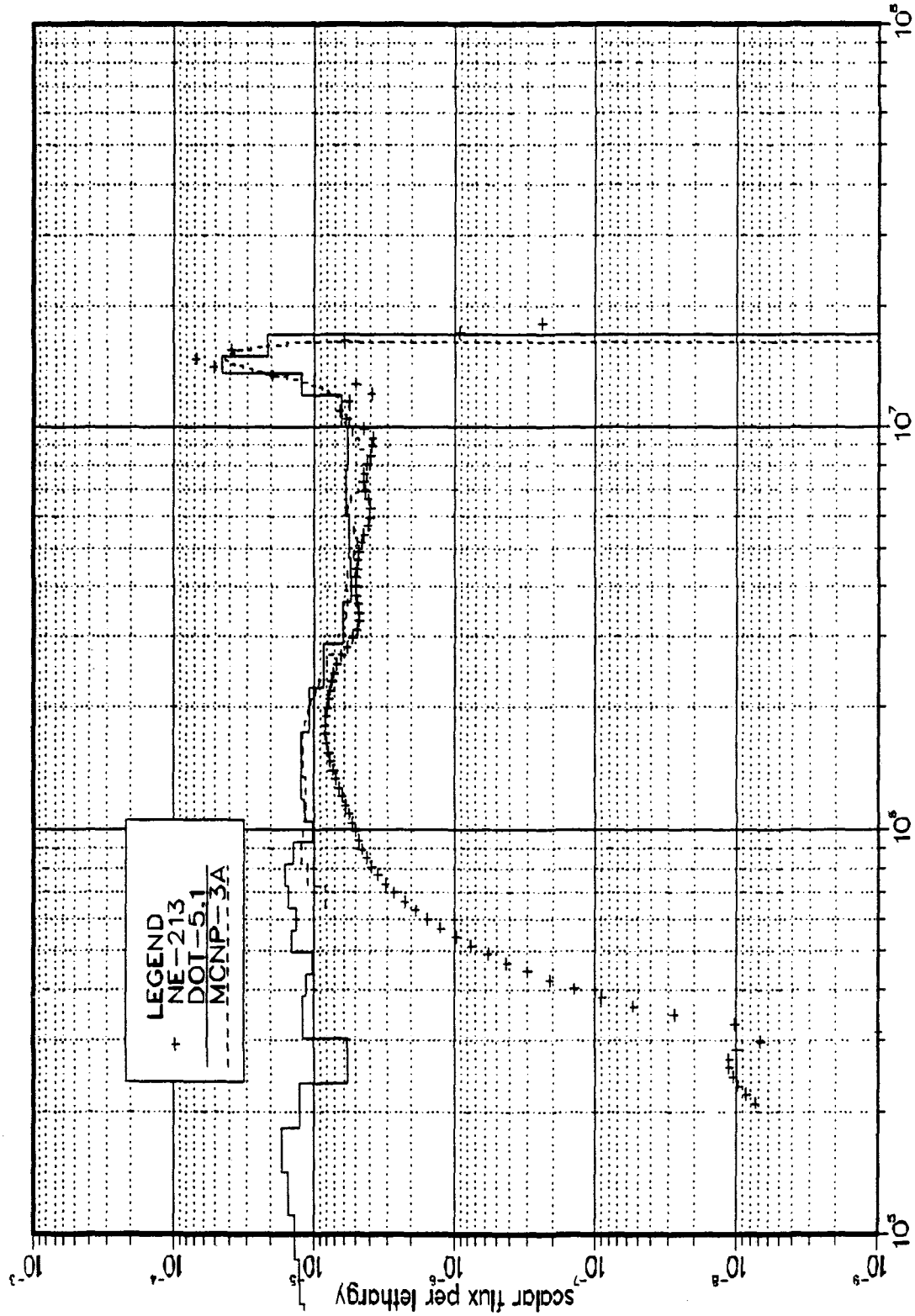

Fig. VII.29: Neutron Spectrum at Z = 5 cm
(BEFWFW System - Phase IIB)

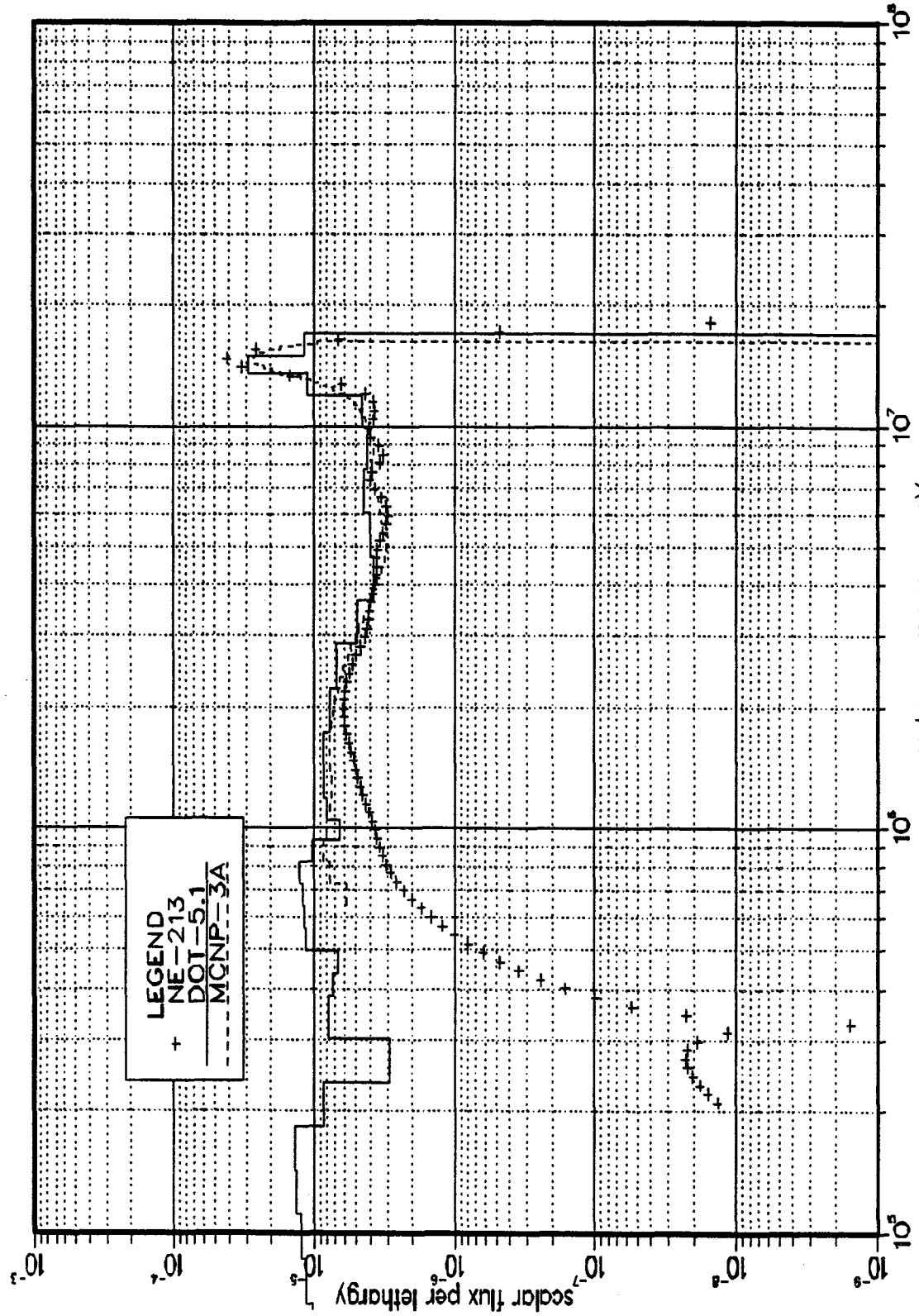

Fig. VII.30: Neutron Spectrum at Z = 10 cm
(BEFWFW System - Phase IIB)

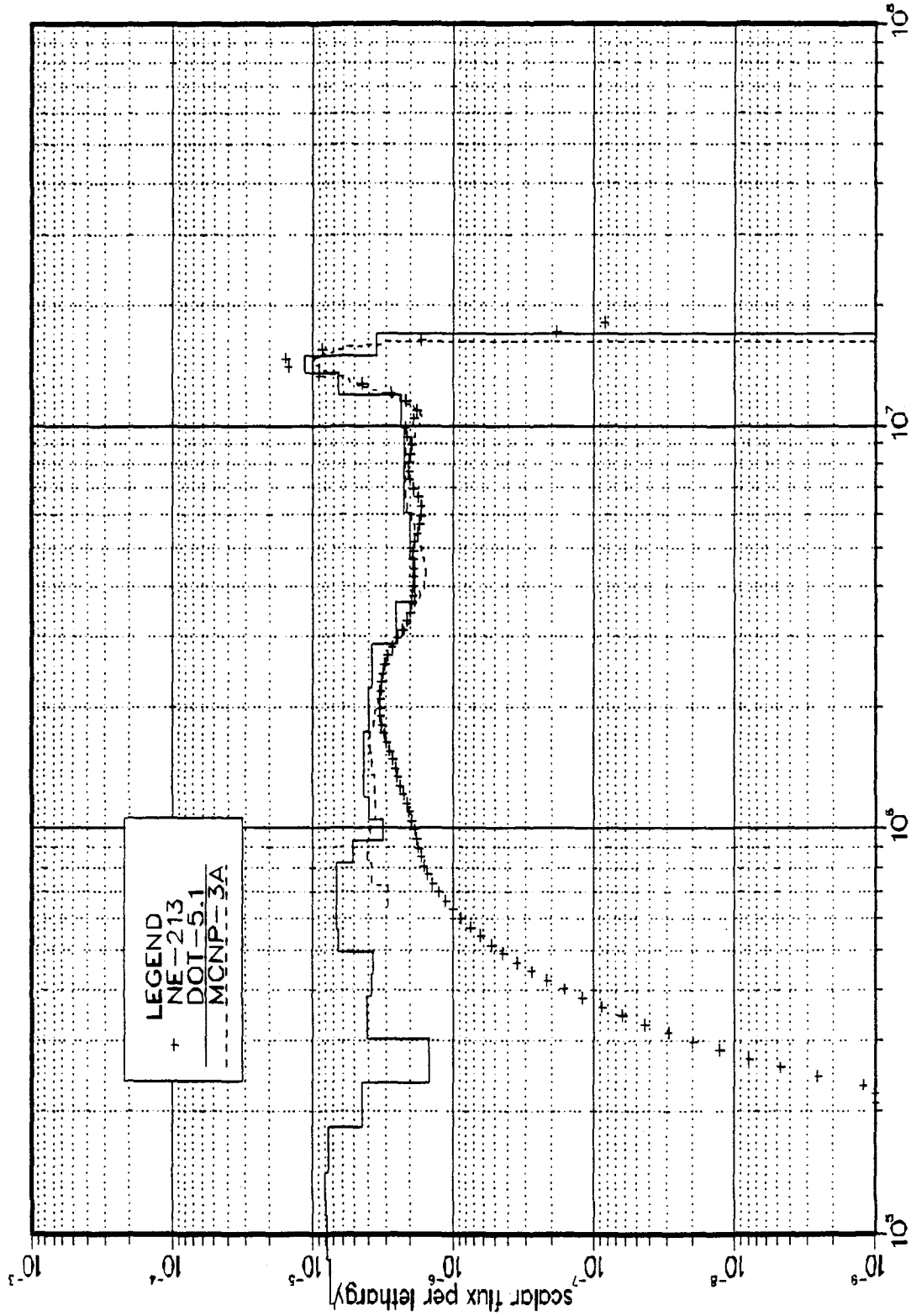

Fig. VII.31: Neutron Spectrum at Z = 20 cm
(BEFWFW System - Phase IIB)

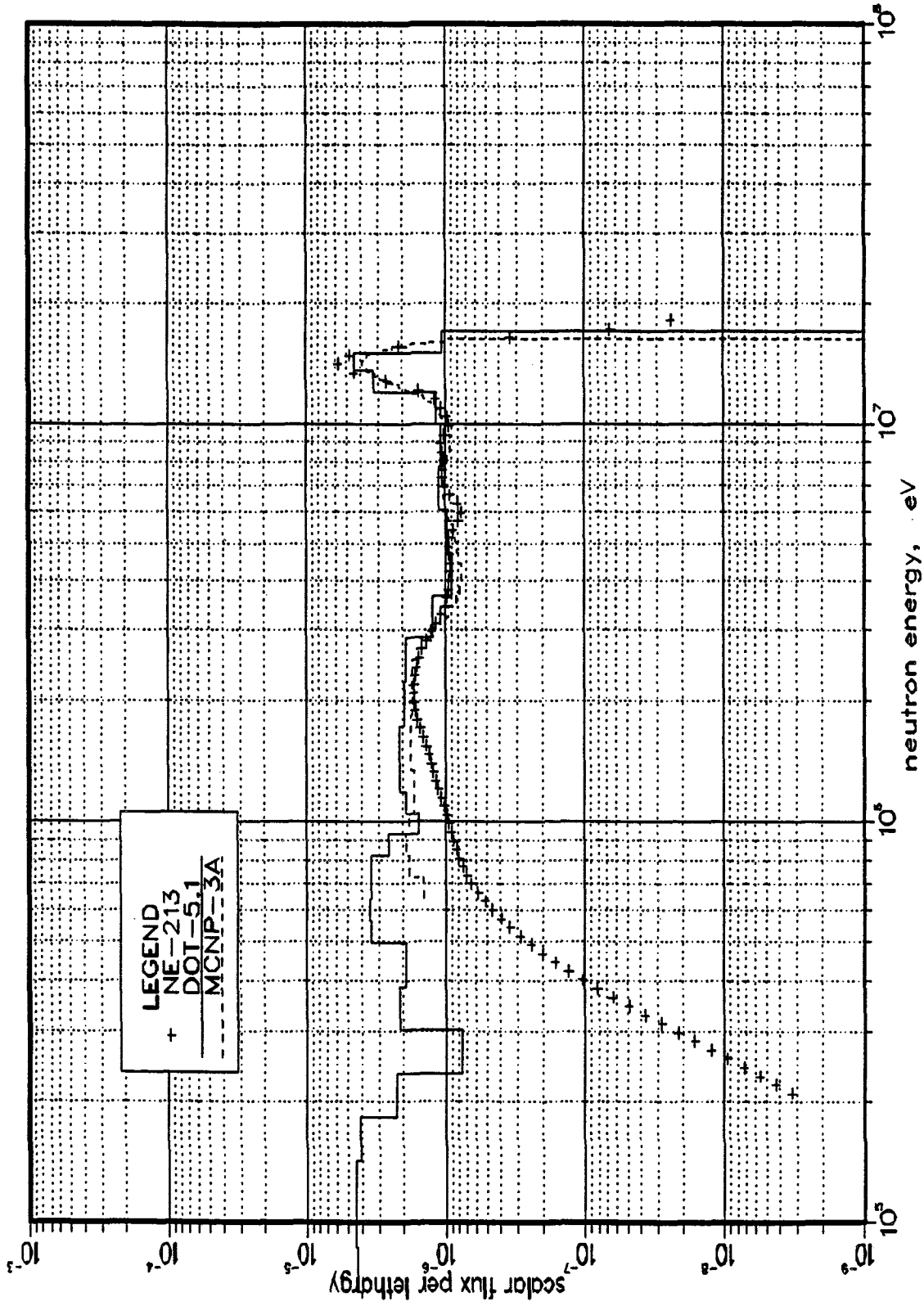

Fig. VII.32: Neutron Spectrum at Z = 30 cm
(BEFWFW System - Phase IIB)

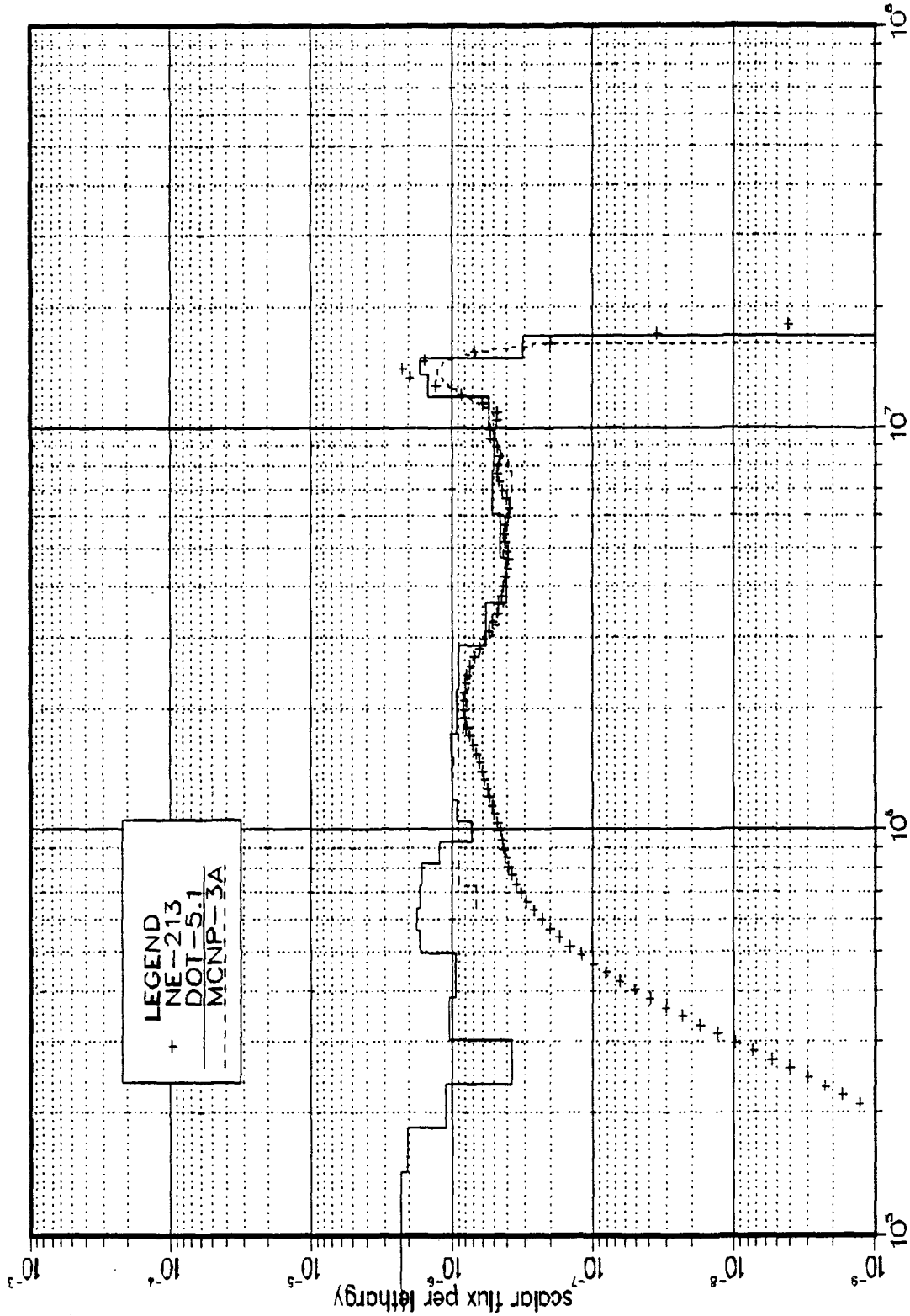

Fig. VII.33: Neutron Spectrum at Z = 40 cm
(BEFWFW System - Phase IIB)

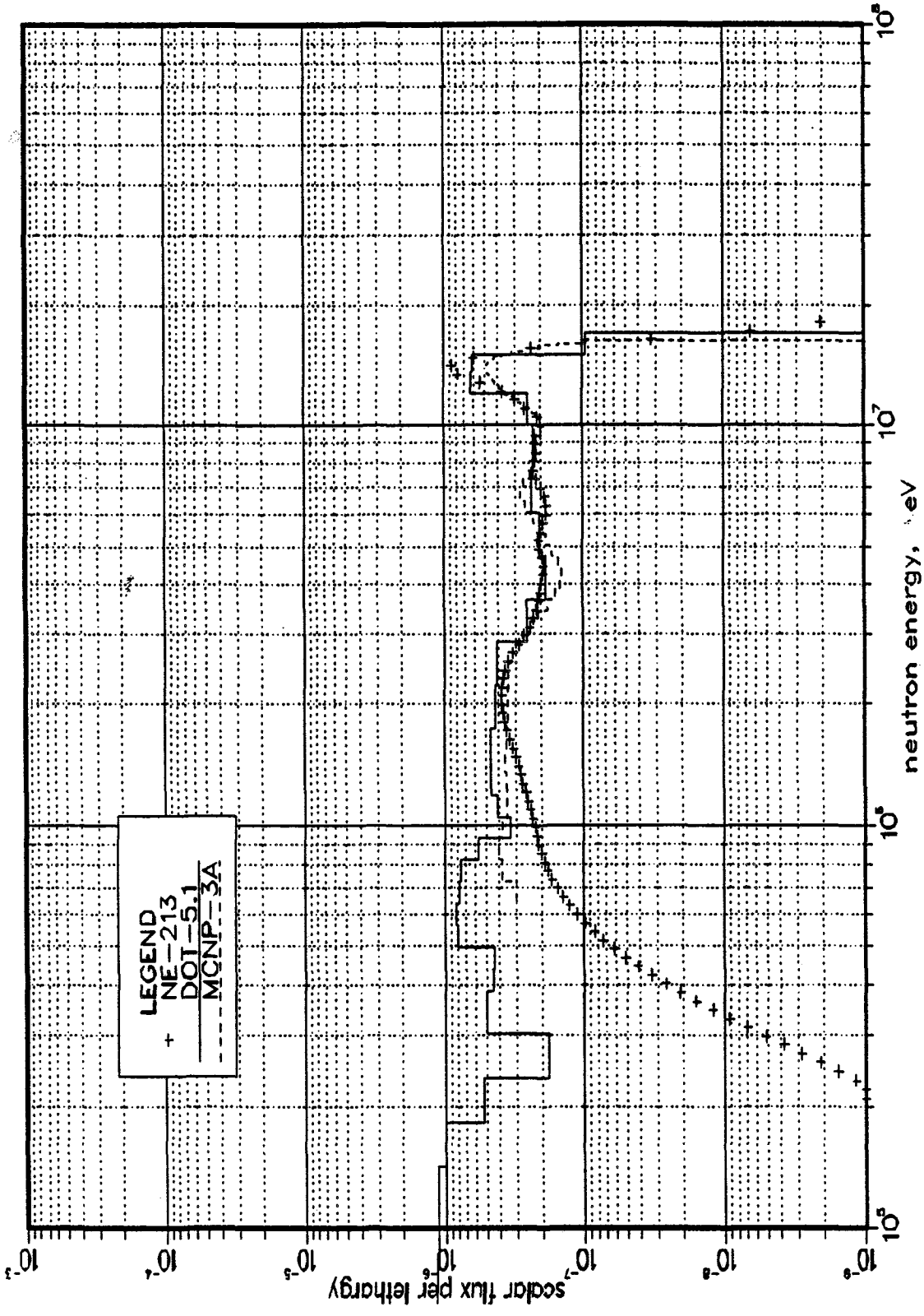

Fig. VII.34: Neutron Spectrum at Z = 50 cm
(BEFWFW System - Phase IIB)

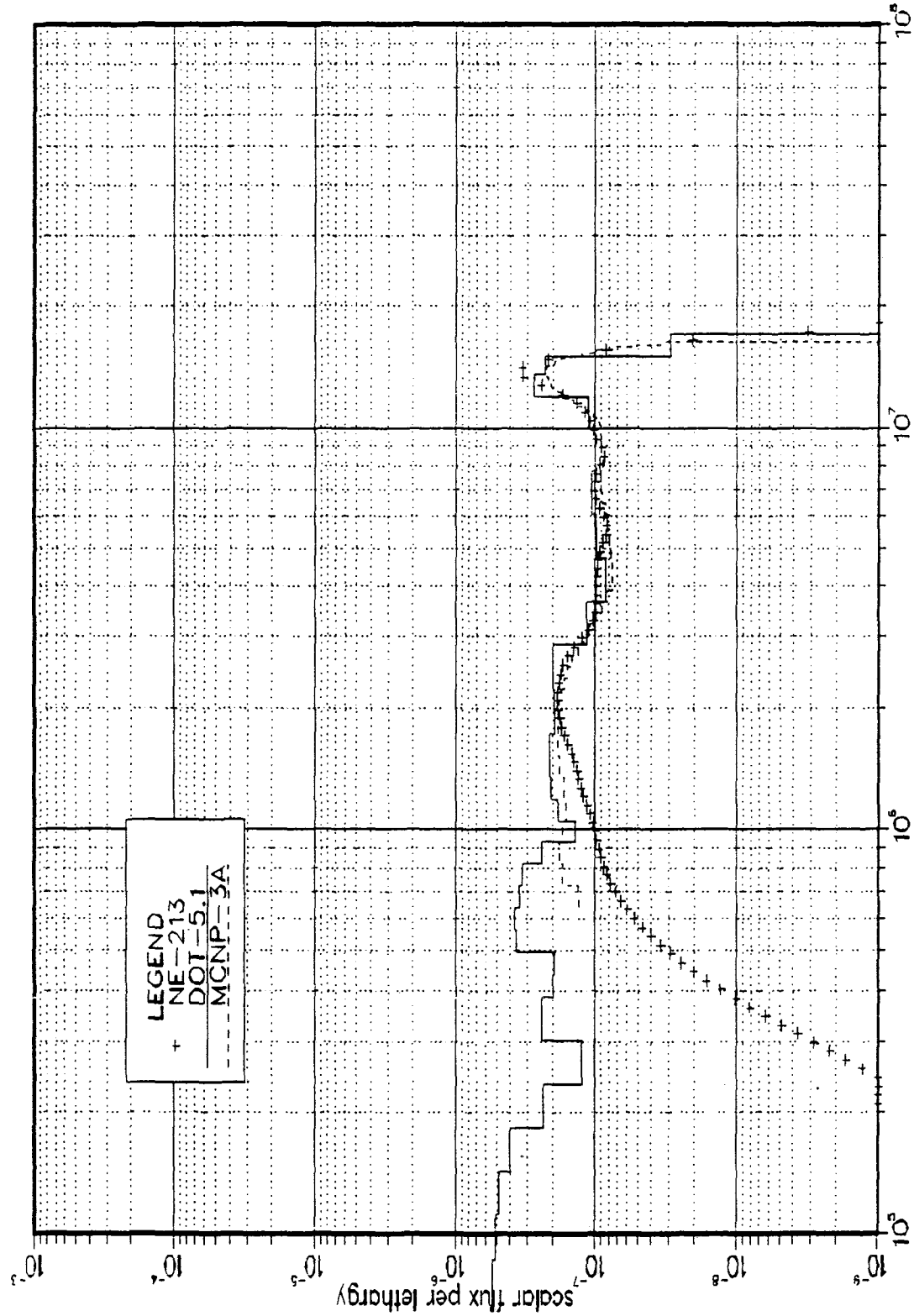

Fig. VII.35: Neutron Spectrum at Z = 60 cm
(BEFWFW System - Phase IIB)

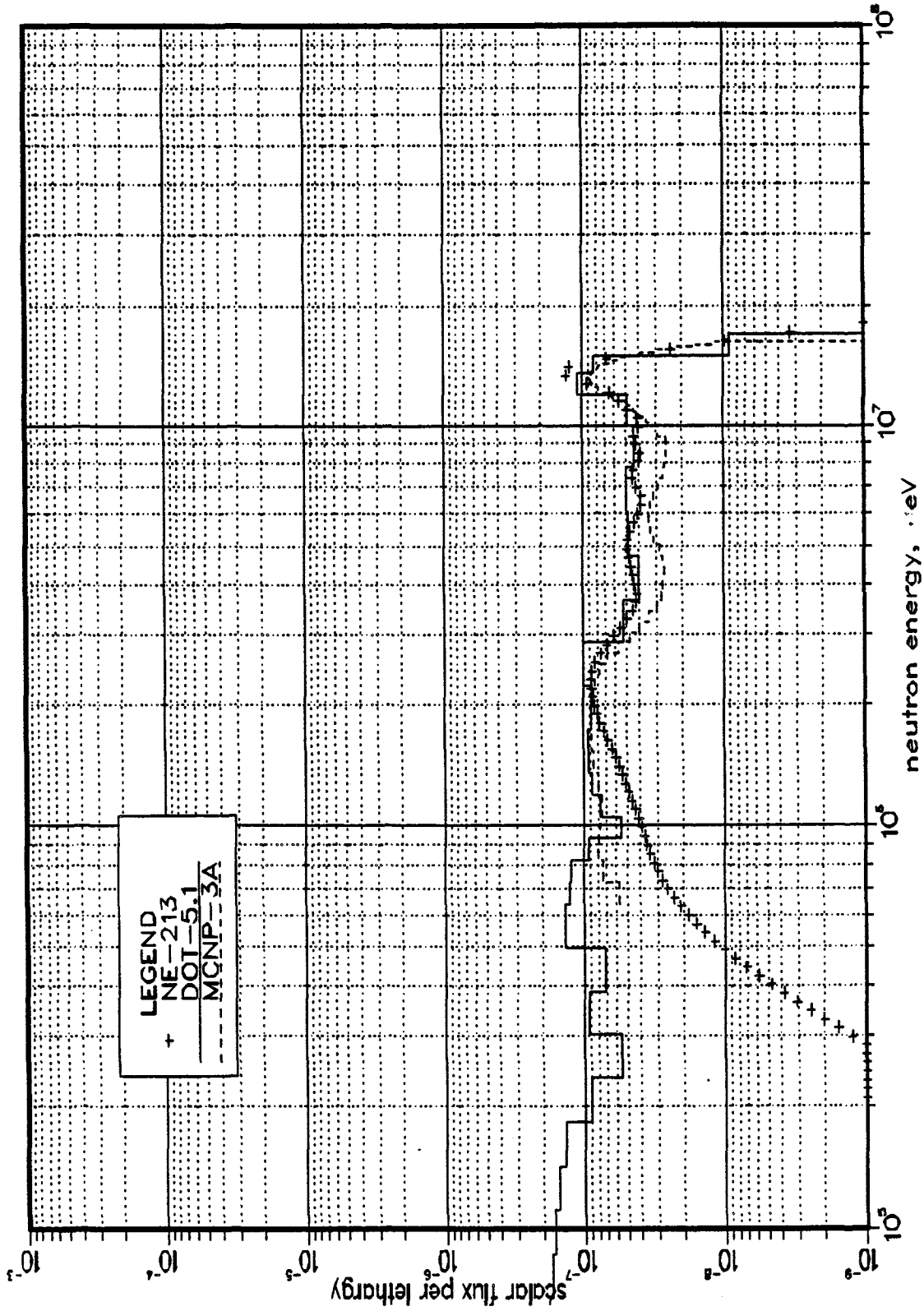

Fig. VII.36: Neutron Spectrum at Z = 70 cm
(BEFWFW System - Phase IIB)

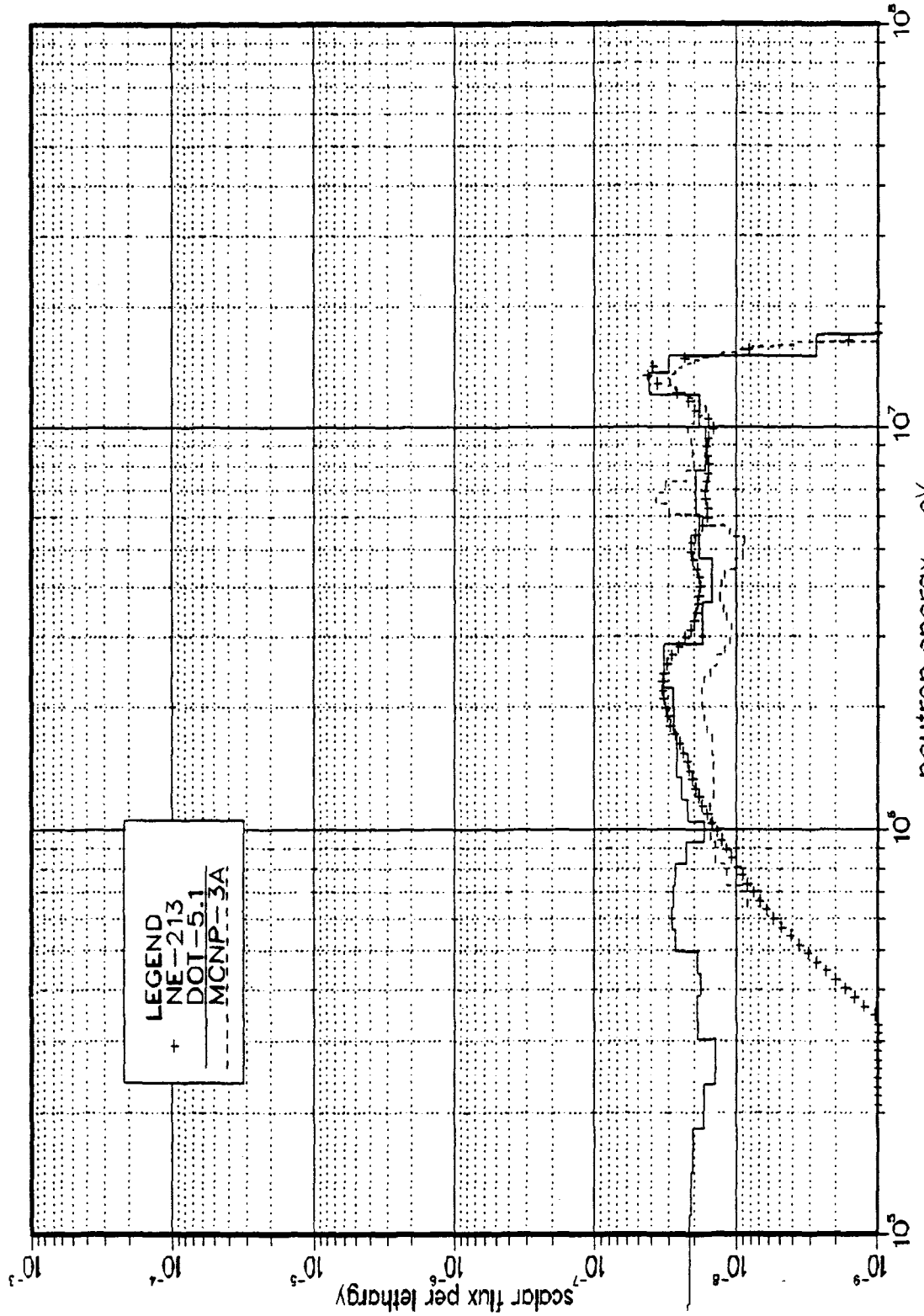

Fig. VII.37: Neutron Spectrum at Z = 80 cm
(BEFWFW System - Phase IIB)

Figs. VII.17 to VII.26 show a comparison between the calculated spectrum (by MCNP and DOT codes) and the measured one in the REF system of Phase IIB at depth Z = 0, 5, 10, 20, 30, 40, 50, 60, 70, and 80 cm from the front surface of the test assembly. Note from Fig. VII.17 the large low-energy component of the incident spectrum. Figs. VII.27 to VII.37 show the same comparison but in the Be-front system (W/FW,BEFWFW). Close comparison of the results contained in these figures, at each of the corresponding locations, reveals the following:

(1) The incident spectrum (at location Z = 0 cm) has larger low-energy component in the BEFWFW system as compared to the REF system of Phase IIB. This is due to the reflected neutrons from the front Be layer that are larger in number than neutrons reflected by the Li_2O material.

(2) The spectrum around the 14 MeV peak is underestimated at all locations in Phase IIB in both systems. This underestimation is more pronounced in Phase IIB than in Phase IIA. This could be due to the large amount of beryllium liner used in Phase IIB for which the total $^9Be(n,2n)$ cross-section is overestimated. This leads to underestimating the number of incident neutrons around the 14 MeV peak.

(3) The 14MeV peak at all locations is lower by 12 - 15% in the BEFWFW system than in the REF system due to the presence of the FW/Be front layer in the BEFWFW system.

(4) When Figs. VII.18 and VII.29 are compared it can be seen that at the location just behind the Be layer (Z = 5 cm), the emerged spectrum has larger component in the energy range 100 KeV - 2 MeV in the BEFWFW system than in the case of the REF system, as predicted by the MCNP calculations.

(5) The agreement between the DOT and the MCNP calculations is generally well, except at deeper locations (Z >50 cm) and in the Li_2CO_3 zone (see Fig. VII.36 and VII.37).

(6) As compared to the NE213 measurements, the spectrum in the energy range 1 MeV - 10 MeV, as predicted by both the MCNP and the DOT codes, is larger than measurements in both the REF and the BEFWFW system and that the overestimation is more pronounded in the BEFWFW system than in the REF system, particularly inside and behind the Be layer. This overestimation tends to be lessened at deeper locations in both systems. This observation is consistent with Oyama and Maekawa's experiment on the Be-slab, as discussed earlier. In the REF system, neutrons that interact with the Be liner and reflected to the Li_2O assembly their number is overpredicted in the energy range 1 - 10 MeV. This is

also true in the BEFWFW system where the overprediction is even larger due to the front Be layer in that system.

As for the PRC measurements, the agreement with the calculations is fairly good in the energy range 30 KeV - 100 KeV, as shown in Figs. VII.38 and VII.39 at the locations Z = 10, and 40 cm in the BEFWFW system. This is consistent with the results in Phase IIA (see Section VII.1 above) where it was shown that good agreement with the PRC measurements is obtained in the energy range 50 - 80 KeV. The calculations give larger spectrum in the energy range 2 - 30 KeV, as it is also the case in Phase IIA.

Generally speaking, the agreement between the calculated spectrum and the measurements is more reasonable in the case of the PRC measurements than in the case of the NE213. The 14 MeV peak is underpredicted, particularly in Phase IIB, which could be related to an overestimation in the ^{9}Be(n,2n) cross-section. Also, the spectrum is overestimated in the energy range 1 - 10 MeV in Phase IIB where large amount of beryllium is used as liner/front layer, and again, this could be related to the secondary energy/angular distribution of neutrons emitted from the ^{9}Be(n,2n) reactions. In the next Section, three evaluations for the cross-sections of beryllium were used to investigate the impact on tritium production, reaction rates, and in-system neutron spectrum.

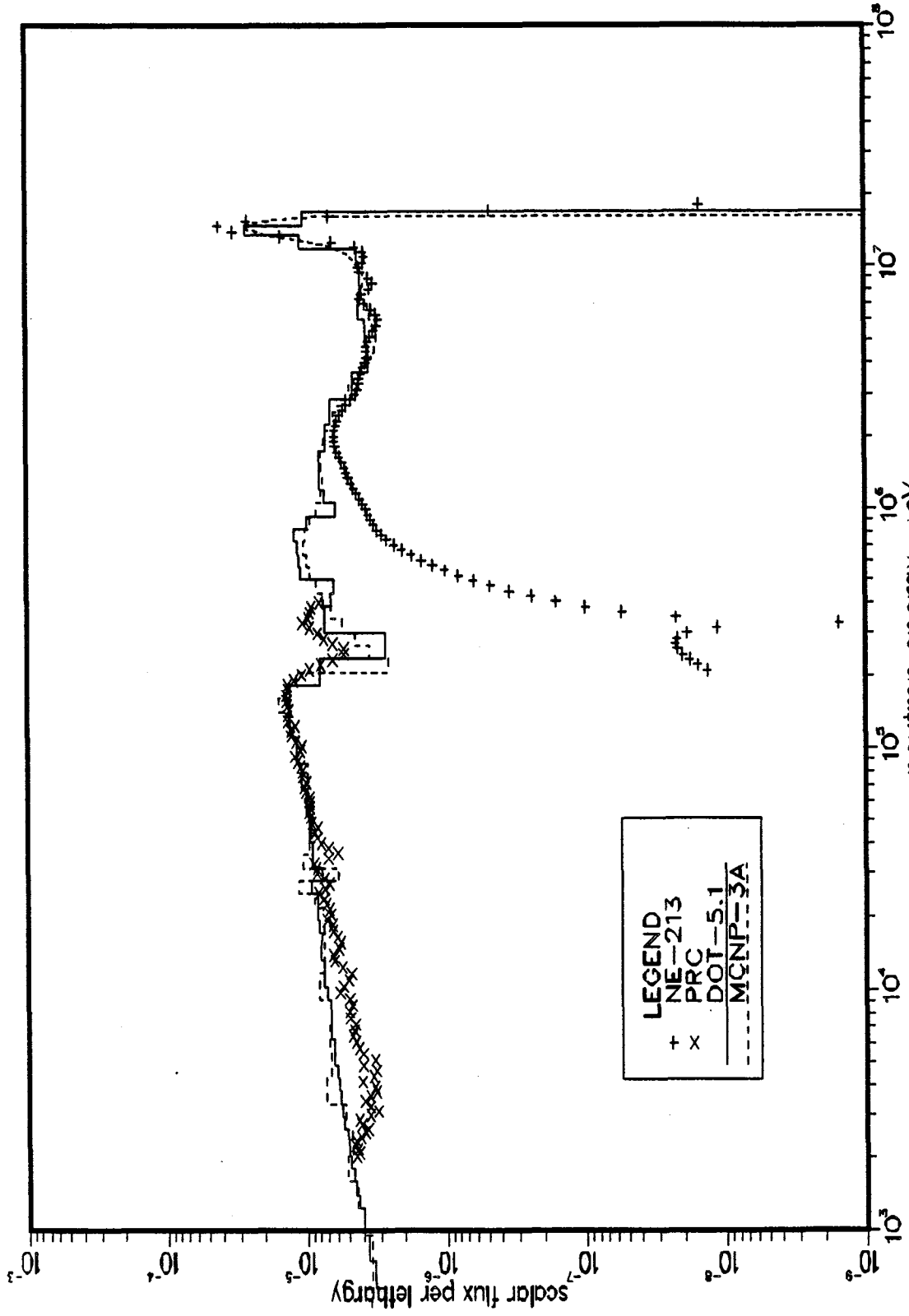

Fig. VII.38: Neutron Spectrum at Z = 10 cm
(BEFWFW System - Phase IIB, NE213 and PRC Measurements)

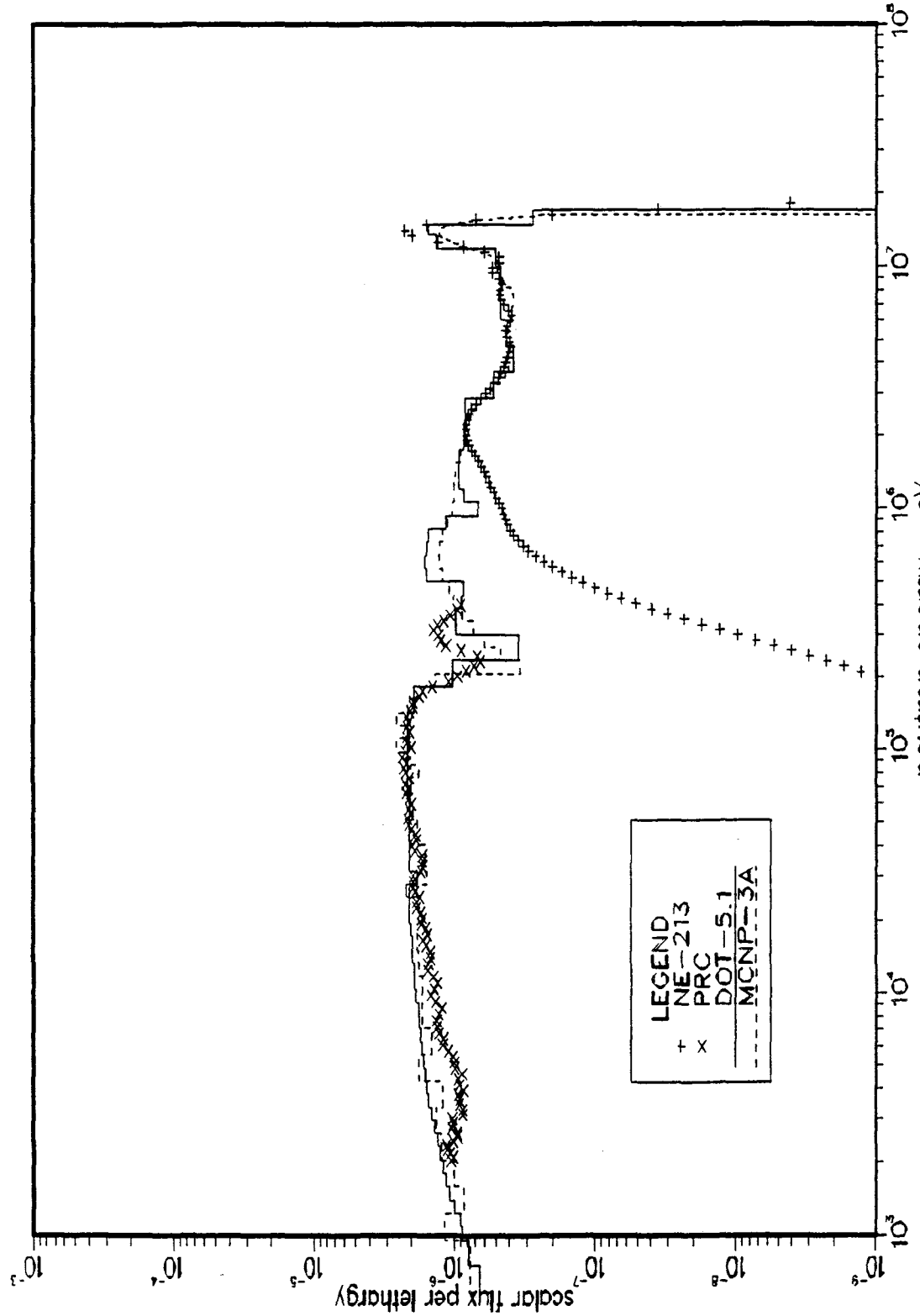

Fig. VII.39: Neutron Spectrum at Z = 40 cm
(BEFWFW System - Phase IIB, NE213 and PRC Measurements)

VIII. Impact of Several Evaluations for the Beryllium Cross-Section on the Neutronics Performance in Phase IIB Experiments

VIII.1 Introduction

Three evaluations for the beryllium cross-sections were used to study their impact on the neutronics characteristics in the beryllium-front system (W/FW, BEFWFW) of Phase IIB. This particular system was chosen for the present study because there is an appreciable amount of beryllium (5 cm-thick) covering the inner surface of the Li_2CO_3 enclosure in addition to a Be layer (5 cm-thick) placed in front of the Li_2O test assembly as shown in Fig. I.3. The neutronics characteristics studied are the tritium production rate (from ^6Li and ^7Li), several activation reactions, and in-system neutron spectrum. The three evaluations are the ENDF/B-V evaluation, the LANL evaluation [performed by Young and Stewart, see ref (27)], and the ENDF/B-VI evaluation. These evaluations are denoted ENDF/B5, LANL(Be), and ENDF/B6 in the present study. As pointed out in Section II, the LANL evaluation was used in both the MCNP and DOT results discussed in this report. The results from the other two evaluations were used for intercomparison. This intercomparison is based on the DOT5.1 calculations performed in the 2-D R-Z geometry shown in Fig. II.7 (with a FW) using the 80-neutron group library in P_5S_8 approximation. Except for beryllium, the cross-sections of other materials are based on ENDF/B-V.

VIII.2 The Status of Beryllium Data

As was discussed in Section V, the integrated (over energy and angle) cross-section for the $^9Be(n,2n)$ reaction is known to a better accuracy than the secondary energy (SED) and Angular (SAD) distributions of neutrons emitted from this reaction. This has direct impact on the neutronics characteristics in the test assembly since subsequent interactions with various nuclides of the transport media depend on the incident neutron energy and direction of these secondary neutrons. In ENDF/B-V, the $^9Be(n,2n)$ cross-section is represented by four inelastic excitation levels in $^{9*}Be$ at 1.68, 2.43, 6.76, and 11.28 MeV (see Fig. V.1), each having zero width and with the energy-angle correlation between the emitted neutrons ignored. In the LANL calculation, this cross-section is represented by 33 inelastic levels that were chosen to fit the neutron emission spectrum measurements of Drake, et.al[38]. The $^9Be(n,2n)$ cross-section is then based on data for a cluster of real levels near E_x = 2.429 MeV and 32 excitation energy bins to represent the (n,2n) continuum levels. The energy-angle correlation for the secondary neutrons was considered in this evaluation while it was ignored in ENDF/B-V, as mentioned earlier. The total

integrated cross-section for the $^{9}Be(n,2n)$ reaction is very similar in ENDF/B-V and LANL evaluation; the difference being in the SED/SAD distribution of the secondary neutrons. In ENDF/B-VI, improvement has been made in the total integrated $^{9}Be(n,2n)$ cross-section, mainly being reduced by ~ 10 - 15% at high incident neutrons energies. Also, the energy/angle correlation for the secondary neutrons was considered in this evaluation and is based on ENDL-86 evaluation performed by Perkins et al.[45] at Lawrence Livermore National Laboratory (LLNL).

Figs. VIII.1 and VIII.2 show the total integrated cross-section for the $^{9}Be(n,2n)$ reaction processed [in 30 neutron group of MATXS5 group structure[21]] from ENDF/B-V, LANL, and ENDF/B-VI (LLNL) evaluations. In the case of LANL evaluation, two processing systems were used, namely, the AMPX processing system[53], and the NJOY processing system[22]. Fig. VIII.2 shows the cross-section at high incident energies (above 2 MeV). Notice for this figure the following:

(1) The ENDF/B-V and LANL data (processd either with AMPX or NJOY processing systems) as very similar

(2) The LLNL data (ENDF/B-VI) are lower than ENDF/B-V and LANL data (by ~ 10 - 15%), as pointed out earlier.

As for the SED, Figs. V-11 to V.13 show this distribution for several incident energies (incident energy group in 30 -group structure) for the three evaluations. As shown, the SED in LLNL evaluation does not extend down below ~ 1 KeV while the LANL evaluation extends down below ~ 1 KeV, but the cross-section in this energy range is negligible. However, in the ENDF/B-V evaluation, the SED extends down to very low energies.

VIII.3 Impact on In-System Neutron Spectrum

The neutron spectrum at five locations was examined with the three evaluations in the BEFWFW system, and the intercomparison to the NE213 measurements is shown in Figs. VIII.3 to VIII.7. These locations are at depth Z = 1.15, 3.68, 6.21, 11.27, and 31.51 cm. The first two locations are inside the front Be layer while the third is at 1.21 cm behind this layer. The following could be observed from these figures:

(1) At the five locations selected, the 14 MeV peak is much smaller than the measured value obtained by the NE213 detector.

(2) The 14 MeV peak obtained by the ENDF/B6 evaluation is larger than that obtained by the ENDF/B5 and LANL evaluations where this peak is basically the same.

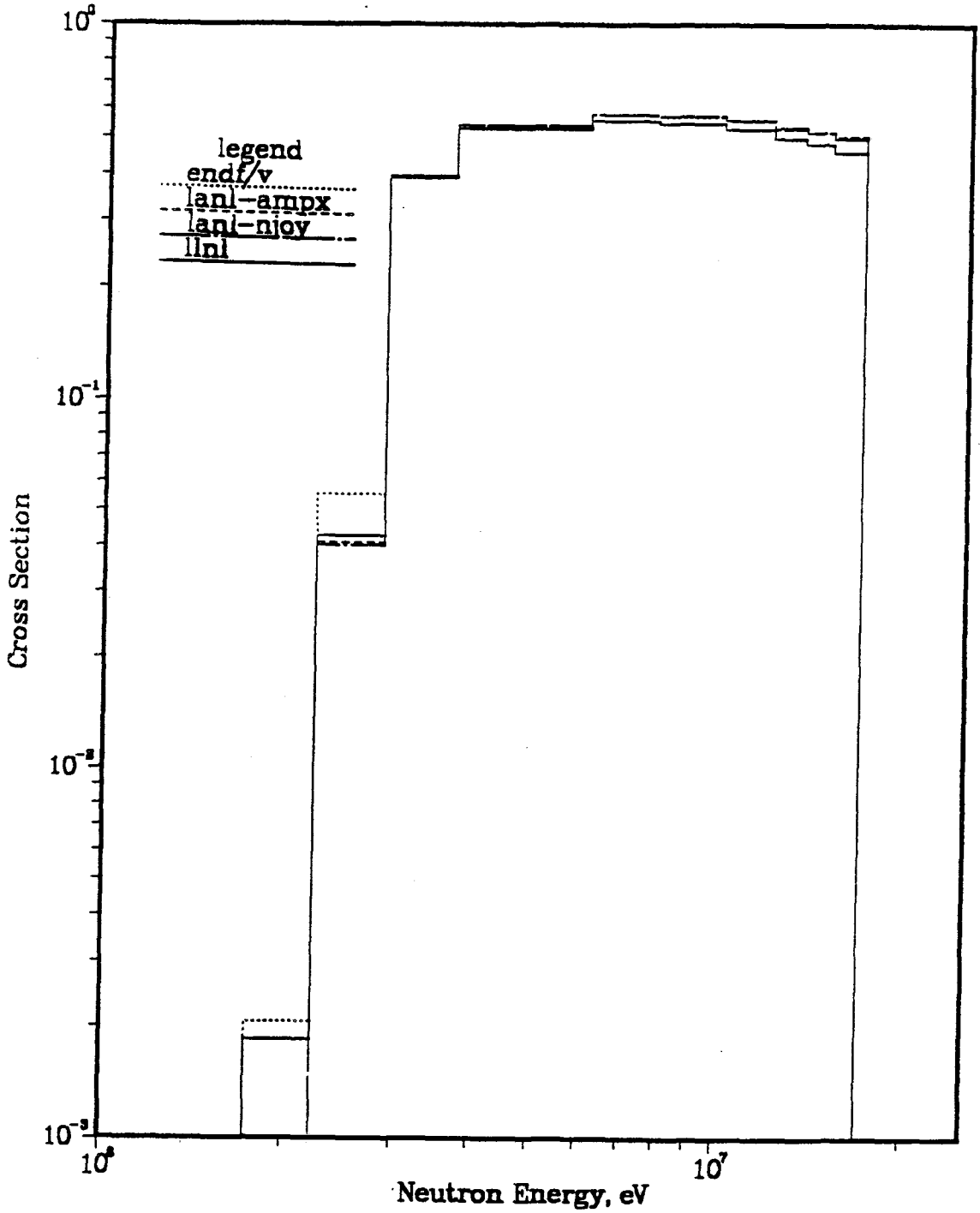

Fig. VIII.1: Processed ^{9}Be(n,2n) Cross-Section with Various Evaluations

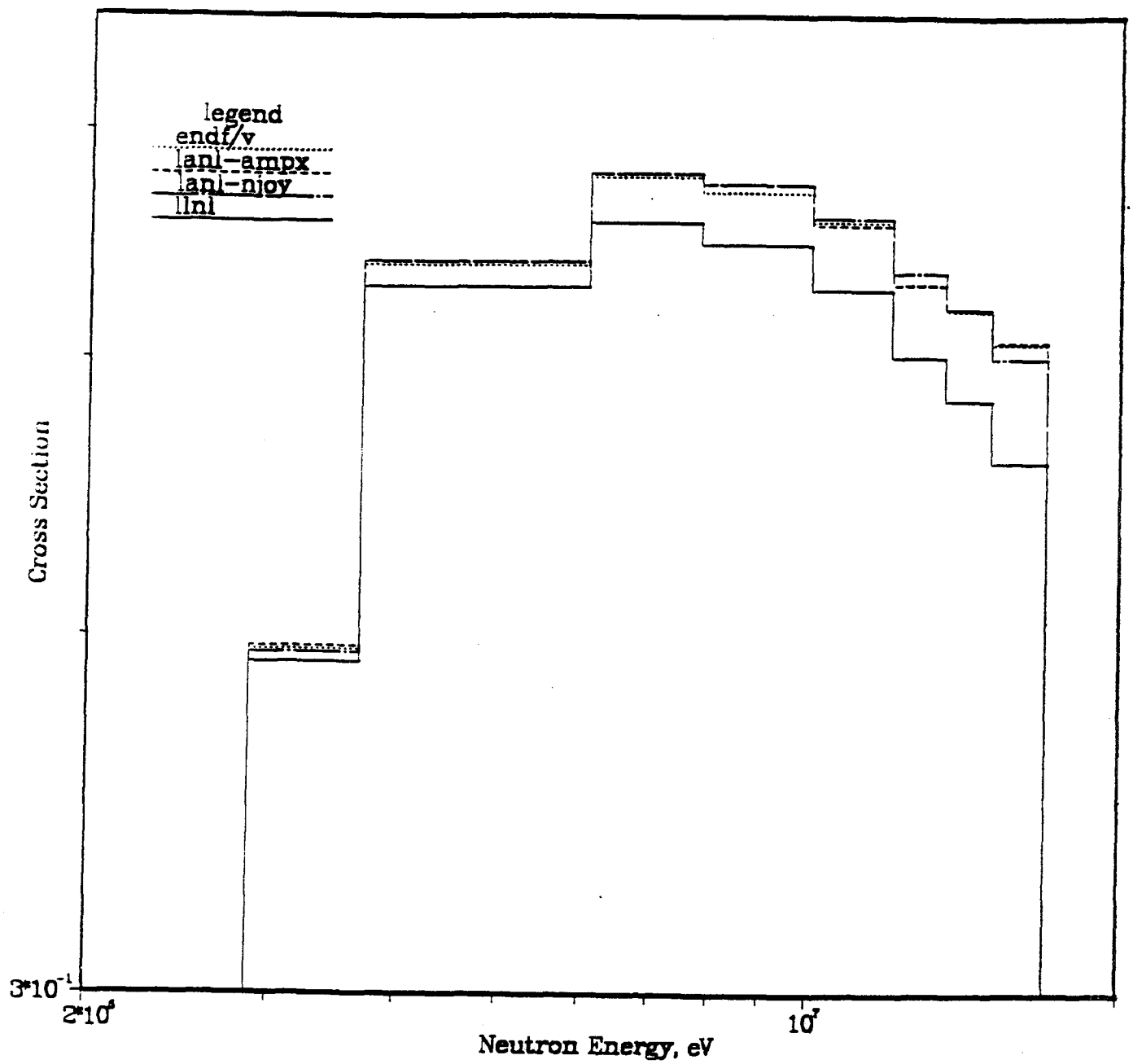

Fig. VIII.2: Processed ^{9}Be(n,2n) Cross-Section with Various Evaluations (Ein > 2 x 10^{6}eV)

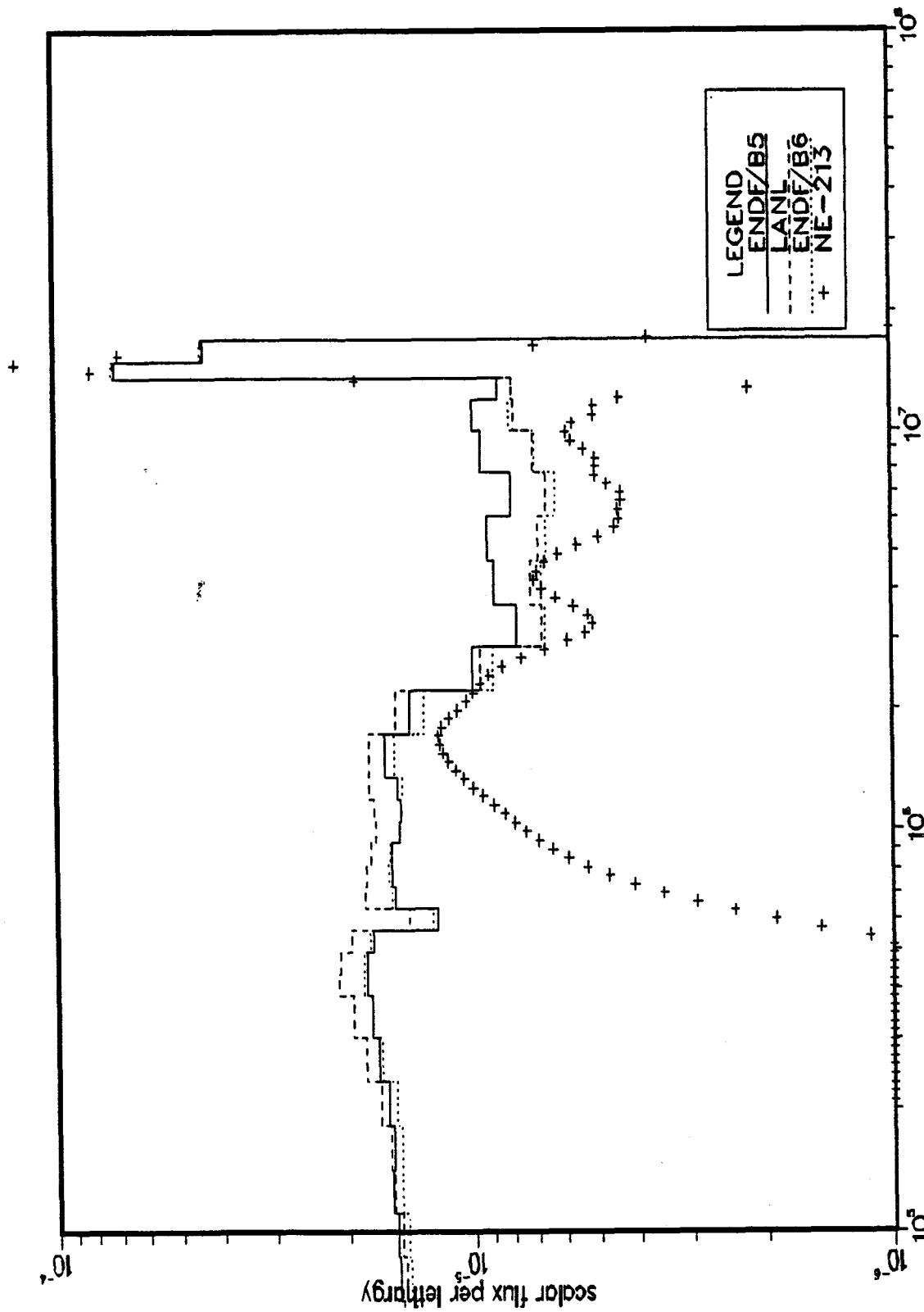

Fig. VIII.3: Neutron Spectrum (DOT5.1) at Z = 1.15 cm with Various Be Evaluations (BEFWFW System - Phase IIB)

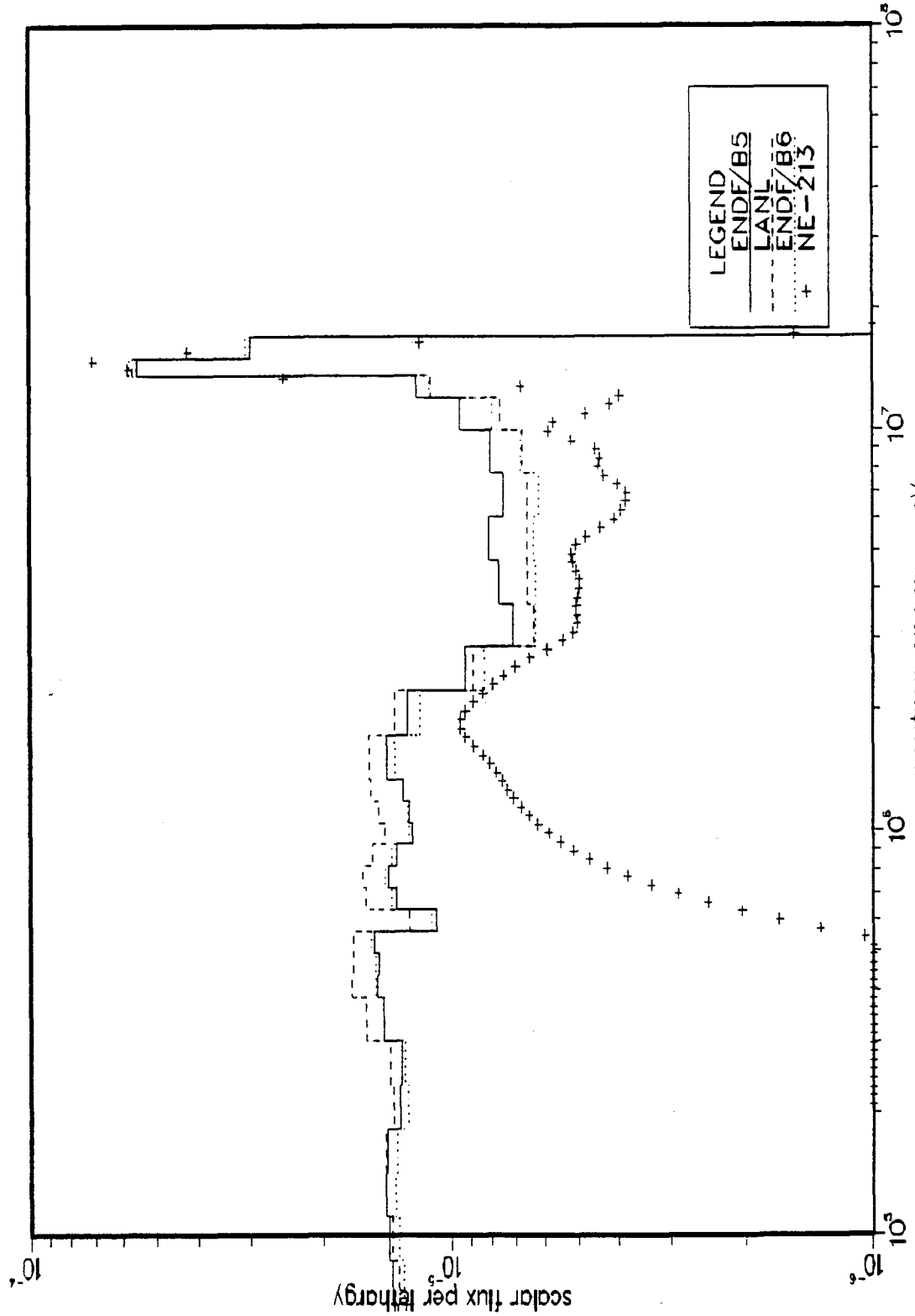

Fig. VIII.4: Neutron Spectrum (DOT5.1) at Z = 3.68 cm with Various Be Evaluations (BEFWFW System - Phase IIB)

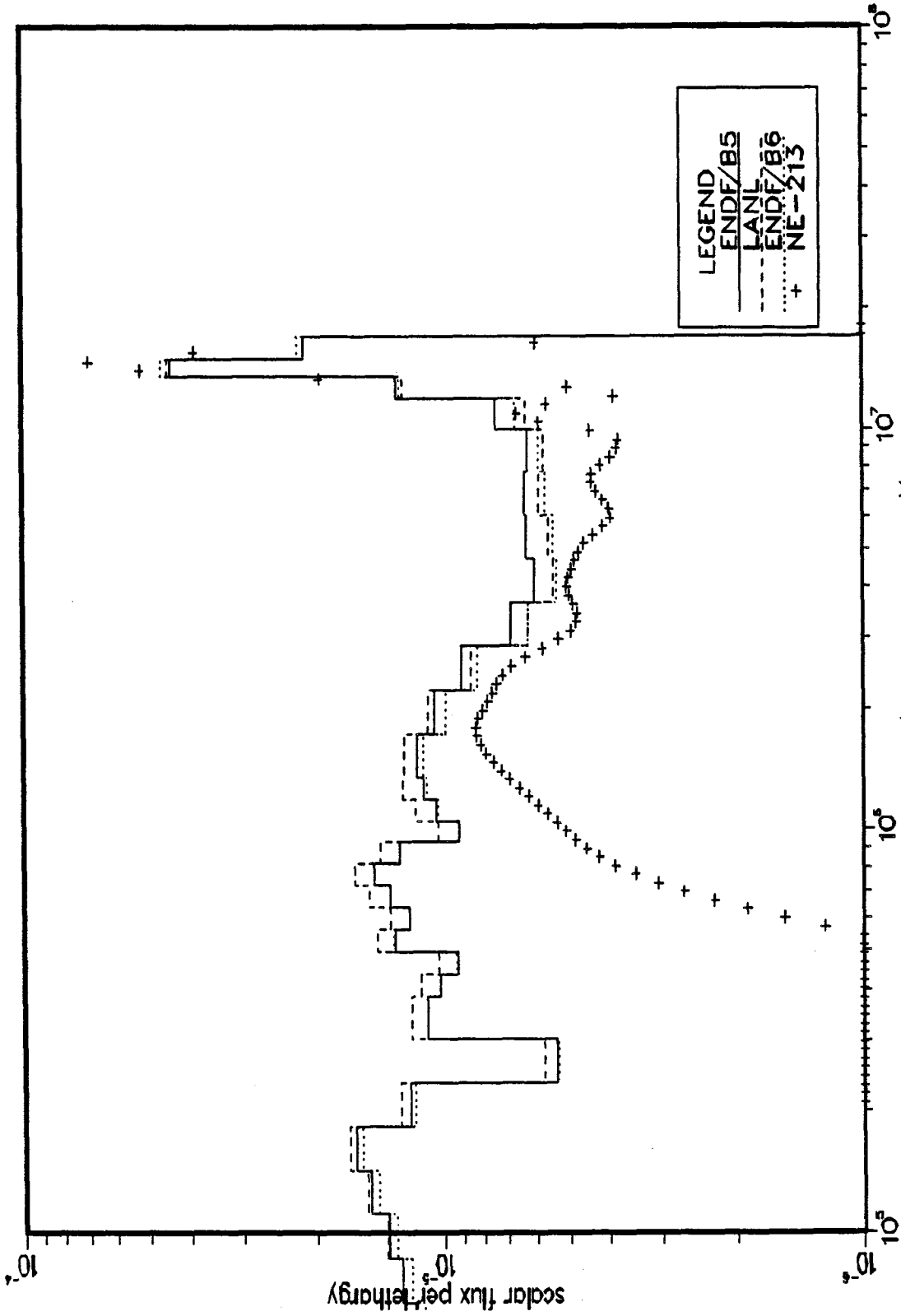

Fig. VIII.5: Neutron Spectrum (DOT5.1) at Z = 6.21 cm with Various Be Evaluations (BEFWFW System - Phase IIB)

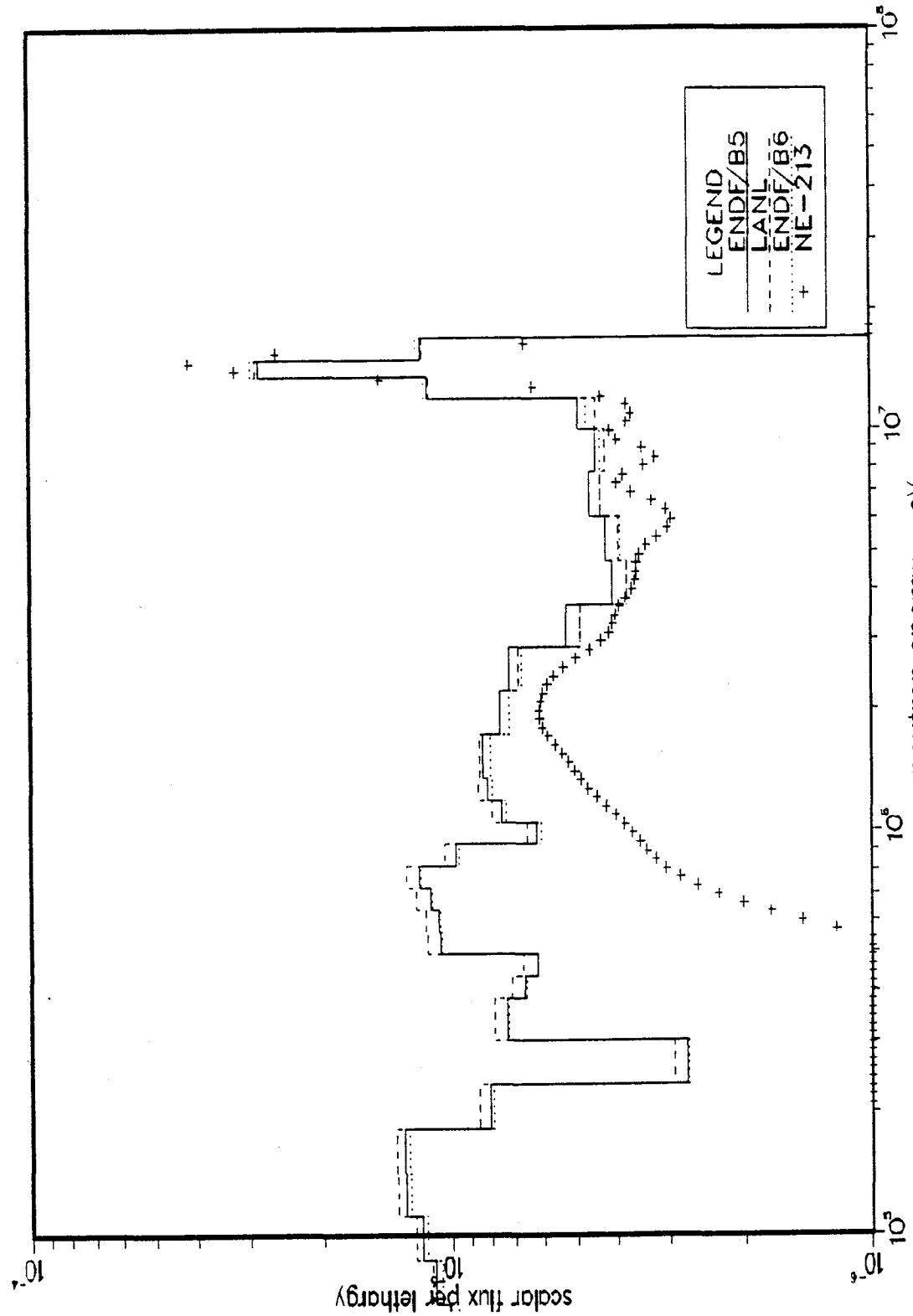

Fig. VIII.6: Neutron Spectrum (DOT5.1) at Z = 11.27 cm with Various Be Evaluations (BEFWFW System - Phase IIB)

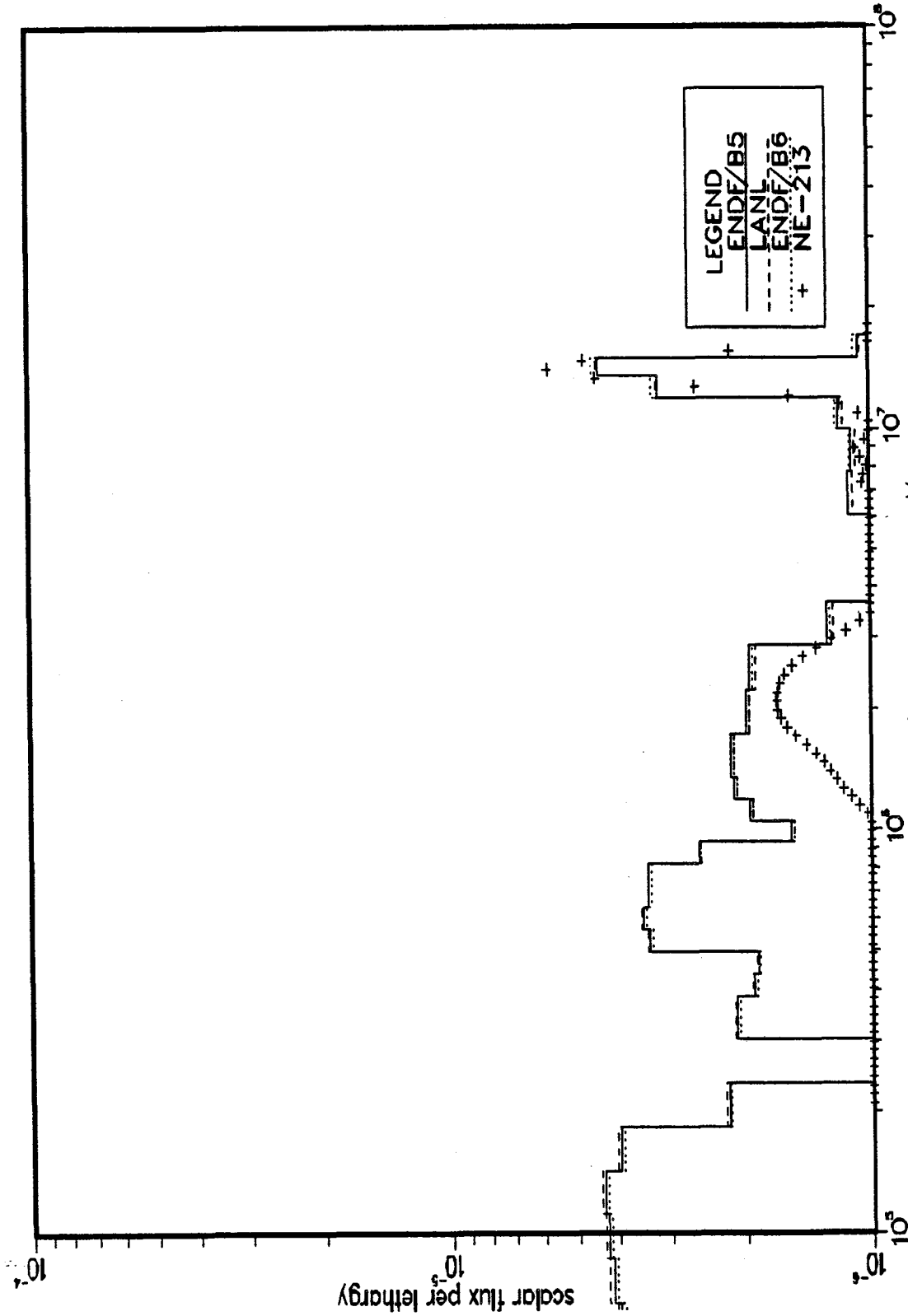

Fig. VIII.7: Neutron Spectrum (DOT5.1) at Z = 31.51 cm with Various Be Evaluations (BEFWFW System - Phase IIB)

(3) The computed spectrum with the three evaluations in the energy range 2 - 13 MeV is larger than the measurements. The ENDF/B5 evaluation gives the largest spectrum in this energy range while the spectrum is comparable with the ENDF/B6 and LANL evaluation.

(4) In the energy range 0.1 - 2 MeV, the neutron spectrum calculated by the LANL evaluation is the largest; ENDF/B6 results are similar (but slightly less) to the ENDF/B5 results in this energy range.

(5) The differences in the spectrum calculated by the three evaluations decrease outside the Be layer, particularly at locations far from this layer (see Fig. VIII.7).

The above intercomparison among the calculated spectrum with the three evaluations for energies below 0.1 MeV is shown in Fig. VIII.8. Also shown in this figure is a comparison to the measurements performed by the PRC. The spectrum calculated by the ENDF/B5 evaluation is always larger than that obtained by ENDF/B6 and LANL evaluations below 0.1 MeV. This could be due to the observation that the SED from the $^{9}Be(n,2n)$ reaction, as it is currently implemented in ENDF/B-V, extends to very low energies in comparison to the two other evaluations, as can be seen from Figs. V.11 to V.13. Note from Fig. VIII.8 that good agreement with the PRC measurements is obtained in the energy range 10 - 100 KeV but larger spectra are obtained by calculations in the energy range 1 KeV - 10 KeV.

Figs. VIII.9 and VIII.10 show the C/E values for the integrated spectrum as obtained by the three evaluations of Be data, in the energy ranges En>10MeV and 1.01 MeV<En<10 MeV, respectively. Inside the Be layer, the C/E values for the integrated spectrum above the 10 MeV is lower than unity by $\sim$ 5% with the three evaluations at depth Z = 1.15 cm, but slightly higher than unity at depth Z = 3.68 cm. From Figs. VIII.3 and VIII.4 one can observe that the underprediction at Z = 1.15 cm is mainly due to the underprediction in the neutron spectrum above 13 MeV which dominates the overprediction in the energy range 10 - 13 MeV. At Z = 3.68 cm, however, the overpredicted part of the spectrum in the energy range 10 - 13 MeV dominates and this leads to the C/E value that is larger than unity (by $\sim$ 5%). Just behind the Be layer (at Z = 6.21 cm.), the integrated spectrum above 10 MeV is underpredicted by the three evaluations, as shown in Fig. VIII.9, and this underprediction is less pronounced in the case of the ENDF/B6 data for Be. In the bulk of the Li_2O zone the C/E values for the integrated spectrum above 10 MeV is also underpredicted (by $\sim$ 5 - 10 %) but the underprediction is less pronounced with the ENDF/B6 data. Since the integrated cross-

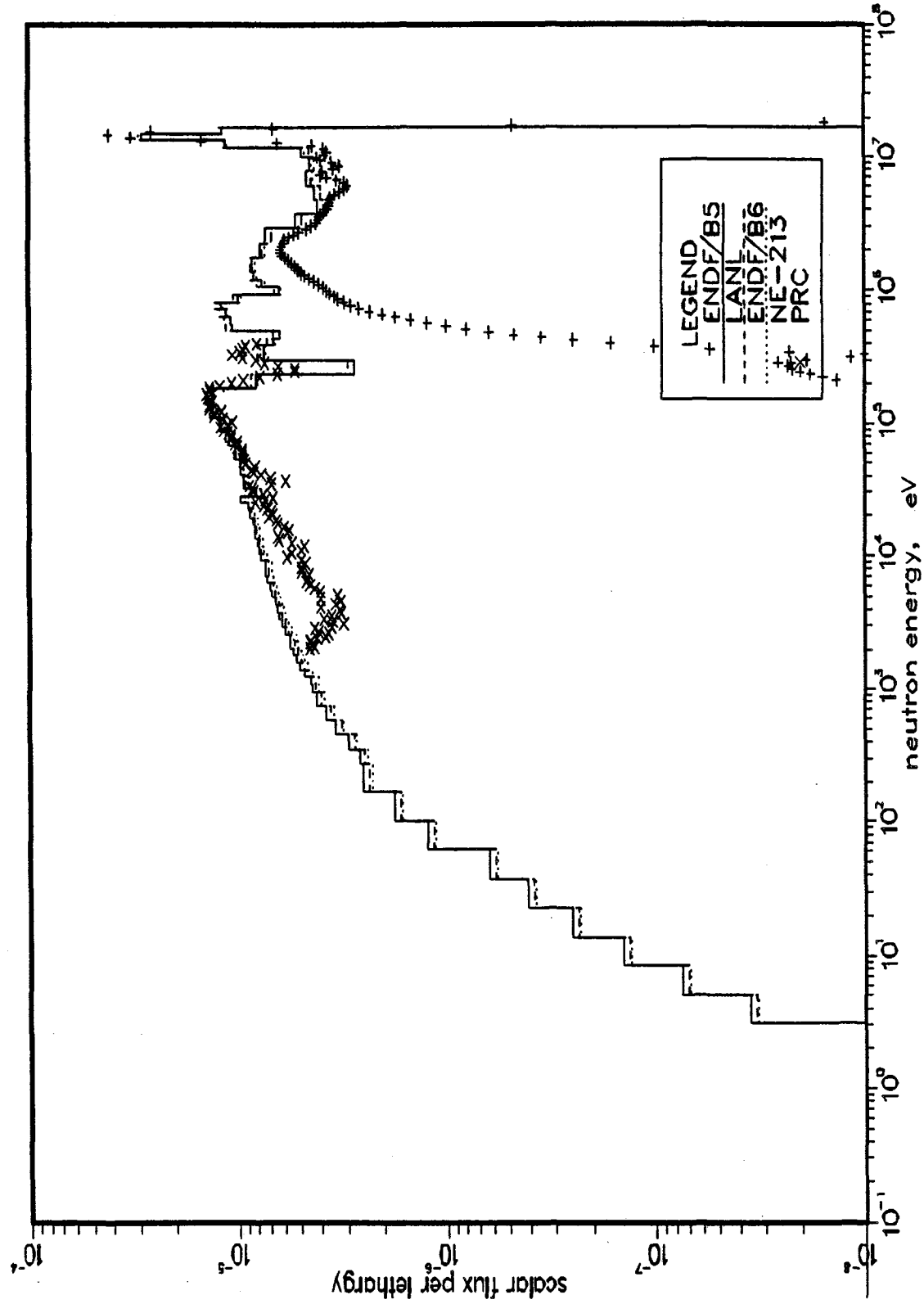

Fig. VIII.8: Neutron Spectrum (DOT5.1) at Z = 11.27 cm with Various Be Evaluations (BEFWFW System - Phase IIB, NE213 and PRC Measurements)

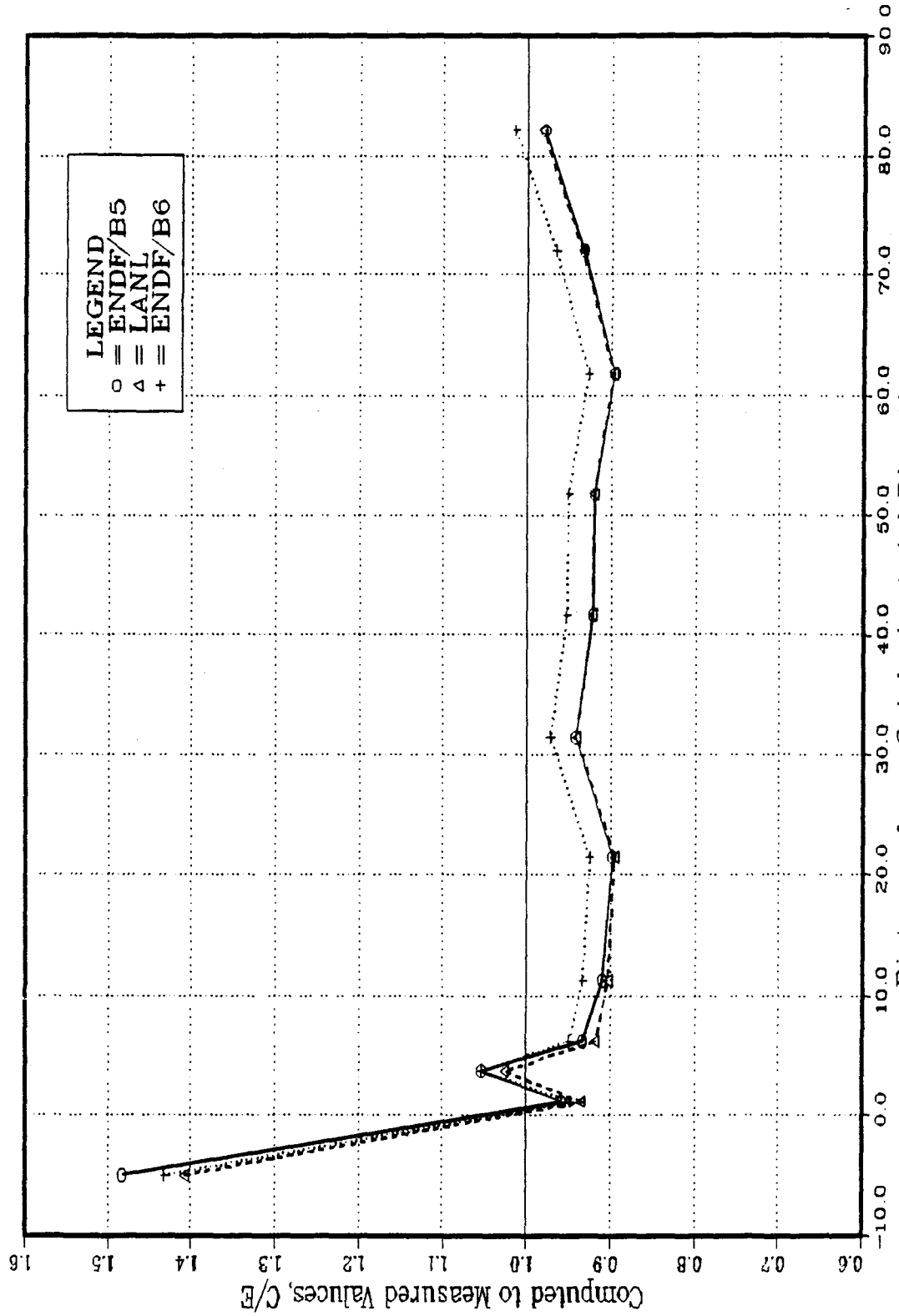

Fig. VIII.9: Integrated Flux (E > 10 MeV) Measured by NE213 in the Central Drawer (BEFWFW System - Phase IIB)

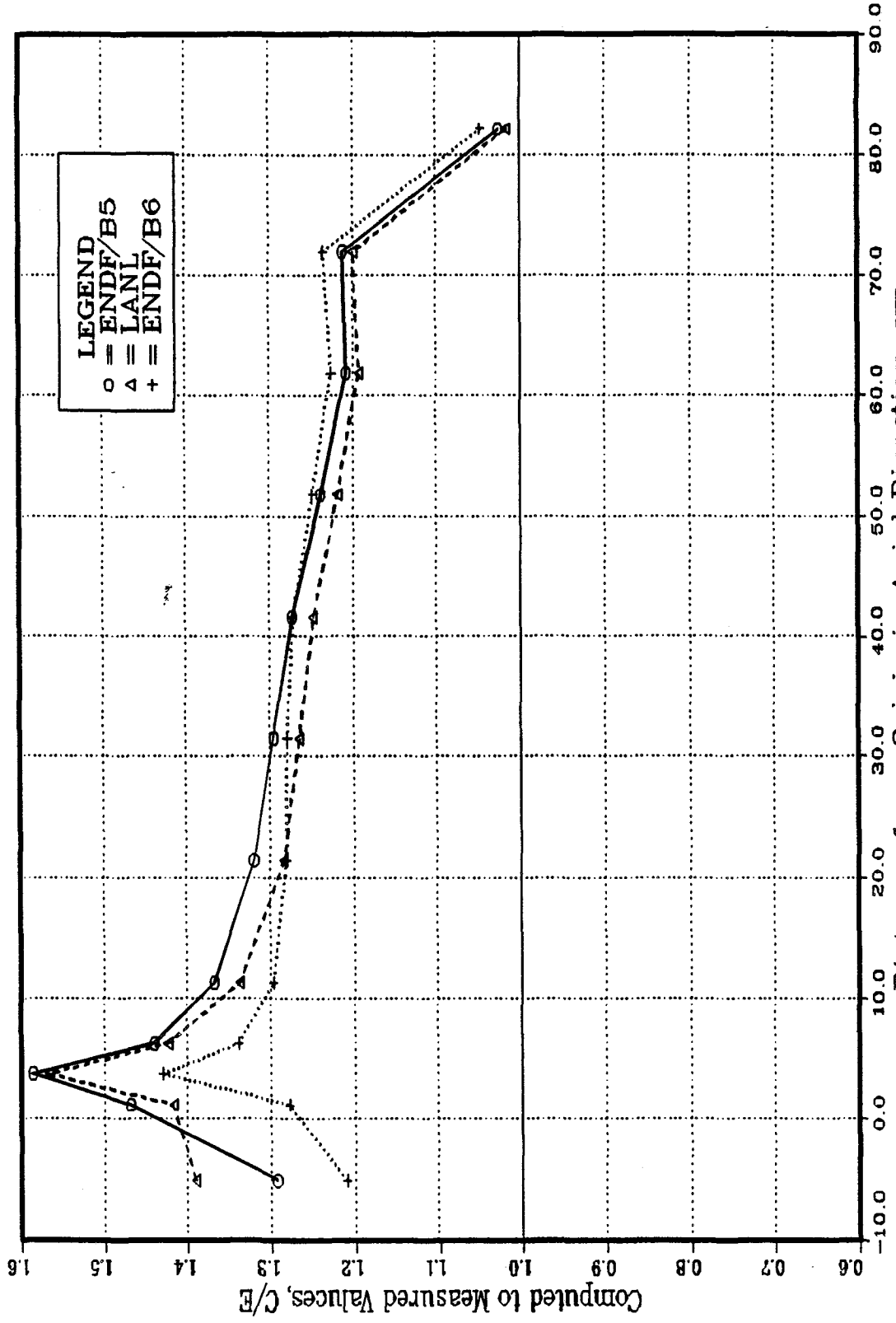

Fig. VIII.10: Integrated Flux (10 > E > 1.01 MeV) Measured by NE213 in the Central Drawer (BEFWFW System - Phase IIB)

section for the $^{9}Be(n,2n)$ reaction is less in the ENDF/B6 data, particularly at high energies (see Figs. VIII.1 and VIII.2), this leads to an improvement in the prediction of the integrated spectrum above 10 MeV, although this component is still underpredicted with the ENDF/B6 data. This suggests that this cross-section may need further reduction at high incident energies.

The integrated spectrum in the energy range 1.01 MeV <En <10 MeV is overpredicted by three evaluations at all locations. In the Li_2O zone, the overprediction is ~ 20% but it is larger (by ~ 60%) inside the Be layer. In the Be region and at Z = 3.68 cm, the overprediction with the ENDF/B5 data is similar to that with the LANL data (by examining Fig. VIII.4, we can see that the spectrum between 1 MeV - 2 MeV is larger with the LANL data while it is smaller in the energy range 2 - 10 MeV as compared to results obtained with the ENDF/B5 data; and this leads to compensation in the integrated spectrum in the energy range 1 - 10 MeV). With the ENDF/B6 data, the integrated spectrum is better predicted since the spectrum in the energy range 1 - 10 MeV is the closest to the experimental values, as can be seen in Figs. VIII.3 to VIII.7, upto a depth of ~ 15 cm. Thus, one can say that the improvement carried out in the Be data of ENDF/B-VI (which is basically due to the improvement in the total and SED of the $^{9}Be(n,2n)$ cross section) leads to better prediction in the neutron spectrum inside and around the Be layer. This improvement is that the integrated $^{9}Be(n,2n)$ cross-section is lower at high incident energies and the SED of the emitted neutrons from the $^{9}Be(n,2n)$ reactions is harder (larger spectrum component above 10 MeV and lower component in the energy range 1 - 10 MeV).

VIII.4 Impact on Activation Reaction Rates

Threshold reactions can give a measure of the differences in the integrated spectrum over a certain range of energy. The C/E curves for the high energy reaction $^{58}Ni(n,2n)$ (E_{th} ~ 12.5 MeV) is shown in Fig. VIII.11 based on the three evaluations for Be data. As mentioned before in Section VI (see Fig. VI.14), the cross-section for this reaction is underestimated in ENDF/B-V by ~ 15 - 20%. Thus, if the entire curves are raised by that value, the C/E values, on the average, will be below unity by ~ 5%. As was noted in Figs. VIII.3 to VIII.7, the spectrum above 13 MeV is underpredicted by all evaluations, and this could explain the underestimation (of ~ 5%) in the C/E curves. Note also from Fig. VIII.11 that the ENDF/B6 evaluation gives the closest C/E values to unity in comparison to the other two evaluations (the C/E values in this case are ~ 3% larger than those obtained with ENDF/B5 and LANL evaluations at all locations except at Z = 0 where

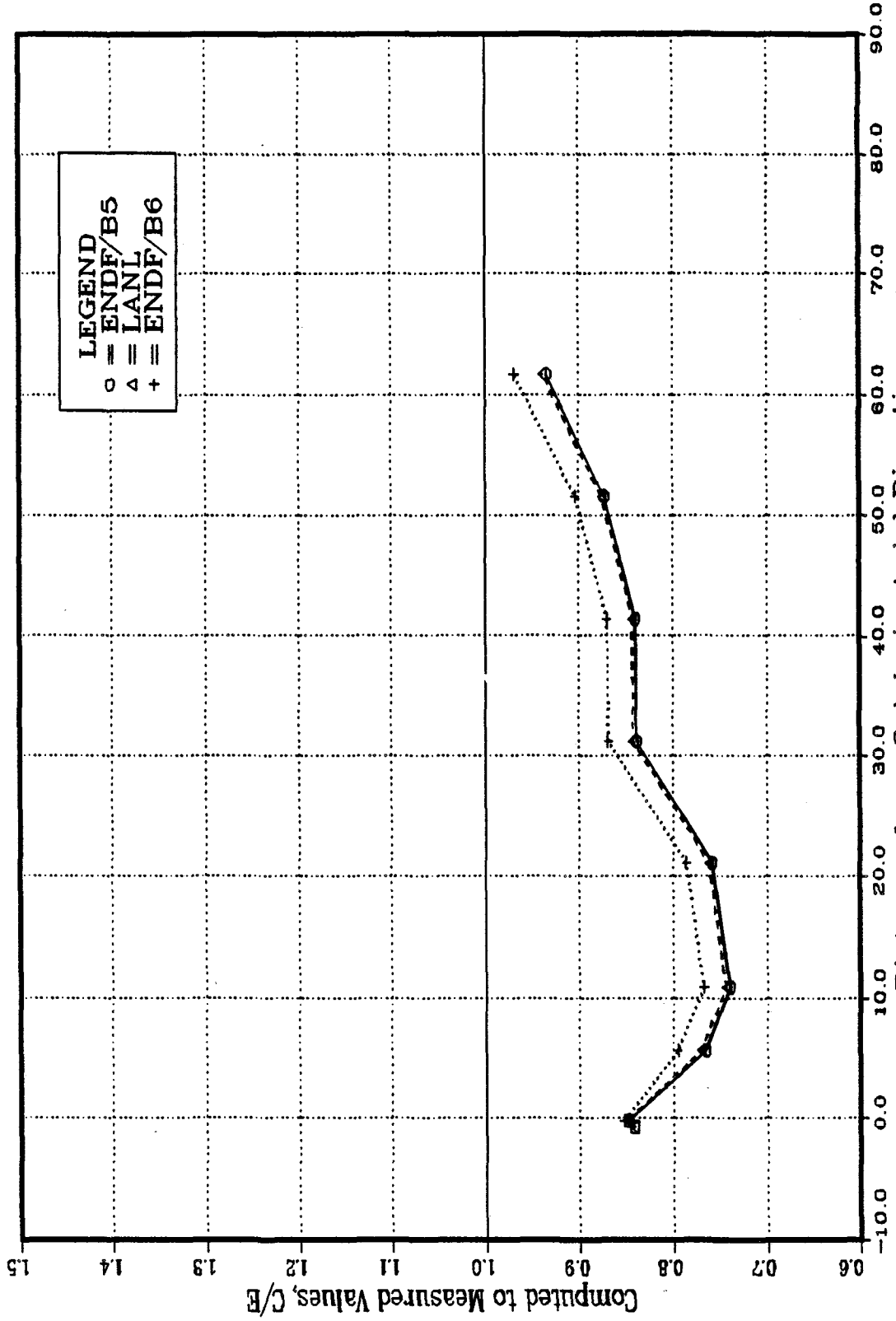

Fig. VIII.11: C/E Values for the $Ni^{58}(n,2n)Ni^{57}$ Reaction in the Central Drawer (BEFWFW System - Phase IIB)

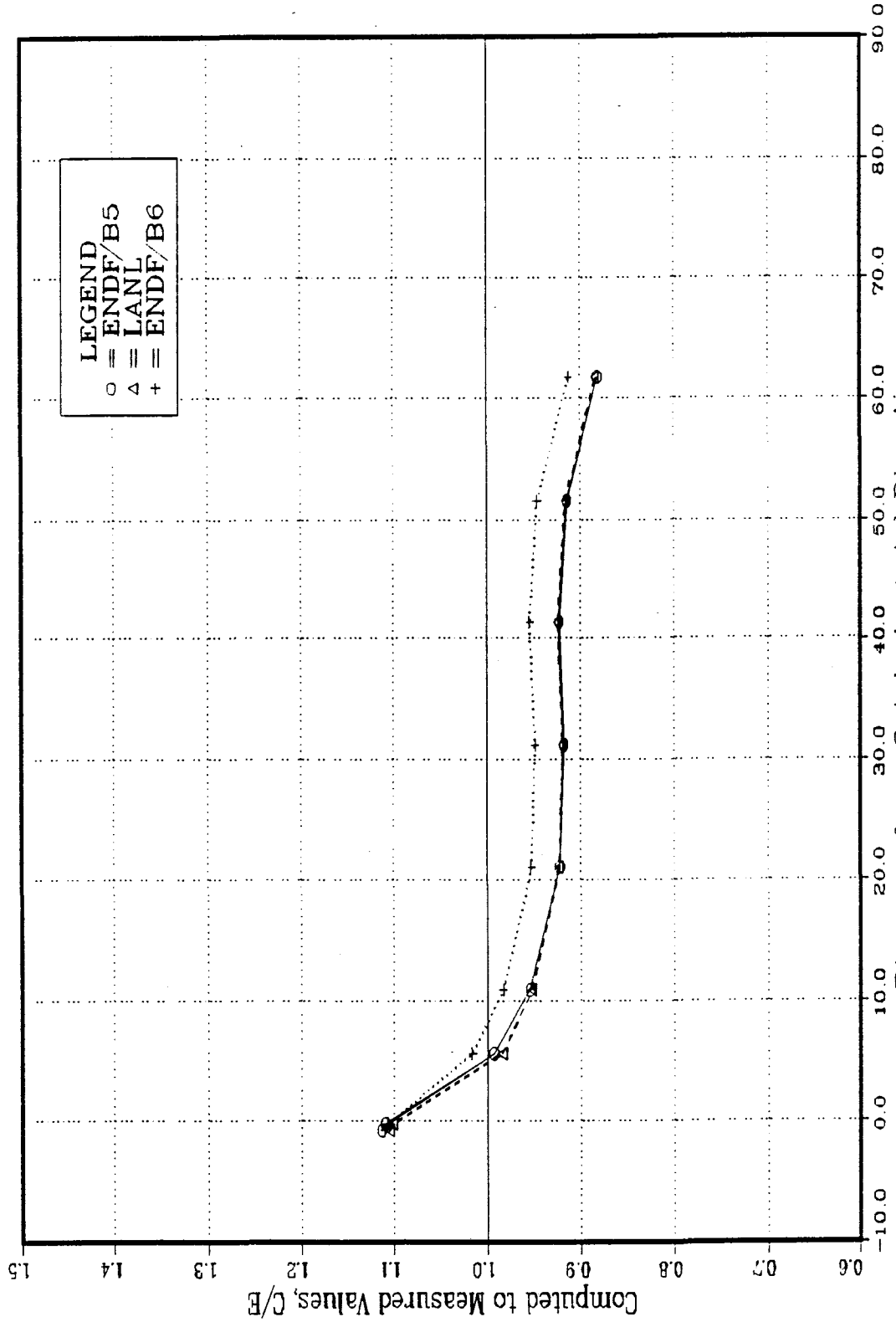

Fig. VIII.12: C/E Values for the $Nb^{93}(n,2n)Nb^{92m}$ Reaction in the Central Drawer (BEFWFW System - Phase IIB)

neutrons enter the test assembly). This is due to the improvement in the high-energy component of the neutron spectrum above 10 MeV where this component is larger than the ones obtained by the ENDF/B5 and LANL evaluations, as was shown and discussed in Fig. VIII.9.

The C/E values for the $^{93}Nb(n,2n)^{92m}Nb$ reaction (E_{th} ~ 8 MeV) are shown in Fig. VIII.12. At the front face of the assembly, and inside the Be layer, the C/E values are larger than unity, but their values drop below unity behind that layer. The ENDF/B6 evaluation for Be gives larger values (by ~ 3%) in comparison to the other evaluations. (Note from the spectrum curves shown in Figs. VIII.3 to VIII.7 that the calculated spectrum above 13 MeV is the largest with the ENDF/B6 evaluation. This is also true for the integrated spectrum above 10 MeV, as was shown in Fig. VIII.9.) However, and in the bulk of the Li_2O zone, the C/E values are less than unity. This could be partly attributed to an overestimation in the total $^{9}Be(n,2n)$ cross-section itself at high energies (which leads to lower neutron spectrum around the 14 MeV peak) and partly to an underestimation in the SED of the emitted neutrons for the $^{9}Be(n,2n)$ reactions above 10 - 13 MeV. The ENDF/B6 evaluation for Be has lower total (n,2n) cross-section (see Figs. VIII.1 and VIII.2) and thus an improvement in C/E curves for the high-threshold reactions takes place, as can be seen in Figs. VIII.11 and VIII.12.

For lower threshold reactions, the characteristics of the C/E curves are different from those of the high-threshold reactions. The C/E curves for $^{27}Al(n,\alpha)^{24}Na$ reaction are shown in Fig. VIII.13. The values are larger than unity inside the Be zone but fall below unity thereafter. The threshold energy for this reaction is ~ 6 MeV, and as was shown in Figs. VIII.3 to VIII.7, the neutron spectrum inside the Be layer is the largest with the ENDF/B5 evaluation in the energy range 2 - 13 MeV, where the threshold energy of this reaction lies. Also, the integrated spectrum in the energy range 1 - 10 MeV is overpredicted with this evaluation than others, as can be seen from Fig. VIII.10. This is reflected on the C/E value inside the Be zone, where the values are the largest with the ENDF/B5 evaluation followed by the ENDF/B6 and LANL data. In the Li_2O zone, the LANL values approach those calculated by the ENDF/B5 while the C/E values obtained by ENDF/B6 evaluation are the largest (by ~ 5%) and closest to unity, as shown in Fig. VIII.13.

Trends similar to those discussed above are observed in the C/E curves for the $^{58}Ni(n,p)^{58}Co$ and $^{115}In(n,n')^{115m}In$ reactions shown in Figs. VIII.14 and VIII.15,

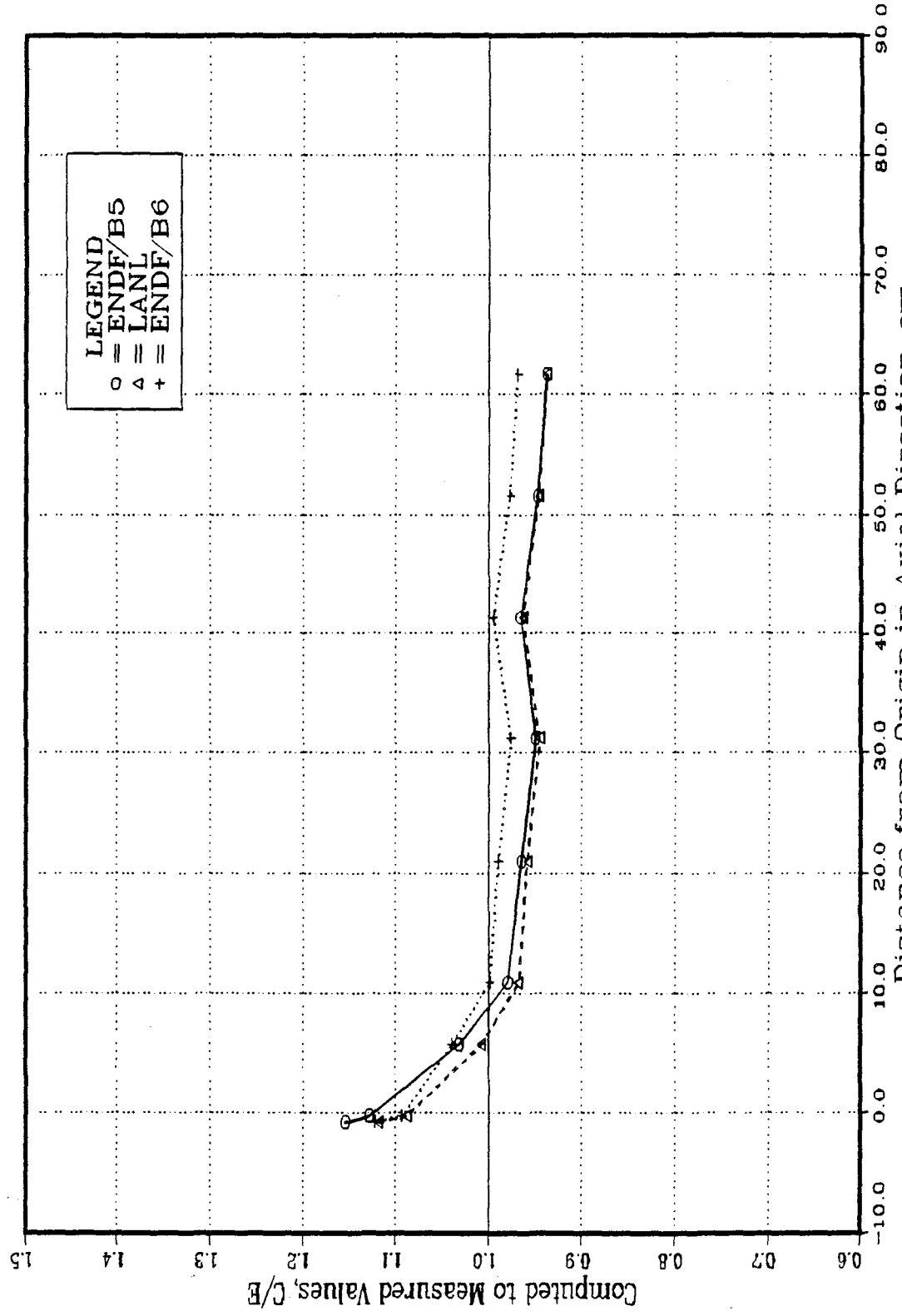

Fig. VIII.13: C/E Values for the $Al^{27}(n,\alpha)Na^{24}$ Reaction in the Central Drawer (BEFWFW System - Phase IIB)

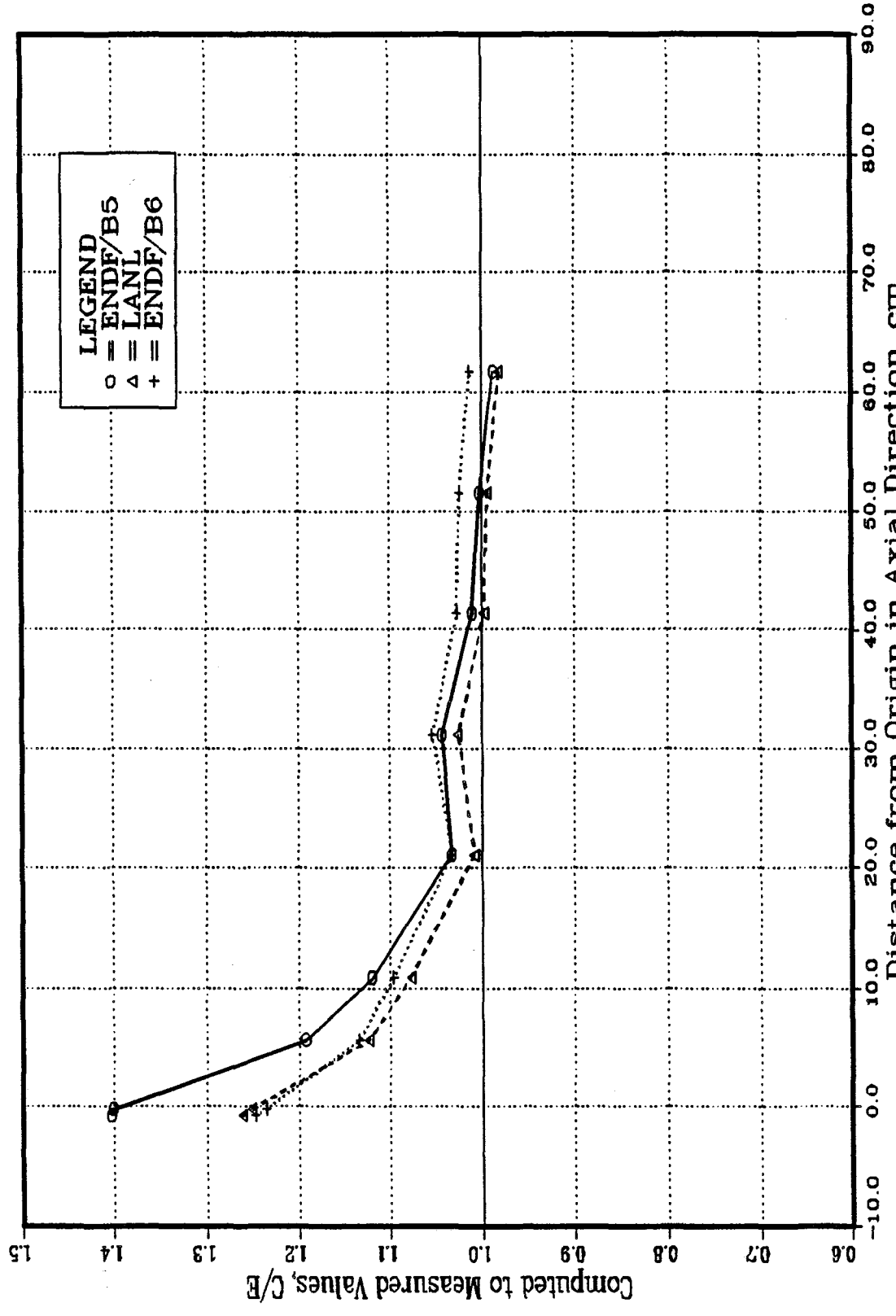

Fig. VIII.14: C/E Values for the $Ni^{58}(n,p)Co^{58}$ Reaction in the Central Drawer (BEFWFW System - Phase IIB)

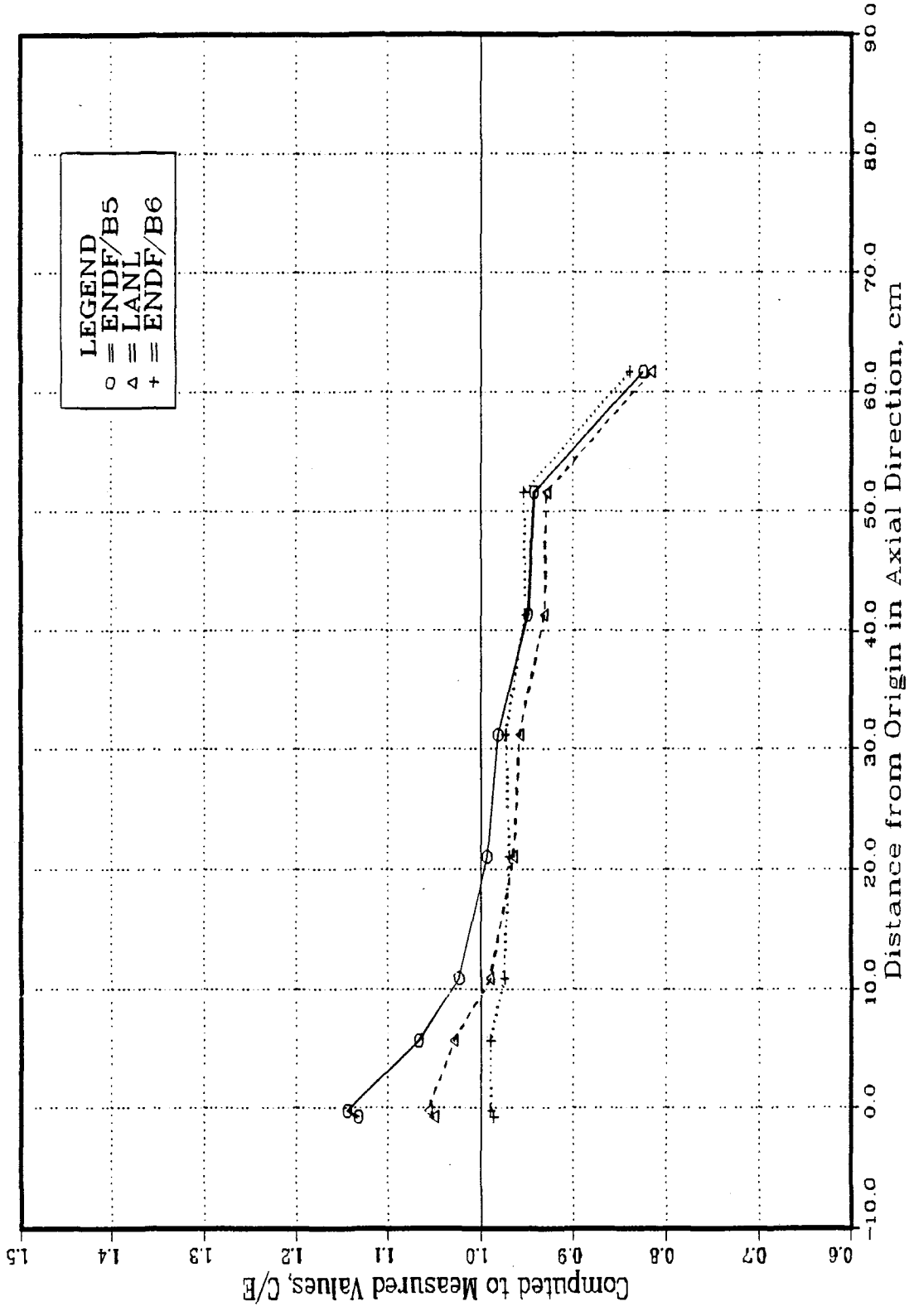

Fig. VIII.15: C/E Values for the $In^{115}(n,n')In^{115m}$ Reaction in the Central Drawer (BEFWFW System - Phase IIB)

respectively. The overprediction of the neutron spectrum in the energy range 2 - 13 MeV by the ENDF/B5 data shows up as the largest C/E values inside the Be layer. At deeper locations, such overprediction in the spectrum is less pronounced, hence, the larger neutron spectrum above 13 MeV predicted by the ENDF/B6 data leads to the largest C/E values. The threshold energy for the $^{115}In(n,n')^{115m}In$ reaction is low (~ 1 MeV) and neutron flux below 2 MeV also makes contribution to this reaction. In the Be zone, the overprediction of this spectrum component (in the energy range 0.1 - 2 MeV) by the LANL data (see Figs. VIII.3 to VIII.7) leads to medium values between those obtained by ENDF/B5 and B6 data. This is also shown in Fig. VIII.10, where the integrated spectrum between 1 and 10 MeV, as predicted by LANL data, tends to be between the ones obtained by the ENDF/B6 and ENDF/B5 data.

VIII.5 Impact on Tritium Production Rates

The C/E curves for T_7 and T_6 are shown in Fig. VIII.16 and VIII.17, respectively, as obtained by the three evaluations for Be. Note that the measured values for T_7 are obtained by folding the neutron spectrum measured by the NE213 detector with the $^7Li(n,n'\alpha)t$ cross-section of the JENDL3-PR1 data.[32] The threshold energy for this cross-section (~ 2.8 MeV) is similar to the $^{58}Ni(n,p)$ reaction and, therefore, the C/E curves have similar trends, that is, larger C/E values obtained with the ENDF/B5 data inside the Be zone (due to the overprediction in spectrum in the energy range 2 - 13 MeV). The C/E values obtained by LANL evaluation approach the values obtained by the ENDF/B5 at deep locations, and the C/E values obtained by the ENDF/B6 are the largest at these deep locations. Note that the last trend is due to the fact that the $^9Be(n,2n)$ cross-section is the smallest at high incident energies in the ENDF/B6 evaluation as compared to the other two evaluations. It was shown in Section V (see Figs. V.33 to V.35) that T_7 has negative integrated sensitivity coefficients for variation in the $^9Be(n,total)$ cross-section. That is, decreasing the total (elastic + nonelastic) cross-section will lead to an increase in T_7, and that increase is more noticeable as one proceeds towards the back end of the test assembly. Also, it was shown that the main contribution to the sensitivity coefficient comes from variation in the $^9Be(n,2n)$ cross-section. Since the $^9Be(n,2n)$ cross-section in ENDF/B6 evaluation is smaller (by ~ 15%) than those of ENDF/B5 and LANL, the T_7 will consequently increase, particularly at deep locations, as shown in Fig. VIII.16. In addition, the relative sensitivity profile for variation in the $^9Be(n,2n)$ cross-section shown in Fig. V.36 indicates that any reduction in this cross-section at high energies above 13 MeV leads to the largest impact (increase) on T_7.

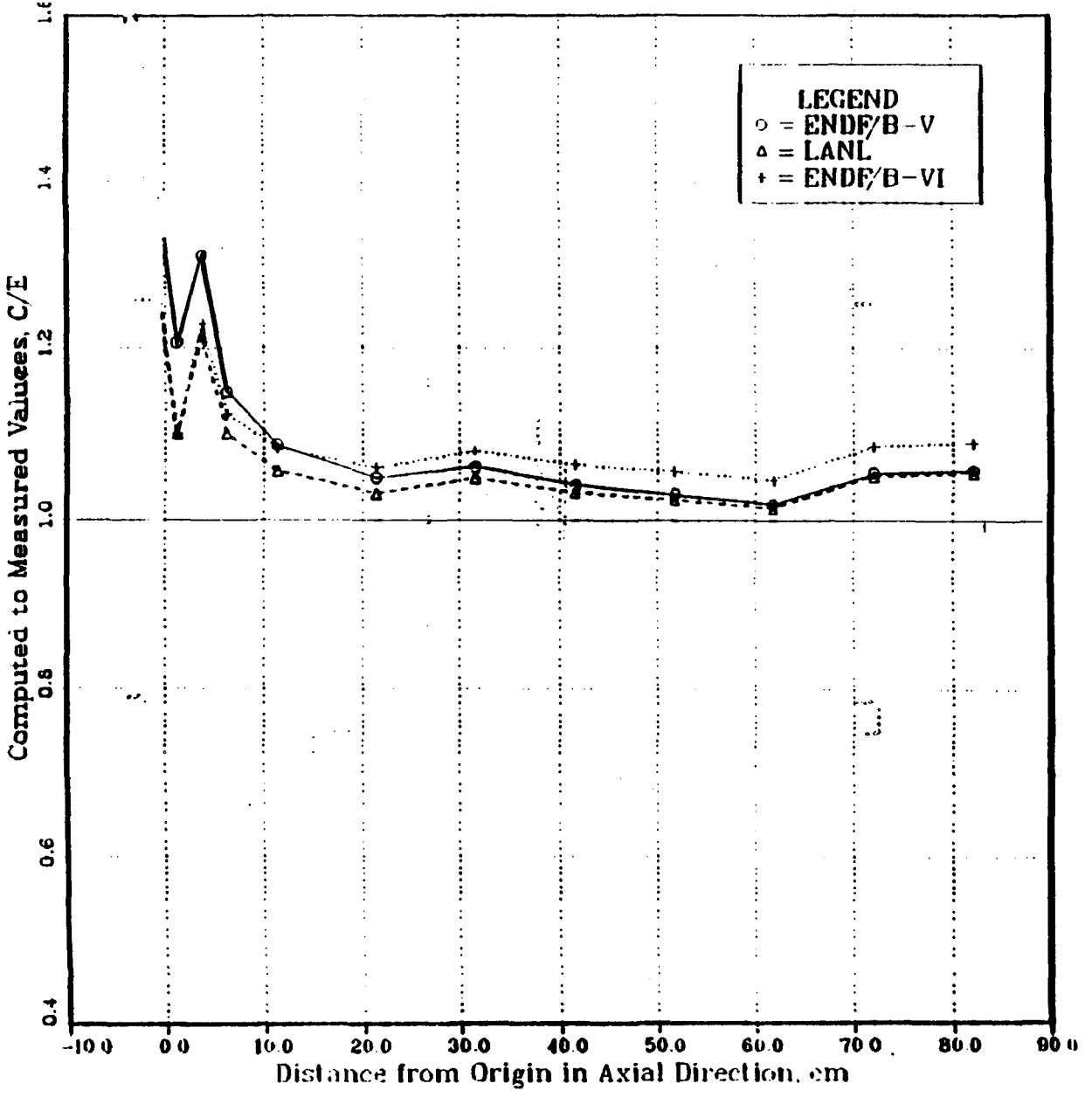

Fig. VIII.16: C/E Values for T_7 Measured by NE213 Detector in the Central Drawer (BEFWFW System - Phase IIB)

The C/E curves for T_6 are very different from those seen for other threshold-type reactions. The lower energy component of the neutron flux plays a significant role on T_6 values. Fig. VIII.17 shows the C/E values as obtained by the three evaluations for Be. It is seen from that figure that the C/E values in the Be layer are as large as 1.6. When corrections due to the self-shielding by the Li-glass scintillator itself and the flux perturbation effect of the detector structure materials are made, it was shown that the C/E values inside the Be region decrease to about unity (see Section IV.3.4). It is clear without such corrections that the magnitude of the C/E values inside the Be layer is in the order, ENDF/B5, ENDF/B6, and LANL, from the largest to the smallest. Just behind the Be layer the sudden drop in the C/E values (to below unity) is more noticeable with the ENDF/B6 evaluation followed by those obtained with the LANL and ENDF/B5, in that order. As was shown in Fig. VIII.8, both the ENDF/B6 and LANL data lead to smaller low-energy component in the spectrum than in the case with the ENDF/B5 evaluation. In addition, it was shown in Figs. V.11 to V.13 that the SED of neutrons emitted from the $^9Be(n,2n)$
reactions does not extend below ~ 1 KeV in the ENDF/B6 evaluation while the LANL evaluation extends below this energy but with insignificant cross-section. On the other hand, the SED in the ENDF/B5 case has the largest component at very low energies as compared to ENDF/B6 and LANL data. The difference in the low-energy component in the neutron spectrum shows up in Fig.VIII.17 as smaller C/E values with the ENDF/B6 and LANL data than those obtained with the ENDF/B5 data at all locations in the Li_2O region. Thus, it is clear from Fig. VIII.17 that the C/E values for T_6 in the bulk of the Li_2O zone have improved upon using the ENDF/B6 data for beryllium, except at locations just behind the Be layer.

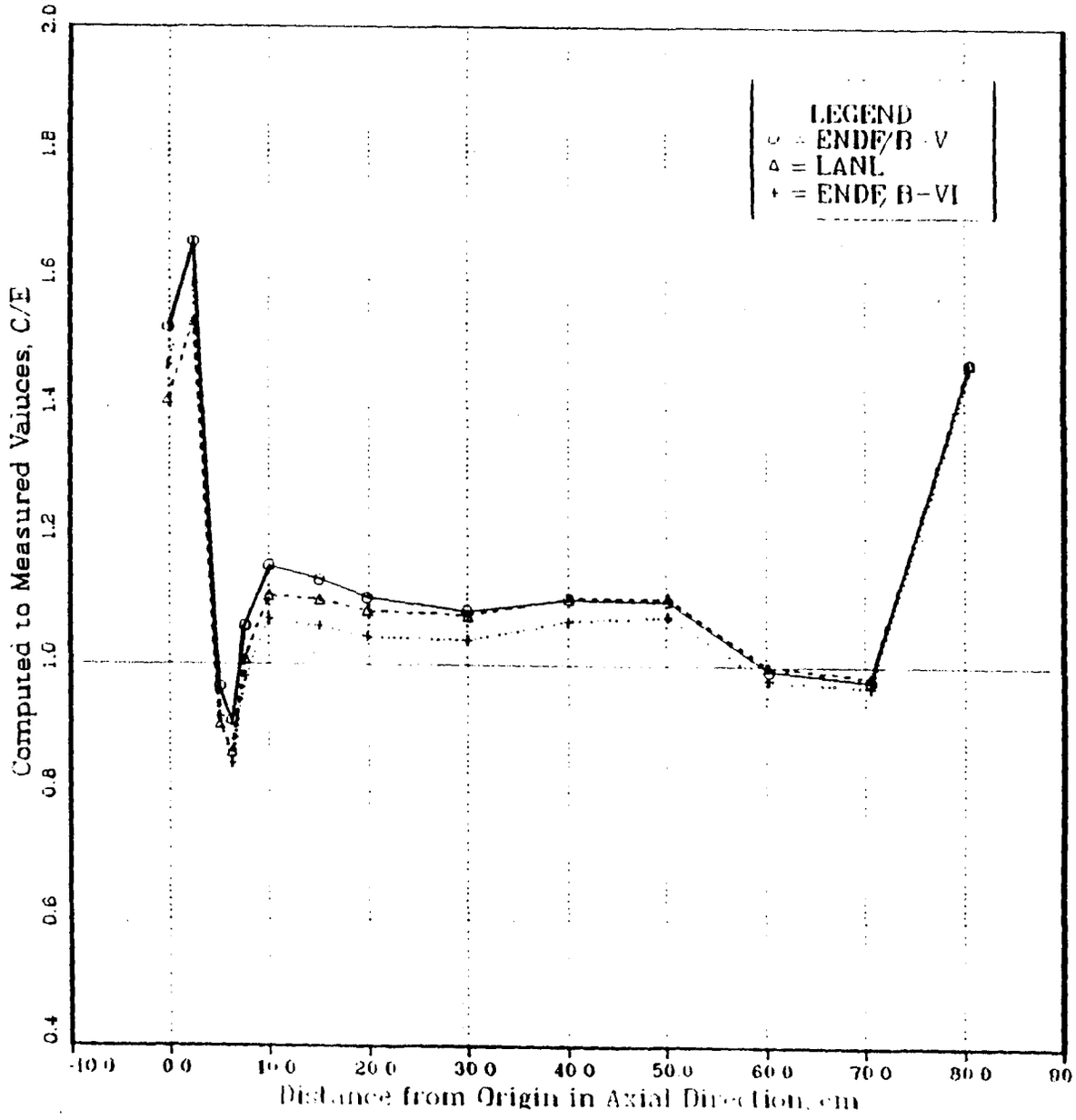

Fig. VIII.17: C/E Values for T_6 Measured by Li-Glass Detector in the Central Drawer (BEFWFW System - Phase IIB)

IX. Concluding Remarks

The analysis for Phase IIA and IIB of the US/JAERI Collaborative Program on Fusion Neutronics has been performed independently by both parties. This report summarizes the U.S. contribution to this analysis while JAERI's contribution is reported separately.[6-7]

The main objective of the program is to derive information on the prediction accuracy of key design parameters relevant to the blanket design of future experimental and commercial fusion reactors. In particular, gaining information on the uncertainty (both experimental and analytical) involved in tritium production rate (TPR) at local spatial locations as well as within integrated spatial zones is crucial in resolving some of the feasibility issues pertaining to the attractiveness of a particular blanket concept such as achieving tritium self-sufficiency in a solid breeder blanket. In addition, results from the integral experiments performed (or to be performed) in this collaborative program will provide a data base for selection of materials, blanket and shield configurations, and advancing the neutronics technology required for the next experimental devices such as FER, ITER, etc. At this stage of the program, emphases were placed on the prediction verification and advancing measuring techniques for local and zonal tritium prediction rate [from ^{6}Li and $^{7}Li(T_7)$], activation reaction rates and neutron spectrum measurements. In Phase IIC (activities on that phase to be reported separately), effort has been initiated to measure radioactivity build-up and after heat in typical structural materials, an issue of a prime importance to the safe operation of a fusion reactor. Furthermore, Phase III experiments, that are scheduled to be carried out during the next two years, will concentrate on the realization of a line source, generated by moving the point source back and forth relative to the test assembly, which in effect, gives better simulation to the angular and energy distribution of the incident neutrons generated in the plasma of a fusion reactor. In that phase, several experiments on nuclear heating and tritium production measurements are planned in addition to neutron streaming through openings in the blanket.

Unlike Phase I Experiments,[1,3-5] the geometrical arrangement for Phase II has been carefully chosen (through pre-analysis) to simulate to a larger degree the incident neutron source that can be found in fusion reactors. The Li_2O test assembly (86 cm x 86 cm x 60 cm) was placed at one end of a rectangular enclosure made of Li_2CO_3 and

the D-T neutron source was placed inside the cavity at a distance of ~ 78 cm from the square front surface of the assembly.

Three experiments were performed in Phase IIA on three configurations, namely: (a) a reference Li_2O test assembly (REF system), (b) a 5 cm-thick beryllium front zone preceeding the Li_2O test assembly (BEF system), and (c) a 5 cm-thick beryllium zone is sandwiched between a 5 cm-thick front Li_2O layer and the rest of the Li_2O test assembly (BES system). It was shown analytically, and verified experimentally, that the integrated TPR in the last system is larger than in the BEF system; an important issue for blanket designes. In Phase IIB, the innter surface of the Li_2CO_3 enclosure was covered by a 5 cm-thick beryllium layer (with a 0.5 cm-thick FW) and three experiments were also performed on three configurations, namely: (a) a reference Li_2O assembly (REF system), (b) a 5 cm-thick beryllium front zone (with no FW) preceeding the Li_2O test assembly (BEFWOFW system), and (c) a 5 cm-thick beryllium front zone (with FW) preceeding the Li_2O test assembly (BEFWFW system). The beryllium liner simulates the inner tiles placed on the inboard shield in a fusion reactor. Again, it was shown through the experiments and analysis that the presence of the Be liner enhances the TPR in the test assembly.

Prior to performing in-system measurements (e.g. local and zonal TPR, activation rate and spectrum measurements), the incident neutron source from the rotating neutron target (RNT) has been characterized by NE213 and proton recoil counter (PRC) measurements at several locations inside the cavity. In addition, several reaction rates were measured at the inner surface of the Li_2CO_3 enclosure and at the front surface of the test assembly and comparison was made to the prediciton by Monte Carlo Calculations. Both Monte Carlo and discrete ordinates methods were used in the analysis of Phase IIA and IIB experiments and the data libraries applied were based on ENDF/B-V evaluation. Special evaluations for the beryllium cross-sections were also used for intercomparison, namely, the LANL and ENDF/B-VI evaluations. The summary of the comparisons between measurements and calculations for the neutronics parameters mentioned above is given below.

IX.1 Source Characterization

Source characterization by foil activation measurements and by spectrum measurements by NE213 and PRC indicated the following:

(1) High-energy threshold reaction rates are reasonably predicted (with some exceptions, see below) in the forward direction but large discrepancies (by a factor of 2) were observed between calculations and measurements at the back locations (behind RNT) due to the improper modeling of the equipment (e.g. motor, water-cooled tubes, etc.) that are placed behind the RNT.

(2) Mapping the $^{58}Ni(n,2n)$ reaction rate at front surface of the assembly and at inner surface of the Li_2CO_3 enclosure indicated that the calculated to measured values (C/E) are below unity by as much as 30%. The cross-section of the $^{58}Ni(n,2n)$ reaction, as presently implemented in ENDF/B-V should be increased by ~ 15 - 30%.

(3) In the forward direction, the C/E values for the $^{93}Nb(n,2n)^{92m}Nb$ reaction and the $^{197}Au(n,2n)$ are reasonably predicted, although some underestimation (by ~ 5%) has been observed. Comparison to the spectrum measured by NE213 indicated that the 14 MeV peak is underestimated in the REF system of Phase IIA. This is also true for Phase IIB, where the incident spectrum above 10 MeV is underpredicted.

(4) The reaction $^{58}Ni(n,p)$ is overpredicted at the front surface of the test assembly (by ~ 7%). Since the threshold of this reaction is relatively low (E_{th} ~ 2 MeV), the overestimation was attributed to an overestimation in the incident spectrum in the energy range 1 - 10 MeV, as was revealed from comparing the calculated spectrum to the measurements performed by the NE213 detectors.

(5) The reaction $^{197}Au(n,\gamma)$, which is sensitive to the low-energy component of the incident neutron spectrum, is underestimated by as much as 30%. The prediction accuracy of the low-energy neutron spectrum tail is largely dependent on the specifications of the epoxy paint used to coat the Li_2CO_3 bricks. Since the prediction accuracy of this reaction is indicative to the prediction accuracy for T_6, the C/E values for T_6 is also lower than unity at the front surface of the test assembly in the REF system of Phase IIA.

IX.2 Tritium Production Rate

(A) Tritium Production from ^6Li, T_6:

The prediction accuracy for T_6 in Phase II has substantially improved as compared to the results from Phase I. The elimination of the uncertainty in predicting the room-returned component of the incident neutron spectrum of Phase I by isolating the test assembly from the room walls resulted in a better prediction for T_6. The C/E values in the bulk of the Li_2O assembly of the REF system of Phase IIA is ~ 1.1 based on the Li-glass measurements and this overprediction still persists when the Li-foil detectors are used to measure T_6 although the C/E values in this case are closer to unity(C/E ~ 1.08). The overestimation in T_6 also appeared in the radial directions where the C/E curves flat (no space dependence).

When a beryllium layer is added (either in the BEF or the BES systems of Phase IIA), the shape of the C/E curves for T_6 has the following featues:

(1) large C/E values inside the Be layer due to the self-shielding effect and flux perturbation by the components of the Li-glass detectors. To improve the C/E values inside the Be layer, it was shown that it is necessary to consider the geometrical details of the detectors used to measure T6 in the calculational model. Ignoring these details could lead to ~ 50% larger T6 inside the Be layer.

(2) There is a sudden drop in the C/E curves for T_6 just behind the Be layer by ~ 10 - 20% below unity. This underestimation continues for 3-5 cm behind the Be layer. Thereafter, the C/E values start to increase where they reach more or less steady values (C/E ~ 1.1) then they start to decrease again. The underestimation in T_6 behind the Be layer should be seriously considered by blanket designers. The inclusion of a Be layer at the front of several blanket concepts is intended to enhance the breeding performance of these blankets and the enhancement from ^6Li basically occurs within a short distance behind the Be layer.

The two features cited above were also apparent in the C/E curves for T_6 in Phase IIB, although the C/E values were generally closer to unity in comparison to Phase IIA. The drop behind the Be layer was investigated by performing extensive sensitivity analysis to variations in the secondary energy (SED) and angular (SAD) distributions of neutrons emitted from the $^9Be(n,2n)$ reactions. The motivation was to explore whether or not the drop observed in the C/E curves is attributed to the current

uncertainties in SED and SAD of the $^{9}Be(n,2n)$ cross-section. It was shown that, although the applied variations could explain the discrepancies between measurements and calculations behind the Be layer, however, the uncertainties in the SED and SAD should be at least ~ 100% to explain the discrepancy of 10% behind that layer. Indeed, when the SED from the $^{9}Be(n,2n)$ reactions at several incident energies were compared among the three evaluations for Be (e.g. ENDF/B-V, LANL, and ENDF/B-VI) it was found that the secondary energy distributions are different by more than an order of magnitude at some exit energy ranges. This means that the current uncertainties in the SED of the $^{9}Be(n,2n)$ cross-section are large. Thus, when these uncertainties are coupled with the SED sensitivities coefficients (whose values are relatively small), large uncertainties in T_6 (and to a lesser extent in T_7) could be obtained. For example, when the calculated spectrum inside and behind the Be layer was compared to the NE213 measurements, it was shown that the spectrum is overpredicted in the energy range 2 - 10 MeV and underpredicted above 10 MeV. These features are consistent with Oyama and Maekawa's experiment on the leakage spectrum from a 5 cm slab where they further indicated that the emerged spectrum from this slab is underpredicted in the energy range 0.1 - 0.5 MeV. By assuming that the observed discrepancies are attributed to the uncertainties in the SED of the $^{9}Be(n,2n)$ reactions, variations were applied to decrease the overpredicted part of the spectrum and to increase the underpredicted part such that the total integrated $^{9}Be(n,2n)$ remains the same. When the resultant sensitivity coefficients for this SED variations were coupled with the estimated uncertainties in the SED of the $^{9}Be(n,2n)$, large uncertainties in T_6 were obtained, in the order of ~ 10%, just behind the Be layer[58]. This could partly cover the observed 10 - 20% discrepancy in T_6 observed at this location.

Another possible source for the discrepancy observed in T_6 behind the Be layer was also explored, that is, the uncertainty in interpolating the calculated values to the exact locations where measurements were taken. At the interface between the Be and Li_2O zones, the T_6 profiles are very steep and a shift of a 1 mm in interpolating the calculated values could lead to ~ 8% drop in the C/E values behind the Be layer.

(B) Tritium Production from ^{7}Li, T_7

As it was found in Phase I, the predictions of local T_7 in Phase IIA are larger by ~ 20 - 25% than the measured values obtained by NE213 indirect method. The prediction by the Monte Carlo method is closer to unity and fluctuates between ± 5 - 20%. Based on T_7 measurements by the Li-foil detectors, the C/E values are lower by

10 - 20% than those based on the NE213 indirect method, and therefore, the C/E values for T_7 obtained by that method in Phase IIA is around unity. Unlike T_6, the C/E values for T_7 do not change drastically between the locations inside and outside the Be layer. In addittion, the microstructure treatment that considers the geometrical details of the detector used (whether the detector is a single foil or multicomponent as is the case of the Li-glass detectors) was shown to be unnecessary for T_7 which depends mainly on high-energy neutrons.

In Phase IIB, the features of the C/E curves for T7 are different. The C/E values tend to be lower than those of Phase IIA (by $\sim$ 10%, based on the NE213 indirect method). In addition, the C/E curves exhibit a slope toward the back locations in the Li_2O assembly where the C/E values fall below unity in the BEFWOFW system. The cross-section sensitivity study indicated that T_7 is most sensitive to variations in the total $^9Be(n,2n)$ cross-sections, and that the sensitivity coefficients are negative and increase in their absolute values as one proceeds towards the back locations. Thus, by reducing the $^9Be(n,2n)$ cross-section, the C/E values that are below unity at the back locations will now become closer to unity. In addition, the C/E values for the high-energy threshold reactions in Phase IIB also exhibit the above mentioned slope where their values fall below unity at deeper locations (e.g $^{93}Nb(n,2n)^{92m}Nb$). Also, close examinatin of the integrated spectrum above 10 MeV indicated that this component is underestimated as compared to the NE213 results, particularly at the back locations. Thus, be decreasing the $^9Be(n,2n)$ cross-section at high incident energies, an improvement occurs in the C/E curves of the high-energy threshold reactions, T_7, and the integrated spectrum above 10 MeV at deep locations. Indeed, this was shown to be the case when the ENDF/B-VI evaluation for the beryllium data was used, where improvement of $\sim$ 3% was achieved in the C/E curves in comparison to the results obtained by the ENDF/B-V and LANL data for beryllium. However, it seems that further reduction in the $^9Be(n,2n)$ cross-section may be required to improve the discrepancies between calculations and measurements for T_7, high-energy threshold reactions, and the integrated neutron spectrum above 10 MeV.

The present study has also indicated that the local enhancement in T_6 upon including the beryllium liner or layer is underestimated in comparison to the local enhancement measured by the Li-glass detector. Also, the decrease in the local T_7 upon the inclusion of the Be liner/layer is overpredicted in comparison to the relative decrease measured by the NE213 indirect method. As a result, the predicted enhancement in tritium breeding upon including the Be multiplier in the BES system of

Phase IIA, for example, is ~ 7 - 8% while measurements indicate an approximately 10% increase in the integrated TPR. The reason for the overprediction in the decrease in T_7 could be explained by the overestimation in the $^9Be(n,2n)$ cross-section, as discussed above. The underprediction in the local enhancement in T6 upon the inclusion of the Be liner/layer could be attributed to the need to improve the SED of the neutrons emitted from the $^9Be(n,2n)$ reactions by increasing the SED below 0.5 MeV, decreasing the spectrum in the energy range 2 - 10 MeV, and increasing the spectrum above 10 MeV. Since some of these improvements have been considered in the ENDF/B-VI data for beryllium, the C/E curves for T_6 have improved with this evaluation and hence improvement occurs in predicting the enhancement in the TPR upon including the Be liner/layer.

In summary, the prediction accuracy for local T_6 is ~ 10% where it is on the overprediction side. As for local T_7, the prediction accuracy is ~ ± 5 - 25% but the prediction accuracy for the integrated zonal TPR from natural lithium is better (3 - 7%)due to error cancellation. Generally speaking, the prediction accuracies of the TPR, reaction rates, and neutron spectrum have improved in comparison to Phase I experiments. However, the results from Phase II analysis have indicated the need to carry out some improvement in the beryllium data, particularly the $^9Be(n,2n)$ cross-section and its associated secondary energy and angular distribution.

Phase III experiments, planned to be carried out during the next two years will involve the simulation of a line source by moving the point source relative to the test assembly. In a situation like this, the modeling of the moving point source could involve some approximations that could add to larger uncertainties. It is a challenging task to estimate the total prediction uncertainties involved in tritium production and heating rates, radioactivity build-up, afterheat, and neutron streaming through openings that are planned for that phase.

X. Reference

[1] T. Nakamura and M.A. Abdou, "Summary of Recent Results from the JAERI/U.S. Fusion Neutronics Phase I Experiments" Fusion Technology, 10, 541-548 (1986).

[2] U.S. ITER Nuclear Group, "ITER Shield and Blanket Work Package Report," ANL/FPP/88-1, Argonne National Laboratory (June 1988).

[3] M. Z. Youssef, et al., "Analysis and Intercomparison for Phase I Fusion Integral Experiments at the FNS Facility," Fusion Technology, 10, 549-563 (1986).

[4] M. Z. Youssef, M. Nakagawa, et al., "Phase I Fusion Integral Experiments, Vol. II: Analysis," UCLA-ENG-88-15, University of California, Los Angeles, (September 1988). See also JAERI-M-88-177, Japan Atomic Energy Research Institute (Aug. 1988).

[5] H. Maekawa, et al., "Measured Neutron Parameters for Phase I Experiments at the FNS Facility," Fusion Technology, 10, 564-572 (1986).

[6] M. Nakagawa, et al., "JAERI/U.S. Collaboratove Program on Fusion Neutronics - Phase II Fusion Integral Experiment Analysis," Japan Atomic Energy Research Institute report, to be published (Aug. 1989).

[7] Y. Oyama, et al., "Phase IIA and IIB Experiment of JAERI/USDOE Collaborative Program on Fusion Blanket Neutronics - Neutron Experiment of Beryllium Configuration in a Full-Coverage Blanket Geometry," Japan Atomic Energy Research Institute report to be published (Aug., 1989).

[8] M.Z. Youssef, et al., "Analysis of Neutronics Parameters Measured in Phase II Experiments of the JAERI/U.S. Collaborative Program on Blanket Neutronics, Part II: Tritium Production and In-System Spectrum," Proc. of the International Symposium on Fusion Nuclear Technology, April 10-15, Tokyo, Japan (1988). Also, see Fusion Engineering and Design, 9, 323-332 (1989).

[9] M. Nakagawa, et al., "Analysis of Neutronics Parameters Measured in Phase II Experiments of the JAERI/U.S. Collaborative Program on Breeder Neutronics, Part I: Source Characteristics and Reaction Rate Distributions," Proc. of the International Symposium on Fusion Nuclear Technology, April 10-15, Tokyo, Japan (1988). Also see Fusion Engineering and Design, 9, 315-322 (1989).

[10] T. Nakamura and M. Abdou, "Overview of JAERI/U.S. DOE Collaborative Program on Fusion Blanket Neutronics Experiments, "Proc. of the International Symposium on Fusion Nuclear Technology, April 10-15, Tokyo, Japan (1988).

[11] Y. Oyama, et al., "Phase IIB Experiment of JAERI/U.S.DOE Collaborative Program on Fusion Blanket Neutronics," Fusion Technology, 15, No. 2, Part 2B, 1293-1298 (1989).

[12] Y. Ikeda, et al., "Determination of Neutron Spectrum in D-T Fusion Field by Foil Activation Technique," Fusion Technology, 15, No.2, Part 2B, 1287-1292 (1989).

[13] M. Z. Youssef, et al., "Comparative Analysis for Phase IIA and IIB Experiments of the U.S./JAERI Collaborative Program on Fusion Blanket Neutronics," Fusion Technology, 15, No. 2, Part 2B, 1299-1308 (1989).

[14] A. Kumar, et.al., "Analysis for the Selection of Experimental Configurations for Heterogeneity and Be Multi-Layered Experimentsof U.S.DOE/JAERI Collaborative Program on Blanket Neutronics," Fusion Technology, 15, No.2, Part 2B, 1309-1314 (1989).

[15] Los Alamos Monte Carlo Group, 'MCNP -- A General Monte Carlo Code for Neutron and Photon Transport," version 3A, LA-7396, Rev. 2, Los Alamos National Laboratory (1986).

[16] W. A. Rhoades and R.L. Childs, "An Updated Version of the DOT 4 (version 4.3) One-and-Two-Dimensional Neutron/Photon Transport Code, ORNL-5851, Oak Ridge National Laboratory, (April, 1982). Also, see CCC-429, Radiation Shielding Information Center, RSIC (1982).

[17] W. A. Rhoades, et al, private communication, Oakridge National Laboratory, (1987).

[18] L. P. Ku and J. Kolibal, "RUFF - A Ray-Tracing Program to Generate Uncollided Flux and First Collision Source Momemts for DOT4, A User's Manual," EAD-R-16, Plasma Physics Laboratory, Princeton University, (1980).

[19] "DOT 3.5: Two-Dimensional Discrete Ordinates Radiation Transport Code, CCC-276, Radiation Shielding Information Center, RSIC," Also, see W.A. Rhoades and F. R. Mynett, "The DOT III Two-Dimensional Discrete Ordinates Transport Code," ORNL-TM-4280, Oak Ridge National Laboratory (September 1973).

[20] M. B. Emmett, "The MORSE Monte Carlo Radiation Transport Code System," Oak Ridge National Laboratory, ORNL-4972 (1975).

[21] R. A. MacFarlane, "TRANSX-CTR: A Code for Interfacing MATXS Cross-Section, Libraries to Nuclear Transport Codes for Fusion Systems Analysis," LA-9863-MS, Los Alamos National Laboratory (February, 1984).

[22] R. MacFarlane, D. Muir, and R. Boicourt, "The NJOY Nuclear Data Processing System," Vol.I and II (ENDF-9303-M, Vol I, LA-9303-M, Vol. II (ENDF-324), Los Alamos National Laboratory (May 1982).

[23] R. T. Santoro, R. G. Alsmiller, Jr., J. M. Barnes, "Monte Carlo Analysis of the FNS (Phase II) Experiments," The US/JAERI Workshop on Fusion Blanket Neutronics, June 16-18, 1987 JAERI, Japan (1987).

[24] "DLS-113/VITAMIN-E: A coupled 174 Neutron, 38 Gamma Ray Multigroup Cross-Section Library for Deriving Application-Dependent Working Libraries for Radiation Transport Calculation," RSIC/DLC-113 Radiation Shielding Information Center, Oak Ridge National Laboratory (1984).

[25] R. T. Santoro, et al., "ORACT: 174-Neutron-Group Activation Cross-Section Library for Fusion and Fission Reactor Design Studies," Oak Ridge National Laboratory, ORNL/TM-9203 (June 1984).

[26] D. Garber, Ed., "ENDF/B-V," BNL-17541 (ENDF-201), National Nuclear Data Center, Brookhaven National Laboratory (October 1975).

[27] P. G. Young and L. Steward, "Evaluated Data for n+^{9}Be Reactions," LA-7932-MS(ENDF-283), Los Alamos National Laboratory. (1979)

[28] P. G. Young, "Evaluation of n+^{7}Li Reactions Using Variance-Covariance Techniques," Trans. Am. Nucl. Soc., 39, 272 (1980).

[29] ENDF/D-VI data for beryllium is based on S. T. Perkins et al. work, see Ref. (45).

[30] J. Benveniste, et al., and J. Zenger, "Information on the Neutrons Produced in the ^{3}H(d,n)^{4}He Reaction," UCRL-4266 (1954). Also, see J. Benveniste et al., Nuclear Instruments and Methods, 7, 306-314 (1960).

[31] Pavik et al., Nuclear Science and Engineering, 90, 186 (1985)

[32] K. Shibata, et al., "Evaluation of Neutron Nuclear Data for ^{6}Li, ^{7}Li, and ^{12}C for JENDL3," JAERI-M-84-198, JAERI-M-84-204, JAERI-M-83-221, Japan Atomic Energy Research Institute (1984).

[33] G. C. Hanna, "The Neutron Flux Perturbation Due to an Absorbing Foil: A Comparison of Theories and Experiments," Nuclear Science and Engineering, 15, 325 (1963).

[34] Y. Oyama and H. Maekawa, "Measurements and Analysis of an Angular Neutron Flux on a Beryllium Slab Irradiated with Deuterium-Tritium Neutrons, " Nuclear Science and Engineering, 97, 220-234 (1987).

[35] T.H.R. Skyrme: AERE reports, MS-91 and MS-91A, 2nd edition (1944).

[36] R. H. Ritchie and H.B. Eldridge, Nuclear Science and Engineering, 8, 300 (1960).

[37] H. Meister, Z. Naturforsh , 10a, 669 (1955).

[38] D. M. Drake, G. F. Auchampaugh, E. D. Arthur, C. E. Ragan, and P.G. Young, "Double-Differential Beryllim Neutron Cross-Sections at Incident Neutron Energiess of 5.9, 10.1, and 14.2 MeV," Nuclear Science and Engineering, 63, 401-412 (1977).

[39] M.Baba, et al. "The Interaction of Fast Neutrons with 9Be," International Conference, Neutron Physics and Nuclear Data, 198, Harwell, U.K., Sept, 1978.

[40] T. K. Basu, V. R. Nargundkar, P. Cloth, D. Fulges, and S. Taczanowski, "Neutron Multiplication Studies in Beryllium for Fusion Reactor Blanket," Nuclear Science and Engineering, 70, 309 (1979).

[41] V. R. Nargundkar, T. K. Basu, O. P. Jonega, M.R. Phiske, and S.K. Sadavarte, "Neutron Multiplication Measurement in BeO for 14 MeV Neutrons," Fusion Technology, 6, 93 (1984).

[42] V. R. Nargundkar, T. K. Basu, and O.P. Jonega, "Reanalysis of Neutron Multiplication Measurements in Thick Beryllium and Graphite Assemblies for 14 MeV Neutrons," Fusion Technology, 12, 380 (1987).

[43] A. Takahashi, E. Ichimura, Y. Sasaki, and H. Sugimoto, "Measurement of Double Differential Neutron Emission Cross Sections for Incident Neutrons of 14 MeV," J. of Nuclear Science and Technology, 25, 215 (1988).

[44] JENDL Compilation Group (Nuclear Data Center, JAERI): JENDL-3T, private communication (1988).

[45] S. T. Perkins, E. F. Plechaty, and R. J. Howerton, "A Reevaluation of the ^{9}Be(n,2n) Reaction and Its Effect on Neutron Multiplication in Fusion Blanket Applications," Nuclear Science and Engineering, 90, 83-98 (1985).

[46] M. Z. Youssef, "Status of Methods, Codes and Applications for Sensitivity and Uncertainty Analysis," Fusion Technology, 8, 1552 (1985).

[47] R. G. Alsmiller, Jr., R. T. Santoro, J. Barish, and T. A. Gabriel, "Comparison of the Cross-Section Sensitivitiy of the Tritium Breeding Ratio in Various Fusion-Reactor Blankets," Nuclear Science Eng., 57, 122 (1975).

[48] D. E. Bartine, R. G. Alsmiller, Jr., E. M. Oblow, and F. R. Mynatt, "Cross-Section Sensitivity of Breeding Ratio in a Fusion-Reactor Blanket," Nuclear Science Eng., 53, 304 (1974).

[49] S. A. W. Gerstl, D. J. Dudziak, and D. W. Muir, "Cross-Section Sensitivity and Uncertainty Analysis with Application to a Fusion Reactor," Nuclear Science Eng., 62, 137 (1977).

[50] M. Z. Youssef, R. W. Conn, and C. W. Maynard, "Impact of Cross-Section Uncertainties on the Nuclear Design of Hybrid Reactors," Nuclear Technology/Fusion, 2, 648 (1982).

[51] M. J. Embrechts, "Two-Dimensional Cross-Section Sensitivity and Uncertainty Analysis for Fusion Reactor Blankets," LA-9232-T, Los Alamos National Laboratory (1982).

[52] D. E. Bartine, E.M. Oblow, and F.R. Mynatt, "Radiation-Transport Cross-Section Sensitivity Analysis -- A. General Approach Illustrated for a Thermonuclear Source in Air," Nuclear Science Eng., 55, 147 (1974).

[53] N. M. Green, et al., "AMPEX: Modular Code System for Generation Coupled Multigroup Neutron-Gamma-Ray Cross-Section Library from Data in ENDF Format," PSR-063/AMPXII, ORNL/TM-3706, Radiation Shielding Information Center, Oak Ridge National Laboratory (1980).

[54] C. R. Weisbin, et al., "Application of FORSS Sensitivity and Methodology to Fast Reactor Benchmark Analysis," ORNL/TM-5563, Oak Ridge National Laboratory (1976); see also "FORSS: A Sensitivity and Uncertainty Analysis Code System," CCC-334, Radiation Shielding Information Center (1983).

[55] R. L. Childs, D. E. Bartine, and W. W. Engle, Jr., "Perturbation Theory and Sensitivity Analysis for Two-Dimensional Shielding Calculations," Trans. Am. Nucl. Soc., 21, 543 (1975).

[56] R. L. Childs, "Generalized Perturbation Theory Using Two-Dimensional Discrete Ordinate Transport Theory," ORNL/CSD/TM-127, Oak Ridge National Laboratory (1980).

[57] "DOT3.5: Two-Dimensional Discrete Ordinates Radiation Transport Code," RSIC/CCC-276, Radiation Shielding Information Center, Oak Ridge National Laboratory (1973).

[58] M.Z.Youssef and P. M. Song, Private Communication, University of California at Los Angeles, (1989)

Distribution List

DOE
S. Berk
A. Davies
R. Dowling
P. Hemming
M. Roberts
L. Whetstoone

ANL
H. Attaya
Y. Gohar
R. Mattas
R. McKnight
K. Porges
Dale Smith
Donald Smith
T. Yule

ORNL
R. Alsmiller
C. Baker
J. Barnes
L. Berry
C. Fu
T. Gabriel
D. Larson
R. Peelle
R. Santoro
J. Schifield
R. White

LANL
J. Anderson
E. Arthur
W. Davidson
R. Haight
R. Krakowski
R. Labauve
R. MacFarlane
D. Muir
P. Young

University of Wisconsin
G. Kulcinski
C. Maynard
M. Sawan

RSIC
R. Roussin

PPPL
L. P. Ku
K. Young

University of Washington
G. Woodruff

BNL
M. Baht
C. Dunford
S. Pearlstein

NBS
A. Carlson

EG&G
D. Holland

RPI
M. Embrechts
D. Steiner

University of Illinois
M. Ragheb

HEDL
F. Mann

Westinghouse
L. Green

EPRI
J. Cummings

Georgia Tech
W. Stacey

LLNL
J. Gilleland
L. Hansen
C. Henning
R. J. Howerton
J. D. Lee
R. Moir
S. T. Perkins

GA Technologies
E. Cheng
K. Schultz

University of Texas
N. Hertel

TRW
R. Whitely

Grumman
D. Berwald

MIT
C. Gung

UCLA
M. A. Abdou
R. Conn
N. Ghoneim
I. Jun
W. Kastenberg
A. Kumar
G. Pomraning
M. Song
M. Youssef

University of Florida
Innovative Nuclear
Space Inst.
Y. Watanabe

Distribution List
(International)

JAERI (Japan)
T. Fuketa
Y. Ikeda
Y. Ishiguro
Y. Kaneko
T. Kosako
H. Maekawa
K. Maki
S. Mori
T. Mori
M. Nakagawa
T. Nakamura
Y. Oyama
Y. Seki
T. Tone
K. Tsuda
S. Yamaguchi
M. Yoshikawa
H. Yoshida (JAERI)

University of Tokyo (Japan)
T. Iguchi
K. Miya
M. Nakazawa
Y. Oka

Kyoto University (Japan)
I. Kimura
K. Shin

Osaka University (Japan)
K. Sumita
J Yamamoto
A. Takahashi

Tokyo Institute of Technology (Japan)
H. Sekimoto

KfK (Karlesruhe, Germany)
U. Fischer
G. Kessler
M. Kuchle
J. E. Vetter

U.K.
University of Birmingham
T. D. Beynon

Canada
P. Gierszewski

Switzerland
R. Brögli (EIR)
S. Pelloni (EIR)
J.P. Schneeberger (EDFL)
J. Stepanek (EIR)

U.S.S.R.
A. Antipekov (ENTER)
V.A. Chujanov (IAE)
A.M. Epinatiev (IET)
V. Khropunov (IAE)
I.V. Lavrentjev (SRIEA)
P.V. Orlov (IET)
G. Shatalov (IAE)
Yu. Strebkov (IET)

China
Du Shu-Hua
J. H. Huang
Jian Wen-Mian
Liu Cheng-An
Qui Li-Jian
Shen Ji-An

Israel
E. Greenspan

Tohoku University (Japan)
K. Sugiyama

Kyushu University (Japan)
H. Nakajima

Italy
G. Casini
C. Ponti
G. Reffo

FRG (Germany)
R. Hecker
K.F.A. Tülich

France
F. Carre
J. P. Schwartz